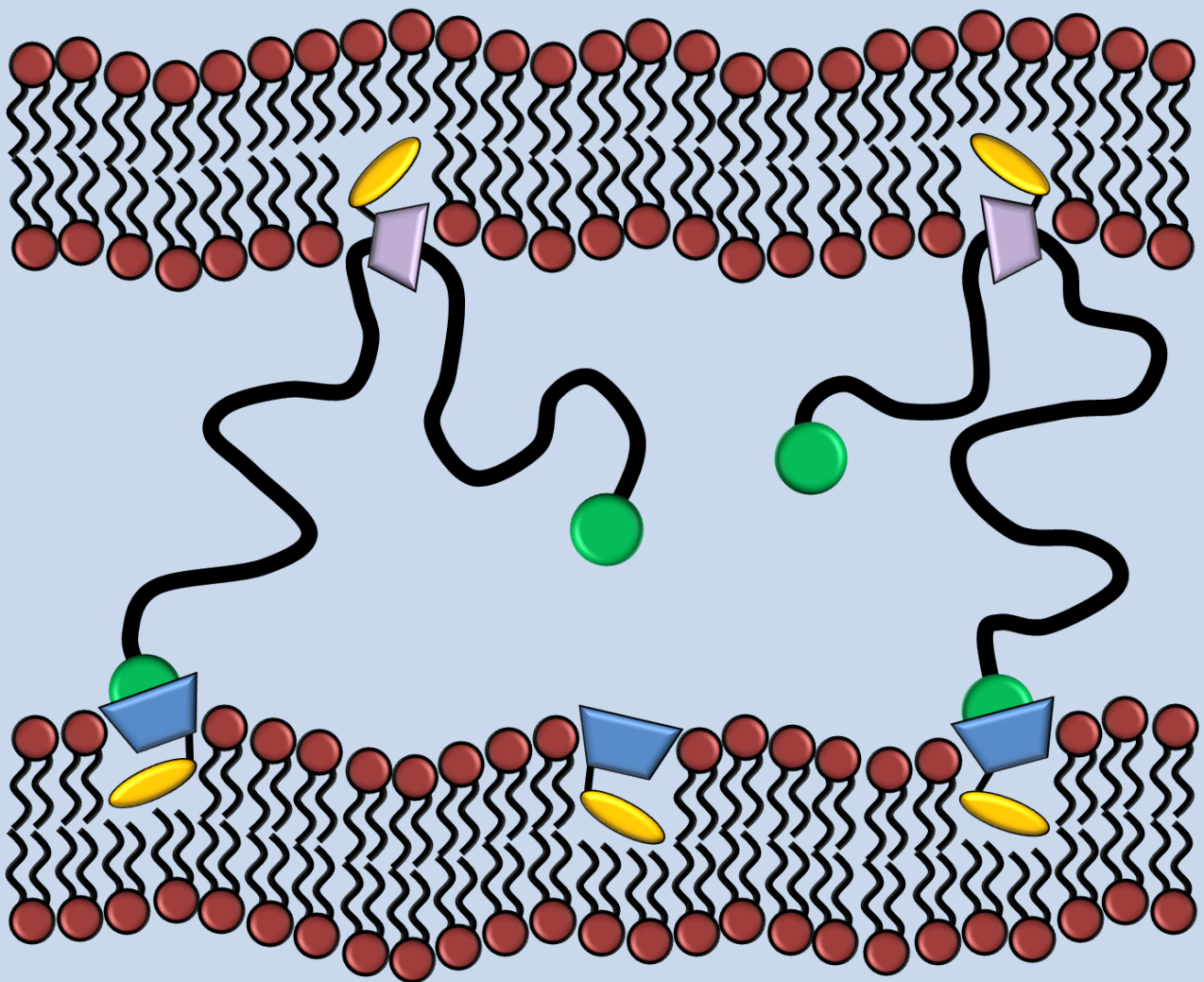


Membrane Functionalisation using Polyrotaxanes with amphiphilic Cyclodextrins



Martin BAUER



Université de Strasbourg

en co-tutelle avec

Université de Regensburg

Fonctionnalisation de Membranes par Polyrotaxanes de Cyclodextrines amphiphiles

Thèse de Doctorat présentée par

Martin Bauer

Discipline: Physique

Le 4 novembre 2011

Membres du Jury:

Rapporteur :	M. Jürgen RÜHE
Rapporteur :	M. Gerhard WENZ
Examineur :	M. Wais HOSSEINI
Directeur de thèse :	M. Carlos MARQUES
Co-Directeur de thèse :	M. Werner KUNZ
Co-Directeur de thèse :	M. Jean DAILLANT



A joint-degree between

University of Strasbourg

and

University of Regensburg

Membrane Functionalisation using Polyrotaxanes with amphiphilic Cyclodextrins

Dissertation by

Martin Bauer

Subject: Physics

4th of November 2011

Committee:

Rapporteur : M. Jürgen RÜHE
Rapporteur : M. Gerhard WENZ
Examiner : M. Wais HOSSEINI
Supervisor : M. Carlos MARQUES
Co-Supervisor : M. Werner KUNZ
Co-Supervisor : M. Jean DAILLANT

Acknowledgments

I would like to express here my deepest appreciation to all those that helped and supported me, thus contributing to the accomplishment of my PhD.

This work has been a collaboration between the Institut Charles Sadron (ICS) in Strasbourg and the Laboratoire Interdisciplinaire sur l'Organisation Nanométrique et Supramoléculaire (LIONS) at the CEA Saclay. I want to thank Dr. Jean-Francois Legrand (ICS) and Dr. Jean Daillant (LIONS) for having given me the possibility to work in their laboratories, respectively. Moreover this thesis has been a joint-degree between the university of Strasbourg and the university of Regensburg. I am deeply thankful to Prof. Dr. Werner Kunz for having supervised this joint-degree and having hosted me several months in his laboratory in Regensburg. Besides I gratefully acknowledge the CEA Saclay and the région Alsace for funding my PhD scholarship.

I want to thank the jury members for having shown such a great interest in my work: Prof. Dr. Weis Hosseini for giving me the honor of being president of the jury, as well as Prof. Dr. Jürgen Rühle and Prof. Dr. Gerhard Wenz for having accepted to be examiners of my thesis.

First and foremost I would like to thank both of my supervisors in Saclay, Dr. Jean Daillant and Dr. Christophe Fajolles, as well as my supervisor in Strasbourg, Dr. Carlos Marques, for 3 years of excellent supervision and for their commitment to guide me through my research. I greatly appreciate the time they spent on helping me with scientific and non-scientific questions, as well as for their enduring support. Special thanks go to Jean for his excellent and very efficient supervision, as well as explaining many concepts of physics, especially neutron and x-ray reflectivity techniques. I am also very thankful to Christophe for always having been accessible for discussion and his precious expertise on the synthetic part of my research. I would like to thank Carlos for managing a great deal of the PhD administration at the university Strasbourg during my time in Saclay. Furthermore I am deeply grateful to him for helping me understand the concepts of polymer physics, which was essential for the last part of my thesis.

I very much appreciated the support of Dr. Thierry Charitat during the neutron experiments and their analysis. It is also an honor to acknowledge Dr. Patrick Kékicheff with whom I have performed the SFA experiments. I also would like to express my gratitude to Dr. Giovanna Fragneto for her precious help during the neutron experiments at the ILL in

Grenoble. I am likewise thankful to Christian Blot and Patrick Haltebourg for helping to solve technical problems with the X-ray experiment and the Brewster Angle Microscope, as well as producing sample cells for the Atomic Force Microscope.

Working at three different laboratories in Saclay, Regensburg and Strasbourg, there are many people with whom I was not directly collaborating, but which have made the last three years such a great and memorable experience.

I would like to thank all the people at the laboratory LIONS, for their help and their support as well as the inspiring atmosphere they have created. Thanks to Dr. Julien Barriet, for the time we spent together in the organic laboratory, his kindness and his help. Thanks to Dr. Corinne Chevillard, Dr. Patrick Guenoun and Elodie Collard for their help in various questions I had and for explaining different types of microscopes. Beyond, I would like to thank Hermann, Jean Christophe, Olivier, Aude, Andi, Gaëlle, Aline Kévin and many others for the nice moments we spent together.

My PhD could not have been completed without all the help, support and smiles from my friends at the ICS in Strasbourg. Especially I want to thank my office colleagues Laure and Philippe, as well as George, Constantin, Andreas and many more, I had the pleasure to meet.

I am especially grateful to Patricia, for her motivation and enduring support while I was writing my thesis. And of course, infinite thanks go to my family for their kind support in every way. Special thanks to my parents, Judith and Patricia which made my PhD celebration a full success.

Contents

1	Introduction	1
2	Fundamentals	5
2.1	Membranes	5
2.1.1	Introduction	5
2.1.2	Lipids	6
2.1.3	Model Membranes	9
2.1.4	Interactions between Membranes	12
2.2	Cyclodextrins	20
2.2.1	Introduction	21
2.2.2	History	21
2.2.3	Synthesis, Structure and Properties	22
2.2.4	CD complexes	23
2.2.5	Modified CDs	26
2.2.6	Amphiphilic CDs	28
2.3	Rotaxanes	31
2.3.1	Introduction	31
2.3.2	CD-based rotaxanes	32
2.3.3	CD-based polyrotaxanes	33
2.3.4	Characterisation of Rotaxanes	38
3	Experimental Techniques	43
3.1	Chemicals	43
3.2	Langmuir Film Balance	44
3.2.1	Langmuir Isotherms	44
3.2.2	Isotherm Analysis	44
3.2.3	Film Deposition	45
3.3	Brewster Angle Microscopy	46
3.3.1	Principle	46
3.4	Atomic Force Microscopy	48
3.4.1	Principle	48
3.4.2	Atomic Force Spectroscopy	51
3.5	Scattering Techniques	57
3.5.1	Interactions of Neutrons with matter	57
3.5.2	Interactions of X-rays with matter	59

3.5.3	Specular Reflectivity at interfaces	60
3.5.4	Thin films	62
3.5.5	Instrumental aspects	63
3.6	Nuclear Magnetic Resonance (NMR) Spectroscopy	65
3.6.1	Theoretical background	65
3.6.2	One-dimensional NMR	66
3.6.3	Two-dimensional NMR	68
3.7	Infrared reflection absorption microscopy	71
3.7.1	Principle	72
3.8	Surface Force Apparatus	74
3.8.1	Principle	74
3.8.2	Instrumental Aspects	78
4	Amphiphilic behavior of cholesteryl CDs	81
4.1	Interfacial behavior of pure cholesteryl CDs	81
4.1.1	Amphiphilic properties	81
4.1.2	Reflectivity measurements	83
4.1.3	AFM	86
4.1.4	Monolayer morphology	87
4.1.5	Hydration of CD-headgroup	90
4.2	Membrane insertion properties of amphiphilic CDs	91
4.2.1	Monolayers	92
4.2.2	Bilayers	97
4.2.3	Miscibility and fluidising effect of cholesteryl CD	101
4.2.4	Membrane insertion at the molecular level	102
4.2.5	Bilayer nano-mechanical properties	104
4.3	Conclusion	107
4.4	Appendix	109
5	Synthesis of sliding tethered ligands	117
5.1	Strategy	117
5.2	Development of end-capping technique	119
5.2.1	Introduction	119
5.2.2	Blocked isocyanate	120
5.2.3	Condensation of carboxylic acids with the aid of DMT-MM	122
5.3	Polyrotaxanes	124
5.3.1	Choice of reaction conditions	125
5.3.2	Synthesis	126
5.3.3	Characterisation	127
5.3.4	Optimisation of reaction parameters	134
5.4	Clicking of the lipophilic anchor	139
5.4.1	Click Chemistry	139
5.4.2	Preparation of cholesteryl succinic acid propargylamide	140
5.4.3	Clicking of the cholesteryl succinic acid propargylamide	141
5.5	Conclusion	143

5.6	Experimental	144
5.6.1	Used Chemicals	144
5.6.2	Synthetic procedures	144
5.7	Appendix	150
6	Sliding tethered ligands: Insertion in membranes and interactions	165
6.1	Interfacial properties	165
6.1.1	Langmuir Isotherms	166
6.1.2	Film morphology	170
6.1.3	IRRAS	172
6.2	Neutron Reflectivity	179
6.2.1	Data Analysis	179
6.2.2	Films containing PEG without cholesteryl anchor	181
6.2.3	Films containing STLs	183
6.2.4	Available surface area per polymer	186
6.2.5	Sliding effect	186
6.3	Sliding tethered ligand receptor interactions	188
6.3.1	Sample architecture	188
6.3.2	Force profiles	190
6.3.3	Compression behavior	195
6.3.4	Adhesion properties	198
6.4	Conclusion	201
6.5	Appendix	202
7	Conclusion	205
	List of Publications	209
	Bibliography	237

Chapter 1

Introduction

The clinical utility of most conventional chemotherapeutics is limited either by the inability to deliver therapeutic drug concentrations to the target tissues or by severe and harmful toxic effects on normal organs and tissues. Many of the pharmacological properties of conventional (“free”) drugs can be improved through the use of drug delivery systems (DDS). Therefore such DDS are also of high potential industrial impact. Different approaches have been attempted to overcome these problems by providing selective delivery to the affected area. The ideal solution would be to target the drug only to those organs, tissues, or cells affected by the disease [1].

Selected carriers, such as molecular conjugates and colloidal particulates, can be suitable for this purpose [2]. These include polymer-drug conjugates and microspheres based on synthetic [3] and natural polymers [4] or dendrimers [5]. Furthermore there are various lipid based carriers, such as liposomes, micelles, lipid emulsions, and lipid-drug complexes [6].

Among these drug delivery and carrier systems, liposomes represent a promising technological tool to deliver active molecules to the site of action. Their attraction lies in their composition, which makes them biocompatible and biodegradable. They can be engineered to have specified sizes and permeability properties. Moreover, drugs with different lipophilicities can be encapsulated into liposomes: strongly lipophilic drugs are entrapped almost completely in the lipid bilayer, strongly hydrophilic drugs are located exclusively in the aqueous compartment, and drugs with intermediate partition coefficient easily partition between the lipid and aqueous phases, both in the bilayer and in the aqueous core [7].

For a long time a major problem for broad medical utility of liposomes has been their inherent instability in biological fluids due to recognition and destruction by the host’s immune system. Yet since liposomes were first developed (around 1980) the related technology has made considerable progress. Using formulations with high cholesterol content, as well as phospholipids with high phase transition temperatures, liposome stability has been increased and drug leakage minimised [8]. Especially the discovery that liposomes coated with appropriate polymer avoid detection by the body’s immune system (specifically, the cells of reticuloendothelial system) greatly augmenting the liposomes circulation time in the body, can be considered a breakthrough. Because they are virtually invis-

ble to the defense mechanisms of the body they have been named “stealth®” liposomes. Among the different polymers investigated in the attempt to improve the blood circulation time of liposomes, poly-(ethylene glycol) (PEG), a polymer already used for a variety of other applications in the biomedical field, has been proved to be the most effective. It can be attached to the liposomal surface in different ways. The most widely used method to produce “stealth®” liposomes is the application of liposomal formulations composed of mixtures of normal and pegylated lipids. Pegylated lipids are lipids with a cross-linked PEG tether and a whole variety of different conjugates is now commercially available, e.g. PEG- distearoylphosphatidylethanolamine (DSPE) [9]. At present several formulations using “stealth” liposomes are already in clinical use, such as Doxil®, which is an encapsulated form of the anti cancer drug doxorubicin [10].

Pegylated lipids have also found application in the construction of polymer cushioned supported lipid membranes [11]. Supported lipid bilayers provide an excellent model system for studying the surface chemistry of the cell due to their robustness and stability. Nevertheless a inherent disadvantage is that the membrane properties are strongly influenced by the underlying solid support. The addition of a soft and hydrophilic polymer layer effectively decouples the membrane from the surface. This enables the incorporation of transmembrane proteins and allows their investigation by a number of surface science techniques. Moreover polymer cushioned bilayers better mimick natural membranes since its fluctuations are less influenced by the substrate [12]. Typically, the lipopolymer is covalently bonded to the substrate. But it is also possible to exploit ligand-receptor interactions between a receptor coated surface and ligand modified polymer tethers to anchor the bilayer to the substrate [13]. An exciting and newly emerging field in solid supported lipid bilayers is the development of air-stable lipid membranes. They are of great interest because they present promising platforms for sensing applications, using incorporated pegylated lipids to create protection cushion to provide for stability in air [11]. Additionally to improving liposome formulations and properties of supported membranes, PEG-modified lipids can also be used as emulsifiers and stabilizers of microspheres in aqueous solutions.

To increase drug accumulation in desired tissues, producing higher and more selective therapeutic activity, the use of targeted DDS and especially liposomes has been suggested. This involves the coupling of targeting moieties capable of recognizing target cells, binding to them, and inducing the internalization of liposomes or encapsulated drugs. Targeting moieties include monoclonal antibodies or fragments, peptides, growth factors, glycoproteins, carbohydrates, or receptor ligands [14]. However it has been found that directly surface bound targets increase the clearance rate of liposomes from the body, hindering their accumulation in target tissues. This shortcoming can be circumvented by attaching the ligand with appropriate spacer groups, placing the ligands far from the surface and at the same time providing them with significant freedom of movement for effective binding [8]. A great deal of research is now focused on developing PEG spacers which carry ligands for targeting liposomes to specific tissues and at the same time preserving their stealth ability.

In order to effectively direct liposomes to specific targets in the body, the control and

understanding of the molecular recognition mechanisms is a scientific challenge. Biorecognition in living organisms is mediated by ligand receptor pairs, which build lock and key complexes through the formation of specific, non-covalent bonds. They play a crucial role in cell adhesion events that allow the communication, proliferation, differentiation and migration of cells [15]. The thermodynamic and kinetic constants for reactions between ligand receptor pairs are well known when both species are in solution, or one of them is attached to a wall [16]. However, in most relevant practical situations both of the molecules are attached to surfaces, e.g. bound to cell surfaces in living systems or grafted to colloid interfaces in medical assays. For practical purposes, it is important to control not only when and if binding and unbinding occur, but also the behavior of the bound complexes with respect to mechanical load leading to rupture or adhesion. Thus the fundamental question is how to design a pair that will lead to a specified force-distance profile, with given prescribed binding kinetics. This is usually achieved by controlling the nature of the spacer that tethers the ligand to the interface. Flexible polymers such as PEG are good candidates to mimic the behavior of natural spacers, and as such, they are employed in experiments on model systems [17]. The polymer tether turns the short-range, lock-and-key type interaction into a long-range, specific interaction. This has important implications to the equilibrium as well as the dynamic properties of adhesion [18]. So the design of new polymer tethers for ligands, as well as new polymer tethers for lipids remains a fundamental challenge for nanotechnology application in the fields of drug delivery, medical diagnostics and construction of soft nano-interfaces.

Inspired by the fact that ring like molecules, such as cyclodextrins (CDs) can form topological complexes with polymers, a new family of polymer spacers could be derived, where the polymer is attached to the surface by a CD ring. Such an interfacial structure would provide the grafted chain with an additional degree of freedom to slide through the ring. Theoretical work on the behavior of such sliding grafted polymer layers demonstrated that these sliding polymer tethers would adapt their conformation to external conditions [19]. Therefore the design of a new family of polymer spacers for ligands, based on this concept could bring an unprecedented flexibility to the ligand-receptor bond. The flexibility, promoted by the sliding character of the topological complex formed by a polymer and a ring, should translate into a new type of force-distance profiles characterized by weak force amplitudes over ranges comparable to the polymer size and a strong force for distances above. This would allow to finely tune the interaction range, forces and kinetics in the different systems where ligand-receptor interactions play an important role. For instance, one anticipates larger adhesion efficiency when two corrugated surfaces are brought together, or a better support of a fluctuating membranes by a cushion of sliding ligands.

The goal of this thesis is the synthesis and characterisation of a new family of tethered ligands, called sliding tethered ligands (STLs). The key structure of the STLs are inclusion complexes of a suitable ring molecule and a polymer. When endcapped with bulky stopper molecules, such molecular necklace structures are called polyrotaxanes. These topological complexes are well known and especially polyrotaxanes between α -CD and PEG have been studied intensively [20,21]. The assembly of STLs requires polyrotaxanes

based on PEG complexed with a low number of modified CDs, which are functionalised with a hydrophobic anchor suitable to insert them into lipid membranes. Furthermore the polymer tether needs to be endcapped with appropriate ligands to provide for molecular recognition ability. Using the concepts of CD-inclusion polymer complexation, with the tools for the chemistry of biorecognition molecules and the manipulation of amphiphile self-assembly, STLs are a new biotechnological tool for building soft nanoscale materials. They might find application in the fields of stealth liposome technology for drug delivery, model supported bilayers and nanoparticle stabilization.

In the first chapter we provide background information about the major elements required to assemble and study the STLs.

It is followed by a description of the materials and experimental methods that were used along this work.

Subsequently we present a detailed study of the insertion of cholesteryl CDs into model membranes. The detailed understanding about the anchoring strength and their conformational behavior in lipid bilayers is of great importance since similar compounds are used as the membrane anchors for the STLs.

In the next part we focus on the assembly of the STLs. It involves three major synthetic challenges which have to be overcome. Firstly we present new capping techniques allowing to prepare polyrotaxanes with ligands as stopper groups. Then we describe a new method to synthesise polyrotaxanes with modified CDs furthermore enabling us to control the threading ratio to very low numbers of CD. Finally we present a method for the attachment of the hydrophobic anchor to the modified CDs via click chemistry.

The last chapter of the thesis is dedicated to the characterisation of the membrane insertion properties of the STLs. We demonstrate that STLs firmly anchor into lipid membranes and we investigate the STL's polymer tether conformation, when grafted to a model membrane surface. Moreover we study the influence of the sliding polymer spacer on the interactions between STLs and receptors inserted into phospholipid bilayers.

Chapter 2

Fundamentals

We introduce in this chapter the key elements to assemble and investigate STL induced interactions. The system studied here is illustrated in Figure 2.1.

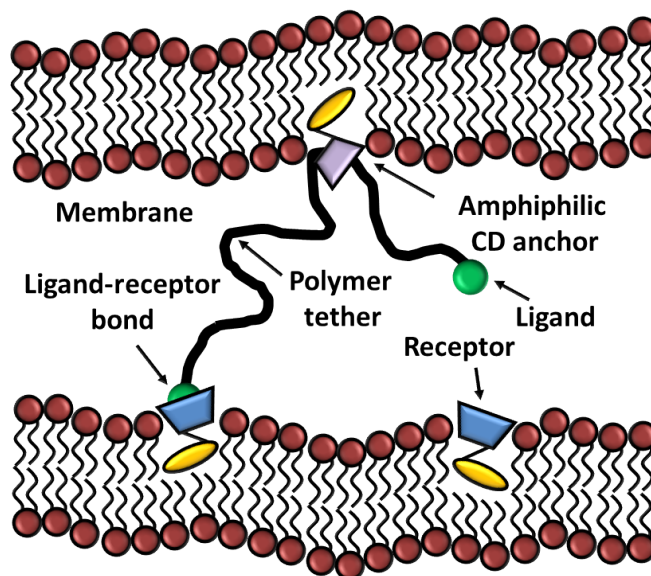


Figure 2.1: Schematic illustration of the STL

It comprises model phospholipid membranes, that we describe first, as they are the insertion matrix for the STLs and their complementary receptors. CD and amphiphilic CDs as membrane anchors will be presented, followed by an overview about CD inclusion complexes with polymers, called polyrotaxanes. Finally polymer layers grafted to surfaces and tethered ligand-receptor interactions will be discussed.

2.1 Membranes

2.1.1 Introduction

Biological membranes, e.g. the cell membrane, are thin separating layers, which act as selective barriers in cells. They regulate the passage of molecules into and out of the cells, maintain relevant concentration gradients, and host a number of metabolic and biosynthetic activities, such as adhesion and signaling cascades. A key feature of cell membranes

is that they are both fluid but still highly ordered in the membrane plane, as has been captured in the early conception of the fluid mosaic model of biological membranes [22]. Different cellular membranes may vary between each other significantly, e.g. with respect to their surface charge, lipid composition, cholesterol and protein content or membrane curvature. Natural membranes are very complex systems composed of a bilayer of lipids (80%) into which proteins (20%) are inserted (Figure 2.2). The lipid fraction in cell membranes includes a surprisingly wide spectrum of lipid species and the reason for this diversity is not at all clear [15]. To further add to the compositional complexity, the lipids are asymmetrically distributed between the two membrane monolayers.

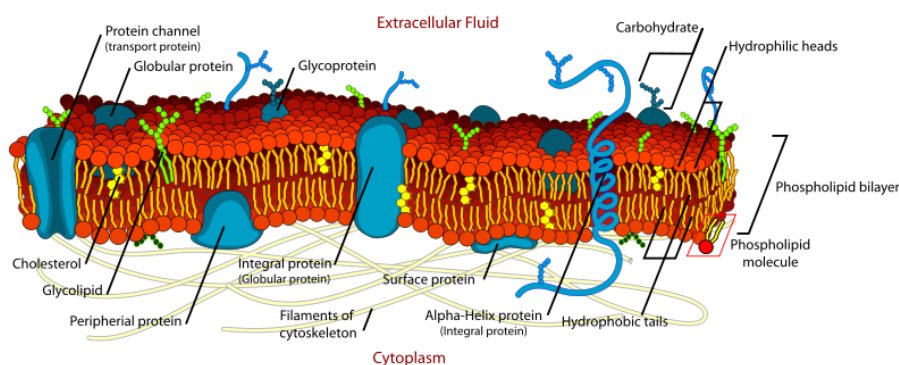


Figure 2.2: Schematic illustration of a cell membrane and its components [23]

2.1.2 Lipids

Lipids in cell membranes belong to the very large family of amphiphilic molecules. The so called amphiphiles are compounds with two distinct regions, one having high and the other low affinity for the solvent. As the amphiphilic behavior is most pronounced in the very polar solvent water, such molecules are typically composed of polar, ionic or zwitterionic headgroups and nonpolar side chains. The main lipid classes found in cellular membranes are various types of phospholipids (PLs) and cholesterol.

Phospholipids

Phospholipids are the most common structural lipids in membranes of certain types of cells, like lung cells and are divided into two classes. The glycerophospholipids are amphiphilic molecules made of a phosphate containing hydrophilic head, connected to two hydrophobic tails by a glycerol group. Phosphosphingolipids possess a sphingosine backbone. The hydrophilic head can be neutral, charged or zwitterionic. The carbon chain length varies between 10 and 20 methylene units and may be unsaturated.

Typical representatives for zwitterionic phospholipids are e.g. 1,2-dipalmitoyl-syn-glycero-3-phosphocholine (DPPC) or 1,2-dioctadecanoyl-syn-glycero-3-phosphoethanolamine (DSPE). The former one is composed of a zwitterionic hydrophilic phosphatidylcholine headgroup, whereas the latter one possesses an ethanolamine headgroup. Both compounds have two hydrophobic aliphatic side chains which are connected to the glycerol backbone by ester bonds (Figure 2.3).

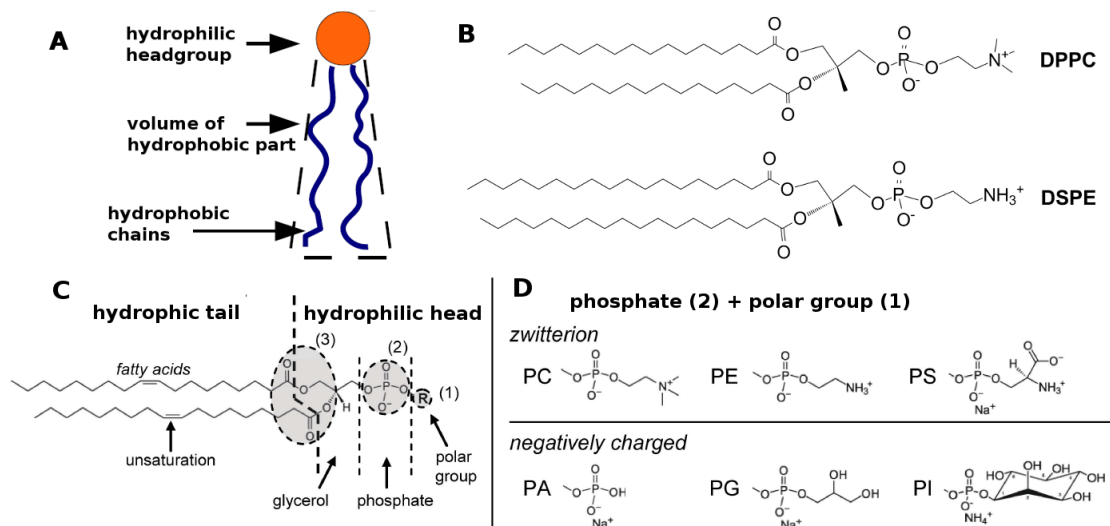


Figure 2.3: A. Schematic drawing of a phospholipid. B. Chemical structure of 1,2-dipalmitoyl-sn-glycero-3-phosphocholine (DPPC) and 1,2-dioctadecanoyl-sn-glycero-3-phosphoethanolamine (DSPE). C. Characteristic chemical structure of a phospholipid, composed of two hydrophobic tails connected via ester bonds (3) to a hydrophilic head formed by a polar group (1) and a negative phosphate group (2). D. Chemical formula of the different polar head groups (1) of phospholipids: phosphatidylcholine (PC), phosphatidylethanolamine (PE), phosphatidylserine (PS), phosphatidic acid (PA), phosphatidylglycerol (PG) and phosphatidylinositol (PI)

Cholesterol

Sterols, in particular cholesterol, are essential structural components of cell membranes. Their characteristic structure differs from the other membrane lipids because they are composed of a steroid nucleus consisting of three six-membered and one five-membered ring fused together, with an aliphatic chain attached to it. In the case of cholesterol, additionally to the hydrophobic hydrocarbon body, a hydrophilic hydroxyl group at the C₃ atom is responsible for its amphiphilic character (Figure 2.4).

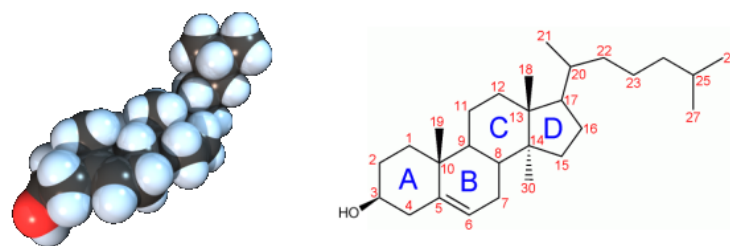


Figure 2.4: Space filling model and chemical structure of cholesterol

The cholesterol molecule is almost planar and rather rigid as the fused rings do not allow rotation around the C-C bonds [24]. Cholesterol forms membranes only in mixtures with other lipids. The insertion of the sterol into a phospholipid bilayer alters the membrane's physicochemical properties. The polar head group encounters the aqueous phase and the steroid ring is incorporated in the hydrocarbon chains of the phospholipids. In the biologically relevant liquid-disordered state it increases the degree of orientational order and reduces the rate of motion of the phospholipid hydrocarbon chains which leads to a more condensed membrane with increased mechanical strength and decreased permeabil-

ity [25]. Recent studies have revealed that cholesterol seems to play a crucial role in the formation of so called lipid rafts which can be considered as small, cholesterol enriched, liquid ordered phase micro-domains in biological membranes [26]. Since membrane proteins are found to accumulate in these domains they appear to be important in cell signaling, molecular trafficking and other cellular processes [27].

But cholesterol, additionally to its function as a membrane constituent, also serves as precursor for many hormones which regulate gene expression and participate in cellular signaling. Furthermore bile salts, acting as detergents for fat digestion in the intestine, are cholesterol derivatives as well [24].

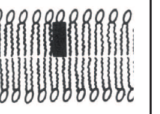
Lipid	Single-chained lipids (surfactants) with large head-group areas: SDS in low salt, ...	Single-chained lipids with small head-group areas: SDS and CTAB in high salt, nonionic lipids, ...	Double-chained lipids with large head-group areas, fluid chains: phospholipids (PC, PE, PS, PA, PG and PI), ...	Double-chained lipids with small head-group areas, anionic lipids in high salt, saturated frozen chains	Double-chained lipids with small head-group areas, nonionic lipids, poly(cis) unsaturated chains, high temperature
Critical packing parameter (V/s^2L_c)	$< 1/3$	$1/3 - 1/2$	$1/2 - 1$	~ 1	> 1
Critical packing shape	cone 	truncated cone 	truncated cone 	cylinder 	inverted truncated cone or wedge 
Structures formed	spherical micelles 	cylindrical micelles 	flexible bilayers, vesicles 	planar bilayers 	inverted micelles 

Figure 2.5: Some examples of possible structures of lipids in aqueous solution, based on geometrical arguments concerning the shape of the lipids [28].

Phospholipid self association

Above the critical micellar concentration ($\sim 10^{-10}$ mol/l [28]), lipids are not soluble anymore in water. In stead they self-assemble due to hydrophobic interactions in order to limit the contact between hydrophobic tails and water. On the contrary, due to steric or electrostatic repulsion, hydrophilic heads tend to escape from one another, so as to increase their contact area with water. Thus, the self-assembly is the result of two competing forces. It can be shown that this results in an optimal surface area s occupied by the headgroup. As displayed in figure 2.5, the formed structures are diverse and are essentially governed by the geometrical criterion V/sl_c , the so called critical packing parameter [28]. It is defined by the ratio between the carbon chain volume V and the optimal head area s multiplied by the chain length l_c . In water the cylindrical shape of phospholipids induces the preferred formation of structures with low radius of curvature. This leads to the aggregation of bilayers, composed of two monolayer films with opposite orientation, in form of vesicles or lamellar phases. They can be regarded as essentially 2-dimensional systems with a thickness of 4 - 5 nm and a lateral extension of the order of micrometers [29].

2.1.3 Model Membranes

In order to study the fundamental properties of membranes it is useful to examine simplified models. While at first research was mainly focused on understanding the physical properties, later studies started assigning a biomimetic role to model membranes by inserting biologically active moieties, such as proteins [29]. The model systems can be classified into monolayers, planar bilayers and vesicles or liposomes. All model systems have their own advantages and limitations, but all can give important insights into the function of biological membranes.

Monolayers

Insoluble amphiphiles, like phospholipids, form monomolecular films at the air-water interface which are also called Langmuir monolayers. They are obtained by spreading the compound dissolved in a volatile organic solvent on the interface. As the surface active molecules are insoluble and have low volatility they rest at the surface. Using a Langmuir balance with movable barriers allows to vary the surface area per molecule A while the corresponding surface pressure Π is measured. The resulting Langmuir films show a rich phase behavior, which can be assigned to structural changes in the monolayer: e.g. translational order, presence or absence of tilt or variations of tilt azimuth, which has been confirmed by microscopic methods or reflectivity measurements [30].

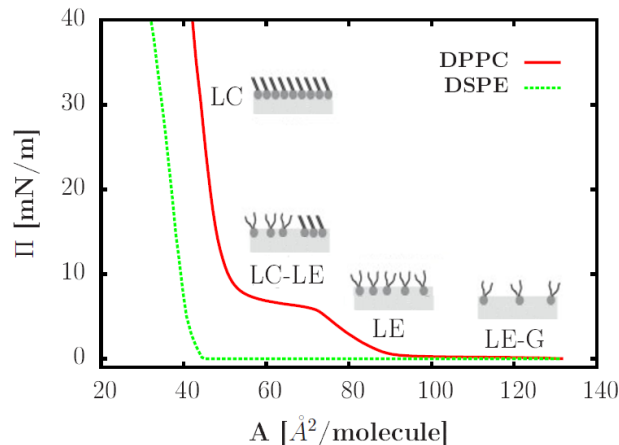


Figure 2.6: Langmuir isotherms for DPPC and DSPE at 20°C. The different phases occurring for DPPC are indicated

Figure 2.6 displays generic Langmuir isotherms for DPPC and DSPE at 20°C. For DPPC different phases can be identified: For low compression the gaseous phase coexists with a liquid expanded phase (LE-G) which transforms into pure liquid expanded phase (LE). The amphiphiles are in a similar state as in liquid crystalline bilayers and the chains behave liquid like. The plateau region indicates the transition of liquid expanded into liquid condensed phase (LE-LC) until for high surface pressures only liquid condensed state remains [31]. Specific to phospholipids with the bulky phosphocholine headgroup, the alkyl chains are tilted around 35° with respect to the surface normal in the liquid condensed state [32]. The compressibility of the different phases decreases with increasing pressure. So analogous to three-dimensional phases the gaseous phase shows a much higher compressibility than the liquid phases, whereas the solid phases are almost incompressible

[33]. For very high surface pressures the film eventually collapses. The required surface pressure depends on the headgroups. Due to the large and charged phosphatidylcholine head group the film collapse occurs at molecular areas around $45 \text{ \AA}^2/\text{molecule}$. The DSPE isotherm does not show a plateau region at room temperature, since it is already in a state of partial two-dimensional condensation at areas per molecule even larger than 1000 \AA^2 . The isotherm steeply rises at high compressions to collapse around $35 \text{ \AA}^2/\text{molecule}$ since the ethanolamine headgroup is smaller compared to the phosphocholine [34].

The main limitation of monolayers as model membranes are the high surface tensions at the air-water interface, because the hydrocarbon chains are in contact with air. In order to achieve comparable molecular areas per lipid, the surface pressure is unrealistically high compared to real membranes where the surface tensions are almost zero [35]. As described in detail in section 3.2, monolayers can be transferred to solid supports and if transferred several times multilayers can be obtained.

Supported bilayers

In order to obtain a controlled small number number of bilayers and defined orientation, bilayers deposition can be achieved on a solid substrate like silicon, mica or glass. The lipid layers are usually prepared by the Langmuir-Blodgett (LB) technique or by spontaneous vesicle fusion on inorganic substrates [36]. In this way lipid bilayers can be formed from a large variety of lipids. The density of molecules in a monolayer can be varied by choosing the appropriate film pressure and the phase state of the bilayer can be adjusted by the temperature or choice of lipids.

The biggest advantage of supported bilayers is their stability and also the possibility to prepare asymmetric membranes. They will remain largely intact even when subjected to high flow rates or vibration and the presence of holes will not destroy the entire bilayer. This allows them to be studied with methods which require direct physical interaction with the sample. Bilayers can e.g. be studied by Atomic Force Microscopy (AFM) or the Surface Force Apparatus (SFA) in order to probe nanomechanical properties or measure interactions between membranes [29]. The planar bilayer geometry is a prerequisite for many fluorescence-based techniques [37] and scattering experiments [38,39].

The supported bilayer is a planar structure sitting on a solid support, from which the slab close to the substrate is only separated by a thin water layer (0.5 - 2 nm, depending on the substrate [12]). Therefore the membrane dynamical properties are influenced by the substrate [40]. It has been investigated that e.g. the substrate induced decoupling of the two bilayer leaflets leads to a broadening and shift of the main transition temperature T_m to higher temperatures [41]. Furthermore for incorporating and maintaining the fluidity of transmembrane proteins the gap width between bilayer and substrate is not enough [12]. Hence several methods have been developed to disconnect the bilayer from the substrate and decrease its influence on the membrane (Figure 2.7).

The first method is to prepare two membranes by consecutive transfer of four monolayers on a support [42]. Yet these samples are very fragile. Another approach is to cushion the bilayer by water-soluble polymers (e.g. PEG), either by simple physisorption or covalent attachment to one the surface by forming tethers between the substrate and the membrane. This is e.g. achieved by deposition of a first lipid monolayer containing a

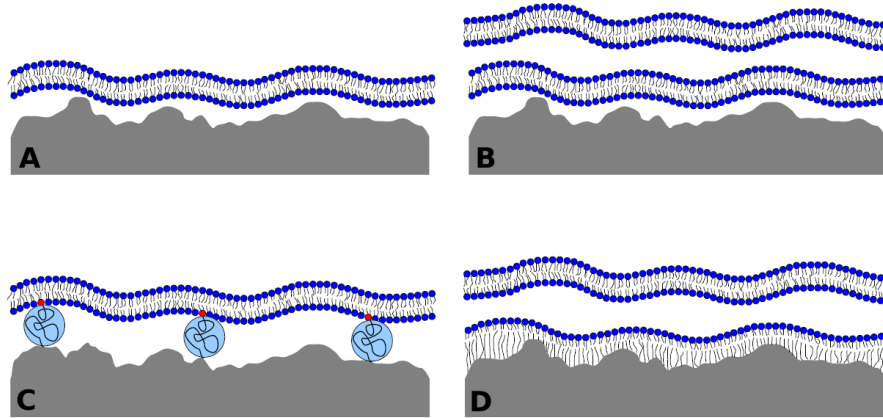


Figure 2.7: A. Simple bilayer, B. Double bilayer formed by four consecutive monolayer transfers, C. polymer-supported bilayer, D. Mixed lipid/OTS double bilayer

small fraction of lipopolymers [43]. Moreover it is possible to modify the substrate surface with a hydrophobic octadecyltrichlorosilane (OTS) layer and transferring three monolayers resulting in a first mixed OTS/lipid bilayer tightly bound to the substrate and a free floating bilayer on the top [44].

Bilayers show an interesting phase behavior. The temperature is a key parameter that drives the ordering of phospholipids in the bilayer. X-ray studies have revealed several phase transitions with transition temperatures, specific for each type of lipid, mainly governed by the structure of the tails.

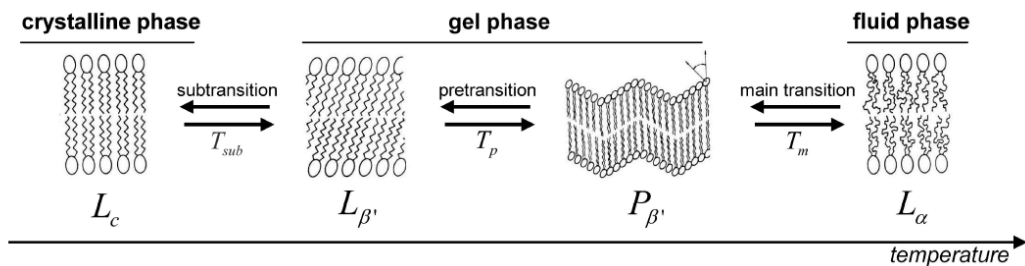


Figure 2.8: Schematic structure of a bilayer in different phases: Crystal phase L_c , gel phases L_β , rippled phase P_β and fluid phase L_α

For the temperatures above the so called main transition temperature T_m , the bilayer resides in its fluid state L_α . Decreasing the temperature induces a transition into gel phase, where the gel phases L_β and the rippled phase P_β can be distinguished with the pre-transition temperature T_p . The gel phase is characterised by a tilt angle of the chains in the order to of 30° and by an increase of bilayer thickness, as well as a decrease of surface area. At the subtransition temperature T_{sub} , the membrane undergoes a transition to a crystalline state in which fatty acid tails are fully extended and the packing is highly ordered [29].

Vesicles

In a flat bilayer, hydrophobic chains from lipids positioned at the edges are exposed to the solvent. In order to overcome this energetically unfavorable situation edges can be avoided by closing the membranes into spherical vesicles or liposomes. It is possible to produce vesicles with different sizes ranging from nanometers to tens of micrometers in diameter depending on the used preparation technique. Vesicles can be multilamellar or unilamellar. The latter ones are divided in three main classes: Small Unilamellar Vesicles (SUVs; 20 to 100 nm, Large Unilamellar Vesicles (LUVs; 100 to 500 nm) and Giant Unilamellar Vesicles (GUVs; 0.5 to 100 μm). The former two can be viewed in analogy to model cellular organelles (vesicles of secretion, of transport, ...). They are also utilised as protective capsules for biomedical applications.

The main disadvantages of using lipid vesicles as biomimetic model membranes are that the lipid asymmetry found in native biological membranes cannot be mimicked and that the final lipid composition of the vesicles may be relatively different from the initial lipid mixture used for vesicle formation [45].

2.1.4 Interactions between Membranes

Intercellular adhesion is essential for many biological processes. Tissue formation, immune defense and many other functions in the living realm involve complex cell adhesion processes. Additionally to non-specific interactions, also known for colloidal and polymeric systems, they are mediated by a set of specific molecules called cell adhesion molecules such as selectins, integrins, and cadherins. Each of these adhesion molecules has a different function and recognizes different ligands [46]. Due to the complexity understanding cell adhesion is a formidable task and simple membrane models are typically used to study interactions between membranes.

Non-specific adhesion

The forces between two phospholipid bilayers without specific adhesion molecules are governed by van der Waals and electrostatic interactions and can be quantified by the DLVO theory named after Derjaguin, Landau, Verwey and Overbeek. The theory describes the force between charged surfaces interacting through a liquid medium. Van der Waals forces is a collective term for all forces induced by dipolar interactions between any combination of molecules. It is the sum of the force resulting from interaction between two permanent dipoles (Keesom forces F_K), between a permanent dipole and a corresponding induced dipole (Debye forces, F_D) and between two instantaneously induced dipoles (London dispersion force, F_{disp}).

$$F_{vdW} = F_K + F_D + F_{\text{disp}}. \quad (2.1)$$

The latter one is usually the dominating term since it is always present. All three interaction potentials decay quickly with the distance r proportional to r^{-6} , resulting in the van der Waals pair potential

$$w_{vdW}(r) = \frac{C}{r^6}, \quad (2.2)$$

with the coefficient in the particle-particle pair interaction C . The rigorous way to treat the van der Waals interaction between solid bodies is the Lifshitz theory [47]. Typical values for the Hamaker constants of lipid films calculated from the Lifshitz theory are in the order of $5 - 10 \times 10^{-21} \text{J}$ [48]. A simple approximation based on the pairwise summation of interaction potentials is the Hamaker theory. In order to determine the interaction potential between two macroscopic solids made of A and B with a molecule density ρ_A and ρ_B respectively, one calculates at first the van der Waals energy between a molecule A and an infinitely extended body with a planar surface made of molecules B. Then one integrates over all molecules in the solid A. For two planar surfaces made of A and B separated by a distance D , the van der Waals energy per unit area is given by

$$w_{vdW} = -\frac{A_H}{12\pi D^2} \quad (2.3)$$

with the Hamaker constant $A_H = \pi^2 C_{AB} \rho_A \rho_B$. The detailed calculation of w for different geometries and A_H can be found elsewhere [33]. w depends on the sign of the Hamaker constant. So the van der Waals force can be attractive or repulsive. However for two identical surfaces interacting across a vacuum or liquid, the van der Waals forces are always attractive.

Phospholipid bilayers, as most surfaces in water, are charged, either by dissociation of surface groups or by adsorption of charged molecules from the bulk solution. This results in a wall surface potential, which attracts counter-ions from the surrounding solution and excludes co-ions in order to balance the surface charge. The region near the surface of increased counterion concentration is called the electrical double layer. It can be approximated by a sub-division into two regions. Ions closest to the charged wall surface are strongly bound to the surface. This immobile layer is called the Stern or Helmholtz layer with a surface potential ϕ_0 . The region adjacent to the Stern layer is called the diffuse layer and contains loosely associated ions that are comparatively mobile. The total electrical double layer due to the formation of the counterion layers results in electrostatic screening of the wall charge and minimizes the Gibbs free energy of double layer formation. The electrostatic interactions can be mathematically described with the help of the Poisson-Boltzmann equation

$$\frac{d^2\phi}{dx^2} = -\frac{1}{\varepsilon_0\varepsilon_r} \sum_i c_i^0 z_i e \exp\left(-\frac{z_i e \phi}{kT}\right). \quad (2.4)$$

ε_0 and ε_r are the dielectric constants of free space and the solution, c_i^0 the concentration of ions i in the bulk solution, z_i the valency of the ion species i and e the electron charge. Solving the differential equation for two flat surfaces with overlapping electric double layers as surfaces approach and adding the attractive van der Waals interactions (although they are in principle not additive) yield the following expression

$$w = \frac{64c^0 kT}{\kappa} \cdot \tanh \frac{e\phi_0}{4kT} \cdot \exp(-D\kappa) - \frac{A_H}{12\pi D^2}. \quad (2.5)$$

Since the Debye-Hückel inverse length $\kappa = (2e^2 c^0 z^2)/(\varepsilon_0\varepsilon_r k_B T)^{1/2}$ for a symmetric electrolyte, increases with the concentration of ions, the repulsion due to double layer overlap decreases. Figure 2.9 shows a very weak attraction at large distances with a

secondary energy minimum, an electrostatic repulsion at intermediate distance with an energy barrier for a dilute solution of highly charged surfaces, and a strong attraction at short distance with the primary minimum at the contact. With increasing salt concentration, the energy barrier significantly decreases and even completely vanishes. Forces between bilayers can be measured using the surface force apparatus (SFA), atomic force microscopy (AFM) and the osmotic pressure technique [36, 49].

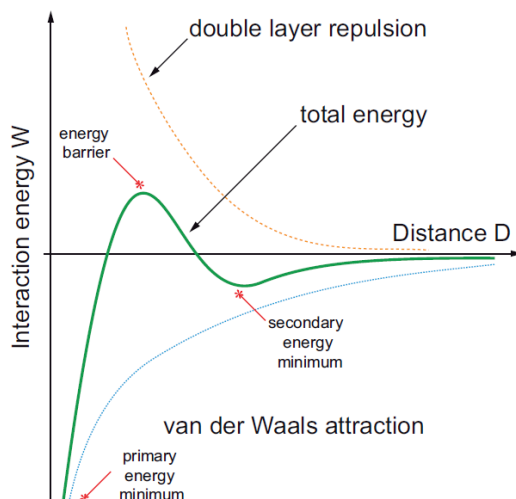
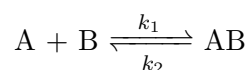


Figure 2.9: Forces profile for a flat charged surface in a polar solvent. The van der Waals force is purely attractive while the electrostatic repulsion is purely repulsive. The net force exhibits one deep minimum close to the surface, a positive repulsive maximum at some distance from the wall and a second, attractive minimum

Although there is a strong attraction at short distance, further approach is prevented by hydration forces to avoid atomic contact. This so called hydration pressure can be measured e.g. in multilayer systems, where a pressure of 10^8 Pa has to be applied to obtain bilayer separations below 1 nm [49]. Since in supported and lamellar bilayers the membranes are confined by the substrate or adjacent bilayers, also entropic effects like steric repulsion due to membrane fluctuations, described by Helfrich, play a role and contribute to repulsion between bilayers at short distances [50].

Ligand-receptor interactions

The formation and dissociation of specific noncovalent interactions between a variety of macromolecules embedded in the cell membrane play a crucial role in the function of biological systems. The specific binding with high affinity between certain molecules that have a perfect geometrical fit are called "lock and key" or "ligand-receptor" (see Figure 2.10). The binding occurs by intermolecular forces, such as ionic bonds, hydrogen bonds and van der Waals forces to give rise to very strong physical bonds, opposed to covalent or metal chelating-bonds, with minimal expenditure of energy and is short-ranged [51]. From a thermodynamic perspective, ligand-receptor interactions between ligand A and receptor B in solution can be described as a conventional chemical equilibrium



with the kinetic constants of association k_1 and dissociation k_2 accounting for forward and reverse reaction according to following reaction

$$\frac{d[AB]}{dt} = k_1[A][B] - k_2[AB] \quad (2.6)$$

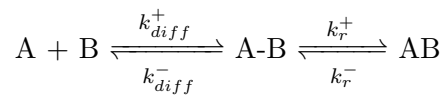
yielding the definition of the affinity equilibrium constant K_a

$$K_a = \frac{k_1}{k_2} = \frac{[AB]}{[A][B]}, \quad (2.7)$$

which can be related to the free binding energy ΔG by

$$\Delta G^\circ = -RT \ln K_a. \quad (2.8)$$

A first approach to describe the kinetics of ligand-receptor interactions which are attached to surfaces has been developed by Bell [16]. This is achieved by splitting the binding process into two steps with a diffusion-controlled formation of an encounter complex followed by the ligand-receptor bond formation



with k_{diff}^+ , k_{diff}^- and k_r^+ , k_r^- the rate constants of diffusion complex and the ligand/receptor bond formation/dissociation respectively. By assuming that the reaction rate for free and bound molecules is equal, as well as a steady state approach for the formation of the diffusion complex A-B and by treating the diffusion phase with a standard Smoluchowski approach in 2 dimensions, it is then possible to roughly quantify the rate of bond formation between membranes [16]. However more sophisticated models comprehend the possible variation of membrane distance and also the redistribution of binding molecules in the contact area. Furthermore it has to be taken into account that the rate of bond dissociation is dependent on the applied force, according to the expression

$$k_r(F) = k_r^0 \exp\left(\frac{\gamma F}{kT}\right), \quad (2.9)$$

where F is the applied force and γ a parameter related to the interaction range of the ligand-receptor bond (usually $< 1\text{nm}$) [52].

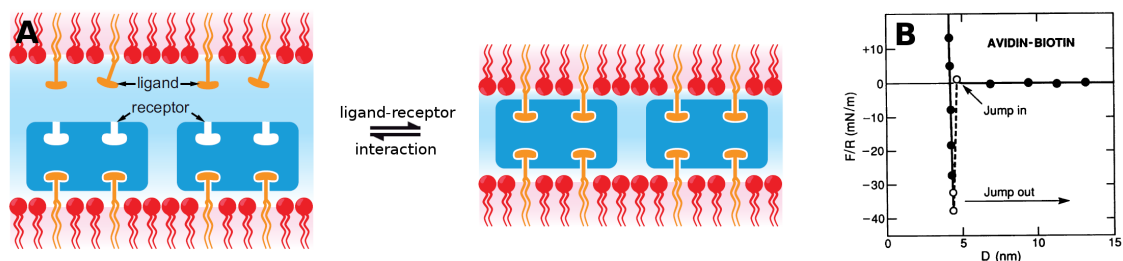


Figure 2.10: A. Schematic illustration of ligand-receptor interaction between two membranes of avidin and biotin before and after they have locked together to form a symmetrical ligand-protein-ligand junction that is strongly and irreversibly adhesive, B. Corresponding force profile [53].

Nowadays AFM [54], SFA [53] and various other experimental methods [51] allow a direct monitoring of ligand-receptor interactions up to the single molecule level. Computational studies using molecular dynamics and Monte Carlo simulations have provided more

direct physical pictures of the binding and unbinding processes [52]. Antigen-antibody couples are typical examples of ligand-receptor pairs, with affinity constants normally ranging between $10^4 - 10^{10} \text{ M}^{-1}$ and a typical lifetime of ms [51]. The interactions between biotin ligands and streptavidin or avidin receptors are the strongest and most-thoroughly studied ligand-receptor systems, with a binding constant of 10^{15} M^{-1} (88 kJ/mol , $\sim 35 k_B T$ per bond) and a bond lifetime of 12 days. When inserted into phospholipid membranes the binding is essentially irreversible, since the ligand-receptor bond is stronger than the energy required to pull out a lipid from the bilayer ($26 k_B T$) [53]. Yet when applying external force the lifetime can be diminished to ms [55]. Molecular recognition with artificial ligand-receptor pairs, such as CD host-guest complexes will be described in detail in section 2.2. A selection of typical ligand-receptor bond energies and corresponding distribution of intrinsic bond lifetimes are displayed in Figure 2.11 [56].

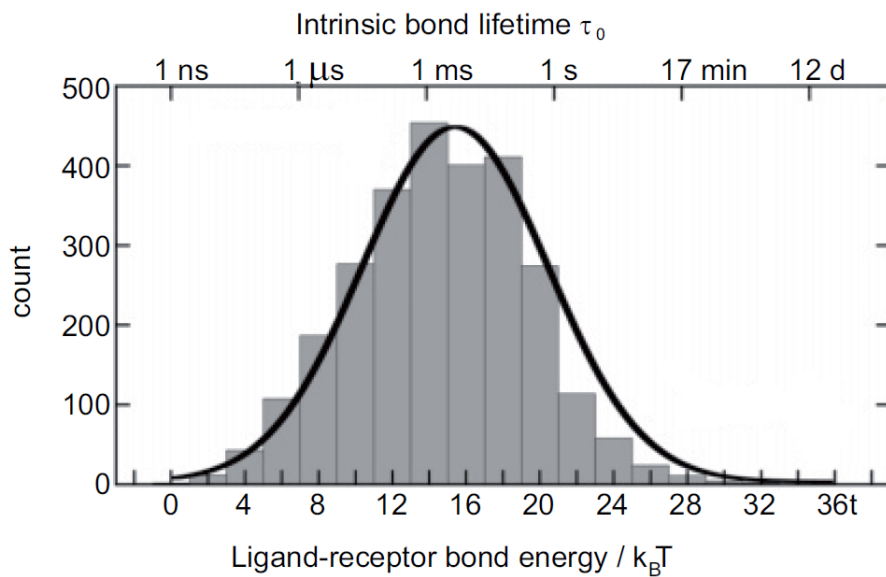


Figure 2.11: The distribution of ligand-receptor bond energies and corresponding distribution of intrinsic bond lifetimes. Based on data reported for 2756 ligand-receptor pairs [56].

Polymer tethered ligand-receptor interactions

In many biological systems, ligands are attached to the ends of flexible or semiflexible tether groups rather than fixed or immobilised on a surface or macromolecule [15]. These tethers play an important role in controlling the range of the ligand-receptor interactions and its kinetics. In order to mimic nature in many systems designed for selective targeting, flexible polymers are used as tethers. Hence a better modulation of the short-ranged, specific interactions can be achieved and their role can be compared to theoretical predictions. Using SFA, Israelachvili and coworkers [57,58] made the first direct measurement of the interaction potential between polymer-tethered ligands (biotin) on one surface and receptor sites (streptavidin) on an opposing surface (Figure 2.12).

The interaction between two surfaces due to tethered ligand-receptor binding involves two qualitatively different levels of physics. The specific binding between the ligand and the receptor is governed by the binding potential of the ligand and receptor groups, which is short-ranged in the order of a few Angstroms. The binding also depends crucially on

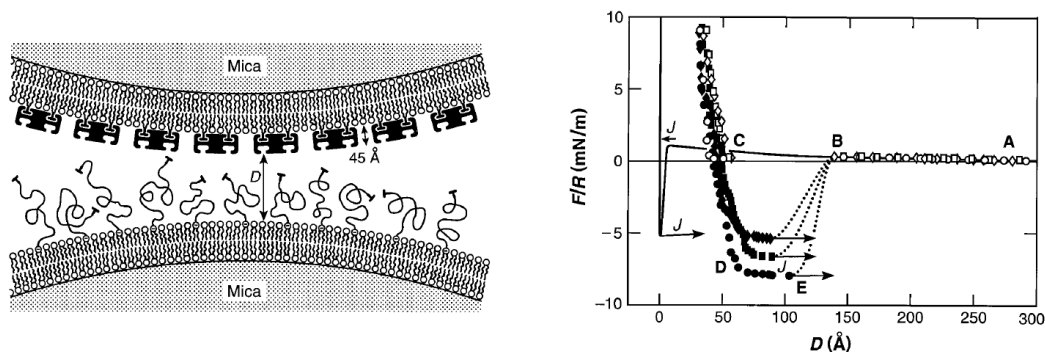


Figure 2.12: left: Schematic illustration of tethered-ligand-receptor interaction between two surfaces of streptavidin and PEG-tethered biotin. right: Corresponding force profiles between PEG-biotin and streptavidin (dotted curves) and biotin without PEG and streptavidin (solid curve) [57]

whether the receptor sites are mobile or frozen on the substrate. Receptor sites can be regarded as immobile, e.g. when their diffusion is sufficiently slow compared to the time scales for binding and conformation relaxation of the tether. Mobile receptor sites, e.g. those attached to a fluid lipid membrane, will be attracted by the ligands, leading to a rearrangement of their distribution [59].

On the other hand, if the terminal ligand moiety is small compared to the tether, the interaction depends on the length and flexibility of the tether. The flexible tether connecting the ligand allows it to reach receptor sites that are some distance away from the anchoring location of the tether on the surface, thus dramatically increasing the range of attraction between the two surfaces (Figure 2.12). The binding occurs at separations that are comparable to the fully stretched chain length of the tether polymer [57]. Combining Monte Carlo simulation with reaction rate theory, the effect of flexible tethers on the kinetics and spatial range of multiple-receptor binding have been assessed both qualitatively and quantitatively. It has been demonstrated that ligand cannot be described simply with a diffusing particle approach, but that the dynamics of the tether chain have to be taken into account. Thus, a combination of the specific ligand-receptor pair interaction and the dynamics of the tethering chains determines the overall range, rate, and ultimate strength of complementary multiple bond formation [58].

Grafted polymer layers

As described above the polymer tether length and flexibility has a big influence on the ligand-receptor interaction profile. So it is crucial to know the polymer distribution of grafted STL layers prior to force measurements. For this purpose neutron reflectivity is carried out. The chain conformation of the STLs can then be determined by applying appropriate models which will be discussed in the following paragraphs.

Let us at first consider the behavior of traditional polymer grafts fixed with one end-point to the surface. If chains are grafted to a surface in low density, they do not interact and they behave similar to isolated grafted chains. This regime is called the “mushroom regime” (Figure 2.13 a). In first approximation they are not affected by the presence of the surface and their mean height is in the order of the Flory radius $R_F = aN^{3/5}$ (a is the length of a monomer and N the number of monomers). If σ is the surface density

of grafted polymers (in the brief theoretical description of grafted polymers σ is dimensionless and normalised with respect to a^2), the distance separating two chains is $D \simeq a\sigma^{-1/2}$. When D decreases, chains start to interact for $D \leq R_F$. Therefore the chains are forced to elongate perpendicular to the surface under the action of the excluded volume interactions, which is counterbalanced by the entropic elastic force of the chains.

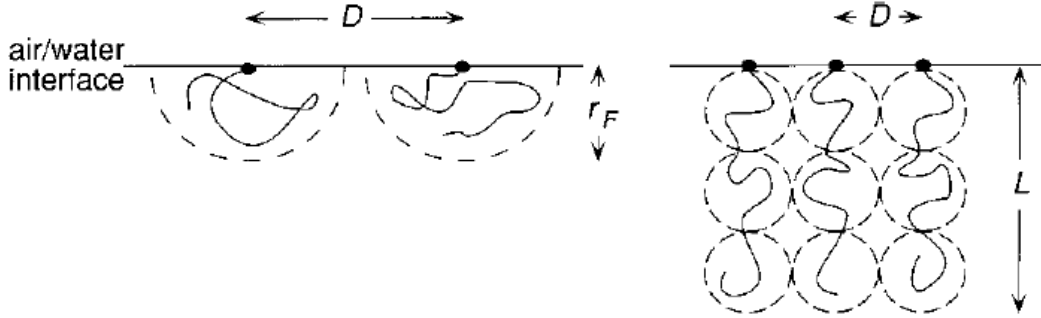


Figure 2.13: Schematic representation of the “mushroom regime” (a) and “brush regime” (b) conformations of surface-grafted polymers.

For this so called “brush regime” Alexander [60] and de Gennes [61] proposed a simple description. They supposed that the volume fraction of the polymer ϕ is constant in the brush, while it extends a certain distance H from the surface. The volume fraction is

$$\phi = \frac{aN\sigma}{H}. \quad (2.10)$$

The extension of the brush can be calculated from the free energy of the chain F_{ch}

$$F_{ch} \simeq \frac{aN^2\sigma}{H} + \frac{H^2}{a^2N}, \quad (2.11)$$

with the first term related to the excluded volume due to monomer packing and the second term depending on the chain elasticity, which is minimised for a brush height

$$H \simeq aN\sigma^{1/3}, \quad (2.12)$$

in equilibrium. Applying equations (2.10) and (2.12) the polymer volume fraction in the brush is fixed by the grafting density according to $\phi = \sigma^{2/3}$, which is independent of the brush height.

It is however unrealistic to situate all polymer extremities at the end of the brush. A brush where the polymer ends are distributed in the whole brush should result in a volume fraction profile dependent on the brush height. Such a model has been presented by Milner et coll. [62] and Skvortsov et al. [63] by introducing a self-consistent field $V(z)$ which only depends on the distance of the surface z and which takes into account the excluded volume interactions. In the mean-field approach, V is proportional to the volume fraction of polymer in the brush

$$V(z) = v\phi(z), \quad (2.13)$$

with the effective volume of a monomer v . This problem is similar to the one of an ideal polymer chain to which an exterior potential field is applied. It can be demonstrated that the mean field approach results in a parabolic profile [62, 63]:

$$\phi(z) = \frac{\pi^2}{8N^2v} \left[1 - \left(\frac{z}{H} \right)^2 \right], \quad (2.14)$$

with the polymer volume fraction at the interface ϕ_0 expressed by

$$\phi_0 = \frac{\pi^2}{8N^2v}. \quad (2.15)$$

In this model the brush thickness equals

$$H = \left(\frac{12}{\pi^2} \right)^{1/3} (v\sigma)^{1/3} N. \quad (2.16)$$

It can be seen that the brush extension H dependence on σ and N is identical with the Alexander-de Gennes approach, since equation (2.12) translates the local equilibrium between the chain elasticity and the excluded volume interaction. These are the same parameters as in the Alexander-de Gennes model. So applying equations (2.14) and (2.16), the brush height H should scale with the volume fraction ϕ_0 at the surface ($z = 0$) as follows:

$$H \sim \sigma^{1/3} \sim \phi_0^{1/2}. \quad (2.17)$$

Sliding polymer layers

The additional conformational freedom in sliding grafted polymer layers induces important differences in the equilibrium and dynamic behavior compared to polymer tethers grafted on a fixed point [19]. At first fixed sliding links with low grafting densities in mushroom regime shall be considered, with the total number of monomers N . Thus, one branch has n monomers, the other branch has $N - n$ monomers 2.14.

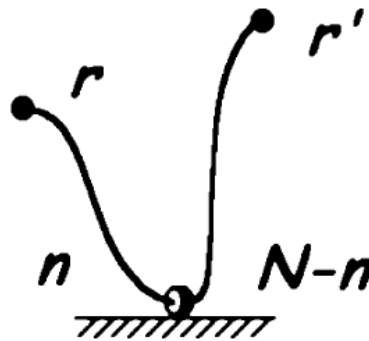


Figure 2.14: Schematic picture of a Gaussian chain grafted to a surface by a sliding link [19]

The polymer concentration profile for conventional grafted mushrooms is given by equation

$$c(z, N) = \frac{N\sqrt{\pi}}{R_g} \left[\operatorname{erfc} \left(\frac{z}{2\sqrt{N}} \right) - \operatorname{erfc} \left(\frac{z}{\sqrt{N}} \right) \right], \quad (2.18)$$

where as R_g is substituted by $R_g = \sqrt{\frac{Na^2}{6}}$. For sliding mushrooms (assuming Gaussian chains), it can be demonstrated that the low density grafts adopt mainly symmetric con-

configurations with equal number of chains at each side of the sliding ring. This results in following expression for the polymer concentration profile at the surface:

$$c(z, N) = \frac{2N}{\sqrt{\pi}R_g} \left[2 \exp\left(-\frac{z^2}{4R_g^2}\right) - \frac{3\sqrt{\pi}}{R_g} \operatorname{erfc}\left(\frac{z}{2R_g}\right) \right] - \frac{2N}{\sqrt{\pi}R_g} \left[2 \exp\left(-\frac{z^2}{R_g^2}\right) - \frac{2z\sqrt{\pi}}{R_g} \operatorname{erfc}\left(\frac{z}{R_g}\right) \right]. \quad (2.19)$$

Figure 2.15 displays the concentration profiles of sliding mushrooms and conventional mushrooms with the same N , as well as conventional mushrooms with $N/2$ but double concentration. It demonstrates that the sliding effect translates into a decreased polymer layer thickness compared to conventional polymer grafts with same N . Compared to conventional grafts with $N/2$, the thickness is similar, however the sliding layer can explore larger z/a .

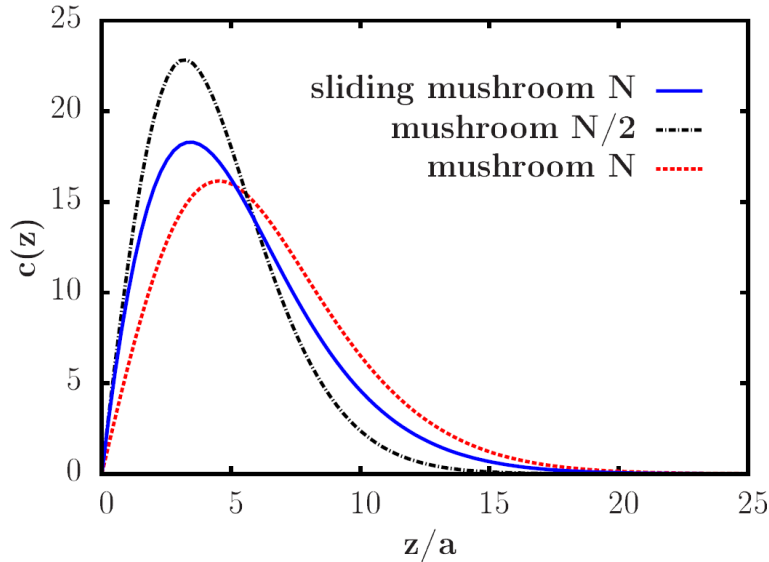


Figure 2.15: Comparison between the concentration profiles $c(z)$ of a normal mushroom and a sliding mushroom with the same number of monomers N and a normal mushroom with $N/2$ but double surface concentration $2c(z)$. The thickness z/a is normalised with respect to the size of a monomer a .

Furthermore it has been shown that sliding chains in a densely grafted brush adopt stretched asymmetric configurations [19]. Therefore they should essentially behave like normal polymer brushes grafted with a fixed link. Thus they should be well described by parabolic profile given by equation (2.16).

2.2 Cyclodextrins

CDs and especially amphiphilic derivatives capable of inserting into phospholipid membranes are key components for the assembly of the STLs. Therefore they will be described in detail in this section.

2.2.1 Introduction

Supramolecular chemistry is a new rapidly progressing field on the crossroads among chemistry, biochemistry, physics and technology. Its foundations were laid less than half a century ago and its founding fathers Pedersen, Cram and Lehn, were awarded the Nobel prize in chemistry 1987 for their work on molecular recognition [64,65]. Very often supramolecular chemistry is referred to as the chemistry beyond the molecule, where in contrary to covalent bonds in classical organic chemistry, non-covalent interactions play a crucial role. These reversible interactions, such as Coulomb, van der Waals, hydrophobic interactions as well as hydrogen bonds, are characterised by much smaller energies than covalent chemical bonds (200 - 400 kJ/mol). They give rise to the formation of supramolecular assemblies which are comprised of many molecules, e.g. micelles, vesicles and liquid crystals, but also defined supramolecular structures with few molecules (most of the times two), which are termed host-guest complexes [66], between complementary molecules. Supramolecular compounds based on host-guest recognition are of great importance to design molecular systems which can be used as intelligent drug carriers [67], chemical sensors [68] or conformational switches [69]. Among other hosts, like crown ethers, cryptands or cyclic peptides [70], cyclodextrins (CDs) can be regarded as one of the most important and potent host molecules. The seminatural compounds are able to form inclusion complexes with many different hydrophobic and amphiphilic guests in water [71]. CDs are readily available in both high purities and large quantities. Furthermore, CDs can be modified by a wide variety of synthetic methods and they are water-soluble as well as biocompatible. Therefore they have been serving as model compounds to study the inclusion phenomenon and they have been extensively researched in the last decades giving rise to many applications in food industry, pharmaceuticals and cosmetics. CD and their inclusion compounds will be described in detail in the following sections.

2.2.2 History

CDs were first isolated in 1891 as degradation products of starch by Villiers [72] and identified as cyclic oligosaccharides by Schardinger in 1904, which would form colorful adducts upon treatment with iodine solution [73]. For this reason these cycloamyloses are also named Schardinger dextrins, especially in the older literature.

In the 1930s the structure of the CDs was finally clarified by means of hydrolysis experiments. The results led to the conclusion that CDs are made of glucose units which are linked by 1,4-glycosidic bonds. Also the ring structure of the CD-molecules with a central cavity, the molecular weight of the most common α , β and γ -CD, were determined in the following years, mostly by the efforts of Freudenberg and French. By the 1950s the basic structural and physicochemical properties, as for example the cavity size, solubility, reactivity and complexation ability were well characterised and described in Cramer's book on CD-"Einschlussverbindungen" [74]. And short after first patents were filed for the use of CDs in drug formulations by exploiting their solubilisation abilities for lipophilic substances.

Beginning from the mid 1970s CDs became more and more popular for industrial applications especially in Japan and a little later in Europe. This was mainly due to advances in biotechnology which now allowed producing and purifying the different CDs selectively in

an efficient manner. The prize for the most frequently used β -CDs dropped about 400 fold from 2000 \$/kg in 1970 to several \$/kg today [75]. Today CDs and their derivatives are used in an industrial scale e.g. as solubilisers and stabilisers in food, pharmaceutical and agricultural industry [76]. Currently the annual production is more than 10000 tons/year and still expected to rise in the future [77].

2.2.3 Synthesis, Structure and Properties

As already mentioned earlier CDs are a family of cyclic oligosaccharides consisting of 6, 7, 8 or more α -D-glucose units linked by α -1,4-glycosidic bonds, which are called α -, β -, γ -CDs and so on, respectively (Figure 2.16 left). They are produced by enzymatic degradation of starch with CD glycosyl transferases (CGTases) which are obtained from bacterial strains such as *Bacillus macerans*, *Klebsiella oxytoca* and *Bacillus circulans* [75]. CGTases can synthesize all forms of CDs. Thus the product of the conversion results in a mixture of the three main types of cyclic molecules and traces of larger rings, in ratios that are strictly dependent on the enzyme used. The 6, 7 and 8 membered rings can be isolated from the reaction mixture by specific precipitation agents (1-decanol, toluene and cyclohexadec-8-en-1-one for α -, β -, γ -CDs respectively) in purities of >99% [78]. Higher cyclic oligosaccharides are described [79] but they need to be isolated by elaborate chromatographic methods. For steric reasons, smaller rings do not naturally occur. But e.g. the cyclopentaose built of 5 glucose has been chemically synthesised [80].

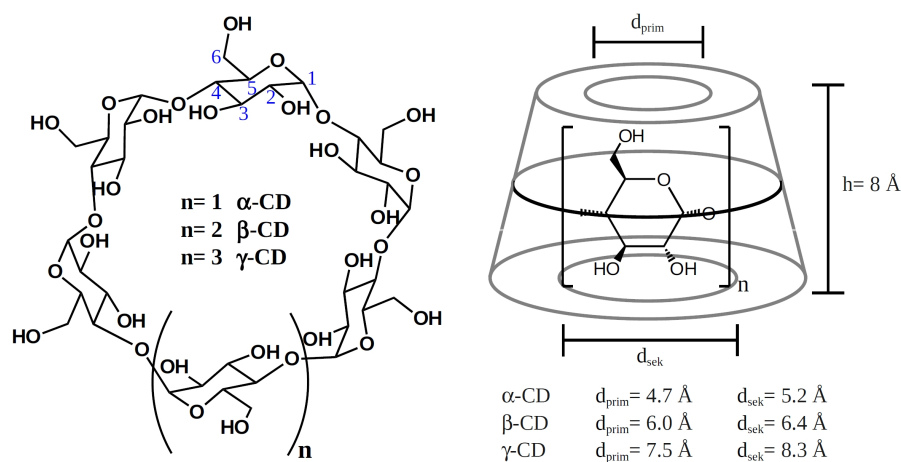


Figure 2.16: Chemical structure (left) and schematic illustration of cone shape (right) of the CD

On the basis of x-ray studies the structure of the CDs with ring sizes $n = 6, 7$ and 8 resembles a rather rigid truncated cone with a planar ring of glycosidic oxygen atoms exhibiting C_n symmetry. As a consequence of the 4C_1 (“chair”) conformation of glucose units the primary hydroxyl groups of the C_6 atoms are located at the narrow side of the cone. The secondary hydroxyl groups of the C_2 and C_3 atoms are situated on the wider rim. The latter form systematic intramolecular, inter-glucose hydrogen bonds which stabilise the CD’s round conformation. The height is similar for α -, β - and γ -CDs in the order of $0.8 - 0.9 \text{ nm}$ [79]. The H_3 and H_5 atoms of the sugar units are inward-directed to form the hydrophobic cavity. The diameters of the inner cavity depend on the ring size and range from 4.5 to 8 nm . Since the rotation of the primary hydroxyl groups is in

contrast to the secondary ones not restricted, the effective diameter of the cavity on the primary side of the molecule is reduced. Thus the cavity is, like the exterior, conically shaped with a constriction in the middle (Figure 2.16) [81]. Owing to the hydroxyl group positioning at both outer rims of the torus the CD exterior is hydrophilic. On the other hand the inside of the cavity is rather hydrophobic because it is lined with skeletal carbons and oxygens of the glycosidic bonds in the sugar monomers. Sometimes CDs are referred to as endolipophilic and exolipophobic molecules.

The CDs are fairly water soluble and highly soluble in strongly polar solvents like DMF, DMSO and pyridine [78]. Interestingly the β -CD is the least soluble in water among the three most common CDs (Table 2.1). In β -CD a complete intramolecular hydrogen bond belt is formed by the secondary hydroxyl groups owing to its more rigid structure compared to the 6 and 8 membered derivatives.

The time-averaged structure determined by “slow” spectroscopic techniques, like NMR indicate that the C_n symmetry of the CDs prevails in solution. However modeling by molecular dynamics simulations shows that, although the torus is stabilised by intramolecular hydrogen bonds, it is still flexible enough to permit considerable deviations from the regular toroidal shape [82]. The most important properties of α -, β - and γ -CD are summarised in table 2.1.

	α -CD	β -CD	γ -CD
Number of glucose units	6	7	8
Molecular weight [g/mol]	972	1135	1297
Approximate inner cavity diameter in Å	4.7 - 5.2	6.0 - 6.4	7.5 - 8.3
Approximate outer diameter in Å	14.6	15.4	17.5
Approximate volume of cavity in Å ³	174	262	427
Approximate height in Å	7.9	7.9	7.9
$[\alpha]_D$ at 25°C	150	162.5	177.4
Solubility in water at room temperature in g/L	145	18.5	232
Surface tension in mN/m	71	71	71
Melting temperature range in °C	255 - 260	255 - 265	240 - 245
Water molecules in cavity	6	11	17
Hydrolysis by <i>A. oryzae</i> α -amylase	negligible	slow	rapid
Crystal forms (from water)	hexagonal plates	monoclinic parallelograms	quadratic prisms

Table 2.1: Characteristic properties of the three most common CDs (after [75,83])

2.2.4 CD complexes

The feature that makes CDs so special is their ability to form inclusion complexes with a wide range of solid, liquid and gaseous compounds, which gives them a remarkable capacity for molecular recognition. These kind of complexes are often called host-guest complexes between the host CD cavity and a guest molecule. Some examples for different topologies of CD complexes are illustrated in Figure 2.17. Most of the research has been carried out in aqueous environment since the complexes are the most stable in water and it is most important for applications. The hydrophobic cavity provides a lipophilic micro-environment into which appropriately sized, non-polar (less polar than water) molecules or parts of molecules can enter. CDs form complexes with a whole variety of compounds. With purely hydrophobic guests water insoluble channel inclusion compounds are obtained, where the CDs are stacked into columns held together by intermolecular hydrogen

bonds, e.g. complexes of α -CD with n-pentane or n-hexane (Figure 2.17 a). They also form inclusion compounds with amphiphilic guests. These are water soluble since repulsion between the hydrophilic headgroups prevents aggregation of the complexes (Figure 2.17 c). CDs are also good hosts for so called bola-amphiphiles which are molecules with two hydrophilic headgroups (Figure 2.17 b). However the inclusion dynamics are slowed down compared to common amphiphiles because a considerable activation energy has to be overcome since the penetration of one of the hydrophilic endgroups through the hydrophobic cavity is required [84]. Compounds which cannot enter the cavity sometimes form sandwich like inclusion complexes with CDs (Figure 2.17 d) [78].

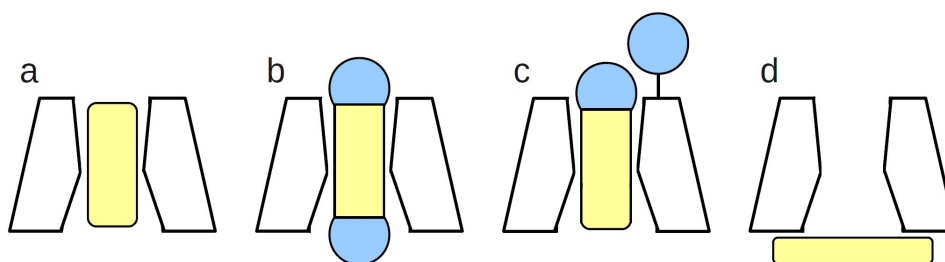


Figure 2.17: Schematic illustration of formation different CD complexes: inclusion compound a. native CD with hydrophobic guest, b. native CD with bola amphiphile, c. modified CD with amphiphilic guest and d. association compound with native CD

Due to the different sizes of their cavities, the α -CD complexes rather small molecules with low molecular weight or compounds with aliphatic side chains. β -CD will form complexes with aromatic compounds and heterocycles, whereas γ -CD can include big molecules like macrocycles or steroids. Modified CDs, e.g. methylated CDs or amphiphilic CDs, also form inclusion complexes. Even when there are no guest compounds present CDs usually incorporate some solvent molecules into the cavity [85]. The complexes are held together by non-covalent interactions such as van der Waals interactions, hydrophobic interactions, hydrogen bonds, other electrostatic interactions and steric effects.

Another interesting type of complexes are so called polyrotaxanes and pseudo polyrotaxanes between a polymer and CDs, which are arranged like beads on a string, and depending on the length of the polymer, stoichiometries of 1:n (polymer : CD) are observed. They will be described in detail in section 2.3.

Complexation thermodynamics

The main driving force for the complex formation arises from penetration of the hydrophobic moiety of an appropriately sized guest into the CD cavity and from dehydration of the guest. Both are usually summarised as the hydrophobic effect. H-bond interactions also play a role if the guest molecule possesses functionalities able to form H-bonds. Two more factors accounting for the stabilisation of the complex are release of enthalpy rich water from the cavity and the conformational changes which lead to a release of ring strain in the CD molecule [71].

Numeric values for the thermodynamic properties of the complex formation can be either directly measured by microcalorimetry or by sampling the temperature dependence of the equilibrium constant K_C . So through the relationship

$$\Delta G^\circ = -RT \ln K_C, \quad (2.20)$$

the free Gibbs energy change (ΔG°) can be calculated with the ideal gas constant R and the temperature T . By assuming a temperature independent heat capacity using the van't Hoff equation

$$\frac{d \ln K_C}{dT} = \frac{\Delta H^\circ}{RT^2}, \quad (2.21)$$

the enthalpy change (ΔH°) can be determined. And finally by the application of expression (2.22)

$$\Delta G^\circ = \Delta H^\circ - T \Delta S^\circ, \quad (2.22)$$

the entropy for the complexation can be evaluated [71,76]. The thermodynamic parameters for host-guest complexes of the CDs with many different compounds have been measured and a collection can be found in reference [71]. E.g. for complexes of β -CD with adamantane carboxylic acid in water at pH 7 and 298K following values have been found: $\log K = 4.6$, $\Delta G^\circ = -26.2$ kJ/mol, $\Delta H^\circ = -21.8$ kJ/mol and $T \Delta S^\circ = 4.4$ kJ/mol. The thermodynamic stability of the complexes is the discriminating feature for the molecular recognition of guest molecules by CDs. It is sensitive to the size, chirality, shape and polarity of the included compound. Molecular recognition can also derive from kinetic effects. E.g. using so called bola-amphiphiles (Figure 2.17 b.) the inclusion becomes an activated process governed by an activation energy due to steric hindrance from bulky groups. Thus complexation and dissociation rate varies with the size of the terminal groups [84].

In aqueous solution a dynamic equilibrium in the form



between the CD, the guest molecule (G) and the complexes (CD-G) is established. It can be described by the stoichiometry (m,n) of the complex and the complex stability constant K_C which is defined by

$$K_C = \frac{[(CD)_m G_n]}{[CD]^m [G]^n}. \quad (2.24)$$

The most common complexes have a 1:1 stoichiometry (Figure 2.17). However other ratios between host and guest molecule have been described, for example stoichiometries (CD:guest) 1:2, 2:1 and 2:2 [86]. Some higher order complexes derive very often from the formation of non-inclusion complexes between the normal inclusion complexes and additional guest molecules. Some 2:1 and 2:2 complexes have been shown to be composed of a mixture of inclusion and non-inclusion complexes. Also more recent studies suggest that the CD complexes, like native CDs themselves, are able to self-associate and form aggregates in solution. Therefore the model of free CD/guest complexes in ideal solution is in many cases too simple [87].

Characterisation of CD complexes

Many physicochemical properties like UV-absorbance, fluorescence, NMR chemical shifts, chromatographic retention and solubility, vary sufficiently between the free and complexed molecules. This can be exploited to determine numerical values for the stoichiometry and the equilibrium constant K_C by measuring these differences [86–88].

The structure of CD complexes is usually studied by X-ray and neutron crystallography, as well as NMR and optical spectroscopy [78]. As the diffraction experiments are carried out in solid state it has to be taken into account that the results may differ from the actual structure in dilute solution. Usually CD inclusion complexes when crystallised are able to form two different kinds of crystal lattices. In the “cage” mode the cavities of the CDs are blocked on both sides by their neighbors, whereas in the “channel” mode the oligosaccharides are stacked on top of each other like coins on a roll to generate channels in which the guest compound is embedded [79]. The crystal environment produced by these kinds of arrangements may inflict differences in structure compared to a solution of the complexes and also a rather rigid structure of the CD complex.

In NMR experiments and with optical methods, like UV absorption, circular dichroism and fluorescence, the structure can be directly surveyed in solution. Combining data obtained from different spectroscopic and diffraction experiments in solid state and solution allows some general structural features to be established. It is commonly accepted that the CD usually acts as a one-site ligand. The wider rim of the compound with the secondary hydroxyl groups displays the end where the substrate can enter. Furthermore the guest molecule owns one or more binding sites depending on the number of parts which sterically fit into the cavity. So complexation of CDs at various binding sites of the substrate leads to isomeric clathrates with distinct structures. The magnitude of inclusion of the guest into the cavity depends on its size and the optimisation of contact of its polar and unpolar portions with the solvent and the CD interior respectively [86]. In addition most of the experimental results as well as theoretical calculations suggest that the macrocycles are rather non-rigid so that a kind of induced fit model can be adopted for the host-guest complex. This is not surprising as the relatively rigid glucose monomers are connected by interglycosidic bonds where rotation is easily possible [83].

2.2.5 Modified CDs

CD are derivatised for a variety of reasons, such as improvement of the solubility in water or organic solvents or increasing their molecular recognition potential by tailoring a CD host to a particular guest, to meet specific requirements in the host-guest complex. Usually the native CDs serve as scaffolds where modification is achieved by electrophilic attack of the nucleophilic hydroxyl groups in primary (C-6) or secondary position (C-2 and C-3) [89]. But the large set of hydroxyl groups available on the two different sides of the CD make the challenge of selective conversion a daunting task because numerous regioisomers are possible.

Random modification

For industrial applications in drug formulation random modifications of hydroxyl groups to hydroxypropyl, sulfobutyl or carboxymethyl groups for enhanced water solubility and to silylethers for increased solubility in organic solvents can be readily achieved. But the products are difficult to reproduce and characterize because of their heterogeneity. In order to be of use to investigate supramolecular behavior of CD derivatives the compounds need to be pure and well characterised [83].

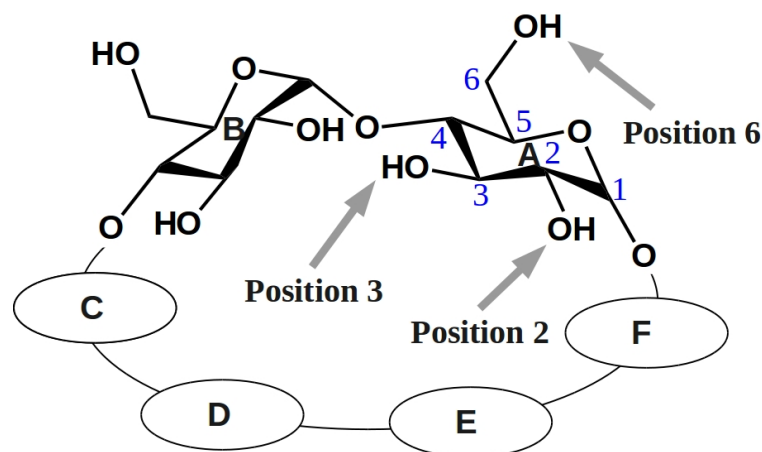


Figure 2.18: Labeling of the positions in a CD molecule

Selective modification

Derivatisation of well defined CDs can be carried out by exploiting their unique chemistry. Moreover careful choice of reaction conditions, solvents and regioselective reagents strongly influence the product distribution. Bulky reagents preferably react with the primary hydroxyl groups (OH-6) since they are the most accessible, as well as the most nucleophilic. The secondary hydroxyl groups (OH-2) are the most acidic ones, and so well-directed access can be achieved by selective deprotonation under anhydrous conditions. Selective modification of the least reactive secondary hydroxyl groups (OH-3) is only possible after blocking the OH-2 and OH-6 positions. Another option is to exploit complex formation of the reagent with the CD cavity to direct the functionalisation. However in most of the cases chromatographic purification is still necessary in order to obtain the desired compounds. The separation is easiest for substituents which are hydrophobic, so that the polarity of the various derivatives differs significantly [78, 89].

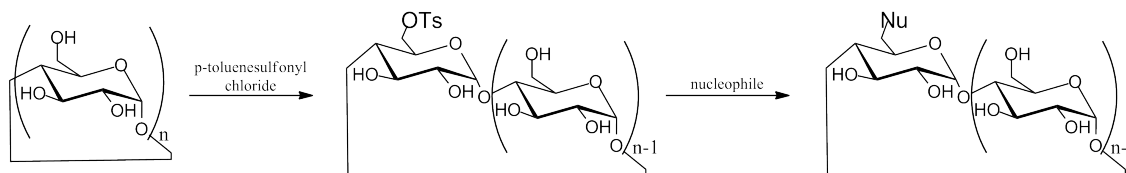


Figure 2.19: Different possibilities of mono-functionalisation of CDs; Nu = -I, -NH₂, -SR, -CHO, -NHR, -N₃

The classical way to prepare monosubstituted CDs at the 6-position are tosylates for α - and β -CDs, as well as 2,4,6-triisopropylbenzene sulfonate for γ -CD [90, 91]. These O-6

sulfonates are valuable precursors for a variety of modified CDs by nucleophilic displacement with suitable nucleophiles to afford 6-azido, 6-amino [90], 6-iodo [92] or 6-thioether derivatives [93]. Using sulfonylchlorides, also 10 trisubstituted CDs and the different disubstituted positional isomers (AB, AC, AD) can be synthesised. A more elegant method to access disubstituted regioisomers is the dealkylation of permethylated and perbenzylated CDs with diisobutylaluminium to selectively obtain A-B [94] or AD type diols [95]. Per-halogenated oligosaccharids, like per-6-iodo-6-deoxy-CDs are important intermediates for *n*-substituted derivatives at the primary rim and can be directly prepared by reaction of CDs with triphenylphosphine/I₂ [92].

Selective modification of the secondary rim is more difficult since there is twice the number of hydroxyl groups present. Again sulfonates are the reagents of choice and very often complex formation between reagent and CD is exploited to direct substitution to the 2 or 3 position. E.g. *m*-nitrophenyl tosylate preferentially yields the 2 substituted CD, whereas naphthalenesulfonyl chloride reacts with β -CD to give the 3-substituted product [89].

Alkylated CDs

Alkylation of CDs can be achieved by reaction of CD alkoxide ions with alkyl halides in presence of a strong base to produce the corresponding CD ethers in good yields. The complete substitution of all hydroxyl groups requires drastic reaction conditions such as a large excess of the reagent, increased reaction temperature and complete exclusion of water but can be achieved in very high yields [96]. The synthesis of dialkylated derivatives is more subtle because it requires selective alkylation. In the case of heptakis(2,6-di-O-methyl)- β -CD (DIMEB), the absolutely pure product (with 14 methyl groups) is only obtained by separation with HPLC. Especially methylated CDs exhibit some interesting properties. Methylation increases both the solubilities in water and organic solvents compared to the native compounds. β -CD DIMEB shows the highest solubility, whereas the permethylated analogue's solubility is slightly lower. Furthermore in contrary to other CD derivatives the water solubility correlates inversely with the temperature and methylated CDs possess a lower critical solution temperature (cloud point) [84]. Moreover because of the absence of the stabilising H-bond network due to methylation, these CD derivatives exhibit a much larger structural flexibility than the native compounds, allowing the glucose units to spin about its glycosidic oxygen atoms [97]. So sterical constraints result in a rather distorted structure with a greatly reduced cavity volume [98, 99].

2.2.6 Amphiphilic CDs

Amphiphilic CDs represent a class of CD derivatives, modified with polar groups, lipophilic groups and conjugates. The resulting amphiphiles are host molecules, which additionally to their molecular recognition capacities are capable of forming all the supramolecular assemblies expected of amphiphiles. By now examples of these macrocyclic amphiphiles are known that form thermotropic liquid crystals, while lyotropic assemblies include micelles, unimolecular micelles, nanoparticles, monolayers and bilayer vesicles. Regarding STLs, amphiphilic CDs able to insert into phospholipid bilayers are of special importance. The amphiphilic CDs can be divided into different classes.

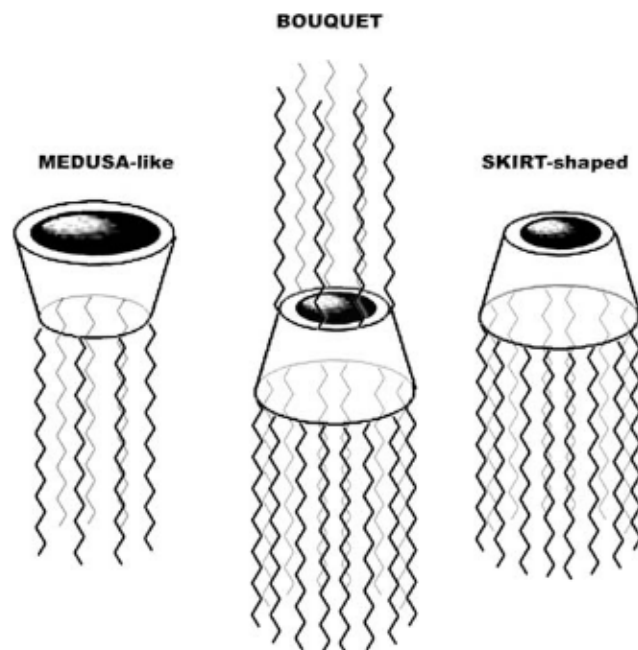


Figure 2.20: Different classes of polysubstituted amphiphilic CD's [100]

Polysubstituted amphiphilic CDs

These cyclic oligosaccharid compounds are synthesised by persubstitution of the primary and/or secondary hydroxyl groups with hydrophobic chains [101]. “Medusa-like” compounds (Figure 2.20) are synthesised by complete substitution of the primary side with amino-, amido-, sulfo- or alkyl chains. Sometimes also fluoroalkyl chains are used to render the CD amphiphilic [102]. Most of these molecules can establish stable monolayers at the air-water interface, and persubstituted thioethers are able to form thermotropic liquid crystals [103]. Furthermore it has been demonstrated that nanospheres of β -amido-alkyl CD derivatives still maintain the ability to incorporate drugs [104].

So called “Skirt shaped” CDs (Figure 2.20) are prepared by linking alkyl chains e.g. via ester bonds to the secondary hydroxyl groups. Derivatives with carbon chain lengths varying between C_6 and C_{12} have been confirmed to behave like surfactants and to form stable monolayers on water [105]. They have already found application to encapsulate drugs as they easily self-assemble to nanospheres or nanocapsules. Also very interesting for their application as drug carriers is their potential biodegradability. Moreover persubstituted hexanoyl derivatives have been shown to incorporate into DMPC membranes [106].

By modification of both sides of the cavity e.g. with on one side hydrophobic O-alkyl and on the other side hydrophilic polyethylene chains “bouquet-like” CD amphiphiles (Figure 2.20) are obtained with enhanced amphiphilic character. With the resultant increase in the size and hydrophilicity of the CD headgroup, the amphiphiles acquired a range of self-assembly properties previously not seen with CDs, forming bilayer vesicles, micelles or nanoparticles [101]. Instead of the nonionic polyethylene group, anionic or cationic hydrophilic headgroups are applied to give rise to e.g. amino or sulfonated amphiphilic CDs which are able to form vesicles with positive and negative surfaces, respectively [100]. Furthermore glycosylation of amphiphilic CD provides for compounds which can be recog-

nised by carbohydrate-specific lectin proteins and might be therefore of use for directed drug targeting [107].

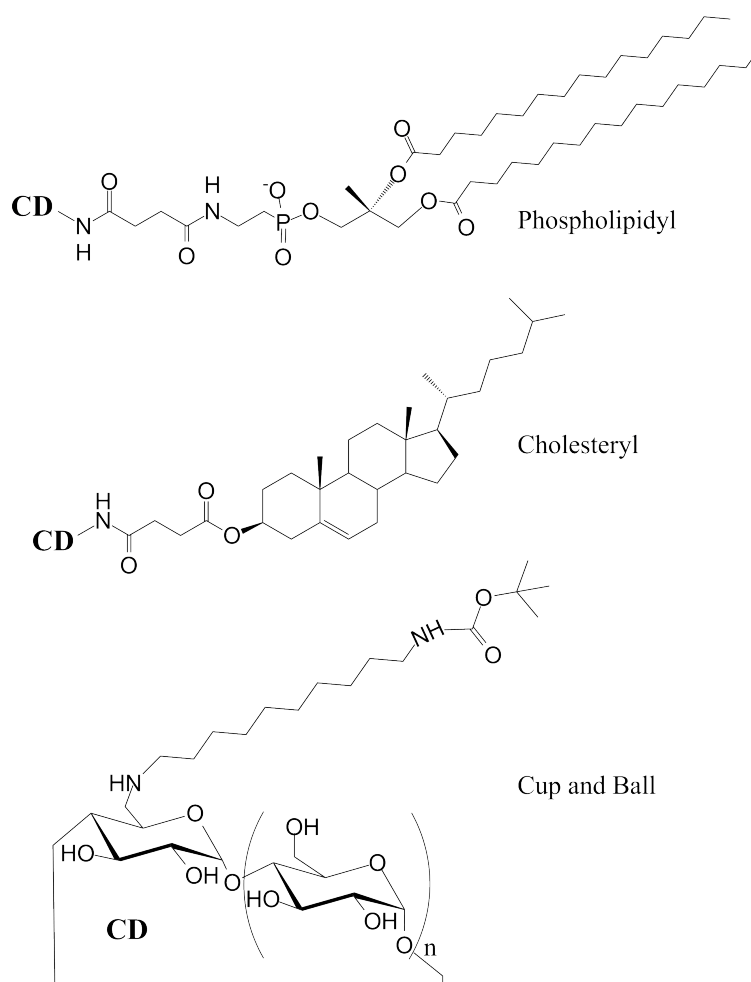


Figure 2.21: Different classes of mono-substituted amphiphilic CD's

Monosubstituted amphiphilic CDs

A different class of amphiphilic derivatives which is able to include itself into lipid membranes is created by furnishing mono-functionalised CDs with one single or two hydrophobic anchors [108, 109]. Usually the anchor is attached to the primary side to leave the secondary face unhindered for guest molecules to enter (Figure 2.21). The first examples were called "lollipops" as the lipophilic alkyl chain readily inserts into the cavity to give an intramolecular complex. To prevent this behavior, a bulky Boc amino protective group has been introduced at the end of the anchor residue. This "cup and ball" compounds (Figure 2.21) can be integrated into phospholipid membranes even with guest molecules in the cavity [110]. To enhance insertion properties into lipid membranes, derivatives with lipid-like anchors, like dilauryl aspartic [100], asymmetrical lauryl leucine [111], phospholipidyl [108] and cholesteryl chains [112] have been developed. Especially the cholesteryl CDs are very valuable compounds to combine the inclusion properties of the CD with membrane insertion properties [101, 113]. The 2,6-di-O-methyl β -CD for example is highly water soluble

and aggregates to spherical micelles consisting of 24 molecules in average [114] which maintain the capacity to include guests [115]. Yet it seems that water soluble methylated lipidyl β -CDs show a detergent effect on lipid membranes [108]. Water-insoluble permethylated di-cholesteryl β -CDs have been demonstrated to form stable monolayers and readily insert into phospholipid membranes [109, 116]. Native cholesteryl as well as phospholipidyl CDs however smoothly self-assemble into lipid membranes and induce a phase separation into a CD-rich L_{CD} phase and a lipid phase [117]. The composition, meaning the amount of lipid which can be found in the new phase, is dependent on the hydrophobic anchor. The stability seems to be conditioned by the CD-headgroup interactions.

Amphiphilic CDs are promising new compounds for improving drug administration and targeting. They are able to form a whole variety of supramolecular structures like micelles, vesicles and nanoparticles depending on the shape and length of their attached chains. In many cases the CD cavities of the nano-assemblies additionally keep their full complexation capacity. This gives a high loading capacity not only for hydrophobic but even for hydrophilic drugs [101, 113].

The emergence of mechanically interlocked molecular structures based on fabrication of rotaxanes with CDs which allow to construct functional molecular machines could open another area of application for these amphiphilic macrocycles. As they can self-organise on surfaces they could serve as the ideal material to interface the supramolecular assemblies with macroscopic structures like membranes, metallic surfaces or porous materials [113].

2.3 Rotaxanes

A distinctive feature of the STL is the sliding ability of its polymer tether. This is achieved by forming a polyrotaxane with a CD which functions as sliding ring grafted to a surface. These unique topological complexes are presented in the following sections.

2.3.1 Introduction

From the various supramolecular structures the ones having a topologically interlocked structure are of particular interest. They are characterised by high freedom of mobility of the mechanically linked components, which can be deduced from their predicted structures (Figure 2.22). Among these topological compounds, so called rotaxanes have attracted much attention because they can be used to construct functional molecular devices of high sophistication [118–120].

They are consisting of one or more rings and one or more axes where the dissociation of the rings is hindered by bulky stopper-groups at both ends of the axis. Although there exist no covalent bonds between axes and rings, rotaxanes are very stable molecules, since a high energy barrier ΔG_{diss}^\ddagger (>150 kJ/mol) has to be overcome for the dissociation of the rings (Figure 2.23). Compounds are only termed rotaxanes if the energy to surmount for the dethreading is higher than 50 RT, otherwise the molecules are called pseudo-rotaxanes [84].

The specific nomenclature for polyrotaxanes denotes the total number of molecules involved in the non-covalent complex within a set of square brackets. A rotaxane with only one macrocycle and one axle is termed a [2]rotaxane, two macrocycles and one axle

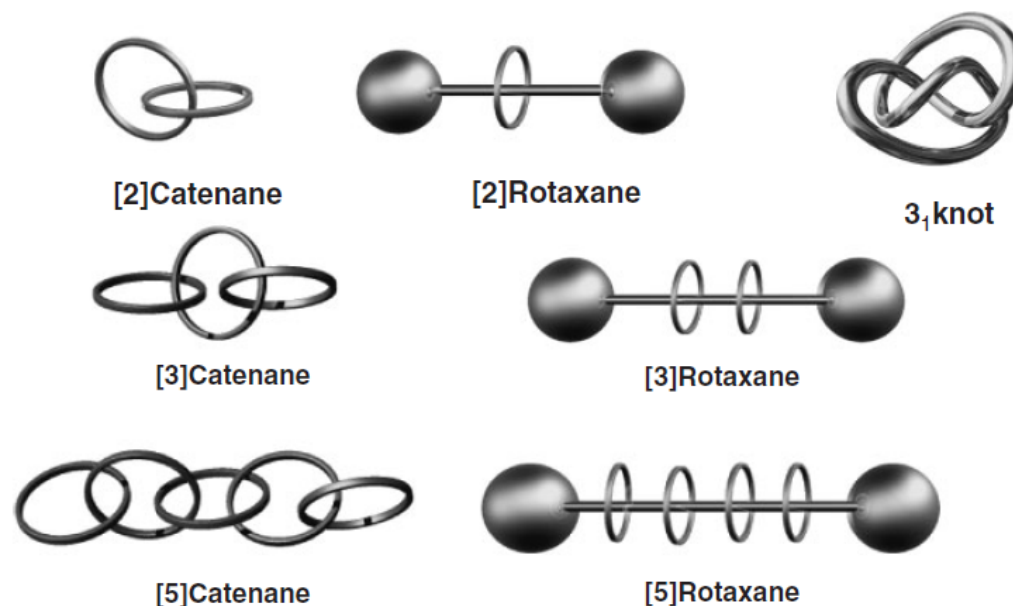


Figure 2.22: Different classes interlocked supramolecular structures [121]

a [3]rotaxane, and so on up to [5]rotaxane. If there is a larger or intermediate number of rings present on a polymeric guest, the compounds are denoted as polyrotaxanes [122]. Rotaxanes are prepared by threading the axis through the ring. Usually a so-called template method is applied, where host-guest interactions between the rotaxane constituents provide for high yields. Complexes of various organic host compounds such as crown-ether complexes [121], hydrogen bond complexes of cyclic peptides [123] or donor - acceptor complexes [124] have been used to synthesise rotaxanes. But the by far most common host molecules are CDs [21, 125, 126]. As already described in section 2.2, they offer several advantages since they are able to form complexes with a whole range of guests, are readily available and can be selectively functionalised. So the following sections will focus on CD based rotaxanes.

2.3.2 CD-based rotaxanes

Generally there are three different approaches to the construction of rotaxanes. Attaching bulky substituents to the ends (the so called rotaxanation reaction) after “threading” is by far most common method to produce CD based rotaxanes (Figure 2.24 a). The “slipping” approach (Figure 2.24 b), involving threading of the CD over a dumbbell shaped template, mostly leads to pseudo-rotaxanes. For CD-based rotaxanes the so called “clipping” is not practical, since the acyclic oligosaccharide precursor would only interact weakly with the guest and the cyclisation reaction would even further decrease the yield [125].

There are several limitations that render the production of CD-containing rotaxanes a rather challenging task. At first axis and ring have to form stable host guest complexes, which implies most importantly that the guest molecule fits into the host cavity. Furthermore the axis has to exceed the CD cavity to allow the functionalisation with stoppers. To provide for stable complexes the complexation needs to be carried out in water or other strongly polar solvents like DMF or DMSO which do not cause or only

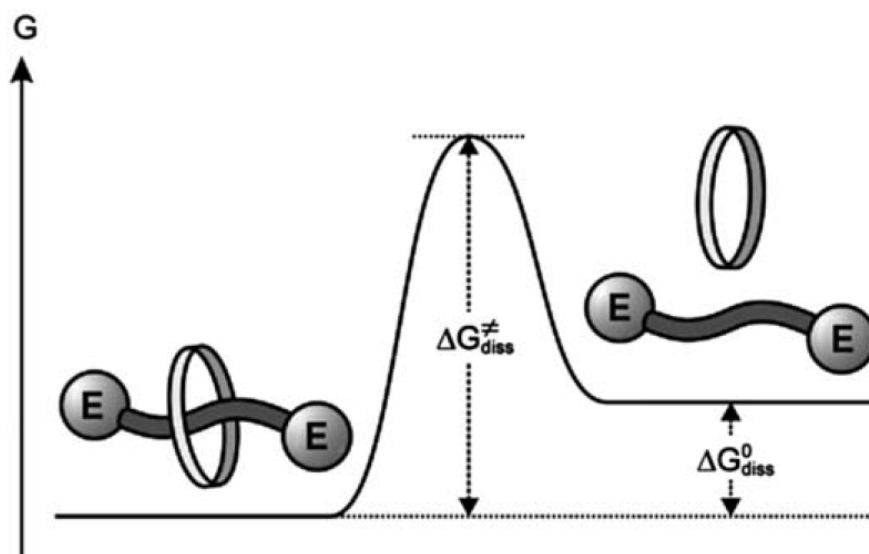


Figure 2.23: Energy diagram for the dissociation of a [2]-rotaxane into its components. E indicates the endgroups [21]

limited dissociation. Moreover the rotaxation reaction needs to be performed in one of these solvents and give high yields with a suitable end-group bulky enough to prevent dethreading. Bola amphiphiles such as bis-amino-alkanes, longer than 1 nm are the most suitable guest molecules because of their solubility and readily modified terminal functional groups. E.g. one of the first syntheses of CD rotaxanes has been carried out with 1,10-diaminodecane threaded through α -CD in DMSO solution, being end-capped with bulky bis(ethylenediamine)-Co(III) complexes [125]. But also rotaxanes with β - and γ -CD are reported which obviously require larger stopper groups due to the increased cavity diameters, e.g. naphthalene-3-6 disulphonate (β -CD) [21] and m-terphenyl-4,4'-dicarboxylic acid (γ -CD) [84].

2.3.3 CD-based polyrotaxanes

Polymers which incorporate CD rings as covalently bound monomers within linear and cross-linked macromolecules are well-known. They have been already briefly described in section 2.2. The most common approach to create novel polymeric structures containing CD rings is to take advantage of their supramolecular properties. An obvious extension of CD-based [2]rotaxanes is in the direction of [n]rotaxanes or polyrotaxanes. But also rotaxane formation with branched polymers or supramolecular polymers built of monomers with an axis covalently linked to a ring are possible architectures and will be discussed in the following sections (Figure 2.25).

Pseudo polyrotaxanes

Typically linear pseudo polyrotaxanes are obtained by threading of CDs onto a polymeric chain. It has also been reported that monomeric inclusion compounds in solution or channel inclusion complexes of monomers in solid state can be polymerised, which is a challenge

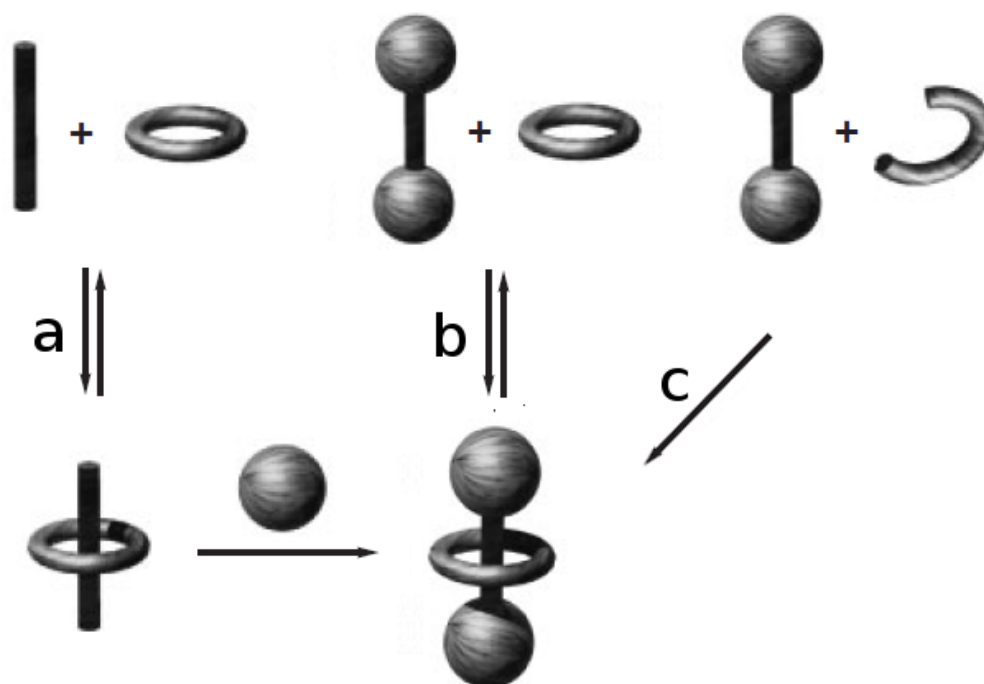


Figure 2.24: Methods for rotaxane formation: a. threading, b. slipping and c. clipping approach [121]

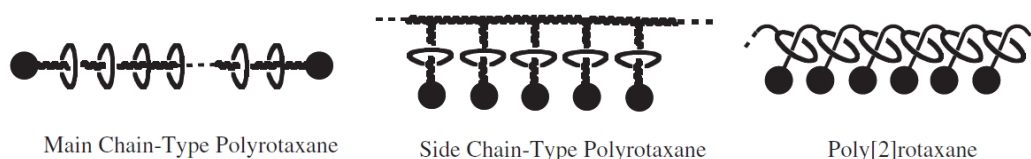


Fig. 2.25: Different CD based polyrotaxane architectures [121]

since polymerisation and complexation conditions rarely match [127, 128].

Threading of polymers with CDs is the easiest and most common way to get access to linear pseudo polyrotaxanes. They have been first described by Harada et al. who synthesised insoluble crystalline channel like inclusion complexes with PEG and α -CD from concentrated aqueous solutions of the compounds [129]. In order the complexes to be formed, a minimum degree of polymerisation of 4 is required and the rate of complexation reaches a maximum for MW around 10^3 g/mol. Generally for fully covered complexes the stoichiometry depends on the length of CD unit and the length of the polymer repeat unit, which is 2:1 (two ethylene glycol units to one α -CD) for the system PEG/ α -CD [20]. Due to kinetic reasons inclusion gets increasingly more difficult with rising MW and becomes virtually impossible for polymers larger than 10^5 g/mol. For PEGs of MW > 2000 g/mol gel-like structures are formed [130] and for MW > 8000 g/mol thermodynamically stable hydrogels are obtained [131].

But also many other polymers have been successfully included into the different CDs. The main criterion for the complexation is that there is good match between the cross-sectional areas of the CD cavities and the polymer [21]. E.g. β -CD forms pseudo

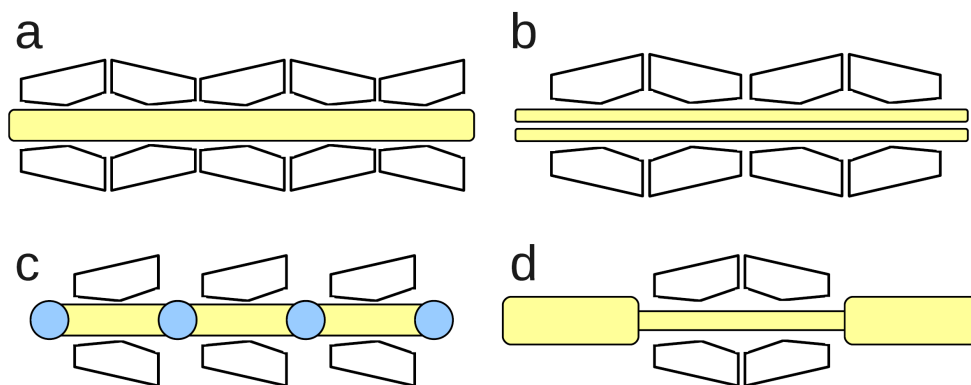


Fig. 2.26: Schematic drawing of pseudo polyrotaxane complexes: a. channel-like complex, b. double-stranded complex, c. soluble poly-bola-amphiphile complex, d. block-copolymer complex

polyrotaxanes with with polypropylene glycol (PPG) and γ -CD with polyisobutene and many more examples can be found in literature [21, 125, 126]. A remarkable effect upon complexation is observed in the case of γ -CD and PEG modified with two naphthylacetyl residues as end groups since double-stranded inclusion compounds are formed [132]. Water-soluble complexes can be prepared from CDs and polyelectrolytes such as charged poly(iminooligomethylenes) [133]. The charged groups within the polymer prevent dense channel-like packing of the CDs. These complexes can be seen in analogy to bola-amphiphile complexes and can therefore also be called poly-bola-amphiphiles. By using block-co-polymers site-selective threading has been achieved, where the CDs occupy the segment which fits best into their cavity. E.g. pseudo polyrotaxanes have been prepared with PPO-PEO-PPO tri-block co-polymers where the α -CD preferentially occupies the PEO part [134, 135].

Instead of using a linear polymers it possible to form so called side-chain polyrotaxanes with polymers where binding sites are grafted as side-groups to the main chain (Figure 2.25 b). The threading of the side group polymers is much faster compared to the linear macromolecules since the binding events occur independently of each other. Likewise the dissociation proceeds much easier. Therefore the inclusion process is considered to be very similar to monomeric guests mainly governed by the same parameters as described in section 2.2 [136].

Threading Process

Threading of the CDs on the polymer chains is a complex process which is subject to kinetic and thermodynamic control [137]. Since usually a large excess of CDs is employed the threading can be regarded as a pseudo-first-order process



where σ^\ddagger represents the rate-determining transition state, indicating an unstable intermediate structure that corresponds to an activation energy to be overcome for the pseudopolyrotaxane to form. With the help of turbidity measurements thermodynamical parameters for several pseudopolyrotaxane systems of different MW, and CD sizes have been established [137].

Generally the inclusion of polymer guests is a reversible process which is mainly driven by a highly negative binding enthalpy ($\Delta H \approx -105$ kJ/mol [138]). It mainly arises from hydrophobic and van der Waals interactions between polymer and CD, as well as from intermolecular hydrogen bonds between the threaded CDs. Since the van der Waals forces decrease significantly with the distance, strong complexes are only formed when the cross-sectional areas of the CD cavity (A_{CD}) and the polymer (A_{pol}) match. This can be quantified with the help of the so called space filling quotient $\Phi = A_{pol}/A_{CD}$, which is normally found to be in the order of 0.9 - 1.2 for compounds which form polyrotaxanes. To maximise the hydrogen bond stabilisation, densely packed channel pseudo polyrotaxanes are predominantly threaded in head to head and tails to tails conformation. The strong intermolecular hydrogen bonding is also the key reasons why pseudo polyrotaxanes exhibit poor solubility. Pseudo polyrotaxanes with modified CDs and substituents which disrupt the intermolecular hydrogen bond formation (e.g. methylated CDs) improves their solubility but generally renders the complexes less stable [21].

Entropic contributions usually favor the dissociation of the complexes because both, the polymer as well as the CD, lose conformational flexibility upon threading since the macrocycle enforces more trans conformations along the polymer chain [136]. The threading is entropically disfavored which is reflected by the process getting less efficient with increasing temperatures consequently increasing the entropies of solvent, CD and polymer.

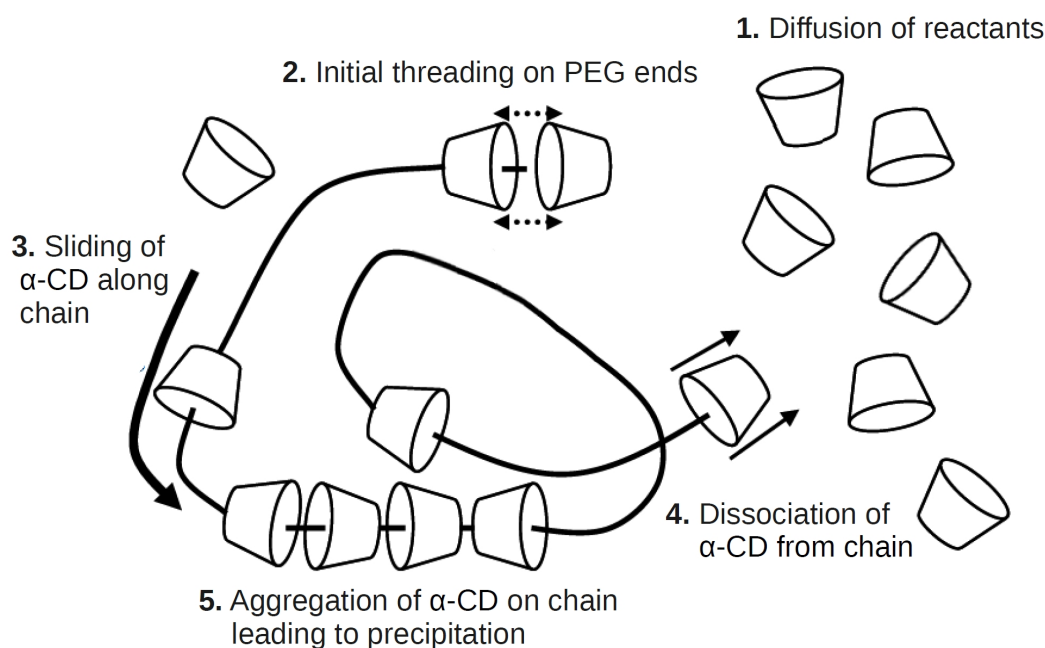


Fig. 2.27: Schematic representation of threading process

The threading process for linear polymers can be regarded as a serial process in which the different steps are dependent on each other like displayed in Figure 2.27 [139]. It involves (1) the diffusion of the polymer and CD molecules in the solvent medium. Furthermore it requires (2) the initial threading of the host molecules on the guest chain, which needs at least a partial stretching of the random coil polymer chain in solution. Simultaneously the solvating water molecules from the surface of the polymer and the CD cavities have to be released. Then (3) the CD molecules have to slide along the polymer

chain so that more cavities can be penetrated. In this step, the CDs force the polymer chain to stretch further to avoid direct contact between the polymer and the aqueous environment [140]. The packing of the CDs on the template chain leads to a more rod-like conformation and decrease in flexibility, leaving the chain ends more accessible for complexation [141]. Since it is an equilibrium process, partial dissociation (4) of a few CDs from the polymer ends occurs. However, once the CD molecules have complexed the guest, dethreading is inhibited because of hydrophobic interactions and because the vicinal threaded CD units act as physical stoppers [142,143]. Finally for a uncharged nonlinear polymer due to the hydrogen bonding (5) CD aggregates on the chain are formed which leads to aggregation of several pseudo polyrotaxanes in bundles that eventually precipitate [137].

Among different factors, like solvent, MW of the polymer and salt effects, the temperature plays a crucial role in the threading process and effects the different steps in various ways. Heating of precipitated pseudo polyrotaxanes leads to redissolution by dissociation of the inclusion compounds since the hydrogen bonds are weakened. Generally the complexation rate decreases with increasing temperature, as well as MW and decrease in concentration [20]. Applying temperature cycles, such as heating followed by cooling, during the threading process allows to control the number of CDs threaded on the chain and higher threading ratios for high MW polyrotaxanes can be obtained. This has been explained by the formation of sparsely complexed soluble pseudo polyrotaxanes at high temperatures, which serve as active nucleation centers to further auto-catalyse the final complexation when the temperature is decreased to lower temperatures leading to more complexed polymers [141].

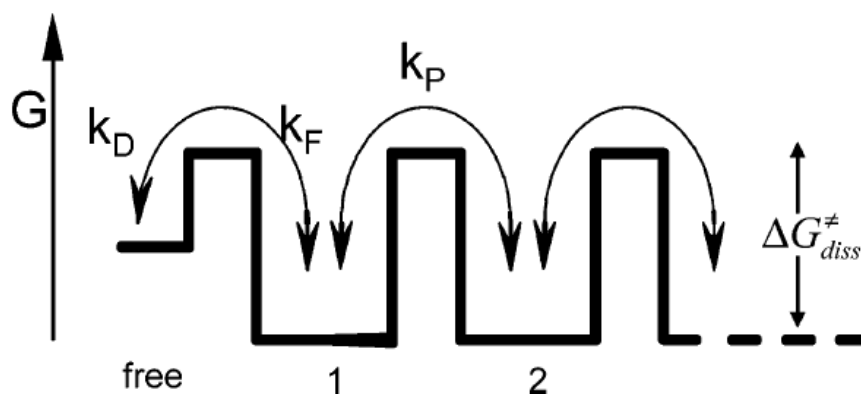


Fig. 2.28: Schematic representation of hopping model for poly-bola-amphiphiles. The free energy, G , of a CD ring as a function of its location on the polymer. 1, 2: Segments 1 and 2 on the polymer, free: free CD; k_D , k_F , and k_P are rate constants of dissociation, formation, and propagation; $\Delta G_{diss}^{\ddagger}$: free activation energy for dissociation and propagation [84]

For soluble linear poly-bola-amphiphiles with ionic groups the threading rate of CDs is strongly decreased with the degree of polymerisation. In this case the threading process can be described by a hopping model, where the CDs move from one hydrophobic segment to another (Figure 2.28). For each hopping step a high activation energy, similar to the one for monomeric bola-amphiphiles has to be overcome leading to a “molecular traffic jam”, so that polymers with large ionic groups can only be threaded in a reasonable time at high temperatures. At room temperatures such compounds are almost kinetically stable [21,84].

Polyrotaxanes

To transform the pseudo polyrotaxanes in kinetically stable polyrotaxanes, bulky stoppers have to be attached to the polymer so that the rings are mechanically interlocked. They can be coupled either at both chain ends or along the chain. However the first approach is by far the most common. Evidently the endgroups have to be large enough to prevent dethreading of the rings. The coupling reaction has to be carried out in the complexation solvent or in a solvent where no dissociation of the pseudopolyrotaxane occurs. Furthermore it should be fast and high yielding. The polymer chain has to be functionalised at both ends with terminal groups with orthogonal reactivity compared to the OH groups. This is important since the stopper molecules must be bound with severe selectivity only to the end of the polymer chain and not to the CD rings. Although polymers with other terminal functionalities are reported, very often amino-end groups are used since they do not disturb the threading process and a whole variety of coupling reactions exist. Since the end-capping reaction is a significant step that governs the yield and/or characteristics of the obtained polyrotaxane, various synthetic approaches have been explored, as displayed in Figure 2.29. It should be noted that almost all of the polyrotaxanes synthesized to date comprise PEG or PEG-containing block copolymers, in spite of the numerous reports on pseudopolyrotaxane formation by a wide variety of polymers, as stated in the previous section.

Another synthetic technique for producing polyrotaxanes is the polymerization of pseudorotaxanes. This route is only useful for the few cases where the polyrotaxane is end-capped with a self-reactive functional group. Subsequently an entity is formed that is large enough to block the CD dethreading process (Figure 2.30)

Yet another approach to generating polyrotaxanes is to randomly block the threaded polymer along its length in a process called statistical end-capping (Figure 2.31). This was the route originally pioneered by Wenz and coworkers who developed one of the first polyrotaxanes [150]. The major advantage of this procedure is that the stoppering reactions do not necessarily need to be quantitative. The polymer requires many reactive sites in the chain and a loose coverage with CDs so that they remain accessible for the stopper. Pseudopolyrotaxanes of poly(bola-amphiphile)s, e.g. polyamines are the most suitable molecules for such reactions. The reaction produces threaded segments of random length, consequently leading to highly heterogeneous polyrotaxanes.

2.3.4 Characterisation of Rotaxanes

Scattering techniques

Once the polymer is threaded through the CDs, the high molecular weight complex usually precipitates out of solution. This characteristic of pseudo polyrotaxanes makes turbidity analysis a convenient technique to study the rate of threading or dethreading reactions [20]. By observing the change in turbidity of a pseudopolyrotaxane suspension as a function of time, the kinetics of the threading process may be determined [137, 139].

Although suitable crystals, in particular for polyrotaxanes are rarely obtained, the best

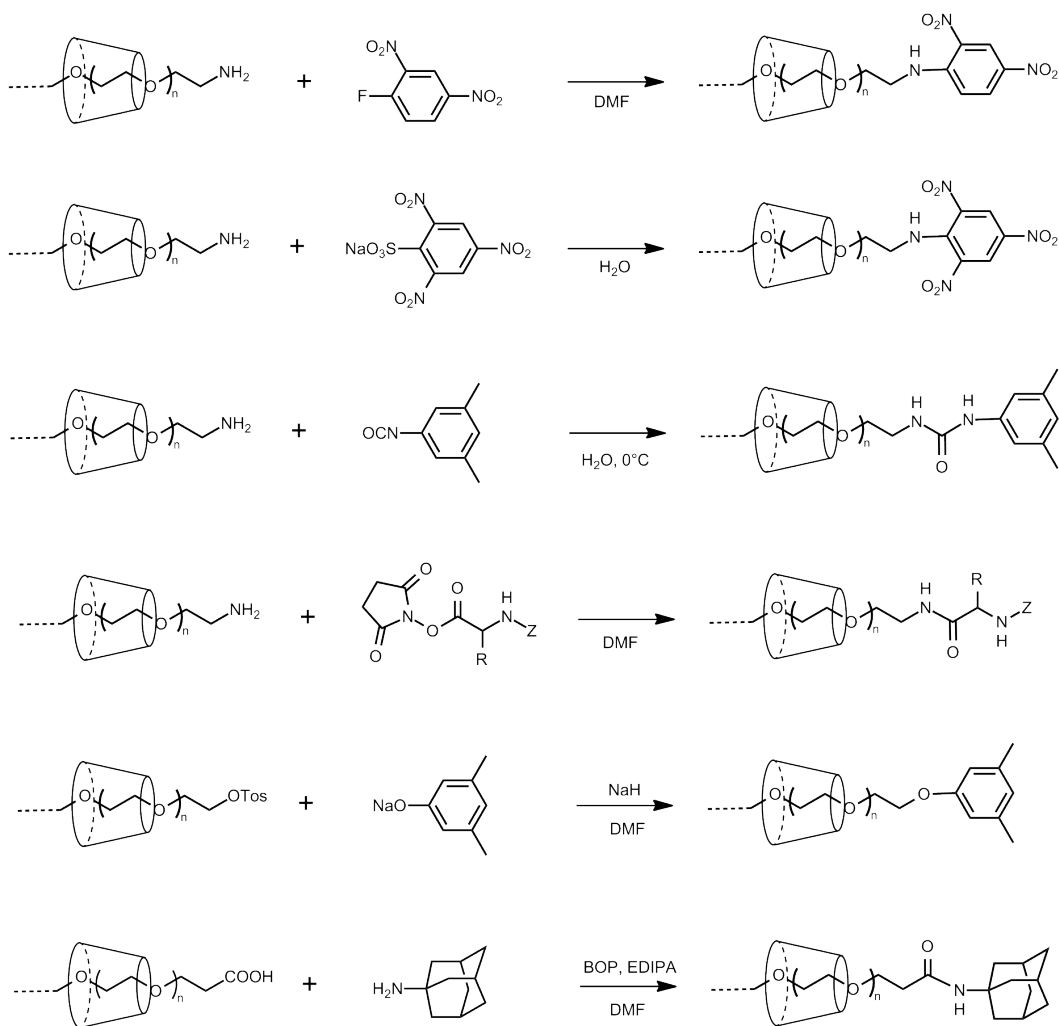


Fig. 2.29: Examples for terminal end-capping reactions [141,144–148]

evidence for formation of rotaxanes is a detailed x-ray structure. Yet it requires large enough rotaxane single crystals which are most of the times not available. Especially for polyrotaxanes which form insoluble channel inclusion compounds this is seldom the case since they rapidly precipitate as form of powders. Therefore only very few extensively characterised x-ray structures are available, which demonstrate, that suitable stoppers only have to be slightly larger than the cavity diameter [21,151]. For polyrotaxanes only more soluble loosely complexed structures are known which clearly show that the CDs are arranged in a head-to-head and tail-to-tail conformation [152].

In most cases, powder x-ray diffraction (XRD), one of the original techniques used to

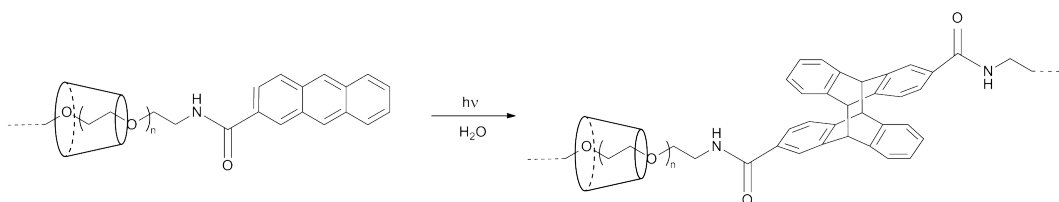


Fig. 2.30: Example for self end-capping reaction [149]

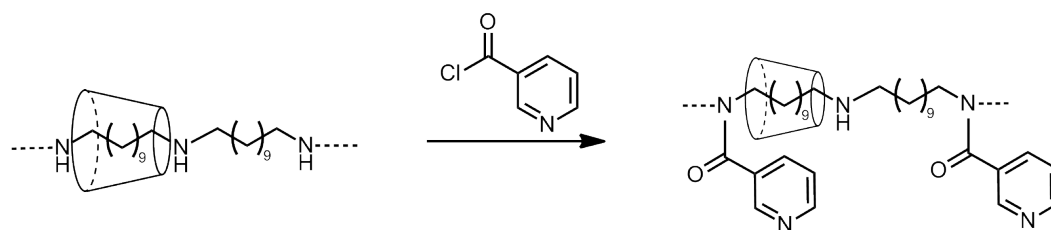


Fig. 2.31: Example for statistical end-capping [150]

characterize these structures, is usually the most informative [20]. With this method it is possible to distinguish free CDs with its typical herringbone structure in solid state from inclusion compounds which produce a hexagonal column type structure. Thus the more symmetric channel inclusion complexes show powder diffractograms with less reflections and characteristic peaks at $2\Theta = 20^\circ$ [129, 153]. It has also been reported that there are two crystalline states during the precipitation of α -CD - PEG complexes. The first one is the expected head-to-head and tail-to-tail arrangement, which slowly reorganises in the second one, which is a columnar structure with a head-to-tail arrangement [154]. Powder diffractograms of β -CD-based polyrotaxanes produce less structured XRD patterns since β -CD possesses a lower symmetry and is therefore less capable of packing into symmetric structures [155].

Other scattering techniques like Small Angle Neutron and X-ray Scattering (SANS and SAXS respectively) or dynamic light scattering (DLS) are used to get insight into the structure of polyrotaxane gels and to understand the mechanism of the aggregation [126, 156].

NMR spectroscopy

NMR spectroscopy is a useful tool for characterisation of the inclusion compounds. For rotaxanes direct proof for rotaxanation can be obtained due to splitting of the signals of the axis atoms due to the asymmetric environment provided by the surrounding CD ring. NMR techniques exploiting the nuclear Overhauser effect (NOE), especially between the internal protons H-3 and H-5 of the CD and the protons of the axis, can provide evidence for the rotaxane formation, as well as information about the preferred location of the ring on the chain can be obtained [21]. For channel inclusion compounds solution NMR can be applied to determine the polymer/CD ratio in the solution. But typically it cannot be convincingly establish whether or not the polymer is included in the macrocycle. By analyzing the CD ^1H NMR T_1 and T_2 relaxation times, however, the relative mobility of the CDs can be determined to indicate whether they are in a rigid (i.e., highly threaded) or mobile (i.e., sparsely threaded) environment [157]. Using diffusion-ordered 2D-NMR spectroscopy (DOSY), the self diffusion coefficients of the compounds in solution can be correlated to each other, proving that CD and axis diffusion coefficients coincide when rotaxanation occurs [147]. Furthermore it has been observed that for PEG the dynamics of the included polymer are faster than the one in solution [158].

Solid state NMR methods are good tools to get access to structural information about crystalline or gelled polyrotaxanes. E.g. with ^{13}C CP/Magic Angle Spinning (MAS) NMR typical peaks of the CD's C-1 and C-4 atoms appear when an inclusion compound

is formed due to its higher symmetry compared to free CDs [20]. MAS 2D ^1H NMR has been used to give information about the nature of polyrotaxane gel structures [156]. Threading of water soluble rotaxanes like poly(bola-amphiphiles)s can be followed by solution NMR. There are signals in ^1H NMR spectrum, which can be distinguished between complexed and free CDs as well as covered and unthreaded polymer axis. The peak assigned to the anomeric protons of the CD's glucose units is particularly useful since it is shifted from 5.05 ppm to 5.10 ppm when the CD is complexed. This allows e.g. to measure the threading kinetics by comparing the integration of free and complexed CDs [21].

Mass spectrometry

Mass spectroscopy (MS) provides further insights into the structure of polyrotaxanes. But it has to be kept in mind that absence of a molecular ion does not necessarily mean that no rotaxane has been formed since ionisation and evaporation might be tricky especially for high MW polyrotaxanes with low solubility and high polydispersity. Also detection of corresponding MW compound might be only caused by an aggregate with a different structure than a rotaxane. Therefore the MS data usually needs to be backed by complementary experiments. Using MALDI-TOF, mass spectra of e.g. β -CD based polyrotaxanes have been obtained [159]. In a special case it was even possible to get mass spectra of a water soluble diblock pseudopolyrotaxane. This is rare in the characterization of polyrotaxane materials since CD-based pseudo polyrotaxanes have very low solubility and are typically dethreaded once the complex is dissolved [160].

Gel permeation chromatography

Gel permeation chromatography (GPC) is widely employed to estimate the approximate molecular weights of polyrotaxanes [141, 148, 161]. GPC can definitively distinguish between a polyrotaxane and a pseudopolyrotaxane (which dethreads to give the retention times corresponding to the polymer and CDs). Accurate MW determinations need the calibration of the GPC with adequate MW standards. This is a difficult task since high MW, highly threaded, polyrotaxanes behave unlike any commercially available standard available, due to their semi-rigid rod-like morphology. Use of conventional MW standards give rise to molecular mass approximations which are unreasonably high. This problem indicates the necessity of confirming the polyrotaxane MW by other techniques, such as ^1H NMR integration comparison between the polymer and the CDs. Column selection is crucial as some of the highly threaded polyrotaxanes will only dissolve in very polar organic solvents (e.g., DMSO, DMSO with 1% LiCl, or DMAC with 8% LiCl). Thus a column matrix that can withstand these harsh solvents must be selected [126].

Imaging

Using imaging techniques like Scanning Tunneling Microscopy (STM) and Atomic Force Microscopy (AFM) channel-like polyrotaxanes can be visualised with remarkable detail since they are rather stiff and rod-like compounds. STM images have been obtained of the crystal structure of α -CD/PEG pseudo polyrotaxanes. But also single polyrotaxanes have been imaged and the orientations of the CDs threaded on a polyrotaxane with respect

to their neighboring CD has been revealed. Furthermore it has been demonstrated, that individual CDs can be manipulated to slide along the polymer chain as a type of molecular abacus [162]. AFM images have e.g. been reported of β -CD/poly-para-phenylene polyrotaxanes. The observed structures of the tubes have roughly the expected width and height for a CD [159].

Chapter 3

Experimental Techniques

3.1 Chemicals

In order to ensure comprehensibility and legibility throughout the text abbreviations have been introduced for some compounds which are specified in Table 3.1.

Abbreviation	Name of the compound
TASC	6 ^I -(cholesteryl)succinylamido-6 ^I -deoxy-2 ^I ,3 ^I -di-O-methyl-hexakis (2 ^{II-VI} ,3 ^{II-VI} ,6 ^{II-VI} -tri-O-methyl)cyclomaltohexaose
TBSC	6 ^I -(cholesteryl)succinylamido-6 ^I -deoxy-2 ^I ,3 ^I -di-O-methyl-hexakis (2 ^{II-VI} ,3 ^{II-VI} ,6 ^{II-VI} -tri-O-methyl)cyclomaltoheptaose
TBdSC	di-(6 ^I ,6 ^{IV} -(β-Cholesteryl)succinylamido-6 ^I ,6 ^{IV})-deoxy-2 ^I ,3 ^I -di-O-methyl-hexakis (2 ^{II-VI} ,3 ^{II-VI} ,6 ^{II-VI} -tri-O-methyl)cyclomaltoheptaose
DPPC	1,2-Dipalmitoyl-syn-glycero-3-phosphocholine mono-hydrate
DPPC-D62	1,2-Dipalmitoyl-D62-sn-glycero-3-phosphocholine
DSPE	1,2-Distearoyl-sn-glycero-3-phosphoethanolamine
DMT-MM	4-(4,6-Dimethoxy-1,3,5-triazin-2-yl)-4-methylmorpholinium chloride
DMPENOC	2,5 dimethoxyphenyl-1-ethyl isocyanate
PMDETA	N,N,N,N,N-Pentamethyldiethylenetriamine
THPTA	Tris(3-hydroxypropyltriazolylmethyl)amine

Table 3.1: Abbreviations introduced for certain compounds

The chemicals and solvents used throughout the physcial characterisation of the amphiphilic CDs and the STLs are listed in Tables 3.2 and 3.3 respectively.

Name	Formula	Molar Mass [g/mol]	Provider
TASC	C ₈₅ H ₁₄₄ O ₃₂ N	1690,83	own laboratory
TBSC	C ₉₃ H ₁₅₉ NO ₃₇	1883.29	own laboratory
TBdSC	C ₁₂₃ H ₂₀₆ N ₂ O ₃₉	2337.00	own laboratory
DPPC	C ₄₀ H ₈₀ NO ₈ P	734.39	Sigma
DPPC-D62	C ₄₀ H ₁₈ D ₆₂ NO ₈ P	796.43	Avanti Polar Lipids
Deuterium Oxide	D ₂ O	20.03	provided from ILL
Chloroform	CHCl ₃	119.38	Riedel-de Haen
Milipore water(18MΩcm)	H ₂ O	18.02	own laboratory

Table 3.2: Chemicals used for the characterisation of the permethylated cholesteryl CDs

Name	Formula	Molar Mass [g/mol]	Provider
STL 3k			own laboratory
STL 6k			own laboratory
STL 10k-DMPE			own laboratory
STL 10k-Adamantane			own laboratory
STL 20k			own laboratory
Cholesteryl α -CD	$C_{73}H_{118}N_4O_{32}$	1521.65	own laboratory
Cholesteryl β -CD	$C_{79}H_{128}N_4O_{37}$	1783.79	own laboratory
DPPC	$C_{40}H_{80}NO_8P$	734.39	Sigma
DPPC-D62	$C_{40}H_{18}D_{62}NO_8P$	796.43	Avanti Polar Lipids
DSPE	$C_{41}H_{82}NO_8P$	748.07	Avanti Polar Lipids
Deuterium Oxide	D_2O	20.03	provided from ILL
Chloroform	$CHCl_3$	119.38	Riedel-de Haen
Ethanol	C_2H_6O	46.07	VWR
Methanol	CH_4O	32.04	Sigma-Aldrich
Milipore water(18M Ω cm)	H_2O	18.02	own laboratory

Table 3.3: Chemicals used for the characterisation of the STLs

3.2 Langmuir Film Balance

3.2.1 Langmuir Isotherms

The Langmuir Balance is the first method to characterise monolayers of amphiphilic molecules, also called Langmuir films, at the air-water interface. By spreading of an insoluble amphiphilic compound dissolved in a volatile, organic solvent, on a water surface, a monolayer is produced once the solvent is evaporated. Due to their unique asymmetric structure amphiphiles self-assemble with its hydrophilic parts immersed in the water and with their hydrophobic parts projecting into the air. Using the film balance technique it is possible to continuously vary the available area per molecule A at the surface via movable barriers and to study the compression behavior of the monolayer. Caused by the presence of the amphiphiles, the surface tension of the pure subphase γ_0 is lowered and can be expressed by the surface pressure

$$\Pi = \gamma_0 - \gamma. \quad (3.1)$$

The surface pressure Π is in most cases determined using the so called Wilhelmy plate method, which measures the force due to the surface tension on a plate (made of filter paper or platinum) touching the subphase [33]. Thus Langmuir (Π -A) Isotherms can be recorded.

3.2.2 Isotherm Analysis

The free surface area per molecule A is calculated from the concentration of the spread solution c , the surface area of the trough A_S and the spreading volume V_S

$$A = \frac{A_S}{N_A c V_S}, \quad (3.2)$$

with the Avogadro constant N_A .

In order to better identify phase transitions in the isotherms, the derivative of the surface pressure Π with respect to the molecular area A is determined from the isotherms to obtain the isothermal compressibility

$$C_S = -\frac{1}{A} \left(\frac{dA}{d\Pi} \right)_T. \quad (3.3)$$

It is calculated numerically from the data as follows:

$$C_S = -\frac{1}{A_i} \frac{(A_{i+1} - A_i)}{(\Pi_{i+1} - \Pi_i)}, \quad (3.4)$$

where A_i and Π_i are the molecular surface area and surface pressure corresponding to data point i in the isotherm. For further analysis we have taken the reciprocal isothermal compressibility to give the inverse compressibility modulus C_S^{-1} which is a measure for interfacial elasticity. The smaller C_S^{-1} the higher is the film elasticity [163–165]. For better visibility of the two-dimensional phase transition the C_S^{-1} values are plotted in a log scale. To find out about the mixing behavior, the excess free mixing energy ΔG_{mix}^{ex} can be determined from the difference of work of compression between the ideal and real mixed films, which is determined by integrating the experimental Langmuir isotherms (3.5)

$$\Delta G_{mix}^{ex} = \int_0^\Pi [A - (x_1 A_1 + x_2 A_2)] d\Pi, \quad (3.5)$$

where A is the molecular area for the binary mixture. A_n and x_n are the molecular area and molar fraction of the monolayer components [166].

3.2.3 Film Deposition

Apart from being used to study monolayers, the film balance can also be applied to transfer Langmuir films on a solid substrate. This is achieved by modifying the Langmuir balance with a dipper and a well so that the sample can be moved up and down through the monolayer. Following compression, the desired surface pressure is kept constant by a computer controlled feedback system. In the case of Langmuir-Blodgett (LB) deposition the sample is moved vertically through the monolayer (Figure 3.1 a), while with the Langmuir-Schaeffer (LS) method the sample is approach horizontally to the interface (Figure 3.1 b).

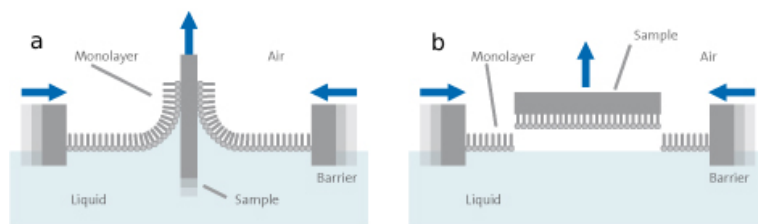


Figure 3.1: Langmuir monolayer transfer on a solid substrate [167]

Depending on the substrate, which can be hydrophobic (e.g. a silanised silicon wafer) or hydrophilic (e.g. SiO_2 or mica), the monolayer adsorbs with its aliphatic chains or headgroups on the surface of the solid support. It is possible to create multi-layered systems of defined composition and thickness by dipping the sample up and/or down several times. Hydrophilic deposition is achieved by rising and hydrophobic deposition by lowering the substrate through the monolayer. So different kinds of distinct deposition patterns can be obtained for multiple monolayers, like supported bilayers or double bilayers [39, 168, 169].

Experimental Setup

The surface pressure - area isotherms have been measured with a temperature controlled Langmuir balance (702BAM Film Balance for Brewster Angle Microscopy, Micro Processor Interface IU4, NIMA Technology) which is used in conjunction with a BAM. The trough as well as the two computer controlled barriers are made of Teflon. It possesses a maximum surface area of 700 cm², a minimum surface area of 80 cm² and is filled with approximately 500 ml ultra pure water subphase. The trough, placed on an anti-vibration table, is covered by a plastic hood to prevent contamination of the surface by dust and subphase evaporation. If not mentioned differently, isotherms are recorded with a compression speed of 15 cm²/min and at a temperature of 20°C. The solution is spread with a Hamilton syringe and the compression is started 15 min after the sample is introduced in order to let the CHCl₃ evaporate.

3.3 Brewster Angle Microscopy

The Brewster Angle Microscope (BAM) is a non-invasive technique which enables the direct visualisation of molecular monolayers at the air-water interface or dielectric substrates. It was developed simultaneously by two groups in Göttingen [170] and Paris [171] in 1991 and is routinely used for imaging ultra-thin films on air-water interfaces.

3.3.1 Principle

Light can be described as a plane electromagnetic wave of wavelength λ with an electric component E and a magnetic component H which are perpendicular to each other. In the case of refraction and reflection phenomena the orientation of the electric field vector with respect to the plane of incidence can be specified, which is called polarisation. The magnetic component of the electromagnetic field is usually irrelevant. Figure 3.2 displays the behavior of a light beam with defined state of polarisation moving through an interface formed by two isotropic dielectric media with refractive indices n_1 and n_2 , whereas $n_1 < n_2$.

The relationship between the angle of incidence Θ_{in} and the angle of refraction Θ_{tr} is described by Snell's law

$$n_1 \sin \Theta_{in} = n_2 \sin \Theta_{tr}. \quad (3.6)$$

With the help of the Fresnel equations the intensity of the reflected light wave can be calculated which is dependent on the polarisation of the incident ray. For s-polarised light, polarised perpendicular to the plane of incidence, the reflectivity R_S is given by

$$R_S = \left[\frac{\sin(\Theta_{tr} - \Theta_{in})}{\sin(\Theta_{tr} + \Theta_{in})} \right]^2 = \left[\frac{n_1 \cos \Theta_{in} - n_2 \cos \Theta_{tr}}{n_1 \cos \Theta_{in} + n_2 \cos \Theta_{tr}} \right]^2 \quad (3.7)$$

and for p-polarised light polarised in the plane of incidence can be written

$$R_P = \left[\frac{\tan(\Theta_{tr} - \Theta_{in})}{\tan(\Theta_{tr} + \Theta_{in})} \right]^2 = \left[\frac{n_1 \cos \Theta_{tr} - n_2 \cos \Theta_{in}}{n_1 \cos \Theta_{tr} + n_2 \cos \Theta_{in}} \right]^2. \quad (3.8)$$

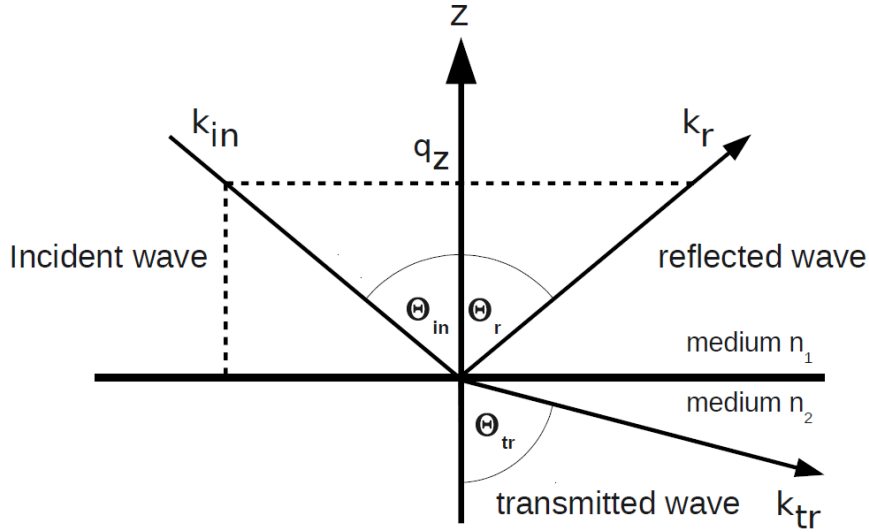


Figure 3.2: Reflection and Refraction of a plane wave at a interface

At a certain angle of incidence $\Theta_{in} + \Theta_{tr} = 90^\circ$ for p-polarised light. In this case the denominator of equation (3.8) becomes ∞ and $R_P = 0$. This angle of incidence, where the electric wave vector of the reflected light has no component in plane, is called the Brewster angle Θ_B

$$\Theta_B = \arctan \frac{n_2}{n_1}, \quad (3.9)$$

which depends on the refractive indices of the two media [172]. For an air-water interface with $n_1 = 1$ for air and $n_2 = 1.3345$ for water (at 20°C , $\lambda = 545 \text{ nm}$) the Brewster angle is defined as

$$\Theta_B = \arctan \frac{1.3345}{1} = 53.15^\circ. \quad (3.10)$$

The BAM is based on irradiating the interface between two isotropic media (e.g. air-water, $\Theta_B = 53^\circ$) with a p-polarised light beam at the Brewster angle Θ_B . In this case the ray is only transmitted through the media and no reflection occurs at the surface and no light is detected. If the optical properties at the interface are altered by spreading a monolayer of organic molecules, the Brewster angle changes and the incident beam is partly reflected. Since the pure water surface produces no signal in the detector, the reflected light on the monolayer can be detected with very high contrast. Different domains in the film which of typical sizes between $10 - 100 \mu\text{m}$ can be visualised (Figure 3.3).

Experimental Setup

The Brewster Angle Microscope (BAM), type PI, C-138K003, Optrel GBR, Berlin, co-aligned with the Langmuir trough, described in section 3.2 is based on the Hoenig and Moebius setup [170]. A green laser (LasNova series 50) with a wavelength of 532 nm , polarised by a polarisation filter is directed onto the water surface at the Brewster Angle

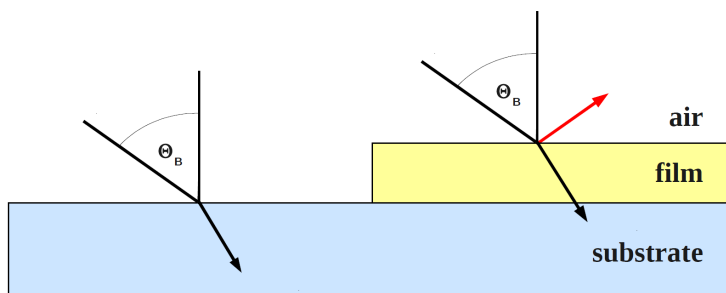


Figure 3.3: Principle of the BAM microscope

(53.1°). The reflected light from the surface, focused by a 10x objective (Mitutoyo), is visualised by means of a CCD camera (EHD@kamPro02) to give images of the monolayer morphology with a size of $480\mu\text{m} \times 599\mu\text{m}$ and a resolution of 480×640 pixel. All BAM images are corrected with a factor of $1/\cos \Theta_B$ in vertical (y-) direction. The whole BAM - Langmuir balance set up is set on an anti-vibrational table and covered with a hood. The focus of the BAM is operated with a computer controlled stepper motor which allows taking images online while recording an isotherm [173].

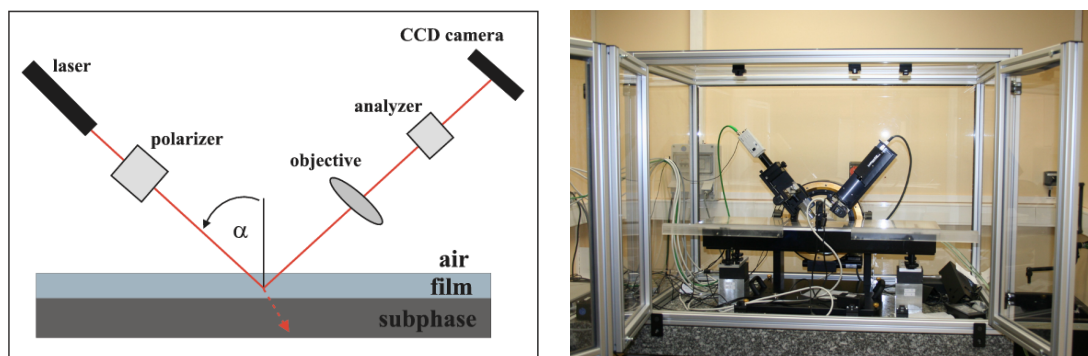


Figure 3.4: Scheme of the BAM setup and picture of BAM in our laboratory

3.4 Atomic Force Microscopy

The Atomic Force Microscope (AFM) can be classified as a scanning probe microscope which skims the surface of an object. Being developed in 1986 by Binnig, Quate and Gerber, AFM allowed for the first time imaging of non-conducting surfaces at an atomic scale [174]. Today it is a standard method for imaging, measuring and manipulating matter in nanometer and even sub-nanometer dimensions.

3.4.1 Principle

An AFM consists of an elastic microscale cantilever with a sharp tip whose size is in the range of micrometers. It acts as probe for sensing the texture of the surface. It is mounted on a piezo-electric element, called the modulating piezo. A piezo-electric scanner moves the sample below the tip with very high accuracy. In order to record the deflection of the cantilever a position sensitive detecting system is necessary. This is usually achieved

by reflecting a laser beam from the top of the cantilever and detecting the motion of the reflected light by a photo diode array. An electronic feedback and detector system enables to control the movement of the piezo-scanner in z-direction and converts the data into an image (Figure 3.5).

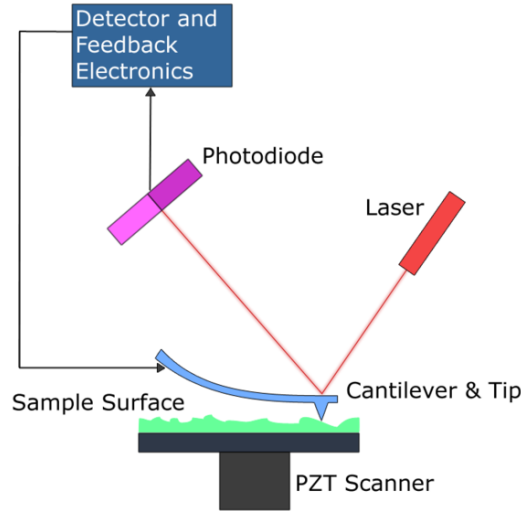


Figure 3.5: Schematic setup of an AFM

The cantilever tip is usually fabricated of silicon or silicon nitride with a tip curvature in the order of tens of nanometers. In close proximity to the sample surface forces F between tip and the specimen cause a deflection z of the cantilever, which can be described by Hooke's law

$$F = -k_c z \quad (3.11)$$

with the spring constant k_c . The forces relevant for AFM are ultimately of electromagnetic origin. However, different intermolecular, surface and macroscopic effects give rise to interactions with distinct distance dependencies (Figure 3.6). In the absence of external fields the dominant forces are van der Waals interactions, short-range repulsive interactions including mechanical contact force, adhesion and capillary forces which are in the order of nano- and picometers.

The resonance frequency f_0 at which the cantilever can oscillate is given by

$$f_0 = \frac{1}{2\pi} \sqrt{\frac{k_c}{m_0}} \quad (3.12)$$

with the cantilever's effective mass m_0 .

AFM can be operated in several different modes depending on the application. The most important ones are contact, non-contact and tapping mode. The former one is a static method, where a static cantilever deflection is used as feedback signal. The latter two are dynamic methods. Here the cantilever is excited by the modulating piezo close to or at its resonance frequency f_0 . This motion can be approximately described by non-linear, second-order differential equation for a forced harmonic oscillator with damping

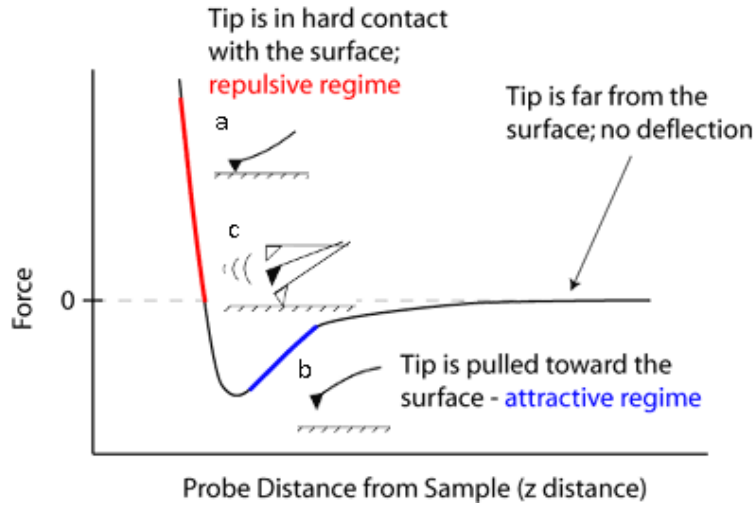


Figure 3.6: Force - distance curve and corresponding AFM modes; a) contact mode, b) non-contact mode, c) tapping mode

$$m_0 \ddot{z} + k_c z + \frac{m 2\pi f_0}{Q} \dot{z} = F_{ts} + F_0 \cos(\omega t), \quad (3.13)$$

where F_0 and ω are the amplitude and angular frequency of the driving force, Q is the quality factor, m_0 the effective mass, k_c the spring constant, f_0 the resonance frequency and F_{ts} the tip - surface forces. This is the classical Newton law, with the second and third term accounting for the elastic cantilever force and the friction respectively. The frequency dependent term describes the cantilever excitation. Since the amplitude and the frequency are altered by the tip - surface forces, either one can be used as feedback signal in order to image the topography.

In the contact mode the tip screens the surface at distances being located in the repulsive region of the curve (Figure 3.6 a). This occurs either at a constant height or with constant force. In the constant height mode the deflection of the cantilever which depends on the topography of the sample is directly measured. In the constant force mode the cantilever is actuated by the z-piezo controlled by the electronic feedback system so that the force between the apex and the specimen remains the same. The contact mode can only be applied for characterising samples which are not ruined by the scratching of the tip.

For soft-matter and biological samples non-contact or tapping mode is preferred. As both modes are dynamic methods, the cantilever is excited close to its resonance frequency. For non-contact mode the frequency is typically around 100 - 400 kHz with an amplitude smaller than 10 nm. The surface is scanned at a distance where attractive forces prevail (Figure 3.6 b). Depending on the strength of these forces the resonance frequency and the amplitude are modulated and can be translated into an image. Although giving good insight into short range attractive forces, the major drawback of the non-contact mode is, that it does not acquire direct information about the surface due to the lack of direct contact.

This problem is addressed in the tapping mode by applying larger cantilever excitation amplitudes in the range of several hundred Angstroms. The tip impacts the surface once during each vibration and therefore oscillates periodically between the attractive and the repulsive regime in the force-distance curve (Figure 3.6 c). The difference between the exciting frequency, close to its resonance and the frequency close to the surface is then measured. In this mode the observables are the amplitude of the cantilever oscillation and the phase shift compared to the excitation of the cantilever. Additionally to the topographical information, analysis of the phase shift provides a tool to discriminate between different types of material at the sample surface [175, 176].

3.4.2 Atomic Force Spectroscopy

Atomic force microscopy can be used to determine, at every location of the sample, the dependence of the interaction on the probe-sample distance. To determine the spatial variation of the tip-sample interaction, force curves may be recorded at a large number of locations with atomic force spectroscopy (AFS). Using AFS it is possible to obtain the following information: First of all the magnitude of the force which depends on long-range attractive and adhesive forces can be probed. Moreover the point of tip-sample contact, the tip-sample contact area and the elastic modulus, as well as viscoelasticity of thin and thick films can be determined. In order to analyze force-mapping experiments, it is important to understand how force-distance curves are obtained and the information provided regarding tip-sample interaction [177].

Force Curves

In order to measure a force curve the cantilever is extended towards and retracted from the surface at a particular location on the sample. At the same time the deflection of the cantilever is monitored as a function of piezoelectric displacement.

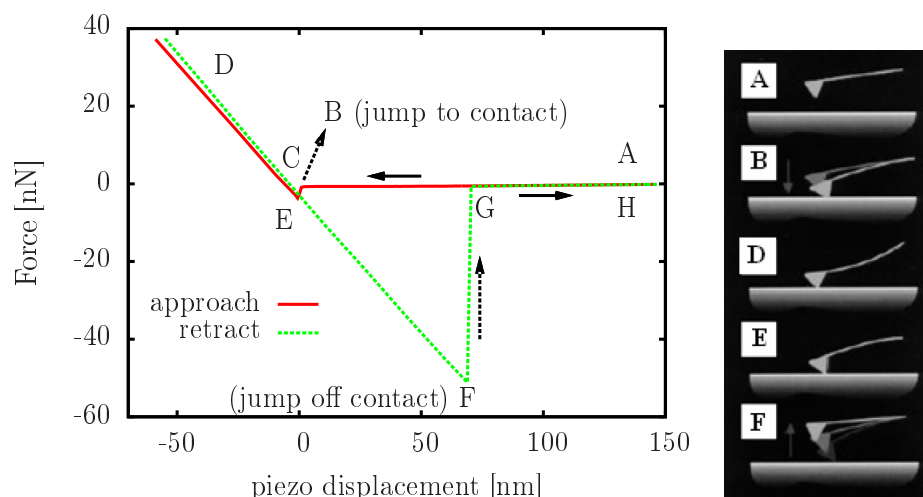


Figure 3.7: Schematic cantilever displacement - distance curve illustrating the points where jump-to-contact (approach) and jump-off-contact (withdrawal) occur and the maximum values of the attractive forces (pull-on force and pull-off force)

A schematic force curve is shown in Figure 3.7. At large tip-sample separations, there

is no interaction and the cantilever remains in its noninteracting equilibrium state (A). This region is also called zero line. While the tip is approaching the sample at a constant speed, it reaches a point close to the sample surface where attractive forces between surface and tip set in. If the force gradient is larger than the effective elastic constant, the cantilever becomes unstable and a jump-to-contact discontinuity is observed (B - C). At point (D), the tip is in contact with the surface and the deflection is dominated by mutual electronic repulsion between overlapping molecular orbitals of the tip and sample atoms. For rigid samples, much stiffer than the cantilever, its deflection becomes proportional to the piezo-displacement with further approach towards the surface (A - D is the approach curve).

In the contact region (also referred to as contact line), the shape of the curve is determined by the elastic properties of the sample and the geometries of tip and sample. The subsequent sample deformation is consistent with elastic asperity deformation and/or the presence of a thin layer. Therefore these region of the curve can be used to extract the elastic modulus of the sample. Given a calibrated sensor response, the shape of segment (C - D) indicates whether the sample is deforming in response to the force from the cantilever. If there is a hysteresis between approach and retract curve in the contact region conclusions about irreversible plastic deformation of the sample can be drawn.

During withdrawal, adhesion or bonds formed during contact with the surface cause the tip to adhere to the sample up to distances far beyond the initial contact point on the approach curve (E - F). As the piezo-tube continues retracting, the spring force of the bent cantilever overcomes the adhesion forces, and the cantilever pulls off sharply, springing upwards to its non-deflected or noncontact position (G). This is the jump-off-contact discontinuity. Finally, the tip completely loses contact with the surface and returns to its starting equilibrium position (H) (D - H is the withdrawal curve) [36, 178].

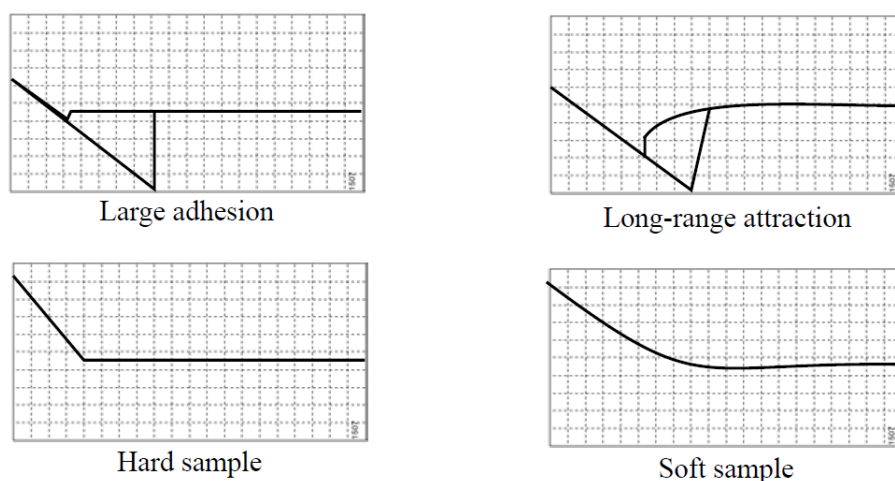


Figure 3.8: Examples of typical shapes of force curves for different materials [179]

Obviously the force plot features correlate with surface characteristics such as adhesion, hardness and the sample environment. E.g. in liquids, the adhesion is normally drastically decreased due to absence of capillary forces. Some examples for typical force curves are displayed in Figure 3.8.

Calibration of spring constants

In order to convert the cantilever deflection z into to the corresponding force F , Hooke's law can be applied providing the knowledge of the tip's force constant k_c . The accuracy of force measurements depends in part on the sensitivity of the AFM, but also in part on the precise knowledge of the spring constant. In principle the spring constant can be calculated from the geometry of the cantilever. There are a number of approximations relating the spring constant of a thin rectangular plate to its dimensions and Young's modulus. However due to difficulties in controlling the thickness of the cantilever at a particular stage of the manufacturing process and deviations in geometry from cantilever to cantilever, the calculated values are often inflicted with larger errors [36]. Thus many methods have been developed to measure the cantilever spring constant. These include the measurement of the static deflection of the cantilever, as well as dynamic measurements in the determination of the spring constants. There are also methods which require the placement of spheres of different masses at the tip of the cantilever and measuring the resultant resonant frequency [180]. But the most simple and today most widely used method involves the measurement of the thermal fluctuation of the cantilever [181,182]. In this approach it is assumed that the cantilever can be described as a simple harmonic oscillator with one degree of freedom (neglecting higher modes of oscillation). Applying the equipartition theorem to the cantilever potential energy leads to following expression

$$k_c \langle z^2 \rangle = k_B T \beta, \quad (3.14)$$

which relates the spring constant of the cantilever k_c to its mean square deflection $\langle z^2 \rangle$ caused by the thermal motion in the vertical direction. k_B is the Boltzmann constant and T the temperature. β is a correction factor, which accounts for the cantilever being a non-ideal spring and depends among others on its geometry. By transforming the time series data to the frequency domain, the Lorentzian form is obtained around the resonance frequency ω_f as shown in the power spectral density plot in Figure 3.9.

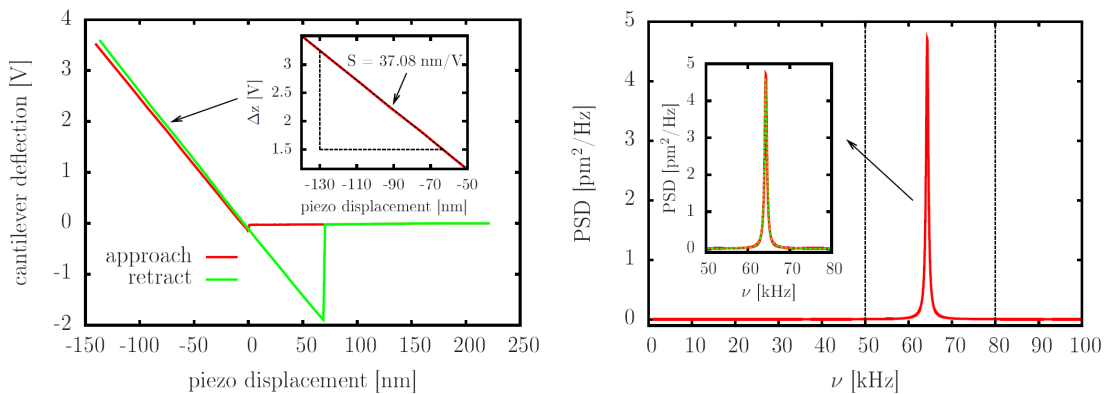


Figure 3.9: Force curve for a mica substrate in air used for cantilever sensitivity calibration (left). Power spectrum density (PSD) plot for a triangular Si_3N_4 tip (nominal spring constant $k = 0.6 - 0.8 \text{ N/m}$) (right). The data is fitted with a Lorentzian curve around the angular resonance frequency $\omega_f = 64 \text{ kHz}$. The calculated spring constant $k = 0.69 \text{ N/m}$ for $T = 20^\circ\text{C}$.

The area below this peak is taken to be equal to the mean square $\langle z^2 \rangle$ of the fluctuations in the time series data. So it is fitted with a Lorentzian curve and the mean square deflection of the first peak is obtained by integration. Prior to measuring the intensity of

the thermal noise, the cantilever's sensitivity S needs to be calibrated. The contact region of a force curve on a hard sample (e.g. mica) can be used, where the piezo-displacement can be considered proportional to the cantilever deflection. Applying the relation $z = Sz_V$, the cantilever deflection, initially measured in volts (z_V), can be converted into the deflection z in nm 3.9. The accuracy of the force constant computation can be further improved by accounting for assumptions that go into the theory with several correction factors [36]. The use of the thermal noise method has been confirmed experimentally and it usually gives values for spring constants with higher accuracy than provided by the manufacturer.

Probing nanomechanical properties

From the contact lines of force-displacement curves it is possible to draw information about the elastic-plastic behavior of materials. For an ideally elastic material, the tip deforms the sample by a depth δ , also called indentation. This results in a deviation from a straight line due to elastic deformation, which can be analyzed. When samples have a partially plastic behavior a "loading-unloading hysteresis" is observed, usually manifested in the force of the unloading curve being less than the force of the loading curve at a given penetration depth [36].

For samples where plastic deformations can be neglected, the tip-sample interactions can be modeled with elastic contact mechanics. The system can be described by means of its potential energy E

$$E = E_{cs}(D) + E_c(Z_c) + E_s(\delta) = E_{cs} + \frac{1}{2}k_c z_c^2 + \frac{1}{2}k_s \delta^2 \quad (3.15)$$

with the tip-sample interaction potential caused by surface forces E_{cs} , the cantilever's bending energy E_c and the elastic deformation energy of the sample E_s . k_s is the sample stiffness and k_c the cantilever spring constant. The actual sample-tip separation D can be calculated using the piezo-displacement z_p , the cantilever deflection z and sample indentation δ

$$D = z_p + z + \delta. \quad (3.16)$$

At contact $D = 0$ and in equilibrium equation (3.15) reduces to $\frac{1}{2}k_c z^2 = \frac{1}{2}k_s \delta^2$. Substituting leads to following expression, which relates the slope of the force-displacement curve to the stiffness of the sample:

$$k_c z = -\frac{k_c k_s}{k_c + k_s} z_p = k_{eff} z_p. \quad (3.17)$$

Relationship (3.17) shows, that for $k_s \gg k_c$ the piezo-displacement is directly proportional to the cantilever deflection. This is why this scenario is used to calibrate the cantilever sensitivity S , like described in the previous section. Furthermore it demonstrates that the elastic properties of the sample can be probed when z and δ are proportional for $k_s \ll k_c$.

The stiffness of the sample depends on the contact area, Young modulus E_i and Poisson ratio ν_i of sample and tip respectively, via

$$-k_s = \frac{3}{2}E_r a \quad (3.18)$$

with

$$\frac{1}{E_r} = \frac{3}{4} \left(\frac{1 - \nu_s^2}{E_s} + \frac{1 - \nu_c^2}{E_c} \right), \quad (3.19)$$

where a is the contact radius. In order to describe the plastic deformation several assumptions have to be made and the relations between the applied load F and the contact radius a or the deformation δ can be described by several theories. The three most common ones to characterise the deformation of the sample, and the adhesion force for a spherical tip on a plane surface are the Hertz [183], the Johnson-Kendal-Roberts (JKR) [184] and the Derjaguin-Müller-Toporov (DMT) models [185].

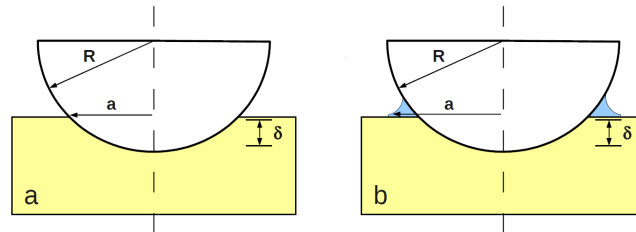


Figure 3.10: The Hertzian model describes the deformation of two elastic bodies. (a) A virtually incompressible sphere of radius R is pressed by a force F on an elastic sample, which reacts by an indentation δ to give a contact area with radius a . (b) Additional adhesive forces, like van der Waals attraction or capillary forces between sphere and sample by wetting, lead to a larger contact area and to an additional load e.g. taken into account by the DMT model

In the Hertz-model the adhesion between tip and surface is neglected, whereas the latter two theories take into account the adhesion outside (DMT) or inside (JKR) the contact area. Therefore the Hertz model can only be applied when the adhesion force is much smaller than the maximum load. In the two other theories, the work of adhesion w can be estimated from the jump-off-contact if the tip radius R is known. Using these models it is possible to calculate the contact area as a function of the reduced Youngs modulus E_r (taking into account contributions from the sample and the tip) which can finally be converted into the Youngs modulus as a function of δ [36, 178]. The Hertzian model of a sphere-plane contact can be applied for a routine estimation of the elastic modulus for small indentation depths. Since the elastic moduli of the tip material and the substrate are very high, the only detectable indentation should be the indentation of a soft material, like the bilayers adsorbed on the mica. Thus the elastic indentation of the tip and the mica can be neglected. Using the Hertzian contact model for a spherical indenter the loading force F_0 is related to the indentation δ by following equation

$$\delta^3 = \frac{9}{16} \frac{(1 - \nu^2)}{RE^2} F_0^2, \quad (3.20)$$

where R is the tip radius (in our case $R \approx 10$ nm, like indicated by the manufacturer), ν the Poisson ratio (which has been assumed to be 0.5 for bilayers on mica [186], like for a perfectly incompressible media). The cantilever indentation is calculated by subtraction of the piezo-displacement Z_p from the cantilever deflection Z_d

$$\delta = Z_d - Z_p \quad (3.21)$$

to convert the force curves into force vs indentation curves. These can then be fitted using equation (3.20) to extract the Young modulus E .

Experimental Setup

In order to image the monolayers at a desired surface pressure, the films are at first transferred onto freshly cleaved hydrophilic mica wafers (11 x 11 x 0.15mm, purchased from Agar Scientific). The dipping speed is set to 2 mm/min and transfer ratios for good monolayers are usually close to 1. The samples are imaged with a NanoScope V (Veeco) atomic force microscope (Figure 3.11).



Figure 3.11: Image of the used NanoScope V (Veeco)

Monolayers

To obtain a monolayer the immersed mica is pulled out of the water. For tapping mode imaging in air, standard cantilevers with a conical silicon etched probe tip (NSC15, μ masch) with spring constants in the order of 40 N/m and typical resonance frequencies in the order of 350 kHz are used. Images of scan sizes between $1\mu\text{m} \times 1\mu\text{m}$ and $50\mu\text{m} \times 50\mu\text{m}$ are recorded with scan rates of 0.5 - 1 Hz, depending on the scan size. Working in contact mode, cantilevers with a conical silicon etched probe tip (NSC19, μ masch) with typical spring constants in the order of 0.7 N/m are used.

Bilayers

The bilayers are obtained by depositing a second film on the monolayer by immersing the mica into water. The mica with the deposited film is then transferred under water into a sample holder, made of teflon, placed into the dipping well prior to the experiment. The sample holder has been fabricated in our laboratory with dimensions to allow for imaging with the AFM, while keeping the bilayer sample wet at all times. It is of special importance that the mica sheet is properly fixed to the surface to avoid drifts in the images and the force curves. After several tests a sampler holder layout allowing to fix the mica sheet with a teflon screw has proved to be the most suitable for our purpose.

In order to image and measure force curves of bilayers in water, triangular silicon nitride cantilevers with reflective gold coating (DNP-S10, Veeco) are used. Typical spring constants are in the order of 0.06 N/m, verified prior to the experiments by the thermal resonance method [182]. Images with scan sizes ranging from $1\mu\text{m}\times 1\mu\text{m}$ to $10\mu\text{m}\times 50\mu\text{m}$ are recorded with a scan rate of 1 Hz.

3.5 Scattering Techniques

Reflectivity methods, in particular neutron and x-ray reflectivity, are applied to analyse the structure of surfaces, like liquid surfaces or thin solid films. These powerful techniques allow studying e.g. micro-emulsion and polymer surfaces, magnetic films, biological membranes as well as Langmuir monolayers in detail. Irradiating the surface of a flat sample with a collimated beam of thermal neutrons or x-rays allows the detection of the intensity of the reflected radiation as a function of wavelength or angle, giving access to its scattering length density or electron density profile. Generally, films of thicknesses ranging from 1 - 200 nm are accessible. A major advantage of neutron scattering is the possibility of varying the contrast by isotopic substitution. Moreover the technique is non-destructive. However x-ray scattering usually provides access to a larger q-range because its radiation intensity is larger. Very often both methods are applied together as complementary experiments.

3.5.1 Interactions of Neutrons with matter

Due to the wave-particle duality a neutron in vacuum (or air) can be described theoretically as a plane wave with a time-independent wavefunction

$$\psi_0(x) = A_0 e^{ik_0 x} \quad (3.22)$$

with the wavevector

$$k_0 = \frac{2\pi}{\lambda}, \quad (3.23)$$

where λ is the wavelength. The corresponding energy is:

$$E = \frac{\hbar^2 k_0^2}{2m}. \quad (3.24)$$

The wave function of the particle obeys the Schrödinger equation

$$\frac{\hbar^2}{2m} \frac{d^2\psi}{dr^2} + [E - V(r)]\psi = 0, \quad (3.25)$$

where m is the mass of the neutron and V is the interaction potential (which is 0 in vacuum) between the neutron and the scatterers in the medium in which it is propagating. The interactions are mainly the strong interaction with the nuclei and the magnetic interaction with the existing magnetic moments. In the case of non-magnetic systems the mean interaction potential can be derived by integration of the Fermi-pseudo-potential [187] to give

$$V = \frac{2\pi\hbar^2}{m}\rho, \quad (3.26)$$

with ρ as the scattering length density which is defined by the equation

$$\rho = \sum_i N_i b_i. \quad (3.27)$$

N_i is the number of atoms of the sort i per unit volume and b_i is the scattering length of the nucleus i [188]. The scattering length b is actually a complex number of the form

$$b = b' + ib'', \quad (3.28)$$

where the imaginary part b'' describes the absorption of neutrons.

Since in an extended object the scattering relies on the direction of observation, it is useful to introduce the differential scattering cross-section. If the neutrons only interact once with the sample (Born approximation), then expression (3.29) can be applied for the differential scattering cross-section

$$\frac{d\sigma}{d\Omega} = \left| \sum_i N_i b_i e^{iqr} \right|^2, \quad (3.29)$$

which corresponds to the unit incident flux at a fixed angle $d\Omega$, where

$$\vec{q} = \vec{k}_{sc} - \vec{k}_{in} \quad (3.30)$$

where \vec{k}_{sc} is the wave vector of the scattered neutrons and \vec{k}_{in} of the incident neutrons. The scattering cross-section is composed of a position dependent coherent part and an incoherent part originating from the random distribution of isotopes and nuclear spin states in a material. The latter part appears as a constant background in the neutron experiment which has to be subtracted from the data.

For non-magnetic systems due to the wave behavior of neutrons they can be treated with classical optics. Neutron refractive indices n_i can be introduced similarly to optical ones. This is justified by the fact that the Schrödinger equation (3.25) can be written as a Helmholtz equation very much alike the electromagnetic field:

$$\frac{d^2\psi}{dr^2} + k^2\psi = 0, \quad (3.31)$$

with the wave vector in the medium

$$k^2 = \frac{2m}{\hbar^2}[E - V] = 0. \quad (3.32)$$

In this case the optical index for neutrons can be defined as the ratio of the wave vector in the medium k to that in the vacuum k_0

$$n^2 = k^2/k_0^2. \quad (3.33)$$

By substituting (3.33) with (3.32) and (3.24) the expression

$$n^2 = 1 - \frac{V}{E} = 1 - \frac{\lambda^2}{\pi} \sum bN \quad (3.34)$$

is derived, whereas the latter part is obtained by substituting E and V by (3.24) and (3.26) as well as k_0 expressed by λ . For slow neutrons with wavelengths in the order of \AA , n differs from 1 by only 10^{-5} and so the approximation

$$n \approx 1 - \frac{\lambda^2}{2\pi} Nb = 1 - \frac{\lambda^2}{2\pi} \rho_b \quad (3.35)$$

is valid. As the scattering lengths for the different atoms and even isotopes vary throughout the periodic table it is possible to alter the refractive index of the medium by isotopic substitution thus providing a higher contrast. Especially the large difference between hydrogen and deuterium is of particular utility in soft matter research [187–189].

3.5.2 Interactions of X-rays with matter

The electromagnetic x-ray radiation interacts with the electron cloud of an atom in the form of elastic scattering, which is called Thompson scattering. The intensity of the scattered radiation from an object can be calculated considering a linearly polarized plane incident wave hitting a free electron, described by the electric field

$$\mathbf{E}(\mathbf{r}) = E_0 \mathbf{e} \exp(-i\mathbf{k}_{in}\mathbf{r}) \quad (3.36)$$

with the polarisation of the incident wave, orthogonal to the incident wave vector \mathbf{k}_{in} . In the far field, the electromagnetic wave scattered by a particle of charge e can be approximated by a spherical wave:

$$\begin{aligned} E_r(r) &= \frac{-e^2 E_0}{4\pi\epsilon_0 m c^2 r} \exp(-ik_{sc}r) \\ &= -\frac{r_e E_0}{r} \exp(-ik_{sc}r), \end{aligned} \quad (3.37)$$

which is the solution of the Helmholtz equation

$$\nabla^2 E - k_0^2 E = \frac{k_0^2}{e_0} \delta P, \quad (3.38)$$

where the electric dipole moment δP is defined as

$$\delta P = \frac{e^2}{m k_0^2 c^2} \quad (3.39)$$

for a charge e in a field E . The scattering length is the classical Thompson radius of an electron r_e :

$$r_e = \frac{e^2}{4\pi\epsilon_0 m_e c^2} = 2.818 \text{fm}, \quad (3.40)$$

where m_e is the mass of an electron.

X-rays interact only very little with the nuclei because they are several orders of magnitude heavier than electrons (equation (3.37)). So the effective cross-section of the nuclei can be neglected compared to the electrons: $\sigma_{pr} < 3 \times 10^{-7} \sigma_{el}$. This is why only electrons are

considered. In analogy to the neutron case r_e is the scattering length for electrons. The refractive index is therefore

$$n = 1 - \frac{\lambda^2}{2\pi} r_e \rho, \quad (3.41)$$

where ρ_e is the electron density [189].

3.5.3 Specular Reflectivity at interfaces

For both x-ray and neutron reflectivity an interface is defined as the position between media of two different refractive indices. The incidence beam with wave vector k_{in} and an angle of incidence Θ_{in} gets reflected resulting in a reflected beam with wavevector k_r and angle of reflection Θ_r (Figure 3.12).

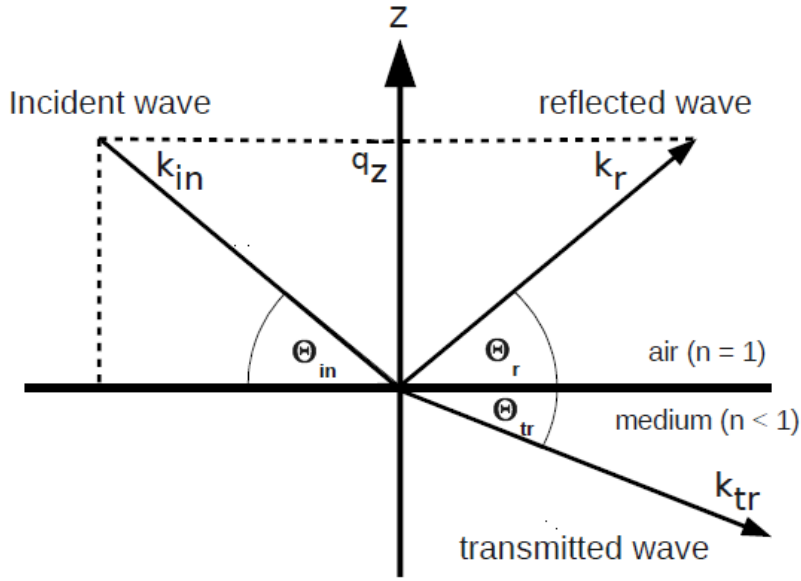


Figure 3.12: Reflectivity on a perfect surface

In general the diffraction index of a medium is described by

$$n = 1 - \delta - i\beta. \quad (3.42)$$

It depends on the type of the wave, as well as its energy. As seen before, the definitions of δ and β are the same for x-rays and neutrons:

$$\delta = \begin{cases} \lambda^2 \rho_d / (2\pi) & \text{for neutrons} \\ \lambda^2 \rho_e r_e / (2\pi) & \text{for x-rays} \end{cases} \quad (3.43)$$

with the wavelength λ , the scattering length density ρ_n , the electron density ρ_e and the Thompson radius r_e .

$$\beta = \begin{cases} \lambda \mu_n / (4\pi) & \text{for neutrons} \\ \lambda \mu_x / (4\pi) & \text{for x-rays} \end{cases} \quad (3.44)$$

μ_n and μ_x are the absorption lengths of the media for neutrons and x-rays respectively. The reflectivity index is always close to 1 because values for δ and β are found to be

between 10^{-5} and 10^{-8} .

In order to describe the relationship between the angles of incidence Θ_{in} and refraction Θ_{tr} when an incident wave passes the interface between two isotropic media with reflective indices n_1 and n_2 , Snells law can be applied:

$$n_1 \cos \Theta_{in} = n_2 \cos \Theta_{tr}. \quad (3.45)$$

Below the critical angle Θ_c , the incoming beam arriving from medium with n_1 is totally reflected at the interface and hence $\Theta_{tr} = 0$. Therefore equation (3.45) reduces to

$$\frac{n_2}{n_1} = \cos \Theta_c. \quad (3.46)$$

If $n_1 = 1$, like for air and Θ_c is very small, a Taylor expansion for the cosine function can be carried out. Then with (3.35) following expression can be obtained:

$$\Theta_c = \sqrt{\frac{\rho}{\pi}} \lambda. \quad (3.47)$$

In reflection geometry, the momentum transfer

$$q = q_z = \frac{4\pi}{\lambda} \sin \Theta_{in} \quad (3.48)$$

and inserting (3.47) into (3.48) the critical momentum transfer

$$q_c = \frac{4\pi \sin \Theta_c}{\lambda} = 4\sqrt{\pi\rho} \quad (3.49)$$

is derived.

The reflectivity is defined as the ratio between the intensities of the reflected and incident beam r , which can be obtained from the Fresnel reflection coefficient r for a flat and infinitely thin interface:

$$r = \frac{n_1 \sin \Theta_{in} - n_2 \sin \Theta_{tr}}{n_1 \sin \Theta_{in} + n_2 \sin \Theta_{tr}} = \frac{k_{0z} - k_{trz}}{k_{0z} + k_{trz}}. \quad (3.50)$$

The Fresnel reflectivity R_F is then given by the square modulus of the reflection coefficient, as the intensity is defined by the square modulus of the amplitude

$$R_F = \left| \frac{A_r}{A_{in}} \right|^2 = \left| \frac{k_{in,z} - k_{r,z}}{k_{in,z} + k_{r,z}} \right|^2. \quad (3.51)$$

Using expression (3.48), R can also be written as a function of q

$$R(q) = \left[\frac{q - \sqrt{q^2 - q_c^2}}{q + \sqrt{q^2 - q_c^2}} \right]^2. \quad (3.52)$$

With the help of equation (3.52) R_F can be calculated e.g. for an air-D₂O interface, displayed in Figure 3.13.

It can be clearly seen that for $q < q_c$ the reflectivity equals one because no transmission occurs. For $q > q_c$ the reflectivity decays asymptotically as q^{-4} .

So far only infinitely sharp interfaces have been considered which is very seldom the case for real samples. The boundary between two materials may be rough with peaks and troughs

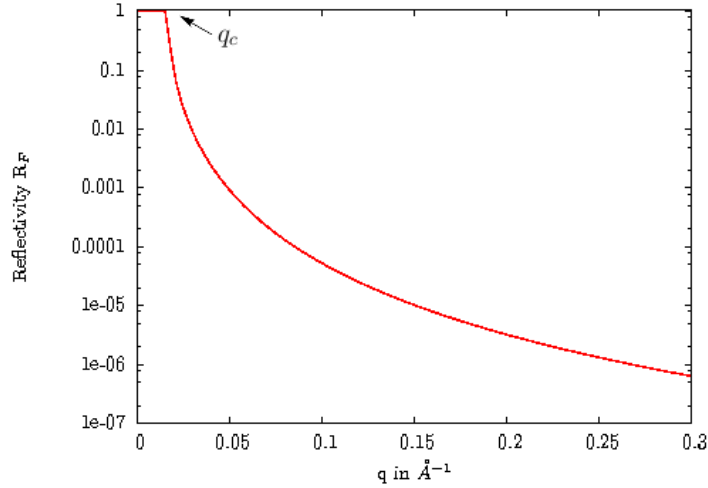


Figure 3.13: Calculated Fresnel reflectivity for air - D₂O interface

over a large range of length scales. It might be also extended by inter-diffusion processes between two layers. In the case of specular reflectivity the two types of roughnesses can not be distinguished and therefore both problems can be addressed in the same manner if the size of the surface's imperfection is small compared to $1/q^2$. It can be shown that the reduction of the reflectivity due to interface roughness can be well described by

$$R = R_F e^{-q^2 \sigma^2}. \quad (3.53)$$

$\exp(-q^2 \sigma^2)$ is called the Debye-Waller factor and σ is the roughness [189].

3.5.4 Thin films

If the system is composed of a stacking of several slabs of thickness z_i separated by a planar interface, with constant refraction index each, the specular reflection includes a form factor due to the interference between the waves reflected at each interface (Figure 3.14). The scattering length density profile or electron density profile ρ_i is determined by the atomic nuclei and electrons in the slab i , respectively. In the limit of thin slabs the reflectivity function $R(q_z)$ can be expressed in terms of the Fourier transform of the density profile $\rho(z)$ along the normal z to the interface:

$$R(q_z) = R_F(q_z) e^{-(\delta q_z)^2} \left| \frac{1}{\rho_\infty} \int_{-\infty}^{+\infty} dz \frac{\partial \rho}{\partial z} e^{iq_z z} \right|^2. \quad (3.54)$$

Knowing only the modulus and not the phase of its Fourier components (equation (3.54)), the density profile $\rho(z)$ cannot be directly derived from the experimental data. Instead appropriate models have to be applied and by fitting the experimental curves the density profile is obtained. However the interpretation of the simulated graphs should be carried out cautiously because very often several consistent fits can be obtained for different density profiles. This problem is usually addressed by including as much complementary information as possible into the deployed model, e.g. obtained from theoretical evaluations or other measurements [42, 189].

Very often the the interfacial structure can be well approximated by a slab model in which layers of thickness (z_i), scattering length density (ρ_i) and roughness ($\sigma_{i,n+1}$)

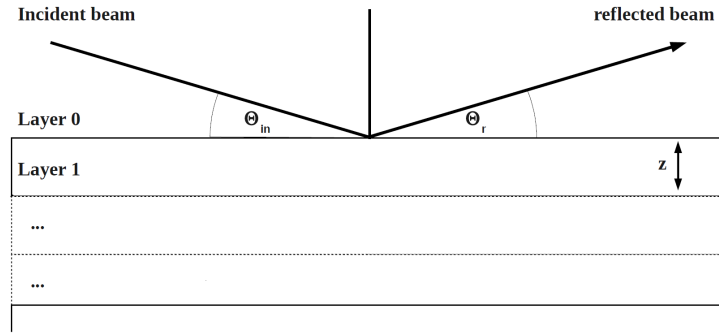


Figure 3.14: Multi-layer-model with air as 0th and the substrate as (m + 1)th layer

are sandwiched between the super- and subphase (Figure 3.14). A refinement procedure to minimise the differences between the theoretical and measured reflectivity curves is then used, by changing the parameters that describe each layer. The reflectivity can be calculated with the Abeles matrix method for stratified interfaces [190]. Using equation (3.50) and taking into account the roughness between the layers the Fresnel coefficients between layer i and $i+1$ are expressed by

$$r = \frac{k_i - k_{i+1}}{k_i + k_{i+1}} e^{-2k_i k_{i+1} \sigma_{i,i+1}}. \quad (3.55)$$

Introducing a phase factor β which accounts for the thickness of each layer

$$\beta_i = k_i z_i \quad (3.56)$$

a characteristic matrix c_i is calculated for each layers

$$c_i = \begin{pmatrix} e^{\beta_i} & r_i e^{\beta_i} \\ r_i e^{-\beta_i} & e^{-\beta_i} \end{pmatrix} \quad (3.57)$$

The resultant matrix is defined as the product of these characteristic matrices, from which the reflectivity is calculated.

$$M = \prod_0^i c_i \quad (3.58)$$

$$R = \left| \frac{M_{00}}{M_{10}} \right| \quad (3.59)$$

The data were fitted with the Motofit package run with the program IGOR Pro 6.0 (Wavemetrics, OR), where the specular reflectivity is calculated by the Abeles matrix method for stratified interfaces [190]. A detailed description of the Motofit software is given elsewhere [191].

3.5.5 Instrumental aspects

The experiments have been conducted at three different instruments which are described in the following:

Figaro

The neutron reflectivity experiments at the air-water interface are carried out at the time of flight reflectometer Figaro (Fluid Interfaces Grazing Angles Reflectometer) at the ILL, Grenoble [192]. The incoming beam comprises wavelengths between 2 Å and 30 Å, and $M = 4$ supermirrors are used to deflect the beam. For our samples a q -range from 0.005 - 0.35 Å⁻¹ has been achieved by joining together two measurements with a reflection angle, $\Theta_1 = 0.62^\circ$ and $\Theta_2 = 3.82^\circ$ with a resolution of 5.6% determined by the chopper openings. The samples are measured in a Langmuir trough (Nima) aligned with the beam. The reflectivity is normalised by direct beams in a transmission geometry through the windows of the Langmuir trough lid, and corrected for incoherent background scattering.

D17 reflectometer

The measurement of bilayer samples has been conducted at the D17 reflectometer operated in time of flight mode at the ILL, Grenoble with a wavelength range from 2 to 20 Å, giving a q -range for specular reflectivity of 0.005 - 0.3 Å⁻¹. Each measurement is performed at two reflection angles, $\Theta_1 = 0.7^\circ$ and $\Theta_2 = 3^\circ$ to be joined together with a resolution defined by two choppers of $\Delta t/t = 1\%$ and 4%. The beamline has been already described in detail by Cubitt et al. [193].

The detector efficiency is calibrated with H₂O. For the actual experiment the neutron beam enters the silicon substrate through one 5 x 1 cm² side of the block, hits at grazing incidence the polished 5 x 5 cm² face on which the layer under study has been deposited, and goes out through the opposite 5 x 1 cm² side [42]. Two direct beams have been measured for both angles of incidence for data normalization.

X-ray reflectivity

Complementary to neutron reflectivity, the thickness and vertical composition of the monolayers were also characterized by x-ray reflectivity. The monolayers were spread on a water subphase in a homemade teflon trough with a maximum and minimum area of 462 cm² and 161 cm² respectively, suitable to fit into a Siemens powder diffractometer D5000. A movable teflon barrier allows to compress the monolayer to the desired surface pressure for the x-ray reflectivity measurement. The trough and the diffractometer are operated with a home-made software. The Cu K_α beam (wavelength $\lambda_x = 1.54$ Å) is first collimated using 100- μ m slits. A graphite monochromator is placed after the sample in front of the NaI scintillator detector. A homemade Langmuir trough was mounted on the sample stage of the diffractometer and covered with a plastic hood to avoid evaporation and dust exposure.

Sample preparation

Monolayers

The samples are spread in a Langmuir trough (Nima, maximum and minimum area are 930 cm² and 254 cm² respectively), perfectly aligned with the neutron beam and sealed

with a Plexiglas hood. The spreading solvent is allowed to evaporate for 15 min. Then the film is compressed at the desired surface pressures and the reflectivity curve is recorded.

Bilayers

The bilayers are prepared on $5 \times 5 \times 1 \text{ cm}^3$, homogeneously n-doped silicon single crystals, oriented [111] on the side where the film is deposited and atomically smooth with a roughness $< 5 \text{ \AA}$, as determined by the polisher (SILTRONIX, Archamps, France). Prior to each deposition the silicon block is cleaned with chloroform, alcohol and water then treated with UV/ozone for 30 min to reach a maximum hydrophilicity. For all bilayers deuterated DPPC-D62 is used.

The double layer deposition is carried out on a NIMA 611 trough available in the ILL soft matter lab ($30 \times 20 \text{ cm}^2$). The first layer is deposited by the classical Langmuir Blodgett technique, whereas the second layer is deposited by the Langmuir-Schaefer method (horizontal sample) and the temperature is kept constant at 20°C . All layers are deposited at 40 mN/m . The samples are then inserted into a teflon sample cell, which is put into an aluminum box to be mounted on the neutron reflectometer and thermostatted using a water circulation bath. The cell is connected to a solvent circuit by means of a peristaltic pump in order to be able to change the subphases for different contrast. More detailed information about the substrate and sample preparation is given elsewhere [42]. The measured samples are listed in Table 4.4.

3.6 Nuclear Magnetic Resonance (NMR) Spectroscopy

3.6.1 Theoretical background

NMR spectroscopy is one of the most important methods for structure elucidation of organic molecules. It exploits the fact that atomic nuclei with an odd number of protons or neutrons exhibit an intrinsic magnetic moment μ and an angular momentum m . It is described by the spin quantum number I for the nucleus. The magnetic moment

$$\mu = \gamma I \quad (3.60)$$

is associated with the spin I by the gyromagnetic ratio γ , which is specific for each nucleus. The angular momentum m is quantised and can take values from $-I$ to $+I$ corresponding to a total of $2I + 1$ different states which are all degenerate as long as there is no external field applied. If a nucleus is placed in a static external magnetic field B_0 the different states no longer possess the same energy E . This is called the Zeeman-effect. Then the energy of the magnetic moment along the z-axis μ_z of a nucleus is given by

$$E = -\mu_z B_0 = -m \hbar \gamma B_0 \quad (3.61)$$

and is determined by the spin state m of the nucleus. For a nucleus with spin $I = \frac{1}{2}$ (e.g. ^1H , ^{13}C) there are two different energy levels with a energy difference

$$\Delta E = \hbar \gamma B_0 = \nu_L B_0, \quad (3.62)$$

dependent on the external magnetic field B_0 and the gyromagnetic ratio γ . The Larmor frequency ν_L is the frequency of the electromagnetic radiation necessary to achieve resonant absorption which is typically in the radio frequency range of the electromagnetic spectrum. The magnetisation can be visualised considering the external magnetic field along the z-axis of the coordinate system and the spin vectors rotating either parallel or antiparallel respective to the external field. More atoms result in two cones of spin vectors, one for parallel spin (α) and one for antiparallel spin (β) possessing different energies (Figure 3.15).

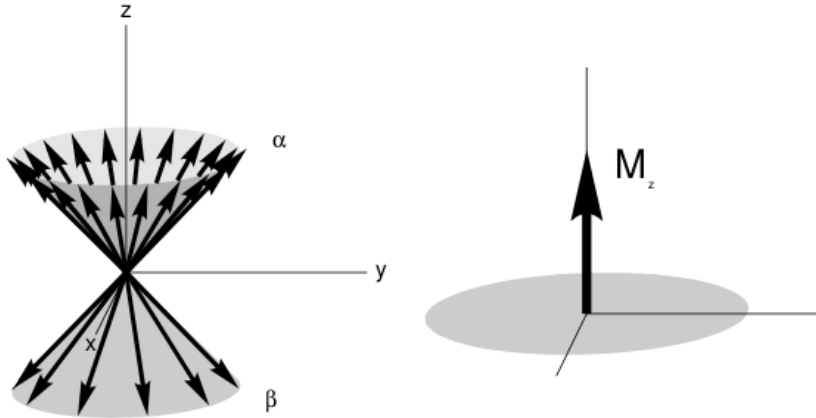


Figure 3.15: Schematic spin diagram

In thermal equilibrium the population difference between the energy states with low N_α and high energy N_β respectively can be calculated by the Boltzmann distribution

$$\frac{N_\beta}{N_\alpha} = e^{-\frac{\Delta E}{k_b T}}, \quad (3.63)$$

which shows that at room temperature the lower energy state is slightly more populated leading to an equilibrium net magnetisation vector M_z in direction of the applied magnetic field.

3.6.2 One-dimensional NMR

In order to obtain a NMR signal a radio frequency pulse in the range of the Larmor frequency is applied to the sample, exciting its spins. The magnetisation vector M_z this means it is deflected from its equilibrium position in x,y-direction. The degree of deflection is dependent on the duration and the intensity of the pulse. The out of equilibrium magnetisation vector M_{xy} precesses perpendicular to the plane of the applied static external magnetic field. And the oscillating magnetisation can be detected by the induction of an electric current in the detector which produces an electric signal oscillating at the NMR frequency. After the application of the pulse the magnetisation vector returns to its equilibrium position by two characteristic relaxation processes. There is the transversal relaxation with the time constant T_2 which refers to the decay of the detected signal and the longitudinal relaxation with its time constant T_1 describing the return of the nuclei into the Boltzmann equilibrium, whereas $T_1 > T_2$. The measured signal is called free induction decay (FID) which has to be transferred from the time domain into the frequency domain by Fourier transformation in order to get the NMR spectrum. The FID is modulated by

frequency variations caused by the chemical shift and the coupling of the nuclei in the sample.

The chemical shift δ in the spectrum is the frequency shift in ppm of the sample signal ν_s compared to a reference ν_{ref} . Tetramethyl silane (TMS) or a secondary reference of known chemical shift can be used instead of TMS. The most common secondary references are the residual solvent signals. The chemical shift is calculated as shown in equation (3.64),

$$\delta = \frac{\nu_s - \nu_{ref}}{\nu_0} 10^6, \quad (3.64)$$

where ν_0 is the frequency of the spectrometer. The reason for the chemical shift is the different chemical environment of the atoms depending on the electron density of the molecule because electrons partially shield the nuclei from the external magnetic field. So the local magnetic field is slightly altered compared to the applied field producing the shift of the signals.

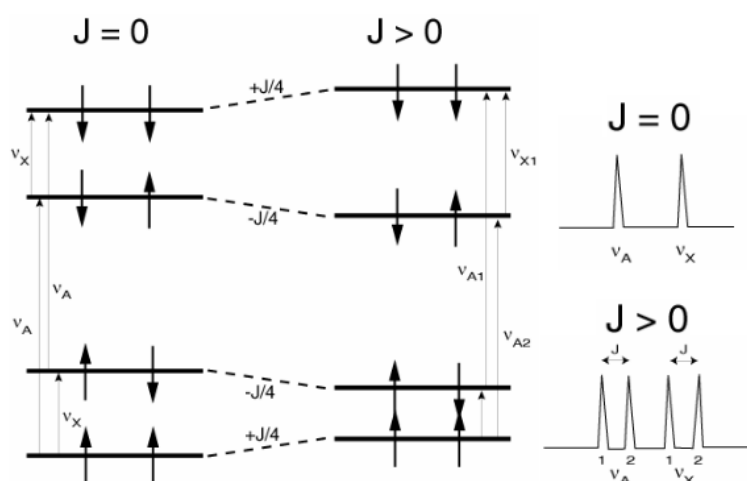


Figure 3.16: Schematic representation of origin of scalar coupling for a two spin system

Spin-spin coupling occurs when the spins of nuclei in close proximity to each other interact and adjust themselves respectively. This interaction can either be transmitted through the binding electrons (scalar coupling) between the atoms or directly through space (dipolar coupling). Depending on the number of the interacting nuclei n and their spin quantum number I the signal splits up into a characteristic number of signals which is called multiplicity

$$m = 2nI + 1 \quad (3.65)$$

and its relative intensity can be extracted from the Pascal's triangle. The coupling constant J describes the characteristic distance between the multiplets and is independent from the external magnetic field. Figure 3.16 illustrates the origin of the scalar coupling J for a two spin system.

A problem of the NMR spectroscopy is its relatively low sensitivity. Generally this is due to the very low population difference between the energy levels determined by the Boltzmann equilibrium (3.63) which is close to one even for low temperatures. The sensitivity can be expressed by the signal to noise ratio

$$\frac{N}{R} = n\gamma_{ex}(\gamma_{de}(NS)B_0)^{\frac{3}{2}}T_2T^{-1} \quad (3.66)$$

with the number of detected atoms n , the gyromagnetic ratios of the excited nucleus γ_{ex} and the detected nucleus γ_{de} , the static magnetic field B_0 , the number of scans NS , the temperature T and the characteristic time constant T_2 for spin-spin relaxation. Equation (3.66) shows which parameters have to be optimised in order to make the NMR experiment sufficiently sensitive. Therefore it is desirable to detect nuclei with high γ_{de} (if possible protons as they possess the largest γ), to use strong magnets with high B_0 and as long accumulation times NS as possible. Since N/R is also dependent on the number of detected atoms n their natural abundance plays a role as well. This explains the relative low sensitivity for ^{13}C -NMR compared to ^1H -NMR because the ^{13}C isotope only makes up about 1.1% of the total carbon whereas the protons consist to fractions higher than 99% of the ^1H isotope [194, 195].

3.6.3 Two-dimensional NMR

The invention of pulse-Fourier-Transformation-NMR-spectrometers enabled the development of multi-dimensional NMR spectroscopy which allows to extract many different kinds of information about a molecule. Thus problems like peak-overlapping in one-dimensional spectra could be addressed and structures of complex molecules like proteins and drugs have become amenable.

The application of pulse sequences of various shape, frequency and duration allow a magnetisation transfer between different nuclei. Figure 3.17 shows the general structure of a two dimensional experiment.

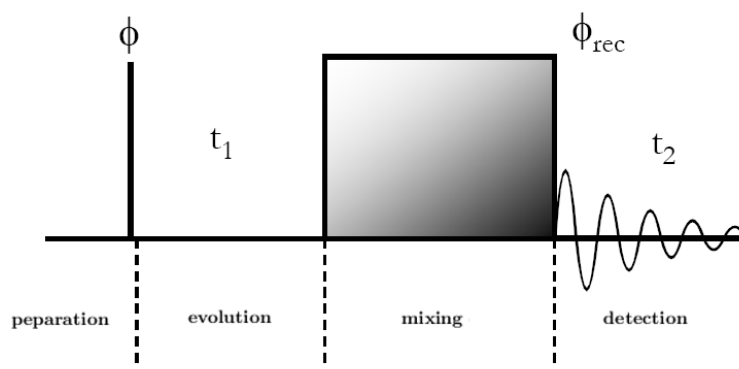


Figure 3.17: General structure of a 2D NMR experiment, ϕ describes the phase of the pulses

It is always composed of preparation, evolution (t_1), mixing and detection (t_2). Preparation means the excitation of the spins with pulses. During the evolution the spins develop only by the influence of the static magnetic field and their interactions among each other. The mixing period is designed so that transversal magnetisation (which is the one being able to be detected) can be observed during the final detection period. By the right choice of specific mixing times different correlations between the spins can be made visible and detected. Thus it is possible to correlate the various nuclei by for example their scalar coupling, dipolar coupling or chemical shift.

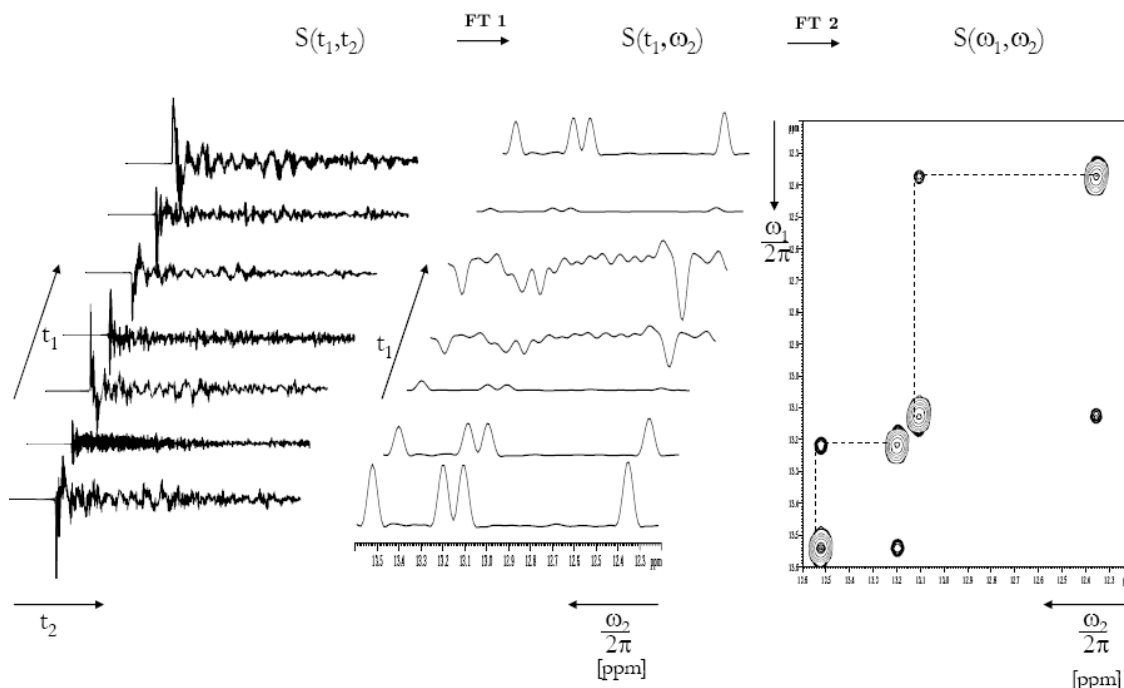


Figure 3.18: General principle how a 2D NMR spectrum is obtained

Besides the acquisition time t_2 , the evolution time t_1 is the second time dimension which is incremented. Thus a two-dimensional NMR experiment is basically a line up of many one-dimensional NMR experiments differing in evolution time t_1 . The two time domains are converted into the corresponding frequency domains by successive Fourier transformation. Figure 3.18 illustrates the principle for obtaining 2D-NMR spectra [196]. In following paragraphs some of the most important 2D-NMR experiments and their application in structure analysis are introduced.

COSY (homonuclear correlation spectroscopy)

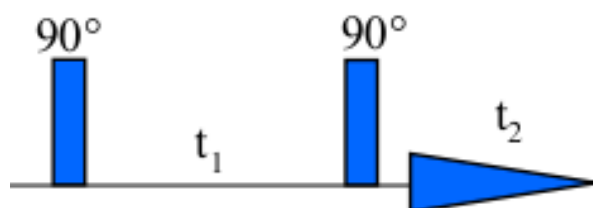


Figure 3.19: Pulse sequence for a standard COSY experiment

In the COSY experiment a pulse sequence is applied which correlates nuclei of the same sort (mostly ^1H) by their scalar coupling. Usually all geminal, vicinal and some long range couplings will appear as off-diagonal signals in the COSY spectrum. The latter ones can be identified by their low intensity whereas the former ones can be removed from consideration by other experiments like HSQC. So it is possible to deduce structural fragments in a molecule because the COSY experiment reveals the connectivity of protons

on adjacent carbon atoms which couple through three bonds. A related technique is the TOCSY (total correlation spectroscopy) method which allows to determine all the different spin system in a molecule.

HSQC (heteronuclear single quantum correlation)

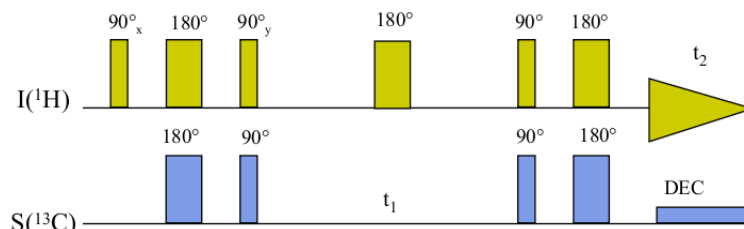


Figure 3.20: Pulse sequence for a standard HSQC experiment

This two-dimensional one-bond heteronuclear correlation experiment correlates the chemical shift of different sorts of nuclei (e.g. ^1H and ^{13}C), which show scalar coupling. Each peak in the spectrum (with a carbon and a proton axis) represents the shift of every proton and its directly attached carbon. The phase sensitive nature of HSQC allows to distinguish between carbon atoms bonded to an even or odd number of protons since they show a different phase being indicated by a color. A major advantage of the HSQC experiment is that overlapping multiplets very often become clearly separated because the peaks are now spread out over two dimensions. A complementary two-dimensional NMR method to the HSQC is the HMBC (heteronuclear multiple-bond correlation) experiment. It reveals longer range correlations of protons connected to carbon atoms by two or more bonds. It is particularly useful because it reveals quaternary carbons and connectivity between separated spin systems. As mentioned before it is desirable for heteronuclear correlation experiments to design the pulse sequence in a way to be able to detect the protons as they show the greatest gyromagnetic ratio. In this work a nowadays less popular phase sensitive multiquantum sequence (HMQC) is used, which fits well with the spectrometer configuration.

NOE (Nuclear Overhauser effect)

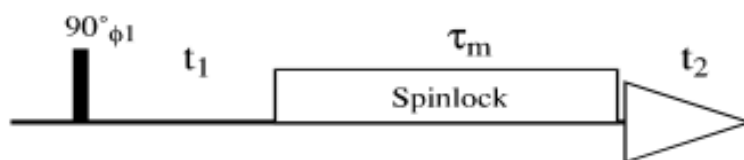


Figure 3.21: Pulse sequence for a standard ROESY experiment

Generally NOE describes the transfer of spin polarisation from one proton to another via cross-relaxation. In a NOE experiment, this is observed when a proton is selectively excited and saturated by a pulse at its resonance frequency and thereby its Boltzmann equilibrium is disturbed. Due to dipolar coupling the relaxation behavior of an adjacent proton can be influenced so that its signal intensity increases up to 50%. This only occurs

for protons which are in close proximity to the saturated one since the dipolar coupling interaction decreases strongly with distance ($\sim r^{-6}$). To clearly identify the increased intensity of the peaks NOE-difference spectroscopy is used where the NOE spectrum is subtracted from a normal spectrum and the saturated proton occurs as negative peak while the protons in close proximity are positive. As it is sometimes difficult to selectively saturate protons with very similar signals, a two-dimensional experiment has been developed to overcome this problem. In this so called NOESY (NOE spectroscopy) experiment all the protons which are interacting by dipolar coupling appear as non diagonal peaks. It can detect chemical and conformational exchange as well. Yet it has to be paid attention to COSY artifacts in the data analysis. Intermediate sized molecules however, like for example the modified CD we are using in this laboratory, only show a weak NOE and hence this method is not applicable. For such compounds the ROESY (rotating frame NOE spectroscopy) experiment is preferably carried out. A ROESY spectrum might contain TOCSY artifacts and artifacts due to chemical exchange of protons which has to be kept in mind for interpretation [196]. Therefore t-ROESY and off-resonance ROESY (used in our experiment) have been developed [197]. The latter is routinely used in the lab.

Experimental Setup

The ^1H -NMR experiments have been performed at 300 MHz using a Bruker DMX300 spectrometer run with xwinNMR and a Bruker AVANCE DPX400 spectrometer run with Topspin (using a broad band (BB) probe in both experiments). If not stated differently, measurements have been carried out at 25°C under careful temperature regulation (Eurotherm thermostat). Deuterated chloroform, D_2O and DMSO- D_6 have been obtained from Euriso-Top (France). The duration of the 90° pulse was ca. 11 ms. 1D NMR spectra were collected using 16 K and 64 K data points for the 300 and 400 MHz instruments, respectively. Chemical shifts are given relative to external TMS (0 ppm). The signal of the residual protons of the solvent are used as a secondary reference. The off-resonance ROESY experiment is carried out using the PULSE program available from the Bruker library with 300 ms mixing time. Off-resonance ROESY spectra are treated without symmetrization. All NMR data have been processed and plotted using MestRe-C 4.9.9.9. Typically the NMR data have been treated using a Fourier transformation with exponential apodization and line broadening of 0.3 for ^1H and 3 for ^{13}C . For polyrotaxanes and STL integration, a baseline correction is used in order to avoid a drift due to large PEG and H_2O peaks. The same correction is applied for all spectra. Robustness of the method has been tested. For most experiments, a Whittaker smoother is used with a 100000 smooth factor and automatic selectivity (default 25). This has been applied especially for better measurement of CD content on the polyrotaxanes. In that case, no correction is applied for integration.

3.7 Infrared reflection absorption microscopy

The Infrared Reflection Absorption Microscopy (IRRAS) is a vibrational spectroscopic technique which allows to obtain spectral information of thin films adsorbed to surfaces. Dluhy and Cornell in the mid 1980s were the first to acquire IR spectra from lipid mono-

layers at the air-water interface. This allowed them to extract structural features, which could not have been studied otherwise [198]. The IRRAS technique has steadily improved and it is today widely used as unique method to determine the structure and orientation of molecules at aqueous interfaces [199–201].

3.7.1 Principle

IR spectroscopy detects molecular vibrations accompanied by changing molecular dipole moments. The major types of molecular vibrations are stretching and bending. Linear and non-linear molecules with n atoms give rise to $3n-5$ and $3n-6$ vibrations respectively. Only the vibrations which produce a net change in dipole moment are visible in an IR spectrum.

IR radiation directed on a molecule is absorbed for so called resonant frequencies, when it matches the frequency of a specific vibration in the molecule. The energies are determined by the shape of the molecular potential energy surfaces, the masses of the atoms, and the associated vibronic coupling. In a first approach resonant frequencies are related to the strength of the bond, and the mass of the atoms at either end of it. Thus, particular bond types can be associated to characteristic resonant frequencies. Although the absorption involves discrete, quantized energy levels, the individual vibrational motion is usually accompanied by other rotational motions. These combinations lead to the typical absorption bands, commonly observed in the IR region, rather than discrete lines.

IRRAS spectra of mono-molecular films adsorbed on a reflective substrate are obtained by reflecting the incoming radiation from the three-phase ambient-thin film-substrate system. In contrast to normal IR spectroscopy, it is the reflected intensity which is measured as a function of wavelength. The mid IR region is normally used for IRRAS experiments. The IR absorption is generally presented in wavenumbers $\tilde{\nu}$ in cm^{-1} which are interconverted from the wavelength λ

$$\tilde{\nu} = \frac{1}{\lambda}. \quad (3.67)$$

In the case of a water subphase the reflection-absorbance R/R_0 is defined by the ratio of the sample reflectance R and the reflectance of the film-free water surface R_0 as reference. The reflection spectrum obtained in this manner is a function of wavelength, state of polarisation, film thickness, angle of incidence of the reflected light and the reflective indices of the three phases involved. Due to the complex optical properties of dielectric substrates like water, spectra can be obtained with s-, as well as p-polarised incidence radiation. The reflected intensity is very weak. It may be positive or negative depending on the state of polarization of the incident light, the proximity of the angle of incidence to the Brewster angle, and the direction of the change in the dipole moment during the normal mode [201–203].

A major impediment to the acquisition of good quality IRRAS spectra on aqueous surfaces is the spectral interference from the omnipresent rotation-vibration bands of water vapor. This problem can be addressed by application of the so called sample shuttle approach in which a reference IRRAS spectrum is acquired from a film-free surface. The intensity of light reflected from the film-covered surface is then normalised with respect to the reference spectrum. Thereby the interference from water vapor and other sources of noise is reduced

to very low levels. Furthermore the entire system must be enclosed and purged (e.g. with N_2) to keep the relative humidity levels as low and as constant as possible [201]. An alternative approach is the polarisation modulation-infrared reflection-adsorption spectroscopy (PM-IRRAS). Here the interfering effect of water vapor and carbon dioxide is greatly reduced by irradiating the surface with alternating linear states of polarized light [204].

For the interpretation of the experimental data traditional approaches applied for bulk IR spectroscopy can be adopted. In analogy typical peak-frequencies corresponding to structural features of the monolayer molecules are able to be identified. However band positions measured in IRRAS may differ from those observed in transmission due to effects arising from the optical properties of the substrate. Yet, structural information can be drawn from characteristic shifts in frequency, peak splitting or broadening caused by the occurrence of coupling between identical (or at least very similar) oscillators in the film [200]. E.g. the liquid-gel phase transition of lipids produces a typical splitting of the chain's CH_2 scissoring vibrations (1462 and 1474 cm^{-1}). Moreover it results in an increase of the symmetric CH_2 stretching frequencies from ~ 2848 to 2853 cm^{-1} [205]. Typical peak splits of the amide I band in peptides and proteins are utilised to determine the secondary structure of these biomolecules and is most drastic for antiparallel β -sheet conformation [206].

Band intensities are harder to measure accurately in vibrational spectroscopy than frequencies. In addition their interpretation is more difficult. Nevertheless they can be used to measure e.g. tilt angles of phospholipids or helix tilt angles of proteins [205]. This is achieved by following the dependence of the reflected light's intensity for different polarisation states and angles of incidence. The data can then be fitted by appropriate models derived from various theoretical descriptions of the interface [199].

Experimental Setup

The surface of a Langmuir trough, co-aligned with a Bruker Vertex 70 IR apparatus has been irradiated with p-polarised light from a NIR/MIR source in the range of $8000 - 200\text{ cm}^{-1}$ at an angle of incidence of 40° . The light is detected with a liquid nitrogen cooled MCT detector and the polarisation of the light is controlled by a HINDS PEM-100 polariser. The whole setup is sealed with a Plexiglas hood and purged with nitrogen. In order to avoid interference of water vapor, spreading solvent and CO_2 the trough shuttle technique is applied. The spectra have been analysed with the OPUS 6.0 software (Bruker).

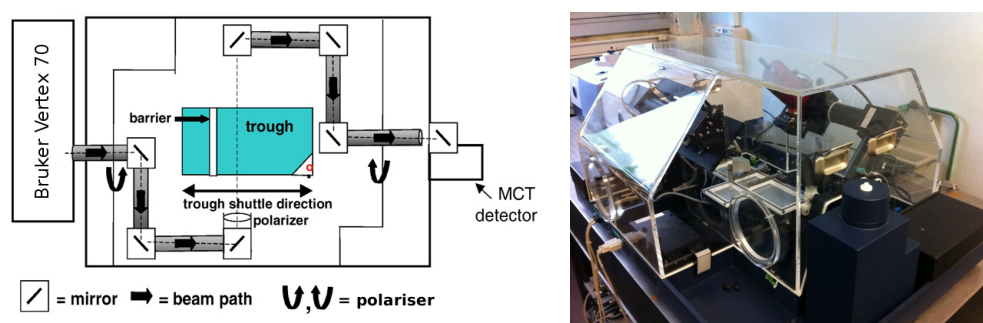


Figure 3.22: Schematic layout of the IRRAS system and photograph of the utilized IRRAS instrument.

The sample trough and reference trough are filled with a milipore water subphase. After spreading of the sample the system has been allowed to equilibrate for 30 min prior to the measurement. The film has been compressed with movable barriers to the desired surface pressure, determined by the Wilhelmy plate method.

3.8 Surface Force Apparatus

All methods involving direct measurement of molecular interactions between macroscopic surfaces, are based on the measurement of two quantities: The force of interaction and the distance that separates them. There are different techniques based on osmotic equilibria, force measurement on individual freely moving particles (total internal reflection microscopy, etc.) and most importantly force measurement devices using macroscopic solid surfaces (AFM, SFA, etc.). With the surface force apparatus (SFA), both attractive and repulsive forces can be measured from the deflection of a sensitive spring (cantilever). In contrast to AFM the separation between the surfaces is exactly defined and accurately determined by means of interferometric techniques. In most cases the force F scales with the radius of curvature of the surfaces R . For the most part the normalised force F/R can be directly related to the interaction free energy E . One of the most powerful techniques to measure the force profile between two surfaces is the interferometric surface force apparatus (SFA) pioneered by Israelachvili et al [207,208] in the mid 70s.

3.8.1 Principle

SFA allows the force measurement as a function of separation between two macroscopic surfaces in air or immersed in liquids. The separation between the surfaces is determined by optical interferometry and the force is read from the deflection of a cantilever spring on which one of the surfaces is mounted and that can be moved to bring the surfaces to a given separation. The principle behind the SFA is depicted schematically in Figure 3.23.

Preparation of the surfaces

Precise force measurements require a pair of surfaces which produces interference fringes yielding resolution of less than a few Angstrom. Thus delicately thin (1 - 3 μm thick), molecularly smooth and optically transparent substrates coated with silver layers need to be prepared. To ensure a contaminant free surface the whole sample preparation is carried out in a clean room.

The preferred substrate in the SFA is muscovite mica, which is a naturally occurring mineral consisting of aluminosilicate layers held together by ionic bonds between potassium. When mica is cleaved along crystallographic planes, the ionic interlayer bonds are broken and large atomically smooth areas (flat to within 0.1 nm) can be obtained. The mica is cleaved to obtain 1 - 3 μm thick sheets possibly free of cleavage steps. Small mica squares (1 cm x 1 cm) are cut with a white-hot platinum wire (0.1 mm diameter) and immediately placed face down on a freshly cleaved, large backing sheet onto which it adheres. In this way the surface of the pieces in contact with the backing sheet are protected from contamination. The backing sheet decorated with the small thin pieces can be transported and coated with a ~ 50 nm silver layer by vacuum deposition (reflectivity > 98% in the

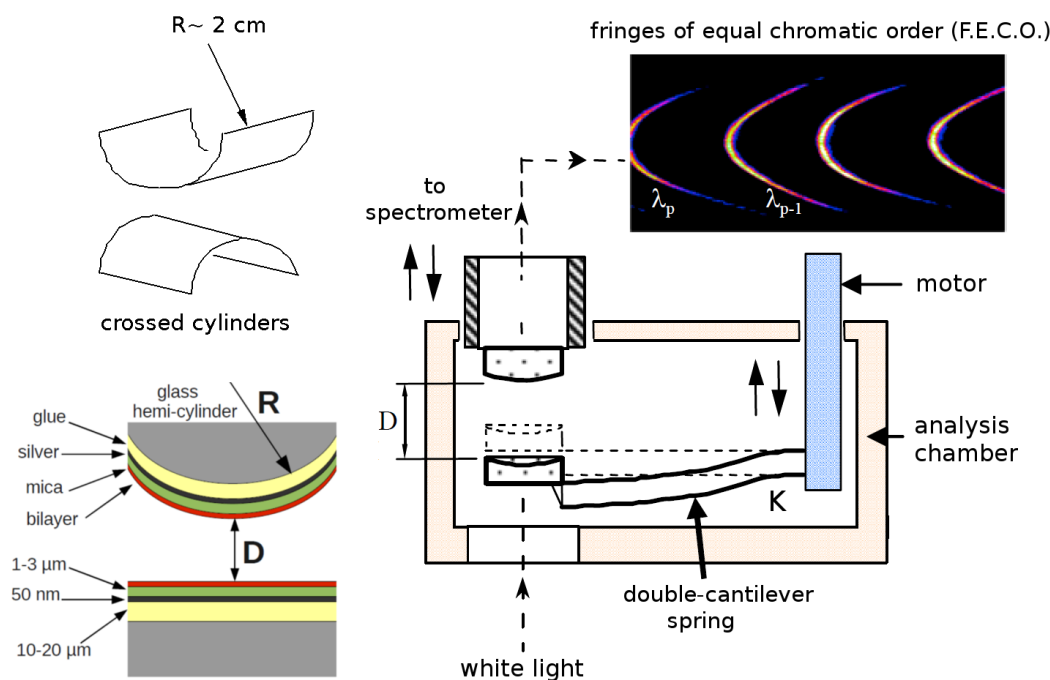


Figure 3.23: A schematic representation of the interferometric surface force apparatus (SFA). The surfaces are attached to a piezoelectric crystal and on a double-cantilever spring, respectively. The crossed cylinder geometry is equivalent to that of a sphere against a flat as the radius of curvature, R (about 2 cm), is much larger than the surface separation D (in the drawing the curvature of the surfaces has been exaggerated). The interference FECO pattern set in incident white light gives the real separation between the surfaces (relative to silver backing) and their local shape

green region of the visible spectrum).

Prior to an experiment the thin mica sheets are glued, silvered side down, to the supporting fused silica cylinders (highly polished to give a cylinder with a radius of 2 cm). As glue the thermosetting resin; Epikote 1004 from Shell Chemical Co. (melting point ca. 100°C) is used. The Epikote resin is very suitable as a glue for three reasons: it is transparent, it does not change its volume as it sets, thus preventing any stress in the glued mica sheet upon cooling and it is not a source for contaminants [209].

Langmuir-Blodgett deposition, like described in section 3.2 can be employed to produce bilayer films on the mica surface attached to the fused silica cylinders. They are then mounted in the SFA, keeping the bilayers in aqueous environment at all times.

Crossed cylinder geometry

The two thin sheets of mica freshly attached to the curved supporting silica disks, are mounted in the apparatus facing each other with the cylinder axes at right angles to each other (Figure 3.23). This geometry allows the precise alignment of two interacting plates and unwanted effects at the edges of the plates are avoided. The geometry of crossed cylinders has an additional advantage. If the region of contact becomes contaminated or locally damaged (for example due to adhesive properties of the surfaces) during the course of an experiment, one surface can be moved, first along the axis of one cylinder and then along the other to reveal a new and pristine contact area. Changing contact position several times under the same solution conditions within the same experiment increases the

statistics of the measured data and the reliability of the results.

The crossed cylinder arrangement is also convenient for the comparison of experiment with theory. R is the inverse Gaussian curvature ($R = \sqrt{R_1 R_2}$). According to Derjaguin the force between crossed cylinders of equal radius R , is the same as the force F between a sphere of radius R and a plane flat surface or between two spheres each of radius $2R$. Further, this force is equivalent to the free energy $E(D)$ of interaction per unit area between two plane parallel surfaces of the same material [210]:

$$\frac{F}{R} = 2\pi E. \quad (3.68)$$

For this reason, forces $F(D)$ measured with the SFA between two crossed-cylinders of mean radius of curvature R are routinely plotted as F/R and are therefore implicitly related to the interaction free energy $E(D)$.

The relation is only valid within certain limitations. The Derjaguin approximation holds provided the range of the force is small compared to the radius of curvature of the surfaces ($R \gg D$). This is always fulfilled in measurements using the SFA ($R \sim 2$ cm and $D \sim 0.1$ nm - several μm). R needs also to be independent of D (the surfaces must remain undeformed) so that $F(D)$ is mathematically well-defined, single-valued and integrable. This may not always be fulfilled. Especially when the surfaces are being deformed due to the action of strong surface forces the comparison between experiments and theory is no longer straightforward. In some cases the application of (3.68) can be questionable. Hence statistical mechanic derivations have to be applied to correctly describe the interactions e.g. for oscillatory structural forces arising between curved surfaces in fluids [210].

Distance measurement

The outer silvered faces of the two mica sheets form an optical cavity (a Fabry-Perot like interferometer) providing the means to measure distances. Collimated white light is directed and impinged normal to the surfaces. Multiple reflections occur between the two reflective films. The transmitted light consists of a spectrum of intensity maxima known as fringes of equal chromatic order (FECO) [211]. If a microscope focuses the light emerging from the interferometer on the entry slit of a grating spectrometer, the fringes are split up according to their wavelength. Analysis of this array allows to measure the optical thickness of the film and simultaneously determine the thickness and the refractive index of each layer in the interferometer.

It should be noted that multiple-beam interferometry requires the presence of two highly reflective thin films separated by one or more dielectric materials of total thickness greater than the wavelength of visible light. The spectrum can be accurately predicted using classical electromagnetic theory, and the FECO wavelengths depend on the thicknesses and the optical properties of the media (refractive indices and their dispersions) [211,212]. Since mica is birefringent, each fringe normally appears as a doublet. Thus one fringe is extinguished by passing the light through a polariser. Corrections to this equation and other analytic expressions exist to account for arbitrary thickness and refractive index for each layer, surface roughness and anisotropic (birefringent or optically active) optical media [213].

The spatial positions of the observed FECO change continuously as the separation be-

tween the surfaces is varied. The separation determined by multiple-beam interferometry is an absolute value relative to the predetermined zero separation (measured distance of contact in air, or in an aqueous solution). This is an important advantage over most of the non-interferometric devices. Under optimum experimental conditions a 0.1 nm resolution can be achieved for surface separations larger than 5 nm.

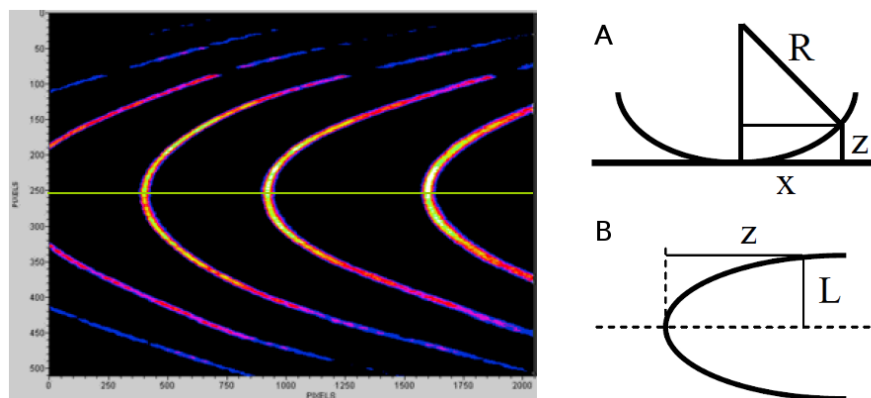


Figure 3.24: Typical interference FECO. Schemes A and B show the relation between sample geometry and fringe shape.

Since the gap between the curved surfaces is not uniform, the shape of the observed FECO is a direct representation of the relative geometry of the surfaces 3.24. In particular the curvatures of the surfaces can be measured along two perpendicular directions in the plane of the surfaces.

The lateral magnification is set by the microscope that focuses the light emerging from the interferometer to the spectrometer slit. Features of lateral dimensions larger than about $1\ \mu\text{m}$ can be observed. E.g. when the surfaces are brought into a strong adhesive contact a flattened region forms, which is easily observed in the FECO fringe pattern because the glue adhering the mica to the discs is rather compliant (Figure 3.24).

Force measurement

In the SFA design schematically displayed in Figure 3.23 one of the surfaces is attached to a piezoelectric tube. The other one is mounted at the end of a double force-measuring spring (force constant $\sim 50\ \text{N/m}$) that can be moved to bring the surfaces to a given separation.

Accurate force measurements require precise control of the surface separation. This is usually realised either mechanically by a system of micrometers and differential springs or by piezoelectric devices. The advantage of the latter ones is, that they displace the surfaces smoothly without causing vibrations. However the piezo-actuators are prone to nonlinearity, hysteresis and creep, which have to be corrected by electronic feedback system to provide a subnanometric precision.

Forces between the surfaces of the crossed cylinders are determined from the deflection of the cantilever spring system and calculated by Hooke's law with the known spring constant. The spring constant is calibrated with an accuracy of 1% after each experiment. Small calibrated weights are placed at the surfaces and the deflection is measured. A double

cantilever is preferable to a single leaf spring because it prevents the curved surfaces from rolling and shearing as the load is varied. The force can be determined with a resolution of about 50 nN. When normalised by the radius of curvature of the surfaces, this is equivalent to 0.002 mN/m, corresponding to a free energy $\sim 0.3 \mu\text{J}/\text{m}^2$ [213].

A force measurement is started with the surfaces separated well beyond the range of any surface force. Then the surfaces are stepwise approached. After each displacement, the surfaces are allowed to come to rest and their true distance is measured by the optical method. This process is repeated and the measured separation profile as a function of the actuator displacement is recorded. A straight line of slope equal to 1 is obtained at large separations where no force of interaction occurs. Repulsive forces are seen as a continuous deflection away from contact and are limited only by the onset of deformation of the surfaces. Strongly attractive surface interactions lead to a mechanical instability. Similar to AFM it occurs when the slope of the attractive interaction exceeds the spring constant of the force measuring spring. As a consequence the technique allows forces to be measured only over the regions where the gradient of the force ($\partial F/\partial D$) is smaller than the spring constant K . Thus only parts of the force curves are directly accessible and the force vs distance profile appears to be discontinuous, with jumps from unstable (e.g. $\partial F/\partial D > K$) to stable mechanical regimes.

3.8.2 Instrumental Aspects

The SFA displayed in Figure 3.25 is home-built by the group of Patrick Kékicheff at the ICS Strasbourg.



Figure 3.25: Image of the SFA.

The upper surface is attached to the piezo actuator (Physik Instrument) with a max. travel of 100 μm and a precision of 0.5 nm, used for fine approach of the surfaces. The lower surface is placed at the end of a double-cantilever spring made of stainless steel with a force constant between 25 - 50 N/m. The sample chamber with a volume of 45 cm^3 is also made of chemical inert stainless steel in order prevent contamination of the sample surfaces or solutions. For coarse alignment the surfaces are moved with screw spindle connected to a computer which allows displacement of the upper surface with a precision of 0.1 μm . In order to avoid thermal drifts of the mechanics, the temperature of

the sample chamber is strictly controlled to 25 °C using a PID controller (Lakeshore 340) which regulates the temperature with a precision of ± 0.5 °C/24h in the laboratory, ± 0.05 °C/24h within the plexiglas confinement and ± 0.001 °C/h within the sample chamber. The temperature of the laboratory is fixed 3 °C lower than the desired temperature of the SFA.

Collimated white light from 150 W halogen lamp is directed in the optical cavity via liquid-core optical fiber. The resulting interference pattern is enlarged by a 16x objective and directed to a Jobin-Yvon spectrometer by the imaging optical fiber (composed of 120000 single fibers). The spectrometer is coupled with a liquid nitrogen cooled CCD camera (2048 x 512 pixels). The spectrometer-camera system is controlled with a computer and the interference patterns are analysed with a home written software.

Sample preparation

The solid support consists of thin, molecularly smooth, back-silvered mica sheets, glued onto fused silica hemicylinders with an average radius of curvature of ~ 2 cm. After thickness calibration of the mica sheets, the bilayer samples are prepared by Langmuir Blodgett deposition.

The isotherms are recorded with a NIMA trough (10 x 30 cm) at a speed of 10 cm²/min at 25°C. As already stated above mica is the most suitable substrate for SFA, being hydrophilic, atomically smooth and with an exchangeable surface charge density of one charge per ~ 45 Å². All samples are prepared with a first layer of DSPE, deposited at 40 mN/m. Phospholipids with the zwitterionic phosphoethanolamine (PE) headgroups bind electrostatically to the negatively charged mica surface. At their highest packing density, the PE headgroups and their two chains have a surface area of 43 Å² closely matching the surface lattice and charge of mica. They provide a particularly smooth hydrophobic surface for deposition of a second monolayer [214]. The second layer is always deposited at 30 mN/m and degassed milipore water is used as subphase. The deposition speed is set to 5 mm/min for the DSPE layer and to 2 mm/min for the second layer.

The surfaces are then mounted under water in the SFA sample chamber filled with degassed milipore water. Force profiles have been recorded between the bilayer samples listed in Table 6.10.

Chapter 4

Amphiphilic behavior of cholesteryl CDs

A first step is to investigate the insertion of the CD anchors into model membranes. In order to understand the effect of the CD, both modified α - and β -CD compounds are studied. Furthermore CDs with a different number of hydrophobic cholesteryl anchors are compared regarding to the anchoring strength into phospholipid membranes. The chemical structure of the used molecules is shown in Figure 4.1.

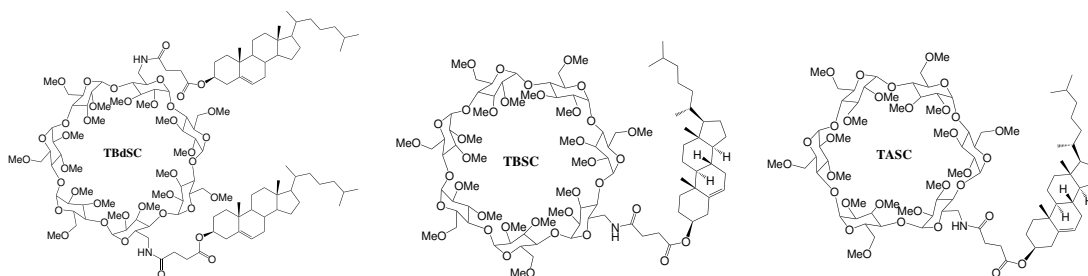


Figure 4.1: Chemical structures of TASC, which is an abbreviation for the trivial name Trimethyl-Alpha-CD-Succinyl-Cholesterol; TBSC for Trimethyl-Beta-CD-Succinyl-Cholesterol and TBdSC for Trimethyl-Beta-CD-diSuccinyl-Cholesterol

4.1 Interfacial behavior of pure cholesteryl CDs

4.1.1 Amphiphilic properties

At first Langmuir isotherms have been recorded for the permethylated β -CD analogues bearing one (TBSC) and two cholesteryl residues (TBdSC), as well as for the permethylated mono-cholesteryl α -CD (TASC). The surface-pressure area isotherms for a. TASC, b. TBSC and c. TBdSC are shown in Figure 4.2. For TASC and TBSC no significant temperature dependence can be observed (unlike to TBdSC) and BAM images feature aggregates which increase in number with the surface pressure Π and decrease in molecular surface area A .

Although the isotherms are reproducible for same spreading conditions and additionally no hysteresis is observed for isotherm cycles, increasing the amount of material spread

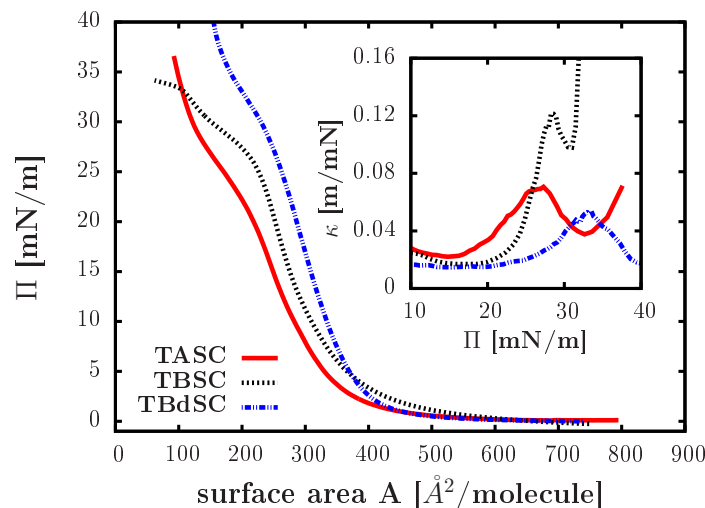


Figure 4.2: Langmuir Isotherms and isothermal compressibility (inlet) at 20°C: a. TASC, b. TBSC, c. TBdSC

on the surface slightly shifts the isotherm to higher surface areas. This effect is however negligible for the spreading volumes used for this study. Moreover the shape of the isotherms always remains the same.

All three isotherms exhibit a sharp rise beginning at $A = 350 \text{ \AA}^2$ for TASC, $A = 380 \text{ \AA}^2$ for TBSC and $A = 400 \text{ \AA}^2$ for TBdSC. They also show a pseudo-plateau at high surface pressures. The isothermal surface compressibility is plotted in the inset of Figure 4.2 in order to emphasize the pseudo-plateau as it shows local maxima for first order phase transitions. The compressibility curves for the three CDs show pronounced peaks for the pseudo-plateau at $\Pi = 25 \text{ mN/m}$ for TASC, $\Pi = 27 \text{ mN/m}$ for TBSC and $\Pi = 32 \text{ mN/m}$ for TBdSC (Figure 4.2). For TBSC the compressibility rises strongly after the pseudo-plateau peak, which, together with the flat continuation of the isotherm, is an indication for a film collapse. The TASC and the TBdSC isotherms look very much alike apart from the rise at different surface areas. Yet the TBSC starts rising slowly already for large surface areas and continues rather flat after the pseudo plateau.

All three investigated amphiphilic CDs show truly amphiphilic behavior and form stable monolayers since isotherms can be recorded up to very high surface pressures before film collapse occurs. The sharp increase of the TASC isotherm occurs for smaller surface areas ($A \approx 350 \text{ \AA}^2$) compared to TBSC ($A \approx 380 \text{ \AA}^2$) and TBdSC ($A \approx 400 \text{ \AA}^2$), which is reflecting the smaller size of the α -CD moiety in the former molecule. This observation, as well as the CDs much larger volume compared to the cholesterol residue leads us to the conclusion, that the shape of the isotherms is mainly determined by the CD part of the molecules. According to literature the β -CDs exhibits a higher structural flexibility compared to α -CD [99, 215]. Indeed in addition to the degrees of freedom due to the unique succinic linker, it is possible for a glycopyranose unit, typically the one grafted by the hydrophobic moiety, to spin about its glycosidic bond [97]. This should be much easier for β -CD than for the more sterically constrained α -CD. This higher deformability is the reason for the different isotherm shapes for TASC and TBSC (Figure 4.2). In TBdSC the rigidity of the usually rather flexible β -CD moiety is restricted by the two cholesteryl residues, explaining an isotherm shape similar to TASC, as well as a similar compressibility

at the pseudo-plateau (Figure 4.2). The slow rise for very large surface areas ($A \approx 600 \text{ \AA}^2$) and the sharp increase for smaller surface areas compared to TBdSC also reflect the greater flexibility of the TBSC.

4.1.2 Reflectivity measurements

Neutron and x-ray reflectivity experiments have been carried out to determine the film thickness and density profile in order to elucidate the nature of the pseudo-plateau in the isotherms.

In order to obtain a better contrast and to avoid incoherent scattering, D_2O has been used as subphase for the neutron reflectivity instead of normal water, which is used for the x-ray scattering. The shapes of the isotherms are very similar for both subphases. Thus the results for both methods can be directly compared. However, due to a limited compression range of the Langmuir trough available for the neutron experiment, more compound had to be spread on the surface to reach the desired surface pressures, leading to a slight shift to higher surface areas (10 - 20 \AA^2) for the isotherms. An isotope effect due to the D_2O might also contribute to the shift [32]. Therefore the surface areas from the isotherms recorded on the D_2O subphase are used for calculations where neutron data is involved.

The reflectivity curves in Figures 4.4, 4.5 and 4.6 show, that for all three modified CDs a minimum appears with increasing surface pressure, related to a structural change in the film. Starting at surface pressures around the pseudo-plateau, the scattering curve minimum drastically deepens. This behavior is most pronounced for TBSC, where we observe a very large step between the curves for surface pressures below and above the pseudo-plateau.

Complementary x-ray scattering experiments have only been measured for TASC and TBdSC for two points in the isotherm, one below and one above the plateau. And similar to the neutron experiment, the curves at low surface pressures are very different from the ones obtained at high pressures (the x-ray curves can be found in the appendix Figure 4.24). The data obtained from neutron and x-ray scattering are fitted with the same model. The measured curves are fitted using a two-layer box model (represented on top in Figure 4.3) with two distinct regions of scattering length densities SLD_1 , SLD_2 and electron density ED_1 , ED_2 respectively, as well as the corresponding thicknesses l_1 , l_2 . The top layer 1 can be assigned to the hydrophobic cholesterol and the bottom layer 2 to the hydrophilic CD residues. For TBSC at $\Pi = 32 \text{ mN/m}$ a third layer had to be added to the model in order to fit the data properly. The subphase roughness was $3 \pm 1 \text{ \AA}$ for all fits and the roughnesses for the CD and cholesterol layers have found to be in the range between 2 - 4 \AA .

Comparing the overall thickness of the films shows, that for low surface pressures the TASC monolayer is $\sim 15 \text{ \AA}$ and that TBdSC, as well as TBSC are $\sim 18 \text{ \AA}$ thick. For high surface pressures the film thickness increases to $\sim 27 \text{ \AA}$ for TASC, to $\sim 29 \text{ \AA}$ for TBdSC and to $\sim 33 \text{ \AA}$ for TBSC. This behavior is clearly visualized in the scattering length density profiles displayed in Figure 4.3.

We now examine in detail the special features of each compound. The detailed results for the three compounds can be found in the appendix in Tables 4.6, 4.8 and 4.7.

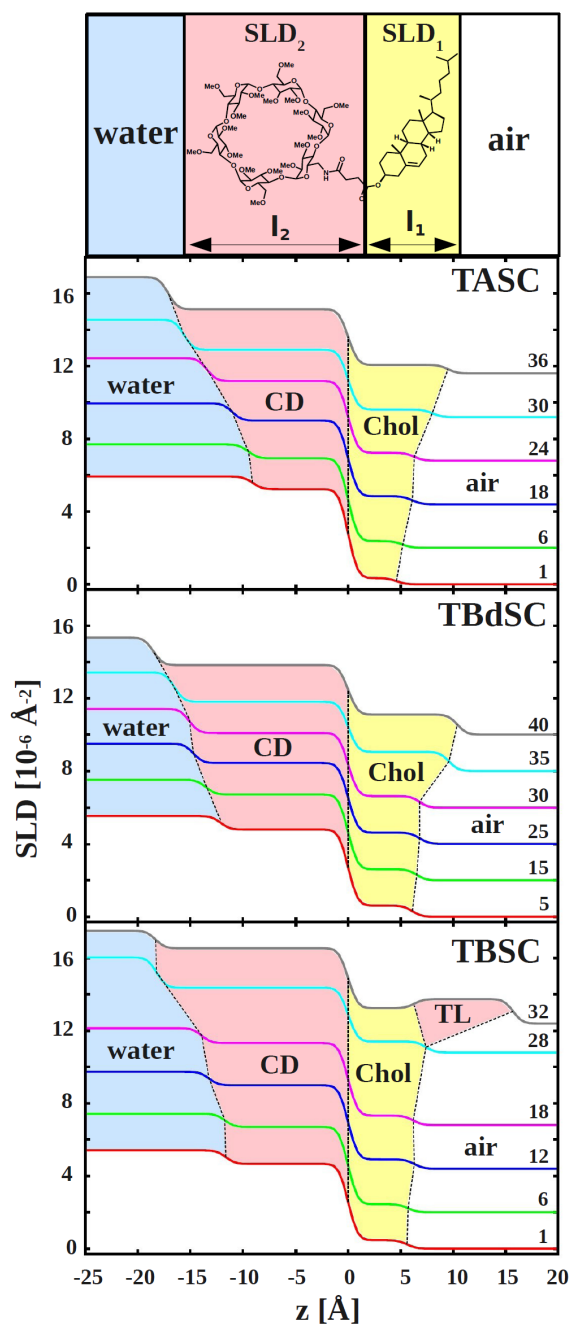


Figure 4.3: SLD profiles at different surface pressures for TASC, TBdSC and TBSC. The surface pressures corresponding to each SLD profile are indicated on the right side of the graph in mN/m. To account for better legibility, the curves have been consecutively shifted by $2 \cdot 10^{-6} \text{ \AA}^{-2}$ with increasing Π . TL signifies the additional layer which had to be added for TBSC at 32 mN/m. The arrows indicate the surface pressure at which the pseudo-plateau in the isotherm occurs.

TASC

The CD part of the monolayer shows a thickness in the range of 10 - 11 \AA up to surface pressures close to the pseudo plateau (4.3 and 4.8). Starting from $\Pi = 21 \text{ mN/m}$ the size of the CD layer increases steadily from 11 \AA to 17 \AA at 36 mN/m. The film compression is accompanied by a drop of the scattering length density from $5.2 \cdot 10^{-6} \text{ \AA}^{-2}$ to $3.6 \cdot 10^{-6} \text{ \AA}^{-2}$. Likewise, the x-ray experiments reveal a jump in electron density from 0.39 \AA^{-3} to

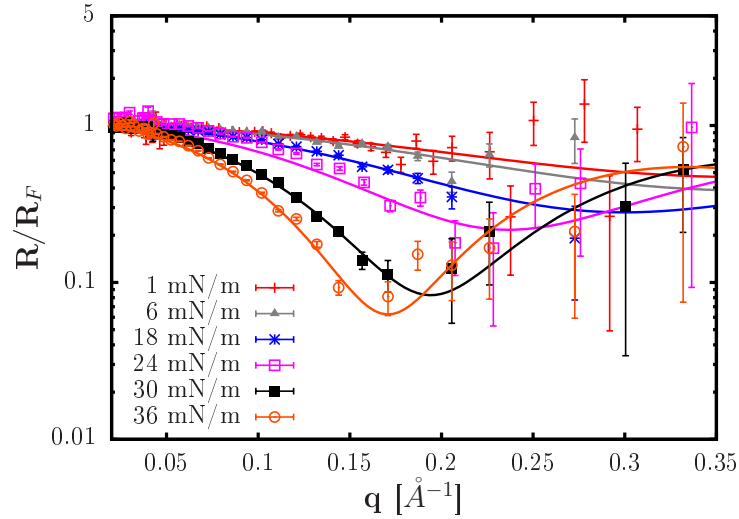


Figure 4.4: Neutron reflectivity curves at different surface pressures for TASC

0.43 \AA^{-3} . X-ray and neutron reflectivity curves are fitted with same model. As the x-ray data extend to higher q values, they better resolve the cholesteryl layer whose thickness has been constrained to the x-ray values for the neutron fits. It increases from $4.5 - 10 \text{ \AA}$ with compression. The scattering length density is found to be in the order of $0.4 \cdot 10^{-6} \text{ \AA}^{-2}$ for all surface pressures.

TBdSC

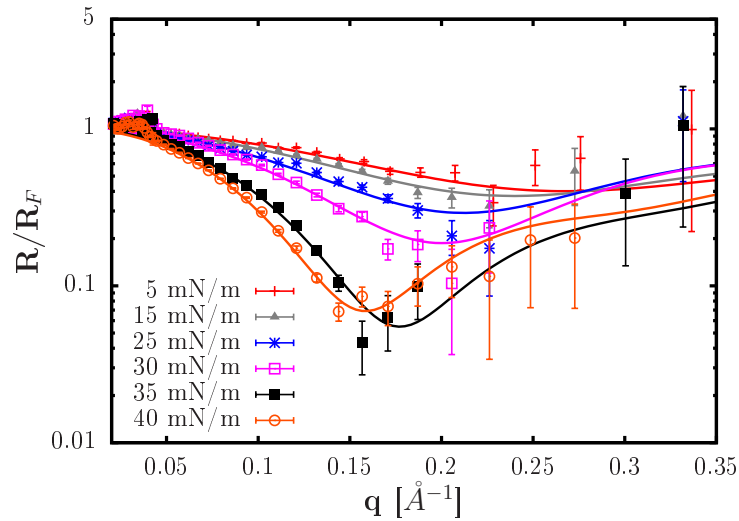


Figure 4.5: Neutron reflectivity curves at different surface pressures for TBdSC

For TBdSC the CD layer is found to be $\sim 12.5 \text{ \AA}$ thick at the beginning of compression (Figure 4.3). Starting from surface pressures close to the pseudo-plateau its size increases significantly to $\sim 18.5 \text{ \AA}$. Furthermore the scattering length density decreases from $4.8 \cdot 10^{-6} \text{ \AA}^{-2}$ to $3.8 \cdot 10^{-6} \text{ \AA}^{-2}$, as well as the electron density increases from 0.38 \AA^{-3} to 0.44 \AA^{-3} . The cholesteryl layer increases from 6 \AA to 10 \AA for $\Pi = 40 \text{ mN/m}$. The x-ray data gives comparable results with a rise from 6 \AA to 11.5 \AA .

TBSC

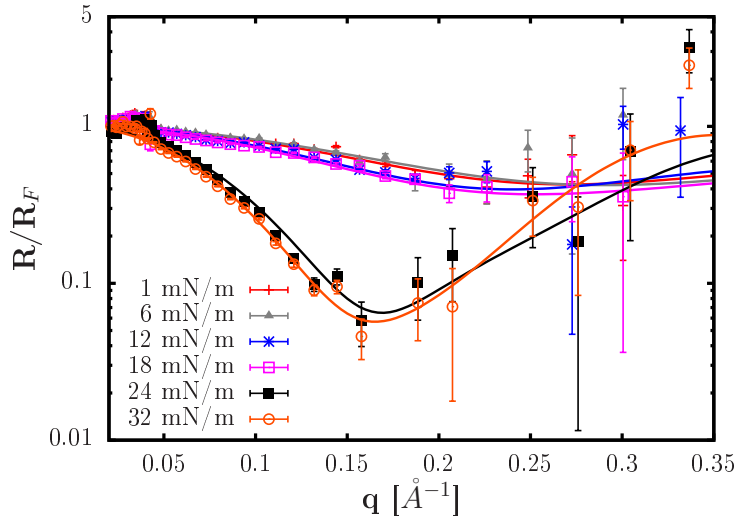


Figure 4.6: Neutron reflectivity curves at different surface pressures for TBSC

The CD layer of TBSC exhibits a thickness between 11.5 Å for low surface pressures up to 13.9 Å at $\Pi = 18$ mN/m. Then the size increases drastically to 18 Å at 28 mN/m (Figure 4.3), like for TASC and TBdSC coming along with a drop in scattering length density from $4.7 \cdot 10^{-6} \text{ \AA}^{-2}$ to $3.6 \cdot 10^{-6} \text{ \AA}^{-2}$. The cholesteryl layer increases from 5.7 Å to 7.4 Å at $\Pi = 28$ mN/m.

For $\Pi = 32$ mN/m a three layer model has to be applied in order to fit the curve. Good fits have only been obtained, adding the layer on top of the cholesteryl layer, whereas fitting the data adding the third layer on the CD side (subphase) has not been successful. We find, that the CD layer remains ~ 18 Å thick. The scattering length density is increased to $4.1 \cdot 10^{-6} \text{ \AA}^{-2}$, which is higher than for $\Pi = 28$ mN/m. For the middle layer a thickness of 6.3 Å and scattering length density of $0.8 \cdot 10^{-6} \text{ \AA}^{-2}$ is found. The additional top layer has a size of 9.4 Å with a scattering length density of $1.3 \cdot 10^{-6} \text{ \AA}^{-2}$. Moreover top-layer roughness (6 Å) is larger than that of the other layers (2 - 3 Å).

4.1.3 AFM

In order to investigate the in-plane structure of the monolayer, several Langmuir Blodgett films on mica have been prepared for different surface pressures and imaged by AFM.

For TASC the monolayer is very flat and homogeneous at low pressure (Figure 4.7 a.). An image at the pseudo plateau (Figure 4.7 b.) shows domains with a height of ~ 7 Å, as well as an increased roughness (~ 3 Å). At 34 mN/m (Figure 4.7 c.) the surface is again homogeneous, whereas the profile indicates that the roughness is larger compared to the low pressure image.

For low surface pressure the Langmuir Blodgett film of TBSC (Figure 4.7 d.) is very flat and homogeneous, similar to TASC. At 28 mN/m (Figure 4.7 e.) there are no domains visible and only a small increase in roughness can be observed. Figure 4.7 f. which is taken on the flat part of the isotherm at 33 mN/m, shows characteristic holes of ~ 15 Å depth and of a diameter of several hundreds of nm. It exhibits similar roughness compared to

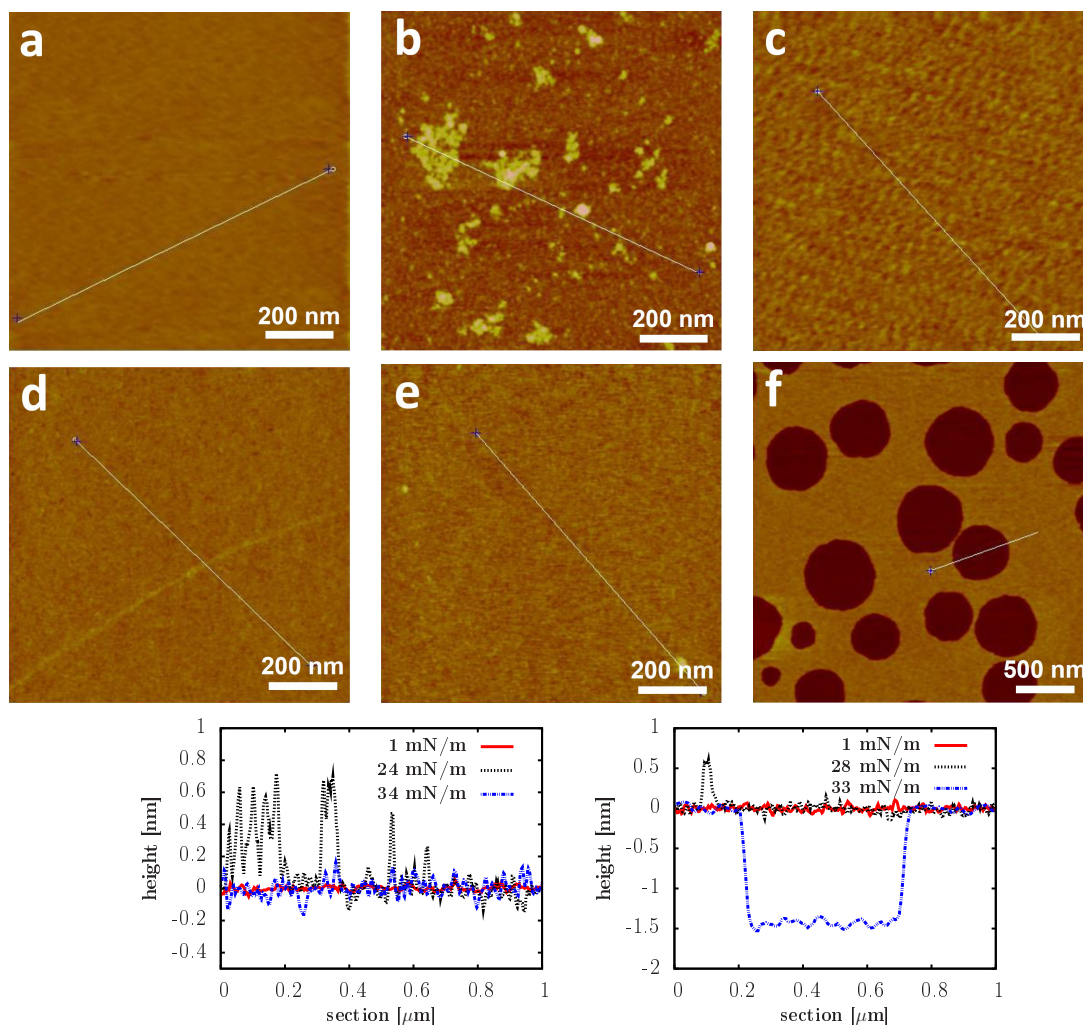


Figure 4.7: AFM images and profiles for TASC a. $\Pi = 1$ mN/m, b. $\Pi = 24$ mN/m, c. $\Pi = 35$ mN/m and TBSC d. $\Pi = 1$ mN/m, e. $\Pi = 28$ mN/m, f. $\Pi = 33$ mN/m

Figure 4.7 e.

4.1.4 Monolayer morphology

CD layer

Every isotherm of the investigated CDs comprises a pseudo-plateau which corresponds to a structural change in the monolayer. Looking at the CD part of the monolayer in more detail reveals for all investigated amphiphiles, that the thickness increases significantly about 6 - 7 Å comparing surface pressures below and above the pseudo-plateau. The compression of the film is accompanied by a drop of scattering length density in the neutron reflectivity experiment which corresponds to an expulsion of water from the film which is further discussed in the following section.

According to literature the torus height for methylated α - and β -CD is increased from 8 Å to 11 Å compared to native compounds due to the methyl groups [216]. Our data

for low pressures correspond well to these values. However we find that for TASC the CD layer is ~ 2 Å thinner compared to TBdSC and TBSC. This suggests that the smaller α -CD headgroup has a small influence on the torus height.

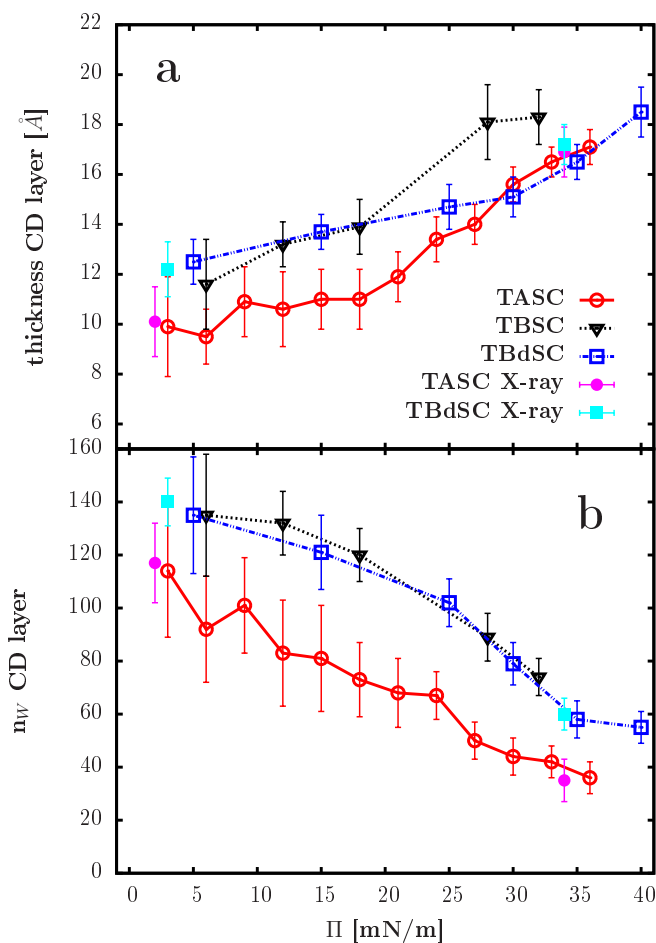


Figure 4.8: a. CD layer thickness and b. number of water molecules per CD for TASC (neutron \circ , x-ray \bullet), TBSC (neutron ∇) and TBdSC (neutron \square , x-ray \blacksquare) during compression

The x-ray and neutron results give a clear interpretation of the pseudo-plateau in the isotherms. The CD layer thickness is indeed equal to the methylated CD height for low surface pressures and to its diameter [75,83] at large surface pressures. The transformation occurring at the pseudo-plateau is a conformational change, where the axis of the CD's cavity rotates from perpendicular to parallel to the surface (Figure 4.9). For non-methylated native amphiphilic CDs such a reorientation has already been confirmed by IRRAS measurements at the air-water interface [217]. The rearrangement occurs gradually, ~ 1.5 Å every 3 mN/m, starting from the pseudo-plateau with the CD's axis being aligned more and more parallel with respect to the surface (Figure 4.9). Furthermore the AFM images for TASC at the pseudo plateau (Figure 4.7 b) exhibit domains with the same distinct height 6 Å corresponding to the difference between CD height and diameter, indicating a coexistence between the two conformations. AFM images at high pressure show again a homogeneous, flat surface, with the whole monolayer aligned in its high pressure conformation.

For TBSC the neutron reflectivity data suggests that the conformational change already occurs for lower surface pressures than for the disubstituted TBdSC. With further compression for surface pressures above 30 mN/m the flat continuation of the isotherm reveals the beginning of the film collapse. This is also reflected in the neutron data at 32 mN/m where an additional third layer on top of the cholesteryl layers is now required to successfully fit the reflectivity data. Since addition of a third layer close to the subphase does not give good fits, film buckling towards the solution is not a likely explanation. The third layer most probably consists of a TBSC double-layer with a very disordered top-layer, indicated by its high roughness (6 Å) compared to the other slabs (3 Å) and all other fits, where the roughness is in the order of 2 - 3 Å. As the transfer ratios are always found to be greater than 90%, the holes in the AFM image at $\Pi = 34$ mN/m (Figure 4.7 f) cannot be due to a loss of material during the transfer. They are consistent with a partial bilayer formation where zones of monolayer remain, also explaining a drastically decreased SLD of the top layer as an average between the holes and the elevated regions is measured [218]. The low scattering length density of the top layer also indicates that the CDs are only very little hydrated compared to the CDs situated in the layer close to the water. This is possible since the methylated CDs itself are known to be surface active.

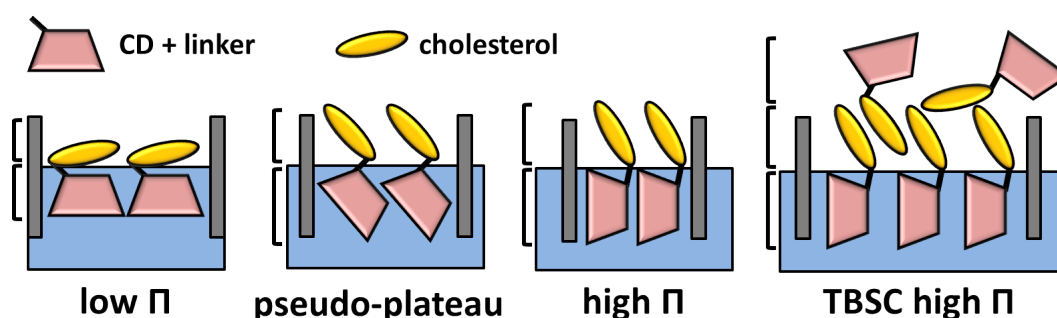


Figure 4.9: Change of conformation in the CD layer

Cholesteryl layer

The thickness of the cholesteryl layer is mainly determined by the available surface area due to the CD moiety. It increases with compression from 4.5 - 10 Å for the monosubstituted α -CD and from 5 - 7.5 Å for the β -CD derivative, as the bulkier β -CD leaves more space for the cholesteryl moiety. Similarly, the two cholesteryl moieties of TBdSC require more space, leading to a more pronounced increase in cholesteryl layer thickness with compression (6 - 11 Å). The more compact packing of the TBdSC's cholesteryl layer is also reflected in the significantly increased scattering length and electron densities for high pressures in contrast to the monosubstituted molecules. Values reported in literature for a fully stretched cholesterol molecule are ~ 17 Å [219]. At least part of the succinyl linker (~ 3 Å) should be assigned to the cholesteryl layer, explaining the elevated average SLD for the "cholesterol" slab compared to the expected cholesterol SLD ($0.2 \cdot 10^{-6} \text{ \AA}^{-2}$ [220]) since the SLD for the succinyl linker can be estimated to be in the order of $2.6 \cdot 10^{-6} \text{ \AA}^{-2}$. The effect seems to be most pronounced for TBdSC in high pressure conformation where the SLD for cholesterol is very much increased.

The tilt angles Θ for the cholesteryl part of the monolayer at maximum compression have been calculated from the expression

$$\cos\Theta = \frac{l_{Chol}}{l_{st}}, \quad (4.1)$$

with the measured thickness of the cholesteryl layer l_{Chol} and the length of the fully stretched cholesteryl molecules l_{st} obtained from literature [219]. The tilt angles decrease in the order TBSC (64°), TASC (55°) and TBdSC (50°) reflecting the available space of the cholesteryl residue in each compound. For low surface pressures the cholesterol moieties are arranged almost flat on the surface. With rising compression the increasingly smaller available surface area forces the cholesterol residues to arrange themselves more upright and for TBdSC increasing the proportion of the linker group in the top layer. However also at elevated pressure, there remains sufficient space for the cholesterol moieties to be tilted, due to the bulky CD residues determining the required surface area of the molecule.

4.1.5 Hydration of CD-headgroup

Methylated CDs are strongly hydrated in aqueous environment [221–223]. Therefore the CD layer in the film contains a large water content. The number of water molecules per CD, n_W , can be calculated using the scattering length, SLD_{CD} , and electron density, ED_{CD} , extracted from the fits starting from following definitions:

$$SLD_{CD} = \frac{SL_{CD} + n_W SL_w}{l_{CD} A}, \quad (4.2)$$

$$ED_{CD} = \frac{N_{CD} + n_W N_w}{l_{CD} A}; \quad (4.3)$$

with the scattering length of the CD SL_{CD} , and D₂O SL_w , the surface area A extracted from the isotherm and the corresponding length of the CD layer l_{CD} . N_{CD} is the number of electrons in the CD residue of the molecule and N_w the number of electrons in heavy water. For the neutron data this leads to the expression (4.4).

$$n_W = \frac{SLD_{CD} l_{CD} A - SL_{CD}}{V_w SLD_w}. \quad (4.4)$$

The scattering length of water is substituted by $V_w \cdot SLD_w$, where V_w is the molecular volume of D₂O (30 Å³) and SLD_w the scattering length density of the subphase, obtained from fitting the reflectivity curves. This is necessary as the values found for SLD_w (see Tables 4.6, 4.7 and 4.8 in appendix) are significantly lower than the literature value for pure heavy water (6.36 10⁻⁶ Å⁻²). As previously observed [224], the D₂O subphase gets enriched with normal water from the atmosphere. This is reflected by a decrease of SLD_w during the experiment. The H₂O content at the air-heavy water interface is calculated to be between 12 - 18 % depending on the duration of the experiment (see Figure 4.25). For the x-ray experiments, n_W is expressed by equation (4.5).

$$n_W = \frac{N_{CD} l_{CD} A - N_{CD}}{N_w}. \quad (4.5)$$

Figure 4.8 shows the calculated number of water molecules per CD in the film for the different surface pressures. The values calculated from the x-ray data correspond very well

to the results from the neutron scattering experiments. The water content decreases with rising compression for TASC from 114 to 36, for TBdSC from 135 to 55 and for TBSC from 193 to 74. The TASC molecule is the least hydrated as it possesses one glucose unit less than the two β -CD derivatives TBdSC and TBSC. The hydration behavior of TBSC and TBdSC is similar (Figure 4.8 b), as expected, because they possess chemically identical headgroups. The number of water molecules per CD we calculated for low surface pressures corresponds well to values reported for methylated CDs in the bulk phase [222]. At high surface pressures we find that the CDs are less hydrated than in the bulk [225]. Looking at Figure 4.8 b the loss of water in the layer occurs slowly for low compression and then more rapidly from the pseudo-plateau in the isotherm.

Knowing n_W , it is possible to calculate x_W , the volume percentage of solvent content in the CD layer

$$x_W = \frac{n_W V_w}{l_{CD} A}. \quad (4.6)$$

By fixing the solvent penetration of the CD layer, the actual scattering length density SLD_{CD-w} and electron density ED_{CD-w} of the CD residues without water can be directly obtained from the fit. Thus we have a means to estimate the molecular volume V_{CD} using equation (4.7) for the neutron and equation (4.8) for the x-ray data.

$$V_{CD} = \frac{sl_{CD}}{SLD_{CD-w}} \quad (4.7)$$

$$V_{CD} = \frac{N_{CD}}{ED_{CD-w}} \quad (4.8)$$

The calculated mean values of the scattering length density SLD_{CD-w} , as well as electron density ED_{CD-w} without water for the CD part and the corresponding molecular volumes V_m , are displayed in Table 4.1.

compound	SLD_{CD-w} [$10^{-6}/\text{\AA}^2$]	V_{CD} [\AA^3]	ED_{CD-w} [\AA^{-3}]	V_{CD} [\AA^3]
TASC	2.15 ± 0.25	990 ± 280	0.539 ± 0.05	1300 ± 250
TBdSC	1.98 ± 0.20	1310 ± 220	0.550 ± 0.05	1530 ± 200
TBSC	1.83 ± 0.25	1320 ± 330		

Table 4.1: Mean SLD_{CD-w} and ED_{CD-w} , as well as corresponding V_m for TASC, TBSC and TBdSC

The SLD_{CD-w} as well as the ED_{CD-w} values are consistent with the ones found for bulk solutions of CDs (β -CD: $V = 1200 \text{ \AA}^3$, dimethyl- β -CD: $V = 1575 \text{ \AA}^3$) by Kuzmin et al. [225]. As expected the V_m for the methylated α -CD in TASC is smaller than for the β -CD derivatives. The V_m values from the neutron data seem to be slightly smaller but within the error bars comparable to what has been reported for bulk solutions [225]. The decreased values could be explained by the fact that we calculated the molecular volume as an average, since we assumed the V_m to stay constant during compression.

4.2 Membrane insertion properties of amphiphilic CDs

In this section the insertion properties of the amphiphilic CDs into phospholipid mono- and bilayers will be investigated. Special emphasis will be given to understanding the

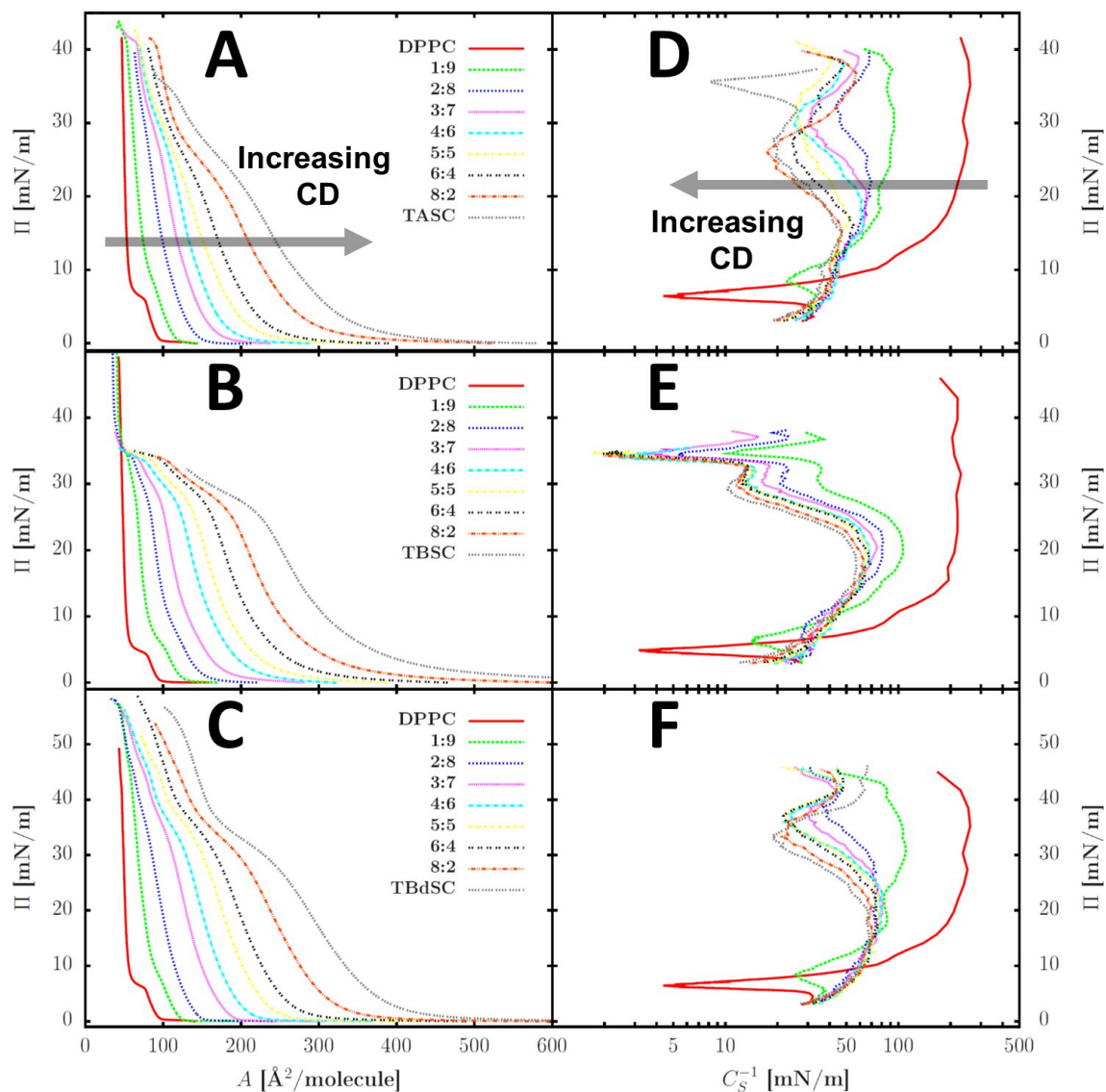


Figure 4.10: Langmuir isotherms (left: A. TASC, B. TBSC, C. TBdSC) and inverse compressibility plots (right: D. TASC, E. TBSC, F. TBdSC) for CD/DPPC mixtures at 20°C.

influence of the CD moiety, as well as the number of cholesteryl anchors on the anchoring strength.

4.2.1 Monolayers

Langmuir Isotherms

Compression isotherms have been recorded for CD/DPPC mixtures with CD molar ratios between 0 and 100 mol% in steps of 10 mol% (Figure 4.10 A - C). Mixed layers containing TASC collapse independently from the mixing ratio at ca. 42 mN/m (Figure 4.10 A). For TBdSC, isotherms can be recorded up to surface pressures even > 50 mN/m (Figure 4.10 C). The TBSC/DPPC isotherms can be compressed up to a plateau around 35 mN/m. For CD ratios smaller than 40% film compression beyond surface pressures > 50 mN/m is possible (Figure 4.10 B). Considering the collapse pressure as criterion for film

stability [226], the TBdSC mixtures are the most stable, followed by TASC and TBSC. The greater stability of the TBdSC films might be caused by the stronger anchoring due to the two lipophilic cholesteryl anchors. Furthermore Figure 4.10 B shows that TBSC monolayers tend to get more stable with increasing DPPC content.

In order to better visualise the phase transitions in the isotherms the data are plotted in terms of surface pressure vs inverse isothermal compressibility (Figure 4.10 D - F). The DPPC plateau (first peak in the inverse compressibility plots) at 6 mN/m, assigned to the liquid expanded (LE) - liquid condensed (LC) phase transition, can only be found for mixtures with a CD content < 20 mol%. However it is less pronounced and shifted to higher surface pressures.

The 10 mol% mixtures for TASC and TBdSC resemble DPPC also at high surface pressures (Figure 4.10 D and F). Yet the maximum C_S^{-1} value is already greatly diminished compared to the pure phosphocholine (250 mN/m), but still in the range of 100-250 mN/m which is typical for the liquid condensed phase according to reference [164]. In contrast TBSC exhibits already the features of pure CD (Figure 4.10 E).

For CD contents > 50 mol% the curves for all compounds almost completely coincide with the ones for pure CD (Figure 4.10 E - F). Maximum values of C_S^{-1} are in the order of 50-60 mN/m, which are similar to phospholipids in the liquid expanded phase [165,227]. The CD's pseudo-plateau (second peak in the inverse compressibility plots) is gradually shifted to higher surface pressures with decreasing CD content. The shifts are most pronounced for TASC and TBdSC. This transition can be assigned to a reorientation of the CD residues from a conformation where their cavities' axes are aligned perpendicular with respect to the interface to a conformation where it is aligned parallel with respect to the interface, like described in section 4.1 for the pure methylated CDs [228].

In order to gain a better understanding of the interactions between the phospholipid and the amphiphilic CDs the excess free energy of mixing ΔG_{mix}^{ex} is calculated from the isotherms and plotted as a function of molar fraction of CD for four different surface pressures (Figure 4.11). Negative values indicate attractive interactions whereas positive ones specify repulsive interactions. Due to rather large error bars for the calculations they can only be interpreted in a qualitative manner. All three different DPPC/CD mixtures are negative for low surface pressures and tend to get more positive with increasing surface pressures. This means that the compounds get less miscible with compression. Looking at the general tendency the values for TBSC are the most negative and the ones for TBdSC the most positive, leading to the assumption that the miscibility with DPPC decreases in the order TBSC, TASC and TBdSC.

Monolayer in-plane morphology

With the help of BAM and AFM the in-plane film morphology can be investigated from μm to nm scale. For low surface pressures no contrast is observed with BAM (Figure 4.12 A) and very flat AFM images without any features are obtained (Figure 4.13 A). At 15 mN/m bright domains appear (Figure 4.12 B) which look alike those for the liquid-expanded (LE) -liquid-condensed (LC) phase transition of pure DPPC [31]. Complementary AFM images

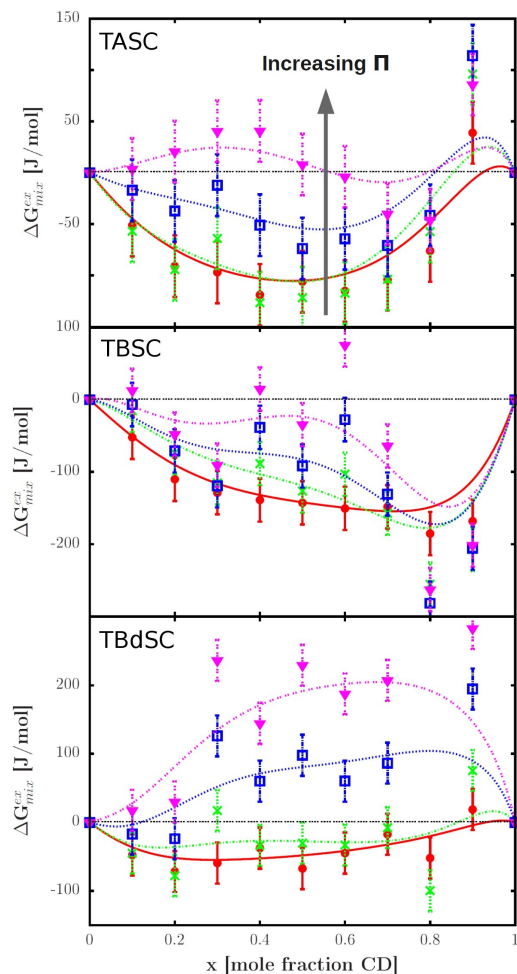


Figure 4.11: ΔG_{mix}^{ex} vs molar fraction of CD for different surface pressures from top to bottom A. TASC (\bullet) 5 mN/m, (\times) 15 mN/m, (\square) 25 mN/m, (\blacktriangledown) 35 mN/m), B. TBSC (\bullet) 5 mN/m, (\times) 15 mN/m, (\square) 25 mN/m, (\blacktriangledown) 33 mN/m) and C. TBdSC (\bullet) 5 mN/m, (\times) 15 mN/m, (\square) 30 mN/m, (\blacktriangledown) 40 mN/m.

(Figure 4.13 B) show a high granularity with small elevated zones of 30 - 80 nm diameter (much smaller than the zones observed in BAM) and a height < 1 nm. With further compression the aggregates visible in BAM become less bright and denser, many of them consisting of a bright core with a dimmer surrounding (Figure 4.12 C and D). These large domains are also visible in the AFM images and they possess a height of 1 nm (Figure 4.13 C). Furthermore there are now additional aggregates, which are 15 - 20 nm high. At the same time the small aggregates, also visible in Figure 4.13 B for lower compression, remain. The friction contrast of the large domains is similar compared to the small ones already visible for 15 mN/m, whereas the tall aggregates which appear for high compression are characterised by a very low friction (see Figure 4.26 in the appendix). The findings for BAM and AFM are similar to what is observed for TBdSC/DPPC mixtures except that there is no contrast inversion for very high surface pressures.

Monolayer structure perpendicular to the surface

Neutron reflectivity experiments are carried out to determine the film thickness and SLD profile of mixed CD/DPPC films for different surface pressures. Some important SLDs

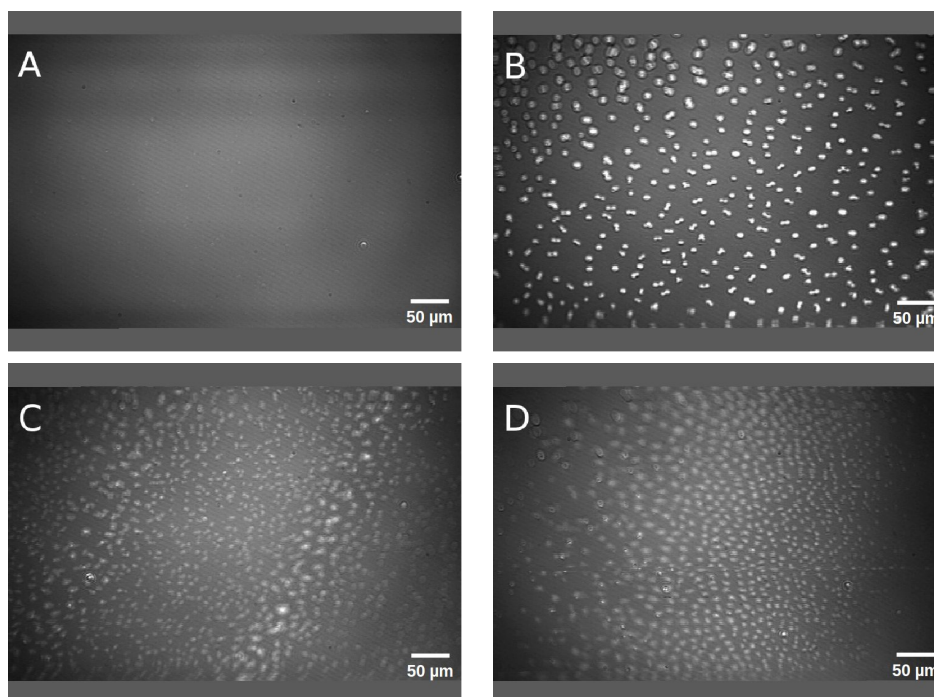


Figure 4.12: BAM images for a DPPC monolayer with 20 mol% TASC, A. $\Pi = 5$ mN/m, B. $\Pi = 15$ mN/m, C. $\Pi = 22$ mN/m, D. $\Pi = 35$ mN/m.

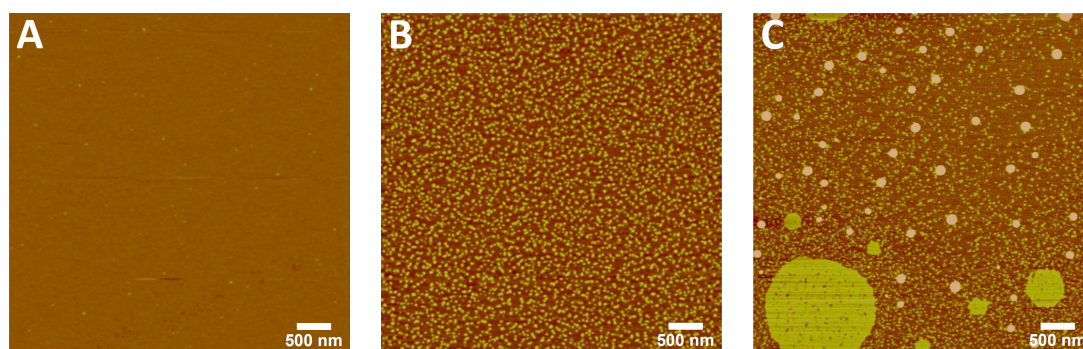


Figure 4.13: AFM height images for a DPPC monolayer with 20 mol% TASC, A. $\Pi = 5$ mN/m, B. $\Pi = 15$ mN/m, C. $\Pi = 35$ mN/m.

are listed in Table 4.2.

In order to obtain a better contrast and to avoid incoherent scattering, D_2O is used as a subphase for the neutron reflectivity instead of normal water. The isotherms' shape is preserved. However it is slightly shifted to higher molecular areas ($\sim 10 \text{ \AA}^2$) compared to isotherms on a H_2O subphase due to an isotope effect affecting the headgroups [32].

The monolayer data (Figure 4.14) is fitted using a two-layer box model with two distinct regions of scattering length densities and corresponding thicknesses. The top layer 1 close to air can be assigned to the hydrophobic tails of DPPC and the cholesteryl moieties of the CD. The 2nd layer should consist of the hydrophilic DPPC head groups and CD residues. The subphase roughness is constrained to 3 \AA . The roughnesses of the two slabs have been constrained to be the same for one surface pressure.

The reflectivity curves for TASC/DPPC- D_{62} in Figure 4.14 clearly show a shift of the scattering curve minimum to lower q values with rising surface pressure, which indicates

material	SLD [10^{-6}Å^{-2}]
Si	2.07
SiO ₂	3.47
D ₂ O	6.34
4MW	4
SMW	2.07
H ₂ O	-0.56
DPPC-palmitoyl tail	-0.41
DPPC-D ₆₂ palmitoyl tail	6.82
DPPC-PC head	1.74
TASC-CD head	2.15
TASC-cholesteryl tail	0.5

Table 4.2: Selected scattering length densities (SLD's) for used materials taken from references [38, 228, 229].

Π mN/m]	l_{head} [Å]	SLD_{head} [10^{-6}Å^{-2}]	water [%]	l_{tail} [Å]	$SLD_{tail-d62}$ [10^{-6}Å^{-2}]	SLD_{tail-H} [10^{-6}Å^{-2}]	roughness [Å]
5	8.0	4.15	56	8.5	4.05	-0.30	1.0
15	8.5	3.95	52	10.5	4.25	-0.05	2
22	9.0	4.00	54	11.0	4.60	0.15	2
30	10.0	3.85	51	11.5	4.90	0.15	3
35	10.5	3.85	51	12.5	5.45	0.20	3
40	12.5	3.70	48	13.0	5.60	0.25	4
errors	± 1	± 0.2	± 5	± 1	± 0.2	± 0.2	± 1

Table 4.3: Fitting results for the DPPC-D₆₂ monolayer with 20 mol% TASC (Figure 4.14 at different surface pressures. l_x is the thickness and SLD_x the scattering length density of slab x

an increase in monolayer thickness.

Expectedly, the total film thickness of the monolayer (Figure 4.15 top) increases from $\sim 16 \text{Å}$ to $\sim 26 \text{Å}$ with surface pressure. Also the film roughness increases from 1Å to 4Å for high compression. Looking at the Π dependence of the SLD profile (Figure 4.14 bottom) reveals that there exists only a small SLD contrast between the hydrophilic and the hydrophobic slabs for the expanded monolayer, which strongly increases when the monolayer is compressed. The thickness of the hydrophilic layer increases from 8Å at 5mN/m to 12.5Å at 40mN/m which is most pronounced between 35 and 40mN/m . It is accompanied by a drop of SLD from $4.1 \cdot 10^{-6} \text{Å}^{-2}$ to $3.7 \cdot 10^{-6} \text{Å}^{-2}$ due to a loss of water from 35 to 11 water molecules per headgroup. The number of water molecules is calculated in the same way as described in section 4.1.5 [228].

The hydrophobic layer thickness increases from 8Å at 5mN/m to 13Å at 40mN/m , at which the tails contribute the most to the rise of film thickness up to 15mN/m . The maximum tail thickness is $\sim 4 \text{Å}$ smaller than described for pure DPPC [32, 230], as well as DPPC/cholesterol mixtures [231]. During compression the SLD increases from $4.0 \cdot 10^{-6} \text{Å}^{-2}$ to $5.6 \cdot 10^{-6} \text{Å}^{-2}$ for deuterated DPPC and from $-0.3 \cdot 10^{-6} \text{Å}^{-2}$ to $0.25 \cdot 10^{-6} \text{Å}^{-2}$ for the mixed layer containing hydrogenated DPPC (see Table 4.3 and Figure 4.15), which is an indication for a more compact arrangement.

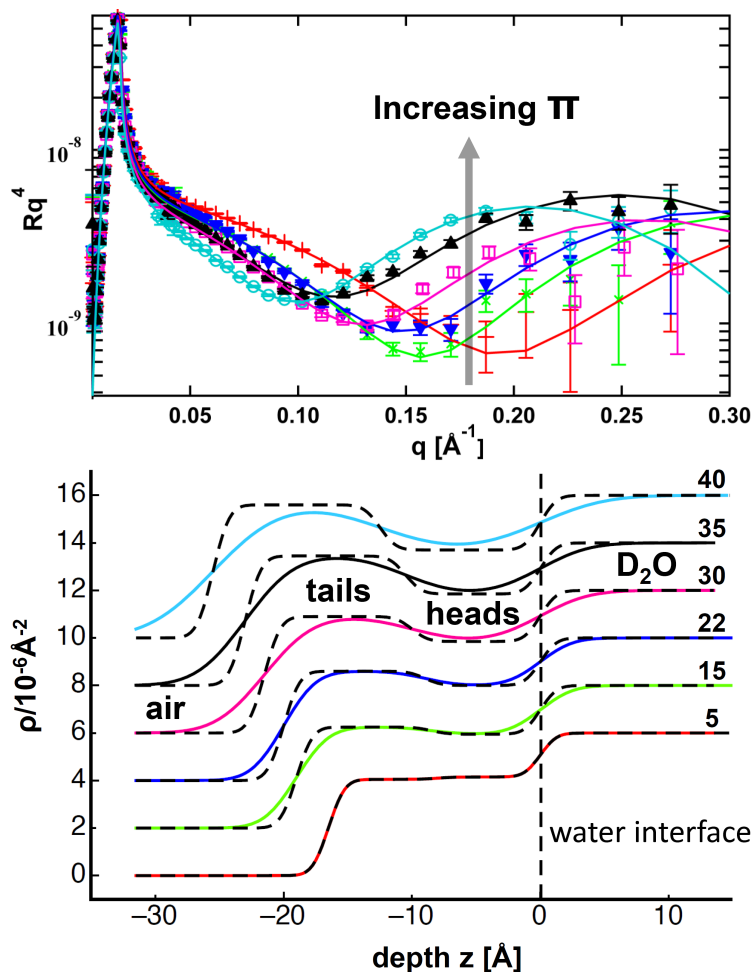


Figure 4.14: Neutron reflectivity curves and SLD profiles from bottom to top with increasing surface pressures for TASC/DPPC-D₆₂ 2:8 (+ 5 mN/m, × 15 mN/m, ▼ 22 is mN/m, □ 30 mN/m, ▲ 35 mN/m, ○ 40 mN/m). The dashed lines in the SLD profile indicate the different slabs of the box model.

4.2.2 Bilayers

Bilayer in-plane morphology

Bilayers deposited on mica substrates with the same compositions as those investigated by neutron reflectivity, have been imaged by AFM in water (Figure 4.16). All three studied bilayers are rather homogeneous and a phase separation is observed, which is consistent with the findings for the monolayers at high surface pressures. The symmetric bilayer displays a height difference between the zones of ~ 1 nm compared to ~ 0.5 nm for the asymmetric ones. In addition there are holes of ~ 5 nm in the 10 mol% TASC sample (Figure 4.16 A), which correspond very well to the bilayer thickness. Like for the monolayers, the friction is greater for the elevated domains (see Figure 4.27 in the appendix). Comparing the asymmetric bilayers with 20 mol% and 50 mol% TASC, the elevated domains get fewer with increasing CD content, leading to the conclusion that the domains mainly consist of DPPC.

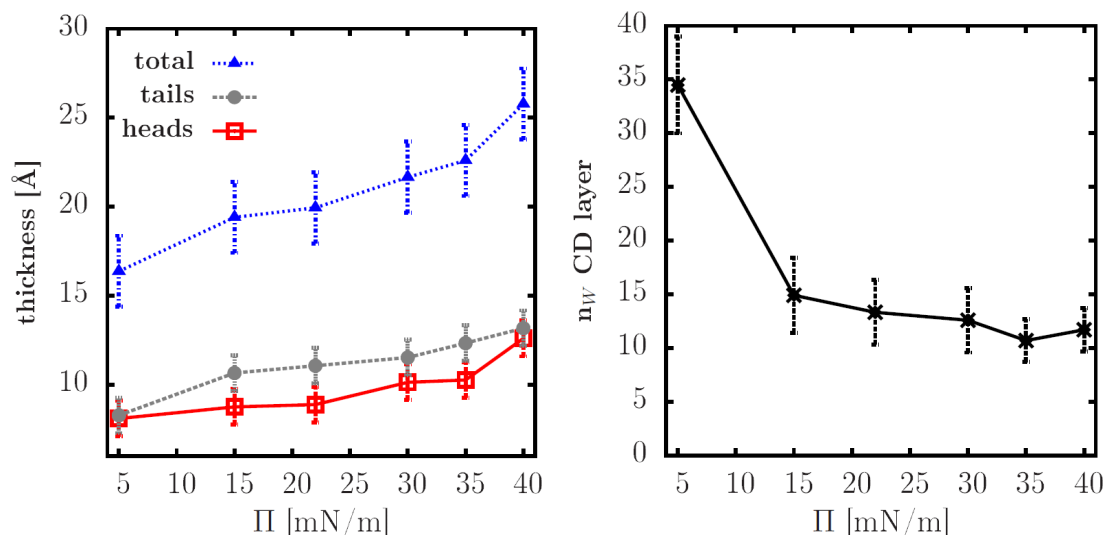


Figure 4.15: Thickness of TASC/DPPC monolayer (left) and water content of head layer (right) in dependence of surface pressure.

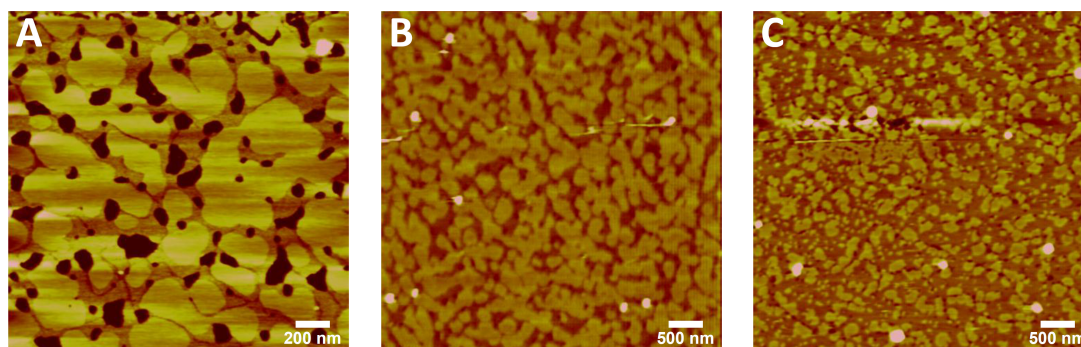


Figure 4.16: AFM height images for TASC/DPPC bilayers deposited at 40 mN/m, A. symmetric 10 mol% TASC, B. asymmetric 20 mol% TASC, C. asymmetric 50 mol% TASC.

Bilayer structure perpendicular to the surface

Symmetric bilayers with the same composition for both leaflets and asymmetric bilayers with a first DPPC monolayer close to the silicon substrate and a second mixed layer exposed to the water subphase are prepared (for details see Table 4.4). For all samples at least one measurement has been carried out for the bilayer in gel phase at 25°C and in liquid phase at 55°C. For annealing, one heating and cooling cycle is performed prior to the actual measurement. For two samples also intermediate temperatures in steps of 5°C have been measured.

sample	1st layer	2nd layer	contrast
1:9 sy	10 mol% TASC	10 mol% TASC	H ₂ O, H ₂ O, SMW
2:8 as	pure DPPC	20 mol% TASC	H ₂ O, SMW
5:5 as	pure DPPC	50 mol% TASC	H ₂ O, 4MW, SMW

Table 4.4: Composition and contrasts used for TASC/DPPC bilayers prepared for neutron reflectivity experiment (sy: symmetric, as: asymmetric).

For symmetric bilayers a 5 layer model is adopted with a SiO₂ layer on the silicon block, a thin water layer between membrane and substrate, two headgroup slabs as well as

a inner membrane layer for the hydrophobic part. For the asymmetric bilayer a 6th layer is added to take into account the inner membrane layer being divided in a slab, which consists only of DPPC tails and another one where the lipid chains are mixed with the cholesteryl residues of the CDs.

The fits for different contrasts have been performed in a coupled manner. For the monolayer only the SLD of the hydrophobic tails is allowed to vary for both contrasts. For the bilayers only the subphase scattering length density is changed for different contrasts. The error bars are determined by varying each parameter of the model and evaluating the χ^2 parameter, as well as visually checking the quality of the fit.

Good coupled fits have been obtained for all measured samples at different temperatures with an exploitable q -range from 0.01 to 0.25 \AA^{-1} . Stable bilayers can be prepared for a symmetric bilayer, with both membrane leaflets containing 10 mol% TASC, as well as asymmetric bilayers with the outer layer containing up to 50% CD (Figure 4.17). The other reflectivity curves, as well as the fitting results for all measured bilayers can be found in the appendix section 4.4).

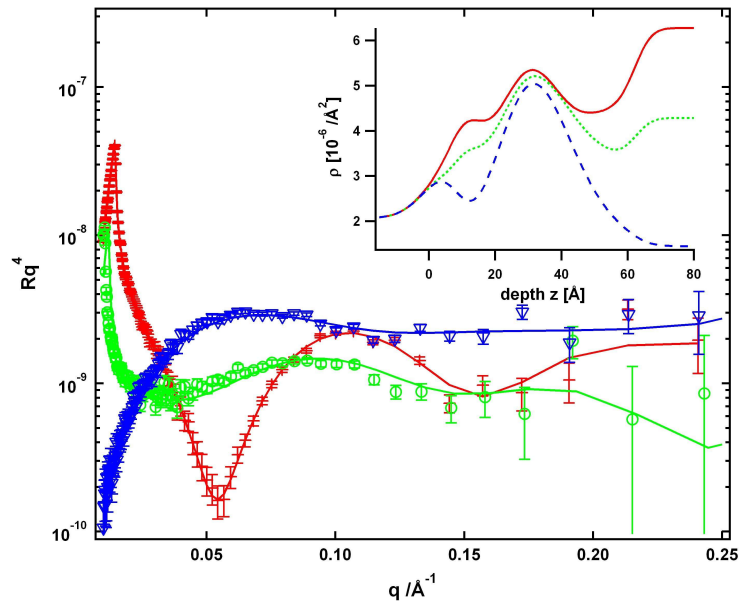


Figure 4.17: Neutron reflectivity curves for asymmetric bilayer with 50 mol% TASC at 55 °C recorded at three contrasts H₂O (+) 4MW (○) and SMW (▽), as well as corresponding SLD profiles for H₂O (—), 4MW (···) and SMW (—).

Silicon substrates are at first characterized, leading to a SiO₂ layer, 8 - 11 \AA thick with a roughness ~ 5 \AA . This parameters have been constrained to these values for fitting the supported bilayer experiments. A water layer of 1.5 - 3.5 \AA thickness with a roughness between 4 - 5 \AA has to be systematically added between substrate and membrane for all samples and temperatures. Compared to symmetric bilayers, the water layer of the asymmetric ones is somewhat elevated (3 - 3.5 \AA) but still smaller than reported in literature [42, 229]. At least for the symmetric layer, due to the strong hydration and the high roughness between the layers the interface might not be very well defined. Thus it is difficult to discern the water film from the headgroups for our experimental resolution.

The box-model for the symmetric bilayer contains two headgroup regions and one

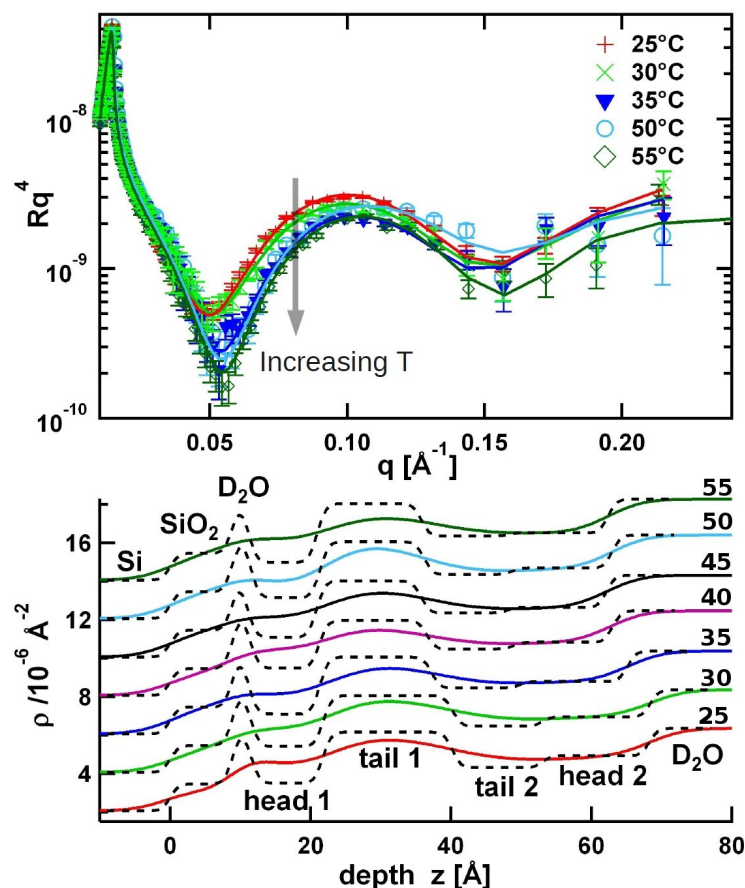


Figure 4.18: Neutron reflectivity curves (to account for better legibility curves for 40 and 45 °C are not displayed) and SLD profiles for asymmetric 50 mol% TASC bilayer from bottom (25°C) to top (55°C) with increasing temperatures in steps of 5°C. The dashed lines in the SLD profile indicate the different slabs of the box model.

single central tail layer. For the asymmetric membranes, the latter one is divided into a slab mainly containing DPPC tails and another one consisting of mixed cholesterol and DPPC tails. For all head and tail boxes a roughness between 4 - 8 Å is found. It increases with temperature, which is very likely due to stronger fluctuations and disorder of the membrane [39].

The total bilayer thickness is several Å larger compared to pure DPPC bilayers [42, 229]. The thickness increases with CD content and decreases with temperature (Figure 4.18 and 4.19). The drop in thickness occurs between 30 - 35°C. This is consistent with known results for the shift of thickness due to the gel-liquid phase transition for phospholipids [42, 229]. The main transition temperature is shifted compared to pure DPPC ($\sim 41^\circ\text{C}$ [232]).

More generally, taking into account the molar ratios of the mixtures, the scattering length densities for the different slabs are in agreement with values found in literature for the pure compounds (Table 4.2). Consequently the mixed head layer's SLD slightly increases with CD content, whereas the SLD of the mixed tail layer decreases with rising TASC content due to the higher cholesterol ratio.

Looking at the mixed headgroup layers, an increase in thickness and water content can be observed with rising CD content and decrease in temperature. The water content for 20

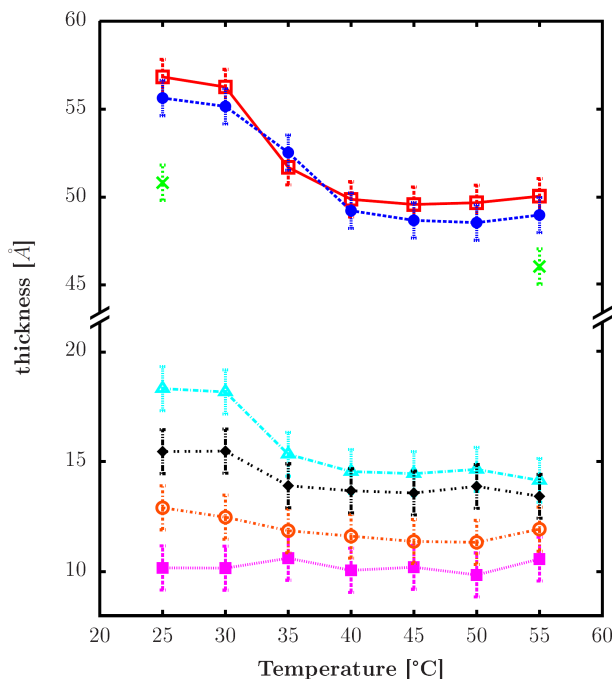


Figure 4.19: Total thickness as a function of temperature for symmetric bilayer containing 10 mol% TASC (\times), the asymmetric bilayers with 20 (\bullet) and 50 mol% TASC content (\square). Below temperature dependence of thickness for the DPPC tail (\blacktriangle) and head group layer (\blacksquare), as well as the mixed headgroup (\blacklozenge) and tail layer (\circ) for the asymmetric 50 mol% TASC bilayer are displayed.

mol% TASC decreases from 58% ($T = 25^\circ\text{C}$) to 51% ($T = 55^\circ\text{C}$) and for 50 mol% TASC it decreases from 68% ($T = 25^\circ\text{C}$) to 60% ($T = 55^\circ\text{C}$). In contrast the headgroup size and water content of the pure DPPC slab (30 - 35%) in the asymmetric bilayers show almost no temperature dependence. The same is observed for the 10 mol% TASC symmetric bilayer. Furthermore it seems that for the symmetric bilayers the headgroup slab close to the silicon substrate is marginally smaller and contains less water (30% close to substrate and 38% close to D_2O).

The tail layer gets thinner with increasing CD ratio. Moreover, as soon as CD is present in the membrane, the change of the tail layer thickness with temperature is significantly smaller compared to pure DPPC tails. A water content between 10 - 20% has been added to account for holes in the bilayer due to defects arising during the bilayer deposition. This is in agreement with what has been reported in literature [233].

4.2.3 Miscibility and fluidising effect of cholesteryl CD

Our results show that all investigated cholesteryl CD analogues readily insert into phospholipid membranes since stable isotherms can be recorded for any kind of molar ratio. In contrast to DPPC films containing cholesterol, there is no strong condensing effect visible in the isotherms [234]. This is because of the large CD moiety, preventing close packing of the film.

Due to the the great structural flexibility of the methylated CD moieties [99, 215] the inverse compressibility of the cholesteryl CD films is very low. Moreover the inverse compressibility of the phospholipid film decreases strongly with cholesteryl CD content. This

is in contrast to DPPC/cholesterol monolayers where the presence of the sterol increases the inverse compressibility of the mixed films [163]. This demonstrates, that the bulky CD moieties, dominate the properties of the mixed layers, rendering the films almost as elastic as pure CD monolayers.

Similar to cholesterol/DPPC films, a fluidising effect of the inserted CDs is observed on the phospholipid layers. It is manifested in monolayers and bilayers, where the LE-LC co-existence region and the main transition temperatures are shifted, respectively.

ΔG_{mix}^{ex} calculations indicate a general demixing tendency of CD and DPPC with increasing compression. Together with the detailed study of the film morphology at various length scales, the phase behavior for CD/DPPC mixtures can be drawn.

For low surface pressures, the compounds are miscible displaying a homogeneous in-plane structure at all scales. At sufficiently high compressions, zones of DPPC in condensed phase appear, from which the CD gets mostly expelled. Consequently the phase surrounding these CD-depleted domains has to be enriched in CD. Yet, due to the fluidising effect of the amphiphilic CDs, already mentioned before, the liquid condensed phase starts to appear at much higher surface pressures than for pure DPPC [31]. This occurs at μm scale (Figure 4.12 B), as well at nano-scale (Figure 4.13 B). With further compression ($> 30 \text{ mN/m}$) more and more condensed phase DPPC domains appear from which the CD is expelled. These DPPC domains grow in size, sometimes around an aggregate core, consisting of CD (Figure 4.12 C, D and 4.13 C). TASC mixtures behave very similar to TBdSC mixtures except that there is no inversion of contrast observed by BAM for surface pressures above 40 mN/m [109]. This might be due to the fact that the film collapses before the α -CD residues can completely re-orientate.

4.2.4 Membrane insertion of the cholesteryl CDs at the molecular level

Structural features of mixed DPPC/CD films

The bilayers get more difficult to prepare with increasing CD content since no stable bilayers could be obtained with TASC molar ratios exceeding 50%. Yet the studied bilayers are sufficiently stable to undergo the gel-liquid phase transition upon heating, which can be followed by looking at the evolution of thickness with temperature. As described in the previous section the transition is shifted compared to pure DPPC due to the fluidising effect of the cholesteryl CD.

The surface pressure dependent SLD profiles (Figure 4.14) show that for low surface pressures almost no contrast between the head and tail layer exists, whereas with further increase a good contrast evolves (Figure 4.14). This indicates a very unordered film structure for low compression, which is getting more ordered at high surface pressures. The hydrophobic tails contribute most to the increase in film thickness up to 15 mN/m , which can be attributed to the DPPC LE-LC phase transition. The sudden rise of the head layer thickness for high surface pressures ($> 30 \text{ mN/m}$) must be related to an at least partial rearrangement of the CD moieties with respect to the interface [109, 228].

It is striking that, for the monolayer at 40 mN/m very similar results are obtained compared to the mixed leaflet of the 20 mol% asymmetric bilayer at 25°C . This is an indication that the insertion of the CD is similar for mono- and bilayers. In both cases the hydration

of the layers containing CD is considerably increased compared to pure DPPC [42, 230], due to the strongly hydrated CD residues, as demonstrated in section 4.1.5. However the bilayer water content is slightly higher, than for the monolayer. This is caused by defects in the supported bilayer, like observed in AFM (Figure 4.16 A), which contribute to the high water ratios for the bilayer.

Furthermore the discrete partitioning between DPPC layer and mixed layer is preserved upon heating and cooling. This shows that there is no significant reorganisation of the asymmetric bilayer. This also means that no or only very few flip-flop events occur, where the amphiphilic CD is exchanged between the leaflets.

When the layers contain TASC, the tail size remains almost unchanged during heating in contrast to pure DPPC. This can be explained by the fluidising effect of the CD since it is already in a very disordered state even for low temperatures. The headgroup thickness however decreases significantly for the disordered liquid phase, since in this state, the 'soft' CD moiety can arrange more freely without being constrained by its hydrophobic cholesteryl anchor being tightly packed in condensed phase. The smaller headgroup size might be also due to less water adsorbed in the layer for high temperatures. The large difference in thickness between the two tail slabs for asymmetric bilayers is mainly attributed to the disordering effect of the CD in the outer mixed layer. Another contribution to the large size disparity is the fact, that the inner DPPC layer tends to be thicker, being strongly adsorbed to the substrate, allowing for a more ordered structure [39].

Molecular model of the insertion

As already mentioned above the insertion of the CD is similar for mono- and bilayers. In order to deduce the molecular arrangement of the CDs with respect to the phospholipids in the film, the measured SLD profiles for monolayers and bilayers are compared to simulated SLD profiles. The model SLD profiles are calculated from the values of the pure compounds (using the the results for TASC described in section 4.1.5 and values found in literature [32, 42, 228, 230]), and taking into account the molar ratio. The asymmetric bilayer's SLD profile is computed from values for a DPPC bilayer and a hypothetical bilayer consisting of a pure DPPC and a pure TASC layer, which in reality cannot be prepared.

For the monolayer and the bilayer a good match between the tail layers of the calculated and the real SLD profile can only be achieved, shifting the pure TASC layer profile into direction of the water subphase. The monolayer is shifted by 8 Å and the bilayer by 4 Å with respect to the DPPC. This is leading to a molecular model of the mixed films like displayed in Figure 4.20, where the CD moiety of TASC protrudes from the headgroup layer. This finding is further supported by the high roughnesses found for the bilayers and monolayers at high surface pressures. However it seems that in the case of the bilayer the CD is more embedded in the film. Of course the fits give only a rather qualitative picture because for producing the model curves it is assumed that the mixtures show the same structural behavior as the pure compounds.

The CD residues partly protruding from the membrane should leave the CD cavities accessible to form complexes. This CD configuration in the bilayer should provide a rather unhindered sliding of a polymer chain threaded through the sliding ring and thus

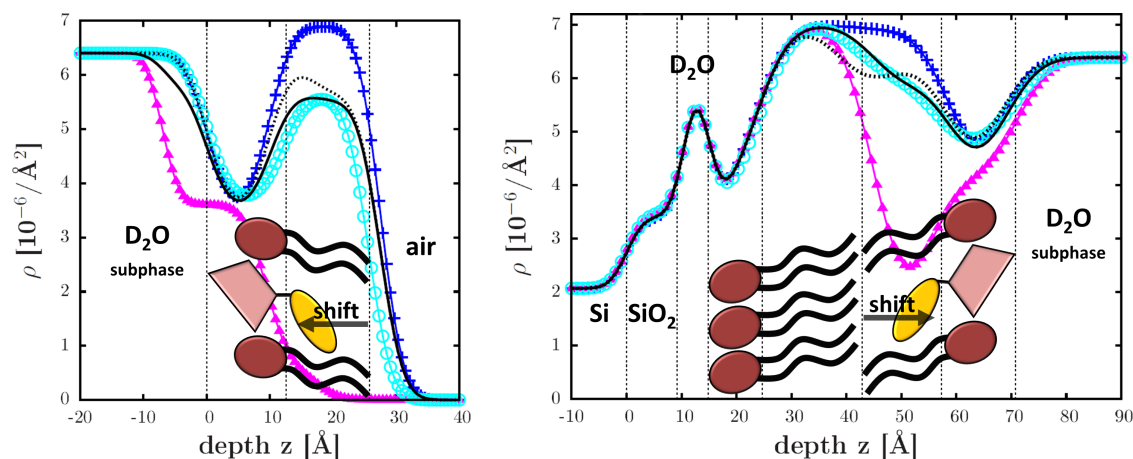


Figure 4.20: A. Monolayer SLD profiles at 40 mN/m for pure DPPC (+), 20 mol% TASC (o) and pure TASC (▲). B. SLD profiles for bilayer of pure DPPC (+), asymmetric bilayer containing 20 mol% TASC (o) and asymmetric bilayer containing pure TASC (▲) as outer layer. In A. and B. the black and the dashed lines correspond to a model SLD profile for the 20 mol% TASC mixture calculated from the pure compounds with (—) and without shifting (···) the TASC layer towards the water interface.

is important for the suitability as STL anchor.

4.2.5 Force spectroscopy

Force curves

Additional to AFM imaging, force curves have been measured for several bilayers. At first the “force volume mode” has been attempted to get a complete set of force curves for each image. However in order to obtain images with satisfactory resolution (at least 64×64 pixel), detailed enough to distinguish features on the surface, the data sampling takes more than 3h due to the large amount of data. Furthermore there is a drift of the piezo tube in x-y as well as in z-direction. Therefore very often detachment of the cantilever has occurred in less than 1h throughout the recording. Due to these instrumental constraints no complete force volumes have been obtained. Instead, the “point and shoot mode” has been used to extract force curves at defined places of the imaged sample (Figure 4.21).

As reference, force curves for bare mica and for DPPC bilayers at 40 mN/m have been taken. Furthermore force curves have been collected for the asymmetric bilayer with 20, as well as 50 mol% TASC, sampling both phases visible in the picture (4.21).

Typical force curves for the four measured samples are illustrated in Figure 4.22. The results displayed in Table 4.5 have been calculated from at least 10 force curves recorded for each sample. For DPPC the force curves show no hysteresis between approach and retract. Neither do they exhibit a jump-in or jump-out related to adhesion (Figure 4.22). The force curves measured on mica and on the CD samples show a hysteresis between approach and retract curve and a jump-out instability. The adhesion force, measured by the difference between the zero line and jump-off minimum of the retract curve, is much higher on mica than for the CD containing samples (Figure 4.22). It should be noted that the jump-out occurs quickly on the mica. But it seems to be slowed down on the CD samples if one compares the slopes of the jump-out events in Figure 4.22. There is only a small difference of ~ 80 pN in adhesion force between the 20 and 50 mol% TASC sample.

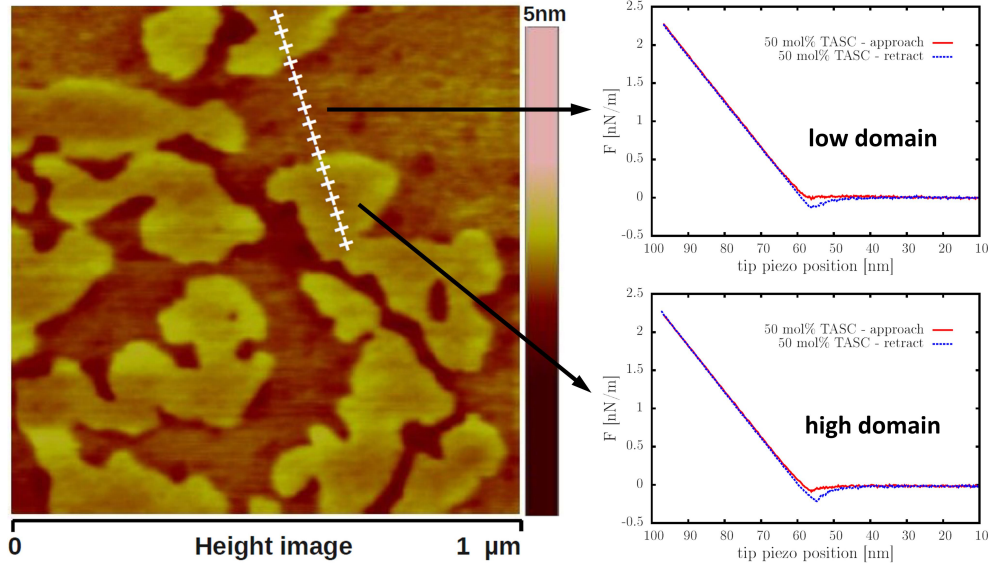


Figure 4.21: AFM height image for 50 mol% TASC bilayer deposited at 40 mN/m. A force curve is recorded for each white cross in the image. Two typical force curves obtained for low and high domains are displayed on the right.

sample	F_{ad}	E [MPa]
mica	1.1 ± 0.2 nN	-
DPPC	-	2.1 ± 1.2
20 mol% TASC	100 ± 25 pN	1.1 ± 0.8
50 mol% TASC	190 ± 35 pN	0.8 ± 0.7

Table 4.5: Results for adhesion force F_{ad} and Young modulus E for fit with Hertzian model. The results are averaged values from at least 10 force curves.

Also comparing the slopes of the jump-out, it occurs more quickly for the 20 mol% sample displayed in Figure 4.22. In all cases, the different domains in the measured CD/DPPC samples have given very similar force curves. Thus it has not been possible to distinguish the two domains by their adhesion forces.

There is a slight deviation from linearity in the contact region in the approach curves of the bilayer sample due to elastic deformation. As the approach curves do not display any adhesion, the elastic deformation of the sample can be related to its Young's modulus E by assuming a Hertzian contact between the tip and the sample for small loading forces [36]. Thus force curves converted into force vs indentation curves via relation (3.21) can be fitted using equation (3.20) to extract the young modulus like displayed in Figure 4.23. The point of contact is also obtained from the fit.

The fit holds only for very small loads ~ 1 nN. The Young moduli extracted for the samples are displayed in Table 4.5. Again the values are averaged values from at least 10 force curves. The elastic moduli are very low and inflicted with a large error, as there is a large spread in the data. The values for pure DPPC are marginally higher than for the mixed CD/DPPC samples. Similar to the adhesion forces, no significantly different values have been obtained for the different phases visible in the TASC/DPPC bilayers.

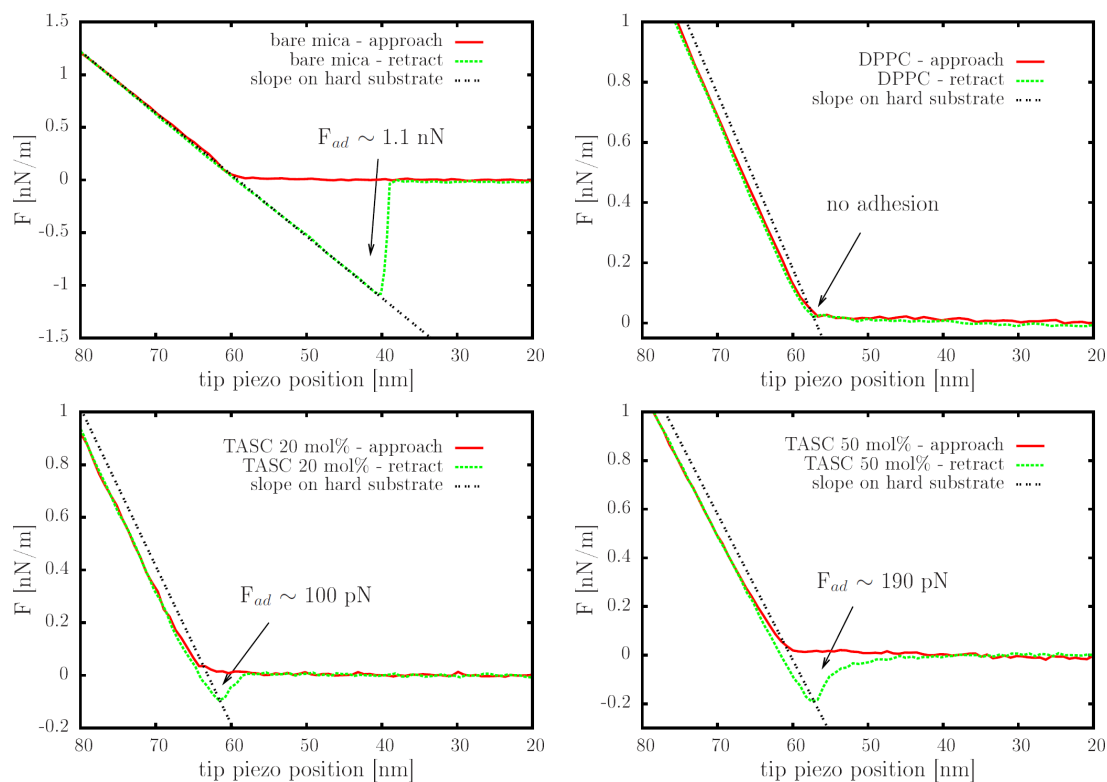


Figure 4.22: Force curves for A. bare mica, B. bilayer DPPC, C. asymmetric bilayer 20 mol% TASC, D. asymmetric bilayer 50 mol% TASC. The dashed line represents the contact line for a perfectly rigid sample.

Bilayer nano-mechanical properties

The force curves taken for mica were clearly qualitatively different compared to the bilayer ones. A particular problem when fitting the approach curves is the determination of the point of contact, which can be difficult especially for soft samples [36]. The poor control of the experimental environment without temperature control and unsealed sample cell, possibly leading to sample contamination, might also account for the poor reproducibility [235]. Therefore the interpretation of the results have to be carried out with care.

The adhesion force for mica ~ 1.1 nN is in the order of what is reported in literature [232, 236]. The DPPC force curves show no hysteresis as no breakthrough occurs in gel

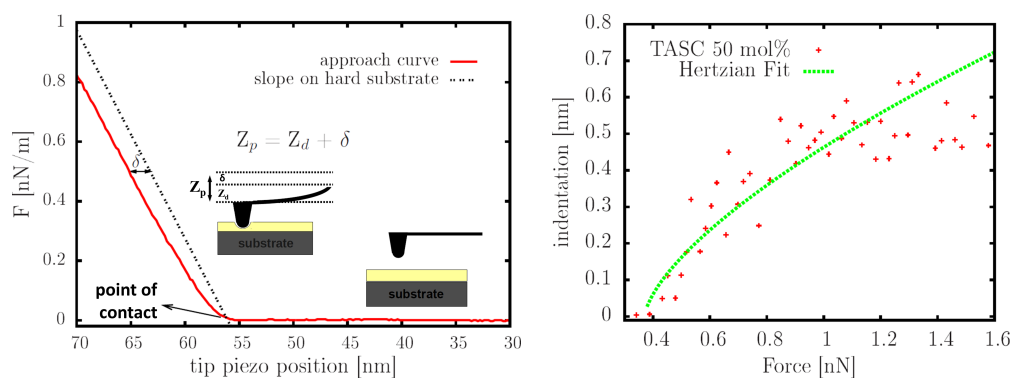


Figure 4.23: left: Schematic drawing of effect on indentation on cantilever deflection and force curve. right: indentation vs force plot fitted with the Hertzian contact model.

phase for the applied loading forces <5 nN [237]. There is a slight rise for the approach curve 0.3 - 0.5 nm before the actual point of contact. Similar behavior for lipid bilayers has been attributed to repulsive hydration forces [48] and electrostatic forces when probed with a Si_3N_4 tip, which is negatively charged at neutral pH [237]. The CD/DPPC bilayers show no attractive forces for the approach. The small adhesion force in the order of several 100 pN, observed upon withdrawal is close to the detection limit. Nevertheless the adhesion seems to increase with CD content.

The other interesting feature in the force curves is the slowing down of the cantilever during liftoff due to a viscous effect, which can be caused by the media or the sample itself [236]. Since all curves are taken in water this effect is even observed for mica. However there seems to be an additional viscous damping which increases with CD content.

The Young moduli extracted from the approach curves for DPPC are smaller than values given in literature [48,237], which are in the order of $10^7 - 10^8$ Pa. As the investigated films are very thin the extracted Young modulus is certainly influenced by the quality of the mica substrate, how well it is fixed to the sample cell and also the used tips. This might account to the observed difference with literature values. Nevertheless having been recorded under the same conditions the samples can be compared among each other. It seems that the Young modulus decreases with increasing CD content, which is in agreement with the fluidising effect of the cholesteryl CDs described before. Yet it has not been possible to discern between the different phases in the CD/DPPC samples by means of analysis of the force curves. The variation of the values for adhesion force and Young modulus have been too large to draw any meaningful conclusions.

4.3 Conclusion

It has been demonstrated that TASC, TBdSC and TBSC form stable monolayers. All three compounds undergo a change of conformation indicated by a pseudo-plateau in the isotherm. With the help of reflectivity measurements it has been demonstrated, that the CD residue rearranges from the cavity's axis aligned perpendicular with respect to the surface to an alignment parallel to the surface (Figure 4.9). TBSC forms a disordered partial bilayer at high surface pressures. The particular behavior of TBSC might be explained by the increased structural flexibility and compressibility if compared to TBdSC and TASC. As expected the methylated CDs are strongly hydrated even for high film compression. Quantification of the number of water molecules gives comparable values to literature and reveals that the α -CD is less hydrated than its β -CD derivative.

A detailed understanding of the insertion behavior of amphiphilic cholesteryl CDs into phospholipid membranes has been achieved from macroscopic to molecular scale. Modified bilayers are stable and are subject to a gel-liquid phase transition upon heating. Depending on the compression, full miscibility of the two amphiphiles is observed for low Π and a clear demixing tendency is apparent during compression. Due to their bulky CD moiety, the amphiphilic CDs exhibit a distinct fluidising effect on the membrane, clearly rendering it more elastic. TBdSC with its two cholesteryl residues seems to be best anchored to the membrane compared to its α - and β -CD analogues with only one membrane anchor. However TASC appears to be more firmly inserted into the membrane than TBSC. With the help of neutron reflectivity a molecular picture of the insertion has been achieved. At

least for high surface pressures and temperatures below the gel-liquid phase transition, the CD residues partly protrude from the membrane, leaving the CD cavities accessible to form complexes.

Thus cholesteryl CDs are indeed good candidates as membrane anchors for the STLs, because the conformational adaptability and accessibility of their CD cavities should be retained, while being inserted into phospholipid membranes.

4.4 Appendix

Interfacial behavior of pure cholesteryl CDs

Reflectivity experiments

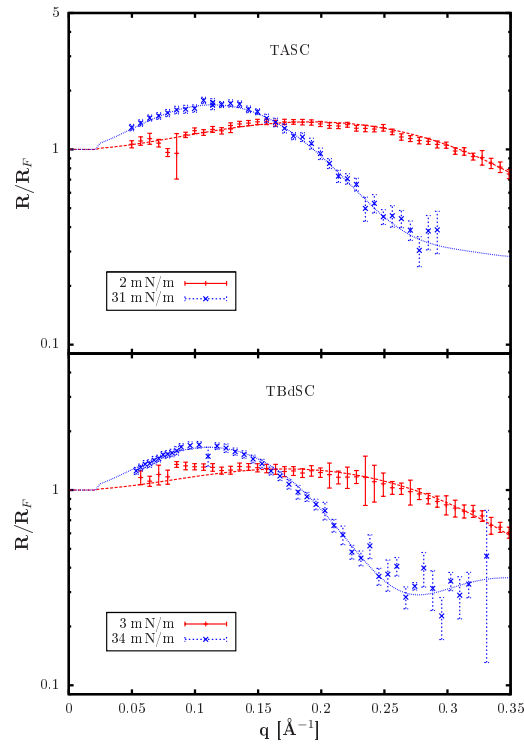


Figure 4.24: X-ray reflectivity curves for TASC and TBdSC for different surface pressures

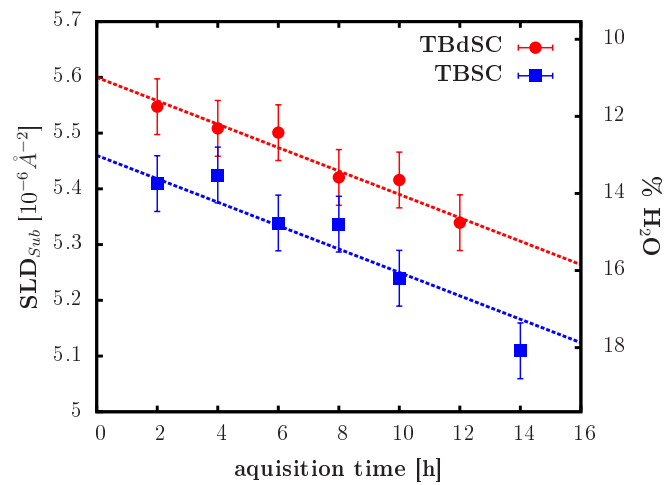


Figure 4.25: Enrichment of heavy water subphase with H₂O during experiment

Π [mN/m]	l_{CD} [Å]	SLD_{CD} [$10^{-6}/\text{Å}^2$]	n_W	l_{Chol} [Å]	SLD_{Chol} [$10^{-6}/\text{Å}^2$]	SLD_{sub} [$10^{-6}/\text{Å}^2$]
1	9.0 ± 2.5	5.23 ± 1.6	176 ± 50	4.5 ± 2.0	0.34 ± 1.1	5.93
3	10 ± 2.0	5.10 ± 1.4	114 ± 25	5.0 ± 2.5	0.37 ± 1.2	5.84
6	9.5 ± 1.0	4.93 ± 1.4	92 ± 20	5.0 ± 2.0	0.42 ± 1.1	5.70
9	11.0 ± 1.5	4.96 ± 1.4	101 ± 18	5.5 ± 1.5	0.37 ± 0.8	5.65
12	10.5 ± 1.5	4.92 ± 1.2	83 ± 20	5.5 ± 2.0	0.38 ± 1.2	5.77
15	11.0 ± 1.5	4.91 ± 1.1	81 ± 20	6.0 ± 1.5	0.43 ± 1.3	5.83
18	11.0 ± 1.5	4.61 ± 0.5	73 ± 14	6.0 ± 2.0	0.44 ± 1.2	5.55
21	12.0 ± 1.0	4.59 ± 0.5	68 ± 13	6.0 ± 1.5	0.41 ± 1.0	5.85
24	13.5 ± 1.0	4.38 ± 0.3	67 ± 9	6.5 ± 2.0	0.43 ± 0.5	5.64
27	14.0 ± 1.0	3.98 ± 0.3	50 ± 7	7.5 ± 1.5	0.45 ± 0.2	5.72
30	15.5 ± 1.0	3.70 ± 0.3	44 ± 7	8.0 ± 1.0	0.41 ± 0.2	5.36
33	16.5 ± 1.0	3.63 ± 0.2	42 ± 6	9.0 ± 1.0	0.41 ± 0.2	5.28
36	17.0 ± 1.0	3.53 ± 0.2	36 ± 6	9.5 ± 1.0	0.45 ± 0.2	5.30
Π [mN/m]	l_{CD} [Å]	ED_{CD} [$e^-/\text{Å}^3$]	n_W	l_{Chol} [Å]	ED_{Chol} [$e^-/\text{Å}^3$]	ED_{sub} [$e^-/\text{Å}^3$]
2	10.0 ± 1.5	0.40 ± 0.05	117 ± 15	4.5 ± 1.5	0.13 ± 0.04	0.335
34	17.0 ± 1.0	0.44 ± 0.05	35 ± 8	10.5 ± 1.0	0.14 ± 0.05	0.335

Table 4.6: Results obtained from fitting neutron scattering and x-ray curves for TASC monolayers at different surface pressures with a 2 layer box model.

Π [mN/m]	l_{CD} [Å]	SLD_{CD} [$10^{-6}/\text{Å}^2$]	n_W	l_{Chol} [Å]	SLD_{Chol} [$10^{-6}/\text{Å}^2$]	SLD_{sub} [$10^{-6}/\text{Å}^2$]
5	12.5 ± 1.0	4.80 ± 0.4	135 ± 22	6.0 ± 1.5	0.62 ± 1.0	5.54
15	13.5 ± 0.5	4.70 ± 0.4	121 ± 14	6.5 ± 1.5	0.61 ± 0.9	5.51
25	14.5 ± 1.0	4.43 ± 0.2	102 ± 9	7.0 ± 1.5	0.63 ± 0.6	5.50
30	15.0 ± 1.0	4.09 ± 0.2	79 ± 8	7.0 ± 1.5	0.61 ± 0.3	5.42
35	16.5 ± 0.5	3.81 ± 0.2	58 ± 7	9.5 ± 1.0	1.04 ± 0.2	5.41
40	18.5 ± 1.0	3.83 ± 0.2	55 ± 6	10.5 ± 0.5	1.10 ± 0.1	5.34
Π [mN/m]	l_{CD} [Å]	ED_{CD} [$e^-/\text{Å}^3$]	n_W	l_{Chol} [Å]	ED_{Chol} [$e^-/\text{Å}^3$]	ED_{sub} [$e^-/\text{Å}^3$]
3	12.0 ± 1.0	0.39 ± 0.04	140 ± 9	6.0 ± 1.5	0.12 ± 0.05	0.335
34	17.0 ± 1.0	0.44 ± 0.05	60 ± 6	11.0 ± 1.0	0.16 ± 0.05	0.335

Table 4.7: Results obtained from fitting neutron scattering and x-ray curves for TBdSC monolayers at different surface pressures with a 2 layer box model.

Π [mN/m]	l_{CD} [Å]	SLD_{CD} [$10^{-6}/\text{Å}^2$]	n_W	l_{Chol} [Å]	SLD_{Chol} [$10^{-6}/\text{Å}^2$]	SLD_{sub} [$10^{-6}/\text{Å}^2$]
1	11.5 ± 2.0	4.66 ± 0.7	193 ± 31	5.5 ± 1.5	0.46 ± 1.0	5.41
6	11.5 ± 2.0	4.70 ± 0.4	135 ± 24	5.5 ± 1.5	0.44 ± 0.7	5.42
12	13.0 ± 1.0	4.59 ± 0.4	132 ± 12	6.5 ± 1.0	0.51 ± 0.4	5.34
18	14.0 ± 1.0	4.48 ± 0.4	120 ± 10	6.0 ± 0.5	0.52 ± 0.5	5.34
28	18.0 ± 1.5	3.57 ± 0.2	89 ± 9	7.5 ± 1.0	0.60 ± 0.2	5.24
32	18.5 ± 1.0	4.14 ± 0.2	74 ± 7	6.5 ± 1.0	0.84 ± 0.2	5.11
layer 3	9.5 ± 1.5	1.34 ± 0.3				

Table 4.8: Results obtained from fitting neutron scattering curves for TBSC monolayers at different surface pressures with a 2 layer box model (for $\Pi=32$ mN/m a 3 layer model has been adopted).

Membrane insertion properties of cholesteryl CDs

AFM

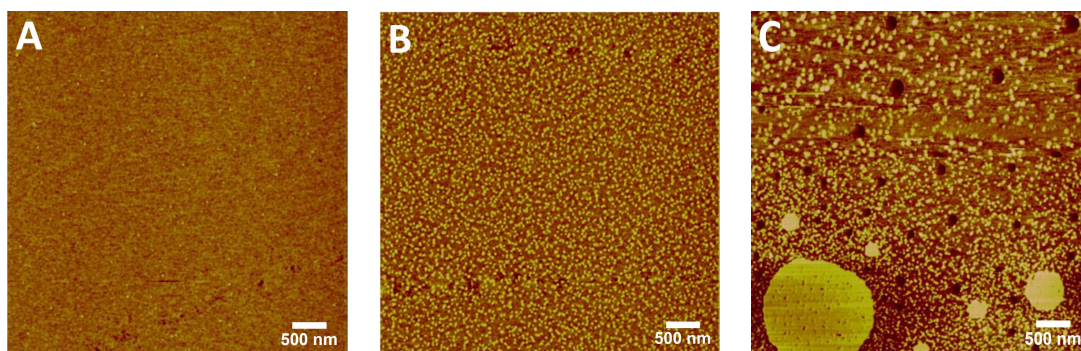


Figure 4.26: AFM friction images for 20 mol% TASC/DPPC mixture, A. $\Pi = 5$ mN/m, B. $\Pi = 15$ mN/m, C. $\Pi = 35$ mN/m.

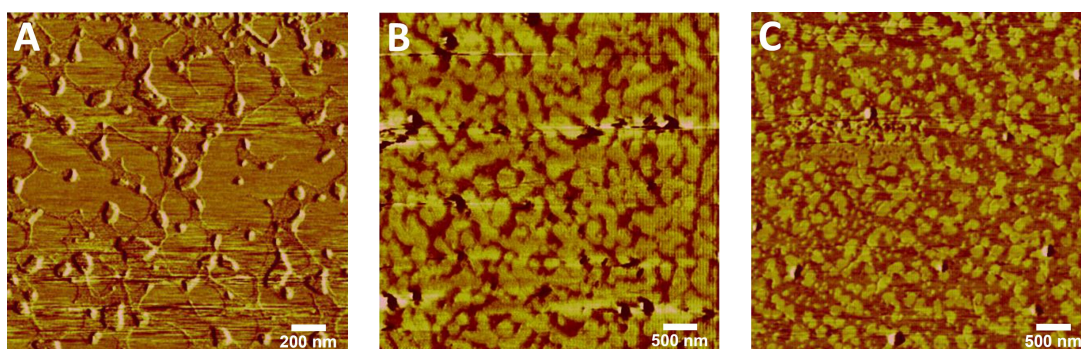


Figure 4.27: AFM friction images for TASC/DPPC bilayers deposited at 40 mN/m, A. symmetric 10 mol% TASC, B. asymmetric 20 mol% TASC, C. asymmetric 50 mol% TASC.

Neutron scattering

sample	thickness [Å]	SLD [10^{-6} \AA^{-2}]	roughness [Å]
10 mol% TASC	10.5 ± 1	3.47	5 ± 1
20 mol% TASC	10.5 ± 1	3.47	5 ± 1
50 mol% TASC	9.0 ± 1	3.47	6 ± 1

Table 4.9: Fitting parameters obtained for SiO_2 layer

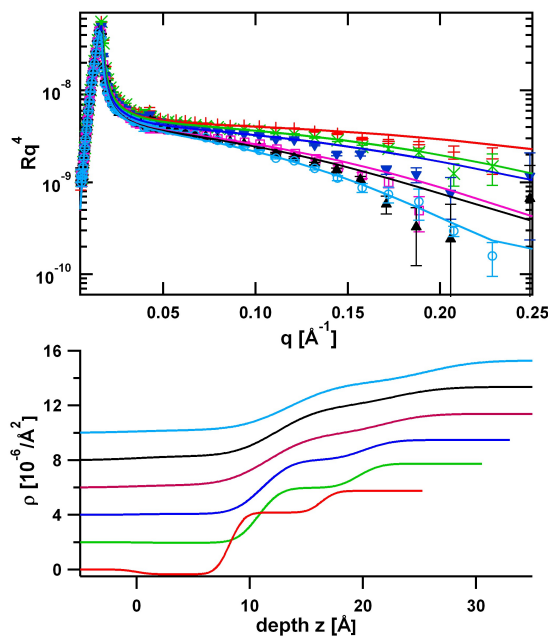


Figure 4.28: Neutron reflectivity curves and SLD profiles from bottom to top (they are shifted by in steps of 2 to account for better legibility) with increasing surface pressures for TASC/DPPC 2:8 (+ 5 mN/m, × 15 mN/m, ▼ 22 mN/m, □ 30 mN/m, ▲ 35 mN/m, ○ 40 mN/m)

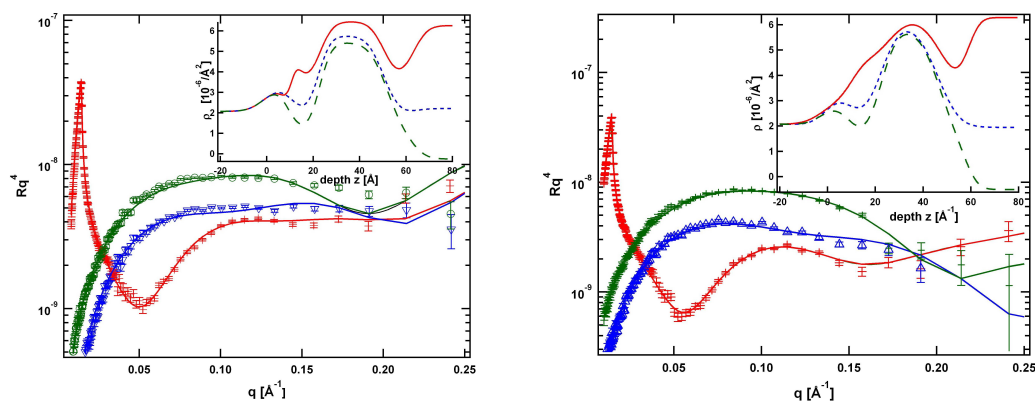


Figure 4.29: Neutron reflectivity curves for symmetric bilayer with 10 mol% TASC at 25 °C (left) and 55 °C (right) recorded at three contrasts D₂O + H₂O ○ and SMW ▼, as well as corresponding SLD profiles for D₂O —, H₂O ··· and SMW - -

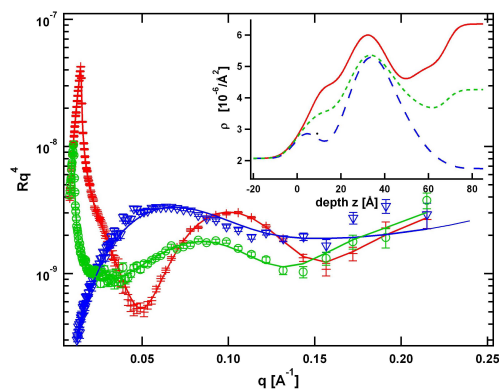


Figure 4.30: Neutron reflectivity curves for symmetric bilayer with 50 mol% TASC at 25 °C (left) recorded at three contrasts D₂O + 4MW ○ and SMW ▼, as well as corresponding SLD profiles for D₂O —, 4MW ··· and SMW - -

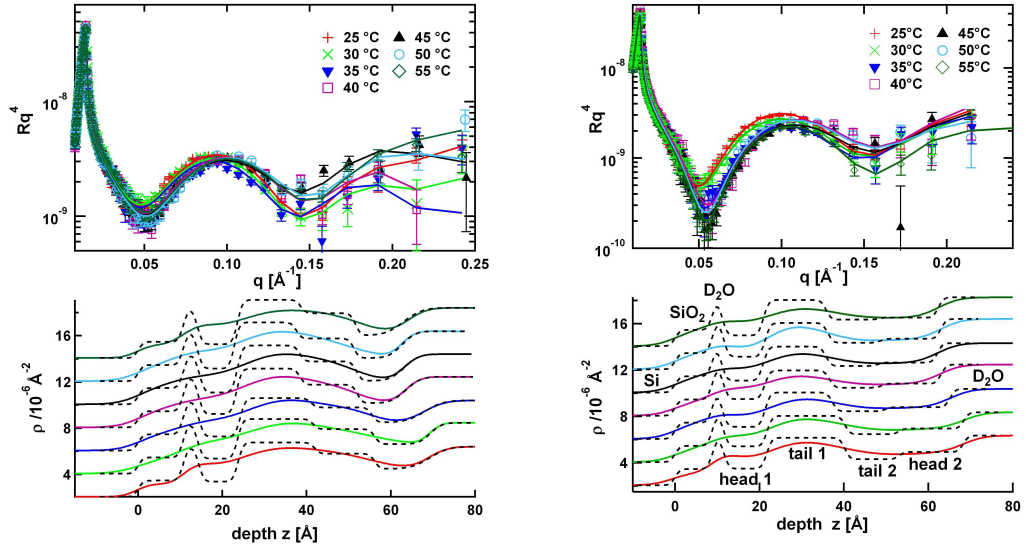


Figure 4.31: Neutron reflectivity curves for asymmetric bilayers with 20 mol% (left) and 50 mol% TASC (right), as well as corresponding SLD profiles from bottom (25°C) to top (55°C) with increasing temperatures in steps of 5°C. The dashed lines in the SLD profile indicate the different slabs of the box model.

symmetric bilayer 10 mol% TASC						
T	layer	water	heads 1	chains 1	heads 2	errors
25 °C	thickness [Å]	1.6	10.0	29.0	12.0	±1
	SLD [10^{-6} Å^{-2}]	-	1.75	6.44	1.75	±0.2
	water [%]	100	29	16	39	±5
	roughness [Å]	6.0	4.8	4.3	5.6	±1
55 °C	thickness [Å]	1.9	9.5	25.0	11.0	±1
	SLD [10^{-6} Å^{-2}]	-	1.75	6.52	1.75	±0.2
	water [%]	100	30	12	37	±5
	roughness [Å]	5.9	6.3	7.1	7.3	±1

Table 4.10: Fitting results for symmetric bilayer 10 mol% TASC

asymmetric bilayer 20 mol% TASC							
T	layer	water	heads 1	chains 1	chains 2	heads 2	errors
25 °C	thickness [Å]	4.0	9.0	18.0	14.0	13.0	±1
	SLD [10^{-6} \AA^{-2}]	-	1.72	7.00	5.90	1.83	±0.2
	water [%]	100	36	15	15	58	±5
	roughness [Å]	4.7	7.6	7.5	6.7	7	±1
30 °C	thickness [Å]	4.0	9.5	18.0	14.0	12.5	±1
	SLD [10^{-6} \AA^{-2}]	-	1.72	6.85	5.84	1.84	±0.2
	water [%]	100	37	15	15	59	±5
	roughness [Å]	5	7.5	8	5.4	6.7	±1
35 °C	thickness [Å]	3.5	8.5	17.0	14.5	12.5	±1
	SLD [10^{-6} \AA^{-2}]	-	1.70	6.46	5.77	1.81	±0.2
	water [%]	100	33	15	15	59	±5
	roughness [Å]	4.6	8.1	8.2	5.6	7.9	±1
40 °C	thickness [Å]	3.5	9.0	15.0	14.0	11.5	±1
	SLD [10^{-6} \AA^{-2}]	-	1.68	7.26	5.70	1.81	±0.2
	water [%]	100	28	10	10	48	±5
	roughness [Å]	4.4	6.9	8.2	7.7	6	±1
45 °C	thickness [Å]	3.5	9.0	15.0	14.0	11.5	±1
	SLD [10^{-6} \AA^{-2}]	-	1.68	7.30	5.69	1.82	±0.2
	water [%]	100	30	10	10	50	±5
	roughness [Å]	4.5	6.8	8.2	7.9	6	±1
50 °C	thickness [Å]	3.5	8.5	14.5	13.5	11.5	±1
	SLD [10^{-6} \AA^{-2}]	-	1.68	7.26	5.70	1.82	±0.2
	water [%]	100	30	10	10	50	±5
	roughness [Å]	4.5	5.4	8.2	7.4	7.1	±1
55 °C	thickness [Å]	3.5	9.5	15.0	13.0	11.5	±1
	SLD [10^{-6} \AA^{-2}]	-	1.70	7.18	5.89	1.83	±0.2
	water [%]	100	28	10	10	51	±5
	roughness [Å]	6.0	6.9	8.4	7.7	6.1	±1

Table 4.11: Fitting results for asymmetric bilayer 20 mol% TASC

asymmetric bilayer 50 mol% TASC							
T	layer	water	heads 1	chains 1	chains 2	heads 2	errors
25 °C	thickness [Å]	3.5	10.0	18.0	13.0	15.0	±1
	SLD [10^{-6}Å^{-2}]	-	1.72	6.75	3.96	2.02	±0.2
	water [%]	100	31	18	18	68	±5
	roughness [Å]	6.0	6.6	7.8	7.3	8.0	±1
30 °C	thickness [Å]	3.0	10.0	17.5	12.0	15.5	±1
	SLD [10^{-6}Å^{-2}]	-	1.7	6.63	3.76	2.07	±0.2
	water [%]	100	33	19	19	68	±5
	roughness [Å]	5.8	6.5	8	8	8	±1
35 °C	thickness [Å]	3.5	10.5	15.5	12.0	13.5	±1
	SLD [10^{-6}Å^{-2}]	-	1.68	6.5	3.72	2.01	±0.2
	water [%]	100	28	2 15	15	62	±5
	roughness [Å]	6	5	8.9	8	7.6	±1
40 °C	thickness [Å]	3.0	10.0	14.5	11.5	11.5	±1
	SLD [10^{-6}Å^{-2}]	-	1.75	6.55	3.94	1.81	±0.2
	water [%]	100	33	13	13	48	±5
	roughness [Å]	5.2	5.7	8.5	8.1	6	±1
45 °C	thickness [Å]	2.5	10.5	14.0	11.0	13.5	±1
	SLD [10^{-6}Å^{-2}]	-	1.74	6.52	3.89	2.02	±0.2
	water [%]	100	29	13	31	61	±5
	roughness [Å]	4.9	5.35	9	7.1	7	±1
50 °C	thickness [Å]	3.0	10.0	14.5	11.5	14.0	±1
	SLD [10^{-6}Å^{-2}]	-	1.68	6.48	3.84	1.96	±0.2
	water [%]	100	29	13	13	61	±5
	roughness [Å]	4.4	5.4	6.4	7	8	±1
55 °C	thickness [Å]	3.0	10.0	14.5	12.0	13.5	±1
	SLD [10^{-6}Å^{-2}]	-	1.68	6.72	3.93	1.96	±0.2
	water [%]	100	29	12	12	60	±5
	roughness [Å]	5.4	5.8	8.0	8.0	8.33	±1

Table 4.12: Fitting results for asymmetric bilayer 50 mol% TASC

Chapter 5

Synthesis of sliding tethered ligands

The full synthesis of the STL schematically illustrated in Figure 5.1 will be presented in this chapter.

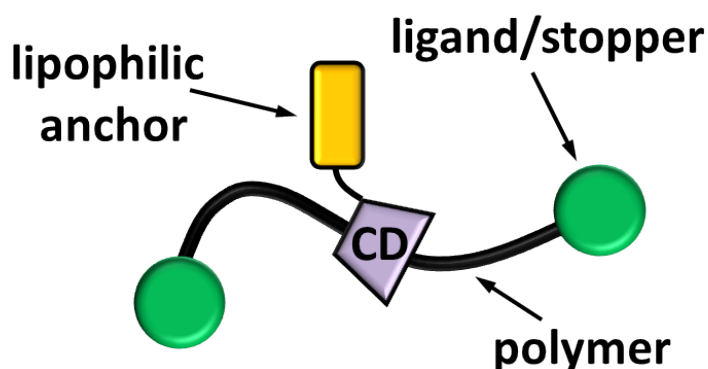


Figure 5.1: Schematic model of a STL

This involves following intermediate steps: a. the development of suitable capping techniques to afford polyrotaxanes with ligands at the chain ends, b. the preparation and study of polyrotaxanes with a low number of modified CDs and c. the attachment of the lipophilic anchor via click chemistry.

5.1 Strategy

At first an appropriate sliding ring/polymer system has to be chosen. Polyrotaxanes based on PEG and α -CDs are particularly useful as scaffolds for the preparation of the STLs. It is one of the most studied polyrotaxane systems [21, 125, 126], as both compounds are easily available and the CDs can be readily modified. Although in most cases polyrotaxanes are formed with a very high density of CDs threaded over the polymer chain, recent strategies for complex formation allow for a low number of CD per chain [141], which is crucial for the synthesis of the STLs. Furthermore both compounds are water soluble and bio-compatible so that the polyrotaxanes can be of use for biomedical applications, e.g.

for drug delivery to protect liposomes of degradation in the body [238, 239].

To allow for end-capping of the polyrotaxane ends, bis-amino-PEG serves as template chain. The amino-functionalised polymers are most commonly used by many researchers, because amino end groups do not interfere with the threading process [20] and they possess a high reaction selectivity with many functional groups in water compared to hydroxyl groups [126]. Polyrotaxanes can be prepared efficiently for a whole range of molecular masses [141, 240] and bis-amino PEGs are commercially available for different molecular masses to be able to adjust the chain length of the STLs.

Polyrotaxanes will be prepared with α -CDs, modified with a single azido group on its primary side to be able to functionalise the threaded CD with an hydrophobic anchor. Azido α -CDs are widely known as valuable precursors for CD modification. They can be prepared from native CDs, via nucleophilic substitution of mono-tosylated CDs [89, 90]. and the azido group is readily transformed into many functional groups. Additionally, the azido group provides orthogonal reactivity towards the terminal amino groups of the PEG and it can be simply modified via click chemistry to couple the lipophilic anchor [241].

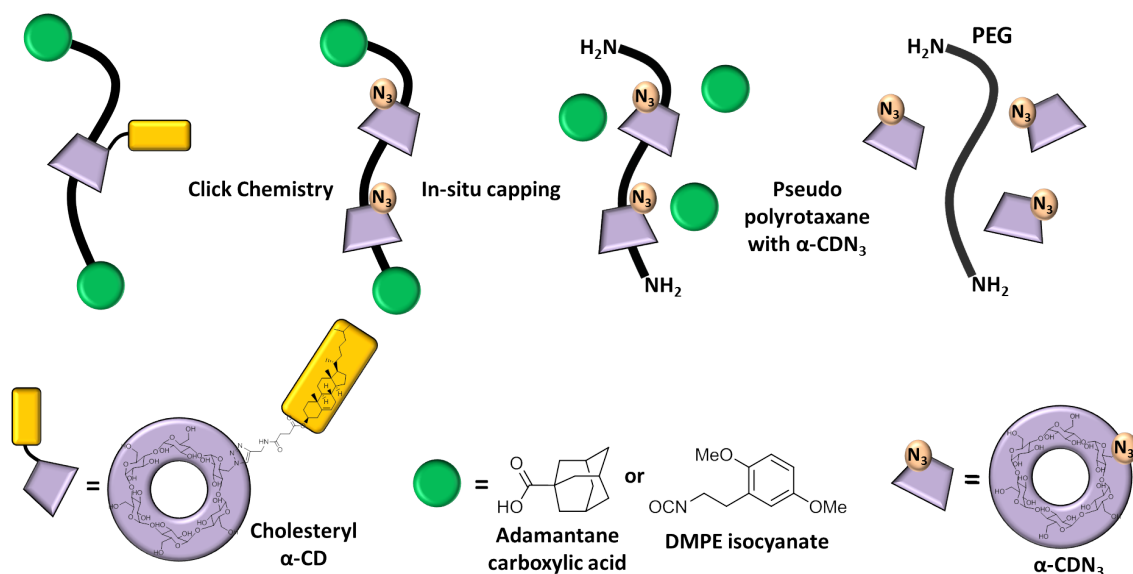


Figure 5.2: Schematic outline of strategy to synthesize the STL

Most of the time, polyrotaxanes are prepared by isolating highly complexed water insoluble pseudo polyrotaxanes, followed by a capping step in a different solvent. In order to obtain soluble polyrotaxanes with a low number of CDs, in-situ capping methods in water have to be applied and only very few methods are described in literature [141, 242]. These methods are hampered by several drawbacks, such as lack of versatility or poor stability. A suitable capping agent needs to be bulky enough to prevent dethreading of the CDs, but nevertheless it has to be water soluble to allow for in situ end-capping of the rotaxane. Moreover the reaction has to be fast and complete in order to, together with the careful choice of complexation conditions, be able to tune the number of CD per polymer chain to obtain the desired low threading ratios.

Two new in-situ stoppering procedures are developed which should be versatile enough to allow for potential application of a whole variety of end-capping molecules. At first a procedure based on blocked isocyanates is applied. After several tests DMPE isocyanate (structure is displayed in Figure 5.2), has been chosen as isocyanate model, which is blocked with phenol sulfonate, rendering the compound water soluble and decreasing its reactivity towards hydroxyl groups. This capping method is mainly used for optimisation of the complexation conditions. Though versatile in principle, access to the different blocked isocyanate proves to be rather tedious.

The second approach involves the synthesis of polyrotaxanes end-capped with suitable carboxylic acids (R-COOH) by amide formation in water applying the condensation agent DMT-MM. Here adamantane carboxylic acid has proven to be a good R-COOH model. Since the reaction is carried out in aqueous environment, a water soluble carboxylic acid derivative has to be used. If this is not the case it has to be solubilised. Adamantane is bulky enough to serve prevent dethreading of α -CDs [148,243]. Furthermore it can act as a ligand with a β -CD as receptor, with a binding constant K in the order of $5 \cdot 10^4$ [244,245]. Both methods can be envisaged depending on the considered capping residue.

The lipophilic anchor of choice is the commercially available cholesteryl-hemi-succinate which needs to be functionalised with a terminal alkyne group so that it can be attached to the azido group of the α -CD by a simple click chemistry approach. From studies about amphiphilic CD's, it is known that the succinyl linker is an adequate spacer molecule [117] and that the cholesterol should provide for a strong incorporation into lipid membranes [109,169,246].

A major difficulty concerning the synthesis is the purification. The polymer and the small molecules can be easily separated by dialysis. However it is difficult to discern between the final product STL, rotaxanes or the native polymer. Therefore it is crucial to chose high yielding reactions and to find ideal reaction conditions for the polymer modification to allow for quantitative yield to avoid elaborate chromatographic purification for each step.

Finally the separation of a batch of rotaxanes with an average threading ratio by their discrete number of CD per chain is a major challenge. Preparation of STLs with a well defined number of sliding rings are preferred for physical characterisation. This is achieved by the development of adequate chromatographic techniques.

5.2 Development of end-capping technique

5.2.1 Introduction

Polyrotaxanes are most of the times synthesised by attachment of bulky stopper groups to the polymer ends of pseudo rotaxanes to prevent the CDs escaping from the chain. The stopper molecules must be bound with severe selectivity only to the end of the polymer chain. A suitable cap needs to be bulky enough to prevent dethreading of the α -CD and not enter into competition with the PEG by forming host-guest complexes with the CD. Furthermore the end-cap reaction should be fast and high yielding in order prevent de-

complexation and therefore very often a great excess of the stopper molecules is used. Most of the times, strategies for polyrotaxane synthesis with high CD content exploit the fact, that pseudo polyrotaxanes become water insoluble with increasing number of α -CD per chain and, depending on their MW, precipitate or form gels [20, 130]. Hence the synthesis is usually carried out by isolating the precipitated pseudo rotaxanes, which can then be taken up in a polar organic solvent, like DMF, where no or very little dethreading occurs, to be end-capped with the stopper. The first CD polyrotaxanes prepared by Harada et al. have been synthesised with 2,4-dinitrofluorobenzene in DMF [144]. Many other different methods, conducted under heterogeneous reaction conditions and providing for polyrotaxanes with a high CD content, are described in literature [126, 247].

For low complexation ratios the pseudo polyrotaxanes remain soluble in water. Therefore all capping methods involving isolation of the pseudo-rotaxane are rendered inapplicable and in-situ end-capping techniques in water are required. Only very few methods using water soluble stopper molecules are specified in literature. A strategy developed by Fleury et al. [141] employs soluble sodium picrylsulfonate to end-cap complexes between bis-amino-PEGs and native α -CDs in water. With their method polyrotaxanes with threading ratios as low as 4 CDs per chain could be obtained, applying proper temperatures and reactant concentrations. Another one pot synthesis in water involves 3,5-dimethylphenyl isocyanate at 0°C to block polyrotaxanes based on bis-amino-PEG and α -CD [145, 242]. Takata et coll. used the same isocyanate to prepare polyrotaxanes on the base of methylated CDs and amine-terminated PEG in various organic solvents [248]. These nucleophilic aromatic substitution reactions are limited to adequate reagents such as picrylsulfonate or isocyanate, as well as particular reaction and solvent conditions. Hence they do not meet our requirements.

To be suitable for the STL synthesis, in-situ end-capping techniques in water have to be developed, which are versatile enough to permit an easy exchange of the stopper molecule (in particular the ligand of the STL) if requested. Moreover the technique should be fast and high yielding under rotaxane complexation conditions to amount to low threading ratios. Two useful strategies have come into mind. On the one hand water soluble blocked isocyanates can meet these requirements and on the other hand amide coupling guided by DMT-MM in water is a promising type of reaction.

5.2.2 Blocked isocyanate

A first class of chemicals which meets the requirements as good capping agents are blocked isocyanates. They derive from isocyanates, electrophilic agents that are highly reactive toward classical nucleophiles such as hydroxyl-, amine- or thiol- containing molecules (including water), which add to the NCO group by N-hydro-C-alkoxy-addition (Figure 5.3).

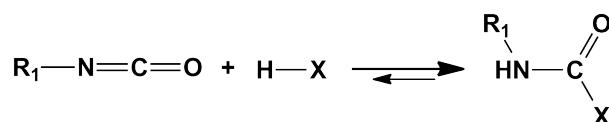


Figure 5.3: Blocking of isocyanates

The highly reactive isocyanates are protected, using hydrogen labile nucleophiles such as phenols, lactams or oximes that can reversibly add on the CN part of the isocyanate

and be reactivated under appropriate thermal conditions [249]. They are routinely used e.g. in textile or paper industrie to protect isocyanates of degradation [250]. In the case of very good leaving groups and nucleophiles, such as primary amines, coupling reactions are possible at room temperature without reactivation (Figure 5.4). Most blocked isocyanates are hydrophobic organic molecules. However using bisulfites or phenol sulfonate, charged water soluble blocked isocyanates can be generated. These compounds retain their reactivity with amino-groups but loose its reactivity towards the CD's OH groups and they are sufficiently stable in water [251, 252].

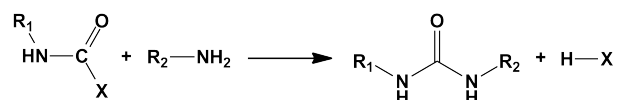


Figure 5.4: Reaction of a blocked isocyanate with an primary amine

Preliminary experiments have directed us to the use of phenolsulfonate together with 2,5 dimethoxyphenyl-1-ethyl isocyanate (DMPENCO), as good isocyanate model. The resulting blocked isocyanate DMPEPhSO₃⁻ has been the easiest to synthesise with high yield and high purity. The formation of other blocked isocyanates has proved to be unsuccessful under the specified reaction conditions (e.g. with adamantane isocyanate) or they have just not been bulky enough to prevent dethreading of α-CD (e.g. 1-Phenylethyl isocyanate).

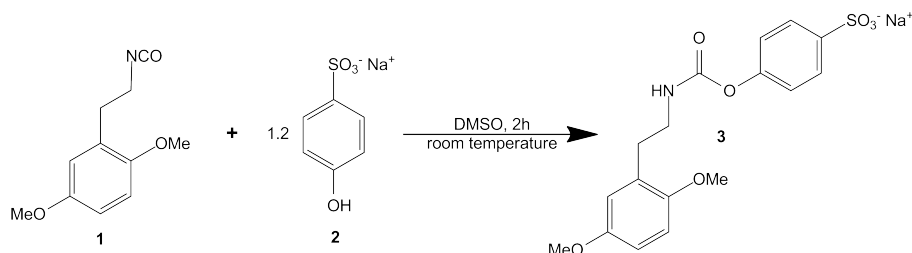


Figure 5.5: Synthesis of DMPEPhSO₃⁻

DMPEPhSO₃⁻ **3** is prepared using DMPENCO, **1** which is just large enough to trap the CDs on the chain. It is treated with a small excess of the good nucleophile 4-phenol sodium sulfonate **2** in DMSO which adds to the isocyanate group to form a carbamate (Figure 5.5). The obtained blocked isocyanate 2,5-dimethoxyphenyl-1-ethyl-4-phenol sodium sulfate (DMPEPhSO₃⁻, **3**) is purified by precipitation in acetone and filtrating an aqueous solution of the precipitate to remove urea side products, produced by self-condensation of the isocyanate. In the final product remain still substantial amounts of 4-phenol sodium sulfonate (40 - 50 mol%), which is simply quantified by NMR (see appendix). But this side product is not removed since it is also a byproduct of the end-capping reaction and it is smoothly removed by dialysis after the coupling has taken place.

To validate the capping method a bis-amino-PEG polymer **4** is endcapped with an excess of DMPEPhSO₃⁻ by stirring the two compounds for 2h in water to give **5**. The more nucleophilic primary amino groups react very likely in an elimination-addition mechanism [249] with the carbamate to create an urea bond. DMPEPhSO₃⁻ is considerably stable under the utilised reaction conditions, as it can still be found in the reaction mixture before dialysis. However it degrades gradually, as substantial amounts of a symmetric urea

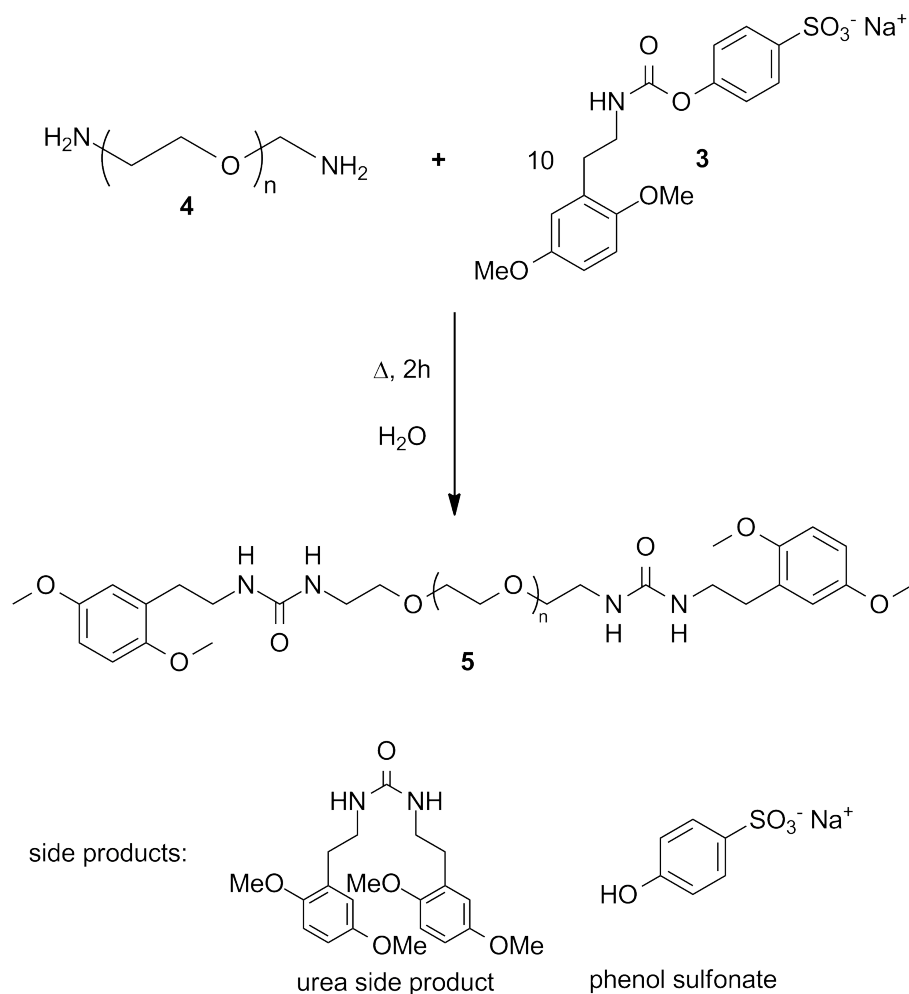


Figure 5.6: Synthesis of PEG endcapped with DMPEPhSO₃⁻

side product are being generated by the reaction of DMPEPhSO₃⁻ itself throughout the reaction (Figure 5.6). These insoluble impurities are removed after dialysis by filtration.

Yet the DMPE end-cap does not fulfill the requirements to be a good ligand. Thus adamantane which can act as ligand to be recognised by β -CD is intended as end-cap. The choice of reaction conditions is delicate in order to block the highly hydrophobic isocyanate with the hydrophilic blocking agent. Thus the synthesis of a blocked isocyanate based on adamantane could not be achieved without major modification of the reaction setup. Therefore the functionalisation of the polymer with an adamantane cap in water is approached using a different strategy.

5.2.3 Condensation of carboxylic acids with the aid of DMT-MM

There are several examples in literature where the bis-amino-PEG is end-capped by condensation of carboxylic acids with the amino groups via activation of the acid moiety to form an amide linkage. But these methods cannot be directly adopted for the synthesis of rotaxanes with low threading ratio, as they use carbodiimides as activating agents in DMF, which require isolation of the pseudo-polyrotaxanes [146, 253].

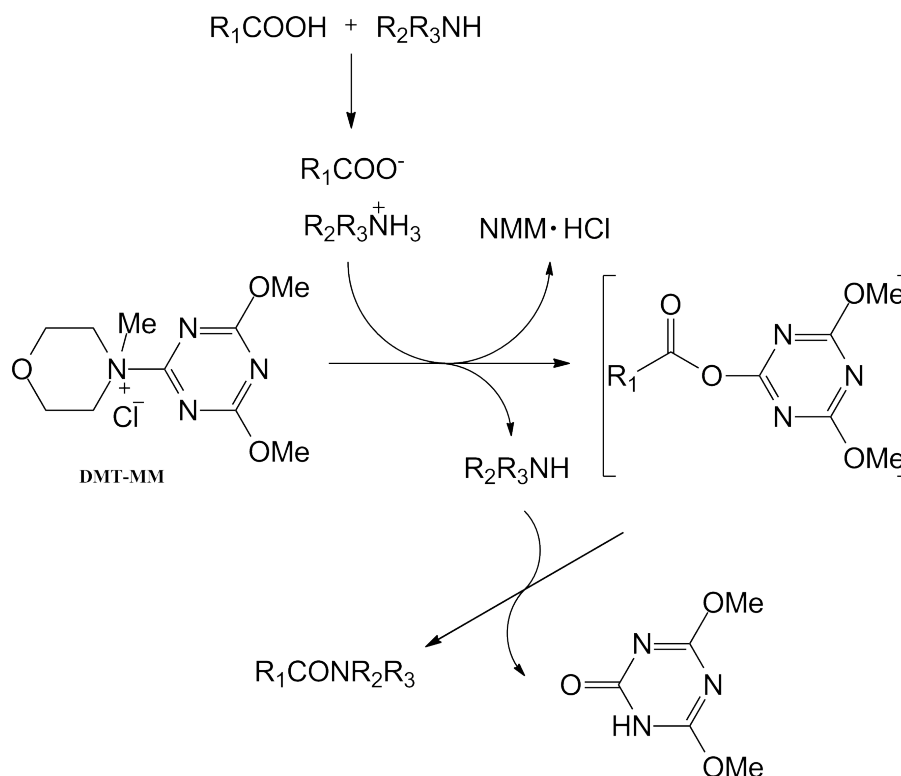


Figure 5.7: Mechanism of carboxamide formation with the aid of DMT-MM

Kunishima et al. demonstrated, that the water soluble 4-(4,6-dimethoxy-1,3,5-triazin-2-yl)-4-methylmorpholinium chloride (DMT-MM) is a useful non-carbodiimid condensing agent, which is unstable in aprotic solvents, yet very stable in protic solvents [254]. It provides for efficient and selective formation of carboxamides in protic solvents, such as water, in a convenient one-step procedure in very high yields with water soluble carboxylic acids and amines. The reaction is thought to be initiated by addition of the carboxylate anion to give an activated ester, which undergoes attack by an amine to the corresponding amide, like illustrated in Figure 5.7. However most carboxylic acids of adequate size to act as stoppers are not water soluble, which is also the case for adamantane carboxylic acid, our ligand of choice. Yet its strong affinity to β -CD can be exploited to form water soluble adamantane carboxylic acid/ β -CD, which are used for the end-capping reaction. The reaction has also been conducted with biotin solubilised both as biotin/ β -CD and biotin/ α -CDN₃ complexes.

In order to test the efficiency of the reaction, bis-amino-PEG polymer **4** has been reacted with an excess of carboxylic acid/ β -CD complex **6** in water to which the DMT-MM **7** is added to obtain the end-capped PEG **8**. Since all side products are water soluble, the pure compound **8** can be simply obtained by dialysis (Figure 5.8). NMR analysis on polyrotaxanes shows that the product is completely end-capped, since N_{CD} are the same for both methods for same conditions. However the yields for the adamantyl PEG **8a** are rather low (<50%) after dialysis. This has been observed in particular for large PEGs > 6000 g/mol, which are dialysed with a dialysis membrane with MW cutoff 2000 g/mol. In contrast the yields for the biotinylated PEGs **8b** are always high (> 90%). So there is a specific effect of the adamantane which seems either to facilitate the escape of the linear

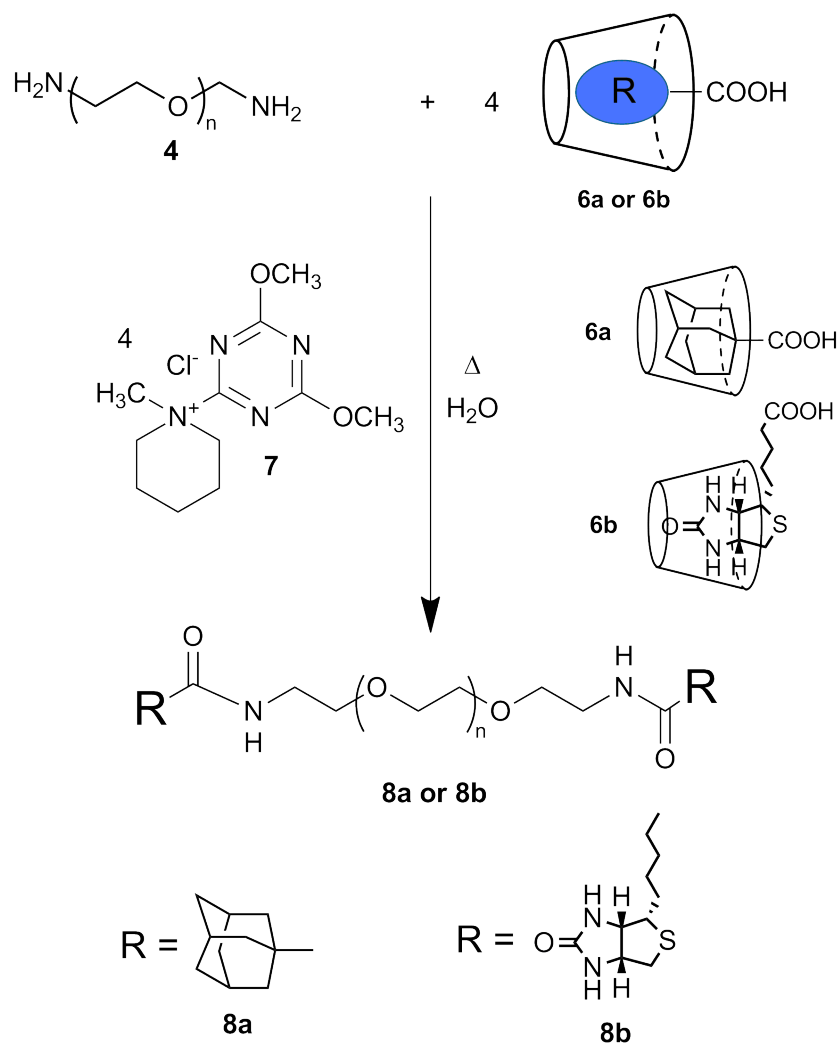


Figure 5.8: Synthesis of PEG endcapped with adamantane or biotin

product from the dialysis tubing or lead to trapping in the dialysis membrane. Preliminary tests to produce polyrotaxanes with biotin **6b** as stopper have not been successful. Characterisation by NMR (see appendix) evidences completely endcapped polymer chains, but no CDs threaded on the chains. This proves that the biotin molecule is not sufficiently large to prevent dethreading of the α -CD. Therefore it is ruled out as suitable stopper.

5.3 Polyrotaxanes

In order to prepare STLs it is necessary to decrease the threading ratio of polyrotaxanes to very few or even one CD per chain. Additionally they have to be synthesised with selectively modified CDs in order to be able to specifically functionalise the molecule with an anchor to allow attachment of the CD to a surface, while retaining their ability to slide through the grafted ring.

5.3.1 Choice of reaction conditions

The inclusion of the PEG into CDs in water is ruled by a subtle interplay between an unfavorable conformational entropy contribution of the polymer chain and attractive interactions between the EO units and the CDs. Hence the threading process is strongly influenced by the complexation conditions.

Fleury et al. [141] have demonstrated that by varying the complexation temperature, the polymer concentration, as well as the initial CD/PEG ratio, it is possible to control the number of native α -CDs per PEG. In this manner they have achieved complexation degrees ranging from 4 - 140 CD/chain using PEG 20k. The lowest threading ratios are achieved using initial CD/PEG ratios of 20 and polymer concentrations of 3 mol/l. Moreover they apply a temperature cycle, which involves at first heating the reaction mixture to 70°C followed by a complexation step at 35°C and a consecutive in-situ endcapping step [141]. Experiments adapting these reaction conditions are carried out with the newly developed stopper molecules. Similar threading ratios are achieved like described in reference [141]. This validates the suitability of our capping systems.

The difficulty in producing polyrotaxanes with azido- α -CD is to overcome its very poor water solubility (~ 10 g/l for azido- α -CD compared to ~ 150 g/l for native α -CD at room temperature). Furthermore auto-inclusion of its azido group into the cavity has been reported [255]. The self-inclusion might be in competition to its complexation with PEG and could be a problem. Thus our first attempts have been quite disappointing. Very recently Yui et coll. [161] efficiently synthesised polyrotaxanes with azido- α -CDs by addition of DMSO as co-solvent. Yet they obtained high threading ratios. So this method is not suitable for our purpose. In order to prepare polyrotaxanes based on Fleury's procedure, the solubility has to be increased in a different manner. Several preliminary tests have been carried out. At first the water solubility of azido- α -CDs is enhanced by salting in with 2M NaNO₃. But only polyrotaxanes with very poor CD content (< 1) are obtained. In a next attempt the azido- α -CD has been solubilised by deprotonation of its OH groups using 2M NaOH as complexation medium. However to avoid degradation of the stopper molecule, the reaction mixture has to be neutralised prior to the addition of the DMPEPhSO₃⁻. This is a delicate task, leading to polyrotaxanes with highly irreproducible complexation ratios. By working at high temperatures the azido- α -CD's solubility in water is significantly enhanced. At 70°C it is ~ 80 g/l which is sufficient to solubilise the CD at given reaction conditions. Precursory experiments showed that skipping the temperature cycle and endcapping directly at high temperatures provides for polyrotaxanes with low threading ratio of ~ 1 CD per chain.

Based on the findings of our preliminary experiments following considerations have been made for the choice of the initial reaction parameters: At first, a high complexation temperature is chosen ($T = 70$ °C). It provides solubility of the azido α -CD. It also results in low threading ratios due to the increased unfavorable entropy contribution in the threading process. In combination with the rather low initial CD/PEG ratios R_0 (20) and low PEG concentrations c_0 (< 10 w%), high temperatures should prevent gelation of the pseudo polyrotaxanes with α -CD for PEGs in the used MW range between 3000 and 20000

g/mol [156]. Complexation times t_C of 30 min for α -CD and 2h for its azido derivative are selected, which are sufficient for complexing only few CDs on the chain. Table 5.1 summarises the reaction parameters which will be referred to as standard conditions in the following.

	T [°C]	R_0	c_0 [mmol/l]	t_c [h]
α -CD	70	20	2.94	0.5
α -CDN ₃	70	20	2.94	2

Table 5.1: Standard reaction conditions for polyrotaxane synthesis

5.3.2 Synthesis

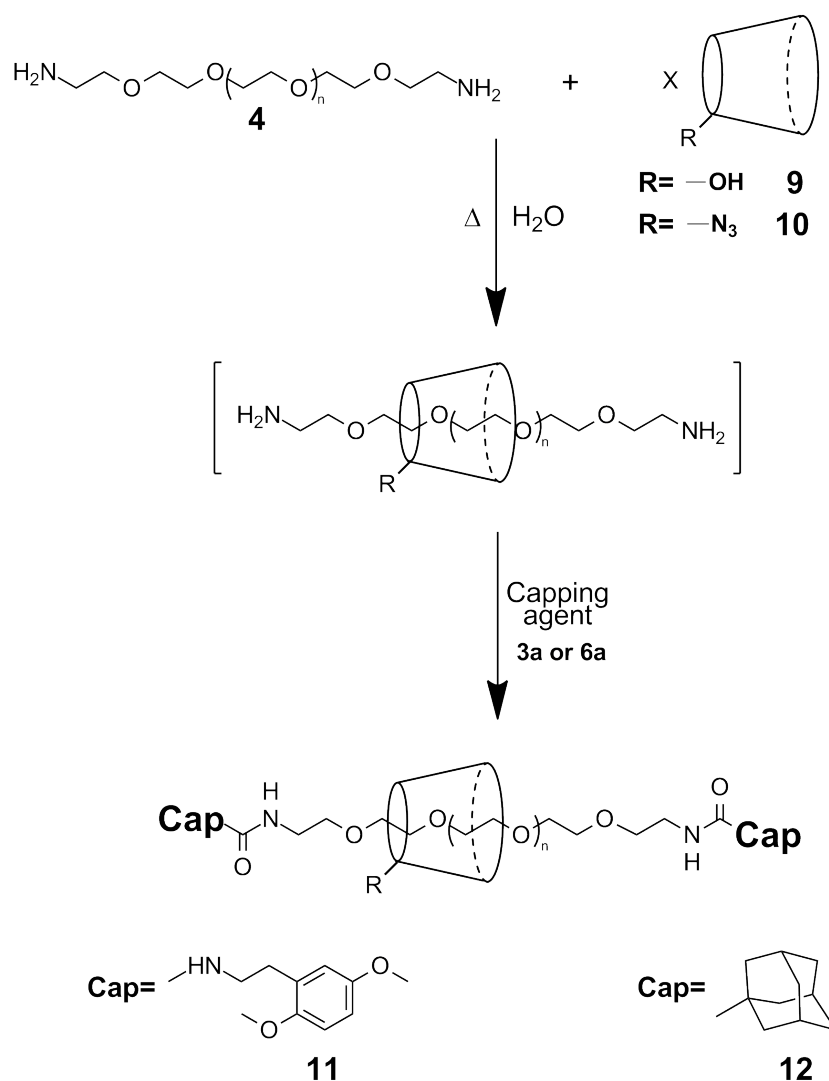


Figure 5.9: Reaction scheme for the preparation of polyrotaxanes, with **9** for native CD (R= OH) and **10** azido-CD (R= N₃). Polyrotaxane **11** is obtained using capping agent **3** described in Figure 5.6 and **12** using capping agent **6** displayed in Figure 5.8.

Polyrotaxanes are synthesised using native **9** or azido α -CD **10**, bis-amino-PEG **4** and capping agent **3** or **6a** shown in the reaction scheme displayed in Figure 5.9. To start the re-

action, the polymer and an excess of CD are heated to a desired complexation temperature, for 30 minutes using native α -CD, or 2h using azido α -CD to form pseudo-polyrotaxanes. The solution remains clear because the scarcely complexed pseudo-rotaxanes are soluble. Maintaining the complexation temperature, they are then end-capped in-situ with an excess of the stopper molecule to ensure quantitative end-capping. In order to purify the product the reaction mixture is dialysed with water to remove the excess CD and unreacted stopper molecules. For polyrotaxanes synthesised with PEG 10 and 20k a dialysis tubing is chosen with a MW cut-off of 3kg/mol and using PEG 3k and 6k a cut-off of 2kg/mol is applied, which is still sufficiently large to let the CDs pass.

Provided the same reaction conditions, both end-capping methods give identical threading ratios. DMPEPSO₃⁻ and adamantane are sufficiently large to prevent dethreading, also for azido α -CD. As already mentioned in section 5.2.3 biotin proves to be too small to serve as stopper for α -CD.

If DMPEPhSO₃⁻ is used for capping, the reaction mixture becomes turbid after several minutes because the water insoluble symmetric urea side product (see Figure 5.6) is formed. It is removed by filtration. Polyrotaxanes blocked with DMPE are obtained with yields in the order of 80 - 90% for PEGs 6, 10 and 20k, whereas for PEG 3k yields in the order of 50 % can be reached since some of the material is lost during the dialysis. Capping with the adamantane stopper results in substantially lower yields after dialysis \sim 40 % for all polymers. Since end-capping with biotin gives high yields (although only complexed polymer) it is unlikely, that the β -CD used to solubilise the carboxylic acids facilitates the escape of the end-capped compounds from the dialysis tubing. It rather seems to be an effect specific to the adamantane stopper. But this effect is not yet fully understood and would require further investigation.

5.3.3 Characterisation

NMR

As already described in section 2.3, there are several different ways to characterise polyrotaxanes. In the case of polyrotaxanes with low CD content, NMR is the fastest and most precise method to characterise these molecules. Only a part of the NMR spectra are shown in this paragraph. A more complete selection can be found in the appendix section 5.7.

Proof of rotaxanation

First of all one can prove the formation of polyrotaxanes. Free and complexed CD can be unambiguously distinguished by a clear shift of the hydroxyl protons OH-2, OH-3 and OH-6 for the native, as well as the azido- α -CD, when measured in DMSO-D₆ (Figure 5.10). The shift is less visible for the latter one since the peaks are not degenerated in contrast to the symmetric native α -CD.

Further proof for the complexation can be drawn from the ¹³C-NMR, where the C-4 and C-6 signals of the CD are clearly shifted (Figure 5.11). When $N_{CD} > 4$, broadening of

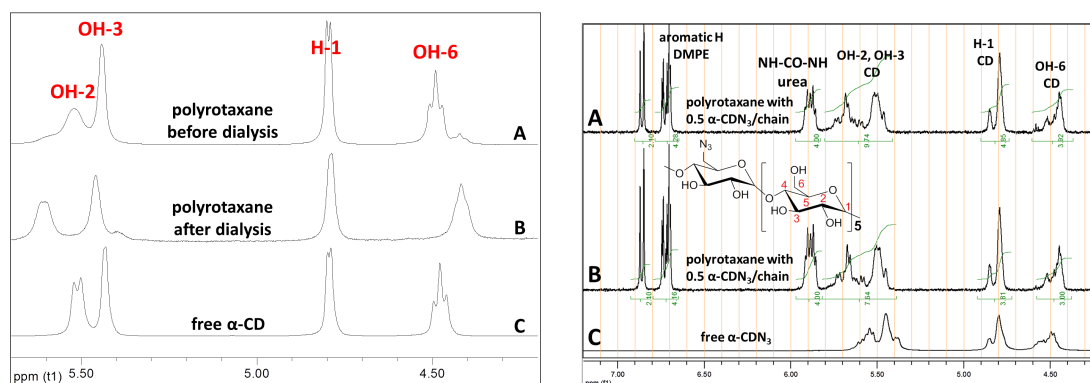


Figure 5.10: left: ^1H -NMR spectrum of OH-region of α -CD for A. polyrotaxane before removal of excess α -CD, B. polyrotaxane after removal of excess α -CD by dialysis and C. pure α -CD right: ^1H -NMR spectrum of OH-region of purified polyrotaxane A. and B. with 0.5 α -CDN₂/chain and C. free α -CDN₃

the signals is observed. This is an indication that aggregation between the threaded native α -CDs occurs (Figure 5.11 B). Moreover the C-2 and C-5 signals can be resolved when they are complexed (Figure 5.11 A, B).

The C-5 shift comes together with the H-5 shift, as assessed by HMQC correlation (Appendix Figure 5.25). It is remarkable that the inner cavity proton H-3, usually shifted in complexes, is nearly not affected. It comes with a small shift of the OH-3 signal. This can be explained by the fact that the more affected OH-2 are closer to the CD axis than the OH-3 protons.

The proximity to the axis also affects the primary OH-6 and H-6, H-6' protons, which

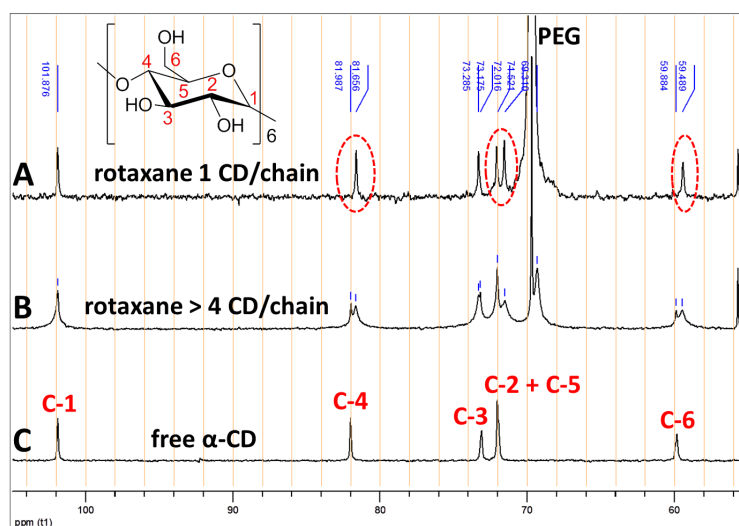


Figure 5.11: ^{13}C -NMR spectra of A. polyrotaxane with 1 CD/chain, B. polyrotaxane with > 4 CD/chain and C. pure α -CD. The CD peaks are labeled with C-1 - C-6

are differentiated as evidenced by a simple COSY experiment (Figure 5.12 for threaded native α -CDs and Figure 5.26 in the appendix for threaded azido α -CDs). Traditional dipolar correlation for H-3, H-5 and the PEG protons has not been observed with our setup because of the strong intensity of the PEG signal.

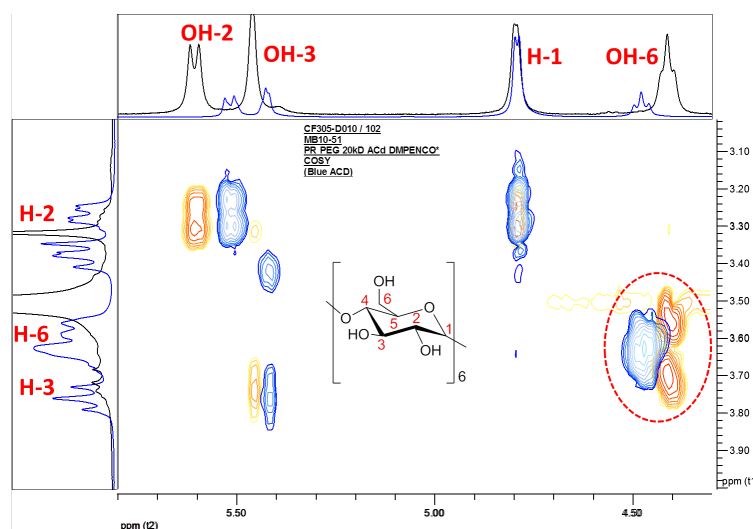


Figure 5.12: Superposition of COSY spectra of a polyrotaxane with α -CD (red) and uncomplexed α -CD (blue). The numbers indicate the corresponding carbons and protons in the glucose units.

Determination of the threading ratio N_{CD}

Furthermore the threading ratio can be clearly assessed by comparing the integration ratio of two well-defined and well-resolved peak areas in the ^1H -NMR spectrum of the complex. Accordingly the average number of CD threaded per chain N_{CD} can be calculated as follows

$$N_{CD} = \frac{A_{CD} H_{Pol}}{A_{Pol} H_{CD}}, \quad (5.1)$$

where A_{CD} is the peak area of a signal assigned to the CD and A_{Pol} the peak area of a signal assigned to the polymer chain. H_{CD} and H_{Pol} are number of protons H corresponding to each peak respectively.

In practice however the peak-integrations are normalised with respect to a well defined-peak which can be assigned to the polymer. Since the capping reactions are quantitative, usually peaks arising from the stopper attached to the chain are chosen, because they can be well identified in the spectrum and intensities in the same order of magnitude as for the CD's H-1 proton are observed. For polyrotaxanes endcapped with DMPEPhSO_3^- the peak integrations are normalised with respect to the urea protons of the end-cap linkage at 5.9 ppm, which amount to 4H or the aromatic protons between 6.7 - 6.9 ppm which represent 6H per chain (Figure 5.13 A). The peak integrations for polyrotaxanes endcapped with adamantane are normalised with respect to its tertiary C-H protons at 1.9 ppm which amount to 6H (Figure 5.13 B). The well-resolved signal of the CD's anomeric H-1 proton at 4.85 ppm is then employed to calculate the number of CDs per chain, simply by dividing the normalised peak area by 6, because it represents 6H per CD molecule.

High performance liquid chromatography (HPLC)

The polyrotaxanes synthesised by the method above are mixtures containing 0, 1, 2, 3, etc. CDs per chain. Depending on the reaction conditions, The composition of these mixtures can be tuned by the reaction parameters, resulting in different average threading ratios.

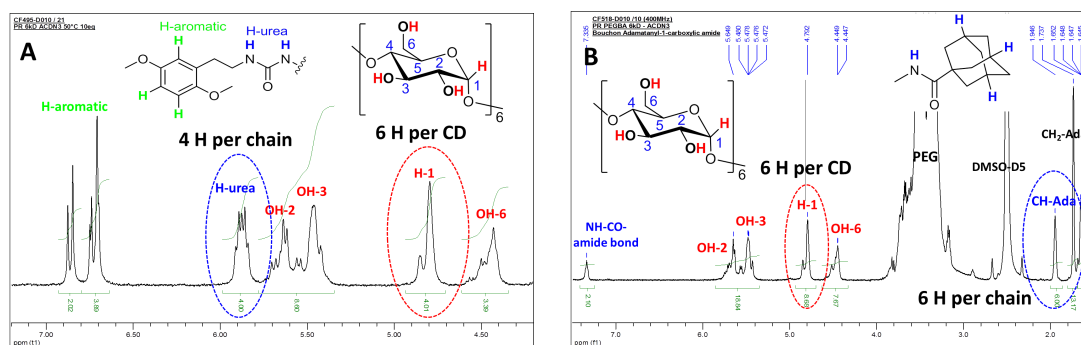


Figure 5.13: ¹H-NMR spectra of polyrotaxanes endcapped with A. DMPEPhSO₃⁻ (0.7 CD/chain) and B. adamantane (1.4 CD/chain) indicating the peaks used to calculate N_{CD} .

Polyrotaxanes with many complexed CDs are routinely separated by size exclusion chromatography (SEC) in order to determine the number of CD/chain and the corresponding MW. Using standard Phenogel columns and a phosphate buffer eluent, separation of samples with polyrotaxanes up to 4 CD/chain has been attempted (see appendix). However this technique proved to be not sensitive enough to distinguish between polyrotaxanes with low N_{CD} and free endcapped polymer. Thus, although MW are markedly different, sizes cannot be easily discriminated by this method.

However, chains bearing 0, 1, 2 or more α -CDs should behave distinctively with respect to their hydrophilic interactions. Each α -CD can potentially interact with its 18 hydroxyl groups (or 17 for azido α -CD) creating H bonds and dipolar moments. Thus polyrotaxane mixtures should be considered as molecules bearing 0, 18, 36, 54 ... OH groups. As the polymer is linear, interaction and discrimination with hydrophilic chromatographic phases should be possible, even if the MW exceeds by far the usual MW barriers (~ 3000 g/mol) considered for classical chromatographic methods. The idea has been validated with silica gel by SPE cartridge or TLC. However, the method was impractical, as affinities are too strong. Thus, we have turned to hydrophilic modified silica. Diol phases have been considered since they are routinely used in our laboratory for control of CDs by HPLC. Trials and errors have led to a method using Betasil diol 100 phase and a gradient elution. Elution starts with acetonitrile and is continued by increasing the percentage of a water/methanol/ethanol mixture. The proportion of each protic solvent depends on the polymer MW and on the modification of the CDs. The method has been validated on analytical and semi-preparative HPLC. Preliminary results show that the chromatographic method should be applicable to columns with larger particle size used for flash chromatography. A complete study cannot be presented so far. However, representative results are displayed in Figure 5.14 and 5.15.

The shift in baseline in the chromatograms is due to the gradient elution, which is necessary to separate the polyrotaxane mixtures. Even small modification of the protocol leads to insufficient separation. The different signals can be clearly assigned to polyrotaxanes with a different number of CDs per PEG, determined from NMR spectra of samples taken for each peak. The first peak always corresponds to endcapped polymer without CD. The following peaks CD 1, CD 2 and CD 3 in the chromatogram displayed in Figure 5.14 correspond to polyrotaxanes with exactly one, two and three threaded CDs, respectively.

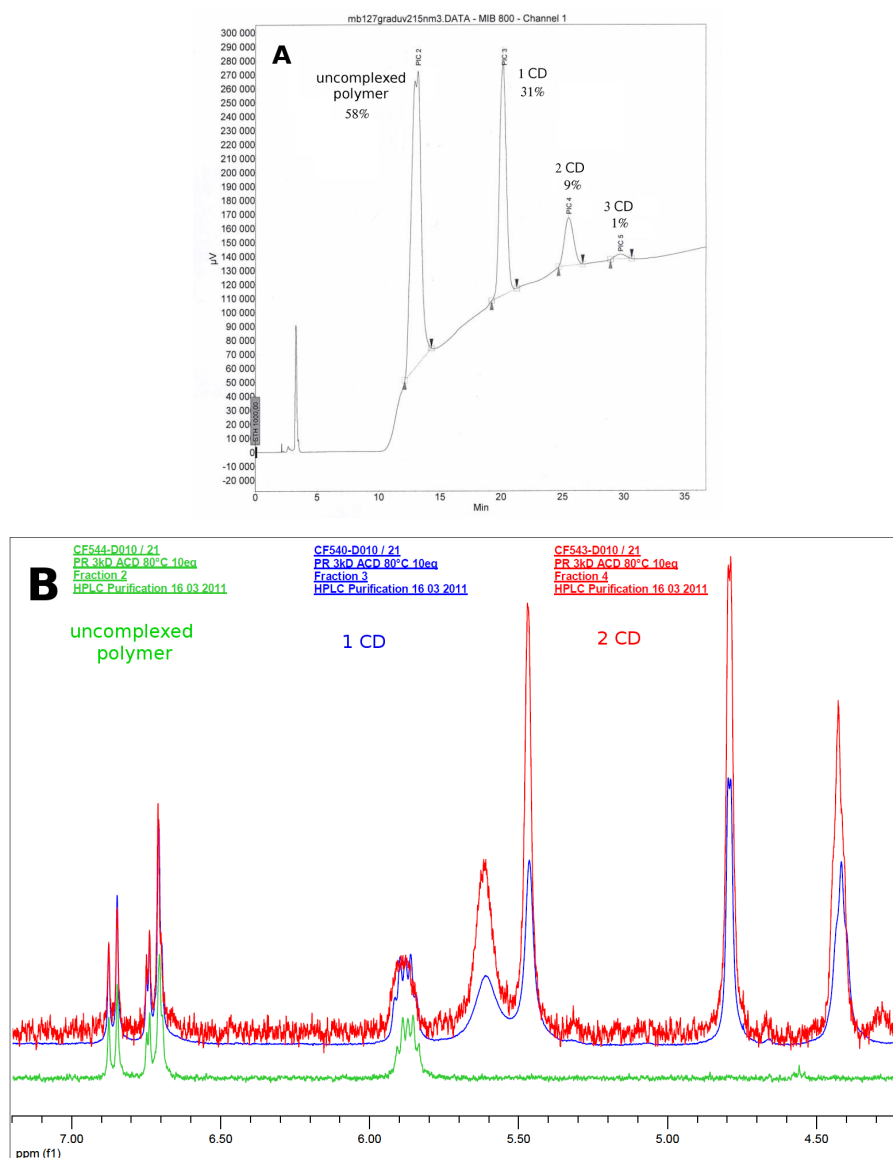


Figure 5.14: A. HPLC chromatogram and B. corresponding ¹H-NMR spectra for each peak of a polyrotaxane with average threading ratio of 0.6 CD per chain synthesised with a PEG of molecular weight 3k and 20 eq α -CD at 80°C

Since a UV detector is applied, the peak intensities in the chromatograms can be used to determine the relative composition of the polyrotaxane samples. Hence the polyrotaxane with $N_{CD} = 0.58$ shown in Figure 5.14 is composed of 58% uncomplexed polymer, 31% polyrotaxane with 1 CD, 9% with 2 CD and 1% with 3 CD/chain.

Figure 5.15 A displays a chromatogram for a polyrotaxane with $N_{CD} = 1.1$. Again peaks corresponding to exactly 1, 2 and 3 CD/chain can be identified (Figure 5.15 B). Additionally the peaks Ag 1, Ag 2, Ag 6 are small rotaxane fractions with 3 or more CDs. The NMR peaks are broadened, which makes peak integration and therefore exact quantification difficult (Figure 5.15 C). However this clearly indicates that in these fractions the CDs are aggregated. Furthermore the peaks Ag 1 - 3 with each $N_{CD} > 3$ appear among the peaks CD 1 - 3. Hence the retention time for the aggregated fractions is reduced. Due to the aggregation, less H-bonds are available to interact with the column. Furthermore

the aggregation leads to a stiffening of the chain. Thus the cannot enter the small pores of the stationary phase leading to a reduced retention time.

No aggregated fractions can be evidenced for polyrotaxanes with low average CD ratio, as well as for polyrotaxanes with azido α -CDs. Consequently these compounds might be more conveniently purified on preparative scale.

So far the method is mainly analytical and only semi-preparative quantities of the different polyrotaxanes fractions can be obtained, sufficient to be characterised by NMR. Expectedly, uncomplexed polymer is present in all samples, but its fraction gets smaller with increasing N_{CD} . The composition of the polyrotaxanes is important for the choice of samples, used for the STL synthesis and the physical characterisation.

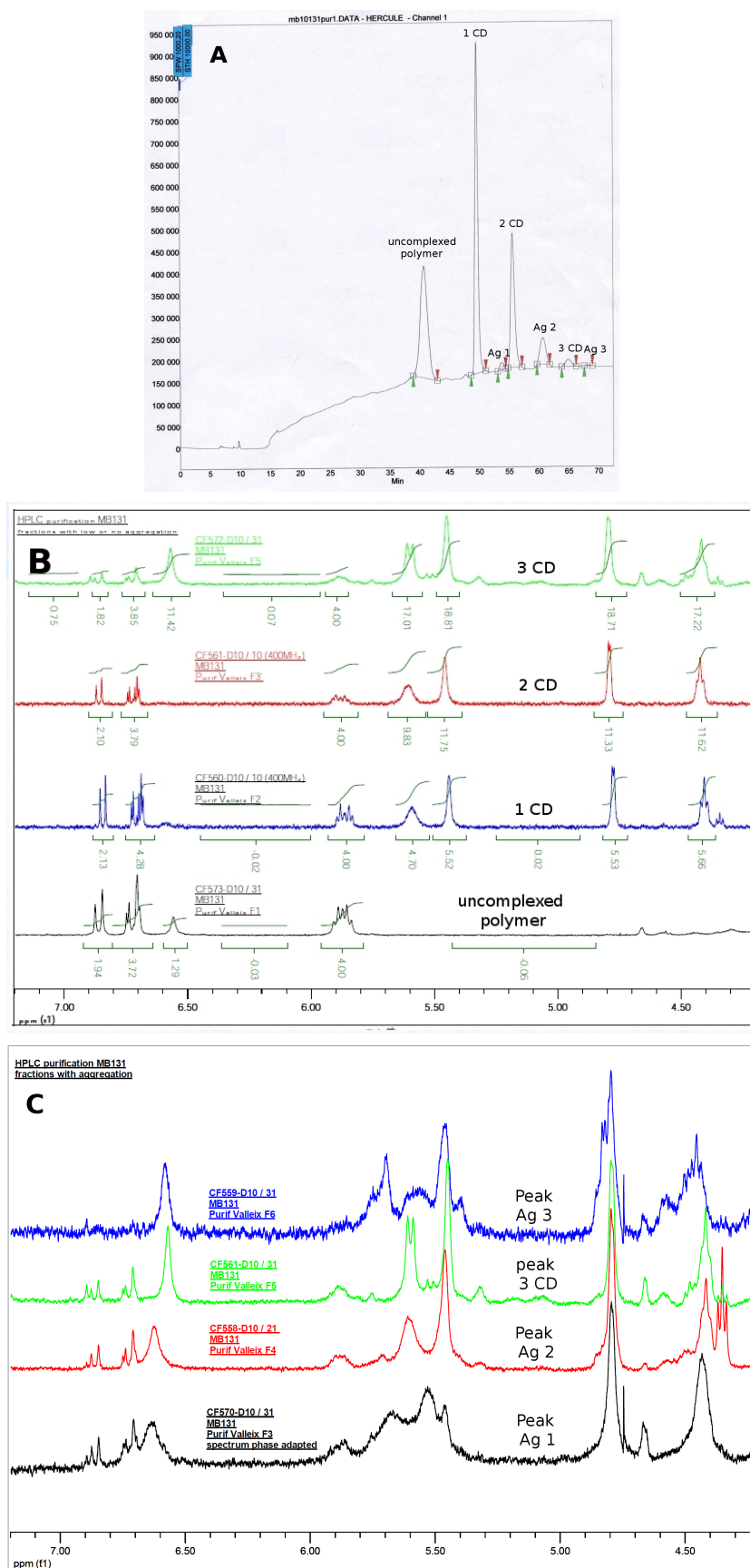


Figure 5.15: A. HPLC chromatogram and B. corresponding $^1\text{H-NMR}$ spectra for the peaks in the chromatogram without aggregated CDs, as well as C. for the peaks in the chromatogram with aggregated CDs for a polyrotaxane with average threading ratio of 1.1 CD per chain synthesised with a PEG of molecular weight 6k and 20 eq α -CD at 90°C.

Mass spectroscopy

Mass Spectroscopy (MS) has been attempted to characterise the polyrotaxanes apart from NMR and HPLC. Only polyrotaxanes synthesised with PEG 3k and 6k have been analysed with $N_{CD} = 1.2$ and $N_{CD} = 1.4$ azido α -CD, respectively. Polyrotaxanes prepared with the small MW PEGs display the largest change of MW per threaded CD large. Furthermore uncharged molecules are ionised with increasing difficulty the bigger their MW.

ESI-TOF MS (Electrospray Ionisation Time of Flight) has not yielded a spectrum for both compounds because the ionisation even for the smaller polyrotaxane has not been achieved by electrospray ionisation. Thus MALDI-TOF (Matrix Assisted Laser Desorption Ionisation - Time of Flight) MS has been attempted. Ionisation was not successful for the 6k polyrotaxane. Yet a MS spectrum has been measured for the 3k compound and is shown in Figure 5.16.

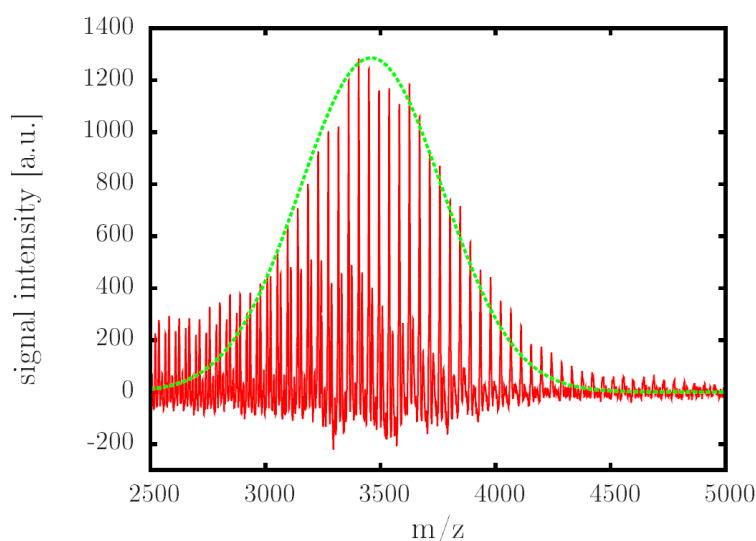


Figure 5.16: MALDI-TOF MS spectrum for polyrotaxanes synthesised with PEG 3k and azido α -CD ($N_{CD} = 1.2$). The maximum of the polymer's Gaussian distribution is at 3450 M/z, which corresponds very well to the endcapped polymer without CD.

It clearly shows the Gaussian distribution of the polymer. The maximum is at $M/z \approx 3450$, which corresponds very well to the Na-adduct of the endcapped polymer without CD (3420 g/mol). Therefore it is suspected that the polyrotaxane is unstable on the matrix. Consequently the complexed CDs must have been dethreaded throughout the ionisation process. Successful detection would require further optimisation of the instrumental parameters. Especially the choice of the matrices and solvents is a delicate task. Due to these difficulties this characterisation method has not been pursued any further.

5.3.4 Optimisation of reaction parameters

The impact of the different reaction conditions on the threading ratio N_{CD} is investigated in order to be able to finely tune the number of complexed CDs. DMPEPSO₃⁻ is used as stopper of choice for the experiments to optimise the reaction conditions. On the one hand because it has been the first working endcap available. But more importantly it results in higher yields than Adamantane.

Starting from the standard reaction conditions, displayed in Table 5.1 (section 5.3.1), the

influence of the different reaction parameters on the threading ratio N_{CD} are investigated. In particular the dependence of N_{CD} on the MW of the PEGs, the temperature, the initial CD/PEG ratio R_0 , the initial concentration of reactants c_0 and complexation time t_c are surveyed.

Complexation time

Prior to the investigation of the complexation time, the kinetics of the capping reaction has been verified by NMR. DMPEPSO₃⁻ degrades instantly (< 5 min, verified by NMR) by quenching the reaction mixture with 0.1M NaOH. At first DMPEPSO₃⁻ is added to the reaction mixture. Subsequent addition of NaOH after 15 min or 24h yields identical threading ratios. This shows, that the end-capping reaction is complete in less than 15 min.

Thus it is possible to study the influence of the complex formation time t_c on the number of CD/chain for $t_c > 15$ min. Shorter complexation times can not be investigated because complete endcapping is not ascertained. Native α -CD and PEG 6k are used, varying the delay time before adding the stopper molecule DMPEPSO₃⁻ to the solution. The results are presented in Table 5.2.

t_c [h]	0.25	0.5	2	6	24	48
N_{CD}	1.16	1.13	1.16	1.09	1.17	1.20

Table 5.2: Influence of complex formation time t_c on N_{CD} at 70°C

N_{CD} does not change significantly between 15 min and 2 days of complexation. This proves that the threading kinetics are very fast. Our findings suggest a very rapid accommodation of complexing equilibrium for soluble polyrotaxanes with low complexation ratios. Nevertheless all the following experiments have been carried out with $t_c = 30$ min using native α -CD and with $t_c = 2$ h using α -CDN₃. It has been assumed that this delay time is sufficiently large to allow for reaching the equilibrium, also when polymers with different MW or different reaction temperatures are used.

MW dependence

It is well known that the polymer size influences the threading efficiency [20]. Thus the effect of the polymer chain length on the number of CD/chain is investigated. Applying identical reaction conditions for each polymer, experiments are conducted for PEGs with a MW of 3, 6, 10 and 20k, using native, as well as azido- α -CD.

The curves for the native and the modified CDs are almost identical. N_{CD} increases with the MW of the polymer. However it increases not exactly linear as the rise is less pronounced between 6 and 20k (Figure 5.17 A). The graph in Figure 5.17 B displays the MW dependence of the number of EO units per CD threaded onto the polymer N_{CD}/N_{EO} . If it is only the number of monomers, which determine N_{CD} it should be equal for all four polymers. For complete coverage of the polymer the maximum possible ratio is $N_{CD}/N_{EO} = 0.5$. Thus the lower N_{CD}/N_{EO} , the lower the threading efficiency. The curve shows a maximum for 6k followed by a strong decrease for higher MW.

Qualitatively the threading efficiency shows similar behavior compared to what is reported for polyrotaxanes which form insoluble channel like inclusion compounds (maximum for

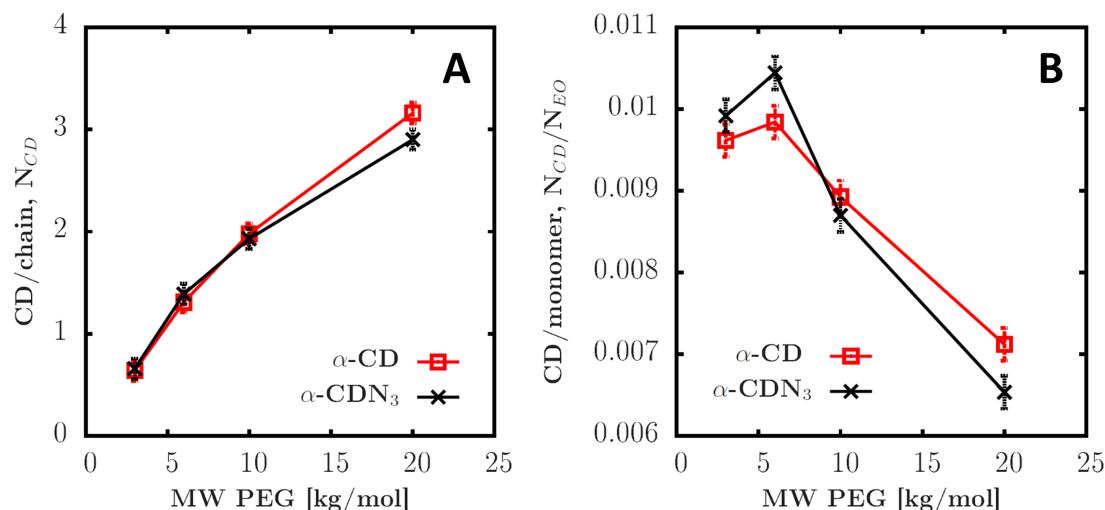


Figure 5.17: Influence of PEG chain length on CD/chain N_{CD} (A) and number ethylene oxide units per CD threaded on the chain N_{CD}/N_{EO} (B)

MW \sim 2 kg/mol) [20]. The difference might be caused by lack of H-bonds between adjacent CDs changing the subtle interplay of entropy and attractive host-guest interactions which is governing threading process. For small PEGs the dissociation might be more important. Whereas for high MW the unfavorable threading entropy [143] and the less available PEG ends are the main factors determining to the N_{CD} . Hence an optimum is reached for the PEG 6k where both effects balance each other.

Temperature dependence

The influence of the reaction temperature on N_{CD} is studied for native and azido α -CD (Figure 5.18 A and B, respectively). The reaction conditions are the same as mentioned in Table 5.1 for the experiments with native α -CD. To ascertain solubilisation of the azido α -CD for temperatures lower than 70°C, initial CD/PEG ratios CD/PEG $R_0 = 10$ for PEG-6k and $R_0 = 15$ for the PEG-20k are used. N_{CD} is determined prior and after the removal of the symmetric urea side products for polyrotaxanes synthesised with native α -CD. Polyrotaxanes prepared with azido α -CD can only be characterised after removal of the urea because the peaks used to determine the threading ratio are not separated enough.

At first native CDs are investigated. Figure 5.18 A illustrates, that with decreasing temperature N_{CD} increases slowly. N_{CD} prior to filtration rises drastically below 50°C. Furthermore below 50°C, threading ratios found before and after filtration start to diverge significantly for PEG 20k and PEG 6k. It reaches a plateau values for filtered polyrotaxanes (\sim 3.5 CD/chain for PEG 20k and \sim 1.5 CD/chain for PEG 6k), which are substantially smaller compared to the N_{CD} determined prior to the filtration. At sufficiently low temperatures, H-bonds contribute more to the stabilisation of the CD-PEG complexes. This leads to aggregation of the CDs on the chain and to formation of insoluble polyrotaxanes. These fractions are then eliminated in the filtration step together with the urea side product.

Using azido α -CD, only $T \geq 50^\circ\text{C}$ can be investigated as azido α -CD is not sufficiently

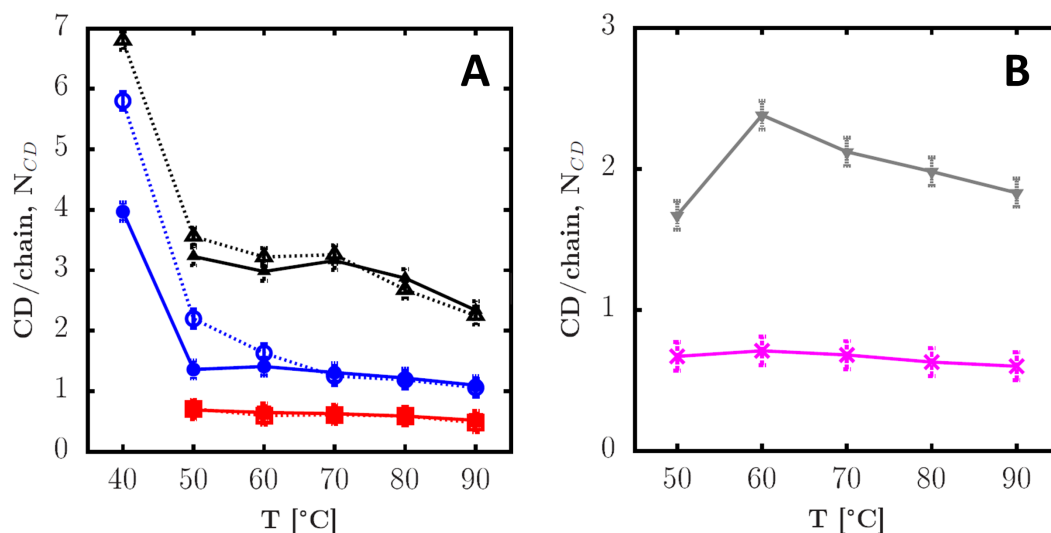


Figure 5.18: Influence of complexation temperature on threading ratio N_{CD} : **A.** native α -CD: PEG 3k filtered (■), not filtered (□); PEG 6k filtered (●), not filtered (○) and PEG 20k filtered (▲), not filtered (△); **B.** azido α -CD: PEG 20k (▼), 6k (×)

soluble for temperatures below. N_{CD} augments with decreasing temperature (Figure 5.18 B). Yet, in contrast to native CDs a decrease in N_{CD} is observed for $T < 60^\circ\text{C}$. In this case the solubility limit of the CD derivative might already be exceeded. Although this is certainly the main reason for the decrease in N_{CD} there are two other contributions, which might explain the different behavior compared to native α -CD. In azido α -CD, the azido group is preventing the formation of a H-bond network similar to native threaded α -CD. Furthermore it is known that azido-CDs partially self-include the azido residue into their cavity [255]. This effect, possibly diminished at high temperatures, might add to the reduced threading ratios at low temperatures.

The observed increase in N_{CD} with decreases in temperature, reflects that the complexation is entropically disfavored for both compounds [21]. Nevertheless, even for $T = 90^\circ\text{C}$ polyrotaxanes are obtained. This can be simply explained by statistical threading in absence of strong interactions between polymer and CD. Such sparsely complexed polyrotaxanes have also been reported by Fleury et al., which in their case further catalyse complexation, when cooled down in a second “complexation step” [141].

Initial ratio CD/PEG

Since polyrotaxanes with azido α -CD are of main interest for the STL synthesis, R_0 is only studied for the modified CD. Due to the low solubility of azido α -CD it is difficult to investigate high R_0 . In order to examine $R_0 > 20$ two different methods are applied to enhance the solubility of the modified CD. Using PEG 20k, supersaturated azido α -CD solutions are used which are prepared by heating to 90°C . The mixture is then cooled down to 70°C before adding the polymer. In the test series using PEG 6k, NaNO_3 (1 mol/l) is added. The addition of the salt augments the azido α -CD solubility by breaking its intramolecular H-bonds to be able to investigate high CD/PEG ratios.

R_0 increases the threading ratio for both investigated polymers (Figure 5.19). This

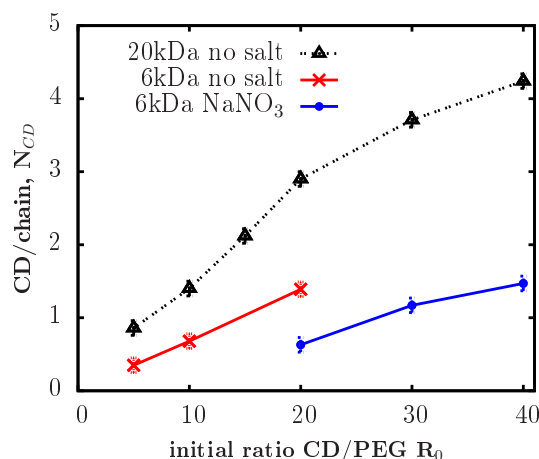


Figure 5.19: Influence of initial ratio CD/PEG R_0 on average number of CD per chain N_{CD} for azido α -CD, complexation time $t_0 = 2$ h at 70°C

can be explained by the CD/PEG ratios increasing the probability of the CD to encounter the PEG ends. Thus the threading equilibrium shifted to higher N_{CD} . For $R_0 > 20$, applying the supersaturated solutions, the increase in N_{CD} is slowed down. This is caused by slowly precipitating the azido- α -CD, thereby reducing the effective R_0 . Comparing the curves for PEG 6k in Figure 5.19 clearly shows that adding salts lowers the threading ratio. This might be caused by a salting-in effect of NaNO_3 , which would weaken the host-guest interactions between polymer and CD [256].

Polymer concentration

Finally the influence of the polymer concentration c_{PEG} (and keeping R_0 constant) is investigated. In order to prevent crossing the solubility limit of the azido α -CD for $R_0 = 20$ at 70°C , the maximum polymer concentration is constrained to 2.9 mmol/l. Taking this concentration as a reference, experiments have been carried out with a dilution factor of 2, 5, 10 and 100, using PEG 6k. Figure 5.20 illustrates, that N_{CD} decreases drastically in a linear fashion the PEG concentration. This result reflects that the probability of the CD to face one of the PEG ends is decreases strongly along with the concentration, leading to less complexed polyrotaxanes.

Remarks

Adequate choice of reaction parameters allows to efficiently control the average threading ratios N_{CD} between 0 - 5 CDs for polyrotaxanes with native, as well as azido α -CD. Applying the same reaction parameters, polyrotaxanes with both CD derivatives exhibit similar threading ratios, as long the conditions afford sufficient solubility of the azido α -CD. Furthermore the poor solubility limits the threading ratio for polyrotaxanes with azido α -CD to few CD/chain. So this method is perfectly suitable in order to produce the desired polyrotaxane precursors for the STLs.

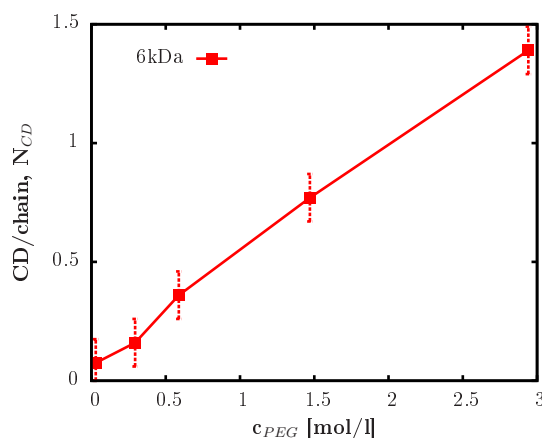


Figure 5.20: Influence of the polymer concentration c_{PEG} on average number of CD per chain N_{CD} for azido α -CD at 70°C and a complexation time $t_0 = 2$ h

5.4 Clicking of the lipophilic anchor

Polyrotaxanes with azido α -CD have been chosen as precursors for the final STL synthesis because they possess several advantages. At first they exhibit orthogonal reactivity to the bis-amino PEG in the retrosynthetic pathway. Moreover azido α -CD is the most readily available selectively modified α -CD. But most importantly, the click chemistry approach can be exploited for further modification of the azido α -CD based polyrotaxanes in a single step process.

5.4.1 Click Chemistry

Click chemistry has been introduced by Sharpless [257] with the goal to develop a set of synthetic tools for reliably and quickly joining together modular units to generate new conjugates. Reactions useful in this context usually possess a high thermodynamical driving force (> 20 kcal/mol), so that they are fast, stereospecific and highly selective for a single product. Furthermore they should be wide in scope, give very high yields and easy to purify [257]. Among these, the 1,3-dipolar cycloaddition reaction of azido compounds with alkyne derivatives has emerged, as one of the most potent ones for ligating two molecules in a general, fast and efficient process. The discovery, that the strictly thermal Huisgen cycloaddition which additionally requires strongly activated alkynes, can be extremely accelerated by several metal species, cleared the way for broad application. Especially the Cu(I) catalysed azide-alkyne cycloaddition (CuAAC), first published by Meldal et al. in 2002 [258], is today widely used because quantitative yields are obtained at moderate temperatures with high regioselectivity for the 1,4 triazole [259].

The reaction takes place in many different solvents, including water, alcohols, DMF, DMSO, etc. and has a high tolerance against other functional groups (only groups which are themselves reactive or yield stable Cu(I) complexes interfere with the process). The only constraint is that the compounds desired to be clicked have to be completely soluble in the reaction media. As catalyst either commercial Cu(I) salts such as CuI can be used or the Cu(I) species can be produced in situ from a Cu(II) compound, e.g. CuSO_4 , with a reducing agent. In general, addition of amino bases further accelerates the reaction by facilitating the formation of the Cu(I)-acetylide complex and by weakly complexing the

labile Cu(I) to protect it from oxidation [241].

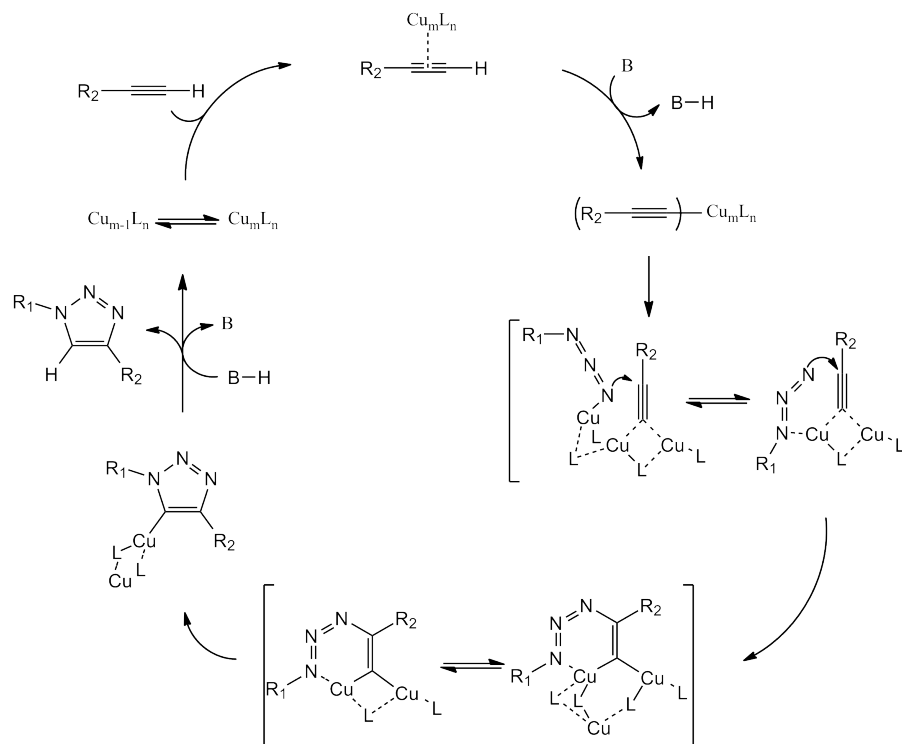


Figure 5.21: Schematic mechanism of azide-alkyne cycloaddition (B= amine base, L= ligand)

Figure 5.21 displays the likely mechanism for Cu(I) catalysed azide-alkyne click reactions, first proposed by Sharpless et al. 2002 [260] and then further refined by computational [261] and kinetic studies [262] in the following years. Since the reaction shows at least second-order kinetics with respect to the concentration of the copper species, at least two copper centers are involved in this reaction, probably linking two acetylenes by a μ -bridge. Furthermore a formation of copper-acetylide is proposed which shows an important contribution to the rate acceleration.

The azide-alkyne reactions has found wide-spread applications, e.g. pharmaceutical, polymer [241] and bio-chemistry [263, 264]. It has been also exploited to synthesise polyrotaxanes. A beautiful example is the endcapping of α -CD/PEG complexes, functionalised with acetylene groups at the polymer ends with azido- β -CD stopper molecules [265].

5.4.2 Preparation of cholesteryl succinic acid propargylamide

To be able to click a cholesterol moiety as the required hydrophobic anchor, a terminal alkyne has to be added to a cholesterol derivative. The succinate linker has been determined as proper linker allowing sufficient mobility (or degrees of freedom) to ensure conformational adaptability for supramolecular applications [112]. Thus coupling the commercial cholesteryl hemisuccinate and propargylamine, leads to a slightly extended linker with an amide bond, which is chemically very stable and biocompatible. Previous bad experience in the formation of amides from cholesteryl hemisuccinate have led us to the application of an alternative method to the classical use of carbodiimides..

A new coupling method described recently by Mukaiyama et al. [266] for forming car-

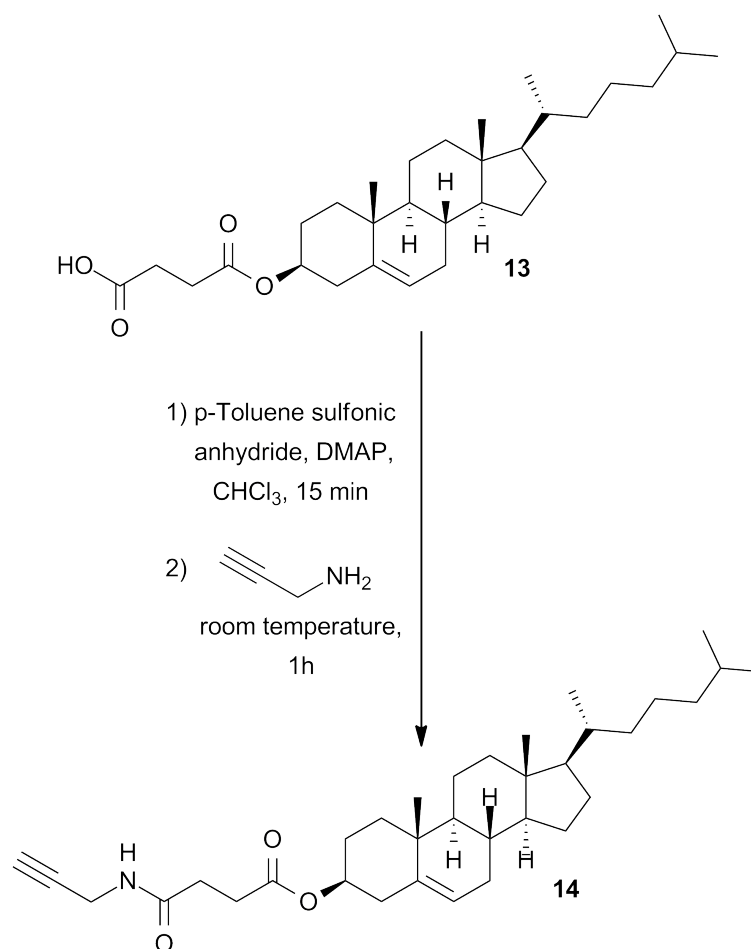


Figure 5.22: Preparation of cholesteryl succinic acid propargylamide

boxamides is adopted in order to synthesise the cholesteryl succinic acid propargylamide **14** from propargylamine and cholesteryl hemisuccinate **13** (Figure 5.22). For this purpose following modifications have been adopted. The solvent is changed from CH₂Cl₂ to CHCl₃. Instead of benzenesulfonic anhydride, p-Toluene sulfonic anhydride (p-Ts₂O) is used because it is commercially available. p-Ts₂O is a good sulfonylation agent owing to its leaving ability and activates the carboxyl group of the cholesterol derivative to give a mixed anhydride. Since p-toluene sulfonic acid is produced in stoichiometric quantities, the weak base DMAP is applied in order to control the acidity. This compound also acts as a nucleophilic catalyst (Steglich catalyst) for the formation of the amide in the presence of the reactive anhydride and the propargylamine. In order to obtain the pure final product **14** the water soluble byproducts are removed by aqueous work up and the compound is finally recrystallised in ethyl acetate.

5.4.3 Clicking of the cholesteryl succinic acid propargylamide

In the last decade numerous procedures have been described in order to click molecules via the azido-alkyne cycloaddition. In order to find a method which suits best our purposes, azido CDs are coupled with compound **14** to refine the reaction conditions. Furthermore, thereby obtained amphiphilic CDs are of importance as reference materials for the

physical characterisation of the STLs. The cholesteryl α -CD is useful to compare the STL's membrane insertion properties to the amphiphilic anchor molecule without polymer. Cholesteryl β -CD serves as perfect receptor molecule for STLs functionalised with adamantane, as they form very stable inclusion complexes [71, 245, 267]. Therefore they are needed to analyse the ligand-receptor binding properties of the STLs.

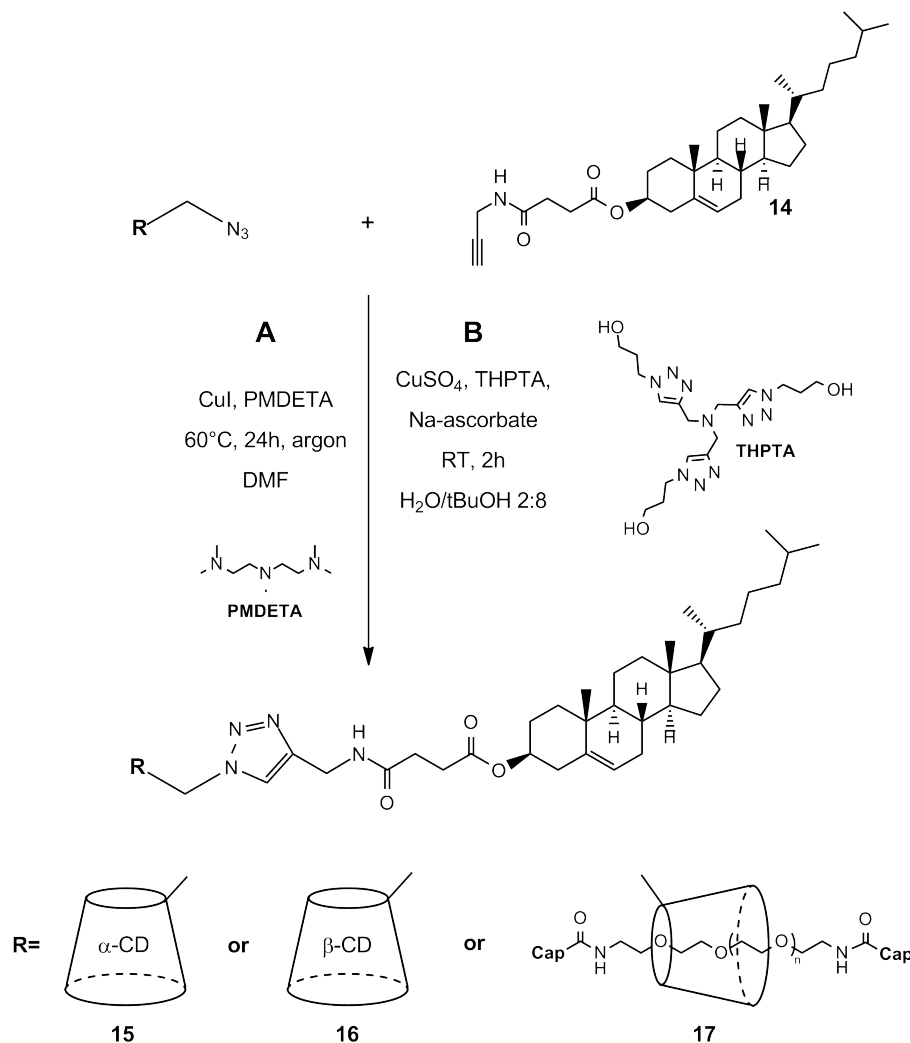


Figure 5.23: Synthesis of cholesteryl CDs **15**, **16** and STL **17**. Both methods are applicable for all compounds. However pathway B is preferred since yields are higher and reaction is faster.

At first we have implemented a procedure, already successfully used to functionalise ethylene dimethacrylate polymers with azido β -CD in DMF [268]. DMF is one of the few solvents, which is able to solubilise the hydrophilic modified CD and the lipophilic cholesteryl derivative. In order to click cholesteryl alkyne with an azido CD, both compounds are dissolved in ultrapure, dry DMF (redistilled and degassed prior to use), employing Cu(I) as catalyst and the amino base PMDETA as ligand (Figure 5.23 pathway A). The reaction is carried out at 60°C for 24h under argon atmosphere to avoid deactivation of the Cu(I) catalyst by oxidation with oxygen. However no quantitative yields have been obtained by this approach. The insoluble product **16** has to be purified by several washing steps; at first with water to remove unreacted CD, the Cu salt as well as PMDETA and

with acetone to withdraw the cholesteryl succinic acid propargylamide. The incomplete reaction might be caused by oxidation of the catalyst since the laboratory is not equipped to work under strictly inert conditions.

In order to avoid elaborate purification in the STL synthesis a completely quantitative method is needed. Hence a new procedure is required to be applicable as universal protocol for STL and cholesteryl CD synthesis. To circumvent inert conditions, a method described by Finn et coll. [259] is adopted which can be carried out at ambient temperatures using in situ generation of the Cu(I) catalyst from CuSO_4 by reduction with ascorbate. The use of a 5-fold excess of the ligand THBTA protects reagents from oxidation by Cu-mediated generation of oxygen species, which is a problem often encountered when working under these conditions [269]. THBTA is not commercial and needs to be prepared like described in detail in reference [259]. The solvent system DMSO/ H_2O used in reference [259] is not able to dissolve all reactants. So it is replaced by another solvent system, which solubilises the cholesteryl alkyne, as well as the azido-CD and the rotaxane, respectively. This is achieved by applying a mixture of water and tBuOH in ratio of 2:8, which are both well known media for the CuAAC [270]. The reaction works very well and quantitative yields are achieved in less than 1h, using 5 - 10 mol% catalyst. It is important to elude alkyne concentrations higher than 5 mM to avoid catalyst poisoning. The general reaction outline is illustrated in pathway B in Figure 5.23.

In the case of cholesteryl CDs the purification of the final product is conducted like explained for the synthesis under inert conditions. When clicking rotaxanes the final product **15** is worked up as follows: At first reaction mixture is dialysed with water to remove the Cu salt, ligand and ascorbate. Then the product is washed with ether in order to eliminate the excess cholesteryl succinic acid propargylamide. By adapting the HPLC method for the polyrotaxanes, it is also possible to separate the STL regarding to the exact number of cholesteryl CD after the clicking step.

5.5 Conclusion

STLs have been successfully synthesised with PEG of different MW and different number of CD anchors. The reaction scheme for the complete synthesis of a STL with an adamantane ligand which can be recognised by β -CD is displayed in Figure 5.24.

The principle building blocks of these new molecules are polyrotaxanes with a controlled, very low threading ratio formed with azido α -CD, as sliding rings, threaded onto bis-amino-PEG chains in water. A small number of CDs per chain is achieved by forming the PEG/CD inclusion complex at high temperatures, which additionally provides for sufficient solubility of the poorly soluble modified CD. To isolate the polyrotaxanes two novel in-situ capping techniques with water soluble stopper molecules are developed. The first method uses blocked isocyanates, in particular DMPEPhSO_3^- . In an alternative approach adamantane carboxylic acid, rendered water soluble by complexation with β -CD, is coupled to the polymer with the help of the activation agent DMT-MM. Both procedures provide for a high versatility, since they are potentially applicable for any soluble capping molecule in form of an isocyanate or carboxylic acid.

The final product is obtained by attaching a lipophilic anchor to the polyrotaxanes by

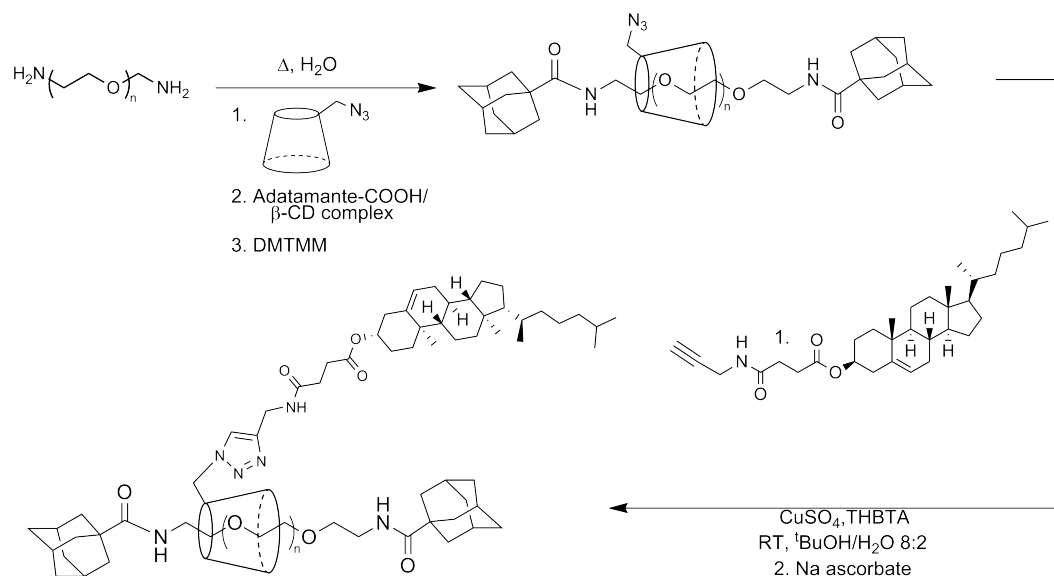


Figure 5.24: Synthesis of STL

exploiting a click chemistry approach. Cholesteryl hemisuccinate, functionalised with an propargylamine group can be coupled to the azido group via a CuAAC in quantitative yields. This method serves also to synthesise cholesteryl CDs, which are needed as reference for the characterisation of the STL's physical properties.

HPLC separation methods have been developed successfully to separate the polyrotaxanes, as well as the STLs according to the discrete number of CDs on the chain. Upscaling should provide pure and well defined STLs. This should be of special importance for studying the effect of the number of sliding rings on the polymer conformation, when inserted into a membrane.

The obtained STLs will be used to study the insertion behavior into DPPC model membranes. The ability of the polymer tether to slide through the CD ring should translate into a new type of tethered ligand-receptor interactions. These can be probed e.g. by force measurements between two phospholipid bilayers one containing STLs modified with an adamantane cap as ligand and the other with cholesteryl β -CD as receptor.

5.6 Experimental

5.6.1 Used Chemicals

The chemicals and solvents used throughout the synthesis are listed in Table 5.3.

5.6.2 Synthetic procedures

Synthesis of $\text{DMPEPhSO}_3^- \mathbf{3}$

3 g (13 mmol, 1.2eq) of 4-phenol sulfonic acid are dissolved in 12 ml DMSO while stirring for 20 min at room temperature. Then 2.3 g (11.1 mmol, 1eq) DMPENCO are added to the solution and left stirring for 4h to give a turbid mixture. The suspension is precipitated with 250 ml of acetone and centrifuged. The residue is taken up in 25 ml of millipore

Name	Formula	Molar Mass [g/mol]	Provider
(+)-Sodium-L-ascorbate	C ₆ H ₇ NaO ₆	198.11	Sigma
1-Adamantanecarboxylic acid	C ₁₁ H ₁₆ O ₂	180.24	Aldrich
4-Dimethylaminopyridine (DMAP)	C ₇ H ₁₀ N ₂	122.17	Fluka
DMT-MM	C ₁₀ H ₁₇ ClN ₄ O ₃	276.72	Aldrich
Acetone	CH ₃ COCH ₃	58.08	Sigma-Aldrich
Acetonitrile	C ₂ H ₃ N	41.05	sds
α-CD	C ₃₆ H ₆₀ O ₃₀	972.84	Wacker
β-CD	C ₄₂ H ₇₀ O ₃₅	1134.98	lab de roquette
tert-Butanol	(CH ₃) ₃ COH	74.12	Fluka
Chloroform	CHCl ₃	119.38	Sigma-Aldrich
Cholesteryl-hemisuccinate	C ₃₁ H ₅₀ O ₄	486.74	Sigma
Copper(I) iodide	CuI	190.45	Sigma-Aldrich
Copper(II) sulfate	CuSO ₄	159.61	Riedel-de Haën
Deuteriochloroform	CDCl ₃	120.38	Eurisotop
Diethyl ether	(CH ₃ CH ₂) ₂ O	74.12	Sigma-Aldrich
N,N-Dimethylformamide (DMF)	C ₃ H ₇ NO	73.09	Fluka
Dimethylsulfoxide-D6 (DMSO-D6)	C ₂ D ₆ OS	84.17	Sigma
DMPENCO	C ₁₁ H ₁₃ N ₃ O ₃	207.23	Sigma-Aldrich
Ethanol	C ₂ H ₆ O	46.07	VWR
Methanol	CH ₄ O	32.04	Sigma-Aldrich
α-CDN ₃	C ₃₆ H ₅₉ N ₃ O ₂₉	997.86	Biocodex
β-CDN ₃	C ₄₂ H ₆₉ N ₃ O ₃₄	1160.00	own laboratory
bis-amino-PEG-3kDa	H ₂ N(C ₂ H ₄ O) _n C ₂ H ₄ NH ₂	3,000	Aldrich
bis-amino-PEG-6kDa	H ₂ N(C ₂ H ₄ O) _n C ₂ H ₄ NH ₂	6,000	Aldrich
bis-amino-PEG-10kDa	H ₂ N(C ₂ H ₄ O) _n C ₂ H ₄ NH ₂	10,000	Aldrich
bis-amino-PEG-20kDa	H ₂ N(C ₂ H ₄ O) _n C ₂ H ₄ NH ₂	20,000	Aldrich
PMDETA	C ₉ H ₂₃ N ₃	173.3	Sigma-Aldrich
Propargylamine	HC ₃ H ₂ NH ₂	55.08	Sigma-Aldrich
Sodium phenylsulfonate	C ₆ H ₅ NaO ₃ S	196.16	Alfa Aesar
p-Toluenesulfonic anhydride	(CH ₃ C ₆ H ₄ SO ₂) ₂ O	326.38	Sigma-Aldrich

Table 5.3: Chemicals used for synthesis

water and filtered at first with a fiberglass filter (1.6 μm) and then with Millex GS filter (0.8 μm). The solution is freeze dried over night to give a white powder. In the final product there is (~ 40 - 50%) 4-phenol sulfonic acid, determined by NMR (see appendix), which is not removed.

Yield: 3.2 g, 71 % (total), 41 % (DMPEPhSO₃⁻)

¹H-NMR (300MHz, DMSO-D6): 9.55 ppm (1H, HO- residual phenolsulfonate); 7.80 ppm (1H, N-H carbamat DMPEPhSO₃⁻); 7.60, 7.57, 7.01 - 6.77 ppm (7H, aromatic H DMPEPhSO₃⁻); 7.43, 7.40 and 6.67, 6.66 ppm (4H, aromatic H residual phenolsulfonate); 5.8 ppm (2H, urea side product); 3.7 ppm (6H, -OCH₃ DMPEPhSO₃⁻); 3.50 (2H, H₂C-CN HCO DMPEPhSO₃⁻); 2.74 (2H, benzylic H₂C DMPEPhSO₃⁻)

Synthesis of DMPE end-capped PEG 5

10 μmol (1eq) of bis-amino-PEG are dissolved in 3.4 ml millipore water. 100 μmol of DMPEPhSO₃⁻ are added to the solution and it is left stirring at 70°C for 4h. The mixture is diluted with 20 ml of millipore water and dialysed four times for 24h at room temperature with 1.5l of millipore water. Finally the turbid solution is filtered with a 0.2 μm filter and freeze dried to give a white powder.

Yield: 55 mg, 86%

¹H-NMR (300MHz, DMSO-D6): 6.95 - 6.75 ppm (6H, H aromatic DMPE); 5.85 ppm (m, 4H, H-urea); 3.7 ppm (s, 12H, -OMe); 3.5 (nH, -OCH₂CH₂- PEG); 2.5 ppm (residual H₂O);

Synthesis of complex β -CD/admantane carboxylic acid 6a

700 mg (0.62 mmol, 1eq) β -CD are dissolved in 50 ml of millipore water, sonicated for 20 min and then heated to 70°C while stirring. Likewise 450 mg (2.5, 4eq) of adamantane carboxylic acid are dissolved in 50 ml of acetone and added slowly to the β -CD solution via a dropping funnel. Then the transparent mixture is sonicated for 45 min and left stirring at 70°C for 3h to completely evaporate the acetone. 30 ml of water are added to the now turbid mixture. Then it is filtered with a 1 μ m fiber glass filter and washed several times with millipore water. Then the transparent solution is freeze dried to give a white powder.

Yield: 710 mg, (87 %)

¹H-NMR (300MHz, DMSO-D6): 5.8 (14H, -OH-1 and -OH-2 CD); 4.8 ppm (7H, H-1 CD); 4.45 ppm (7H, -OH-6 CD); 2.5 ppm (residual H₂O); 1.95 ppm (3H, -C-H adamantane); 1.78 ppm (6H, -CH₂-CCOOH adamantane); 1.65 ppm (6H, -CH₂-CH adamantane)

Synthesis of complex β -CD/biotin 6b

57 mg (0.05 mmol, 1eq) β -CD are dissolved in 10 ml of millipore water, sonicated for 20 min and then heated to 70°C while stirring. Likewise 30 mg (0.12 mmol, 2.5eq) of biotin are dissolved in 30 ml of hot ethanol and added slowly to the β -CD solution via a dropping funnel to give a transparent mixture. After stirring at 90°C for 2h almost all of the solvent is evaporated and a white precipitate is formed. The residue is taken up in 30 ml of water, filtered with a 1 μ m fiber glass filter and washed several times with millipore water. Finally the transparent solution is freeze dried to give a white powder.

Yield: 65 mg, (97 %)

¹H-NMR (300MHz, DMSO-D6): 6.43, 6.35 (2H, urea biotin); 5.8 (14H, -OH-1 and -OH-2 CD); 4.8 ppm (7H, H-1 CD); 4.45 ppm (7H, -OH-6 CD); 4.3 (2H, CH (CH-CH-NH) biotin); 4.1 (2H, CH (CH₂-CH-NH) biotin); 3.5 (nH, -OCH₂CH₂- PEG); 2.5 ppm (residual H₂O); 2.1 ppm (2H, -CH₂-COOH biotin); 1.62 - 1.31 ppm (12H, biotin)

Synthesis of PEG end-capped with adamantane 8a

10 μ mol (1eq) PEG are dissolved in 2 ml of millipore water. Then 40 μ mol (4eq) of adamantane/ β -CD complex, dissolved in 1 ml of millipore water, are added. In order to start the reaction 10 μ mol (4eq) of DMT-MM in 0.4 ml of water are added and the transparent solution is stirred at 70°C during the night. The transparent solution is diluted with 15 ml of millipore water and dialysed 3 times with 1.5l of millipore water at room temperature for 24h. Then the solution containing little white aggregates is freeze dried to give **8a**.

Yield: 17 mg, (27 %)

¹H-NMR (300MHz, DMSO-D6): 7.35 (t, 2H, -NHCO); 3.5 ppm (nH, -OCH₂CH₂); 2.5

ppm (residual H₂O); 1.9 ppm (6H, CH adamantane), 1.7 (24H, CH₂ adamantane)

Trial to produce polyrotaxanes end-capped with biotin **8b**

10 μ mol (1eq) PEG are dissolved in 2 ml of millipore water and 200 μ mol (20eq) CD is added to the clear solution. Then it is left stirring at 70°C for 30 min (α -CD) or 2h (α -CDN₃) to become transparent and after that 40 μ mol (4eq) of biotin/ β -CD complex dissolved in 1 ml of millipore water are added. In order to start the reaction, 10 μ mol (4eq) of DMT-MM in 0.4 ml of water are added and the transparent solution is stirred at 70°C during the night. The transparent solution is diluted with 15 ml of millipore water and dialysed 3 times with 1.5l of millipore water at room temperature for 24h. Then the solution containing is freeze dried to give **8b**. NMR shows that there are no CD threaded on the chain after dialysis (see appendix).

Yield: 98 mg, (94 %)

¹H-NMR (300MHz, DMSO-D₆): 7.8 (2H, -NHCO amide); 6.4 (4H, urea biotin); 4.3 (2H, CH (CH-CH-NH) biotin); 4.1 (2H, CH (CH₂-CH-NH) biotin); 3.5 (nH, -OCH₂CH₂- PEG); 2.5 ppm (residual H₂O); 2.1 ppm (2H, -CH₂-CONH- biotin); 1.62 - 1.31 ppm (12H, biotin)

Synthesis of a polyrotaxane **11**

10 μ mol (1eq) α,ω -diamino PEG is dissolved in 3.4 ml millipore water and 200 μ mol (20eq) CD is added to the clear solution. Then it is left stirring at 70°C for 30 min (α -CD) or 2h (α -CDN₃) to become transparent. 100 μ mol (10eq) DMPEPHSO₃⁻ **3** is added and it is left stirring at 70°C over night. The reaction mixture is taken up in 15 ml of millipore water and dialysed 4 times with 1.6l of millipore water for 24h at 50°C. Then the solution is freeze dried to give **11**.

Yield: 60 - 95 % (depending on MW of PEG used)

¹H-NMR (300MHz, DMSO-D₆): 6.96 - 6.74 ppm (6H, aromatic H's DMPE); 5.86 ppm (4H, H-urea); 5.6 ppm - 5.4 ppm (12H, OH-2 and OH-3 CD); 4.8 ppm (6H, H-1 CD); 4.5 ppm (6H, OH-6 CD); 3.1-3.9 (m, nH, -OCH₂CH₂- PEG and H-2, H-5, CH₂-6 CD); 2.5 ppm (residual H₂O)

Synthesis of a polyrotaxane **12**

10 μ mol (1eq) α,ω -diamino PEG is dissolved in 3.4 ml millipore water and 200 μ mol (20eq) CD are added to the clear solution. It is left stirring at 70°C for 30 min (α -CD) or 2h (α -CDN₃) to become transparent. At first 53 mg (40 μ mol, 4eq) adamantane/ β -CD complex and subsequently 12 mg (40 μ mol, 4eq) DMT-MM are added to the transparent solution, which is left stirring at 70°C during the night. The solution is turbid the next day. Then the mixture is diluted with 15 ml of millipore water and dialysed 4 times with 1.5l of millipore water at 50°C. Finally the transparent solution is freeze dried to give **12**.

Yield: 20 - 50 % (depending on MW of PEG used)

¹H-NMR (300MHz, CDCl₃) adamantane stopper: 7.35 ppm (2H, NHCO- stopper); 5.6

ppm - 5.4 ppm (12H, OH-2 and OH-3 CD); 4.8 ppm (6H, H-1 CD); 4.45 ppm (6H, OH-6 CD); 3.1-3.9 (nH, -OCH₂CH₂- PEG and H-2, H-5, CH₂-6 CD); 2.5 ppm (residual H₂O); 1.9 ppm (6H, CH adamantane); 1.7 (24H, CH₂ adamantane)

Synthesis of cholesteryl succinic acid propargylamide **14**

2.5 g (5.1 mmol, 1.1 eq) of cholesterol-hemisuccinate, 1.81 g (5.6 mmol, 1.3 eq) of p-toluenesulfonic anhydride and 1.26 g (10 mmol, 2.2 eq) of DMAP are dissolved in 25 ml of CHCl₃ and after 15 min 0.26 g (4.6 mmol, 1 eq) propargylamine are added. After 1.5h the mixture is quenched with 3 ml of sat. NaHCO₃ solution. The solution is extracted with ethyl acetate and the combined organic layers are washed two times with 50 ml of sat. NaHCO₃, two times with 50 ml of brine and the organic layer is dried over anhydrous Na₂SO₄. The crude product is purified by recrystallisation in ethyl acetate and freeze dried from cyclohexane to give **14**.

Yield: 1.25 g (55 %)

¹H-NMR (300MHz, CDCl₃): 6.2 ppm (1H, -NHCO-); 5.35 ppm (1H, H-6 Cholesterol); 4.6 ppm (1H, H-3 Cholesterol); 4.0 ppm (2H, -CH₂ propargyl); 2.2 ppm (1H, H-alkyne); 0.65 ppm (9H, -CH₃ cholesterol)

Synthesis of a cholesteryl α -CD **15**

100 mg (50 μ mol, 1eq) azido α -CD and 29 mg (60 μ mol, 1.2eq) cholesteryl succinic acid propargylamide are dissolved in 1.5 ml of ultrapure DMF and 160 μ l of a CuI/PMDETA 1:1 solution ($c = 57$ mmol/l in DMF) are added under argon atmosphere. The solution is stirred at 65°C for 24h. The solvent is evaporated and the compound is suspended in 4 ml of phosphate buffer solution (20 mM, pH = 6.5). Then the compound is centrifuged in 3ml of millipore water, as well as 3 times in 2ml of acetone. Finally the compound is taken up in 10 ml of millipore water and freeze dried to give **15**.

Yield: 35 mg (35 %)

¹H-NMR (300MHz, DMSO-D₆): 8.30 (1H, -NHCO-); 7.8 ppm (1H, H-triazol); 5.6 ppm - 5.4 ppm (12H, OH-2 and OH-3 CD); 5.0 ppm (1H, H-1 modified glucose unit CD); 4.8 ppm (5H, H-1 CD); 4.4 ppm (6H, OH-6 CD); 3.2-3.7 (H-2 and H-5, CH₂-6 CD); 2.5 ppm (residual H₂O); 2 - 0.8 ppm (H's of cholesteryl moiety); 0.65 ppm (9H, -CH₃ cholesterol)

Synthesis of a cholesteryl β -CD **16**

Prior to the experiment solutions of CuSO₄ ($c = 0.13$ mol/l) and a THBTA ($c = 63$ mmol/l) are prepared with millipore water. 47 mg (40 μ mol, 1eq) β -CDN₃ and 28 mg (56 μ mol, 1.4eq) cholesteryl succinic acid propargylamide **14** are dissolved in 16 ml of tert-butanol and sonicated for 10 min. Then 228 μ l (13 mg, 30 μ mol, 0.75eq) of the ligand solution and 72 μ l (0.77 mg, 5 μ mol, 0.1eq) of the CuSO₄ solution are mixed in 3.7 ml of water are added to the mixture to give a slightly turbid suspension. 40 mg (200 μ mol, 5eq) of Na-ascorbate are put into the solution and the mixture is stirred for 1h at room temperature. Then the compound is centrifuged 3 times in 10 ml of buffer/EDTA

solution (2 mg EDTA in phosphate buffer pH = 6.5) and three times in 3 ml of acetone. The compound is taken up in 5 ml of millipore water and freeze dried to give **16**.

Yield: 62 mg (90 %)

¹H-NMR (300MHz, DMSO-D6): 8.30, 8.27 ppm (s, 1H, -NHCO-); 7.83, 7.66 ppm (s, 1H, H-triazol); 5.6 ppm - 5.4 ppm (14H, OH-2 and OH-3 CD); 5.0 ppm (1H, H-1 modified glucose unit CD); 4.8 ppm (6H, H-1 CD); 4.4 ppm (7H, OH-6 CD); 3.2-3.7 (H-2 and H-5, CH₂-6 CD); 2.5 ppm (residual H₂O), 2 - 0.8 ppm (H's of cholesteryl moiety); 0.65 ppm (9H, -CH₃ cholesterol)

Synthesis of the STL 17

Prior to the experiment solutions of CuSO₄ (*c* = 0.13 mol/l) and a THBTA (*c* = 63 mmol/l) are prepared with millipore water. The polyrotaxane (3 μmol) and the cholesteryl succinic acid propargylamide (6 μmol, 2eq (per azide)) are dissolved in a mixture of 1.5 ml tBuOH/millipore water 8:2, sonicated for 5 min and heated for several minutes to provide for complete solubilisation of the compounds. Then the ligand solution (1 μmol, 0.3 eq) and the CuSO₄ solution (0.2 μmol, 0.06 eq) are added to the mixture to give a transparent solution. Na-ascorbate (2.5 μmol, 0.8 eq) is added and the solution is left stirring over night at room temperature. The transparent solution is diluted with 5 ml of millipore water and dialysed (cut-off 2 kg/mol) twice with 2l of millipore water for 24h and freeze dried. The crude product is taken up in 5 ml of ether and centrifuged 3 times to eliminate the residual cholesteryl alkyne. The residue is dissolved in 10 ml of tBuOH/H₂O 8:2 and freeze dried to give **17**.

Yield: 50-95 % (depending on MW of polyrotaxane and used stopper)

¹H-NMR (300MHz, CDCl₃) DMPE stopper: 8.3 ppm (s, 1H, -NHCO-); 7.8 ppm (s, 1H, H-triazol); 6.96 - 6.74 ppm (6H, aromatic H's DMPE); 5.86 ppm (4H, H-urea); 5.6 ppm - 5.4 ppm (12H, OH-2 and OH-3 CD); 5.3 ppm (1H, CH sp₂ cholesterol); 5.0 ppm (1H, H-1 modified glucose unit CD); 4.8 ppm (5H, H-1 CD); 4.5 ppm (6H, OH-6 CD); 3.1-3.9 (nH, -OCH₂CH₂- PEG and H-2, H-5, CH₂-6 CD); 2 - 0.8 ppm (H cholesteryl moiety); 0.65 ppm (9H, -CH₃ cholesterol)

¹H-NMR (300MHz, CDCl₃) adamantane stopper: 8.3 ppm (1H, NHCO- succinyl); 7.8 ppm (1H, H-triazol)(1H, NHCO- succinyl); 7.8 ppm (2H, NHCO- stopper); 5.6 ppm - 5.4 ppm (12H, OH-2 and OH-3 CD); 5.3 ppm (1H, CH sp₂ cholesterol); 5.0 ppm (1H, H-1 modified glucose unit CD); 4.8 ppm (5H, H-1 CD); 4.5 ppm (6H, OH-6 CD); 3.1-3.9 (nH, -OCH₂CH₂- PEG and H-2, H-5, CH₂-6 CD); 2.5 ppm (residual H₂O); 1.9 ppm (6H, CH adamantane), 1.7 (24H, CH₂ adamantane); 1.8 - 0.8 ppm (H cholesteryl moiety); 0.65 ppm (9H, -CH₃ cholesterol)

5.7 Appendix

Polyrotaxane Characterisation

NMR

Figure 5.25 shows the HMQC spectrum for a polyrotaxanes with native α -CD. As described in section 5.3.3 it clearly evidences the shift of the C-5 signal together with the H-5 proton for threaded CDs. The inner cavity proton H-3, usually shifted in complexes, is nearly not affected.

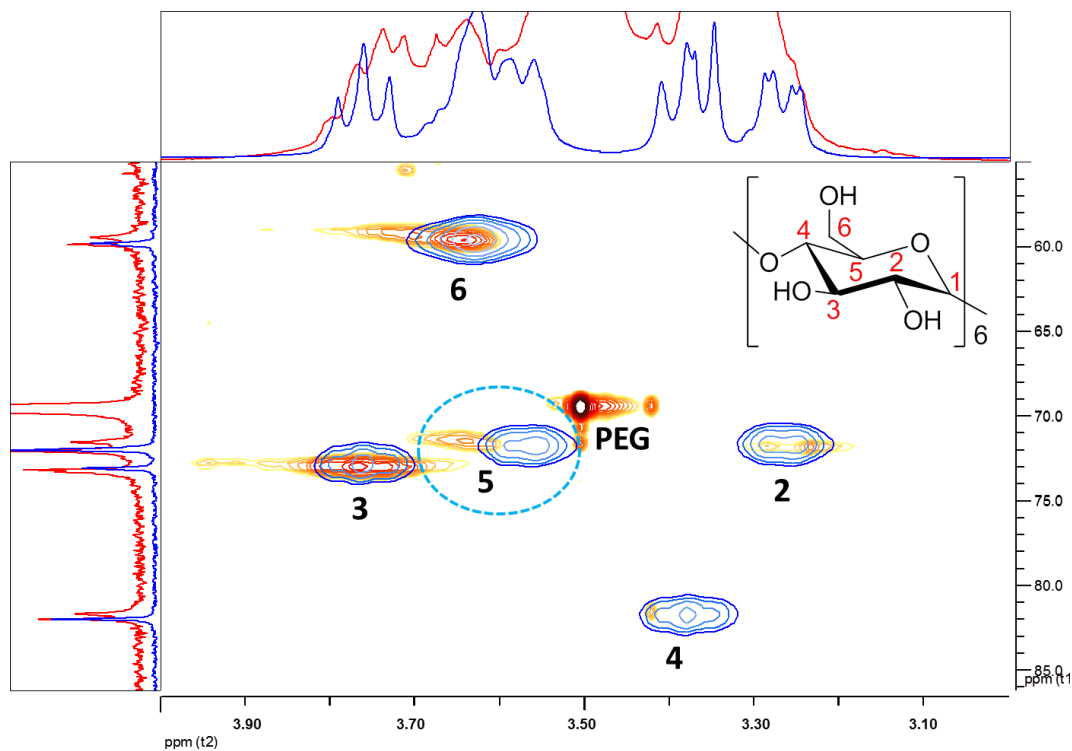


Figure 5.25: Superposition of HMQC spectra for a polyrotaxane with α -CD (red) and uncomplexed α -CD (blue). The numbers indicate the corresponding carbons and protons in the glucose units.

Superposed COSY spectra for a polyrotaxane with azido α -CD (red) and uncomplexed azido α -CD (blue) are shown in Figure 5.26. As observed for polyrotaxanes with native CDs, the H-1 protons remain unaffected upon complexation. There is a small shift of the OH-3 signal and a more pronounced shift for the OH-2 proton because it is closer to the CD axis than the OH-3 protons. The proximity to the axis also affects the primary OH-6 and H-6, H-6' protons, which are displaced.

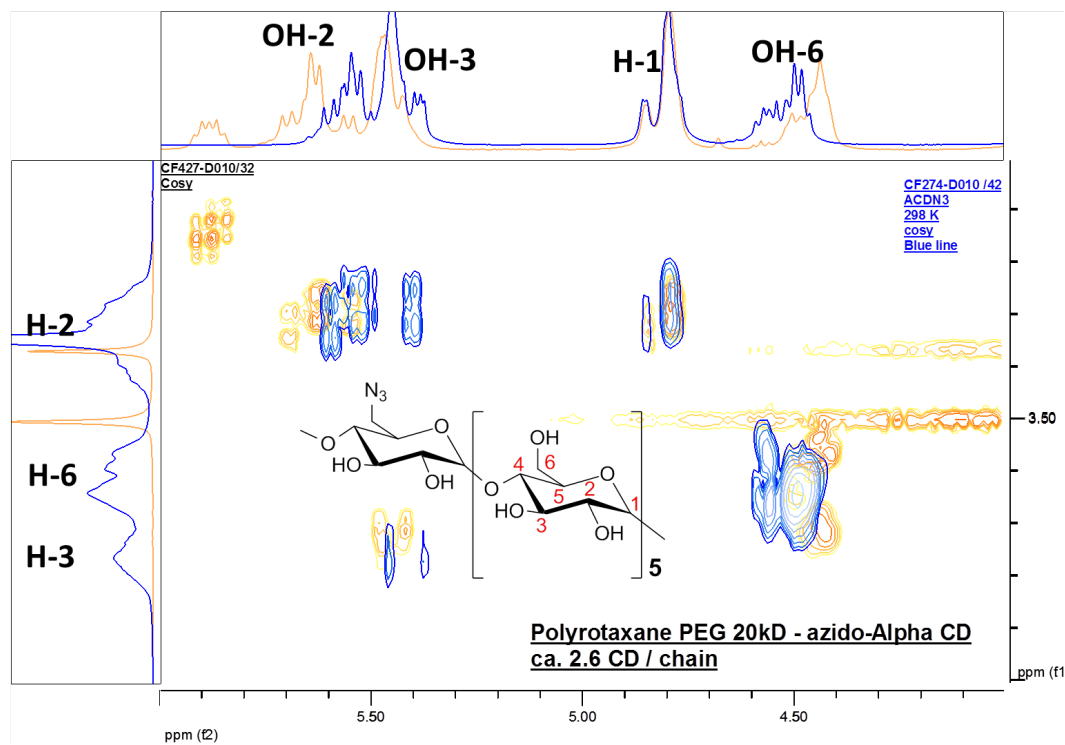


Figure 5.26: Superposition of COSY spectra for a polyrotaxane with azido α -CD (red) and uncomplexed azido α -CD (blue). The numbers indicate the corresponding carbons and protons in the glucose units.

NMR analysis of synthesised compounds

Selected NMR spectra used to characterise the products described in the experimental section (section 5.6.2) are presented in the following paragraphs.

DMPEPhSO₃⁻ **3**

Figure 5.27 shows a typical NMR spectrum for stock DMPEPhSO₃⁻. The peak assignment is illustrated by an overlay of spectra of the starting materials, the side product and DMPEPSO₃⁻ (Figure 5.28). The formation of DMPEPhSO₃⁻ is evidenced by the typical N-H peak of the blocked isocyanate (7.8 ppm) and two aromatic protons of the sulfonate residue (7.6 ppm). Moreover we still find peaks corresponding to non-reacted phenolsulfonate (OH-, 9.5 ppm and aromatic-H, 7.4 ppm) and residual symmetric urea side product (NH-CO-NH, 5.8 ppm). From the peak integrations (Figure 5.27) we have 49 % DMPEPSO₃⁻, 49 % of phenolsulfonate and traces (2%) of symmetric urea side product in final product.

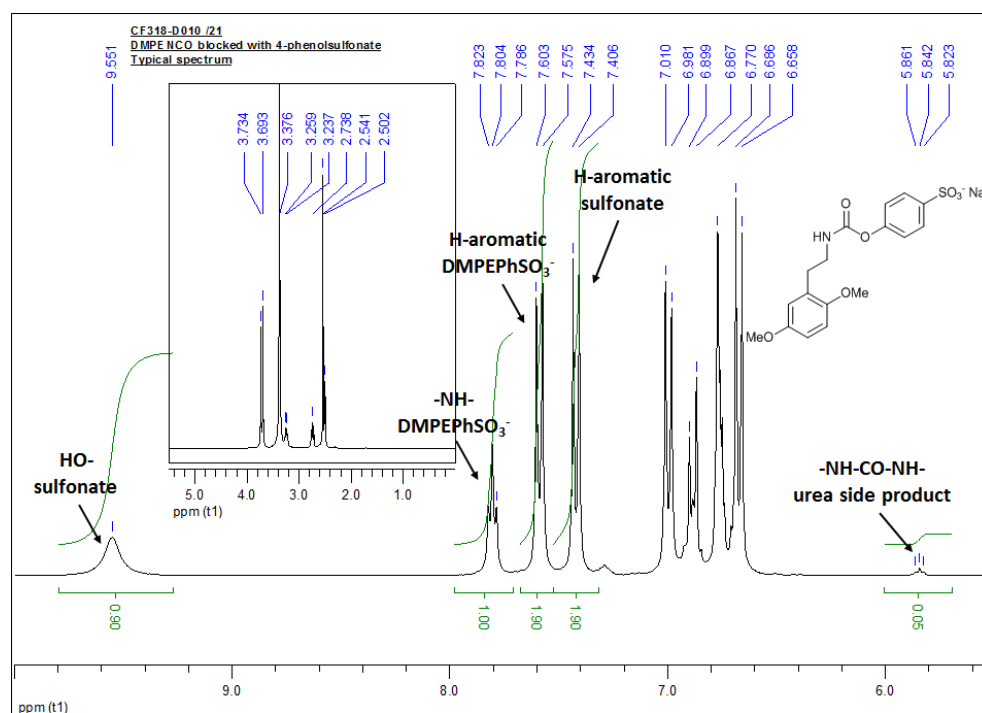


Figure 5.27: Typical ¹H-NMR spectrum obtained for stock DMPEPhSO₃⁻.

The symmetric urea side product appears slowly depending on the age of the DMPEPhSO₃⁻ stock. However it decomposes more rapidly in the NMR tube. The spectrum taken directly after filtration of an aged DMPEPSO₃⁻ solution (Figure 5.27 D) shows no urea and evidences a mixture of DMPEPSO₃⁻ and decomposed DMPEPSO₃⁻.

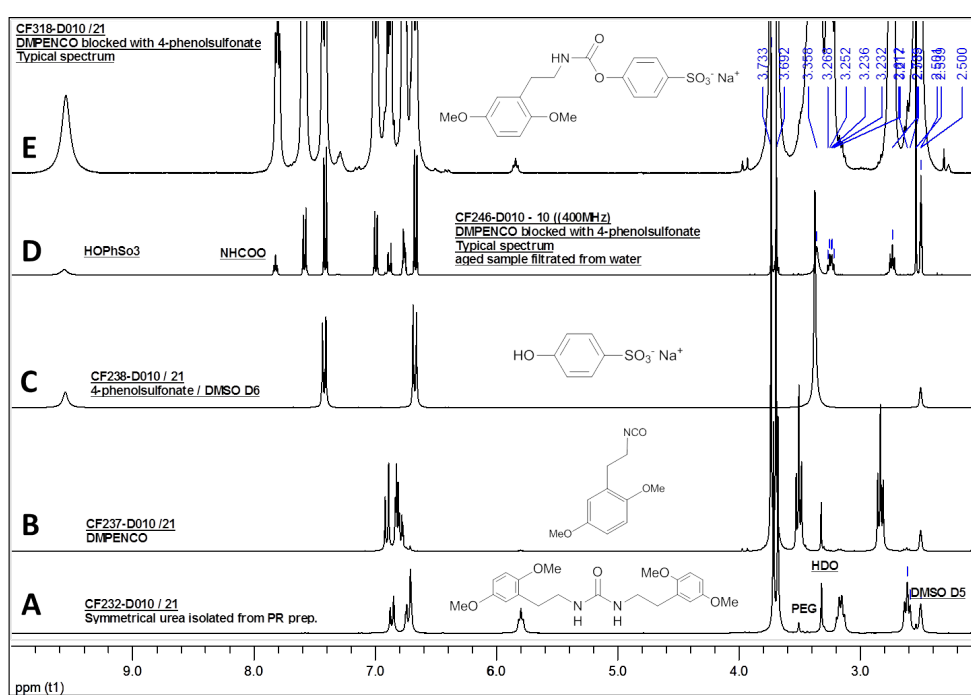


Figure 5.28: Overlaid $^1\text{H-NMR}$ spectra for starting compounds and side products for DMPEPhSO_3^- synthesis from bottom to top A. symmetrical urea biproduct, B. DMPENCO, C. 4-phenolsulfonate, D. and aged DMPEPhSO_3^- freshly filtrated sample and E. DMPEPhSO_3^- after filtration.

PEG end-capped with DMPEPhSO₃⁻ 5

The endcapping is clearly evidenced by the formation of the urea bonds (5.85 ppm) between the DMPE stopper (aromatic protons, 6.95 - 6.75 ppm) and the di-amino PEG (3.5 ppm).

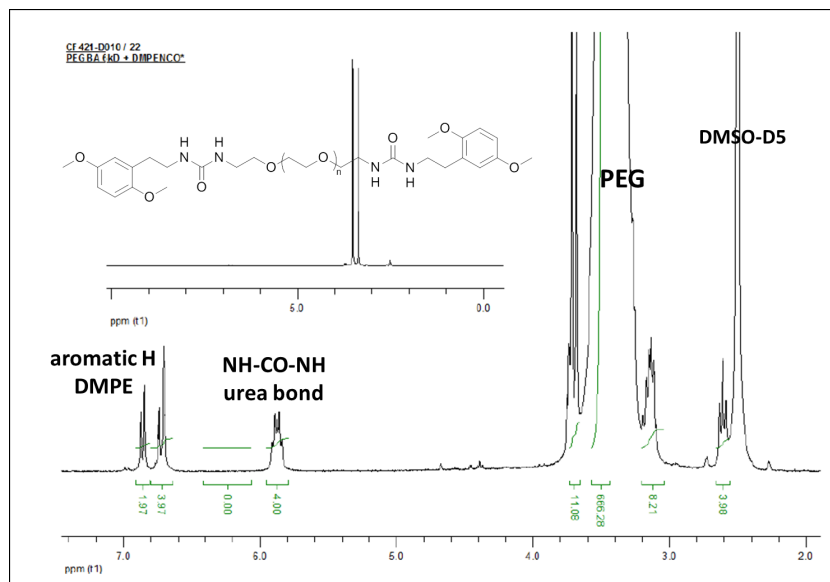


Figure 5.29: ¹H-NMR spectrum for endcapped PEG with DMPEPhSO₃⁻ stopper.

Complex β-CD/adamantane carboxylic acid 6a

The complex formation is evidenced by the appearance of typical signals of β-CD and adamantane carboxylic acid (Figure 5.30). Comparison of the peak integration of the C-H signal for adamantane (1.95 ppm) and the CD's H-1 (5.85 ppm) shows, that a 1:1 complex is formed.

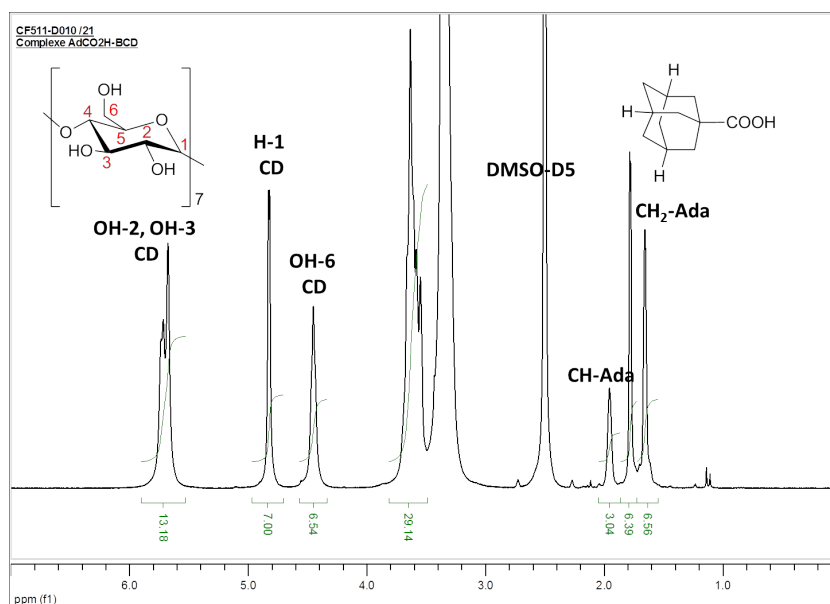


Figure 5.30: ¹H-NMR spectrum for complex β-CD/adamantane carboxylic acid.

Complex β -CD/biotin 6b

The complex formation is evidenced by the appearance of typical signals of β -CD and biotin (Figure 5.31). Comparison of the peak integration for e.g. C-H-S signal for biotin (2.8 ppm) and CD's H-1 (5.85 ppm) shows that we have CD/biotin ratio 1:1.4. So it is very likely that we have obtained a mixture of 1:1 and 1:2 complexes β -CD/biotin.

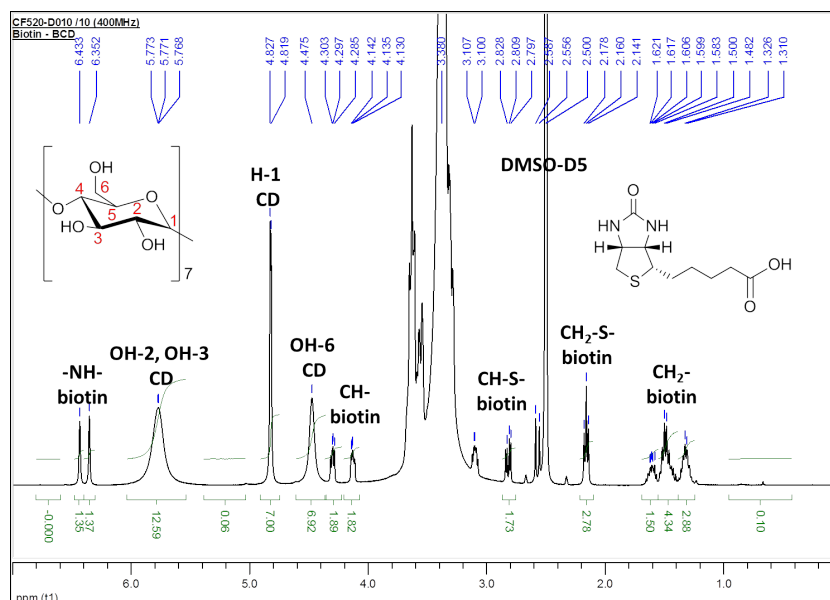


Figure 5.31: $^1\text{H-NMR}$ spectrum for complex β -CD/biotin.

PEG end-capped with adamantane 8a

The endcapping is clearly evidenced by the formation of the amide bonds (7.35 ppm) between the Adamantane stopper (1.95 - 1.65 ppm) and the di-amino PEG (3.5 ppm). Furthermore we find remaining traces of β -CD (H-1, 4.85 ppm) used to solubilise the adamantane.

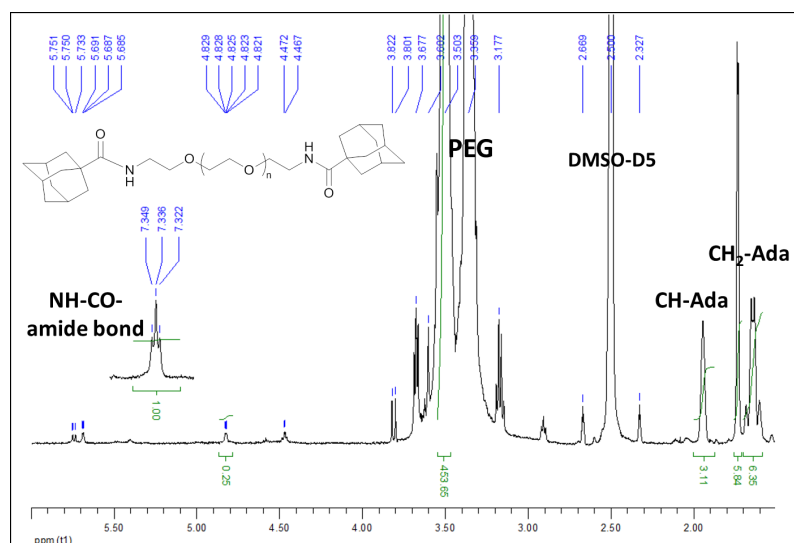


Figure 5.32: $^1\text{H-NMR}$ spectrum for endcapped PEG with an Adamantane stopper.

Attempt to produce polyrotaxanes with a biotin cap

Figure 5.33 shows the spectrum for the attempt to produce polyrotaxanes with a biotin stopper. The capping is clearly evidenced by the formation of the amide bonds (7.35 ppm) between the biotin stopper and the di-amino PEG. The characteristic peaks for the PEG and biotin are both indicated in the spectrum. However there are no signals of CD, which shows that dethreading has occurred during the dialysis.

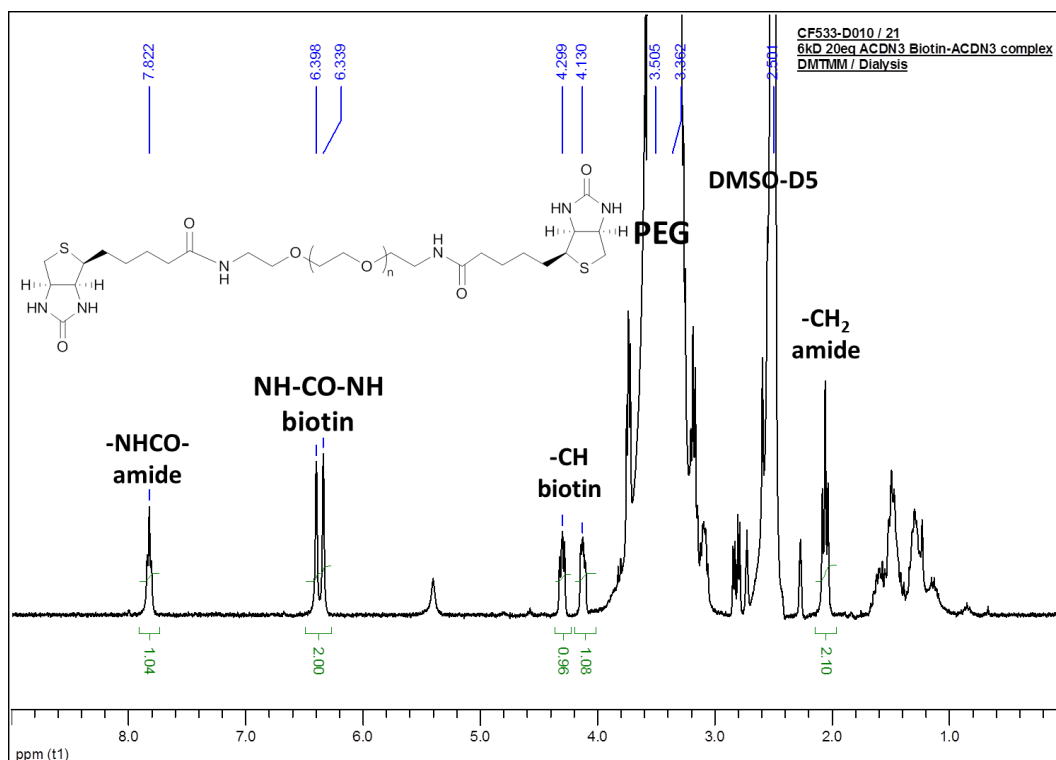


Figure 5.33: ¹H-NMR spectrum for PEG, encapped with biotin stopper.

Polyrotaxanes endcapped with DMPEPhSO_3^- 11

Figure 5.34 displays a typical spectrum for a polyrotaxane with native α -CD endcapped with DMPEPhSO_3^- . As described in section 5.3.3 we find the signals we use to prove complexation (urea bond, aromatic H and CD protons) and to determine the number of CDs. However they are very weak compared to the signals of the PEG (3.5 ppm) and residual water (3.35 ppm).

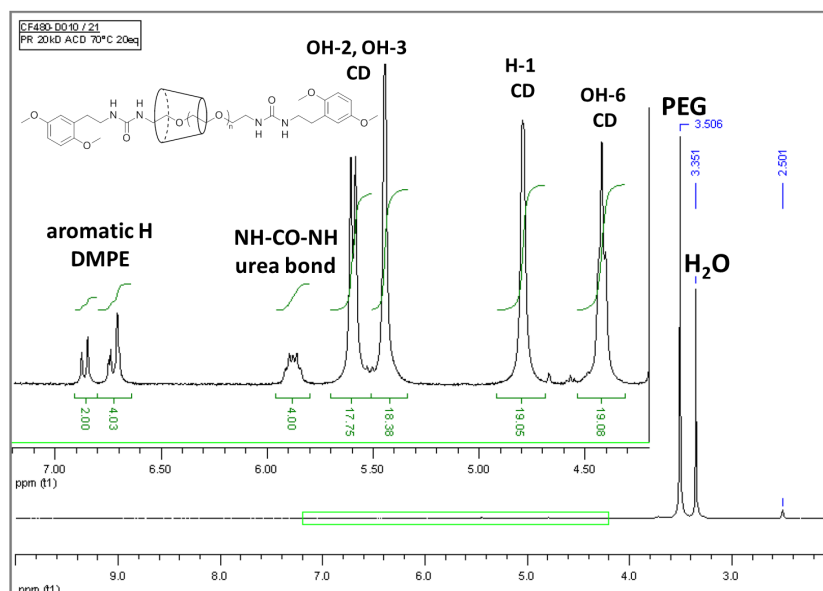


Figure 5.34: $^1\text{H-NMR}$ spectrum for polyrotaxane 20k with native α -CD ($N_{\text{CD}} = 3.1$) endcapped with the DMPEPhSO_3^- stopper.

Figure 5.35 displays a typical spectrum for a polyrotaxane with azido α -CD.

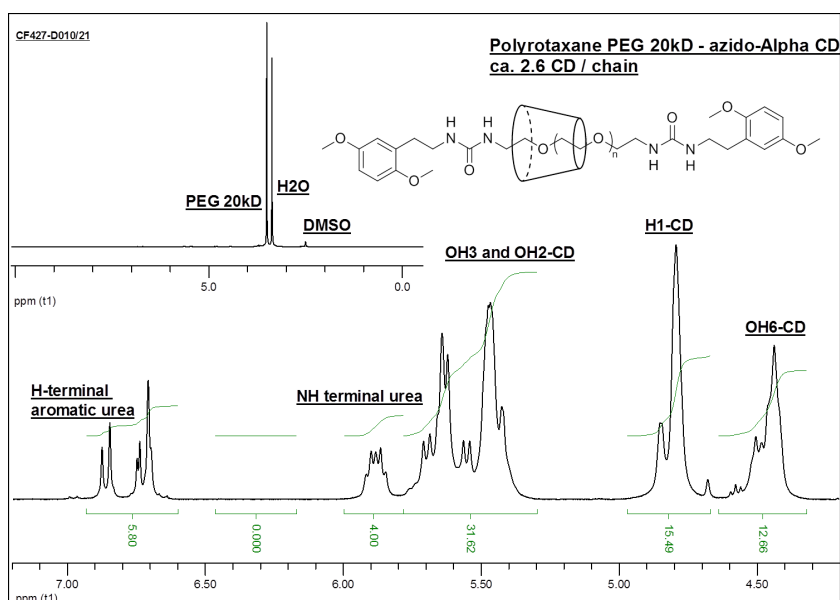


Figure 5.35: $^1\text{H-NMR}$ spectrum for polyrotaxane 20k with azido α -CD ($N_{\text{CD}} = 2.6$) endcapped with the DMPEPhSO_3^- stopper.

Polyrotaxane endcapped with adamantane 12

Figure 5.36 displays a typical spectrum for a polyrotaxane with azido α -CD endcapped with adamantane. Characteristic protons of the amide bond (7.3 ppm), of PEG (3.5 ppm), threaded CDs (5.6 - 4.4 ppm) and the adamantane stopper (1.8 - 1.6 ppm) clearly evidence the polyrotaxane.

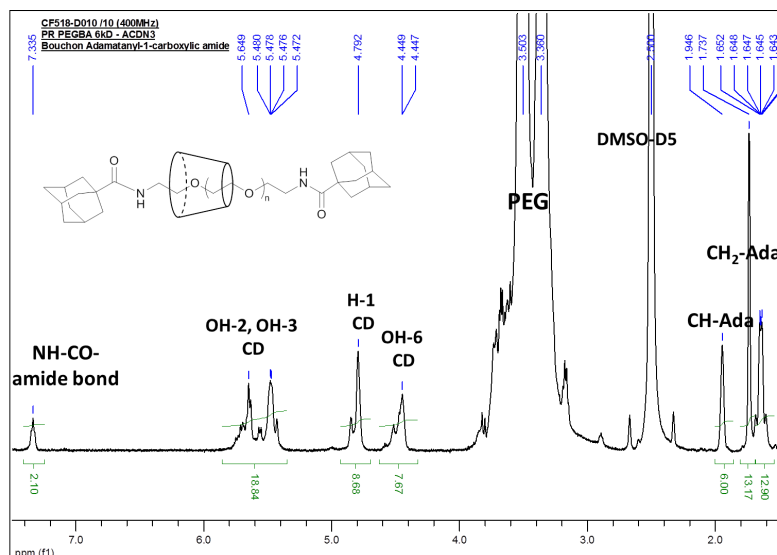


Figure 5.36: $^1\text{H-NMR}$ spectrum for polyrotaxane 6k with azido α -CD ($N_{CD} = 1.4$) endcapped with the adamantane stopper.

Cholesteryl succinic acid propargylamide 14

Figure 5.37 shows a spectrum of cholesteryl succinic acid propargylamide which has been recorded in CDCl_3 . The successful coupling of the propargylamine is evidenced by the formation of the amide (6.2 ppm) and the presence of the characteristic peaks of the alkyne, as well as of cholesteryl hemisuccinate.

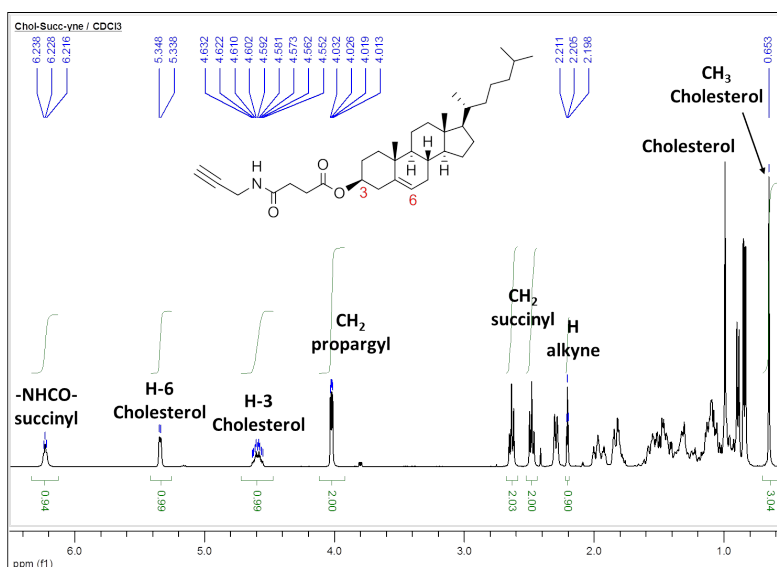


Figure 5.37: $^1\text{H-NMR}$ spectrum of cholesteryl succinic acid propargylamide.

Cholesteryl α -CD 15

Figure 5.38 shows a spectrum of cholesteryl α -CD. The successful coupling of the cholesteryl anchor is evidenced by the triazol signal (8.3 ppm) and the amide bond of the succinyl linker (7.8 ppm). Integration of these two peaks is consistent with a clean product, as no more terminal alkyne (3 ppm) appears in the spectrum. Characteristic CD protons (5.6 - 4.4 ppm) and of the cholesteryl residue are labeled in the spectrum (1.5 - 0.5 ppm).

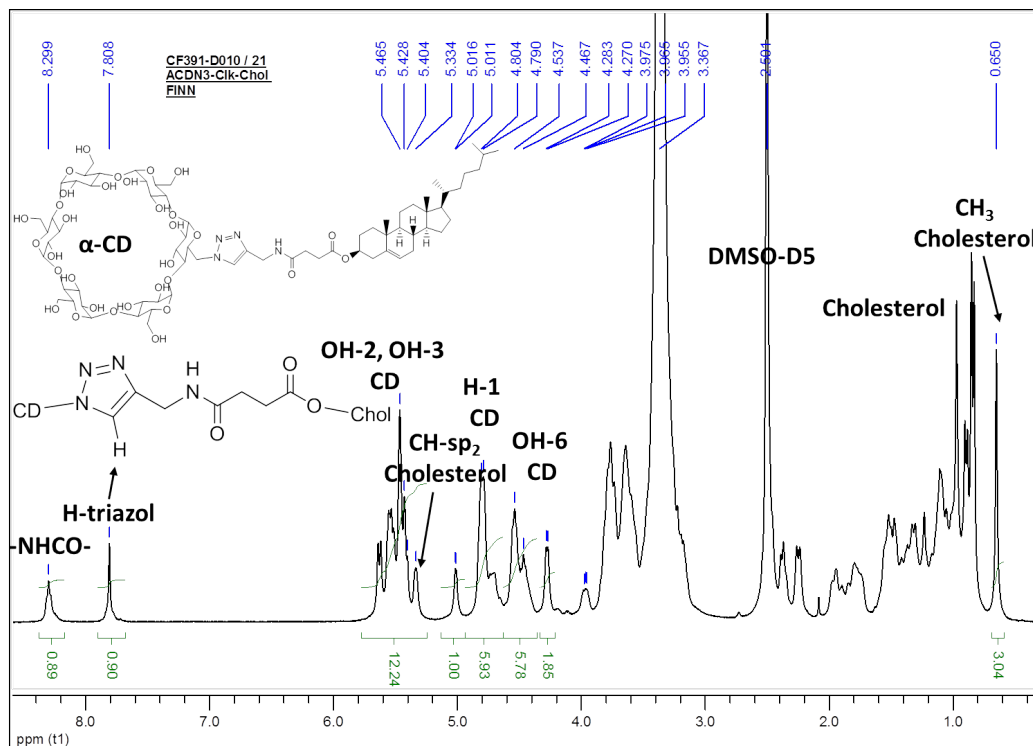


Figure 5.38: $^1\text{H-NMR}$ spectrum of cholesteryl α -CD.

Cholesteryl β -CD 16

Figure 5.39 (top) shows a spectrum of cholesteryl β -CD. Similar to the cholesteryl α -CD derivative, the characteristic protons for triazol, succinyl, cholesterol and CD moieties are indicated in the spectrum. However a peak split of the triazol signal (8.3 ppm) and the amide bond of the succinyl linker (7.8 ppm) occurs, when the spectra are recorded in DMSO-D6. Integration of the peaks amounts to 1. This might be due to a solvent effect favoring particular configurations. It has also been observed for the permethylated β -CD analog. This compound is soluble in both DMSO and Chloroform. As shown in Figure 5.39 (bottom), one peak is observed in CDCl_3 while two exist in DMSO-D6. This phenomenon has not been seen with α -CD (see Figure 5.38). Further NMR experiments should be necessary to identify suspected CD inclusion or capping phenomena. Another explanation might be that we have a mixture of the two regioisomers 1,2 and 1,4 triazol, although the CuAAC should selectively yield the latter isomer.

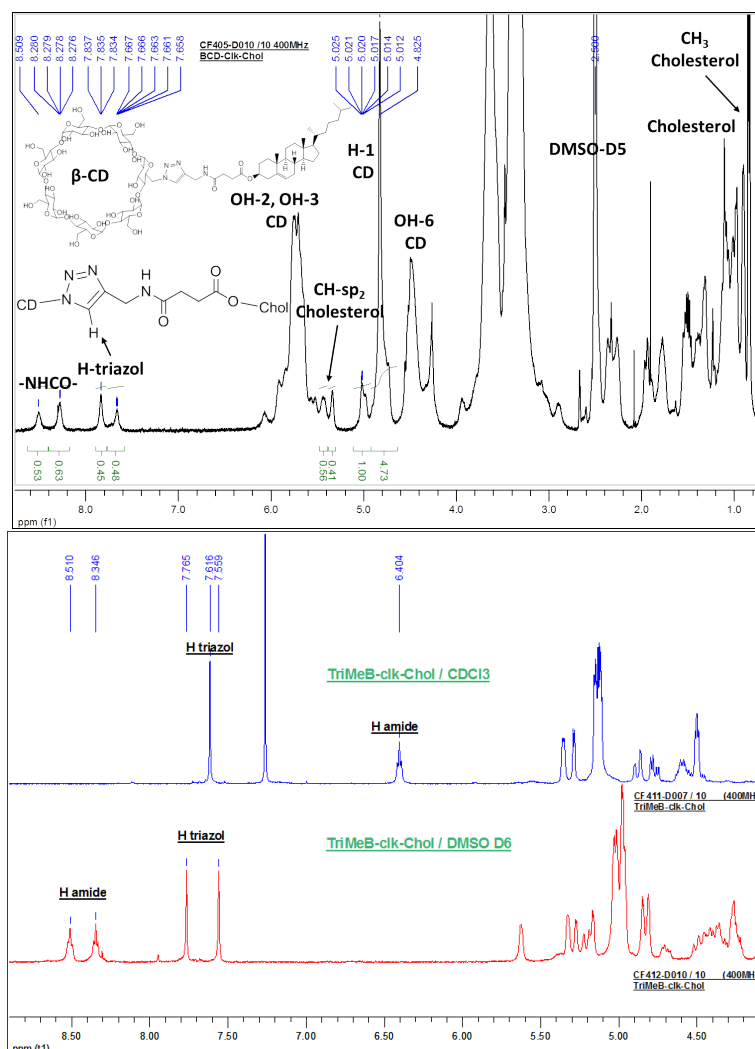


Figure 5.39: top: $^1\text{H-NMR}$ spectrum of cholesteryl β -CD. bottom: $^1\text{H-NMR}$ spectrum of the permethylated cholesteryl β -CD analog in DMSO-D6 and CDCl_3 .

Synthesis of the STL 17

Figure 5.41 shows a spectrum of STL-10k (1.5 CD/chain) endcapped with DMPE. Characteristic protons for PEG, CD, cholesterol and the DMPE stopper are indicated in the spectrum. Figure 5.41 also displays the corresponding HMQC experiment. Even after 48h acquisition time the ^{13}C signals remain weak but nevertheless provide valuable structural information. It is remarkable that the H-1 proton of the modified glucose unit is now clearly distinguishable from the H-1 protons of the unmodified units. The successful coupling of the cholesteryl anchor is evidenced by the triazol signal (8.3 ppm) and the amide bond of the succinyl linker (7.8 ppm). The comparison of the integration of these two peaks with the H-1 (of the modified glucose unit) demonstrates that the reaction is quantitative.

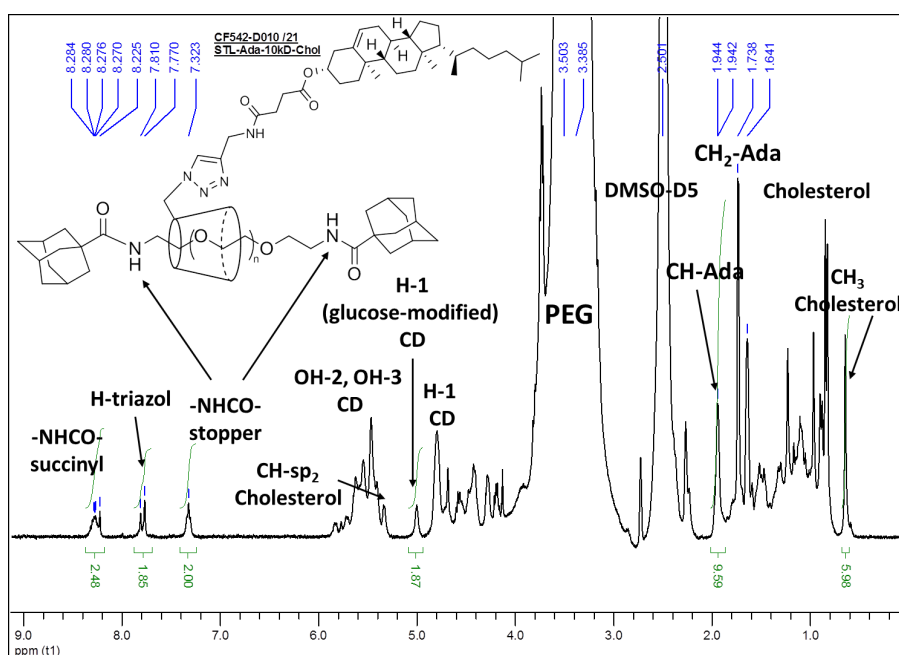


Figure 5.40: ^1H -NMR spectrum of STL-10k (1.5 CD/chain) endcapped with Adamantane.

Figure 5.40 shows a spectrum of STL-10k (1.6 CD/chain) endcapped with adamantane. Characteristic protons for PEG, CD, cholesterol and the stopper are indicated in the spectrum. As described for the STL-DMPE the H-1 proton of the modified glucose unit is again clearly shifted and peak integration of selected peaks show that the reaction is quantitative.

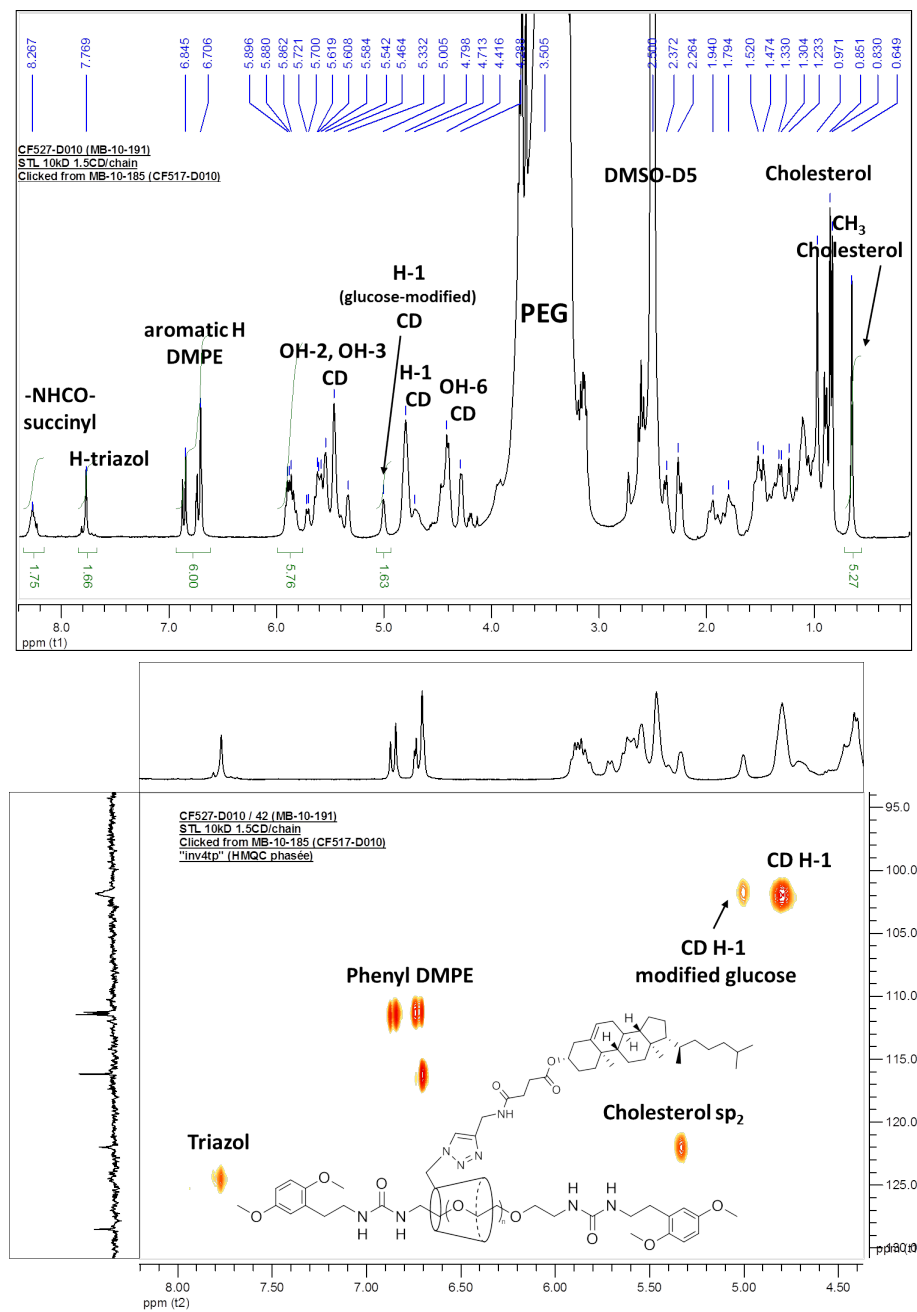


Figure 5.41: ¹H-NMR spectrum of STL-10k (1.5 CD/chain) endcapped with DMPE and below the corresponding HMQC experiment.

Size exclusion chromatography

Figure 5.42 shows size exclusion chromatography (SEC) chromatograms for polyrotaxanes (A. polyrotaxane 6k with 1.6 CD/chain) and B. polyrotaxane 20k with 3.6 CD/chain) and their corresponding uncomplexed polymers endcapped with DMPE. In both cases the uncomplexed compound and the polyrotaxane cannot be distinguished using standard phenogel columns (MW range: 1 kDa - 75 kDa) and a phosphate buffer eluent (pH 7). The peaks have been detected with an UV detector at 230 nm.

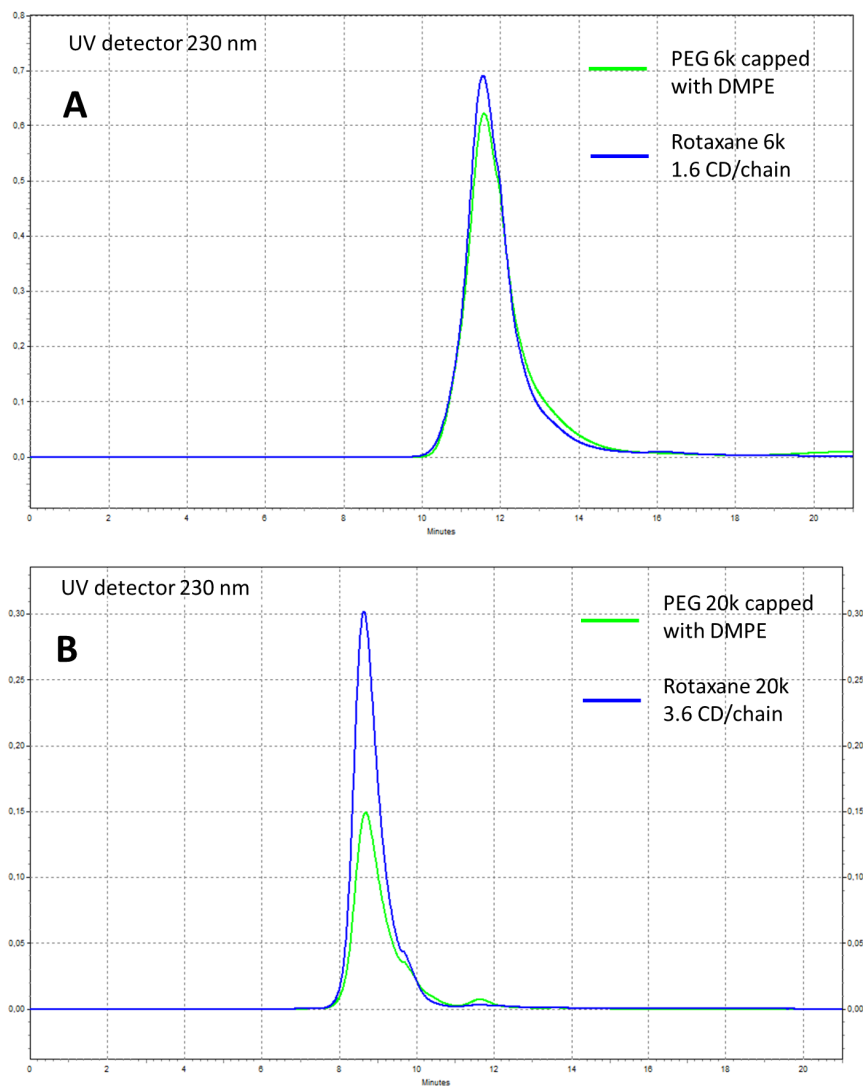


Figure 5.42: SEC chromatograms for polyrotaxanes and their corresponding uncomplexed polymers endcapped with DMPE: A. 6k (1.6 CD/chain) and B. 20k (3.6 CD/chain).

Chapter 6

Sliding tethered ligands: Insertion in model membranes and interactions

So far tethered ligand interactions have been studied on systems where one polymer end is fixed to a grafting point at the surface [17, 58]. The newly synthesised STLs are a new class of molecular units with a sliding ring, which can be grafted to lipid membranes with its lipophilic cholesteryl anchor to form a new kind of topological grafts. Such a system should allow the polymer chain to adapt its conformation to external conditions [19]. This design together with the ligand at the end of the polymer should translate into a new type of tethered ligand-receptor interactions due to an unprecedented adaptability of the spacer length. Therefore in this chapter we investigate the membrane insertion properties of the STLs, as well as the conformational behavior of the polymer chains. Furthermore we characterise the ligand-receptor interactions between membranes modified with adamantane-encapped STLs and membranes modified with β -CD as receptor.

6.1 Interfacial properties

The compounds utilised in this chapter are listed in Table 6.1. STLs end-capped with the dimethoxyphenyl-ethyl (DMPE) stopper are used for studying the interfacial properties. STLs encapped with adamantane are used for the characterisation with of the ligand receptor interactions.

compound	N_{CD}	MW(polymer) [kg/mol]	stopper
STL-3k	1.22	3	DMPE
STL-6k	1.47	6	DMPE
STL-10k	1.48	10	DMPE
STL-10k-Ada	1.76	10	Adamantane
STL-20k	1.40	20	DMPE
STL[2.6]-20k	2.60	20	DMPE
PEG-6k	-	6	DMPE

Table 6.1: Composition of STLs used for characterisation experiments and their abbreviation in the text. DMPE is the abbreviation for the dimethoxyphenyl-ethyl stopper.

It should be mentioned that the number of CD/chain is an average value for each compound. The separation of polyrotaxanes into fractions with a defined number of CDs (section 5.3.3) so far yields too little material to synthesise sufficient quantities of STLs. Therefore studied STLs always contain a fraction of 10 - 20% endcapped polymer without cholesteryl α -CD anchor.

Characteristic length scales of the polymer chains of the STLs with different MW are given in Table 6.2.

PEG	N	L [nm]	R_F [nm]
3k	67	23.4	4.36
6k	133	46.6	6.58
10k	222	77.7	8.95
20k	444	155.4	13.55

Table 6.2: Properties of the studied STL PEG chains. The number of monomers (N) is used with the average length per monomer ($a = 3.5 \text{ \AA}$ [271]) to estimate the contour length ($L = aN$) and Flory radius ($R_F = aN^{3/5}$)

6.1.1 Langmuir Isotherms

The compression ratio of our Langmuir trough (9:1) is not sufficient to record the isotherms for samples with STL molar ratios $> 10\%$ in one run for the whole surface area range. Depending on the composition and MW of the STL, two or three isotherms have been measured for different surface concentrations and joined together to obtain the full isotherm. Especially for high STL ratios and high MW the isotherms for lower surface concentrations have to be shifted with respect to the surface area in order to be connected. We have decided to displace all data with respect to the isotherm recorded with the highest surface concentration, which gives results consistent with literature [272,273]. An example is given in Figure 6.1, which displays the three isotherms joined together to obtain the full isotherm for pure STL-6k. The corresponding shifts are indicated with arrows.

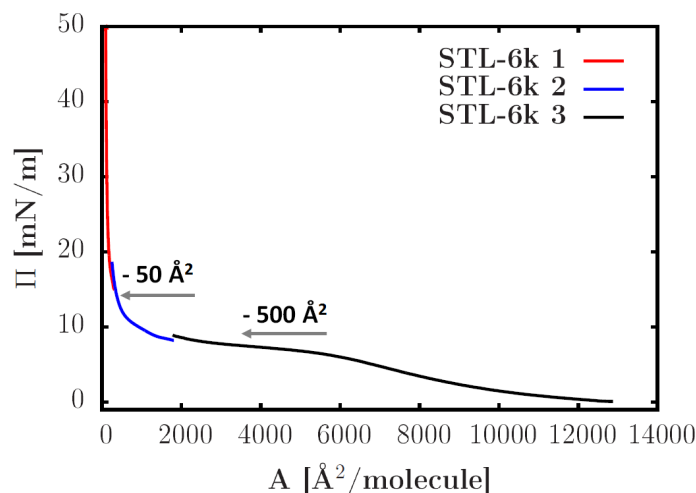


Figure 6.1: Exemplary Langmuir isotherm which is joined together from three different isotherms with different spreading volumes. The required shifts are indicated by the arrows.

A possible explanation for the discrepancies are the substantial amounts of unthreaded PEG, expected in the STL samples. These compounds are continuously lost from the

surface during compression. The loss of material results in an overestimation of the surface area, because the surface area is calculated with the number of molecules initially spread on the surface. This effect increases with the STL ratio in the monolayer.

Pure STLs

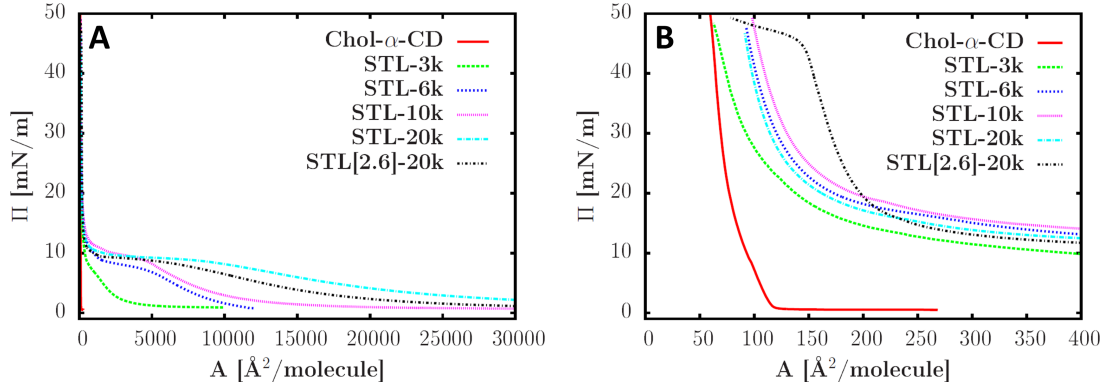


Figure 6.2: A. Langmuir isotherms at 20°C for several STLs compared to the Cholesteryl α -CD anchor without polymer, B. zoom in surface area region between 0 and 400 $\text{\AA}^2/\text{molecule}$

Figure 6.2 shows the Langmuir isotherms for the cholesteryl anchor without polymer and the different STLs listed in Table 6.1. The cholesteryl α -CD anchor itself, as well as the STLs form stable monolayers at the air-water interface. Isotherms can be recorded until film collapse for surface pressures beyond 50 mN/m. This is in contrast to Langmuir isotherms attempted for end-capped PEG without CD anchors, which collapse around 12 mN/m due to loss of PEG molecules into the subphase (isotherms not shown) [274].

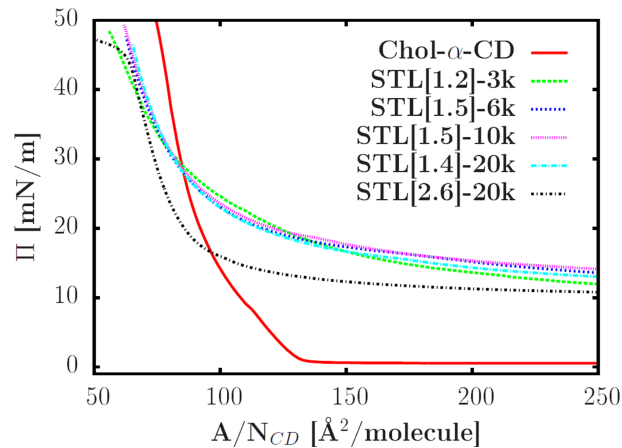


Figure 6.3: Isotherms for pure STLs with surface area normalised with respect to the number of CD A/N_{CD} .

The isotherms for all investigated STLs are qualitatively similar with a plateau region for intermediate surface pressures (~ 10 mN/m) and very large molecular areas. The onset of the surface pressure rise, as well as molecular area range over which the plateau extends, increases with increasing polymer MW (Figure 6.2 A). The shift to larger surface areas simply reflects the increased number of monomers N with MW.

At high surface pressures isotherms for pure STL scale with the average number of threaded

CD which is illustrated in Figure 6.3, where the isotherms are plotted with the surface area normalised with respect to the number of CDs, A/N_{CD} . They all coincide fairly well for $\Pi > 30$ mN/m, yet displaced to smaller areas compared to the isotherm of the pure α -CD anchor, probably caused by the loss of material throughout compression already described above.

Mixed STL/DPPC monolayers

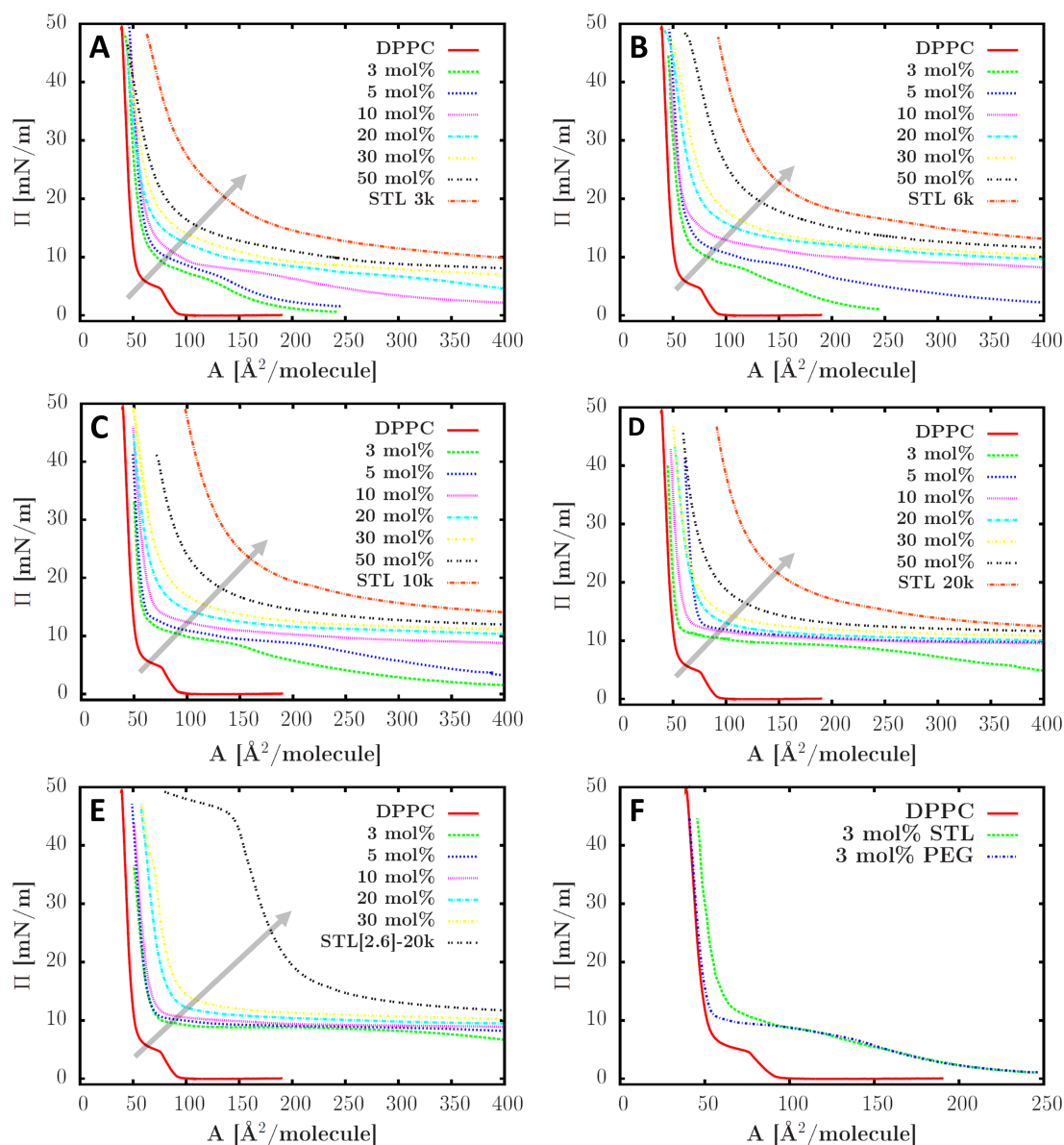


Figure 6.4: Langmuir isotherms for STL/DPPC mixtures at 20°C : A. STL-3k, B. STL-6k, C. STL-10k, D. STL 20k, E. STL[2.6]-20k and F. Comparison between STL-6k/DPPC and PEG-k/DPPC mixtures. The arrows indicate increasing molar ratios STL.

Figure 6.4 A - E shows the compression isotherms for STL/DPPC mixed monolayers at different molar ratios. The plateau, indicating the DPPC liquid - condensed phase transition at 6 mN/m, is not visible anymore when STLs are present. The isotherms for the STL/DPPC mixtures show the same features as the pure STLs. The plateau region

at 10 mN/m is shifted to higher surface areas and surface pressures with increasing STL content (indicated by the arrows in the Figure 6.4), reflecting the increased polymer density ($\sigma = 1/A$) in the monolayer. At high surface pressures they are slightly shifted to larger surface areas with respect to DPPC. For STL molar ratios > 30 mol% the shift is more pronounced.

DPPC mixtures with STL are also compared to mixtures with endcapped PEG without CD anchor. The isotherms for both compounds with identical molar ratio are displayed in Figure 6.4 F. For large surface areas the isotherms coincide and show the typical plateau at 10 mN/m. Upon further compression the STL mixture starts rising more smoothly and is slightly shifted with respect to pure DPPC. In contrast the PEG/DPPC isotherm is identical with the one for DPPC for surface pressures above 12 mN/m, as the PEG gets expelled into the subphase.

Amphiphilic behavior at the air-water interface

The STLs isotherms exhibit three different regions upon compression, which correspond to different chain conformations and are typical for hydrophobically modified PEGs [272]. At low compression (for high surface areas A or low surface densities, respectively), the PEG chains adsorb at the air-water interface, due to the amphiphilic nature of the ethylene glycol (EG) monomers. The interaction between the EG monomers and the interface is attractive, and the EG adsorb at the air-water interface with adsorption energies in the order of $1k_B T$ per monomer [272]. In this regime the pressure and shape of the isotherm is mainly determined by the number of monomers in the layer. At the plateau region the EG-interface interaction becomes increasingly repulsive due to repulsive interactions between EG residues and the cholesteryl CD anchor as well as DPPC molecules, which gradually cover the whole interface upon compression. This promotes the desorption of the EG monomers from the surface so that the PEG chains adopt a mushroom like conformation. At the sharp rise of the isotherms for high compression the PEG is forced into a brush conformation, due to the mutual repulsion of the polymer chains contributing to the rise of surface pressure [275].

The cholesteryl α -CD proves to be suitable to firmly anchor the STLs at the air-water interface up to high surface pressures. Furthermore it allows for insertion of the STLs into phospholipid monolayers, in analogy to the cholesteryl CDs studied in section 4. In contrast the endcapped polymers are expelled to the subphase, which proves that anchoring of the STLs is truly governed by the cholesteryl CD anchor and not mediated by the hydrophobic DMPE stopper molecules. The isotherms for pure STLs and STL/DPPC mixtures are in good agreement with isotherms for comparable hydrophobically modified PEGs described in literature, such as styrene-PEG block copolymers [272] or pegylated lipids [273, 276].

6.1.2 Film morphology

Mixed STL/DPPC monolayers

Using BAM and AFM the in-plane film morphology can be investigated from μm to nm scale. Mixtures with STLs of different MW give comparable results for similar surface densities. At low surface pressures large bright domains of $\sim 50 \mu\text{m}$ diameter are visible (Figure 6.5 A). Complementary AFM images show, that there is also a heterogeneity at much smaller scale in the order of tenth of nanometers (Figure 6.6 A). With further compression those domains vanish and starting at $\Pi > 8 \text{ mN/m}$ small ($10 \mu\text{m}$) brighter domains appear, which grow in number (Figure 6.5 B). These brighter domains, visible for all molar ratios and regardless the MW of the STLs, correspond to the LE-LC phase transition, typical for DPPC [31]. These domains are also displayed in corresponding AFM images (Figure 6.6 B).

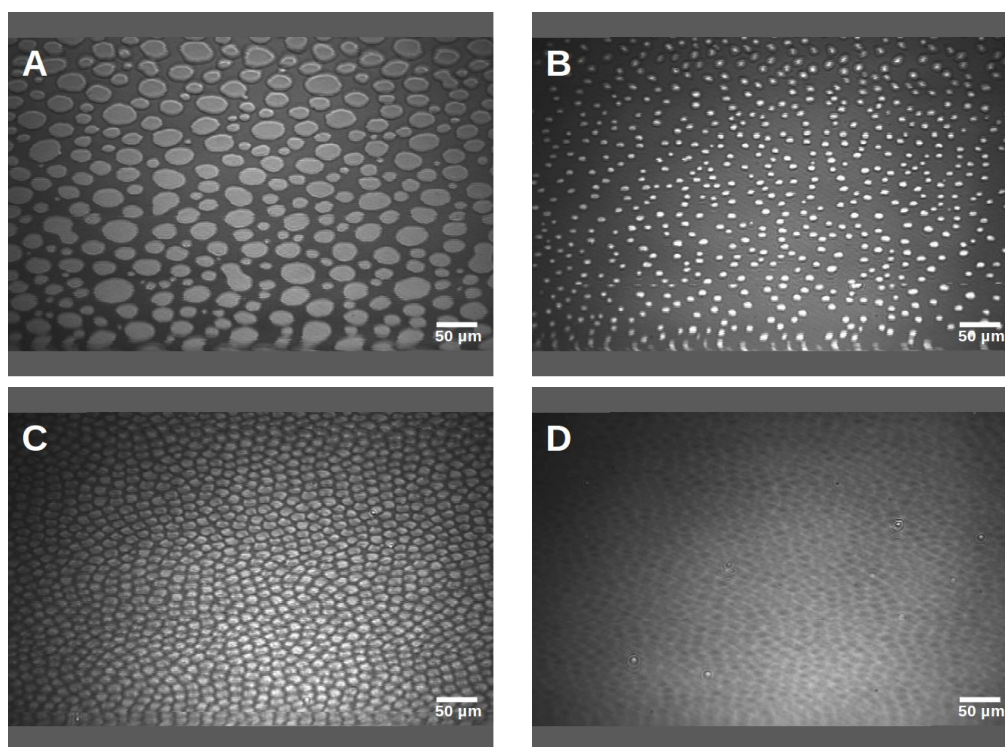


Figure 6.5: BAM images for the mixture 3 mol% STL-6k/DPPC at A. 5 mN/m, B. 9 mN/m, C. 13 mN/m, D. 30 mN/m

They become denser with further rise of Π (Figure 6.5 C and Figure 6.6 C), and an inversion of contrast occurs for $\Pi \sim 20 \text{ mN/m}$ to result in a honey comb like pattern, which prevails up to very high surface pressures (Figure 6.5 D). For higher STL molar ratios the bright domains visible at 13 mN/m are less dense and the inversion of contrast occurs at lower surface pressure to give the same honey comp like pattern only with higher contrast (Figure 6.40 E and F in the appendix). Interestingly for molar ratios $> 30 \text{ mol}\%$ BAM images do not display a contrast for high surface pressures. The AFM images for high surface pressures do not display the patterns observed in BAM, but many aggregates are visible (Figure 6.6 D). The aggregates (height 5 - 10 nm) increase in number with STL molar ratios and they are oriented in the direction of deposition. This clearly signifies, that

the deposition has an effect on the monolayer structure probably inducing a rearrangement of the polymer, when transferred from the aqueous environment onto the mica in air.

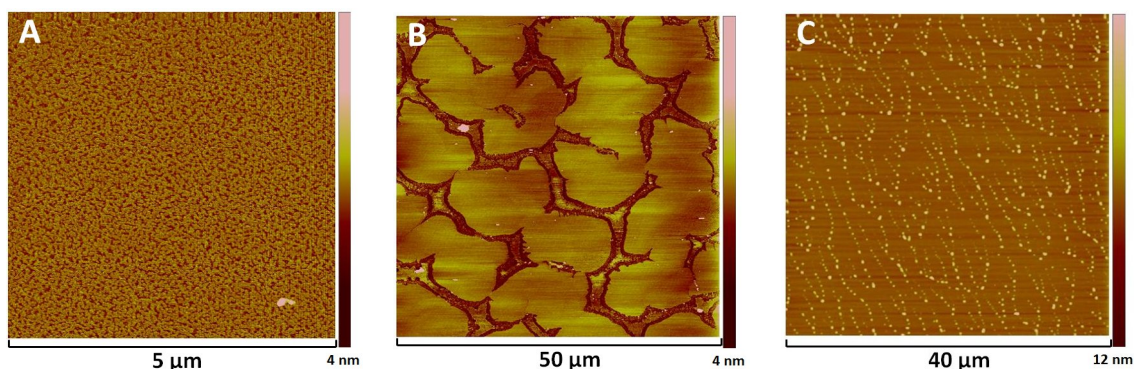


Figure 6.6: AFM images for the mixture 3 mol% STL-6k/DPPC at A. 5 mN/m, B. 13 mN/m, C. 35 mN/m

Mixed PEG-cap/DPPC monolayers

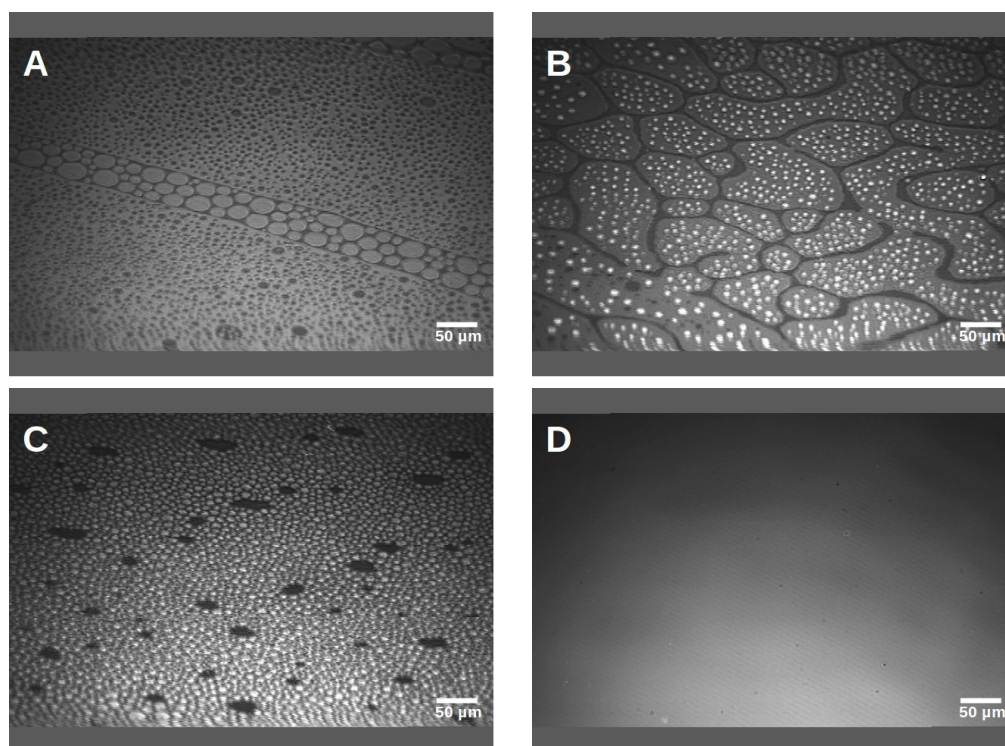


Figure 6.7: BAM images for the mixture 3 mol% PEG-6k-cap/DPPC at A. 5 mN/m, B. 9 mN/m, C. 13 mN/m, D. 30 mN/m

The monolayer morphology is also investigated for PEG-cap/DPPC mixtures. At low surface pressures similar domains compared to the STL mixtures are visible in BAM (Figure 6.7 A), as well as AFM images (Figure 6.8 A). Starting at ~ 8 mN/m brighter domains appear corresponding to the DPPC LE-LC transition (Figure 6.7 B). Continuing increase of surface pressure leads to merging of the large bright domains and the brighter domains become more densely packed (Figure 6.7 C), which is also observed by AFM

(Figure 6.8 B). Further rise of Π leads to loss of contrast at ~ 15 mN/m, which prevails until the end of compression (Figure 6.7 D). Complementary AFM images for very high surface pressures also display a very homogeneous, flat surface, with few aggregates (Figure 6.8 C).

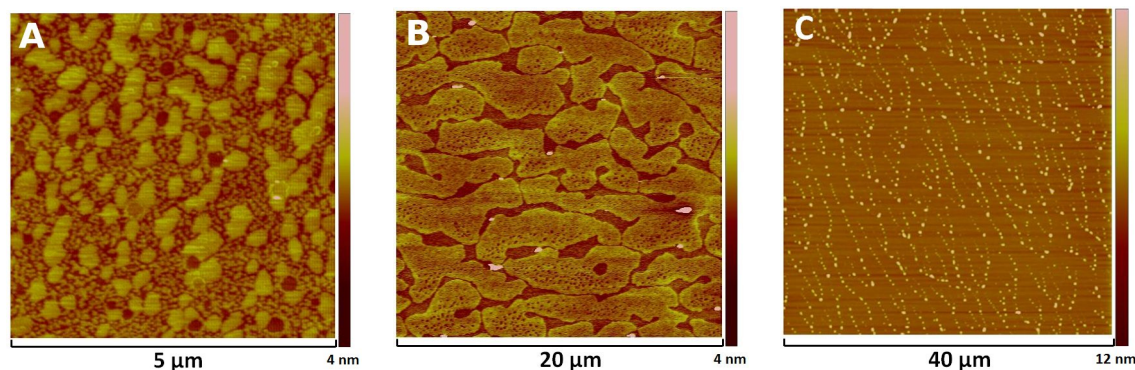


Figure 6.8: AFM images for the mixture 3 mol% PEG-6k/DPPC at A. 5 mN/m B. 13 mN/m, C. 35 mN/m

Phase behavior

Considering the images for STL and PEG-cap/DPPC mixtures, our findings can be summarized as follows: At surface pressures below the desorption transition plateau, STL and PEG/DPPC mixtures behave similarly. For both a phase separation is observed between the phospholipids and the polymer chains adsorbed to the surface. Although the typical plateau for the LE - LC of DPPC is not visible in the isotherms, the phase change is clearly evidenced by the images. Increasing molar ratios of STL influence the alkyl chain condensation because the appearance of DPPC LC phase is shifted to higher surface pressures.

It is striking that for PEG mixtures the DPPC LC phase domains only occur on the large bright domains. This indicates that these bright domains are made of rich in LE phase DPPC, surrounded by a phase rich in PEG adsorbed to the interface. Upon further compression above the desorption transition the PEG is forced into the subphase and the dark zones vanish until it is completely expelled from the interface for $\Pi > 15$ mN/m. The now visible uniform surface consists of pure LC DPPC.

In STL mixtures the LC phase domains are evenly distributed on a uniform surface, consisting of mixed LE DPPC and STL. Upon further compression the LC domains grow and become denser until a contrast inversion is observed to a honey comb like pattern. At high surface pressures we find a phase separated mixed monolayer of DPPC in LC state and the STL cholesteryl-CD anchor with its PEG tether submerged into the subphase. The film morphology at high surface pressures and especially the behavior compared to PEG without CD anchor are good evidence that the STLs are firmly anchored into DPPC monolayers.

6.1.3 IRRAS

With the help of IRRAS we want to get further insight into the monolayer insertion behavior of the STLs. At first, IRRAS spectra have been measured for monolayers of

DPPC and cholesteryl α -CD. They will be used as reference to better analyse the data for pure STL-6k and a 30 mol% STL-6k/DPPC mixtures during film compression. The whole spectra can be found in the appendix (Figure 6.42). All spectra are baseline corrected and corrected for water vapor interference. The data are plotted as transmittance R/R_0 , where R is the single-beam reflectivity spectrum from the film-covered surface and R_0 is the reflectivity from the clean water surface.

DPPC

At first we investigate a pure DPPC monolayer. Figure 6.9 shows the typical methylene peaks from the DPPC alkyl chains. They are composed of the symmetric and asymmetric CH_2 stretching modes at $\nu_s\text{CH}_2 \sim 2850$ and $\nu_{as}\text{CH}_2 \sim 2920 \text{ cm}^{-1}$, respectively, along with the asymmetric methyl stretch at $\nu_{as}\text{CH}_3 \sim 2960 \text{ cm}^{-1}$. Increasing Π leads to increased intensity (Figure 6.9). The increase in intensity is predominantly due to an increase in the number of molecules in the IR beam. However, the intensity of the CH_2 stretching modes is also sensitive to acyl chain orientation. A decrease in the average tilt angle of the acyl chains with respect to the surface normal also results in an intensity increase [200].

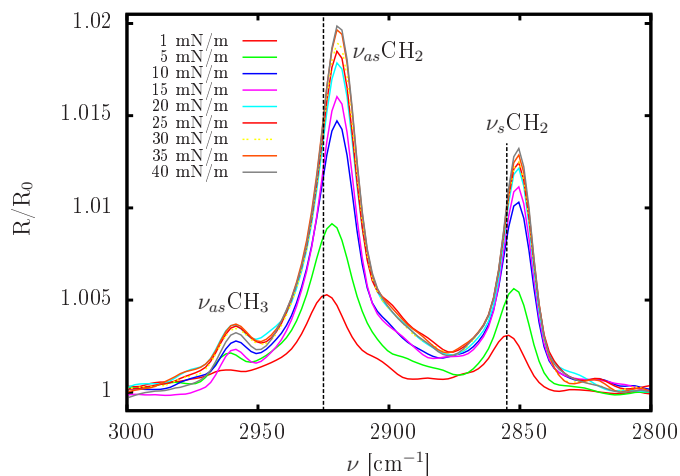


Figure 6.9: Overlaid IRRAS spectra of the methylene stretching region upon compression. The surface pressure ranges from 0 to 40 mN/m from the least to most intense bands, respectively, at a pressure interval of 5 mN/m. Vertical lines are drawn to emphasize the frequency downshift upon monolayer compression.

Furthermore the peaks display a characteristic shift in frequency related to the molecular order of the chains (Figure 6.9) [277]. The exact peak frequencies are determined by fitting the IRRAS signals with a Voigt type profile [278], like illustrated e.g. for the 30 mN/m spectra in Figure 6.10. During the DPPC LE-LC phase transition the conformational order increases and thus $\nu_s\text{CH}_2$ shifts from 2855 cm^{-1} to 2850 cm^{-1} and $\nu_{as}\text{CH}_2$ from 2924 cm^{-1} to 2919 cm^{-1} (Figure 6.10, for corresponding values see appendix). Therefore these signals can be used as qualitative measure for the phase transition. They will be used to draw conclusions about the influence of the STL on the lipid ordering in mixed STL/DPPC monolayers.

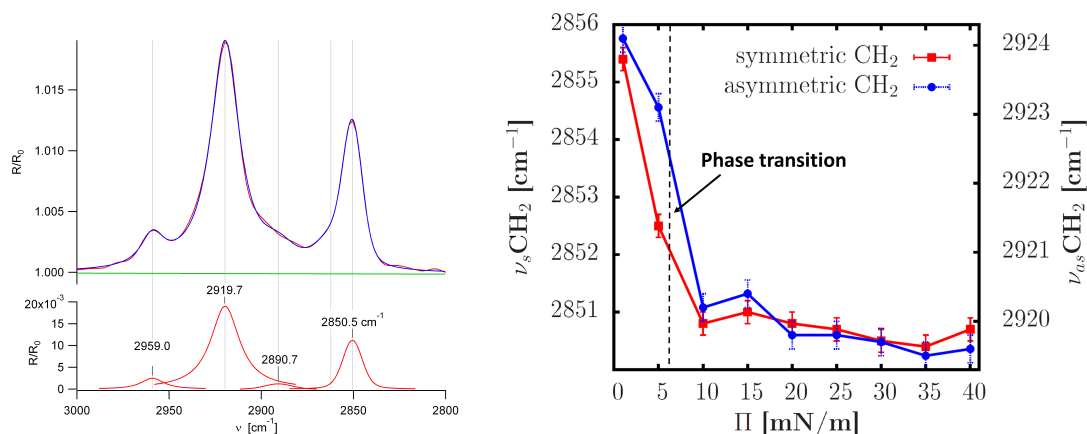


Figure 6.10: left: Fit of the DPPC methylene stretching region for the spectrum taken at 30 mN/m. right: Frequencies for asymmetric $\nu_{as}\text{CH}_2$ and symmetric $\nu_s\text{CH}_2$ stretching vibrations in dependence of the surface pressures determined by fitting the methylene peak between 3000 - 2800 cm^{-1} . The errors are around $\pm 0.2 \text{ cm}^{-1}$.

Pure cholesteryl α -CD

In order to identify characteristic peaks for the cholesteryl α -CD anchor IRRAS spectra of pure a cholesteryl α -CD monolayer are recorded during film compression for surface pressures between 0 - 40 mN/m. There are intense and broad absorption peaks observed in the region between 1200 - 1000 cm^{-1} , as soon as the surface pressure starts rising steeply (Figure 6.11 left). They are correlated to various C-O vibration modes within the CD moiety [217] and their intensity increases with surface pressure. In the literature the occurrence of the intensive peaks has been explained by the arrangement of the CD moieties in a very ordered structure at the interface [217]. The cholesteryl moiety does not give rise to readily identified peaks.

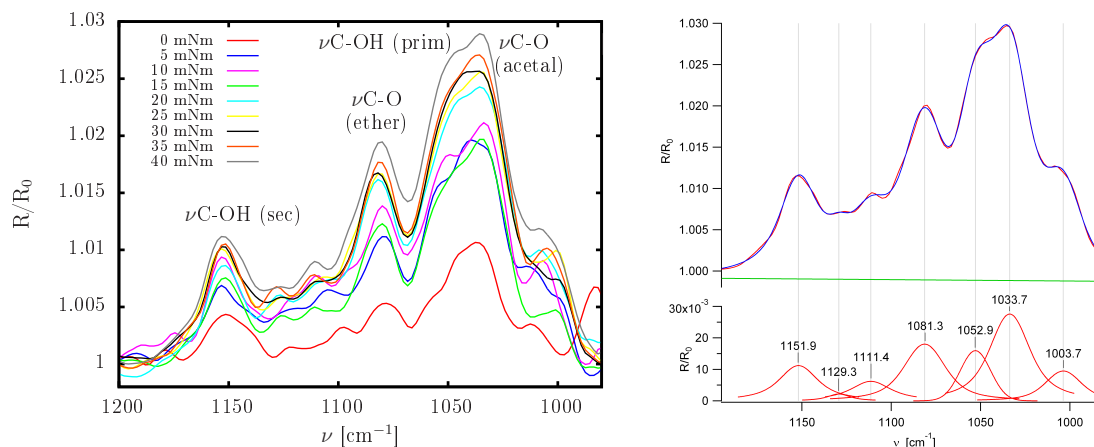


Figure 6.11: left: IRRAS spectra of the C-O stretching region obtained during the compression of a Cholesteryl α -CD monolayer. The surface pressure ranges from 0 to 40 mN/m from the least to most intense bands, respectively, at a pressure interval of 5 mN/m. right: Fit of the Cholesteryl α -CD C-O stretching region at 40 mN/m, allowing to extract the frequencies for the $\nu\text{C-OH}$ (sec), $\nu_{as}\text{C-O}$ (ether), $\nu\text{C-OH}$ (prim) and $\nu\text{C-O}$ (acetal) vibrations.

In order to assign the different vibrations to structural features in the CD, the large C-O peak is deconvoluted by fitting with a Voigt type band shape model. An example is given in Figure 6.11. There is no significant shift of the peaks with compression therefore average peak frequencies extracted from the fits between 5 - 40 mN/m are displayed in

vibration	ν C-OH (sec)	ν_{as} C-O (ether)	ν C-OH (prim)	ν C-O (acetal)
ν [cm ⁻¹]	1152 ± 1	1081 ± 1	1053 ± 1	1034 ± 1

Table 6.3: Frequencies for the ν C-OH (sec), ν_{as} C-O (ether), ν C-OH (prim) and ν C-O (acetal) vibrations extracted from the fits and averaged over all surface pressures above 5 mN/m.

Table 6.3. The peaks for the primary and secondary C-OH stretching vibration, as well as the acetal C-O-C vibration which are characteristic for the CD, can be clearly identified. The peaks between 1082 - 1129 cm⁻¹ can be related to the ether C-O vibration, which according to literature can be decomposed into four different subpeaks [279]. However due to the complexity of the peak only the asymmetric C-O vibration ν_{as} C-O can be unambiguously assigned.

Thus with the primary and secondary C-OH stretching vibration, as well as the acetal C-O-C vibration we have three characteristic peaks which can be used to identify the CD anchor in the STL.

Pure STL-6k

The IRRAS spectra measured below the pancake-mushroom transition at 10 mN/m display only very weak absorption signals. They are almost not discernible from the background noise, reflecting the very low STL surface densities for low compressions. Above the plateau region ($\Pi > 10$ mN/m) two broad and intense absorption peaks in the methylene region (Figure 6.12 left) and the C-O stretching region (Figure 6.13 left) appear, which both increase in intensity with the surface pressure.

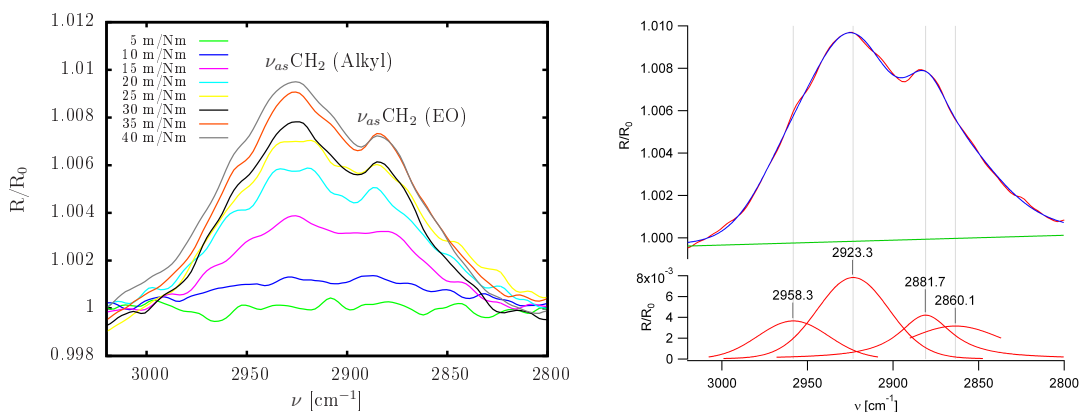


Figure 6.12: left: Overlaid IRRAS spectra of the CH₂ stretching region obtained during the compression of a STL-6k monolayer. The surface pressure ranges from 5 to 40 mN/m from the least to most intense bands, respectively, at a pressure interval of 5 mN/m. right: Fit of the methylene stretching region for the spectrum taken at 40 mN/m.

The peaks in the methylene vibration region do not show a distinct shift with compression. Deconvolution of the broad peak demonstrates, that it is mainly composed of the usual asymmetric and symmetric alkyl stretching vibrations ν_{as} CH₃ = 2958 cm⁻¹, ν_{as} CH₂ = 2923 cm⁻¹, ν_s CH₂ = 2860 cm⁻¹. Additionally an asymmetric ether dependent stretching vibration ν_{as} CH₂ = 2880 cm⁻¹ (Figure 6.12 B) is identified which is characteristic for PEG [276].

Applying the results from the deconvolution of the cholesteryl α -CD C-O peak, the C-O stretching band of the STL can be decomposed into signals arising from the threaded

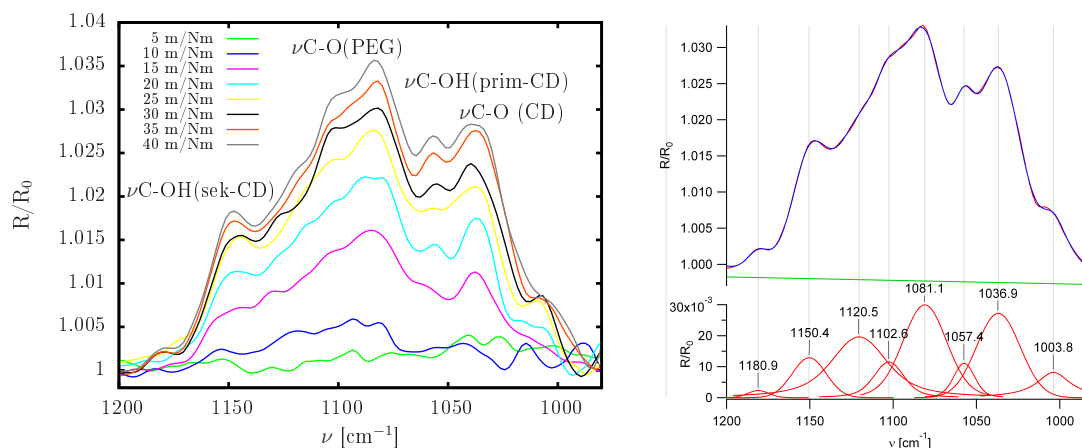


Figure 6.13: left: Overlaid IRRAS spectra of the C-O stretching region obtained during the compression of a STL-6k monolayer. Spectra are measured for surface pressures at an interval of 5 mN/m from 5 to 40 mN/m. right: Fit of the C-O stretching region for the spectrum taken at 40 mN/m. $\nu\text{C-OH (sec)} = 1150.4 \text{ cm}^{-1}$, $\nu\text{C-OH (prim)} = 1057.4 \text{ cm}^{-1}$, $\nu\text{C-O-C (acetal)} = 1036.7 \text{ cm}^{-1}$ and $\nu\text{C-O (PEG)} = 1081.3 - 1120 \text{ cm}^{-1}$

vibration	$\nu\text{C-OH (sec)}$	$\nu_{as}\text{C-O (PEG)}$	$\nu\text{C-OH (prim)}$	$\nu\text{C-O (acetal)}$
$\nu \text{ [cm}^{-1}\text{]}$	1151 ± 1	1081 ± 1	1057 ± 1	1037 ± 1

Table 6.4: Frequencies for the $\nu\text{C-OH (sec)}$, $\nu_{as}\text{C-O (ether)}$, $\nu\text{C-OH (prim)}$ and $\nu\text{C-O (acetal)}$ vibrations extracted from the fits and averaged over all surface pressures above 10 mN/m.

CD and the strong ether C-O-C vibration modes typical for the PEG (Figure 6.13 right). Since the peaks do not shift systematically with compression, average values for the determined frequencies are displayed in Table 6.4.

The ether band is much more intense for the STL compared to the signal found for cholesteryl α -CD alone, due to the presence of the PEG chains, which contribute most to this peak. Again the complexity of the broad C-O absorption peak allows only the identification of three subpeaks of the C-O ether vibration (instead of four described in the literature [276]), and only the asymmetric vibration $\nu_{as}\text{C-O} \sim 1081 \text{ cm}^{-1}$ can be unambiguously assigned. The broad shape of the C-O band without sharp peaks are typical for an amorphous PEG structure [280] and corresponds very well to observations made for polymer brushes formed with lipopolymers [276].

The primary C-OH peak is systematically shifted to higher frequencies in the STL ($\nu\text{C-OH (prim)} = 1057 \text{ cm}^{-1}$) compared to the pure cholesteryl α -CD ($\nu\text{C-OH (prim)} = 1052 \text{ cm}^{-1}$), which might be due to the complexation of the CD on the polymer. The presence of the strong signals from the CD anchors for high compressions, is furthermore an indication that the cholesteryl α -CD anchor must form a rather well organised layer at the interface, in analogy to pure cholesteryl α -CD.

The presence of the characteristic peaks for the CD anchor and PEG up too high compressions are a qualitative proof that the STLs are firmly anchored at the interface. The signals observed for the polymer moiety are typical for PEG polymer brushes [276, 281]. The characteristic CD peaks suggest that the CD anchors form a rather densely packed layer at the interface with the PEG tethers forced to stretch into the subphase.

Mixture STL-6k/DPPC

Having studied all pure components we now investigate the STL/DPPC mixtures. Similar to the pure STL, the IRRAS spectra exhibit only very weak signals for surface pressures below the pancake-mushroom transition at 10 mN/m (Figure 6.15 and 6.17), which can barely be distinguished from the background noise. Moreover the absence of the very intensive bands of the methylene stretching modes of the DPPC alkyl chains illustrates the strong perturbation of the phospholipid ordering by the adsorbed PEG at low surface pressure.

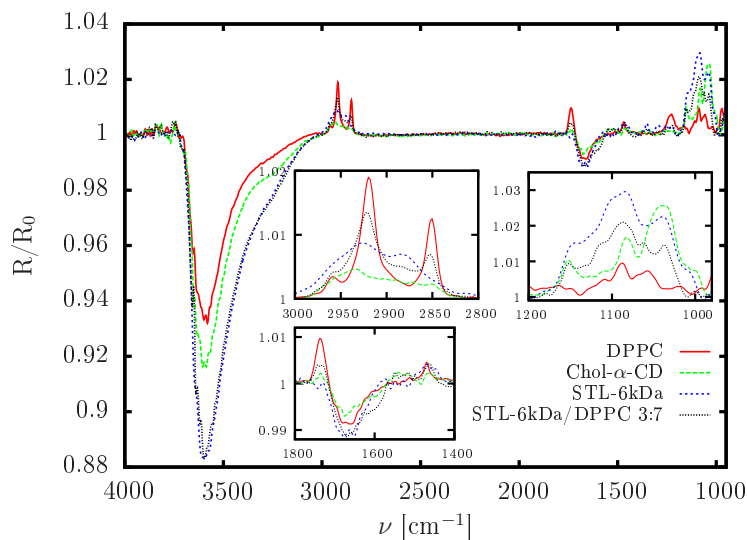


Figure 6.14: Comparison of the spectra recorded at 30 mN/m for DPPC, cholesteryl α -CD, pure STL and the 30 mol% STL-6k/DPPC mixture.

Starting from $\Pi > 10$ mN/m signals appear in the spectrum which increase in intensity with surface pressure (Figure 6.15 and 6.17). Figure 6.14 shows an overlay of spectra recorded at 30 mN/m for DPPC, cholesteryl α -CD, pure STL and the 30 mol% STL-6k/DPPC mixture to better visualise the contribution of each compounds' structural features to the spectrum of the mixture. The insets display magnifications of the most important regions of the spectrum. Strong bands can be observed in the methylene region between 3000 - 2800 cm^{-1} and the typical carbonyl stretching at $\nu_{\text{CO}} \sim 1735$ cm^{-1} of the DPPC fatty acid ester bonds. Furthermore we observe a C-O stretching band similar to the pure STL between 1200 - 1000 cm^{-1} (Figure 6.14).

As demonstrated before the DPPC methylene vibration frequencies are sensitive to the molecular order of the alkyl chains and we will use these peaks to draw conclusions about the influence of the STL on the lipid ordering and phase transition. The CH_2 stretching region displays the sharp, intense $\nu_s\text{CH}_2$ and $\nu_{as}\text{CH}_2$ peaks typical for DPPC, as well as the asymmetric stretching vibration arising from the PEG.

Both the symmetric and asymmetric methylene peak frequencies decrease with increasing surface pressure indicating alkyl chain ordering (Figure 6.15) during compression. Figure 6.16 shows a graph, where the methylene shifts for pure DPPC and the STL mixtures are compared. The characteristic shift of the DPPC methylene peaks occurs at much higher surface pressures for the film containing STL (> 15 mN/m for the 30 mol% mixture compared to > 5 mN/m for pure DPPC). Furthermore the shift is less pronounced indicating

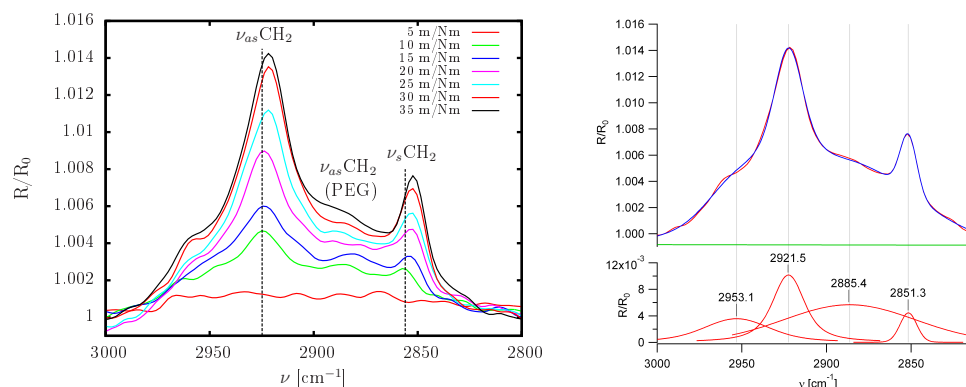


Figure 6.15: left: Overlaid IRRAS spectra of the CH₂ stretching region obtained during the compression of a 30 mol% STL-6k/DPPC mixed monolayer. The surface pressures are measured at an interval of 5 mN/m from 5 to 35 mN/m, from the least to most intense bands, respectively. right: Fit of the methylene stretching region for the spectrum taken at 35 mN/m.

that the STLs perturb the alkyl chain ordering. Like evidenced for cholesteryl CD/DPPC mixtures in section 4, it is likely that not only the PEG chains but also the cholesteryl CD residues influence the DPPC phase transition. Yet, it is difficult to distinguish the effect of the polymer tether and the effect of the cholesteryl anchor on the alkyl chain ordering.

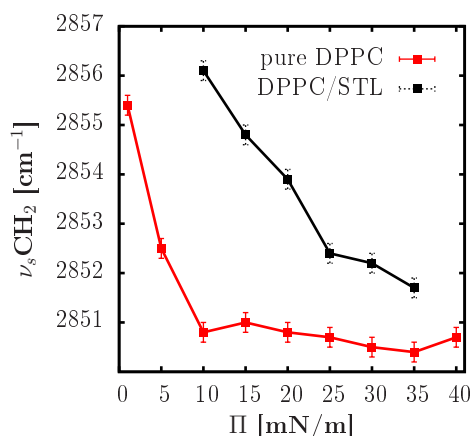


Figure 6.16: Comparison of frequency shift of symmetric ν_s CH₂ stretching vibrations between pure DPPC and DPPC/STL mixture in dependence of the surface pressures. The frequencies have been determined from fits of the methylene region between 3000 -2800 cm^{-1} . The errors are around $\pm 0.2 \text{ cm}^{-1}$.

The CO stretching region is very similar to pure STL. By fitting we can readily identify the four major bands, arising from the STL's CD and PEG moieties (Figure 6.17). Since the peaks do not shift systematically with compression, average values for the determined frequencies are displayed in Table 6.5. The primary C-OH vibrations are even further shifted to higher frequencies compared to pure STL and cholesteryl α -CD, which might be due to interactions with the DPPC headgroups. As already discussed for the pure STL monolayer, the broad shape of the CO band can be assigned to the formation of polymer brushes.

The presence of the characteristic peaks for the STL and the DPPC show that the STLs are well inserted into the phospholipid monolayer up too high compressions. The STLs has a fluidising effect on the monolayer, shifting the LE-LC phase transition and decreasing the alkyl chain ordering. The polymer chains form polymer brushes, whose

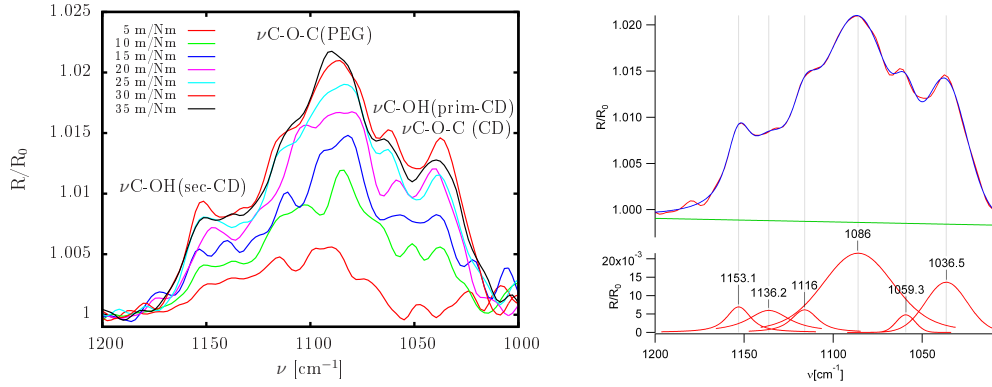


Figure 6.17: left: Overlaid IRRAS spectra of C-O stretching region obtained during the compression of a 30 mol% STL-6k/DPPC mixed monolayer. The surface pressures are measured at an interval of 5 mN/m from 5 to 35 mN/m, from the least to most intense bands, respectively. right: Fit of the methylene stretching region for the spectrum taken at 35 mN/m.

vibration	ν C-OH (sec)	ν_{as} C-O (PEG)	ν C-OH (prim)	ν C-O (acetal)
ν [cm^{-1}]	1153 ± 1	1085 ± 1	1061 ± 1	1036 ± 1

Table 6.5: Frequencies for the ν C-OH (sec), ν_{as} C-O (ether), ν C-OH (prim) and ν C-O (acetal) vibrations extracted from the fits and averaged over all surface pressures above 20 mN/m.

structure will be investigated by neutron scattering, described in the following section.

6.2 Neutron Reflectivity

The film structure perpendicular to the surface has been studied for monolayers containing STLs or binary mixtures with DPPC using neutron reflectivity at the air-water interface. This should provide us with a means to study the influence of the PEG tether's sliding ability on the chain conformation by modeling with the appropriate theoretical descriptions, introduced in section 2.1.4. The studied monolayers are specified in Table 6.6

sample	Π [mN/m]	contrast
DPPC pure	8, 16, 22, 40	D ₂ O
3 mol% STL-6k	8, 14, 30	D ₂ O
10 mol% STL-6k	10, 15, 40	D ₂ O, 4MW, SMW
30 mol% STL-6k	15, 40	D ₂ O
10 mol% PEG-6k-cap	10, 15, 40	D ₂ O
pure STL-6k	10, 15, 40	D ₂ O

Table 6.6: Monolayer samples measured with neutron reflectivity.

Some important scattering length densities (SLD) for this experiment are summarised in Table 6.7.

6.2.1 Data Analysis

Monolayer model

An appropriate monolayer model has to be chosen in order to fit the data. The data obtained for the pure DPPC and the PEG-cap/DPPC mixture have been fitted with the

material	SLD [10^{-6} \AA^{-2}]
D ₂ O	6.06
4MW	4.8
ZMW	0.1
DPPC-D ₆₂ palmitoyl tail	7.66
DPPC-PC head	1.74
CD head + inserted PEG	2.4
cholesteryl anchor	0.5
PEG	0.6

Table 6.7: Important SLDs for the materials used in the experiment. SLDs for D₂O, 4MW and ZMW are obtained from the fit. The SLD for the CD is calculated, using $V(\text{CD})=1000 \text{ \AA}^3$ and its scattering length $b=189 \text{ fm}$ and adding the SLD of the inserted PEG. The other values are from references [38, 233].

same two layer model used for the amphiphilic CDs, described in section 4.1.2.

In order to fit the data from the experiments with STLs, additionally to one layer each for the hydrophobic tails and hydrophilic headgroups, a third layer representing the PEG chains has to be added, as illustrated schematically in Figure 6.18.

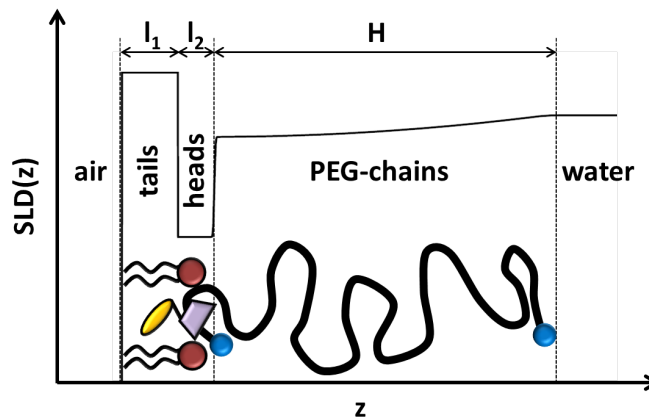


Figure 6.18: Schematic representation of the box model that was used to fit the reflectivity data of the STL-lipid monolayers.

In agreement with literature [282], the data for STLs (with PEGs tethers of MW = 6 kg/mol) can not be well fitted, using a simple steplike for the polymer layer (constant polymer concentration, ϕ_0 in the brush). Instead we use functional forms obtained from the theoretical description of the sliding grafted layers presented in section 2.1.4.

STL polymer brushes should behave like normal chains grafted with one end to the surface [19]. Thus we use the standard parabolic density profile to describe the polymer layer [282, 283], based on equation (2.16) introduced in section 2.1.4. Since we know N (133) and the scattering length density of PEG ($SLD_{PEG} = 0.64 \cdot 10^{-6} \text{ \AA}^{-2}$), the polymer layer is determined by two independent fitted parameters, the brush thickness H and the polymer fraction at the headgroup-PEG interface ϕ_0 .

For low polymer surface densities (3 mol% STL/DPPC monolayer), we additionally have tested fitting the data with the polymer profile, obtained for sliding mushrooms using equation 2.19 described in section 2.1.4. In this case the polymer layer is defined by the single adjustable parameter ϕ_0 .

Fitting procedure

We use the parameters obtained for the DPPC monolayer as reference for fitting the mixed films. The results for the head and tail layers are used as starting values, which are then refined. The roughness is constrained to be the same for heads and tails. To account for capillary waves at the air-water interface, the subphase roughness is fixed to 3 Å.

For the 10 mol% STL-6k monolayers three different subphase contrasts (D_2O , 4MW and ZMW) were measured. The fits have been conducted in a coupled manner with only the SLDs of the subphase allowed to vary (Figure 6.19). The error bars were determined by varying each parameter of the model and evaluating the χ^2 parameter, as well as visually checking the quality of the fit.

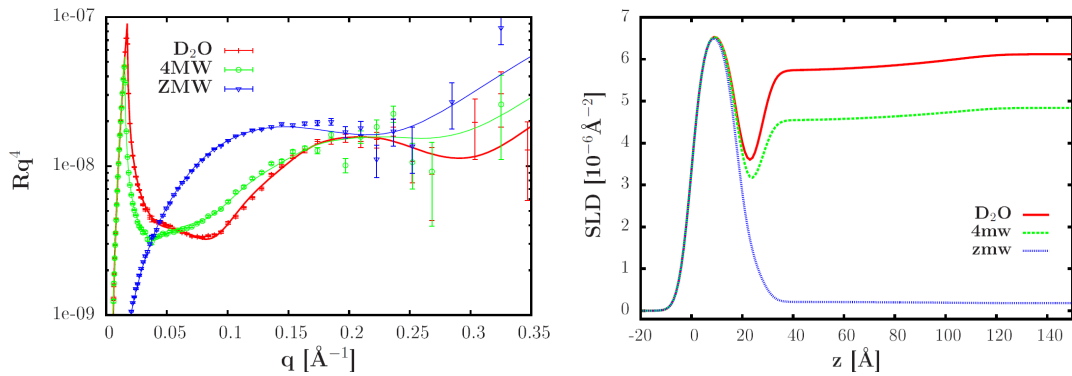


Figure 6.19: Neutron reflectivity curves (left) and corresponding SLD profiles (right) for 10 mol% STL-6k at 40 mN/m measured for three different contrasts.

The water content of the headgroup layer is calculated in the same manner as already described in section 4.1.5, using the scattering length density of the subphase SLD_{sub} and the theoretical scattering length density for the headgroup layer. The latter one is estimated from the ratio of DPPC/STL in the monolayer using the values for SLD_{PC} and the CD residue of the STL listed in Table 6.7.

6.2.2 Films containing PEG without cholesteryl anchor

Pure DPPC-D62 monolayers at different surface pressures are investigated and compared to mixed films of DPPC with 10 mol% PEG-6k-cap without cholesteryl CD anchor. Figure 6.20 displays neutron reflectivity curves and corresponding fits of both monolayers at the same surface pressures. The fits to the experimental data are represented as solid lines. The best-fit parameters using a 2 layer box model, are listed in Table 6.8.

The lipid chain layer thickness for pure DPPC-D62 increases with surface pressure showing a pronounced increase for LE-LC phase transition which occurs at 17 - 19 mN/m (estimated from the plateau region of the isotherm on D_2O recorded simultaneously to measuring the scattering curves). Furthermore the compression is accompanied by a decrease of hydration of the CD layer (Table 6.8). The observations are in agreement with literature values [32, 230].

The mixed DPPC/PEG film exhibits a very small tail layer thickness, as well as a decreased SLD compared to pure DPPC, resulting from substantial amounts of PEG adsorbed to the interface for $\Pi < 10$ mN/m, below the desorption transition. At high surface pressures,

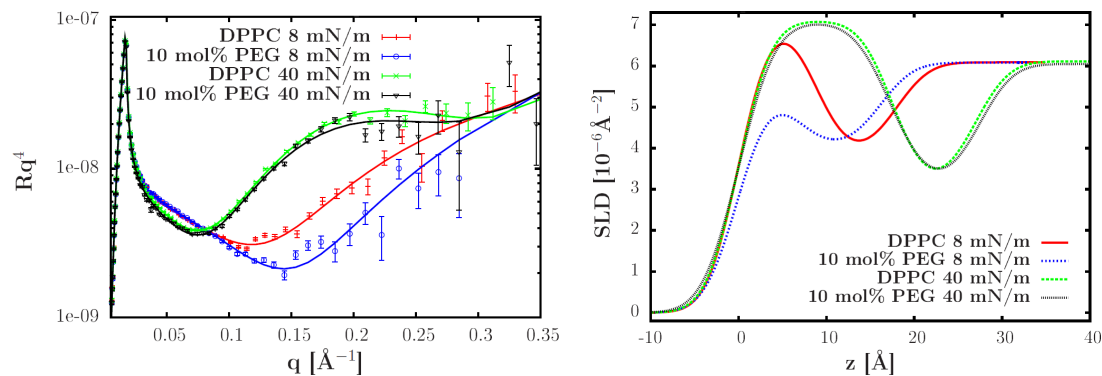


Figure 6.20: Neutron reflectivity curves (left) and corresponding SLD profiles (right) for pure DPPC and 10 mol% PEG-6k-cap monolayers at $\Pi = 8$ and 40 mN/m, respectively.

Π [mN/m]	A_{iso} [\AA^2]	l_{head} [\AA^2]	SLD_{head} [10^{-6}\AA^{-2}]	water [%]	l_{tail} [\AA]	SLD_{tail} [10^{-6}\AA^{-2}]	roughness [\AA]
pure DPPC-d62							
8	78	9.2	3.86	49	9.0	7.15	3.0
16	62	9.4	3.57	42	12.0	7.21	3.0
22	46	9.3	3.12	32	16.0	7.24	3.0
40	42	9.4	3.08	31	17.5	7.12	3.0
PEG-6k-DMPE 10 mol%							
8	120	10.0	4.04	-	6.0	5.70	3.0
40	45	10.3	3.15	-	17.5	7.06	3.5
errors	± 5	± 0.5	± 0.2	± 5	± 0.5	± 0.2	± 0.5

Table 6.8: Fitting results for the DPPC-D₆₂ and 10 mol% PEG-DMPE/DPPC-D₆₂ mixed monolayers at different surface pressures. l_x is the thickness, SLD_x the scattering length density of slab x.

scattering curves and SLD profiles are obtained, which are identical to pure DPPC at corresponding surface pressures (Figure 6.20 and Table 6.8).

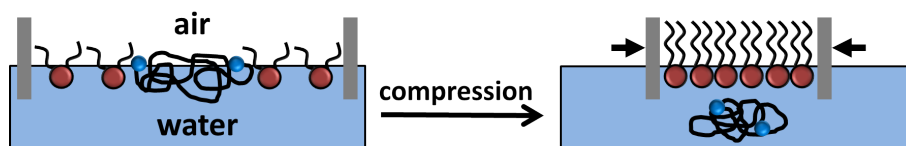


Figure 6.21: Schematic representation of expulsion of endcapped PEG without cholesterol α -CD anchor from the interface during compression

Comparing the results between pure DPPC and mixtures of the phospholipid with endcapped PEG (without cholesterol anchor) upon compression leads to the schematic monolayer structure displayed in Figure 6.21. For surface pressures below the desorption transition, PEG is adsorbed to the interface together with the phospholipids, due to its amphiphilic character [272, 274]. With further compression the polymer is expelled from the surface. This is unambiguously proved by identical SLD profiles for pure DPPC and the PEG mixture at high surface pressures and in agreement with the morphological evidence discussed in the previous section. It also demonstrates that the hydrophobic polymer stoppers alone are not sufficient to fix the polymer at the interface and that it behaves similar to unmodified PEG [274].

Π [mN/m]	A_{iso} [\AA^2]	A_n [\AA^2]	ϕ_0	H [\AA]	l_{head} [\AA]	SLD_{head} [10^{-6}\AA^{-2}]	water [%]	l_{tail} [\AA]	SLD_{tail} [10^{-6}\AA^{-2}]	roughness [\AA]
pure STL-6k										
9	2000	-	-	-	-	-	-	10.1	4.3	3.0
16	200	560	0.16	134	10.4	3.41	28	9.6	0.12	6
40	120	270	0.26	178	10.6	3.10	20	11.6	0.16	6.5
STL-6k 3 mol%										
8	5500	-	-	-	9.3	3.98	-	6.7	5.86	3.0
15	2333	8190	0.02	65	9.3	3.45	40	11.5	6.95	3.7
30	1667	5910	0.03	74	9.5	3.15	33	17.3	6.96	3.5
STL-6k 10 mol%										
10	1200	6600	0.04	53	9.3	3.65	43	8.8	6.55	3.6
15	700	2520	0.06	81	9.4	3.41	38	11.2	6.63	3.5
40	500	1960	0.07	88	9.8	2.98	28	17.9	6.58	4
50	450	1570	0.08	99	9.7	2.92	27	18.7	6.64	4
STL-6k 30 mol%										
16	233	690	0.14	130	10.4	3.6	40	9.9	6.38	3.8
40	167	1290	0.09	110	9.45	3.35	34	17.8	6.35	3.9
errors	± 10	± 100	± 0.01	± 10	± 0.5	± 0.2	± 5	± 0.5	± 0.2	± 0.5

Table 6.9: Fitting results for the STL/DPPC-D₆₂ monolayers at different surface pressures. l_x is the thickness, SLD_x the scattering length density of slab x, H the polymer layer thickness and ϕ_0 the volume fraction of polymer at the head-polymer layer interface.

6.2.3 Films containing STLs

All fitting results are summarised in Table 6.9. We now describe in detail the special features of the different films.

Pure STLs

For surface pressures below the STLs desorption transition (curve recorded at 9 mN/m) one box with a thickness of $\sim 10 \text{\AA}$ and a SLD, expected for a combination of highly hydrated PEG and the cholesteryl CD anchor, is sufficient to fit the data. This shows that the PEG chains are adsorbed to the interface together with the CD anchor.

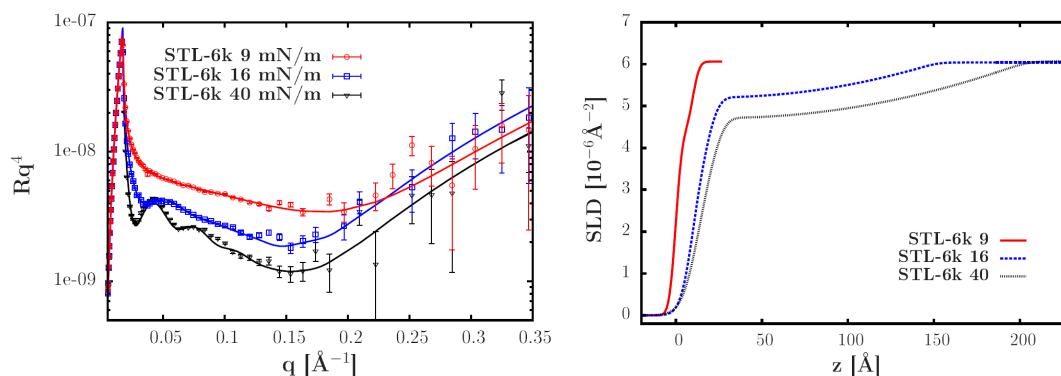


Figure 6.22: Neutron reflectivity curves (left) and corresponding SLD profiles (right) for pure STL-6k monolayers at different Π .

For surface pressures above the desorption transition, the curves are very well fitted with the three layer model, consisting of a tail layer with very low SLD corresponding to the cholesteryl anchor, a hydrated headgroup layer which mainly consists of the CD with

the complexed polymer in its cavity and polymer part, best described with a parabolic density profile for polymer brushes (Figure 6.22).

The cholesteryl slab thickness increases slightly with surface pressure. The head layer thickness remains constant. However its hydration decreases upon compression. Furthermore a very high roughness $\sim 6.5 \text{ \AA}$ is found. Similar behavior has been observed for pegylated lipids [282,283]. The polymer volume fraction ϕ_0 , as well as the brush thickness H increases with compression, due to the increase in polymer density.

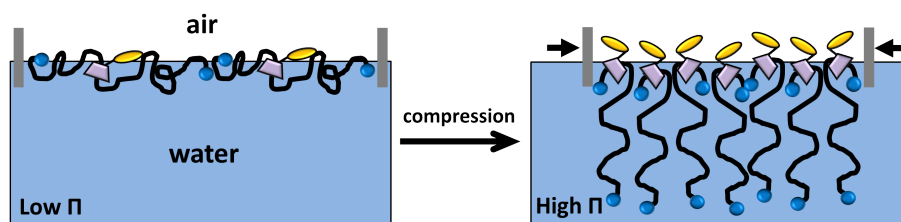


Figure 6.23: Schematic representation of the pure STL monolayer during compression.

The neutron data confirms that pure STL films are firmly anchored to the interface. In agreement with the Langmuir isotherms and the IRRAS measurements, we propose a monolayer structure during compression as schematically illustrated in Figure 6.23. Below the desorption plateau we find the STL in a configuration where the anchor and the polymer chains are adsorbed at the interface. Upon compression we observe a well defined cholesteryl CD layer at the interface where the PEGs form a polymer brush which increases in thickness with Π .

STL/DPPC monolayers

Below the desorption transition the data can be fitted well with a simple two box model without polymer layer similar to the DPPC/PEG mixtures without anchor. The SLD profiles and the low thickness of the tail layer clearly indicate adsorbed STL polymer chains together with DPPC at the interface (see results for 3 mol% STL at 8 mN/m in Table 6.9).

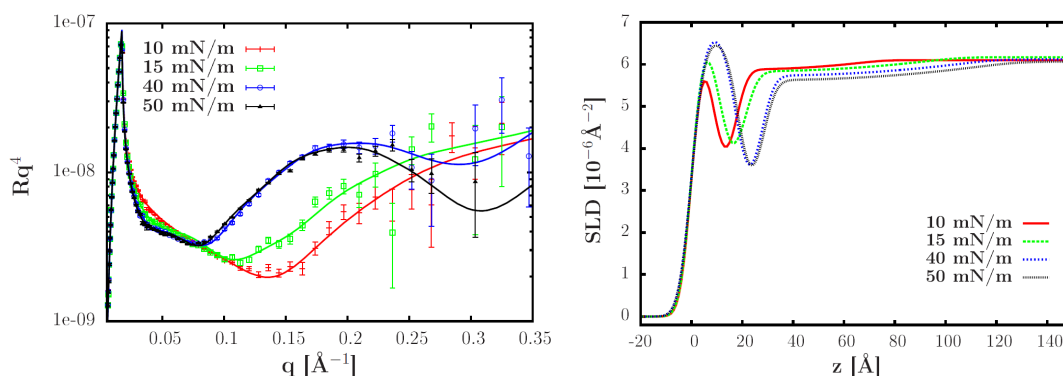


Figure 6.24: Neutron reflectivity curves (left) and corresponding SLD profiles (right) for the STL-6k 10 mol% mixed monolayer at different surface pressures.

Above the desorption transition ($\Pi > 10 \text{ mN/m}$) all STL/DPPC curves can be fitted very well with the parabolic profile for polymer brushes (Figure 6.25 and 6.24). Two well

defined slabs correspond to the DPPC layer with the incorporated cholesteryl α -CD moiety of the STL. The tail SLD is decreased according to the molar ratio of the incorporated STL cholesteryl anchor with its low SLD. The head group layer is similar to the one found for pure DPPC since the thickness and SLD of the CD are not very different from the DPPC headgroup. The roughness is elevated compared to pure DPPC, yet smaller than for pure STL.

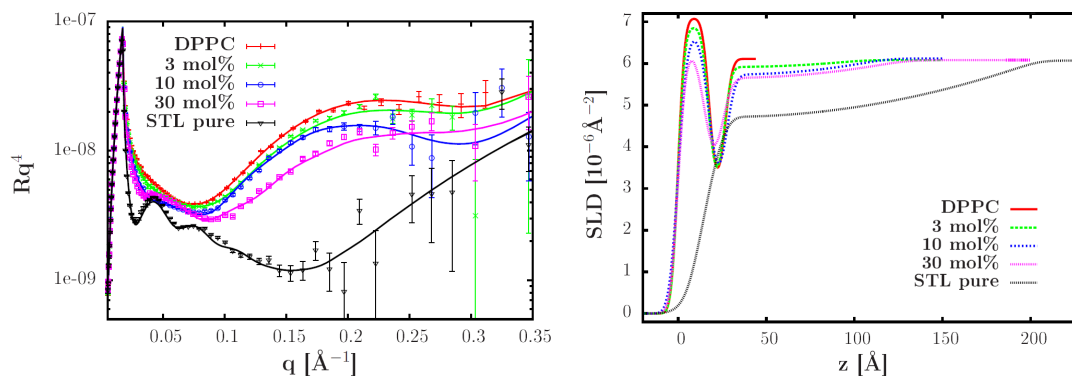


Figure 6.25: Neutron reflectivity curves (left) and corresponding SLD profiles (right) for STL-6k/DPPC monolayers with different molar ratios STL-6k at $\Pi= 40$ mN/m.

The brush height H and volume fraction ϕ_0 both increase with the polymer surface density controlled by the STL molar ratio (Figure 6.25) and the compression of the monolayer (Figure 6.24). Only for the 30 mol% mixture a smaller brush is found for higher surface pressures, probably due to loss of some of the STLs into the subphase for high compressions. Also for surface pressures between 10 - 20 mN/m (above the desorption transition of the polymer and below the LE-LC phase transition of DPPC) polymer brushes are observed. This demonstrates that the STL is also well anchored in LE phase DPPC and that the desorption of the polymer is independent from the phase state of DPPC.

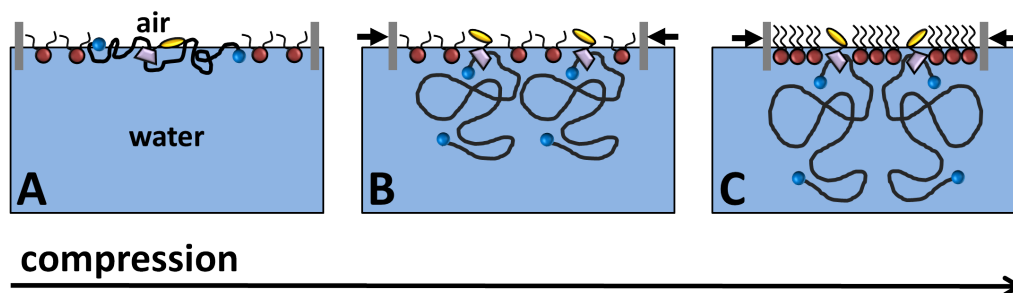


Figure 6.26: Schematic representation STL/DPPC film during compression: A. Monolayer for Π below desorption transition, B. above desorption transition and below DPPC phase transition and C. for Π above DPPC LE-LC transition.

As already evidenced by the Langmuir isotherms and complementary IRRAS measurements, the neutron data clearly shows that the STLs are well inserted into phospholipid monolayers and that the PEG chains form a polymer brush. With the obtained structural information we suggest following monolayer structure upon compression, displayed in Figure 6.26. Below the desorption plateau the polymer is adsorbed to the interface. Above the desorption transition a well defined DPPC layer with the incorporated cholesteryl α -

CD anchor of the STL is formed at the interface. Now the PEG chains form a polymer brush, which increases in thickness with STL surface density.

6.2.4 Available surface area per polymer

To investigate the possible dissolution of STL molecules in the subphase, the available polymer surface area A_{iso} , estimated from the isotherms is compared to the area per chain A_n calculated from the neutron data. A_{iso} is obtained using the surface area A from the isotherm and the molar fraction of STL, x_{STL} :

$$A_{\text{iso}} = A/x_{\text{STL}}. \quad (6.1)$$

A_n is calculated from the reflectivity data by integrating the volume fraction profile $\phi(z)$:

$$A_n = \frac{Nv_{EG}}{\int_0^H \phi(z) dz} \quad \text{with} \quad \phi(z) = \phi_0 \left[1 - \left(\frac{z}{H} \right)^2 \right] \quad (6.2)$$

where N is the chain length and $v_{EG} = 61.4 \text{ \AA}^3$ is the volume of an EG monomer [282]. A large difference is obtained between the surface area occupied per STL, calculated from the neutron data A_n and the one calculated from the isotherms A_{iso} . A_n from the different measurements are between 3 - 4 times larger than A_{iso} (Table 6.9). Nevertheless A_n should be the more reliable value since it reflects the actual amount of substance at the interface [282].

As already discussed in section 6.1.1, this discrepancy can be attributed to the loss of material into the subphase during compression. There is indication, that additionally to the loss of PEG without cholesteryl CD anchor, also some of the STL is expelled from the interface. This is manifested in the decreased brush thickness for high surface pressure found for the 30 mol% STL monolayer. However the question remains if loss of material is the only reason for the large discrepancy between A_n and A_{iso} .

6.2.5 Sliding effect

Sliding mushrooms

As described in section 2.1.4, the sliding ability of the STLs has the greatest impact on the polymer conformation in the mushroom regime. For the used STL-6k we should find the PEG tethers in mushroom regime, when the available surface area per polymer fulfills the criterion $A \geq R_F^2$ ($R_F^2 \approx 5000 \text{ \AA}^2$). Thus, attempting to fit data with STL ratio larger than 3 mol% ($A < R_F^2$) with the sliding model, results in very bad fits. Fitting the data for the mixed STL/DPPC monolayer with 3 mol% STL, where $A \geq R_F^2$ holds, gives almost as good results with the sliding model (Figure 6.27). Thus the polymer concentration profile can be described by both the sliding and the brush model.

This suggests, that for 3 mol% STL the PEG chains are in an intermediate regime between non-interacting sliding mushroom and brush configuration. Hence smaller STL ratios would need to be tested with polymer densities low enough to unambiguously find the tethers in mushroom regime. However we find that already for the 3 mol% STL film, the impact of the polymer tether on the scattering curves is small close to the detection limit. Thus lower STL ratios should even lead to a weaker contrast of the PEG

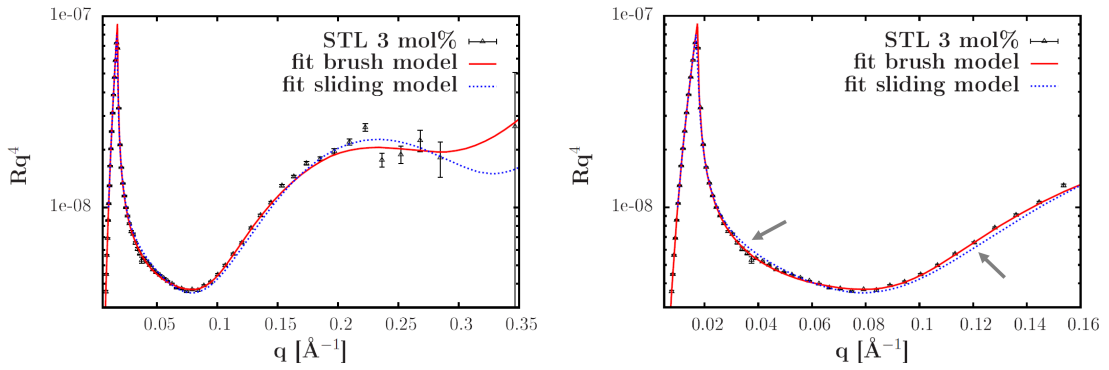


Figure 6.27: Comparison between fits using the sliding model and the parabolic model for the STL 3 mol% monolayer at 40 mN/m. On the left the whole curve and on the right a zoom into the q -range between 0 - 0.16 \AA^{-1} . The arrows highlight the regions where the sliding model reproduces the data with slightly less quality than the parabolic profile.

layer. Therefore it would be difficult to draw any meaningful conclusions about the PEG conformation under the applied experimental conditions.

Sliding brushes

For the brush regime the theory of sliding grafted monolayers predicts, that they behave like normal brushes, which are described by the mean field theory. In this case the brush height H scales linearly with $\sqrt{\phi_0}$ (equation (2.17)), as demonstrated in section 2.1.4. The relation also holds if material is lost into the subphase since H and ϕ_0 are only dependent on the actual polymer density. Figure 6.28 displays the scaling between brush height H and $\sqrt{\phi_0}$ for all curves, measured above the desorption transition and successfully fitted with the parabolic profile.

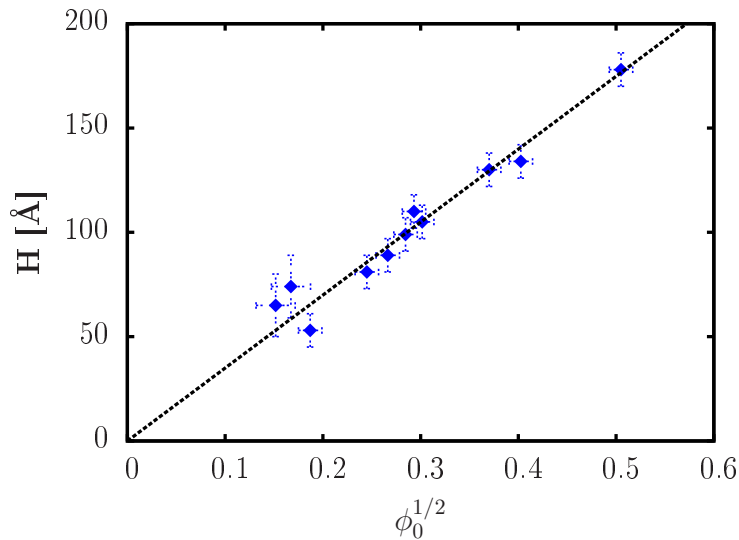


Figure 6.28: Scaling of the brush height H on $\sqrt{\phi_0}$. The dashed line represents the best linear fit. The plotted data can be found in Table 6.9.

Within the error bars all points follow the scaling predicted by the mean field theory. Thus this is a good proof, that in the brush regime the sliding ligands indeed behave very similar to terminally grafted polymers. Furthermore this is in good agreement with results

for pegylated lipids of similar MW [282].

6.3 Sliding tethered ligand receptor interactions

We have performed force measurements with a SFA to probe the sliding tethered ligand - receptor interactions between a membrane modified with STL-10k with two adamantane ligands as end-caps (STL-Ada), and a second opposite membrane modified with cholesteryl β -CD as receptor (Figure 6.29).

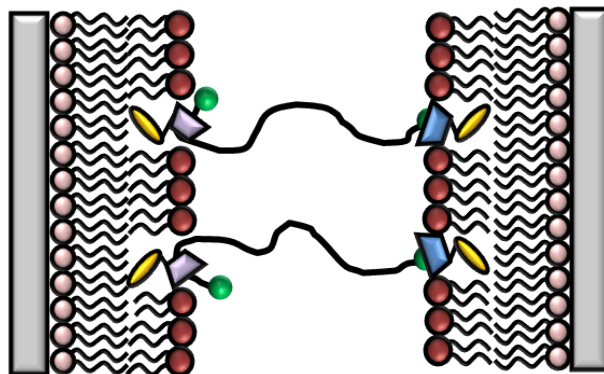


Figure 6.29: Schematic illustration of the STL - cholesteryl β -CD ligand-receptor interaction.

Adamantane/ β -CD inclusion complexes are well studied with an association constant $K_a \approx 5 \cdot 10^4 \text{ M}^{-1}$, or corresponding energy per bond $E_{ad} \approx 10k_B T$ [245].

6.3.1 Sample architecture

Sample composition

In order to understand the effect of the different elements that contribute to the STLs, we have conducted several experiments between supported bilayers with different molecular configuration. The schematic sample architecture is displayed in Figure 6.30.

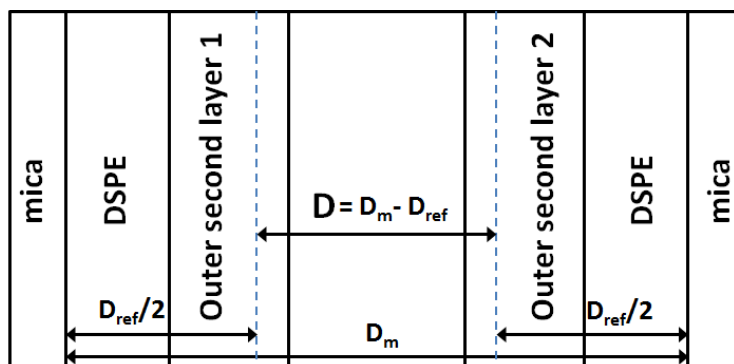


Figure 6.30: Schematic illustration of the sample architecture at contact. D_{ref} is the thickness of two bilayers DSPE-DPPC to which the thickness D is referenced. The dashed line represents the single DSPE-DPPC bilayer thickness $D_{ref}/2$.

The monolayer close to the mica substrate is always made from DSPE. The composition of the outer monolayer for each bilayer is specified in detail in Table 6.10. At first force curves between a DSPE/DPPC bilayer on one surface and a DSPE-DPPC/STL bilayer

on the other surface is measured. Then the force profile between a DSPE/DPPC bilayer and a DSPE-Chol- β -CD bilayer is determined. Both experiments serve as reference to characterise any non-specific interactions. Furthermore force profiles are recorded between a DSPE-DPPC/STL bilayer on one surface and another one with a DSPE-DPPC/Chol- β -CD bilayer in order to study ligand - receptor interactions between those samples. Two experiments are performed with different surface concentrations of STL and Cholesteryl β -CD, respectively.

Experiment	outer second layer bilayer 1	outer second layer bilayer 2
β -CD-ref	DPPC	DPPC/Chol- β -CD 90:10
STL-ref	DPPC	DPPC/STL-Ada 95:5
β -CD/STL 1	DPPC/Chol- β -CD 90:10	DPPC/STL-Ada 94:6
β -CD/STL 2	DPPC/Chol- β -CD 95:5	DPPC/STL-Ada 97:3

Table 6.10: Composition of the outer second layer in the investigated bilayer as displayed in Figure 6.30. The ratios for the mixed monolayers are given in mol%.

Isotherms

The bilayers have been transferred on the mica substrates by Langmuir Blodgett deposition. The isotherms of the mixtures used to prepare the bilayers are displayed in Figure 6.31. The cholesteryl β -CD/DPPC isotherms are shifted to larger surface areas according to the cholesteryl β -CD ratio (Figure 6.31 A). They exhibit the typical plateau corresponding to the LE-LC phase transition of DPPC. At deposition surface pressures of $\Pi = 30$ mN/m the DPPC is expected in LC state.

The STL-10k-Ada isotherms are very similar to the ones already shown in section 6.1.1, which indicates that the different stopper has no influence on the amphiphilic properties of the STL (Figure 6.31 B).

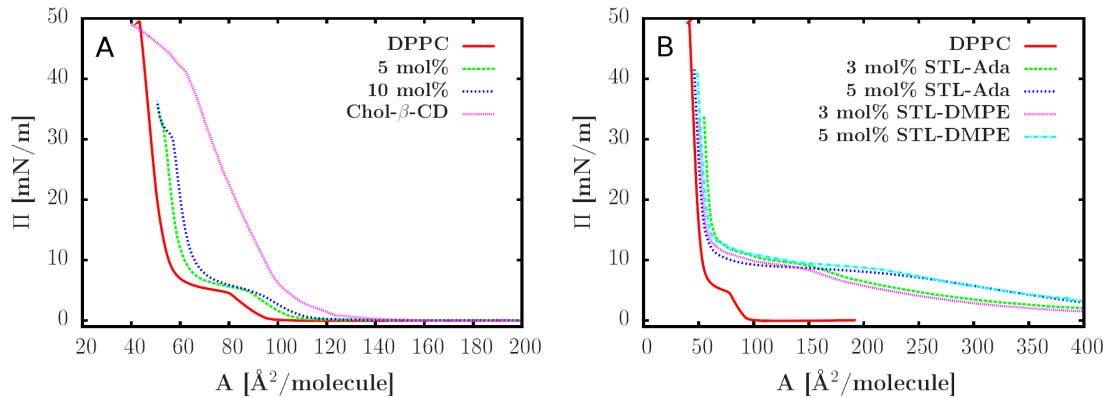


Figure 6.31: A. Isotherms for Cholesteryl β -CD/DPPC mixtures and B. STL-10k-Ada/DPPC mixtures (in comparison to STL-10k with DMPE cap) used to prepare the bilayers measured with SFA.

The surface area per PEG chain A_{iso} calculated from the isotherms corresponds to 2000 and 1000 \AA^2 for the 3 mol% and 6 mol% STL samples, respectively ($A \approx 60$ \AA^2 and using equation (6.2)). As discussed in section 6.2 the actual available surface area per STL might be considerably larger. But already for 3 mol% STL-6k mixtures polymer brushes have been evidenced by neutron scattering (see section 6.2). Thus the polymers

are expected to be in the brush regime at the chosen STL ratios and deposition surface pressures of $\Pi = 30$ mN/m.

6.3.2 Force profiles

To provide better statistics, the positions between crossed cylinders have been changed at least three times recording three independent force measurements. Furthermore several approach and retract runs have been performed for the same sample position. The uncertainties for the different parameters extracted from the force curves have been calculated from the different runs. All force profiles are plotted as normalised force F/R (force normalised with respect to the mean radius of curvature R of the fused silica cylinders determined individually for each experiment) vs the separation D . D is defined as

$$D = D_m - D_{ref}, \quad (6.3)$$

where D_m is the separation calibrated with respect to the bare mica surfaces, obtained from the raw data and D_{ref} the thickness of two pure bilayers DSPE-DPPC ($D_{ref} = 9.6$ nm), measured in preliminary experiments (see Figure 6.30). This definition is useful since we are mainly interested in the gap thickness between bilayers, which reflects the polymer contribution for small separations. The uncertainty in measured forces is typically $\pm 10\%$ and the surface separation can be determined with an accuracy of ± 2 Å. For each sample the contact distance D_0 is determined by the onset of the very steep repulsive barrier due to the steric wall. The thickness of the modified bilayer L_x at full compression then amounts to

$$L_x = D_{ref}/2 + D_0. \quad (6.4)$$

The convention is that the loading force F_c should never be higher than 10 mN/m. Artifacts occur for higher loads due to deformation of the glue used to attach the mica on the fused silica cylinders. For sample β -CD-ref $F_c > 1$ mN/m do not result in significant further change of D_0 . However for the polymer samples D_0 might be inflicted with an error of ± 1 nm when comparing D_0 obtained for maximum loads presented in the curves with D_0 measured for $F_c \approx 5$ mN/m.

Forces between a DSPE-DPPC and a DSPE-DPPC/Chol- β -CD bilayer

The surface force profile for experiment β -CD-ref (Table 6.10) is shown in Figure 6.32. A long range electrostatic repulsion extends for several hundred nm until a strong steric-hydration repulsion occurs, when the two bilayers are in contact. The contact position D_0 is at 0.2 nm, which shows that the CD contributes to a slightly increased bilayer thickness compared to pure DSPE-DPPC bilayers. Thus using relation (6.4) the thickness of the cholesteryl β -CD bilayer amounts to $L_{CD} = 5.0$ nm.

The withdrawal curve exhibits adhesion and a jump-out at $D_{jump} = 1$ nm. The adhesion can be assigned to van der Waals attraction forces which are very short-ranged $D_{vdW} = D_{jump} - D_0 \approx 0.8$ nm. Using Hooke's law, with the calibrated spring constant $K/R = 0.21 \cdot 10^4$ N/m² and the jump distance $\Delta D \approx 94$ nm we estimate an adhesion force $F_{ad}/R \approx -0.20$ mN/m. Applying the Derjaguin relation ($F/R = 2\pi E$), this amounts to

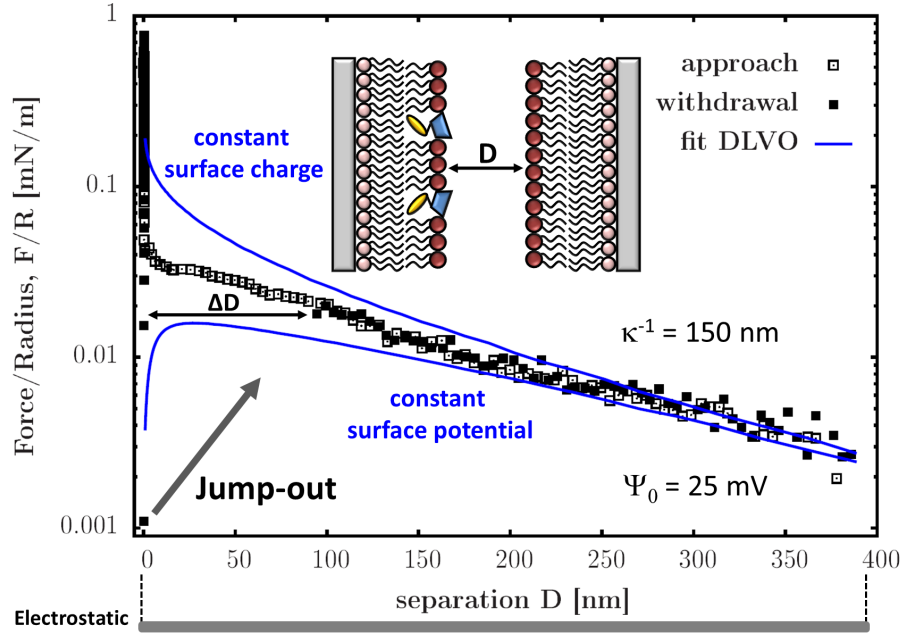


Figure 6.32: Force profile between a DSPE-DPPC and a DSPE-DPPC/Chol- β -CD bilayer. The blue lines represent the boundary conditions at constant surface charge (upper curve) and constant surface potential (lower curve) of the fit.

an adhesion energy $E \approx 31 \mu\text{J}/\text{m}^2$. The profile and short ranged van der Waals adhesion force is comparable to the one measured previously for pure lipid bilayers [284]. After the jump-out the approach and attraction curve are completely reversible.

The solid lines in Figure 6.32 represent the theoretical force obtained by a numerical DLVO calculation, fitting the long-range (large-distance) parts of the curves. The electrostatic component is obtained by numerical solutions of the nonlinear Poisson-Boltzmann equation under constant surface charge σ_0 or constant surface potential ϕ_0 boundary conditions and applying the dielectric constant of pure water, $\epsilon = 78.4$. The attractive van der Waals force is obtained with a non-retarded Hamaker constant $A_{121} = 1 \times 10^{-20} \text{ J}$. As expected for a pure water subphase in equilibrium with dissolved CO_2 , confined between two lipid layers, coating mica semi-finite substrates, the best fit is obtained for very low surface potential $\psi_0 = 25 \text{ mV}$ and very large screening length $\kappa^{-1} = 150 \text{ nm}$ [285]. Important parameters from the force curve are summarised in Table 6.11.

sample	D_0 [nm]	L_{CD} [nm]	D_{jump}	ΔD	F_{ad} [mN/m]	E [$\mu\text{J}/\text{m}^2$]
β -CD-ref	0.2 ± 0.2	5.0 ± 0.2	1.0 ± 0.2	93.6 ± 1	0.20 ± 0.02	31 ± 3

Table 6.11: Important parameters from the force curve of sample β -CD-ref.

Forces between a DSPE-DPPC and a DSPE-DPPC/STL-10k-Ada bilayer

The measured force curves for experiment STL-ref with one bilayer modified with 6 mol% STL-10k-Ada are displayed in Figure 6.33. The force profiles are significantly different from the ones described above. Here no adhesion is observed, only a long range electrostatic repulsion as surfaces are approached and a steric repulsion when the polymer layer is compressed. At full compression we measure $D_0 = 3.7 \text{ nm}$. Since the separation D is

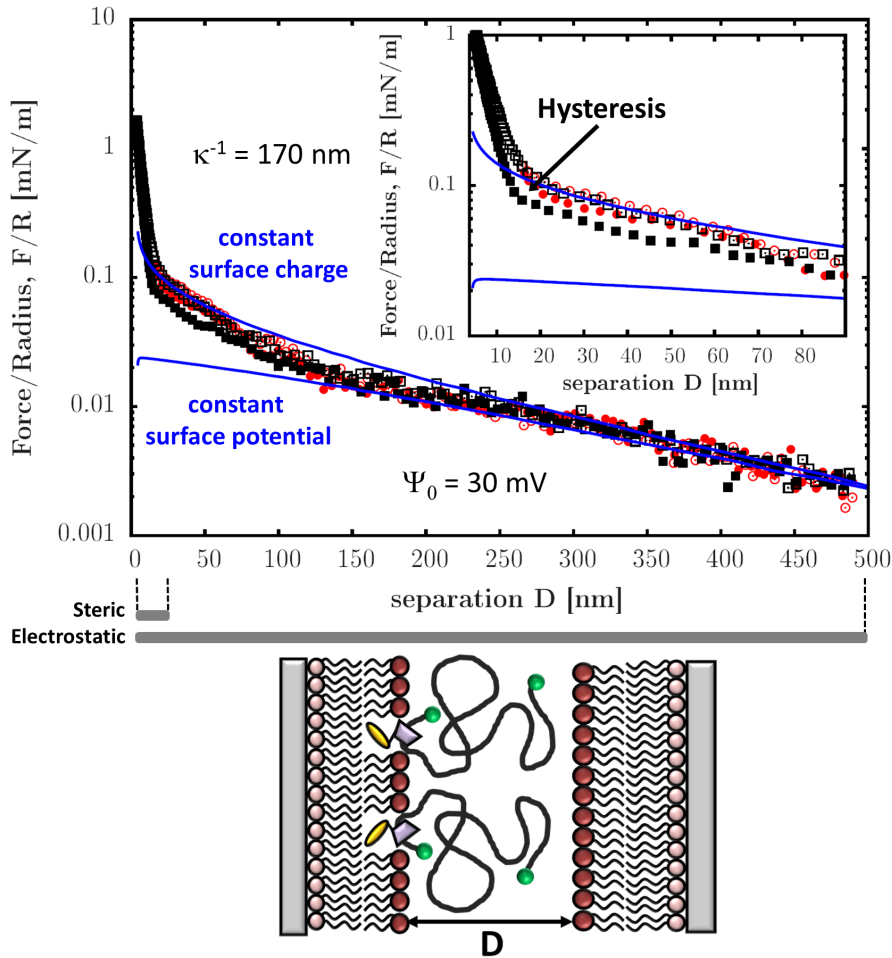


Figure 6.33: Force profiles between a DSPE-DPPC and a DSPE-DPPC/STL-10k-Ada bilayer; (○) approach and (●) withdrawal for low F_0 , (□) approach and (■) withdrawal for high F_0 . The zoom in the contact region shows the hysteresis for high F_0 . The blue lines represent the boundary conditions constant surface charge (upper curve) and constant surface potential (lower curve) of the DLVO fit. Below graph: Distance regimes over which each force is significant.

measured with respect to the DSPE-DPPC double bilayer thickness, D_0 reflects the polymer layer thickness at full compression, assuming that the contribution of the cholesteryl α -CD anchor negligible. Using equation (6.4) we find $L_{STL} = 8.5$ nm. Upon withdrawal no adhesion can be observed because the van der Waals attraction is overcome at all separations by the steric and electrostatic repulsion of the polymer chains.

The weak electrostatic repulsion, observed for large separation, approaches the constant surface charge boundary condition below a threshold separation of $D \approx 60$ nm. Similar to the force curves with CD modified bilayers, a very low surface potential and very large screening length ($\psi_0 = 30$ mV, $\kappa^{-1} = 170$ nm) are obtained from the fit. The electrostatic bilayer force, determined by the DLVO fit, can be subtracted from the total measured force. The remaining force is only due to the steric repulsion of the polymer chains (see Figure 6.37). The strong polymeric repulsion due to the confinement of the PEG chains, sets in at a gap thickness $D_{rep} \approx 11$ nm. The study of the polymer compression behavior will be presented in detail in section 6.3.3.

It is noteworthy that there is a detectable hysteresis between the approach and with-

drawal curves in the force profile. The repulsive force measured upon withdrawal is less than the one measured during the approach. This hysteresis is smaller for the run stopped right after the inset of the polymer-induced repulsion at $D \approx 10$ nm (Figure 6.32). This phenomenon has been already observed for grafted polymer layers [271, 286]. Proposed explanations involve nonspecific adhesion of PEG to the surface, transformation of the PEG backbone into the less ordered gauche configuration or compression-induced phase segregation [271].

sample	D_0 [nm]	L_{STL} [nm]	D_{rep} [nm]
STL-ref	3.7 ± 1	8.5 ± 1	11 ± 1

Table 6.12: Important parameters from the force curve of sample STL-ref.

Forces between a DSPE-DPPC/Chol- β -CD and DSPE-DPPC/STL-10k-Ada bilayer

In this section we present the force profiles measured between bilayers modified with the STL-10k-Ada ligand and the cholesteryl β -CD, respectively. Figure 6.34 shows two examples of force curves recorded for sample STL-1 at different sample positions. The curves are displayed in a non-logarithmic F/R scale to better visualise the adhesive region. Furthermore a second experiment (STL-2) has been conducted, with halved STL and cholesteryl β -CD concentrations in both bilayers (see Figure 6.36).

Similar to experiment STL-ref, a long-range electrostatic repulsion is observed for both samples, when the surface separation is greater than the polymer brush extension. It approaches the constant surface charge boundary condition already for large separations. For both samples a very low surface potential and very large screening length (STL-1: $\psi_0 = 40$ mV, $\kappa^{-1} = 120$ nm and STL-2: $\psi_0 = 34$ mV, $\kappa^{-1} = 135$ nm) are obtained from the fit.

The electrostatic repulsion is followed by a strong steric repulsion when the polymer layer is compressed. For applied loads > 5 mN/m the separations at full compression are $D_0 = 7.0$ nm and $D_0 = 6.2$ nm for experiment STL-1 and STL-2, respectively (Table 6.13). The polymer induced repulsion sets in at $D \approx 15$ nm for STL-1 and at $D \approx 14$ nm for STL-2 and reflects the different polymer densities in the sample.

Withdrawing the surfaces, a comparable steric repulsion is followed by an adhesive regime which extends to $D \approx 45$ nm until the pull-off occurs (indicated by the arrow in Figure 6.34). In most cases the adhesion has been reversible for subsequent approaches at the same place. The long-ranged adhesion is in contrast to the very short ranged van der Waals attractive forces (< 1 nm) observed for sample β -CD-ref. The adhesion force F_{ad} corresponds to the minimum in the force profile. The minimum is located several nm before the jump-out (perpendicular dashed line in the inlet of Figure 6.34). The jump-out occurs after the turning point to a force regime with a slope of positive sign, as soon as the gradient of the force exceeds the spring constant. This is visualised by the tangent of the force profile close to the jump-out with slope K/R (Figure 6.34).

Figure 6.35 shows different force profiles corresponding to several withdrawals at the same spot for experiment STL-1. The DLVO part of the total force is subtracted from

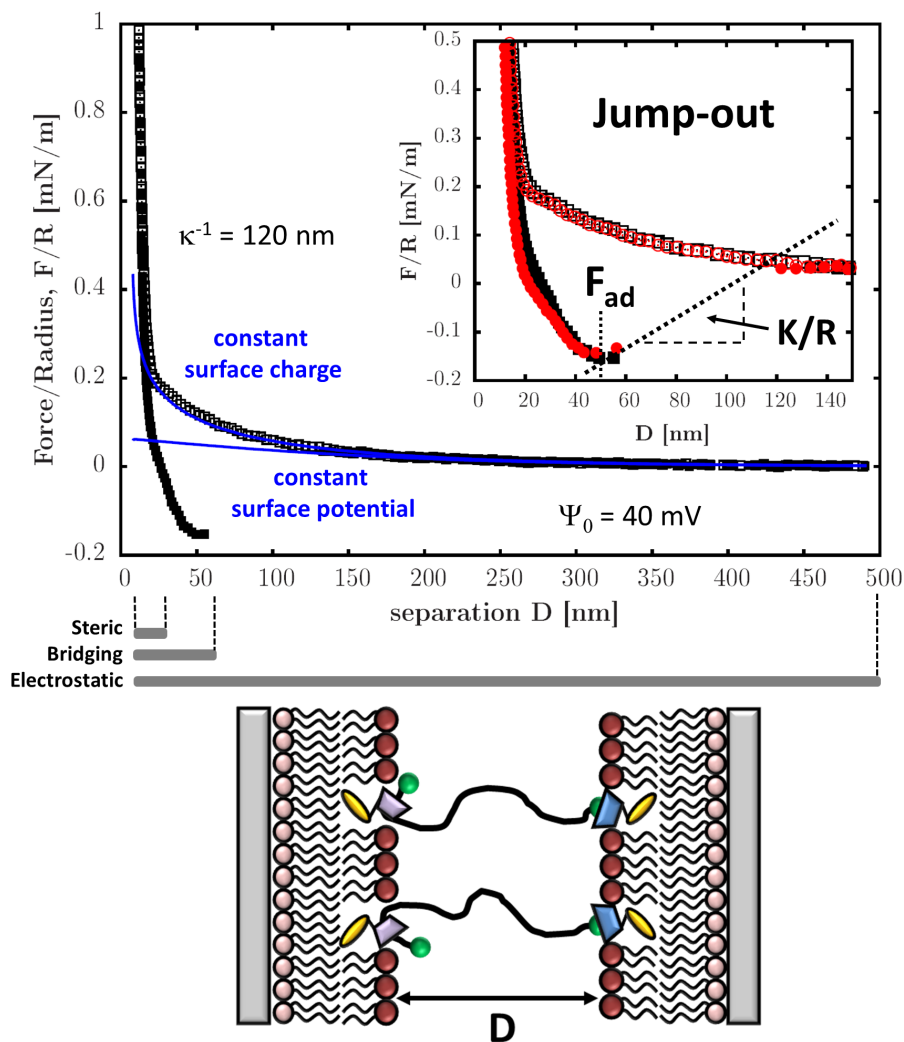


Figure 6.34: Force profiles between a DSPE-DPPC/Chol- β -CD and a DSPE-DPPC/STL-10k-Ada bilayer; (\circ , \square) approach and (\bullet , \blacksquare) withdrawal for two different positions at the sample and similar F_0 . In the big section only one run is displayed for better legibility. The blue lines represent the boundary conditions constant surface charge (upper curve) and constant surface potential (lower curve) of the DLVO fit. The arrow marks the discontinuity in the withdrawal curve due to the instability of the cantilever spring. Below graph: Distance regimes over which each force is significant.

the curves to better visualise the polymer contribution and adhesion force. The return distance D_r is the separation where the approach curve is stopped before withdrawal. D_r is consecutively decreased from $D_r = 20$ nm up to maximum compression at $D_r = D_0 = 7.0$ nm. The contact time before withdrawal has been kept to a few minutes. In some measurements a longer contact time has been used. But no peculiar change on the adhesion value has been observed. For large D_r (20 and 17 nm) find only very small adhesion forces. Hence the gradient of the adhesion force is smaller than the force constant and the whole force profile can be measured. For separations of $D_r = 14$ nm and below a jump-out occurs (indicated by the arrows in Figure 6.35). The adhesion force F_{ad} increases progressively with further approach. But notably the minima of the force profiles where a jump-out occurs can always be found at the same position (see Table Figure 6.35).

Figure 6.36 displays force profiles for experiments STL-1 and STL-2, which have been recorded for identical loads. The separation is normalised with respect to the double

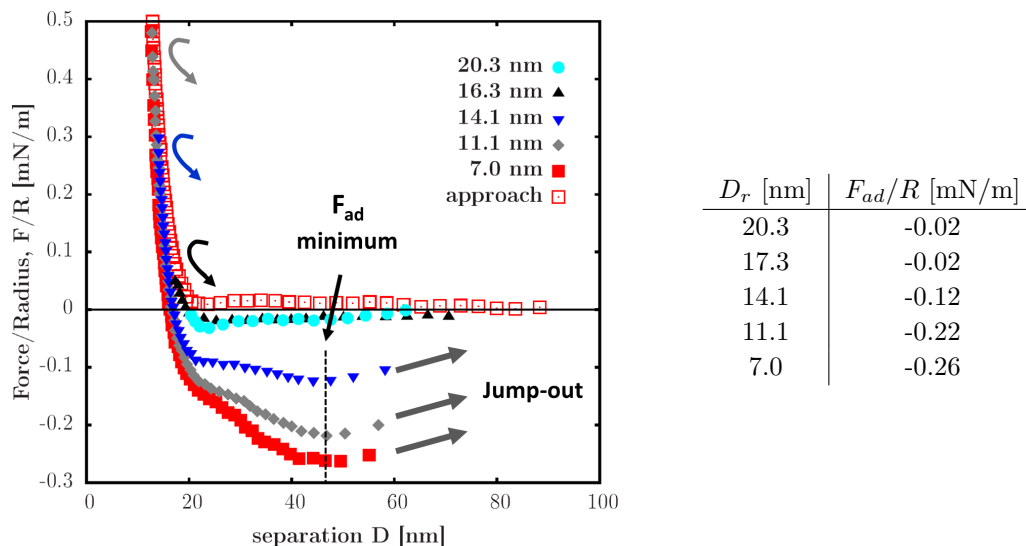


Figure 6.35: Force profiles, after subtraction of the DLVO force, for several withdrawals at the same sample spot consecutively decreasing the return point D_r . Only the approach curve for $D = 7.0$ nm is displayed. D_r and corresponding F_{ad}/R are listed in the table on the left.

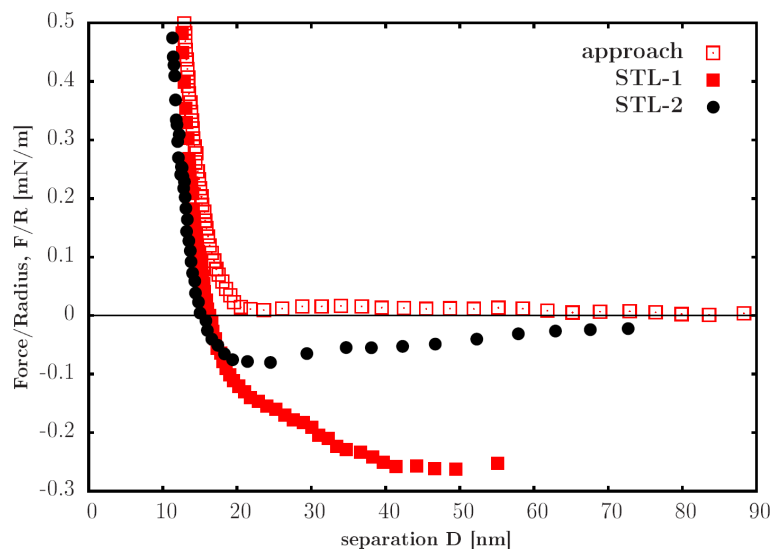


Figure 6.36: Force profiles for experiments STL-1 and STL-2 after subtraction of the DLVO contribution.

bilayer thickness measured for experiment β -CD. The adhesion is much smaller for sample STL-2 with lower STL and cholesteryl β -CD concentration. The force profiles do not exhibit a jump-out and resemble the ones for large return distances in sample STL-1.

6.3.3 Compression behavior

We now compare the compression behavior of the polymer layer in the three STL samples. In order to analyse the approach curves, we use the Milner-Witten-Cates (MWC) theory for the compression of polymer brushes [62, 287] to fit our data. According to the MWC theory the force required for compression of ideal monodisperse polymer brushes is given by following expression:

sample	D_0 [nm]	L_{STL} [nm]	F_{ad}/R [mN/m]
β -CD/STL 1	7.0 ± 1	16.6 ± 1	-0.26
β -CD/STL 2	6.2 ± 1	15.8 ± 1	-0.10

Table 6.13: Important parameters from the force curves at maximum applied load.

$$\frac{F}{R} = 2\pi N^{-4} \left(\frac{k_B T}{a^2} \right) \left(\frac{\pi^2}{12} \right)^2 \left(\frac{H}{a} \right)^5 \left[\frac{H}{D} + \left(\frac{D}{H} \right)^2 - \frac{1}{5} \left(\frac{D}{H} \right)^5 - \frac{9}{5} \right], \quad (6.5)$$

with N the number of monomers ($N = 222$), a the size of the monomer ($a = 3.5 \text{ \AA}$), the separation D and the brush height H , which is related to the polymer density σ by

$$\sigma = \left(\frac{H}{N} \right)^3 \left(\frac{\pi^2}{12} \right). \quad (6.6)$$

It is known however that H is very sensitive to the polydispersity [287]. Therefore we also fit our data using an expression of the MWC theory, which is numerically corrected for polydispersity, like described by Marques et al. [288], applying a polydispersity index $\text{PDI} = 1.25$ (which is in the typical range for the used polymers).

Figure 6.37 shows typical approach curves for the sample STL-ref and the two STL/ β -CD samples in double logarithmic scale. For each curve the DLVO force has been subtracted from the total force. The separation D directly corresponds to the polymer layer thickness upon compression. The dashed lines represent the separation D_0 at onset of the steep repulsive barrier at full compression.

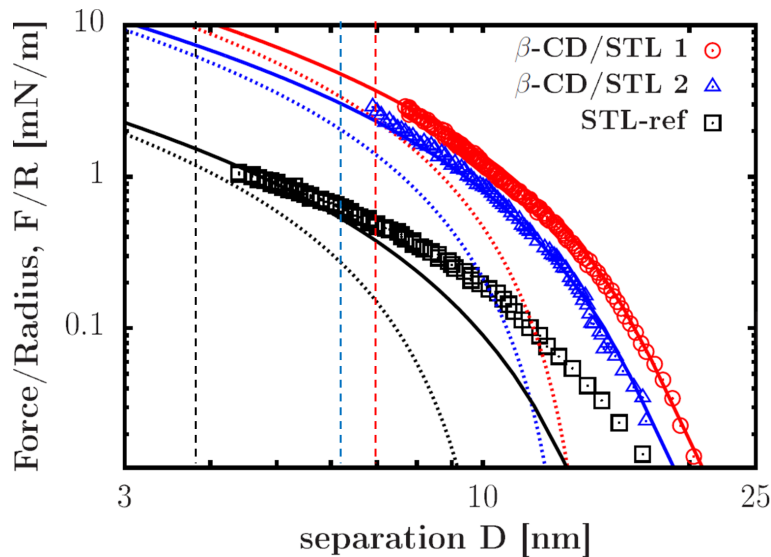


Figure 6.37: Comparison between approach curves for samples STL-1, STL-2 and STL-ref with logarithmic F/R scale. The dashed lines correspond to MWC fits with equation (6.5) for monodisperse polymers. The full lines represent to numerical MWC fits which are corrected for polydispersity ($\text{PDI} = 1.25$).

The dotted lines in Figure 6.37 represent fits using equation (6.5) and the full lines represent numerical MWC fits, which are corrected for polydispersity ($\text{PDI} = 1.25$). Applying the same H for both fits, the monodisperse fits are shifted to the left. Thus not taking into account the polydispersity would lead to an overestimation of H .

For STL-1 and STL-2 very good fits are obtained using $\text{PDI} = 1.25$. For STL-ref the fits deviate for low compressions. This might be caused by the uncertainties in subtraction of the DLVO contribution, which has a great influence on this part of the curve.

The brush height H extracted from the fits, the corresponding surface densities σ (calculated from equation (6.6) and the corresponding available surface areas per PEG A_{SFA} ($A_{\text{SFA}} = 1/\sigma$) are displayed in Table 6.14.

sample	H [nm]	σ [\AA^{-2}]	A_{SFA} [\AA^2]	A_{iso} [\AA^2]
STL-1	14.7	$4.5 \cdot 10^{-4}$	2200	1000
STL-2	13.5	$3.8 \cdot 10^{-4}$	2800	2000
STL-ref	11.0	$1.9 \cdot 10^{-4}$	5400	1000

Table 6.14: Parameters obtained from fitting the SFA approach curves in the polymer compression region after subtraction of the DLVO contribution using the polydispersity corrected MWC theory ($\text{PDI}=1.25$).

Since the brush height H scales linearly with N for identical surface densities, the values can be directly compared to the ones obtained for the neutron experiment (Table 6.9) and they are in good agreement. Similar to the neutron results we find that the surface areas calculated from the isotherms, A_{iso} , are considerably smaller than A_{SFA} , obtained from fitting the force curves.

As expected we find larger H and thus smaller A_{SFA} for STL-1, than for STL-2 with half the amount of STL. Yet instead of A_{SFA} being twice as large as for STL-2 compared to STL-1, we find the surface area only enlarged by the factor 1.25. Furthermore there is a very large discrepancy between H and A_{SFA} of sample STL-ref compared to STL-1. This is unexpected because both samples are prepared with the same STL ratio. The differences observed in H and A_{SFA} are also reflected in the measured separation at full compression D_0 (represented by the dashed vertical lines in Figure 6.37), which are directly related to the amount of material in the gap. D_0 for STL-2 is slightly smaller compared to STL-1. D_0 for STL-ref is by far the smallest.

Thus we obviously deposit less material on the surfaces than expected. Furthermore it seems that the loss of material is larger for deposition of higher STL ratios. Although using the same stock solutions for the samples and applying the exact same deposition conditions, we seem not to be able to exactly control the amount of STL deposited onto the surface. Two main factors may contribute to the discrepancies. At first we certainly lose the polymer fraction without cholesteryl anchor, throughout the isotherm compression prior to the Langmuir Blodgett. Secondly, the Langmuir Blodgett bilayer deposition seems not to be not completely reproducible. Indeed the film deposition in SFA experiments is very delicate since it involves the deposition on curved surfaces and mica sheets which possess different sizes and shapes for each experiment.

Despite the fact that we cannot completely control the amount of STL in the bilayers we clearly evidence dense polymer brushes with H ranging between $1.5 - 2 R_F$. As demonstrated we can estimate the real available surface area per monomer A_{SFA} from the compression of the polymer layer.

6.3.4 Adhesion properties

The observed U-shaped force profile is typical for tethered ligand receptor interactions [17, 57]. The adhesion is generated by the formation of inclusion complexes between the STL's adamantane cap and the cholesteryl β -CD, bridging the two surfaces. Upon withdrawal the tethers are continuously stretched until the bond breakage occurs in the flat part of the interaction profile (Figure 6.34). The observed reversible force profiles show that in our system the rupture of the adamantane/ β -CD bond with its low binding energy of $10k_B T$ is indeed the weakest part in this system.

Adhesion energy

When the two surfaces, linked by tethered ligand receptor bonds are withdrawn, there is a successive buildup of attractive force until the energy required to extend the tethers exceeds the energy of the ligand-receptor bond. Given that the time-scale of the experiment is larger than the typical bond-formation time, the experimentally measured force $F(D)/R$ between two surfaces in SFA experiments is given by

$$\frac{F(D)}{R} = 2\pi\sigma \int_D^\infty \rho(h)f(h)dh, \quad (6.7)$$

where $\rho(h)$ is the fraction of chains bound for a tether extension h , $f(h)$ is the elastic force contribution from each individual chain and $\rho(h)$ the bound fraction of ligand-receptor pairs [58]. Figure 6.38 illustrates the relation between the measured force profile $F(D)$, the elastic force of the chains and bound fraction of chains.

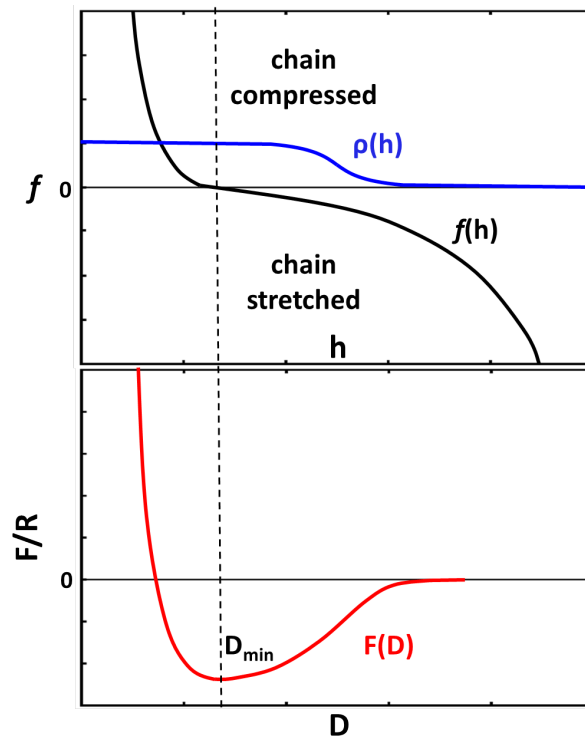


Figure 6.38: Generic representation of the evolution of the measured force $F(D)$ in dependence of the elastic force of an individual chain $f(h)$ of equation (6.7) described by of equation (6.7). The minimum of $F(D)$ occurs when $f(h) = 0$, indicated by the dashed line.

For separations exceeding the minimum of the force profile (dashed line in Figure 6.38), all chains are stretched and the elastic energy per chain $F/(2\pi R\sigma)$ is equal to the adhesion energy of one chain, determined by the ligand - receptor interaction E_{ad} . Then the expected measured adhesion strength can be estimated from

$$\frac{F_{ad}}{R} = -2\pi\sigma\rho E_{ad}, \quad (6.8)$$

where ρ is the fraction of β -CD/adamantane complexes actually formed at the surface. Inserting the relevant values for our experiment ($E_{ad} \approx 10k_B T$, $\sigma = 1/2200 \text{ \AA}^{-2}$) we find $F_{ad}/R \approx 12 \text{ mN/m}$. Compared to the maximum measured $F_{ad}/R = -0.26 \text{ mN/m}$ (6.35) the calculated value is 50x smaller resulting in a bound fraction of ligands $\rho \approx 0.02$. Even when considering the uncertainties of the surface density, this shows that only a small fraction of β -CD/adamantane complexes in the order of 2 - 3 % are formed at the surface. This is considerably smaller compared to $\rho \approx 0.1$ for the system streptavidin/biotin [57].

PEG tether extension

At the minimum of the force profile the force curve of a single chain vanishes (Figure 6.38) [58]. From Figure 6.35 (dashed line) we know that the tether extension is $l = 45 \text{ nm}$ at the minimum of the force profile. The maximum tether extension should be found for distances beyond this minimum. Due to the finite tether length, the maximum chain extension is defined by the interaction energy of the ligand - receptor bond and the number of monomer per chain. Jeppesen et al. [58] have calculated the energy $E(N, x)$ in the region of strong stretching of a PEG chain with finite extensibility for different numbers of monomer N . Using their results we have $E(N_1, x) = N_1/N_2 E(N_2, x)$, where x is the relative extension of the polymer $x = l/L$. For our system adamantane/ β -CD we expect bond rupture for chain stretching energies exceeding $10k_B T$. Comparing their results for a PEG with $N_1 = 142$ ($L = 50 \text{ nm}$ and $l = 21 \text{ nm}$ for $E = 10k_B T$) with our STL-10k ($N_2 = 222$ and $L = 77 \text{ nm}$) we estimate a tether extension $l = 28 \text{ nm}$. This is too small compared to the tether extension at the minimum in the force curve. But again we need to take the considerable polydispersity of the STL tethers into account. Thus the maximum tether extension is certainly underestimated, since the experiment detects the largest masses of the polydispersity distribution. Applying the Flory-Schulz chain length distribution for polymer chains [289] with a typical PDI = 1.25, predicts that 5% of the largest chains have a MW 90% larger than the average. Thus we have to consider that our STL contains chains with at least $N = 400$ ($L = 140 \text{ nm}$). This results in a maximum tether extension $l = 50 \text{ nm}$, which is beyond the minimum of the force profiles. This shows that our measurements are consistent with the expected molecular parameters (PDI = 1.25 and $E_{ad} = 10k_B T$) for our system. In order to quantitatively determine the exact tether extension, numerical modeling of the obtained force curves would be required.

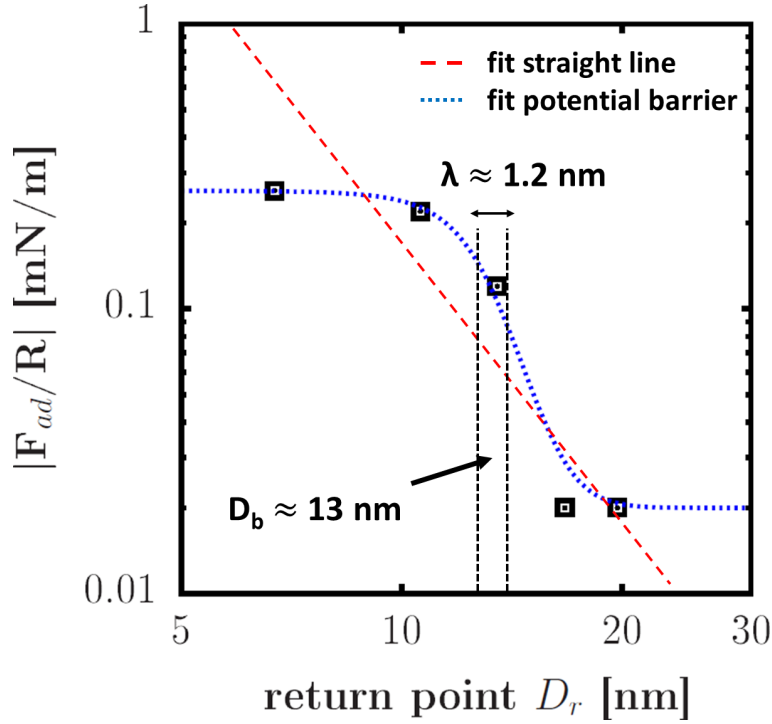


Figure 6.39: Double logarithmic plot of the $|F_{ad}/R|$ in dependence of the return point D_r from the force profiles in Figure 6.35.

Bond formation upon compression

Adhesion forces are only observed for the withdrawal curves, when the surfaces are approached at close contact. They increase successively upon compression (and decrease in D_r). Therefore a considerable activation barrier has to be overcome before ligand-receptor interactions are formed. If one assumes that the polymer is uniformly distributed in the gap between the two surfaces, the available surface concentration c varies as $1/D_r$. Thus if the measured force increases simply with the concentration upon approach of the surfaces, it should follow the relation

$$\frac{F_{ad}}{R} \sim c = \sigma \frac{1}{D_r}. \quad (6.9)$$

Hence a logarithmic plot of F/R vs D_r should give a straight line with negative slope if the increase of adhesion is simply due to the increased surface concentration of ligands. Figure 6.39 shows that the adhesion behavior upon compression is clearly non-linear. Instead the curve is well fitted by an empirical formula inspired from the expected equilibrium distribution between two energy states

$$F(D) = a + \frac{b - a}{1 + \exp\left(\frac{D - D_b}{\lambda}\right)}, \quad (6.10)$$

where a and b are two constants corresponding to the two adhesion regimes, determined by the minimum and maximum measured adhesion force, respectively. D_b corresponds to the threshold separation, where strong adhesion forces set in and λ gives the distance range for which the transition to the strong adhesion regime sets in. We find that the transition from low binding to strong binding regime occurs at a threshold thickness $D_b \approx 13$ nm

in a very narrow range of $\lambda \approx 1.2$ nm. Comparing D_b with the $H = 15$ nm for sample STL-1 shows that strong binding only occurs when the brush is compressed ~ 2 nm which correlates to threshold loading force $F/R = 0.2$ nm.

Our interpretation is that the compressions induces a change in activation energy or number of available binding sites for reaction. On a molecular scale this could be explained by a compression induced change of conformation of the CD moieties, similar to the reorientation of the CD residues observed in section 4, which renders the cavities more accessible for bond formation.

6.4 Conclusion

The in detail study of the monolayer properties, unambiguously proves that the cholesteryl α -CD is suitable for anchoring the STLs at the air-water interface and insertion into DPPC monolayers. For sufficiently high polymer surface densities they form polymer brushes, which follow the scaling laws predicted by the mean field theory. The STL layers resemble conventional grafts fixed with one end to the surface. This is in agreement with the theoretical description for grafts of sliding polymer tethers, where asymmetric chain conformations are predicted for high surface densities. In mushroom regime theory foresees symmetric chain conformations which lead to reduced polymer layer thickness compared to layers fixed at one chain end. The distinct behavior of sliding grafts has not been verified so far due to experimental constraints of the methods used for the STL characterisation. Although the STLs seem to be firmly anchored to the interface a loss of material into the subphase has been evidenced by comparing the polymer surface areas from the isotherms with the ones calculated from the neutron data. On the one hand the loss can be assigned to the polymer fraction without cholesteryl CD anchor present in each of the investigated samples. Yet there are indications, that also STLs might be partly lost during compression. This can only be investigated, when STLs with an exactly defined number of cholesteryl CDs per chain will be available in the future.

Surface force measurements show that supported phospholipid membranes modified with the ligand - receptor pair STL-10k-Adamantane and cholesteryl β -CD give rise to adhesion. Analysis of the approach curves demonstrates, that our surfaces contain dense STL brushes. However it seems that we do not completely control the fraction of STL deposited on the surface.

The force profiles upon withdrawal are typical for tethered ligand - receptor interactions. Due to the polymer tether, the range of the initially short ranged specific adamantane-CD interaction is extended by the length of the fully extended chain. The force profiles correspond well to the expected molecular parameters of the STL-adamantane/ β -CD ligand receptor pair. Only a small fraction in the order of 2 % of the STLs form complexes at the surface. Furthermore a considerable activation barrier for the bond formation has to be overcome by compressing both surfaces before binding occurs. For more detailed characterisation of the STL-CD interactions a quantitative model would be required to describe the force profiles.

6.5 Appendix

Interfacial properties

BAM

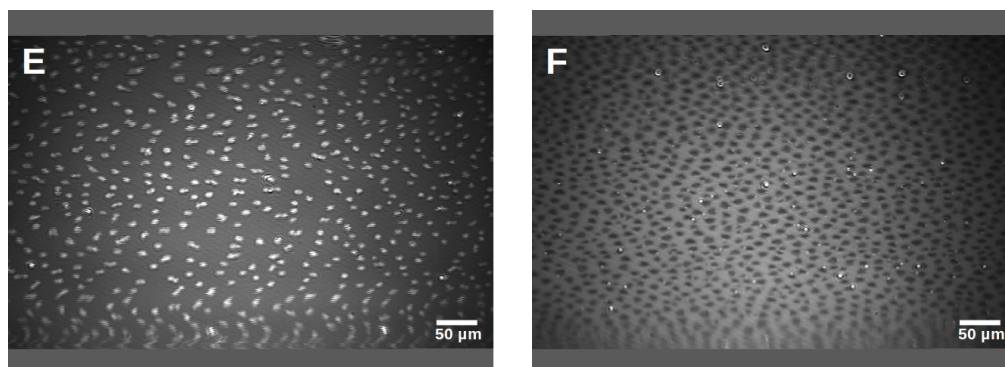


Figure 6.40: BAM images for the mixture 10 mol% STL-6k/DPPC at E. 13 mN/m and F. 30 mN/m

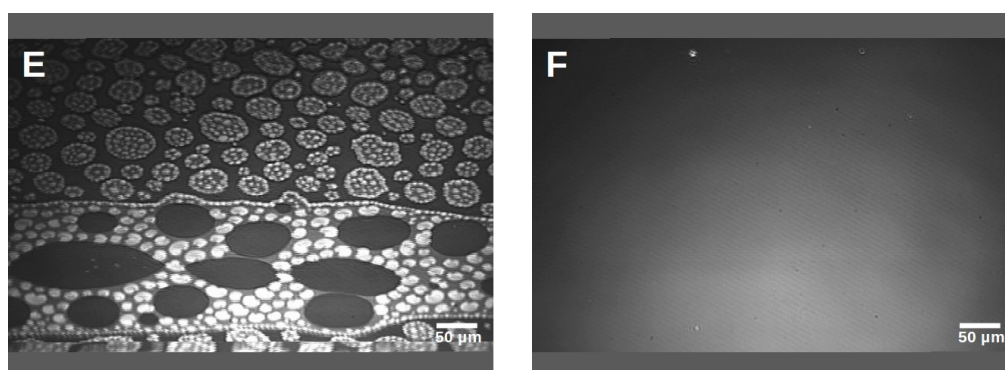


Figure 6.41: BAM images for the mixture 3 mol% PEG-20k-cap/DPPC at E. 9 mN/m, F. 30 mN/m

IRRAS

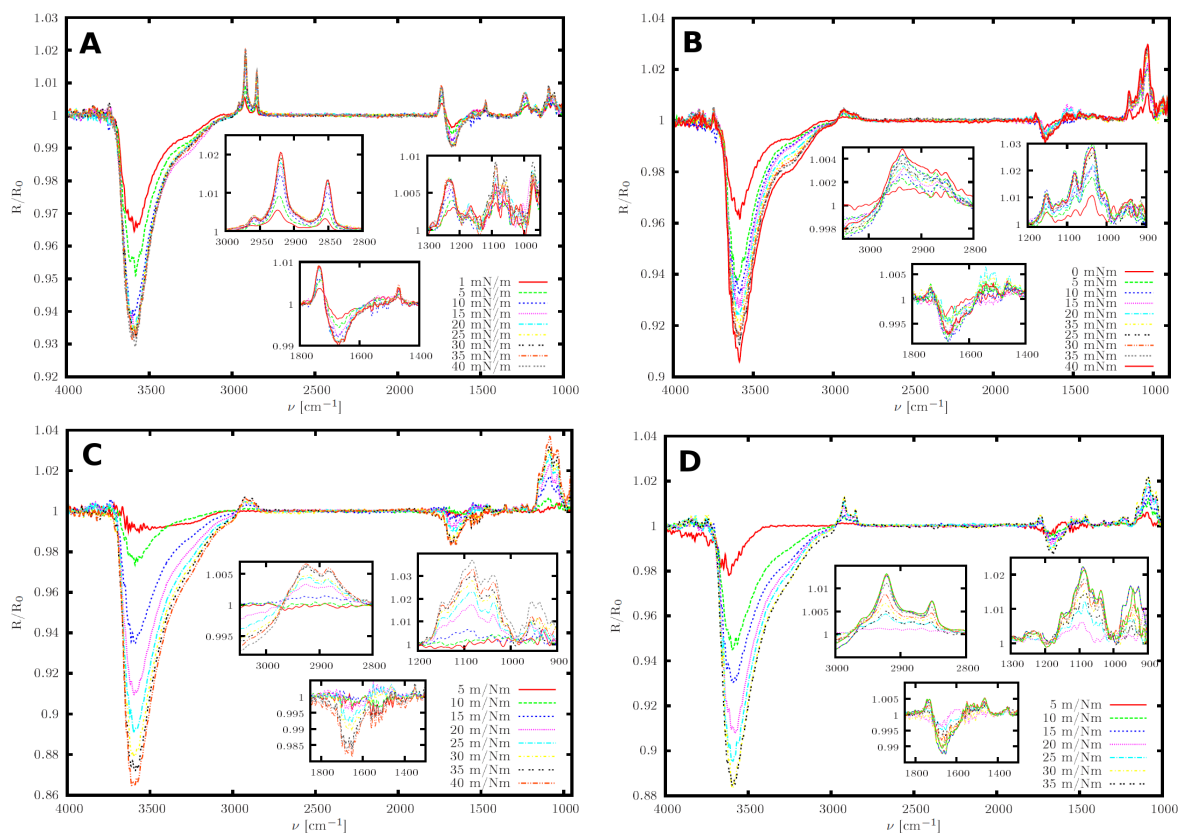


Figure 6.42: IRRAS spectra for monolayers of A. DPPC, B. Cholesteryl α -CD, C. STL-6k and D. 30 mol% STL-6k/DPPC.

Π [mN/m]	pure DPPC		30 mol% STL/DPPC	
	$\nu_{as}CH_2$ [cm^{-1}]	ν_sCH_2 [cm^{-1}]	$\nu_{as}CH_2$ [cm^{-1}]	ν_sCH_2 [cm^{-1}]
1	2924.1	2855.4	-	-
5	2923.1	2852.5	-	-
10	2920.2	2850.8	2924.8	2856.1
15	2920.3	2851.0	2924.4	2854.8
20	2919.8	2850.8	2923.5	2853.9
25	2919.8	2850.7	2922.4	2852.6
30	2919.7	2850.5	2921.8	2852.2
35	2919.5	2850.4	2922.1	2851.7
40	2919.6	2850.7	-	-

Table 6.15: Frequencies shift of asymmetric $\nu_{as}CH_2$ and symmetric ν_sCH_2 stretching vibrations in pure DPPC and 30 mol% STL-6k/DPPC monolayers in dependence of the surface pressures determined by fitting the methylene peak between 3000 -2800 cm^{-1} . The errors are around $\pm 0.2 cm^{-1}$.

Chapter 7

Conclusion

Addressing fundamental challenges that nanotechnology applications face nowadays in the fields of drug delivery and medical diagnostics, this work was aimed at designing and characterizing a new family of polymer spacers for ligands based on topological CD complexes with polymers. Using the concepts of CD-polymer inclusion complexes, with the tools for the chemistry of biorecognition molecules and the manipulation of amphiphile self-assembly, sliding tethered ligands have been obtained, which can be grafted to membranes by a hydrophobic anchor.

In a first step amphiphilic cholesteryl CDs have been investigated, which are suitable candidates as membrane anchors for STLs. In order to understand the effect of the CD, permethylated mono-cholesteryl α -CD (TASC) and its β -CD analogues bearing one (TBSC) and two cholesteryl residues (TBdSC), were studied. Furthermore the CDs with the different number of hydrophobic cholesteryl anchors were compared regarding to the anchoring strength into phospholipid membranes.

It has been demonstrated that TASC, TBdSC and TBSC form stable monolayers. All three compounds undergo a change of conformation indicated by a pseudo-plateau in the isotherm. The plateau is related to a structural change, where the CD residue rearranges from the cavity's axis aligned perpendicular with respect to the surface to an alignment parallel to the surface.

A detailed understanding of the insertion behavior of the amphiphilic cholesteryl CDs into phospholipid membranes has been achieved from macroscopic to molecular scale. Modified bilayers are stable and are subject to a gel-liquid phase transition upon heating. Depending on the compression, full miscibility of the two amphiphiles is observed for low Π and a clear demixing tendency is apparent during compression. Due to their bulky CD moiety, the amphiphilic CDs exhibit a distinct fluidising effect on the membrane. TBdSC with its two cholesteryl residues seems to be best anchored to the membrane compared to its α - and β -CD analogues with only one membrane anchor. A molecular picture of the insertion has been achieved. It has been evidenced that the CD residues partly protrude from the membrane, leaving the CD cavities accessible to form complexes.

Thus cholesteryl CDs are indeed good candidates as membrane anchors for the STLs due to the conformational adaptability and accessibility of their CD cavities, while being inserted into phospholipid membranes.

After having identified the suitability of cholesteryl CDs as membrane anchors, a synthetic pathway for the assembly of STLs has been developed. In particular polyrotaxanes with a very low number of modified α -CDs, threaded on a PEG chain and endcapped with a ligand have been required. Three major synthetic challenges had to be overcome.

At first two new in-situ end-capping techniques in water have been established. The first method uses blocked isocyanates, in particular DMPEPhSO₃⁻. In an alternative approach adamantane carboxylic acid, rendered water soluble by complexation with β -CD, has been coupled to the polymer with the help of the activation agent DMT-MM. Both procedures provide for a high versatility, since they are potentially applicable for any soluble capping molecule in form of an isocyanate or carboxylic acid.

Using the new stoppers a new procedure has been developed allowing the synthesis of polyrotaxanes with azido CDs and limiting the threading ratio to very low numbers of CD per chain. Furthermore a chromatographic method has been established which affords analytical separation of the polyrotaxanes according to their exact number of CDs.

The final product is obtained by attaching a lipophilic anchor to the polyrotaxanes by exploiting a click chemistry approach. Cholesteryl hemisuccinate, functionalised with an acetylene group can be coupled to the azido group via a CuAAC in quantitative yields. Moreover this method is highly adaptable and should be applicable for any kind of molecule functionalised with an acetylene group.

STLs have been synthesised with PEGs of different MW and number of CD anchors. Furthermore the STLs endcapped with adamantane and cholesteryl β -CD provide a suitable tool to probe sliding tethered ligand receptor interactions.

The ability of the polymer tether to slide through the CD ring should translate into a new type of tethered ligand-receptor interactions. Therefore the STLs have been characterised regarding to their membrane insertion properties and ligand-receptor interactions. Due to their cholesteryl α -CD anchor, the STLs are firmly anchored at the air/water interface and readily insert into DPPC model membranes. For sufficiently high polymer surface densities they form polymer brushes, which follow the scaling laws predicted by the mean field theory. In this regime STL layers resemble conventional grafts fixed with one end to the surface. The distinct sliding behavior for low grafting densities could not be unambiguously verified so far due to experimental constraints of the methods used for the characterisation.

Surface force measurements show that supported phospholipid membranes modified with the ligand - receptor pair STL-10k-Adamantane and cholesteryl β -CD give rise to adhesion. Analysis of the approach curves demonstrates, that our surfaces contain dense STL brushes. However it seems that we do not completely control the fraction of STL deposited on the surface.

The force profiles upon withdrawal are typical for tethered ligand - receptor interactions. Due to the polymer tether, the range of the initially short ranged specific adamantane-CD interaction is extended by the length of the fully extended chain. The force profiles correspond well to the expected molecular parameters of the STL-adamantane/ β -CD ligand receptor pair. Only a small fraction in the order of 2 % of the STLs form complexes at the surface. Furthermore a considerable activation barrier for the bond formation has to

be overcome by compressing both surfaces before binding occurs.

In order to get a more complete picture appropriate theoretical models have to be developed which allow quantitative analysis of the force profiles by taking into account the sliding effect of the STLs.

First characterisation of the new class of sliding tethered ligands shows, that they readily insert into phospholipid membranes and give rise to typical tethered ligand-receptor interactions. In order to study these interactions in more detail, there are several improvements to be made regarding the synthesis. To provide STLs with an exactly defined number of CD anchors per chain and a whole range of different PEG spacer lengths, it would be necessary to upscale and refine the chromatographic separation methods. Furthermore STLs with different ligands should be prepared. In this manner a complete tool box of STLs could be obtained in order to investigate the sliding tethered-ligand interactions between ligand receptor pairs of different bond strength, as well as the influence of the tether length. Using different anchor molecules or by directly clicking the polyrotaxanes, all kinds of compounds and surfaces could be modified by STL layers.

A important step towards the development of targeted drug delivery devices based on the new molecules would be to prepare liposomes functionalised with the STLs. They could then be studied regarding to their stability and adhesion properties as well as their suitability to fabricate “stealth “ nanoparticles with new a type of ligand-receptor interactions.

List of Publications

In this section one can find the articles which have already been published using results presented in this thesis.

- A. Klaus, C. Fajolles , **M. Bauer**, M. Collot, JM. Mallet and J. Daillant, “Amphiphilic Behavior and Membrane Solubility of a Dicholesteryl-Cyclodextrin”, *Langmuir*, 2011(27), 7580 - 7586
- **M. Bauer**, C. Fajolles, T. Charitat, H. Wacklin and J. Daillant, “Amphiphilic behavior of new cholesteryl cyclodextrins: A molecular study”, *Journal of Physical Chemistry B*, 2011, DOI: 10.1021/jp205917q
- **M. Bauer**, C. Fajolles, T. Charitat, G. Fragneto and J. Daillant, “Insertion properties of cholesteryl cyclodextrins in phospholipid membranes: A molecular study”, *Soft Matter*, 2012, DOI: 10.1039/C1SM06346D

Amphiphilic Behavior and Membrane Solubility of a Dicholesteryl-Cyclodextrin

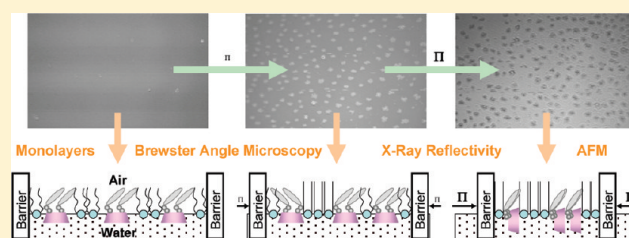
Angelika Klaus,[†] Christophe Fajolles,^{*,†} Martin Bauer,^{†,§} Mayeul Collot,[‡] Jean-Maurice Mallet,[‡] and Jean Daillant^{*,†}

[†]UMR 3299 Commissariat à l'Énergie Atomique et aux Énergies Alternatives (CEA)/Centre National de la Recherche Scientifique (CNRS), SIS2M, Laboratoire Interdisciplinaire sur l'Organisation Nanométrique et Supramoléculaire (LIONS), CEA Saclay, 91191 Gif sur Yvette, France

[‡]UMR 7203, Laboratoire des BioMolécules, 24 Rue Lhomond, 75005 Paris, France

[§]Institut Charles Sadron, ICS(UPR22-CNRS) 23 rue du Loess, 67034 Strasbourg, France

ABSTRACT: Amphiphilic cyclodextrins (CDs) are good candidates to functionalize natural membranes as well as synthetic vesicles. In this paper, we provide a full description of the interfacial behavior of pure 6I,6IV-(β -cholesteryl)succinylamido-6I,6IV-(6-deoxy-per-(2,3,6-O-methyl))cycloheptaose (TBdSC) and how it inserts in dipalmitoyl-L- α -phosphatidylcholine (DPPC) monolayers as a membrane model. Langmuir isotherms of pure TBdSC suggest a reorganization upon compression, which could be clarified using X-ray reflectivity. The CD head can adjust its conformation to the available area per molecule. A compatible model involving a rotation around a horizontal axis defined by the two selectively substituted glucose units is proposed. The in-plane structure is characterized at all scales by Brewster angle microscopy (BAM) on the water surface and atomic force microscopy (AFM) on monolayers deposited on solid substrates. The same tools are used for its mixtures with DPPC. We show in particular that TBdSC seems to be soluble in the liquid-expanded DPPC. However, phase segregation occurs at higher pressure, allowing for sequentially liquid-condensed DPPC and high-pressure conformation of TBdSC. This gives rise to a remarkable contrast inversion in both imaging methods.



1. INTRODUCTION

Cyclodextrins (CDs) are natural cyclic oligosaccharides obtained by enzymatic digestion of starch. Their truncated conical shape is created by the α -1,4-glycosidic link between D-(+)-glucopyranosyl units (glucose). The consequence is that CDs have a hydrophilic exterior and a hydrophobic cavity, because of the inward-directed H3 and H5 atoms of the glucose units (Figure 1) and the interglycosidic oxygen atom. The three main members of the CD family are composed of six, seven, and eight glucose units and are known as α -, β -, and γ -CD.¹

These inside–outside amphiphilic molecules are commonly known and used for their ability to form inclusion compounds.² Applications are numerous and well-documented, mainly in the pharmaceutical and nutritional fields. Their cyclooligomeric structure makes them convenient platforms with a geometry defined by the chosen CD.^{3–6} This symmetrical oligomeric nature, however, brings trouble for synthetic chemists trying to perform controlled transformations of, e.g., 1 hydroxyl group among 21 as for β -CD, and even more trouble for a second one among the remaining 20. Modifying CDs was primarily intended to tune inclusion capacity and solubility of the CDs and their inclusion compounds. Nevertheless, amphiphilically modified CDs have also attracted attention for decades⁷ in an effort to control supramolecular assemblies of CDs. These modifications are mainly restricted to uniformly modified or statistically described mixtures or monosubstituted CDs.⁸

Nowadays, easy access to well-defined permethylated 6A,6D-dihydroxy- and diamino-6A,6D- β -CD^{9,10} prompted us to obtain new insight into amphiphilic CDs from pure disubstituted CDs. Thus, we recently described the synthesis of new β -CD derivatives bearing two grafted cholesterol and preliminary results on the amphiphilic behavior.¹¹

Cholesterol was chosen because monocholesteryl CDs have already been described.^{12,13} Furthermore, cholesterol has also been reported as a convenient membrane-anchoring medium.^{14,15}

Two substitutions were intended to bring double anchoring, allowing for the CD cavity to turn its large rim to open while retaining a good flexibility.¹⁶ It should also preclude, in monolayers, auto-inclusion phenomena specific to permethylated monosubstituted CDs.^{17,18}

Here, we describe the amphiphilic behavior of the pure 6I,6IV-(β -cholesteryl)succinylamido-6I,6IV-(6-deoxy-per-(2,3,6-O-methyl))cycloheptaose, reduced to TBdSC (Figure 1), as a Langmuir monolayer and how it inserts in dipalmitoyl-L- α -phosphatidylcholine (DPPC) monolayers as a membrane model.

Preliminary experiments¹¹ have shown two main features. At first, this compound is able to make stable monolayers in a pure form. Second, it is able to insert into phospholipid DPPC

Received: March 7, 2011

Revised: April 28, 2011

Published: May 19, 2011

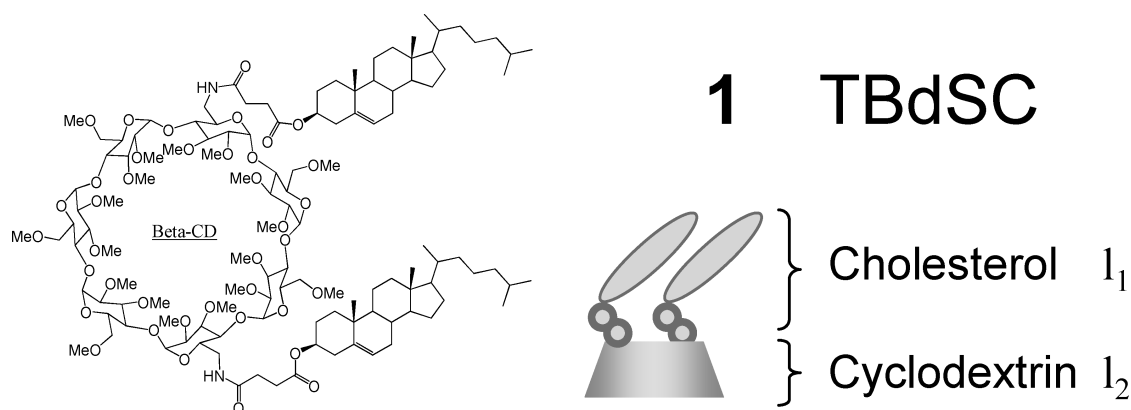


Figure 1. TBdSC acronym stands for compound 1 trivial name trimethyl- β -CD-disuccinyl-cholesterol.

monolayers as well as bilayers. Specific features observed, such as segregation properties toward phospholipids with monocholesteryl-native CDs^{12,19} or surfactant properties of methylated CD amphiphiles,^{20,21} led us to study monolayers of the new dicholesteryl-permethylated CD derivative in detail.

In this paper, we fully describe the interfacial behavior of pure TBdSC and its mixtures with DPPC. Compression isotherms suggest a reorganization upon compression. This is shown by X-ray reflectivity measurements to consist in a reorientation of the CD moiety, whose axis rotates from perpendicular to parallel to the water surface. The in-plane structure is characterized at all scales by Brewster angle microscopy (BAM) on the water surface and atomic force microscopy (AFM) on monolayers deposited on solid substrates. We show, in particular, that TBdSC is fully miscible in fluid DPPC; however, demixing occurs in gel DPPC.

2. EXPERIMENTAL SECTION

2.1. Chemicals. DPPC, chloroform (stabilized with ethanol), and other solvents used for synthesis purposes were purchased from Sigma-Aldrich. Water (18 M Ω) was obtained from a Millipore purification system.

2.2. Synthesis. TBdSC was prepared as previously described from permethylated diamino- β -cyclodextrine.¹¹ As a reference, the mono-substituted analogue TBSC was prepared in the same manner from permethylated monoamino- β -cyclodextrine.

2.3. Preparation of Spreading Solutions. Lyophilized amphiphiles were dissolved in chloroform and stored at +4 °C. Concentrations are 1.186 mM DPPC and 74.45 μ M TBdSC. The 33 mol % TBdSC–DPPC mixture was prepared with 1.000 mL of TBdSC and 0.126 mL of DPPC stock solutions.

2.4. Formation of Langmuir Monolayers and Isotherms. Langmuir films at the air–water interface were prepared on a Langmuir–Blodgett trough (Micro-Processor Interface IU4, NIMA Technology) equipped with a Wilhelmy filter paper plate. The trough was placed on an anti-vibration table with plastic covers for isolation in a closed environment, to avoid dust exposure. Using a Hamilton microsyringe, the required solution was spread on the free water surface and left for a few minutes to ensure complete chloroform evaporation. The temperature was controlled and stabilized by external circulation.

The trough had a total maximum area of 680 cm² and a subphase volume of 500 mL. The spreading volumes were 75, 200, and 150 μ L for DPPC, TBdSC, and the 33 mol % mixture, respectively.

2.5. BAM. Images (480 \times 599 μ m) were taken at the Brewster angle of water with a dedicated microscope (Multiskop, Optrel, Germany).²² Because of the angle between the reflected light and the water surface, only a strip of about 20 μ m is actually in focus. A mechanical translation

of the objective allows for the reconstruction of full images. Resolution is in the micrometer range.

2.6. AFM. Silicon wafers were previously cleaned by the RCA-1 method (H₂O₂–NH₄OH–H₂O).²³ Langmuir films were transferred onto the wafers at different surface pressures by vertical Langmuir–Blodgett deposition. The AFM images of the film were recorded with a Dimension V scanning probe microscope and a NanoScope V controller (Veeco) using the tapping mode in air with a “hybrid head” scanner. Silicon cantilevers, 125 μ m long (Ultraspeed, Micro Marsh), were used with a resonant frequency of 265–400 kHz and a force constant of 20–75 N/m. The radius of curvature is less than 10 nm. The images were typically recorded with scan rates of 0.5–0.7 Hz/line. To minimize artifacts induced by scanner drift and sample deformation, the height profiles were compared to the trace and retrace directions.

2.7. X-ray Reflectivity. X-ray reflectivity²⁴ consists of recording the reflected intensity as a function of the grazing angle of incidence (θ – θ geometry). With this geometry, the wave-vector transfer is normal to the interface. Because the refractive index of matter for X-rays is $n = 1 - (\lambda^2/2\pi)r_e\rho$, where λ is the wavelength (0.154 nm here for Cu K α radiation), $r_e = 2.815 \times 10^{-15}$ m is the Thomson radius of electron, and ρ is the electron density, one obtains access to the electron density profile normal to the interface. The electron density profile of low- and high-pressure TBdSC monolayers on the water surface were determined by X-ray reflectivity using a Siemens powder diffractometer D5000 operated with homemade software.²⁵ The Cu K α radiation is first collimated using 100 μ m slits. A graphite monochromator is placed after the sample in front of the NaI scintillator detector. A homemade Langmuir trough was mounted on the sample stage of the diffractometer and covered with a plastic hood to avoid evaporation and dust exposure. The software allows us to record rocking curves at each point of the reflectivity curve to subtract the background.

3. RESULTS

3.1. Pure TBdSC 1. **3.1.1. Monolayers and Isotherms.** Compression isotherms were recorded at different temperatures from 5 to 30 °C and are shown in Figure 2. The pressure starts to increase at ca. 400 A²/molecule. This is due to the interactions between the large CD headgroups. These isotherms remained similar with an increasing temperature, and no major changes could be observed. A so-called pseudo-plateau or pseudo-transition at ca. 30 mN/m is visible, which will be investigated in more details using X-ray reflectivity, BAM, and AFM. This inflection tends to be more marked with an increasing temperature. At very high pressure, the collapse seems to be announced most likely by a scrambling before multilayer formation, creating a transitory

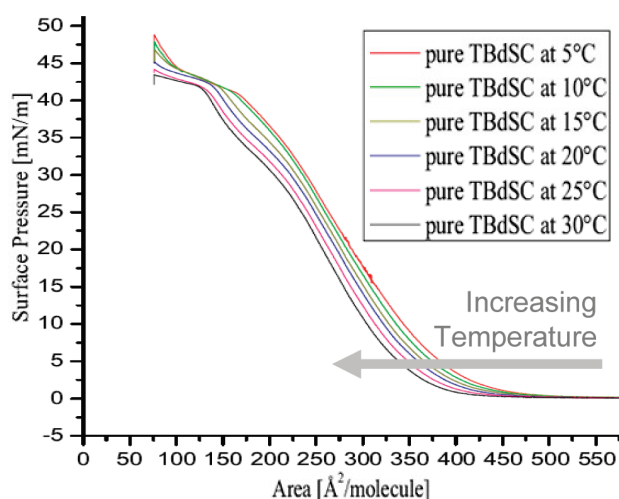


Figure 2. Compression isotherms of pure TbDSC at 5, 10, 15, 20, 25, and 30 °C at the air–water interface as a function of the temperature.

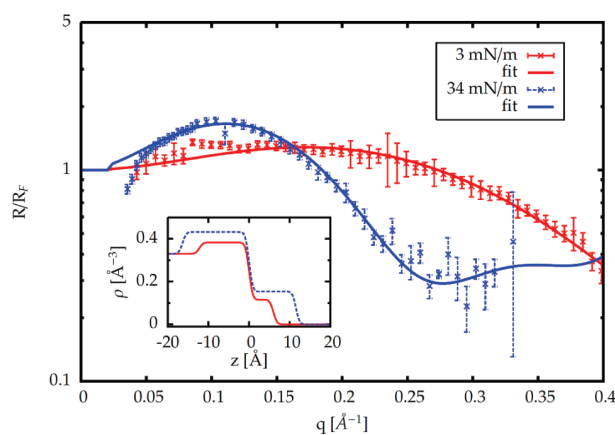


Figure 3. X-ray reflectivity normalized by the Fresnel reflectivity of water for TbDSC at 3 mN/m (red cross, plain error bar) and 34 mN/m (blue cross, dashed error bar) and corresponding best fits using the model described in the text. (Inset) Corresponding electron density profiles.

second plateau. This will not be specifically studied here, but similar behavior was characterized for the TbDSC–DPPC mixture using BAM and AFM.

3.1.2. X-ray Reflectivity. The X-ray reflectivity data were analyzed using a simple model²⁴

$$R = R_F \left| \frac{1}{\rho} \int \frac{\partial \rho}{\partial z} e^{iqz} dz \right|^2$$

where R_F is the Fresnel reflectivity of the air–water interface and q_z ($q_z = 4\pi \sin \theta / \lambda$, where θ is the grazing angle of incidence and λ is the wavelength) is the wave vector transfer (normal to the interface). $\rho(z)$ is the electron density at height z , which has to be determined and ρ_w is the electron density of water. To analyze the data, we assumed that the electron density profile consisted of two homogeneous slabs of constant electron density (Figure 3).

Table 1. Fitting Results from X-ray Curves of TbDSC, Using a Two Layer Model, with Layer 1 Close to Air and Layer 2 Close to Water

Π (mN/m)	ρ_1 ($e^-/\text{Å}^3$)	l_1 (nm)	ρ_2 ($e^-/\text{Å}^3$)	l_2 (nm)	roughness (nm)
3	0.117 ± 0.01	0.60 ± 0.16	0.388 ± 0.02	1.22 ± 0.05	0.1
34	0.156 ± 0.01	1.15 ± 0.1	0.438 ± 0.01	1.64 ± 0.03	0.17

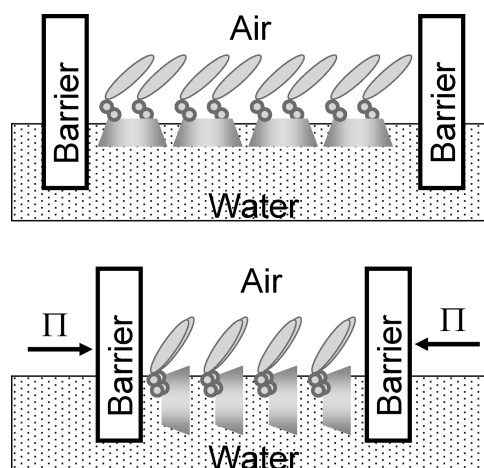


Figure 4. Change in the CD conformation at the isotherm pseudo-plateau according to electron density profile fits.

We first analyzed the pure H_2O (electron density of $0.33 e^-/\text{Å}^3$)–air interface for which R/R_F does not exhibit any feature, as expected.

Because the main objective of these measurements was to elucidate the origin of the pseudo-plateau at 30 mN/m, reflectivity curves were recorded at 3 and 34 mN/m.

Using a two-layer model, good fits for the two surface pressures could be obtained. At 3 mN/m, the model yields $\rho_1 = 0.12 e^-/\text{Å}^3$ and a thickness of 0.60 nm close to air and $\rho_2 = 0.39 e^-/\text{Å}^3$ and a thickness of 1.2 nm close to water. This is in agreement with not too dense TbDSC molecules having their CD moiety close to water and cholesterol pointing to air (Table 1). At 34 mN/m, these values evolve to $\rho_1 = 0.16 e^-/\text{Å}^3$ and a thickness of 1.15 nm close to air and $\rho_2 = 0.44 e^-/\text{Å}^3$ and a thickness of 1.64 nm close to water. This is in agreement with a denser layer, where expulsion of water from the CD layer leads to an increase in electron density. The increase in thickness also implies a reorientation of the CD part, where the cavity axis of CD is now aligned parallel to the interface (Figure 4).

3.1.3. BAM. Brewster angle microscope pictures were taken while recording the compression isotherms to obtain a first characterization of the in-plane film morphology at the micrometer size on the water surface.

At room temperature, aggregates are often visible even before any increase in the pressure. These become bigger and brighter with an increasing pressure (Figure 5). The number of aggregates stays roughly constant upon compression, and the apparent increase in the number on the images is mainly due to the decrease in the area, implying an increase in the concentration.

These aggregates fade away when the water subphase temperature was decreased and were visually absent for temperatures

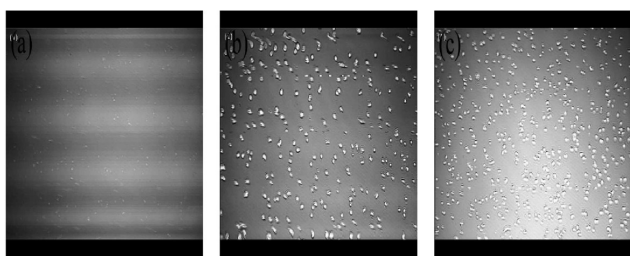


Figure 5. BAM pictures ($480 \times 599 \mu\text{m}$) of TBdSC Langmuir monolayers on water at 20°C and (a) 0 mN/m (left), (b) 21 mN/m (center), and (c) 41.8 mN/m (right).

below 15°C . As mentioned above, their presence does not influence the shape of the isotherms, presumably because only a small number of molecules is involved. The same observations were made for the monocholesteryl analogue, while no aggregates were observed with pure cholesterol monolayers. This temperature effect could be correlated with the inverse solubility coefficient of the methylated CDs.²⁶ However, there are sometimes no aggregates visible at temperatures up to 20°C . This might be explained by the fact that Langmuir monolayers are also known to be dependent upon spreading conditions, e.g., concentration²⁷ or solvent.²⁸

3.1.4. AFM. Langmuir–Blodgett deposition was achieved on hydrophilic silicon wafers, at 20 and 33 mN/m , below and above the pseudo-plateau. A small increase in roughness is observed for the film deposited at 33 mN/m . Figure 6 shows two domains at the same scale for both surface pressures. At first, it appears that domains grow in the horizontal plane. Then, discrete heights of 5 and 10 nm are obtained at a low pressure, and an extra 2.5 nm is obtained at 33 mN/m . The height of compound **1** should be around 2.5 nm with a regular shape. Then, low-pressure steps should correspond to one and two bilayers, which is expected because bilayers should be more stable as a result of the amphiphilic character of the molecules.

Pure TBdSC was also deposited at 43 mN/m (data not shown) as a reference for the high-pressure behavior of DPPC mixtures.

3.2. TBdSC in DPPC Monolayers. As already stated, TBdSC inserts readily in DPPC monolayers. The same experiments were realized with DPPC–TBdSC mixtures from $90:10$ to $10:90 \text{ mol } \%$ with steps of 10% mole fractions.

3.2.1. Monolayers and Isotherms. Compression isotherms were recorded at 20°C for every mixture. Trace of the DPPC liquid-expanded to liquid-condensed phase transition only remains apparent for the $10 \text{ mol } \%$ TBdSC mole fraction mixture at ca. 10 mN/m (Figure 7). The pseudo-plateau is still apparent for all mixtures from 10 to 90% TBdSC mole fractions but at a somewhat higher pressure than for pure TBdSC.

3.2.2. BAM. Related BAM images are displayed in Figure 8.

Image a is reminiscent of the images of pure TBdSC, with small aggregates. In images b–d, starting below the pseudo-plateau, larger domains appear and become brighter. These domains are now reminiscent of the DPPC liquid-expanded to liquid-condensed phase transition.²⁹ The same sequence is observed when a $9 \text{ mol } \%$ solution is deposited, but the domains are much larger according to the DPPC content (data not shown). At a higher pressure, a spectacular contrast inversion occurs in the plateau region. First, contrast completely vanishes at a pressure around 40 mN/m (image e). Then (image f),

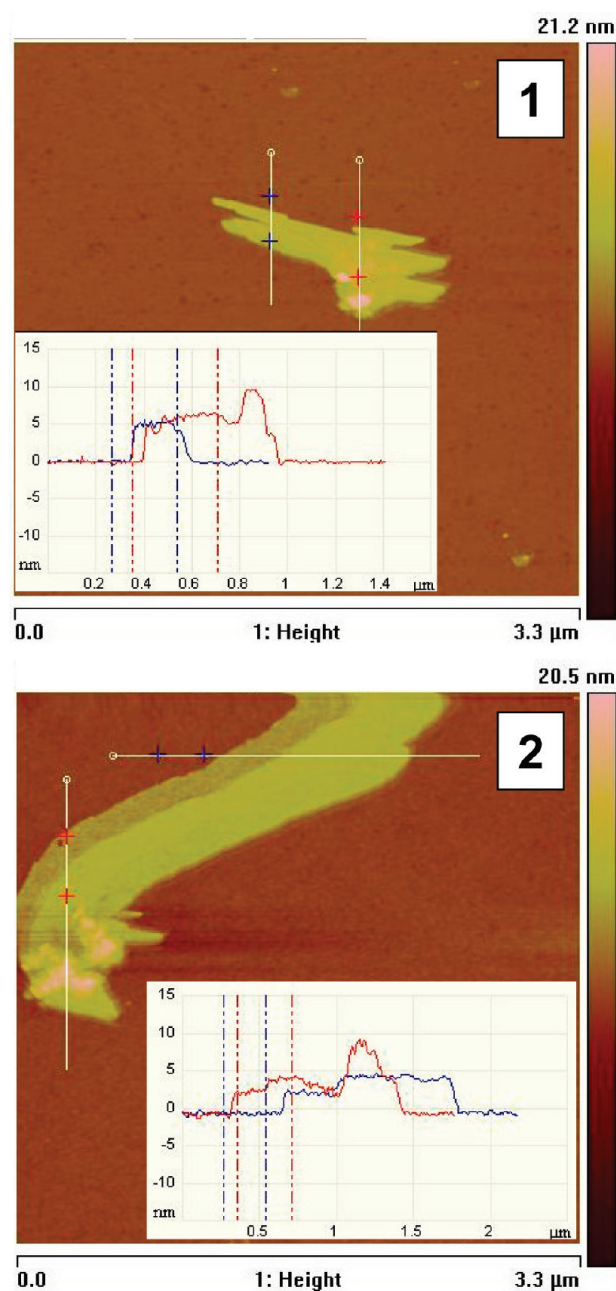


Figure 6. AFM images of TBdSC monolayers deposited at (1) 20 mN/m and (2) 33 mN/m focused on regions containing domains. Sections are taken through domains.

domains appear again with an inverted contrast. Similar features were observed with the monocholesteryl analogue.

3.2.3. AFM. Langmuir–Blodgett wafers were prepared to obtain AFM images of this contrast inversion with a better in-plane resolution. Figure 9 shows the same contrast inversion observed with BAM. Before inversion, the domains are rougher than the surrounding areas. After the inversion, the roughness is inverted as well. The domains are now very flat, while the surrounding areas are rougher comparable to that observed at the same surface pressure for pure TBdSC. While the latter can be foreseen when the pressure comes close to the collapse, the former is more astonishing. It should also be mentioned that the domain size does

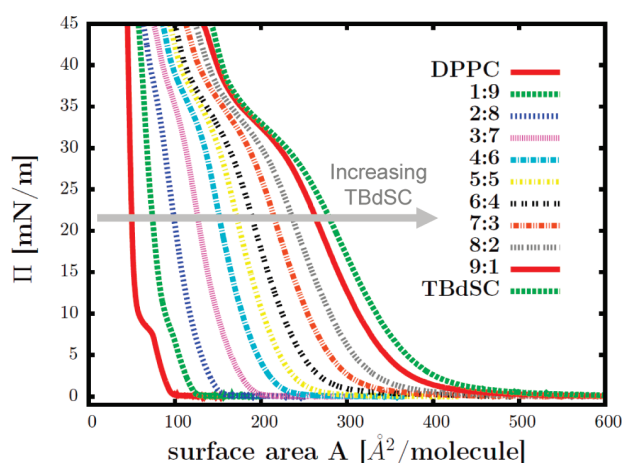


Figure 7. Compression isotherms of pure DPPC–TBdSC mixtures at the air–water interface with steps of 10% mole fractions.

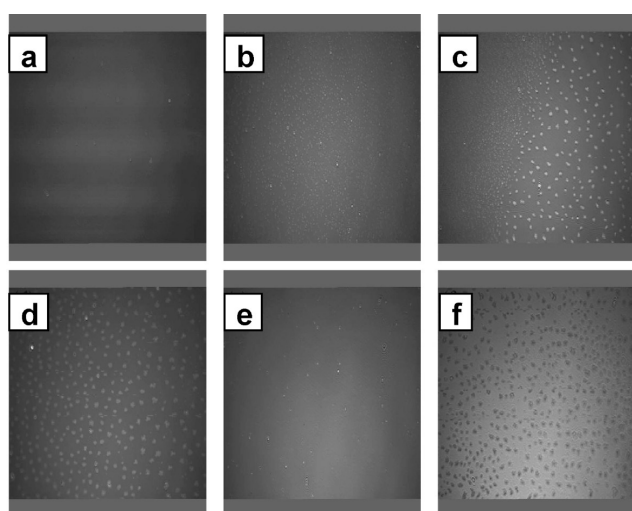


Figure 8. BAM pictures ($480 \times 599 \mu\text{m}$) of 33 mol % TBdSC in DPPC Langmuir monolayers on water at 20°C and from upper left at (a) 0, (b) 14, (c) 22, (d) 34, (e) 40, and (f) 44 mN/m.

not change noticeably. In some cases, the domains seem to grow around aggregates that remain at the center.

4. DISCUSSION

4.1. TBdSC 1 Monolayer. TBdSC behaves as a strongly amphiphilic molecule, retaining the monolayer integrity even at a high pressure.

Moreover, CD reorientation is allowed under pressure even though two lipophilic cholesterol groups are grafted on one CD. A tilt of the CD axis under pressure had already been proposed for monosubstituted amphiphilic CDs.^{13,30} Here, the formal axis between the two grafted glucose units (A and D) allows for a rotation, which can reduce the CD area when a surface pressure is applied. The succinate linker was already claimed to allow for a sufficient degree of freedom to permit CD organization.¹² X-rays bring quantitative information about this rotation. A good electron density contrast is obtained between the cholesterol part and the CD head because of the high oxygen content of the carbohydrate.

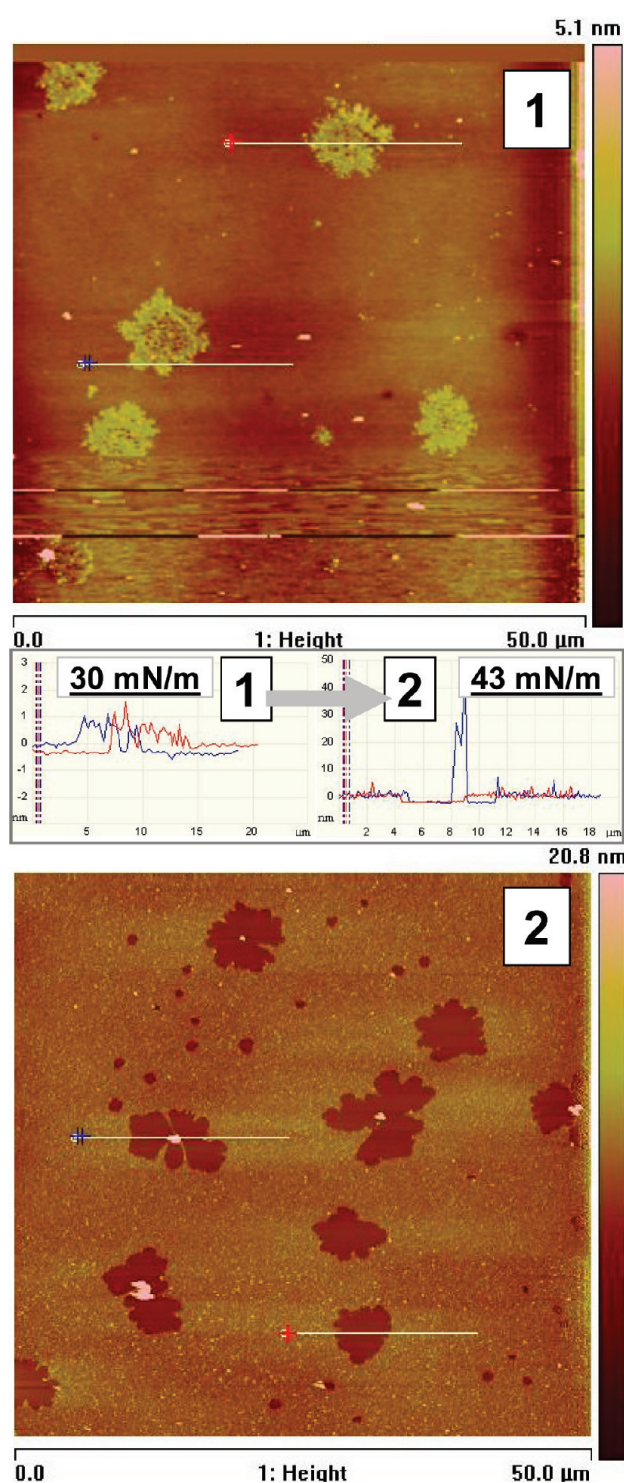


Figure 9. AFM pictures of 33 mol % TBdSC in DPPC Langmuir–Bloggett monolayers transferred on silicon wafer at 20°C and at (1) 30 mN/m and (2) 43 mN/m.

The thickness increase corresponds well to a rotation of the CD cavity axis. Thus, initial and final states of the CD are now established with regard to the pseudo-transition observed on the Langmuir isotherms. It should, however, not be concluded that the CD is submitted to a simple rotation under pressure. Indeed,

methylated CDs are known to be ductile. As an example, simple permethylated β -CD can be crystallized in strongly distorted forms.³¹ In this case and more generally, the water shell explains the behavior of the CD and methylated CDs.²⁶ This is another qualitative piece of information given by X-ray reflectivity data: that the compression and rotation of the CD is accompanied by a strong loss of a water molecule in the CD layer, from nearly 150 to less than 60 per TBdSC molecule, as estimated from the electron density at 3 and 34 mN/m, respectively.

TBdSC then seems well-suited for membrane anchoring and functionalization. This flexibility should allow for good accessibility of the CD cavity, even though it is strongly anchored and close to the surface of the membranes.

4.2. TBdSC–DPPC Mixtures. Considering the TBdSC–DPPC mixtures, our findings can be summarized as follows: The initial aggregates can be attributed to small crystallites of TBdSC. They are also present for the pure compound. These are embedded in the monolayer, in which DPPC and TBdSC seem to be essentially miscible at a low surface pressure, because it shows a homogeneous in-plane structure at all length scales. With an increasing pressure, TBdSC and DPPC become less miscible. At pressures where the liquid-condensed DPPC phase can exist, it first grows around the aggregates as DPPC-rich domains. This could be driven by the condensing effect of cholesterol.³² It appears consistent with the ordering effect observed on ²H nuclear magnetic resonance (NMR) spectra of DMPC-*d*₂₇ vesicles at 25 °C.¹¹ In a 33 mol % mixture, the ratio of area per molecule, because of CD and DPPC choline head, explains that the main part of the surface should be covered by TBdSC. Thus, domains should be surrounded by a DPPC poor phase. At the plateau, TBdSC reorganizes and its length now matches that of DPPC in the liquid-condensed phase; hence, the loss of contrast in the BAM images. Above the inversion pressure, TBdSC is finally expelled from liquid-condensed DPPC domains to either the central aggregates or the TBdSC-rich phase (Figure 9). Domains of most likely pure DPPC are now very flat, with sometimes a TBdSC aggregate at the center. Around these domains, at this very high pressure, TBdSC adopts a high-pressure conformation described above with an even larger roughness before final collapse. The rugosity around the DPPC domains can be compared to that of pure TBdSC at a high pressure, as observed by AFM on Langmuir–Blodgett deposits.

A few comments should be made to compare our results and the first ²H NMR experiments conducted with vesicles (multilamellar) formed from TBdSC and DMPC D27.¹¹ TBdSC was shown to have a fluidizing effect on DMPC, lowering the temperature of its fluid to gel transition. Moreover, no lateral phase separation could be observed. The use of DPPC instead of DMPC and pressure control allowed us to provide evidence of the formation of domains explained by a loss of miscibility in condensed phases but not in expanded phases, such as those found in DMPC vesicles. Then, the liquid-expanded to liquid-condensed transition of DPPC was fading away with as low as 10 mol % TBdSC content, consistent with a fluidizing effect of TBdSC. Condensed DPPC was then observed at a higher pressure.

These results will be extended and further explored on bilayers and vesicles.

5. CONCLUSION

The behavior of amphiphilic CD, TBdSC, as a function of the surface pressure could be clarified using X-ray reflectivity. The CD head can adjust its conformation to the available area per

molecule. Fitting the data leads to a model compatible with a rotation around a horizontal axis defined by the two substituted glucose units. However, possible added deformation of the CD truncated cone has to be taken into account. In any case, this should be accompanied by water exclusion.

The study of the mixed DPPC–TBdSC Langmuir films shows that TBdSC seems to be soluble in the liquid-expanded DPPC. At a high pressure, allowing for high-pressure conformation of TBdSC and liquid-condensed DPPC, both amphiphiles are no longer miscible and phase segregation occurs. The CD water shell was shown to be strongly modified upon compression. Further studies are in progress to understand these changes in more detail and quantitative aspects.

Subsequent studies with various amphiphilic CDs are under study to further understand and tune the solubility parameters of phospholipids and amphiphilic CDs. This involves the control of the conformational changes of the hydrophilic cyclodextrinyl head. This should be of utmost importance to make the best use of amphiphilic CDs as tools on a natural membrane as well as synthetic vesicles.

■ AUTHOR INFORMATION

Corresponding Author

*E-mail: christophe.fajolles@cea.fr (C.F.); jean.daillant@cea.fr (J.D.).

■ ACKNOWLEDGMENT

This work is supported by the French Research Program ANR-07-NANO-016-02 and Région Alsace (Ph.D. Grant).

■ REFERENCES

- (1) Dodziuk, H. *Cyclodextrins and Their Complexes*; Wiley-VCH: New York, 2006.
- (2) Rekharsky, M.; Inoue, Y. *Chem. Rev.* **1998**, *98*, 1875–1917.
- (3) Engeldinger, E.; Armspach, D.; Matt, D. *Chem. Rev.* **2003**, *103*, 4147–4173.
- (4) Ogoshi, T.; Harada, A. *Sensors* **2008**, *8*, 4961–4982.
- (5) Heck, R.; Marsura, A. *Tetrahedron Lett.* **2004**, *45*, 281–284.
- (6) Bjerre, J.; Rousseau, C.; Marinescu, L.; Bols, M. *Appl. Microbiol. Biotechnol.* **2008**, *81*, 1–11.
- (7) Sallas, F.; Darcy, R. *Eur. J. Org. Chem.* **2008**, 957–969.
- (8) Roux, M.; Perly, B.; Djedaini-Pilard, F. *Eur. Biophys. J.* **2007**, *36*, 861–867.
- (9) Lecourt, T.; Mallet, J.; Sinay, P. *Carbohydr. Res.* **2003**, *338*, 2417–2419.
- (10) Armspach, D.; Matt, D.; Peruch, F.; Lutz, P. *Eur. J. Inorg. Chem.* **2003**, 805–809.
- (11) Collot, M.; Garcia-Moreno, M.; Fajolles, C.; Roux, M.; Mauclair, L.; Mallet, J. *Tetrahedron Lett.* **2007**, *48*, 8566–8569.
- (12) Auzely-Velty, R.; Perly, B.; Tache, O.; Zemb, T.; Jehan, P.; Guenot, P.; Dalbiez, J.; Djedaini-Pilard, F. *Carbohydr. Res.* **1999**, *318*, 82–90.
- (13) Janshoff, A.; Steinem, C.; Michalke, A.; Henke, C.; Galla, H. *Sens. Actuators, B* **2000**, *70*, 243–253.
- (14) Soutschek, J.; Akin, A.; Bramlage, B.; Charisse, K.; Constien, R.; Donoghue, M.; Elbashir, S.; Geick, A.; Hadwiger, P.; Harborth, J.; John, M.; Kesavan, V.; Lavine, G.; Pandey, R.; Racie, T.; Rajeev, K.; Rohl, I.; Toudjarska, I.; Wang, G.; Wuschko, S.; Bumcrot, D.; Kotliansky, V.; Limmer, S.; Manoharan, M.; Vornlocher, H. *Nature* **2004**, *432*, 173–178.
- (15) Beugin, S.; Edwards, K.; Karlsson, G.; Ollivon, M.; Lesieur, S. *Biophys. J.* **1998**, *74*, 3198–3210.

- (16) Beulen, M.; Bugler, J.; de Jong, M.; Lammerink, B.; Huskens, J.; Schonherr, H.; Vancso, G.; Boukamp, B.; Wieder, H.; Offenhauser, A.; Knoll, W.; van Veggel, F.; Reinhoudt, D. *Chem.—Eur. J.* **2000**, *6*, 1176–1183.
- (17) Yamada, T.; Fukuhara, G.; Kaneda, T. *Chem. Lett.* **2003**, *32*, 534–535.
- (18) Nishiyabu, R.; Kano, K. *Eur. J. Org. Chem.* **2004**, 4985–4988.
- (19) Roux, M.; Auzely-Velty, R.; Djedaini-Pilard, F.; Perly, B. *Biophys. J.* **2002**, *82*, 813–822.
- (20) Auzely-Velty, R.; Djedaini-Pilard, F.; Desert, S.; Perly, B.; Zemb, T. *Langmuir* **2000**, *16*, 3727–3734.
- (21) Moutard, S.; Perly, B.; Gode, P.; Demailly, G.; Djedaini-Pilard, F. *J. Inclusion Phenom. Macrocyclic Chem.* **2002**, *44*, 317–322.
- (22) Harke, M.; Teppner, R.; Schulz, O.; Motschmann, H.; Orendi, H. *Rev. Sci. Instrum.* **1997**, *68*, 3130–3134.
- (23) Martin, A.; Baeyens, M.; Hub, W.; Mertens, P.; Kolbesen, B. *Microelectron. Eng.* **1999**, *45*, 197–208.
- (24) Daillant, J.; Mora, S.; Sentenac, A. In *X-ray and Neutron Reflectivity*; Daillant, J., Gibaud, A., Eds.; Springer: Berlin, Germany, 2009; pp 133–182.
- (25) Liu, P.; Thebault, P.; Guenoun, P.; Daillant, J. *Macromolecules* **2009**, *42*, 9609–9612.
- (26) Kusmin, A.; Lechner, R.; Kammel, M.; Saenger, W. *J. Phys. Chem. B* **2008**, *112*, 12888–12898.
- (27) Li, J.; Miller, R.; Vollhardt, D.; Mohwald, H. *Thin Solid Films* **1998**, *327*, 84–86.
- (28) Flasiniski, M.; Broniatowski, M.; Romeu, N.; Dynarowicz-Latka, P.; Moreno, A.; Vilas, A.; Martin, M. *J. Phys. Chem. B* **2008**, *112*, 4620–4628.
- (29) McConlogue, C.; Vanderlick, T. *Langmuir* **1997**, *13*, 7158–7164.
- (30) Shtykov, S.; Klimov, B.; Gorin, D.; Pankin, K.; Gets'man, M.; Kurochkina, G.; Glazyrin, A.; Grachev, M. *Russ. J. Phys. Chem.* **2004**, *78*, 1632–1636.
- (31) Caira, M.; Griffith, V.; Nassimbeni, L.; Vanoudtshoorn, B. *J. Chem. Soc., Perkin Trans. 2* **1994**, 2071–2072.
- (32) Quinn, P.; Wolf, C. *Biochim. Biophys. Acta, Biomembr.* **2009**, *1788*, 33–46.

Amphiphilic Behavior of New Cholesteryl Cyclodextrins: A Molecular Study

Martin Bauer,[†] Christophe Fajolles,[†] Thierry Charitat,[‡] Hanna Wacklin,^{§,⊥} and Jean Daillant^{*,†}

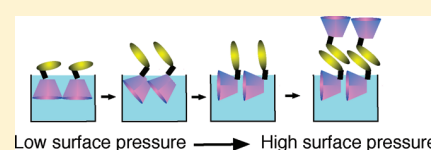
[†]CEA, IRAMIS, SIS2M, LIONS, UMR 3299 CEA/CNRS, CEA-Saclay bât. 125, F-91191 Gif-sur-Yvette Cedex, France

[‡]Université de Strasbourg, Institut Charles Sadron, CNRS, 23 Rue du Loess, BP 84047, 67034 Strasbourg Cedex 2, France

[§]Institut Laue-Langevin, 6 rue Jules Horowitz, BP 156, 38042 Grenoble Cedex, France

S Supporting Information

ABSTRACT: Amphiphilic cyclodextrins (CDs) are good candidates to functionalize natural membranes as well as synthetic vesicles. In this paper, we describe the synthesis of the amphiphilic permethylated monocholesteryl α -CD (TASC). Its interfacial behavior is compared with that of the permethylated mono- and dicholesteryl β -CD analogues (TBSC and TBdSC). Langmuir isotherms suggest a reorganization upon compression for all compounds, which is quantified using neutron as well as X-ray reflectivity. The in-plane structure is characterized by atomic force microscopy (AFM) on monolayers deposited on solid substrates. A model involving a reorientation of the CD with respect to the interface to adjust its conformation to the available area per molecule is proposed. Although we observe for TBSC a rearrangement similar to TASC and TBdSC, it is already achieved at lower surface pressures compared with its disubstituted derivative. This specific behavior is explained by an increased structural flexibility and compressibility compared with TBdSC and TASC. The average number of water molecules per CD was determined using the neutron data and validated from X-ray data, which also allows the determination of the CD's molecular volume. The permethylated CD molecules are strongly hydrated in the film, but the α -CD analogue is less hydrated than the β -CD derivatives, and hydration decreases with compression.



INTRODUCTION

Cyclodextrins (CDs) are natural cyclic oligosaccharides with a truncated cone shape and a hydrophobic cavity that enables them to form host–guest complexes with appropriate molecules. The most abundant α -, β - and γ -CDs are built of six, seven, and eight glucose units, respectively. Since CDs possess a large set of readily modified hydroxyl groups, these cyclic oligosaccharides have become valuable precursors for supramolecular chemistry.¹ The construction of amphiphilic CDs is of particular interest because it combines the CD's ability to act as host molecule with the amphiphiles' capability to self-assemble to supramolecular structures such as vesicles, bilayers, or nanoparticles.^{2,3} Recent advances in CD synthetic modification methods allowed practical preparations of selectively disubstituted α - and β -CDs. This has attracted a new interest in amphiphilic CDs, so far restricted mainly to monosubstituted, statistically or persubstituted derivatives.³

Thus, 6I,6IV-(β -cholesteryl)succinylamido-6I,6IV-(6-deoxy-per-(2,3,6-O-methyl))cycloheptaose, abbreviated TBdSC (Figure 1), which is a disubstituted β -CD bearing two cholesterol residues,⁴ was recently described. It can be readily obtained from permethylated 6A,6D-modified β -CD.⁵ The succinate linker had been determined as an appropriate linker, long enough to ensure relative mobility of the CD and cholesteryl moieties, short enough to avoid self-inclusion, and allowing sufficient mobility (or degrees of freedom) to ensure conformational adaptability.⁶

A close-up study of TBdSC has revealed that it readily inserts into DPPC monolayers to form mixed monolayers for low pressure, whereas segregation occurs for high surface pressure. Moreover, high lateral pressure also induces a reorientation of the CD cavity axis, as demonstrated particularly for monolayers of pure TBdSC. Two selectively grafted cholesterols modify the hydrophilic/hydrophobic balance, but also create a rotation axis defined by the two substituted residues on the CD primary rim, allowing rotation and a consequent decrease of its surface area.⁷

These results prompted us to explore the specific influence of cholesterol and CD, which are the hydrophobic and hydrophilic moieties, respectively, on the amphiphilic behavior. Therefore, monocholesteryl analogues were prepared from permethylated β - and α -amino-CDs. These three molecules were at first studied and compared as pure Langmuir monolayers.

In this paper, we fully describe the air–water interface behavior of pure TBdSC and its monocholesteryl β - and α -CD analogues, called TBSC and TASC (Figure 1). Compression isotherms suggest the same type of reorganization upon compression. By reflectivity measurements, it is shown to consist of a reorientation of the CD moiety, whose axis rotates from perpendicular to parallel arrangement with respect to the water surface. However, the scenarios of these reorganizations are markedly

Received: June 23, 2011

Revised: October 28, 2011

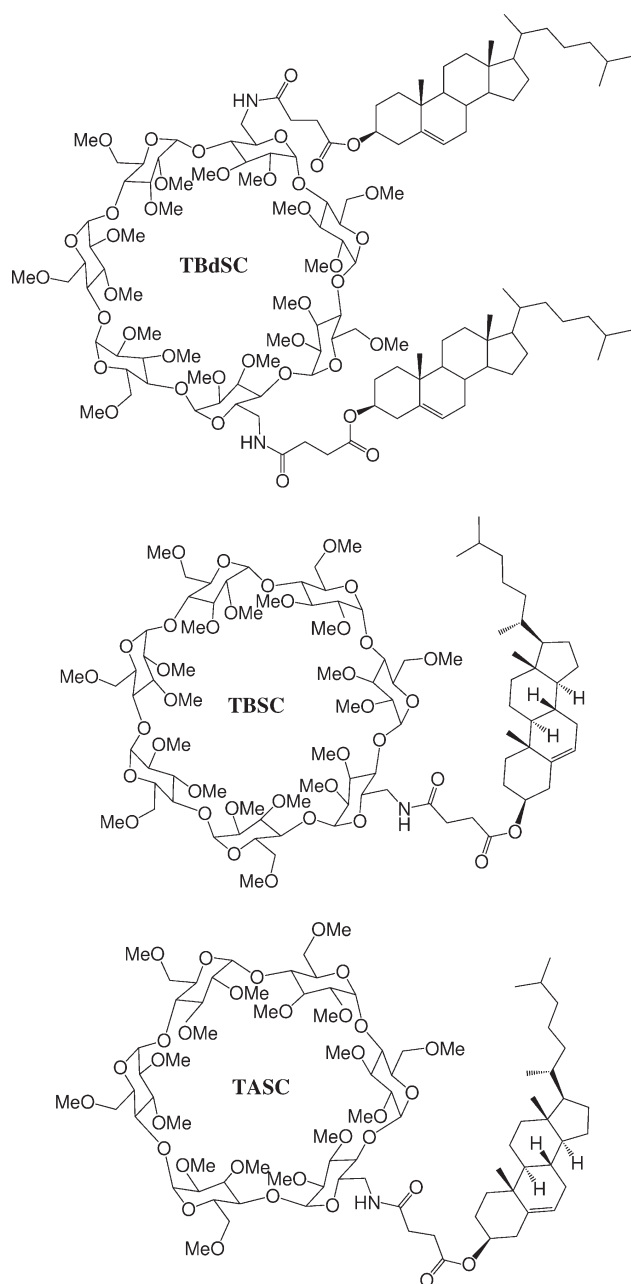


Figure 1. Chemical structure of TBdSC, TBSC, and TASC.

different and strongly depend on flexibility and compressibility, which are determined by the number of attached hydrophobic anchors and the size of the CD. This is evidenced by the isotherm and reflectivity data. It is then correlated to the in-plane structures, which are characterized using atomic force microscopy (AFM) on monolayers deposited on solid substrates.

EXPERIMENTAL SECTION

Synthesis. TBdSC and TBSC are reported in a previous paper.⁷ TASC preparation differs noticeably. Indeed, the common DCC-based coupling method⁴ used to create the amide was found to induce a partial, and still unexplained, oxidation at C-7 on the cholesterol residue as a carbonyl function. Therefore,

TASC 5 (Scheme 1) is alternatively synthesized in three steps, starting from 6^l-azido-6^l-deoxy-cyclomaltohexaose (monoazido- α -CD) **1** (Scheme 1). The first steps are transposed from Jicsinsky's procedure.⁸ A methylation step with methyl iodide and sodium hydride in DMF is followed by a reduction of the azido group to an amine with Pd/C as catalyst and hydrazine hydrate as hydrogen donor. The last step is slightly adapted from a method recently reported by Mukaiyama et al.⁹ to use common reagents. The cholesterol hemisuccinate **4** is in situ activated with toluenesulfonic anhydride (T₂O) as a mixed anhydride in the presence of DMAP to yield the amide in a clean and efficient manner. Procedures and spectra can be found in the Supporting Informations.

Langmuir Monolayers. The surface pressure/area isotherms were measured with a temperature-controlled Langmuir balance (702BAM Film Balance for Brewster Angle Microscopy, Micro-Processor Interface IU4, NIMA Technology) used in conjunction with a Brewster angle microscope (BAM). It possesses a maximum surface area of 700 cm², a minimum surface area of 80 cm², and is filled with ~500 mL of ultrapure water (18.2 M Ω ·cm) subphase. The trough, placed on an antivibration table, is covered by a plastic hood. The compounds are dissolved in chloroform (Riedel-de Haen, EtOH stab.), and the solution is spread with a Hamilton syringe. Typical spreading volumes are 50 μ L. The surface pressure is measured by the Wilhelmy plate method using a filter paper. After 10 min of equilibration of the monolayer, the isotherms are recorded with a compression speed of 10 cm²/min and at a temperature of 20 °C if not mentioned differently.

Atomic Force Microscopy. Langmuir–Blodgett (LB) films of the monolayers were deposited onto hydrophilic, freshly cleaved mica wafers for several surface pressures at the air–water interface with a dipper speed of 1 mm/min. Typically, transfer ratios >0.9 were obtained. The films were then examined in tapping mode with a Nanoscope V (Veeco) AFM. Standard cantilevers with a conical silicon etched probe tip (NSC15, μ masch) with typical spring constants on the order of 40 N/m, as determined by the thermal resonance method, and typical resonance frequencies on the order of 350 kHz were used. Images with scan sizes of 1 μ m \times 1 and 3 μ m \times 3 μ m were recorded with scan rates of 1 and 0.5 Hz, respectively.

Neutron Reflectivity. The neutron reflectivity experiments were carried out at the time-of-flight reflectometer Figaro (Fluid Interfaces Grazing Angles Reflectometer) at the ILL, Grenoble.¹⁰ The incoming beam comprises wavelengths between 2 and 30 Å. For our samples, a q range from 0.005 to 0.30 Å⁻¹ could be achieved by joining together two measurements with a reflection angle, $\Theta_1 = 0.62^\circ$ and $\Theta_2 = 3.82^\circ$ as well as a resolution of 5.6%. The samples were measured in a Langmuir trough (Nima) that is filled with a D₂O subphase. Its maximum and minimum area are 930 and 254 cm², respectively. The reflectivity was normalized by direct beams in a transmission geometry through the windows of the Langmuir trough lid and corrected for incoherent background scattering. The data were fitted with the Motofit package run with the program IGOR Pro 6.0 (Wavemetrics, OR), where the specular reflectivity is calculated by the Abeles matrix method for stratified interfaces.¹¹ A detailed description of the Motofit software is given elsewhere.¹²

X-ray Reflectivity. Complementary to neutron reflectivity, the thickness and vertical composition of the monolayers were also characterized by X-ray reflectivity. The monolayers were spread on a water subphase in a homemade Teflon trough with a

85 S1

86

87

88

89

90

91

92

93

94

95

96

97

98

99

100

101

102

103

104

105

106

107

108

109

110

111

112

113

114

115

116

117

118

119

120

121

122

123

124

125

126

127

128

129

130

131

132

133

134

135

136

137

138

139

140

141

142

143

144

145

146

Scheme 1. Three-Step Synthesis of TASC 5

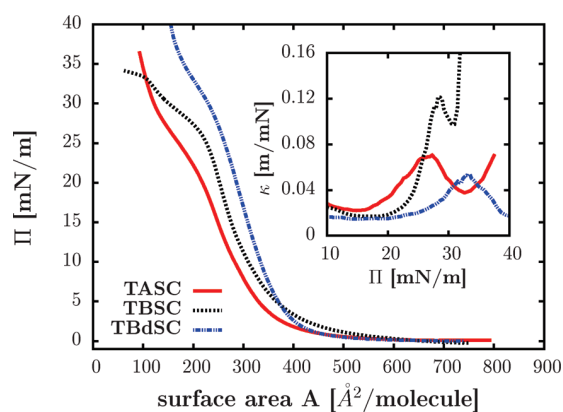
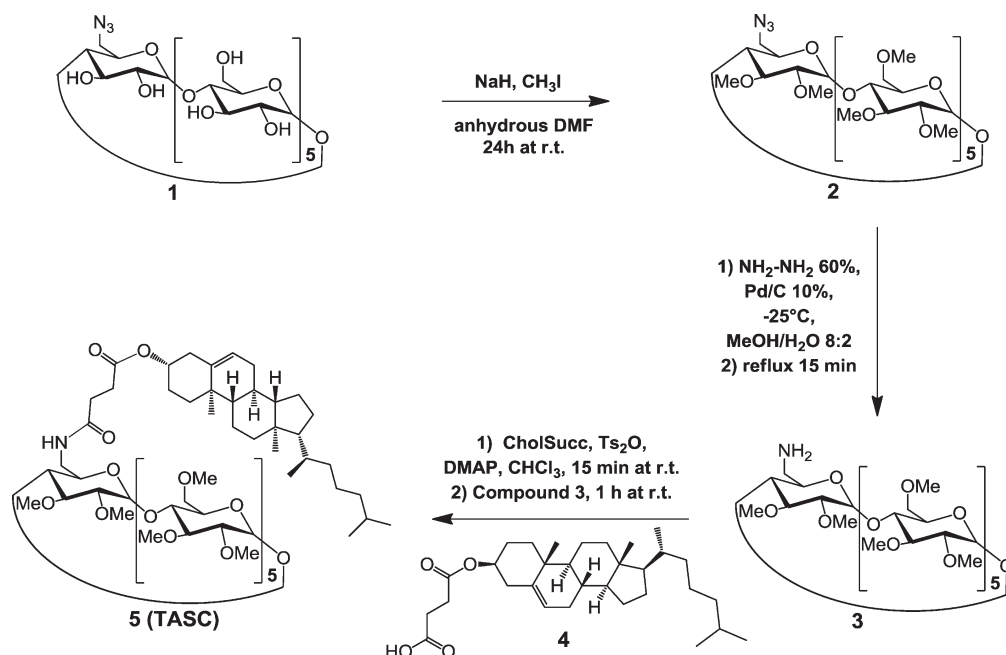


Figure 2. Langmuir isotherms and isothermal compressibility (inset) at 20 °C: (a) TASC, (b) TBSC, and (c) TBdSC.

147 maximum and minimum area of 462 and 161 cm², respectively,
 148 suitable to fit into a Siemens powder diffractometer D5000. A
 149 movable Teflon barrier allows compression of the monolayer to
 150 the desired surface pressure for the X-ray reflectivity measure-
 151 ment. The trough and the diffractometer were operated with
 152 homemade software. The Cu K_α beam (wavelength λ_x = 1.54 Å)
 153 is first collimated using 100 μm slits. A graphite monochromator
 154 is placed after the sample in front of the NaI scintillator detector.
 155 The homemade software allows one to record rocking curves at
 156 each point of the reflectivity curve. The data were also fitted with
 157 the Motofit software applying the same model as used for the
 158 neutron reflectivity.

159 ■ RESULTS

160 **Langmuir Isotherms.** The surface-pressure area isotherms
 F2 161 for (a) TASC, (b) TBSC, and (c) TBdSC are shown in Figure 2.

162 For TASC and TBSC, no significant temperature dependence
 163 can be observed (as opposed to TBdSC⁷), and BAM images feature
 164 aggregates that increase in number with the surface pressure Π
 165 and decrease in molecular surface area A.

166 All the isotherms are reproducible for the same spreading
 167 conditions, and in addition, no hysteresis is observed for iso-
 168 thermal cycles. All three isotherms exhibit a sharp rise beginning at
 169 A = 350 Å² for TASC, A = 380 Å² for TBSC and A = 400 Å² for
 170 TBdSC. They also show a pseudoplateau at high surface pres-
 171 sures. The isothermal surface compressibility,

$$\kappa_S = -\frac{1}{A} \frac{dA}{d\Pi} \quad (1)$$

172 is plotted in the inset of Figure 2 to emphasize the pseudoplateau
 173 because it shows local maxima for first-order phase transitions. κ_S
 174 was calculated numerically from the data obtained from the
 175 Langmuir isotherms as

$$\kappa_S = -\frac{1}{A_i} \frac{(A_{i+1} - A_i)}{(\Pi_{i+1} - \Pi_i)} \quad (2)$$

176 To minimize the noise due to the differentiation of the discrete
 177 data, 10 data points have been averaged to give a smoother
 178 compressibility graph. The compressibility curves for the three
 179 CD's show pronounced peaks for the pseudoplateau at Π =
 180 25 mN/m for TASC, Π = 27 mN/m for TBSC, and Π = 32 mN/m
 181 for TBdSC (Figure 2). For TBSC, the compressibility rises
 182 strongly after the pseudoplateau peak, which, together with
 183 the flat continuation of the isotherm, is an indication for a film
 184 collapse. The TASC and the TBdSC isotherms look very much
 185 alike, apart from the rise at different surface areas, yet the TBSC
 186 starts rising slowly for large surface areas and continues rather
 187 flat after the pseudoplateau.

188 **Reflectivity Measurements.** Neutron and X-ray reflectivity
 189 experiments have been carried out to determine the film thickness

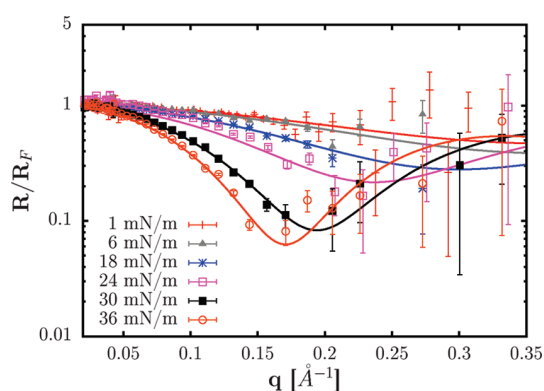


Figure 3. Neutron reflectivity curves at different surface pressures from top to bottom for TASC (red +, 1 mN/m; gray ▲, 6 mN/m; blue ★, 18 mN/m; red □, 24 mN/m; ■, 30 mN/m; red ○, 36 mN/m). Only a part of the recorded scattering curves is displayed in the graph so that they remain distinguishable.

and density profile to elucidate the nature of the pseudoplateau in the isotherms.

To obtain a better contrast and to avoid incoherent scattering, D₂O has been used as subphase for the neutron reflectivity instead of normal water, which is used for the X-ray scattering. The shapes of the isotherms are very similar for both subphases. Thus, the results for both methods can be directly compared. However, due to a limited compression range of the Langmuir trough available for the neutron experiment, more compound had to be spread on the surface to reach the desired surface pressures, leading to a slight shift to higher surface areas (10–20 Å²) for the isotherms. Furthermore Langmuir isotherms are known to be shifted when using D₂O as subphase.¹³ Therefore, the molecular areas from the isotherms recorded on the D₂O subphase are used for calculations with the data from the neutron experiments.

Looking at the reflectivity curves in Figure 3, it can be clearly seen that for all three modified CD's, a minimum appears with increasing surface pressure that is related to a structural change in the film. Starting at surface pressures around the pseudoplateau, the scattering curve minimum drastically deepens. This behavior is most pronounced for TBSC, for which we observe a very large step between the curves for surface pressures below and above the pseudoplateau.

Complementary X-ray scattering experiments have been measured only for TASC and TBdSC for two points in the isotherm, one below and one above the phase transition, and similar to the neutron experiment, the curves at low surface pressures are very different from the ones obtained at high pressures (the X-ray curves can be found in the Supporting Information). The data obtained from neutron and X-ray scattering are fitted with the same model. The measured curves are fitted using a two-layer box model (represented on top in Figure 4) with two distinct regions of scattering length densities (SLD₁, SLD₂) and electron density (ED₁, ED₂), respectively, as well as the corresponding thicknesses *l*₁, *l*₂. The top layer, 1, can be assigned to the hydrophobic cholesterol, and the bottom layer, 2, to the hydrophilic CD residues. For TBSC at Π = 32 mN/m, a third layer had to be added to the model to fit the data properly. The subphase roughness was 3 ± 1 Å for all fits, and the roughnesses for the CD and cholesterol layers are in the range between 2 and 4 Å.

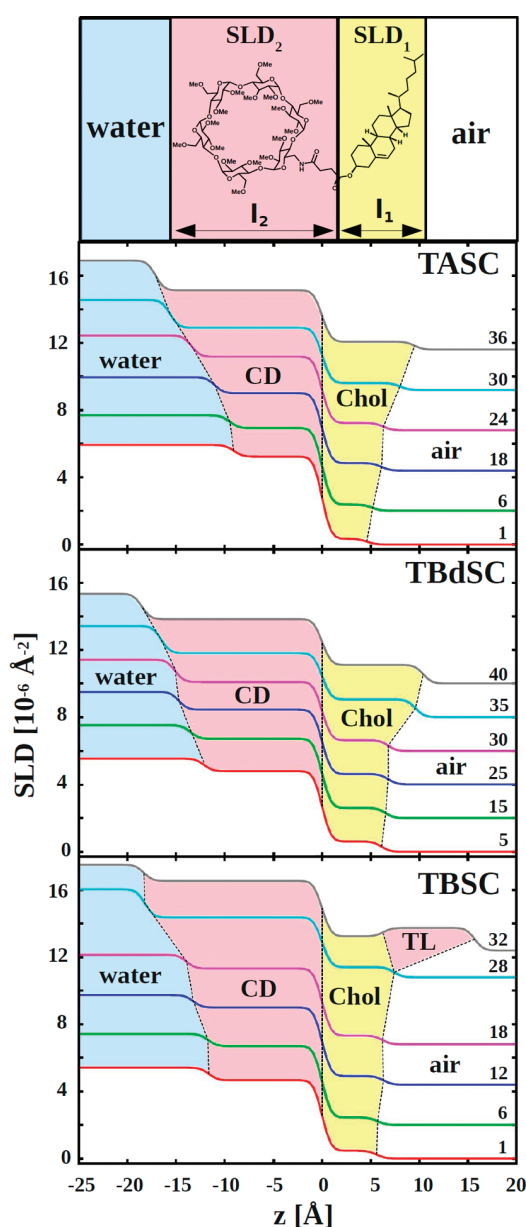


Figure 4. SLD profiles from neutron reflectivity experiments at different surface pressures for TASC, TBdSC, and TBSC. The surface pressures corresponding to each SLD profile are indicated on the right side of the graph in milli-Newtons per meter. To account for better legibility, the curves have been consecutively shifted proportionally to the surface pressure Π (2 × 10⁻⁶ Å⁻² for 5 mN/m). TL signifies the additional layer that had to be added for TBSC at 32 mN/m.

Comparing the overall thickness of the films shows that, for low surface pressures, the TASC monolayer is ~15 Å, and that for TBdSC and TBSC is ~18 Å thick. For high surface pressures, the film thickness increases to ~27 Å for TASC, to ~29 Å for TBdSC, and to ~33 Å for TBSC (all values obtained from the fits can be found in the corresponding tables in the Supporting Information). This behavior is clearly visualized in the scattering length density profiles displayed in Figure 4.

TASC. Having a closer look at the CD part of the monolayer reveals that for TASC, the CD film thickness stays in the range of 10–11 Å up to surface pressures close to the pseudoplateau

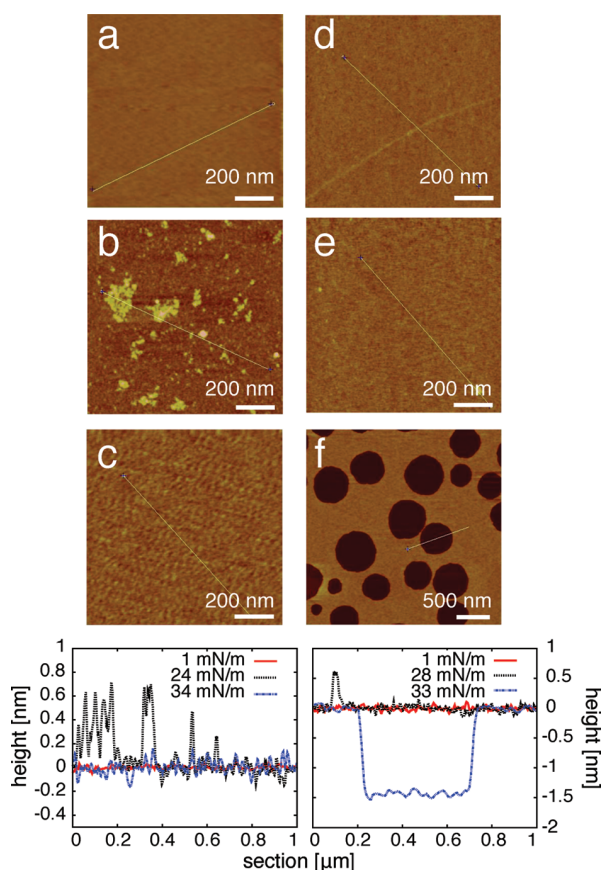


Figure 5. AFM images and profiles for TASC (left) and TBSC (right). $\Pi =$ (a) 1, (b) 24, (c) 35, (d) 1, (e) 28, and (f) 33 mN/m.

(Figures 4 and 7). Starting from $\Pi = 21$ mN/m, the size of the CD layer increases steadily from 11 to 17 Å at 36 mN/m. The film compression is accompanied by a drop in scattering length density from 5.2×10^{-6} to 3.6×10^{-6} Å⁻². Likewise, the X-ray experiments reveal a jump in electron density from 0.39 to 0.43 Å⁻³. X-ray and neutron reflectivity curves are fitted with same model. As the X-ray data extend to higher q values, they better resolve the cholesterol layer whose thickness was constrained to the X-ray values for the neutron fits. It increases from 4.5 to 10 Å with compression (see corresponding data in Supporting Information). The scattering length density is on the order of 0.4×10^{-6} Å⁻² for all surface pressures.

TBdSC. For TBdSC, the CD layer is ~ 12.5 Å thick at the beginning of compression (Figure 4). Starting from surface pressures close to the pseudoplateau, its size increases significantly to ~ 18.5 Å. Furthermore the scattering length density decreases from 4.8×10^{-6} to 3.8×10^{-6} Å⁻², as well as the electron density increases from 0.38 to 0.44 Å⁻³.

The cholesterol layer increases from 6 to 10 Å for $\Pi = 40$ mN/m. The X-ray data gives comparable results, with a rise from 6 to 11.5 Å (see the Supporting Information).

TBSC. The CD layer of TBSC exhibits a thickness between 11.5 Å for low surface pressures and 14 Å at $\Pi = 18$ mN/m. Then the size increases drastically to 18 Å at 28 mN/m (Figure 4), like for TASC and TBdSC coming along with a drop in scattering length density from 4.7×10^{-6} to 3.6×10^{-6} Å⁻². The cholesterol layer increases from 5.5 to 7.5 Å at $\Pi = 28$ mN/m.

For $\Pi = 32$ mN/m, a three-layer model had to be applied to fit the curve. Good fits could only be obtained by adding the layer on top of the cholesterol layer, whereas fitting the data, adding the third layer on the CD side (subphase) was not successful. We find that the CD layer remains ~ 18 Å thick. The scattering length density is increased to 4.1×10^{-6} Å⁻², which is higher than for $\Pi = 28$ mN/m. For the middle layer, a thickness of 6.3 Å and scattering length density of 0.8×10^{-6} Å⁻² is found. The additional top layer has a size of 9.5 Å with a scattering length density of 1.3×10^{-6} Å⁻². Moreover, the top-layer roughness (6 Å) is larger than that of the other layers (2–3 Å).

AFM. To investigate the in-plane structure of the monolayer, several Langmuir–Blodgett films on mica have been prepared for different surface pressures and imaged by AFM.

For TASC, the monolayer is very flat and homogeneous at low pressure (Figure 5a). An image at the pseudoplateau (Figure 5b) shows ~ 7 Å high domains as well as an increased roughness (~ 3 Å). At 34 mN/m (Figure 5c), the surface is again homogeneous, whereas the profile indicates that the roughness is larger compared with the low pressure image.

For low surface pressure, the Langmuir–Blodgett film of TBSC (Figure 5d) is very flat and homogeneous, similar to TASC. At 28 mN/m (Figure 5e), there are no domains visible, and only a small increase in roughness can be observed. Figure 5f, which is taken on the flat part of the isotherm at 33 mN/m, shows characteristic holes of ~ 15 Å depth and diameters of several hundreds of nanometers. It exhibits roughness similar to that of the image in Figure 5e.

DISCUSSION

Amphiphilic Behavior. All three investigated amphiphilic CDs show truly amphiphilic behavior and form stable monolayers, since isotherms can be recorded up to very high surface pressures before film collapse occurs. The sharp increase in the TASC isotherm occurs for smaller surface areas ($A \approx 350$ Å²) compared with TBSC ($A \approx 380$ Å²) and TBdSC ($A \approx 400$ Å²), which reflects the smaller size of the α -CD moiety in the former molecule. This observation, as well as the CDs' much larger volume compared with the cholesterol residue leads us to the conclusion that the shape of the isotherms is determined mainly by the CD part of the molecules. According to the literature, the β -CD exhibits a higher structural flexibility compared with the α -CD.^{14,15} Indeed, in addition to the degrees of freedom due to the unique succinic linker, it is possible for a glucopyranose unit, typically the one grafted by the hydrophobic moiety, to spin about its glycosidic bond.¹⁶ This should be much easier for β -CD than for the more sterically constrained α -CD. This higher deformability is the reason for the different isotherm shapes for TASC and TBSC (Figure 2). In TBdSC, the rigidity of the usually rather flexible β -CD moiety is restricted by the two cholesterol residues, explaining an isotherm shape similar to TASC, as well as a similar compressibility at the pseudoplateau (Figure 2). The slow rise for a very large surface area ($A \approx 600$ Å²) and the sharp increase for smaller surface areas compared with TBdSC also reflect the greater flexibility of the TBSC.

Monolayer Morphology. *CD Layer.* Every isotherm of the investigated CD's shows a pseudoplateau that corresponds to a structural change in the monolayer. Looking at the CD part of the monolayer in more detail reveals for all investigated amphiphiles that the thickness increases significantly, about 6–7 Å, when comparing surface pressures below and above the pseudoplateau.

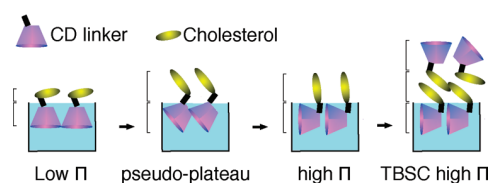


Figure 6. Change of conformation in the CD layer.

The compression of the film is accompanied by a drop in scattering length density in the neutron reflectivity experiment, which corresponds to an expulsion of water from the film, which is further discussed in the following section.

According to the literature, the torus height for methylated α - and β -CD is increased from 8 to 11 Å compared with the native compounds due to the methyl groups.¹⁷ Our data for low pressure correspond well to these values. However, we find that for TASC, the CD layer is ~ 2 Å thinner compared with TBdSC and TBSC. This suggests that the smaller α -CD headgroup has a small influence on the torus height.

The X-ray and neutron results give a clear interpretation of the pseudoplateau in the isotherms. The CD layer thickness is, indeed, equal to the methylated CD height for low surface pressures and to its diameter^{1,18} at large surface pressures. The transformation occurring at the pseudoplateau is a conformational change, where the axis of the CD's cavity rotates from perpendicular to parallel to the surface (Figure 6). For non-methylated native amphiphilic CD's, such a reorientation has already been confirmed by IRRAS measurements at the air–water interface.¹⁹ The rearrangement occurs gradually, ~ 1.5 Å every 3 mN/m, starting from the pseudoplateau with the CD's axis being aligned more and more parallel with respect to the surface (Figure 6). Furthermore, the AFM images for TASC at the pseudoplateau (Figure 5b) exhibit domains with the same distinct height of 6 Å, corresponding to the difference between CD height and diameter, indicating a coexistence between the two conformations. AFM images at high pressure show again a homogeneous, flat surface, with the whole monolayer aligned in its high-pressure conformation.

For TBSC, the neutron reflectivity data suggest that the conformational change already occurs for lower surface pressures than for the disubstituted TBdSC. With further compression for surface pressures above 30 mN/m, the flat continuation of the isotherm reveals the beginning of the film collapse. This is also reflected in the neutron data at 32 mN/m, where an additional third layer on top of the cholesteryl layers is now required to successfully fit the reflectivity data. Since addition of a third layer close to the subphase does not give good fits, film buckling toward the solution is not a likely explanation. The third layer most probably consists of a TBSC double layer with a very disordered top layer, indicated by its high roughness (6 Å) compared with the other slabs (3 Å) and all other fits, where the roughness is on the order of 2–3 Å. Because the transfer ratios are always larger than 90%, the holes in the AFM image at $\Pi = 34$ mN/m (Figure 5f) cannot be due to a loss of material during the transfer. They are consistent with a partial bilayer formation where zones of monolayer remain; they also explain a drastically decreased SLD of the top layer as an average between the holes and the elevated regions is measured.²⁰ The low scattering length density of the top layer also indicates that the CDs are only very little hydrated compared with the CDs situated in the layer close to the water.

Cholesteryl Layer. The thickness of the cholesteryl layer is determined mainly by the available surface area due to the CD moiety. It increases with compression from 4.5 to 10 Å for the monosubstituted α -CD and from 5 to 7.5 Å for the β -CD derivative because the bulkier β -CD leaves more space for the cholesteryl moiety. Similarly, the two cholesteryl moieties of TBdSC require more space, leading to a more pronounced increase in cholesteryl layer thickness with compression (6–11 Å). The more compact packing of the TBdSC's cholesteryl layer is also reflected in the significantly increased scattering length and electron densities for high pressures, in contrast to the monosubstituted molecules. Values reported in the literature for a fully stretched cholesteryl molecule are ~ 17 Å.²¹ At least part of the succinyl linker (~ 3 Å) should be assigned to the cholesteryl layer, explaining the elevated average SLD for the “cholesterol” slab compared with the expected cholesterol SLD ($0.2 \times 10^{-6} \text{ \AA}^{-2}$),²² since the SLD for the succinyl linker can be estimated to be on the order of $2.6 \times 10^{-6} \text{ \AA}^{-2}$. The effect seems to be most pronounced for TBdSC in high pressure conformation where the SLD for cholesterol is very much increased.

The tilt angles, Θ , for the cholesteryl part of the monolayer at maximum compression have been calculated from the expression

$$\cos \Theta = \frac{l_{\text{Chol}}}{l_{\text{st}}} \quad (3)$$

with the measured thickness of the cholesteryl layer, l_{Chol} , and the length of the fully stretched cholesteryl molecules, l_{st} , obtained from the literature.²¹ The tilt angles decrease in the order TBSC (64°), TASC (55°), and TBdSC (50°), reflecting the available space of the cholesteryl residue in each compound. For low surface pressures, the cholesterol moieties are arranged almost flat on the surface. With rising compression, the increasingly smaller available surface area forces the cholesterol residues to arrange themselves more upright. However, for higher pressure, because the bulky CD residues determine the required surface area of the molecule, sufficient space remains for the cholesterol moieties to be tilted. In addition, for TBdSC, we observe an increase in the proportion of the linker group in the top layer.

Hydration of CD Headgroup. Methylated CDs are strongly hydrated in an aqueous environment.^{23–25} Therefore, the CD layer in the film has a large water content. The number of water molecules per CD, n_w , can be calculated using the scattering length, SLD_{CD} (eq 4), and electron density, ED_{CD} (eq 5), extracted from the fits starting from the following definitions:

$$\text{SLD}_{\text{CD}} = \frac{\text{SL}_{\text{CD}} + n_w \text{SL}_w}{l_{\text{CD}} A} \quad (4)$$

$$\text{ED}_{\text{CD}} = \frac{N_{\text{CD}} + n_w N_w}{l_{\text{CD}} A} \quad (5)$$

where SL_{CD} (respectively, SL_w) is the scattering length of the CD (respectively, D_2O), A is the surface area extracted from the isotherm, and l_{CD} is the corresponding length of the CD layer. N_{CD} is the number of electrons in the CD residue of the molecule, and N_w is the number of electrons in heavy water. For the neutron data, this leads to the expression (eq 6).

$$n_w = \frac{\text{SLD}_{\text{CD}} l_{\text{CD}} A - \text{SL}_{\text{CD}}}{V_w \text{SLD}_w} \quad (6)$$

The scattering length of water is substituted by $V_w \times \text{SLD}_w$, where V_w is the molecular volume of D_2O (30 \AA^3) and SLD_w is

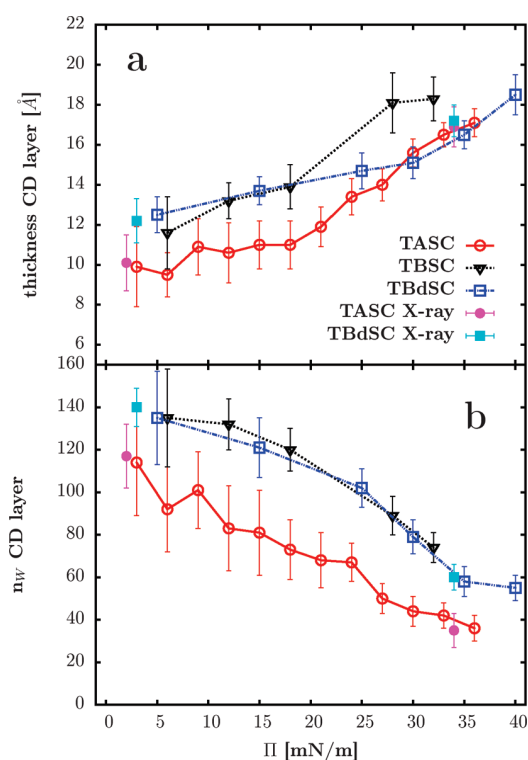


Figure 7. (a) CD layer thickness and (b) number of water molecules per CD for TASC (neutron, red ○; X-ray, red ●), TBSC (neutron, ▼) and TBdSC (neutron, blue □; X-ray, blue ■) during compression.

the scattering length density of the subphase, obtained from fitting the reflectivity curves. This is necessary because the values found for SLD_w (see the Supporting Information) are significantly lower than the literature value for pure heavy water ($6.36 \times 10^{-6} \text{ \AA}^{-2}$).

Reference 26 shows that when the environment of the Langmuir trough is well controlled, there is no noticeable evolution of the bulk SLD. For the experiments described in this paper, using a sealed trough was not possible, and the bulk phase gets more enriched with normal water diffusing from the atmosphere at the D_2O –air interface. This is reflected in a decrease of SLD_w during the experiment (see the Supporting Information). For the X-ray experiments, n_w is expressed by

$$n_w = \frac{N_{CD} l_{CD} A - N_{CD}}{N_w} \quad (7)$$

Figure 7 shows the calculated number of water molecules per CD in the film for the different surface pressures. The values calculated from the X-ray data correspond very well to the results from the neutron scattering experiments. The water content decreases with rising compression for TASC from 114 to 36; for TBdSC, from 135 to 55; and for TBSC, from 193 to 74. The TASC molecule is the least hydrated because it possesses one glucose unit less than the two β -CD derivatives TBdSC and TBSC. The hydration behavior of TBSC and TBdSC is similar (Figure 7 b), as expected because they possess chemically identical headgroups. The number of water molecules per CD we calculated for low surface pressures corresponds well to values reported for methylated CDs in the bulk phase.²⁴ At high surface pressures, we find that the CDs are less hydrated than in the bulk.²⁷ Looking at Figure 7b, the loss of water in the layer occurs

Table 1. Mean SLD_{CD-w} and ED_{CD-w} and Corresponding V_m for TASC, TBSC, and TBdSC

compound	SLD_{CD-w} ($10^{-6}/\text{\AA}^2$)	V_{CD} (\AA^3)	ED_{CD-w} (\AA^{-3})	V_{CD} (\AA^3)
TASC	2.15 ± 0.25	990 ± 280	0.540 ± 0.05	1300 ± 250
TBdSC	2.00 ± 0.20	1310 ± 220	0.550 ± 0.05	1530 ± 200
TBSC	1.80 ± 0.25	1320 ± 330		

slowly for low compression and then more rapidly from the pseudoplateau in the isotherm.

Knowing n_w , it is possible to calculate x_w , the volume percentage of solvent content in the CD layer.

$$x_w = \frac{n_w V_w}{l_{CD} A} \quad (8)$$

By fixing the solvent penetration of the CD layer, the actual scattering length density, SLD_{CD-w} , and electron density, ED_{CD-w} , of the CD residues without water can be directly obtained from the fit. Thus, we have a means to estimate the molecular volume V_{CD} using (eq 9) for the neutron and (eq 10) for the X-ray data:

$$V_{CD} = \frac{l_{CD}}{SLD_{CD-w}} \quad (9)$$

$$V_{CD} = \frac{N_{CD}}{ED_{CD-w}} \quad (10)$$

The calculated mean values of the scattering length density SLD_{CD-w} as well as electron density ED_{CD-w} without water for the CD part and the corresponding molecular volumes V_m , are displayed in Table 1.

The SLD_{CD-w} as well as the ED_{CD-w} values are consistent with the ones found for bulk solutions of CDs (β -CD, $V = 1200 \text{ \AA}^3$; dimethyl- β -CD, $V = 1575 \text{ \AA}^3$) by Kuzmin et al.²⁷ As expected, the V_m for the methylated α -CD in TASC is smaller than for the β -CD derivatives. The V_m values from the neutron data are slightly smaller but within the error bars comparable to what has been reported for bulk solutions.²⁷ The decreased values could be due to the fact that we calculated the molecular volume as an average, since we assumed the V_m to stay constant during compression.

CONCLUSION

We demonstrated that the monosubstituted permethylated α -CD and β -CD derivative TASC and TBSC, like their disubstituted permethylated- β -CD analogue TBdSC, form stable monolayers because we are able to record Langmuir isotherms. The shape of the TASC isotherm resembles the one for TBdSC, with the only difference being that the pseudoplateau is shifted to lower surface pressures. Because of its small α -CD residue, the isotherm is also displaced to smaller surface areas for TASC. Interestingly, the TBSC behaves differently: its isotherm starts rising for large surface areas, and the monolayer collapses shortly after the pseudoplateau. To identify the structural change indicated by the pseudoplateau in the isotherms, we investigated the film morphology by reflectivity measurements and AFM. We found that, for all compounds, the CD residue undergoes a change in conformation during compression. At the phase transition, the CD residue rearranges from the cavity's axis aligned

perpendicular with respect to the surface to an alignment parallel to the surface (Figure 6). Although we observe for TBSC that a rearrangement of the CD layer occurs as for TASC and TBdSC, it is already achieved at lower surface pressures compared with its disubstituted derivative. The specific behavior of the TBSC is explained by the increased structural flexibility and compressibility compared with TBdSC and TASC. Furthermore the evolution of the hydration shell of the hydrophilic permethylated CD groups during compression has been assessed. The permethylated CD molecules are strongly hydrated in the film, and an average number of water molecules per CD could be determined. Considering the hydration of TASC, TBSC, and TBdSC, it is decreased for the α -CD analogue compared with its β -CD derivatives, and it decreases with compression. Knowing the number of water molecules in the film made it possible to calculate the average molecular volume for the CDs and confirm the values found in the literature.

Subsequent studies are underway to determine the insertion modes and solubility parameters of the compounds described here into phospholipid membranes. The knowledge and control of the conformational behavior of the hydrophilic CD head should be of importance to make the best use of amphiphilic CDs as versatile tools on natural or synthetic membranes as well as vesicles.

■ ASSOCIATED CONTENT

S **Supporting Information.** Detailed synthesis of TASC as well as corresponding ^1H NMR, ^{13}C NMR, ROESY, and MALDI-TOF spectra and HPLC chromatogram for TASC derivatives and complementary materials for X-ray and neutron reflectometry. This material is available free of charge via the Internet at <http://pubs.acs.org/>.

■ AUTHOR INFORMATION

Corresponding Author

*E-mail: Jean.Daillant@cea.fr.

Present Addresses

¹European Spallation Source ESS AB, P.O Box 176, SE-221 00 Lund, Sweden.

■ ACKNOWLEDGMENT

This work is supported by the French Research Program ANR-07-NANO-016-02 and Region Alsace (Ph.D. Grant). The authors thank Carlos Marques from the ICS Strasbourg for the coordination of the ANR project and his kind support. The authors also thank Maria Chiriac, Angelika Klaus, Mayeul Collot, and Jean-Maurice Mallet for their intervention in compound synthesis and Alain Valleix for advice in HPLC. In addition, we are grateful for the help and support of Giovanna Fragneto and Richard Campbell during the neutron experiment Figaro at the ILL, Grenoble.

■ REFERENCES

- (1) Szejtli, J. *Chem. Rev.* **1998**, *98*, 1743–1753.
- (2) Roux, M.; Perly, B.; Djedaini-Pilard, F. *Eur. Biophys. J.* **2007**, *36*, 861–867.
- (3) Sallas, F.; Darcy, R. *Eur. J. Org. Chem.* **2008**, *6*, 957–969.
- (4) Collot, M.; Garcia-Moreno, M.; Fajolles, C.; Roux, M.; Mauclair, L.; J., M. *Tetrahedron Lett.* **2007**, *48*, 8566–8569.

- (5) Lecourt, T.; Mallet, J.; Sinay, P. *Carbohydr. Res.* **2003**, *338*, 2417–2419.
- (6) Auzely-Velty, R.; Perly, B.; Taché, O.; Zemb, T. *Carbohydr. Res.* **1999**, *318*, 82–90.
- (7) Klaus, A.; Fajolles, C.; Bauer, M.; Collot, M.; Mallet, J.-M.; Daillant, J. *Langmuir* **2011**, *27*, 7580–7586.
- (8) Jicsinszky, L.; Ivanyi, R. *Carbohydr. Polym.* **2001**, *45*, 139–145.
- (9) Funasaka, S.; Koji Kato, K.; Mukaiyama, T. *Chem. Lett.* **2007**, *36*, 1456–1457.
- (10) FIGARO, Reflectometer at the ILL, <http://www.ill.eu/instruments-support/instruments-groups/instruments/figaro/>.
- (11) Heavens, O. S. *Optical Properties of Thin Solid Films*; Dover Publications Inc.: Mineola, NY, 1992.
- (12) Nelson, A. J. *Appl. Crystallogr.* **2006**, *39*, 273–276.
- (13) Vaknin, D.; Kjaer, K.; Als-Nielsen, J.; Lösche, M. *Biophys. J.* **1991**, *59*, 1325–1332.
- (14) Cairra, M.; Bourne, S.; Mhlongo, W.; Dean, P. *Chem. Commun.* **2004**, *19*, 2216–2217.
- (15) Steiner, T.; Saenger, W. *Carbohydr. Res.* **1996**, *282*, 53–63.
- (16) Nishiyabu, R.; Kano, K. *Eur. J. Org. Chem.* **2004**, *2004*, 4988–4985.
- (17) Immel, S.; Lichtenthaler, F. W. *Starch/Staerke* **1996**, *48*, 225–232.
- (18) Dodziuk, H. In *Cyclodextrins and Their Complexes*; Dodziuk, H., Ed.; Wiley-VCH Verlag: Weinheim, 2006; pp 1–30.
- (19) Vico, R.; de Rossi, R.; Maggio, B. *Langmuir* **2010**, *11*, 8407–8413.
- (20) Coulon, G.; Daillant, J.; Collin, B.; Benattar, J.; Gallot, Y. *Macromolecules* **1993**, *26*, 1582–1589.
- (21) Rapaport, H.; Kuzmenko, I.; Lafont, K.; Kjaer, S.; Howes, P.; Als-Nielsen, J.; Lahav, M.; Leiserowitz, L. *Biophys. J.* **2001**, *81*, 2729–2736.
- (22) Demé, B.; Lee, L.-T. *J. Phys. Chem. B* **1997**, *101*, 8250–8258.
- (23) Sultanem, C.; Moutard, S.; Benattar, J.; Diedaini-Pilard, F.; Perly, B. *Langmuir* **2004**, *20*, 3311–3318.
- (24) Shikata, T.; Takahashi, R.; Satokawa, Y. *J. Phys. Chem. B* **2007**, *111*, 12239–12247.
- (25) Jana, M.; Bandyopadhyay, S. *Langmuir* **2009**, *25*, 13084–13091.
- (26) Romet-Lemonne, G.; Daillant, J.; Guenoun, P.; Yang, J.; Mays, J. *Phys. Rev. Lett.* **2004**, *93*, 148301.
- (27) Kusmin, A.; Lechner, R.; Kammel, M.; Saenger, W. *J. Phys. Chem. B* **2008**, *112*, 12888–12898.

Cite this: DOI: 10.1039/c1sm06346d

www.rsc.org/softmatter

PAPER

Insertion properties of cholesteryl cyclodextrins in phospholipid membranes: a molecular study†

Martin Bauer,^{ab} Thierry Charitat,^b Christophe Fajolles,^a Giovanna Fragneto^c and Jean Daillant^{*a}

Received 16th July 2011, Accepted 3rd October 2011

DOI: 10.1039/c1sm06346d

Amphiphilic cyclodextrins (CDs) are good candidates to functionalize natural membranes, as well as synthetic vesicles. In this paper, we fully describe and compare the insertion properties of the permethylated mono-cholesteryl α -CD (TASC) and its mono- and di-cholesteryl β -CD analogues (TBSC and TBdSC) in dipalmitoyl-L- α -phosphatidylcholine (DPPC) mono- and bi-layers as membrane models from the macroscopic to the molecular scale. By calculating the inverse compressibility moduli and free excess Gibbs energies from the Langmuir isotherms, the influence of the CD type, CD ratio and number of cholesteryl anchors on the membrane properties have been established. TBdSC, with its two cholesteryl residues, seems to be anchored best to the membrane compared to CD derivatives with only one anchor. Furthermore, TASC appears to be more firmly inserted into the membrane than TBSC. The in-plane structure is characterized by Brewster angle microscopy (BAM) at the air–water interface and atomic force microscopy (AFM) of the mono- and bi-layers deposited on mica. Depending on the compression, full miscibility of the cholesteryl CDs and the phospholipids is observed at low surface pressures and a clear demixing tendency is apparent during compression. CD-modified bilayers are stable and are subject to a gel–liquid phase transition upon heating. Due to their bulky CD moiety, the amphiphilic CDs exhibit a distinct fluidizing effect, shifting the DPPC's gel–liquid transition. The structure of the mixed TASC/DPPC mono- and bi-layers perpendicular to the surface is investigated with Ångstrom resolution by neutron reflectivity. In this way a molecular model of the insertion has been established, which suggests that the CD cavities partly protrude into the subphase, which should leave them accessible for complex formation.

1 Introduction

Cyclodextrins (CDs) are natural cyclic oligosaccharides industrially produced by the enzymatic digestion of starch. The most abundant α -, β - and γ -CDs are built of six, seven and eight glucose (D-(+)-glycopyranosyl) units, respectively, which are linked by α -1,4-glycosidic bonds. They possess a truncated cone shape with the primary and secondary hydroxyl groups located at the narrower and wider rims. Consequently, the molecules exhibit a hydrophilic exterior and a hydrophobic cavity due to the inward directed H3 and H5 atoms of the glucose unit (Fig. 1).¹

CDs are known to form inclusion complexes, which is exploited in numerous applications, mainly in the pharmaceutical, cosmetic and nutritional fields.² Their cyclic structure, together with their

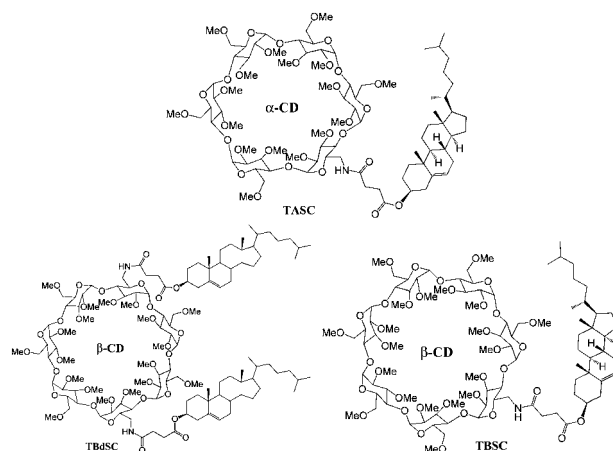


Fig. 1 Chemical structures of TASC, which is an abbreviation for the trivial name Trimethyl-Alpha-CD-Succinyl-Cholesterol; TBSC for Trimethyl-Beta-CD-Succinyl-Cholesterol and TBdSC for Trimethyl-Beta-CD-di-Succinyl-Cholesterol.

^aCEA, IRAMIS, SIS2M, LIONS, UMR 3299 CEA/CNRS, CEA-Saclay bât. 125, F-91191 Gif-sur-Yvette Cedex, France. E-mail: Jean.Daillant@cea.fr; Fax: (+33) 1 6908 6640; Tel: (+33) 1 6908 6481

^bUniversité de Strasbourg, Institut Charles Sadron, CNRS, 23 Rue du Loess, BP 84047, 67034 Strasbourg Cedex 2, France

^cInstitut Laue-Langevin, 6 rue Jules Horowitz, BP 156, 38042 Grenoble Cedex, France

† Electronic Supplementary Information (ESI) available: AFM and neutron reflectivity of the monolayer and bilayer and the structural parameter table. See DOI: 10.1039/c1sm06346d

readily modified hydroxyl groups, makes them convenient templates with a geometry defined by the chosen CD. The primary interest of modifying CDs is to tune their inclusion capacities and their solubility, as well as the solubility of their inclusion complexes. Furthermore, amphiphilic CDs have been designed in order to be able to control the supramolecular assemblies of CDs. But these modifications have mainly been restricted to uniformly functionalised or statistically described mixtures.³ From a synthetic point of view, due to the large number of chemically equivalent OH-groups, the controlled modification, *e.g.* of one or two defined hydroxyl groups, is much more challenging. Today, methods have been developed allowing for the easy access to defined permethylated 6-monosubstituted, as well as 6A,6D-bisubstituted-diamino-CDs so that pure amphiphilic mono- and di-substituted CDs can be obtained. Recently, we described the synthesis of new amphiphilic CD derivatives (Fig. 1), such as TASC, which is composed of a hydrophilic permethylated α -CD part to which a hydrophobic cholesteryl residue is attached by a succinyl linker,⁴ as well as TBSC and TBdSC, which are the permethylated mono- and di-substituted cholesteryl β -CD analogues of TASC.⁵ Cholesterol has been proven to be an efficient membrane anchor. Two substitutions should even allow for double insertion and, thus, an increase in the anchoring strength. Using a succinyl spacer to attach cholesterol to the CD should still be short enough to avoid forming self-inclusion complexes simultaneously, whilst retaining sufficient flexibility.⁶ Previous studies demonstrated that for all three investigated CDs, stable monolayers of the pure compounds can be obtained.^{5,7} We thoroughly studied and compared their amphiphilic behavior and demonstrate that the CD head adjusts its conformation according to the available area per molecule.^{4,5,7} Furthermore, insertion of TBdSC into the phospholipid model membranes⁷ and phase separation has been shown, similar to the native monocholesteryl CDs.^{6,8}

In this paper, we fully describe the interfacial behavior of DPPC mixtures with the amphiphilic CDs, TASC, TBSC and TBdSC, to achieve a complete understanding of the CD insertion properties from a macroscopic to a molecular level, with a special emphasis on the insertion behavior on the molecular scale. By calculating the inverse compressibility modulus and free excess Gibbs energy from the Langmuir isotherms, the influence of the CD ratio, CD type and the number of cholesteryl anchors on the membrane properties has been established. For TASC, the in-plane structure is characterised, on all scales, by Brewster angle microscopy (BAM) at the air–water interface and atomic force microscopy (AFM) of the mono- and bi-layers deposited on mica. Similar to TBdSC, TASC is miscible with the fluid DPPC phase, whereas demixing is observed for the gel phase of DPPC at high surface pressures. Furthermore, we studied the structure of mixed TASC/DPPC mono- and bi-layers perpendicular to the surface with Ångström resolution by neutron reflectivity. In this way a molecular model of the insertion has been established, which suggests that the CD cavities partly protrude into the subphase leaving them accessible for complex formation.

2 Experimental section

2.1 Used chemicals

The amphiphilic CDs were synthesised in our group. TASC (6^l-(α -cholesteryl) succinylamido-(6-deoxy-per-(2,3,6-*O*-methyl))

cyclohexaose was prepared as described recently.⁴ The two β -CD derivatives, 6^l,6^{IV}-(β -cholesteryl) succinylamido-6^l,6^{IV}-(6-deoxy-per-(2,3,6-*O*-methyl)) cycloheptaose (TBdSC) and 6^l-(α -cholesteryl) succinylamido-(6-deoxy-per-(2,3,6-*O*-methyl)) cycloheptaose (TBSC) were synthesised from permethylated amino-cyclodextrin.⁵ DPPC (1,2-dipalmitoyl-*sn*-glycero-3-phosphocholine), chloroform (stabilized with ethanol) were purchased from Sigma–Aldrich. For the neutron reflectivity experiments, DPPC-d₆₂ was bought from Avanti Polar Lipids and deuterium oxide (99.85% D, Euriso-Top) was provided by ILL. Ultra pure water (18.2 M Ω cm) was obtained from a Millipore purification system.

2.2 Langmuir isotherms

The surface pressure–area isotherms were measured with a temperature controlled Langmuir balance (702 BAM Film Balance for Brewster angle microscopy, Micro-Processor Interface IU4, NIMA Technology) used in conjunction with a BAM. Its maximum surface area was 700 cm², the minimum surface area was 80 cm² and it was filled with approximately 500 ml ultra pure water (18.2 M Ω cm) subphase. The trough, placed on an anti-vibration table, was covered by a plexiglas cover. The compounds were dissolved in chloroform and the solution was spread with a Hamilton syringe, typically using spreading volumes between 40 and 60 μ l. The surface pressure, Π , was measured by the Wilhelmy plate method using filter paper. It is defined as

$$\Pi = \gamma_0 - \gamma \quad (1)$$

where γ_0 is the surface tension of the pure subphase and γ is the surface tension in the presence of amphiphiles at the interface. After 15 min of equilibration of the monolayer, the isotherms were recorded with a compression speed of 10 cm² min⁻¹ at a temperature of 20 °C unless stated otherwise.

Isotherm analysis. In order to better identify the phase transitions in the isotherms, the derivative of the surface pressure, Π , with respect to the molecular area, A , has been determined from the isotherms to obtain the isothermal compressibility

$$C_S = -\frac{1}{A} \left(\frac{dA}{d\Pi} \right)_T \quad (2)$$

It has been calculated numerically from the data as follows:

$$C_S = -\frac{1}{A_i} \frac{(A_{i+1} - A_i)}{(\Pi_{i+1} - \Pi_i)} \quad (3)$$

A_i and Π_i are the molecular surface area and surface pressure corresponding to the data point, i , in the isotherm. For further analysis, we have taken the reciprocal isothermal compressibility to give the inverse compressibility modulus C_S^{-1} , which is a measure for interfacial elasticity. The smaller the C_S^{-1} , the higher the film elasticity.^{9–11} For better visibility of the two-dimensional phase transition, the C_S^{-1} values were plotted in a log scale.

To find out about the mixing behavior, the excess free mixing energy $\Delta G_{\text{mix}}^{\text{ex}}$ was determined from the difference in work of the compression between the ideal and real mixed films, which can be

calculated by integrating the experimental Langmuir isotherms (4)

$$\Delta G_{\text{mix}}^{\text{ex}} = \int_0^{\Pi} [A - (x_1 A_1 + x_2 A_2)] d\Pi, \quad (4)$$

where A is the molecular area for the binary mixture. A_n and x_n are the molecular area and molar fraction of the monolayer components.¹²

2.3 Brewster angle microscopy

The Brewster angle microscope (BAM, type PI, C-138K003, Optrel GBR, Berlin) co-aligned with the Langmuir trough was based on the Hoenig and Möbius setup.¹³ A green laser (Las-Nova series 50) with a wavelength of 532 nm was directed onto the water surface at the Brewster angle (53.1°). The reflected light from the surface was imaged by means of a CCD camera (EHD@kamPro02) to give images of the monolayer morphology with a size of 480 μm × 599 μm and a resolution of 480 × 640 pixels.

2.4 Atomic force microscopy

Monolayers. Langmuir–Blodgett (LB) films of the monolayers were deposited onto hydrophilic, freshly cleaved mica wafers (11 × 11 × 0.15 mm³, purchased from Agar Scientific) for several surface pressures from the air–water interface, with a dipping speed of 1 mm min⁻¹. Typically, for good monolayer depositions, transfer ratios close to 1 were obtained.

Bilayers. The bilayer samples were prepared like the monolayers with the Langmuir–Blodgett (LB) technique at $\pi = 40$ mN m⁻¹ and with a dipping speed of 1 mm min⁻¹ for both layers. For the symmetrical bilayers, the first monolayer was deposited by lifting the wafer from the water and subsequently immersing the substrate into the water. For the asymmetrical bilayers, the water surface was thoroughly cleaned after the first deposition and a new monolayer was spread to deposit the second layer by immersing the wafer into the water. Then, the sample was carefully placed into a home-made teflon sample holder, which had been placed into the dipping well before hand in order to transport the sample under water. Typically, transfer ratios of 0.95 were obtained for both depositions.

Imaging. The films were examined with a Nanoscope V (Veeco) AFM in contact mode using cantilevers with a conical silicon etched probe tip (NSC19, MikroMasch) with spring constants in the order of 0.7 N m⁻¹ for imaging the monolayers in air. For water imaging, triangular silicon nitride cantilevers with a reflective gold coating (DNP-S10, Veeco) and spring constants in the order of 0.06 N m⁻¹ were utilised. The spring constants were verified prior to the experiments by the thermal resonance method.¹⁴ Images with scan sizes ranging from 1 μm × 1 μm to 10 μm × 10 μm were recorded with scan rates of 0.5–1.5 Hz.

2.5 Neutron reflectivity

Monolayers. Two mixtures with 20 mol% TASC content were prepared: the first one using hydrogenated DPPC and a second one using deuterated DPPC-d₆₂. The CD/phospholipid samples,

dissolved in chloroform, were spread in a Langmuir trough, which was perfectly aligned with the neutron beam. It was filled with a D₂O subphase and sealed with a Plexiglas cover. For both experiments the spreading volume was 90 μl. The chloroform was allowed to evaporate for 15 min. Then, the film was compressed at the desired surface pressure and the reflectivity curve was recorded.

The neutron reflectivity experiments at the air–liquid interface were carried out on a time-of-flight reflectometer (FIGARO, fluid interfaces grazing angles reflectometer) at the ILL, Grenoble.^{15,16} The incoming beam comprised wavelengths between 2 Å and 30 Å and two incident angles ($\theta_1 = 0.62^\circ$ and $\theta_2 = 3.82^\circ$) were used. We could achieve a q -range from 0.005–0.35 Å⁻¹ with resolutions determined by the chopper openings to be $\Delta q/q \sim 6.5\%$ for θ_1 and $\Delta q/q \sim 8.6\%$ for θ_2 . For details on the variable resolution options of the two instruments please see ref. 15 and 16. The samples were measured in a Langmuir trough (Nima), which was filled with the subphase. Its maximum and minimum areas were 930 cm² and 254 cm², respectively. The reflectivity was normalised by direct beams in a transmission geometry through the windows of the Langmuir trough lid and corrected for the incoherent background scattering.

Bilayers. The bilayers were prepared on 5 × 5 × 1 cm³ homogeneously n-doped silicon single crystals, oriented [111] on the side where the film was deposited and were atomically smooth with a roughness <5 Å, as determined by the manufacturer (SILTRONIX, Archamps, France). Prior to each deposition, the silicon block was cleaned with chloroform, ethanol and water then treated with UV/ozone for 30 min to reach a hydrophilicity as high as possible. For all the bilayers, deuterated DPPC-d₆₂ was used.

The double layer deposition was carried out on a NIMA 611 trough available in the ILL soft matter lab (30 × 20 cm²). The first layer was deposited by the classic Langmuir–Blodgett technique, whereas the second layer was deposited by the Langmuir–Schaefer method (the horizontal sample) at 40 mN m⁻¹ and the temperature was kept constant at 20 °C. The samples were then inserted into a teflon sample cell, which was put into an aluminum box for mounting on the neutron reflectometer. The temperature was controlled using a water circulation bath. The cell was connected to a solvent circuit by means of a peristaltic pump in order to be able to change the subphase for different

Table 1 Selected SLDs for the used materials taken from ref. 4, 19 and 20

Material	SLD [10 ⁻⁶ Å ⁻²]
Si	2.07
SiO ₂	3.47
D ₂ O	6.34
4MW	4.00
SMW	2.07
H ₂ O	-0.56
DPPC-palmitoyl tail	-0.41
DPPC-d ₆₂ palmitoyl tail	6.82
DPPC-PC head	1.74
TASC-CD head	2.15
TASC-cholesteryl tail	0.50

Table 2 The composition and contrasts used for the TASC/DPPC bilayers prepared for the neutron reflectivity experiment (sy: symmetric, as: asymmetric)

sample	1st layer	2nd layer	contrast
1 : 9 sy	10 mol% TASC	10 mol% TASC	D ₂ O, H ₂ O, SMW
2 : 8 as	Pure DPPC	20 mol% TASC	D ₂ O, SMW
5 : 5 as	Pure DPPC	50 mol% TASC	D ₂ O, 4MW, SMW

contrasts. More detailed information about the substrate and the sample preparation have been given elsewhere.¹⁷ Symmetric bilayers, with the same composition for both leaflets, and asymmetric bilayers, with a first DPPC monolayer close to the silicon substrate and a second mixed layer exposed to the water subphase, were prepared (for details see Table 2).

The measurements were conducted on D17 reflectometer¹⁸ operated in the time-of-flight mode at the ILL, Grenoble (France) with a wavelength range from 2 to 20 Å, giving a q -range for the specular reflectivity of 0.005–0.3 Å⁻¹. Each measurement was performed at two reflection angles, $\theta_1 = 0.8^\circ$ (resolution: $\Delta q/q = 2.7\%$) and $\theta_2 = 3.2^\circ$ (resolution: $\Delta q/q$ varied linearly from 3.8% to 13%).¹⁸ The detector efficiency was calibrated with H₂O. For the actual experiment, the neutron beam entered the silicon substrate through one 5×1 cm² side of the block, hit the polished 5×5 cm² face on which the layer under study had been deposited at the grazing incidence, and exited through the opposite 5×1 cm² side.¹⁷ Two direct beams have been measured at two angles of incidence for data normalization.

Different contrasts for various scattering length densities (SLD), such as H₂O (SLD = -0.56×10^{-6} Å⁻²), silicon match water (SMW; SLD = 2.07×10^{-6} Å⁻²), 4 match water (4MW, SLD = 4.0×10^{-6} Å⁻²) and D₂O (SLD = 6.34×10^{-6} Å⁻²) have been measured to remove the ambiguities of the fit (see Table 2).

Furthermore, for all the samples, at least one measurement has been done for the bilayer in the gel phase at 25 °C and in the liquid phase at 55 °C, which was monitored with a thermocouple (equilibration time: 25 min, stability: <0.1 °C, absolute precision: <0.3 °C) in the water-regulated sample chamber described in ref. 17. For annealing, one heating and cooling cycle was performed prior to the actual measurement. For two of the samples the intermediate temperatures, in steps of 5 °C, have also been measured.

Data analysis. Specular reflectivity, $R(q)$, is defined as the ratio between the specularly reflected and incoming intensities of a neutron beam, which is measured as a function of the wave vector transfer ($q = 4\pi/\lambda \sin\theta$) perpendicular to the reflecting surface, where θ is the angle and λ is the wavelength of the incoming beam. $R(q)$ is related to the scattering length density profile across the interface by the square modulus of its Fourier transform. Therefore, the phase is lost and the data needs to be fitted with an appropriate model to obtain the density profile. In this manner it is possible to determine the lipid film profiles with Å precision.^{17,20} The data was fitted with the Motofit package run with the program IGOR Pro 6.0 (Wavemetrics, OR), where the specular reflectivity was calculated by the Abeles matrix method for stratified interfaces.²¹ A detailed description of the Motofit software is given elsewhere.²²

3 Results

3.1 Monolayers

Langmuir isotherms. Compression isotherms have been recorded for CD/DPPC mixtures with CD molar ratios between 0 and 100 mol% in steps of 10 mol% (Fig. 2 A–C). Mixed layers, containing TASC collapse independently from the mixing ratio at *ca.* 42 mN m⁻¹ (Fig. 2 A). Using TBdSC, isotherms can be recorded up to surface pressures of even >50 mN m⁻¹ (Fig. 2 C). The TBSC/DPPC isotherms can be compressed up to a plateau around 35 mN m⁻¹. For CD ratios smaller than 40% the films can be compressed further, up to surface pressures >50 mN m⁻¹ (Fig. 2 B). At least for TBSC, it seems that the monolayers tend to get more stable with an increasing DPPC content and, if one considers the collapse pressure as a criterion for film stability, the TBdSC mixtures appear to be the most stable, followed by TASC and TBSC.²³ The greater stability of the TBdSC films might be caused by the stronger anchoring due to the two lipophilic cholesteryl anchors.

In order to better visualise the phase transitions in the isotherms, the data were plotted in terms of the surface pressure vs. the inverse isothermal compressibility (Fig. 2 D–F). The DPPC plateau (the first peak in the inverse compressibility plots) at 6 mN m⁻¹, which is assigned to the liquid expanded (LE)–liquid condensed (LC) phase transition, can only be found for mixtures with a CD content <20 mol%. However, it is less pronounced and shifted to higher surface pressures. The 10 mol% mixtures for TASC and TBdSC resemble DPPC also at high surface pressures (Fig. 2 D and F). Yet the maximum C_S^{-1} value is already greatly diminished compared to pure phosphocholine (250 mN m⁻¹), although it is still in the range of 100–250 mN m⁻¹, which is typical for the liquid condensed phase according to ref. 10. In contrast, TBSC already exhibits the features of pure CD (Fig. 2 E). For CD contents >50 mol%, the curves almost completely coincide with the ones of the pure CD (Fig. 2 E–F), with maximum values of C_S^{-1} in the order of 50–60 mN m⁻¹, which is similar to phospholipids in the liquid expanded phase at low surface pressures.^{11,24}

At least for TASC and TBdSC, the CD's pseudo-plateau (the second peak in the inverse compressibility plots) is gradually shifted to higher surface pressures with decreasing CD content. This transition can most likely be assigned to a reorientation of the CD residues from a conformation where their cavities' axes are aligned perpendicular with respect to the interface to a conformation where it is aligned parallel with respect to the interface, as previously described for the pure methylated CDs.⁴ The transition occurs at higher surface pressures with decreasing TASC content.

In order to gain a better understanding of the interactions between the phospholipid and the amphiphilic CDs, the excess free energy of mixing $\Delta G_{\text{mix}}^{\text{ex}}$ was calculated from the isotherms and plotted as a function of the molar fraction of the CD for the four different surface pressures (Fig. 3). Negative values indicate attractive interactions, whereas positive ones specify repulsive interactions. Due to rather large error bars for the calculations they can only be interpreted in a qualitative manner. All three different DPPC/CD mixtures are negative for low surface pressures and tend to get more positive with increasing surface

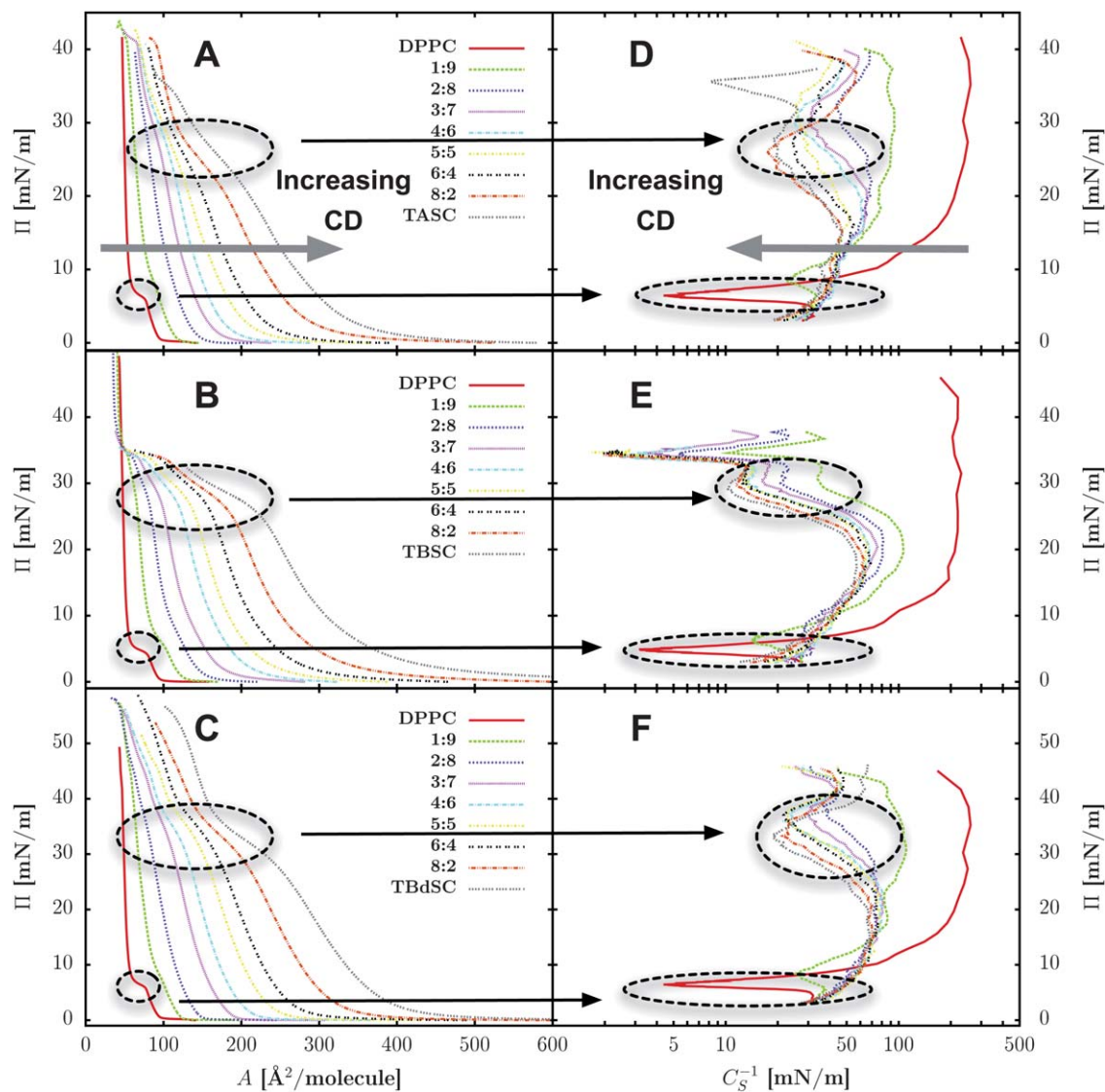


Fig. 2 Langmuir isotherms (left: A. TASC, B. TBSC, C. TBdSC) and inverse compressibility plots (right: D. TASC, E. TBSC, F. TBdSC) for CD/DPPC mixtures at 20 °C.

pressures. This means that the compounds get less miscible with compression. Looking at the general trend, the values for TBSC seem to be the most negative and the ones for TBdSC appear to be the most positive, leading to the assumption that the miscibility with DPPC decreases in the order: TBSC > TASC > TBdSC.

Monolayer in-plane morphology. With the help of BAM and AFM, the in-plane film morphology can be investigated from the μm to the nm scale. For low surface pressures, no contrast is observed with BAM (Fig. 4 A) and very flat AFM images without any features are obtained (Fig. 5 A). At 15 mN m^{-1} , bright domains appear (Fig. 4 B), which look like those for the liquid-expanded (LE) phase–liquid-condensed (LC) phase transition of pure DPPC.²⁵ Complementary AFM images (Fig. 5 B), show that the phase separation occurs also at smaller scales with small elevated zones of 30–80 nm diameter and a height <1 nm. With further compression the aggregates visible *via* BAM

become less bright and denser; many of them consist of a bright core with dimmer surroundings (Fig. 4 C and D). These large domains are also visible in the AFM images and they possess a height of 1 nm (Fig. 5 C). The small aggregates, already visible for the lower compression, remain and, furthermore, there are now additional aggregates, which are 15–20 nm high. The friction contrast of the large domains is similar to the small ones already visible for 15 mN m^{-1} , whereas the tall aggregates, which appear for the high compression, are characterized by a very low friction (see the ESI†). Furthermore, it should be mentioned that the findings for the BAM and AFM are similar to what has been found for TBdSC/DPPC mixtures, except that there is no contrast inversion for the very high surface pressures.⁷

Monolayer structure perpendicular to the surface. Neutron reflectivity experiments were carried out to determine the film thickness and SLD profiles of the mixed CD/DPPC films for different surface pressures. In order to obtain a better contrast

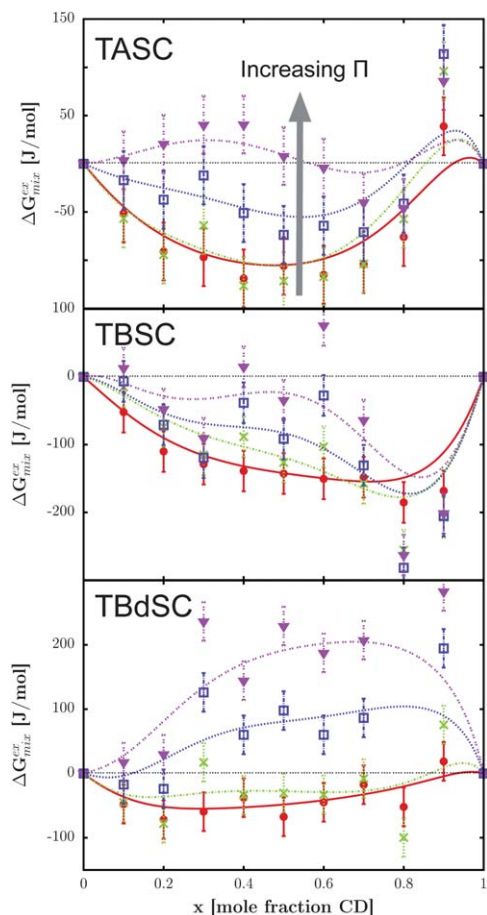


Fig. 3 ΔG_{mix}^{ex} vs. the molar fraction of the CD for different surface pressures from top to bottom A. TASC (\bullet) 5 mN m^{-1} , (\times) 15 mN m^{-1} , (\square) 25 mN m^{-1} , (\blacktriangledown) 35 mN m^{-1}), B. TBSC (\bullet) 5 mN m^{-1} , (\times) 15 mN m^{-1} , (\square) 25 mN m^{-1} , (\blacktriangledown) 33 mN m^{-1}) and C. TBdSC (\bullet) 5 mN m^{-1} , (\times) 15 mN m^{-1} , (\square) 30 mN m^{-1} , (\blacktriangledown) 40 mN m^{-1} .

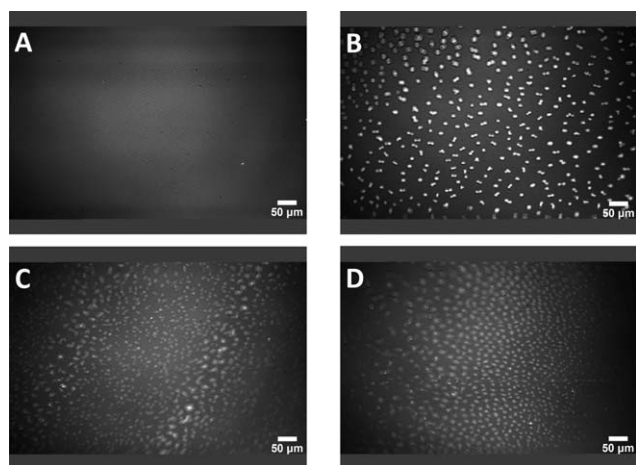


Fig. 4 BAM images for a DPPC monolayer with 20 mol% TASC, A. $\Pi = 5 \text{ mN m}^{-1}$, B. $\Pi = 15 \text{ mN m}^{-1}$, C. $\Pi = 22 \text{ mN m}^{-1}$, D. $\Pi = 35 \text{ mN m}^{-1}$.

and to avoid incoherent scattering, D_2O was used as a subphase for the neutron reflectivity measurements instead of normal water. The isotherms' shape was preserved, however, it is slightly

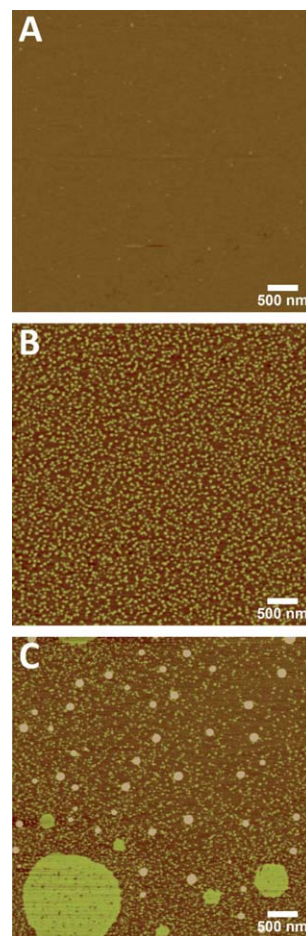


Fig. 5 AFM height images for a DPPC monolayer with 20 mol% TASC, A. $\Pi = 5 \text{ mN m}^{-1}$, B. $\Pi = 15 \text{ mN m}^{-1}$, C. $\Pi = 35 \text{ mN m}^{-1}$.

shifted to higher molecular areas ($\sim 10 \text{ \AA}^2$) compared to isotherms with a H_2O subphase, due to the isotope effect influencing the headgroups.²⁶

The monolayer data (Fig. 6) was fitted using a two-layer box model with two distinct regions of scattering length densities and corresponding thicknesses. The top layer, which is close to the air, can be assigned to the hydrophobic tails of DPPC and the cholesteryl moieties of the CD, whereas the 2nd layer should consist of the hydrophilic DPPC head groups and CD residues. Furthermore, all roughnesses have been constrained to be the same for one surface pressure.

The reflectivity curves for TASC/DPPC- d_{62} in Fig. 6 clearly show a shift of the scattering curve minimum to lower q values with an increasing surface pressure, which indicates an increase in the monolayer thickness.

Expectedly, the total film thickness of the monolayer (Fig. 7, top) increases from $\sim 16 \text{ \AA}$ to $\sim 26 \text{ \AA}$ with the surface pressure. Also, the film roughness increases strongly from 1 \AA to 4 \AA for high compressions. Looking at the Π dependence of the SLD profile (Fig. 7, bottom), it reveals that there exists only a small SLD contrast between the hydrophilic and the hydrophobic slabs for the expanded monolayer.

The thickness of the hydrophilic layer increases from 8 \AA at 5 mN m^{-1} to 12.5 \AA at 40 mN m^{-1} , which is most pronounced

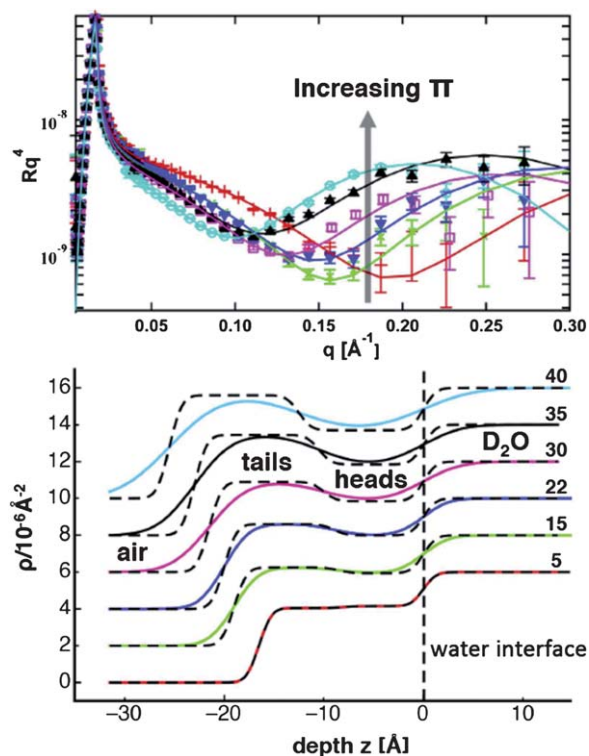


Fig. 6 Neutron reflectivity curves and SLD profiles, from bottom to top, with increasing surface pressures for TASC/DPPC- d_{62} 2:8 (+ is 5 mN m^{-1} , \times is 15 mN m^{-1} , \blacktriangledown is 22 mN m^{-1} , \square is 30 mN m^{-1} , \blacktriangle is 35 mN m^{-1} and \circ is 40 mN m^{-1}). The dashed lines in the SLD profile indicate the different slabs of the box model.

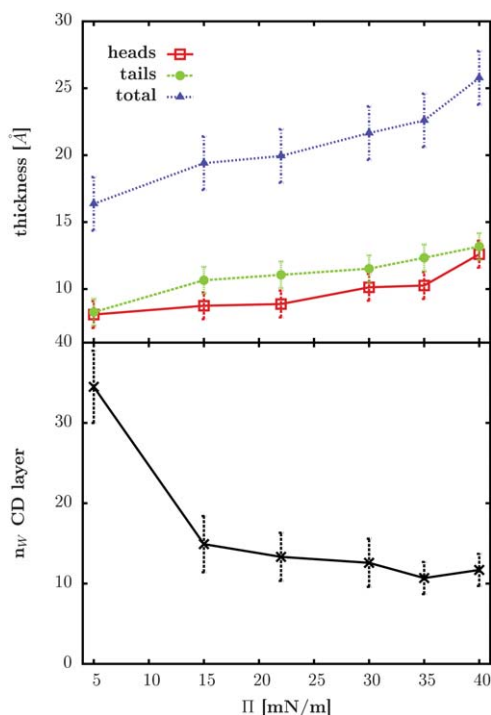


Fig. 7 Thickness of the TASC/DPPC monolayer (top) and the water content of the head layer (bottom) with changes in the surface pressure.

between 35 and 40 mN m^{-1} . It is accompanied by a drop in the SLD from $4.1 \times 10^{-6} \text{ \AA}^{-2}$ to $3.7 \times 10^{-6} \text{ \AA}^{-2}$ due to a loss of water (from 35 to 11 water molecules per headgroup). The number of water molecules was calculated in the same way as described in ref. 4.

The hydrophobic layer thickness increases from 8.3 \AA at 5 mN m^{-1} to 13.2 \AA at 40 mN m^{-1} , at which the tails contribute the most to the increase in the film thickness up to 15 mN m^{-1} . The maximum tail thickness is $\sim 4 \text{ \AA}$ smaller than described for pure DPPC,^{26,27} as well as the DPPC/cholesterol mixtures.²⁸ During compression, the SLD increased from $4.0 \times 10^{-6} \text{ \AA}^{-2}$ to $5.6 \times 10^{-6} \text{ \AA}^{-2}$ for deuterated DPPC and from $-0.3 \times 10^{-6} \text{ \AA}^{-2}$ to $0.25 \times 10^{-6} \text{ \AA}^{-2}$ for the mixed layer containing hydrogenated DPPC (see Table 3 and Fig. 7), which indicates a more compact arrangement.

3.2 Bilayers

Bilayer in-plane morphology. The bilayers, which were deposited on mica substrates with the same compositions as those investigated by neutron reflectivity, were imaged by AFM in water (Fig. 8). All three studied bilayers are rather homogeneous and the phase separation is obvious, which is consistent with the findings for the monolayers at high surface pressures. The symmetric bilayer displays a height difference between the zones of $\sim 1 \text{ nm}$ compared to $\sim 0.5 \text{ nm}$ for the asymmetric ones. In addition, there are holes of $\sim 5 \text{ nm}$ in the 10 mol\% TASC sample (Fig. 8 A), which correspond very well to the bilayer thickness. As observed for the monolayers, the friction is greater for the elevated domains (see ESI†). Comparing the asymmetric bilayers with 20 mol\% and 50 mol\% TASC, the elevated domains decrease with an increasing CD content, which leads to the conclusion that the domains mainly consist of DPPC.

Bilayer structure perpendicular to the surface. For symmetric bilayers, a 5 layer model was adopted with two headgroup slabs, an inner membrane layer for the hydrophobic part, a SiO_2 layer on the silicon block, as well as a thin water layer between the membrane and the substrate. For the asymmetric bilayer, a 6th layer was added to take into account that the inner membrane layer is divided in the slab, which consists only of DPPC tails and another one where the lipid chains are mixed with the cholesteryl residues of the CDs.

The fits for the different contrasts have been performed in a coupled manner. For the monolayer, only the SLD of the hydrophobic tails was allowed to vary for both contrasts. For the bilayers, only the subphase scattering length density was changed for the different contrasts. The error bars were determined by varying each parameter of the model and evaluating the χ^2 parameter, as well as visually checking the quality of the fit. The results fall within the error bars if they still give satisfactory fits for all measured contrasts. Concerning the measurements for temperatures in between 25 and $55 \text{ }^\circ\text{C}$, where only one contrast has been measured, the same error bars have been adopted as those obtained for the samples measured with several contrasts.

Good coupled fits could be obtained for all the measured samples at different temperatures with an exploitable q -range from 0.01 to 0.25 \AA^{-1} . Stable bilayers can be prepared for a symmetric bilayer, with both membrane leaflets containing

Table 3 Fitting results for the DPPC-d₆₂ monolayer with 20 mol% TASC (Fig. 6 at different surface pressures). l_x is the thickness and SLD_x is the scattering length density of slab x

Π [mN m ⁻¹]	l_{head} [Å]	SLD_{head} [10 ⁻⁶ Å ⁻²]	Water [%]	l_{tail} [Å]	$SLD_{\text{tail-d}_{62}}$ [10 ⁻⁶ Å ⁻²]	$SLD_{\text{tail-H}}$ [10 ⁻⁶ Å ⁻²]	Roughness [Å]
5	8.0	4.15	56	8.5	4.05	-0.30	1
15	8.5	3.95	52	10.5	4.25	-0.05	2
22	9.0	4.00	54	11.0	4.60	0.15	2
30	10.0	3.85	51	11.5	4.90	0.15	3
35	10.5	3.85	51	12.5	5.45	0.20	3
40	12.5	3.70	48	13.0	5.60	0.25	4
Errors:	±1	±0.2	±5	±1	±0.2	±0.2	±1

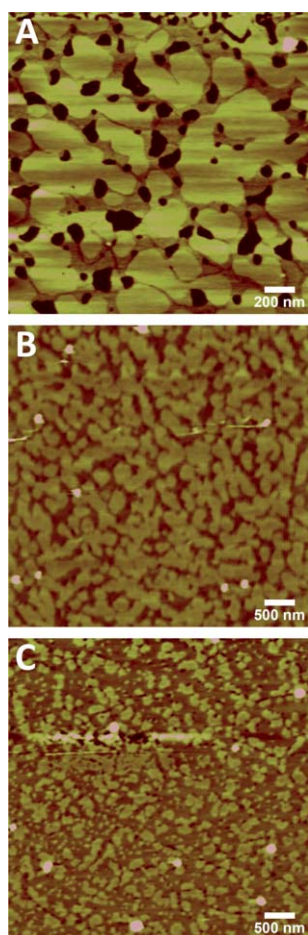


Fig. 8 AFM height images for TASC/DPPC bilayers deposited at 40 mN m⁻¹; A. symmetric 10 mol% TASC, B. asymmetric 20 mol% TASC, C. asymmetric 50 mol% TASC.

10 mol% TASC, as well as asymmetric bilayers with the outer layer containing up to 50% CD (Fig. 9; the reflectivity curves for the other samples, as well as the fitting results, can be found in the ESI†).

The silicon substrates were characterized first, and showed a SiO₂ layer, which was 8–11 Å thick with a roughness of ~5 Å. The parameters have been constrained to these values to fit the supported bilayer experiments. A water layer of 1.5–3.5 Å

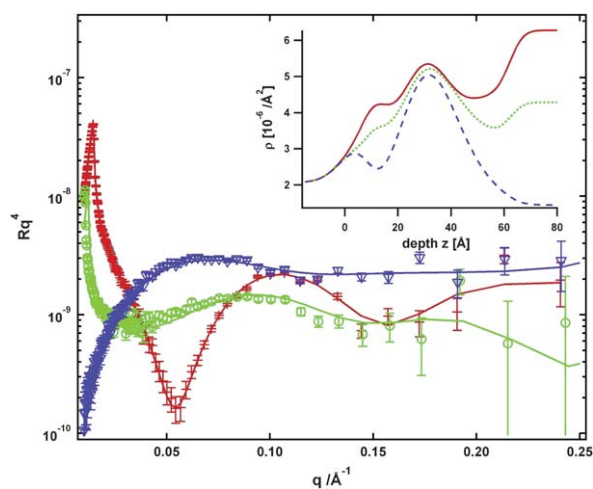


Fig. 9 Neutron reflectivity curves for the asymmetric bilayer with 50 mol% TASC at 55 °C recorded at three contrasts: H₂O (+), 4MW (o) and SMW (v), as well as the corresponding SLD profiles for H₂O (—), 4MW (---) and SMW (-·-).

thickness with a roughness between 4–5 Å had to be systematically added between the substrate and the membrane for all the samples and temperatures. Compared to the symmetric bilayers, the water layer of the asymmetric ones was somewhat elevated (3–3.5 Å), but it was still smaller than what has been reported in the literature.^{17,20} At least for the symmetric layer, due to the strong hydration and the high roughness between the layers, the interface may not be very well defined. Consequently, as the resolution limit of the experiment is reached, it becomes difficult to discern the water film from the headgroups.

The box-model for the symmetric bilayer contains two head-group regions and one single central tail layer. For the asymmetric membranes, the latter is divided into a slab mainly containing DPPC tails and another slab consisting of mixed cholesterol and DPPC tails. For all the head and tail boxes, a roughness between 4–8 Å was found. This increases with temperature, which is very likely to be due to the stronger fluctuations of the membrane.²⁹

The total bilayer thickness expands with the CD content and decreases with heating and it is several Å larger compared to the pure DPPC bilayers.^{17,20} For the bilayer with 10 mol% TASC, the temperature-dependent decrease in the thickness (~4 Å) is less

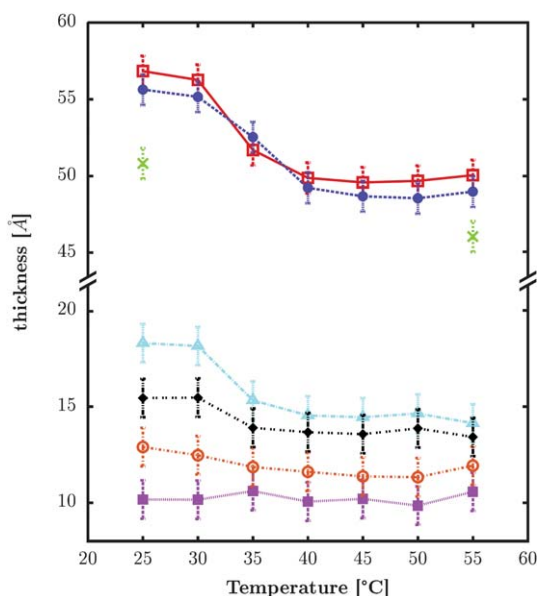


Fig. 10 Top: the total thickness as a function of the temperature for the symmetric bilayer containing 10 mol% TASC (\times) and the asymmetric bilayers with 20 (\bullet) and 50 mol% TASC content (\square). Below: the temperature dependence of the thickness for the DPPC tail (\blacktriangle) and the head group layer (\blacksquare), as well as the mixed headgroup (\blacklozenge) and tail layer (\circ) for the asymmetric 50 mol% TASC bilayer.

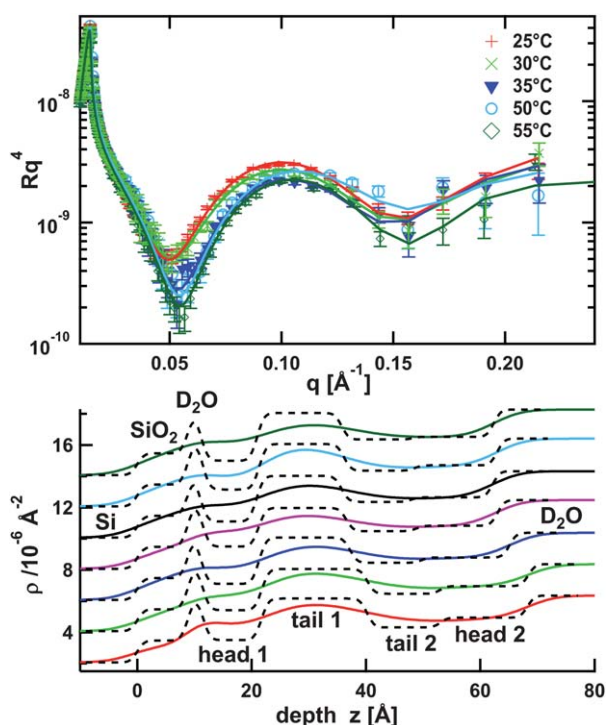


Fig. 11 Neutron reflectivity curves (for clarity, curves for 40 and 45 °C are not displayed) and SLD profiles for the asymmetric 50 mol% TASC bilayer as the temperature increases in steps of 5 °C from the bottom (25 °C) to the top (55 °C). The dashed lines in the SLD profile indicate the different slabs of the box model.

pronounced compared to the two asymmetric bilayers (~ 6 Å) (Fig. 10). For the asymmetric bilayers, the thickness obtained for the scattering curves taken at steps of 5 °C between 25 and 55 °C shows a drop in the thickness between 30–35 °C (which can be seen as two distinct populations in the scattering curves displayed in Fig. 11). This is due to the gel–liquid phase transition of the phospholipids, which is shifted compared to the main transition temperature of pure DPPC (~ 41 °C³⁰). Moreover, due to the less ordered arrangement of the molecules in the liquid phase, the contrast between the tail and head slabs of the mixed layer decreases as the temperature increases (Fig. 11).

Looking at the mixed headgroup layers, an increase in the thickness and water content can be observed with a rising CD content and a decrease in the temperature. So, the water content for 20 mol% TASC decreases from 58% ($T = 25$ °C) to 51% ($T = 55$ °C) and, for 50 mol% TASC, it decreases from 68% ($T = 25$ °C) to 60% ($T = 55$ °C). In contrast, the headgroup's size and water content of pure DPPC (30–35%) in the asymmetric bilayer and the 10 mol% TASC symmetric bilayer show almost no temperature dependence. Furthermore, it seems that, for the symmetric bilayers, the headgroup slab that is close to the silicon substrate is marginally smaller and contains less water (30% close to substrate and 38% close to D₂O, see ESI† for details). Taking into account the molar ratios of the mixtures, the scattering length densities for the hydrophilic regions are in agreement with the values found in the literature for the pure compounds (Table 1). Consequently, the mixed head layer's SLD slightly increases with the CD content.

The tail layer gets thinner with an increasing CD ratio. A water content between 10–20% has been added to account for the holes. This is in agreement with what has been found in the literature.³¹ Moreover, it is obvious that the temperature sensitivity of the thickness is significantly smaller compared to the pure DPPC tails when TASC is present in the membrane. The difference between 10 and 20 mol% TASC is very small, but is very likely to be due to the fact that it is difficult to compare the symmetric and asymmetric bilayers in a strictly quantitative manner. In order to compare the tail layer thickness of the symmetric sample with the asymmetric ones, it has been assumed that the tails of each monolayer contribute equally to the bilayer thickness. The points shown for 10 mol% TASC in Fig. 10 were obtained by dividing the thickness of the symmetric bilayer's tail slab by half. The scattering length densities of the hydrophobic membrane parts are consistent with values which can be found in the literature (Table 1). Consequently, the mixed tail layer's SLD decreases with a rising TASC content due to the higher cholesterol ratio.

4 Discussion

4.1 Miscibility and fluidizing effect of the cholesteryl CD

Previous studies with TBdSC at the air–water interface⁷ and in multilamellar vesicles⁵ show that it readily inserts into phospholipid membranes. Our results show that this is also the case for its mono-substituted cholesteryl α - and β -CD analogues since stable isotherms can be recorded for any kind of molar ratio.

$\Delta G_{\text{mix}}^{\text{ex}}$ calculations indicate a general demixing tendency of CDs and DPPC with increasing compression. Together with the

detailed study of the film morphology at various length scales for the α -CD analogue, the phase behavior of TASC/DPPC mixtures can be examined.

For low surface pressures, the two compounds are miscible and display a homogeneous in-plane structure at all scales. Similar to TBdSC, which is described in detail in ref. 7, at sufficiently high surface pressures, zones of DPPC in the condensed phase appear from which the CD is mostly expelled. Consequently, the phase surrounding these CD-depleted domains has to be enriched with CD. Yet, due to the fluidizing effect of the amphiphilic CDs, as mentioned previously, the liquid condensed phase starts to appear at much higher surface pressures than for pure DPPC.²⁵ This occurs at the μm scale (Fig. 4 B), as well as at the nanoscale (Fig. 5 B). With further compression ($>30 \text{ mN m}^{-1}$), more and more condensed phase DPPC domains appear from which the CD can be expelled and these grow in size, sometimes around an aggregate core consisting of TASC (Fig. 4 C, D and 5 C). So, TASC mixtures behave in a very similar manner to TBdSC mixtures, except that there is no inversion of the contrast observed by BAM for surface pressures above 40 mN m^{-1} . This may be due to the fact that the film collapses before the α -CD residues can completely re-orientate.⁷

The $II - C_S^{-1}$ behavior proves to be a useful tool to gain insight into the monolayer's 2D phase behavior. Caused by discontinuities in the lateral packing at the boundaries and the density fluctuations, a characteristic drop in C_S^{-1} for phase transitions can be detected.¹¹ A fluidizing effect of the amphiphilic CDs can be observed as the peak for the DPPC LE-LC co-existence region is shifted to higher surface pressures for a CD ratio of 10 mol%, which is similar to findings for cholesterol/DPPC films.³² However, there is no strong condensing effect visible in the isotherms, which is usually typical for membranes containing sterols.³³ This is very likely due to the large CD moiety preventing close packing of the film.

The decrease in the inverse compressibility with cholesterol CD contents until it matches those for pure CDs is in contrast to DPPC/cholesterol monolayers with sterol ratios larger than mol 10%⁹ and can be explained by the great structural flexibility of the methylated CD moieties.^{34,35} Due to their much larger size compared to the cholesterol residue as well as the DPPC molecule, they dominate the properties of the mixed layers, rendering them almost as elastic as pure CD films.

4.2 Insertion of the cholesterol CD into membranes at the molecular level

Examining the surface pressure dependence of the mixed monolayer's SLD profile, it is evident that, for low surface pressures, almost no contrast between the head and tail layers exist; however, with further surface pressure increase a good contrast evolves (Fig. 6). This indicates a very disordered film structure for low compressions, which becomes more ordered at high surface pressures.

The hydrophobic tails contribute most to the increase in the film thickness up to 15 mN m^{-1} and can be attributed to the occurrence of DPPC in the LC phase. The sudden increase in the head layer thickness for high surface pressures ($>30 \text{ mN m}^{-1}$)

is probably related to an at least partial rearrangement of the CD moieties with respect to the interface.^{4,7}

A decrease in the water content in the hydrophilic layer is observed with compression. It can be calculated from the SLDs and amounts to 35 water molecules per headgroup in the expanded state to 11 water molecules at a high compression (Fig. 7, bottom). Compared to pure DPPC headgroups,²⁷ where an expulsion of water from the headgroup layer is also observed, the number of water molecules in the mixed layer is significantly higher due to the strongly hydrated CD residues in the layer.⁴

The bilayers seem to get more difficult to prepare with increasing CD content since no stable bilayers could be obtained with TASC molar ratios exceeding 50% and in the AFM images defects are sometimes visible (*e.g.* Fig. 8 A). However, the studied bilayers are sufficiently stable to undergo the gel-liquid phase transition upon heating, which can be followed by looking at the evolution of the thickness with the temperature. The transition is shifted compared to pure DPPC from $41 \text{ }^\circ\text{C}$ ³⁰ to temperatures between $30\text{--}35 \text{ }^\circ\text{C}$. This is in agreement with the fluidizing effect already described for the monolayers, where the LE-LC phase transition is also shifted. Furthermore, the discrete partitioning between the DPPC layer and the mixed layer is preserved upon heating and cooling. This shows that there is no significant reorganisation of the asymmetric bilayer and no, or only very few, flip-flop events occur where the amphiphilic CD is exchanged between the leaflets.

When the layers contain TASC, the tail size remains almost unchanged during heating, which is in contrast to pure DPPC. This can be explained by the fluidizing effect of the CD since it is already in a very disordered state, even at low temperatures. The headgroup thickness, however, decreases significantly for the disordered liquid phase since, in this state, the 'soft' CD moiety can arrange more freely without being constrained by its hydrophobic cholesterol anchor, which is tightly packed in the condensed phase. The smaller headgroup size may also be due to a smaller quantity of water being adsorbed in the layer at high temperatures. The large difference in the thickness between the two tail slabs for asymmetric bilayers is mainly attributed to the disordering effect of the CD in the outer mixed layer. Another contribution to the large size disparity might be the fact that the inner DPPC layer tends to be thicker as it is strongly adsorbed to the substrate and this allows for a more ordered structure.²⁹

For the asymmetric bilayers especially, a very large water content was found and may not only be caused by the strong hydration of the CD heads. Defects in the supported bilayer probably also contribute to the high water content. This explanation is supported by AFM images, which show holes with a depth in the order of magnitude of the bilayer thickness. These defects are also reflected in the $\sim 10\%$ elevated water content of the supported bilayer compared to the corresponding monolayer with 20 mol% TASC, as well as in the necessity to add a similar water content to the tail slabs of the bilayers.

It is striking that, for the mixed leaflet of the 20 mol% asymmetric bilayer at $25 \text{ }^\circ\text{C}$, very similar results are obtained compared to the monolayer at 40 mN m^{-1} , except for the lower water content of the latter. This is an indication that the insertion of the CD is similar for mono- and bi-layers. By comparing the

measured SLD profiles for the monolayers and bilayers with the calculated ones using the SLD profiles of the pure compounds, which are computed with the help of the literature values,^{4,17,26,27} it is possible to deduce the molecular arrangement of the CDs with respect to the phospholipids in the film. The asymmetric bilayer's SLD profile, which was used to fit the real one, was calculated from a DPPC bilayer and a hypothetical bilayer consisting of a pure DPPC and a pure TASC layer, which, in reality, cannot be prepared. For the mixed monolayer, as well as the bilayer, a good match between the tail layers of the calculated and the real SLD profiles can only be achieved when shifting the pure TASC layer profile with respect to the pure DPPC profile by 8 Å and 4 Å, respectively, into the water subphase. This leads to a molecular model of the mixed films like that displayed in Fig. 12, where the CD moiety of TASC protrudes from the headgroup layer. However, it seems that in the case of the bilayer, the CD is more embedded in the film. This finding is further supported by the high roughnesses found for the bilayers and the monolayers at high surface pressures. Of course the fits give only a rather qualitative picture as, in producing the model curves, it is assumed that the mixtures show the same structural behavior as the pure compounds.

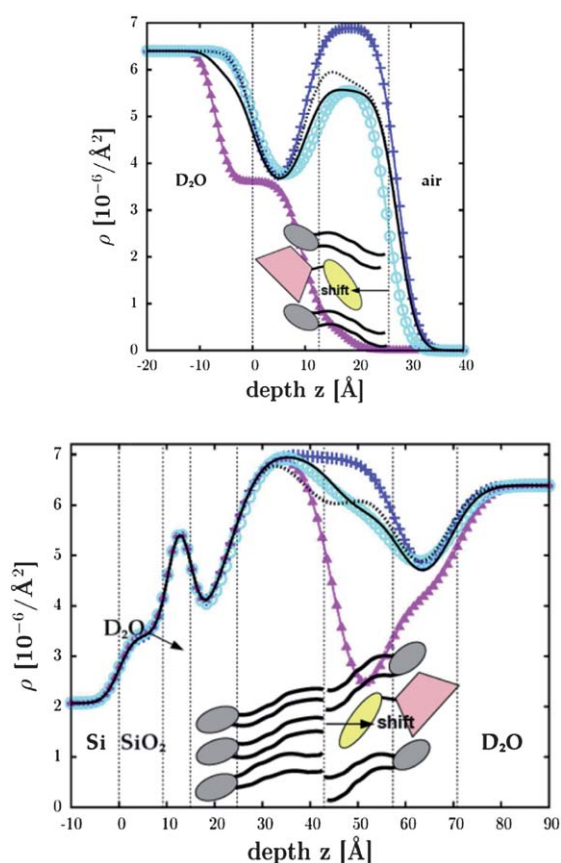


Fig. 12 A. Monolayer SLD profiles at 40 mN m⁻¹ for pure DPPC (+), 20 mol% TASC (o) and pure TASC (Δ). B. SLD profiles for the bilayer of pure DPPC (+), the asymmetric bilayer containing 20 mol% TASC (o) and the asymmetric bilayer containing pure TASC (Δ) as an outer layer. In A. and B. the black and the dashed lines correspond to a model SLD profile for the 20 mol% TASC mixture calculated from the pure compounds with (—) and without shifting (···) the TASC layer towards the water interface.

5 Conclusions

A detailed understanding of the insertion behavior of amphiphilic cholesteryl CDs into phospholipid membranes has been achieved from the macroscopic to the molecular scale. Modified bilayers are stable and are subject to a gel–liquid phase transition upon heating. Depending on the compression, full miscibility of the two amphiphiles is observed for low Π and a clear demixing tendency is apparent during compression. Due to their bulky CD moiety, the amphiphilic CDs exhibit a distinct fluidizing effect on the membrane, which clearly renders it more elastic. TbDSC, with its two cholesteryl residues, seems to be best anchored to the membrane compared to its α - and β -CD analogues with only one membrane anchor. However, TASC appears to be more firmly inserted into the membrane than TBSC. With the help of neutron reflectivity, a molecular picture of the insertion has been achieved. At least for high surface pressures and temperatures below the gel–liquid phase transition, the CD residues partly protrude from the membrane, leaving the CD cavities accessible to form complexes.

Cholesteryl CDs appear to be suitable candidates as tools to functionalize natural membranes and synthetic vesicles. They are readily synthesized with cholesterol as stable and affordable anchors.^{4,5} While being inserted into phospholipid membranes,⁷ the conformational adaptability⁴ and accessibility of the CD cavity prevails. This is crucial with respect to the CD's specific inclusion properties at the membrane surface and its pharmacological relevance regarding its use as a drug delivery vehicle, which should be addressed in future studies.^{3,36} Since CDs are known to form rotaxanes with suitably sized polymers,^{37,38} the cholesteryl CDs could serve as ideal compounds to bridge such supramolecular assemblies with macroscopic structures, like membranes. This could give rise to a new kind of sliding grafted polymer layer, which has been theoretically described by Baulin *et al.*³⁹ Subsequent studies are under way to design and characterize such topological grafts, where the connection between the different elements composing the material is defined by simple topological rules.

6 Acknowledgments

This work is supported by the French Research Program ANR-07-NANO-016-02 and Region Alsace (Ph.D. Grant). The authors wish to thank Carlos Marques from the ICS Strasbourg for the coordination of the ANR project and his kind support. We also wish to thank Maria Chiriach, Angelika Klaus, Mayeul Collot and Jean-Maurice Mallet for their intervention in the compound synthesis. Furthermore, we wish to thank the ILL for beam-time and the use of the PSCM facilities. We are grateful for the help and support of Hanna Wacklin and Richard Campbell during the neutron experiments on FIGARO and D17 at the ILL, Grenoble.

References

- 1 H. Dodziuk, *Cyclodextrins and their complexes*, WILEY-VCA, 2006.
- 2 J. Szejtli, *Chem. Rev.*, 1998, **98**, 1743–1753.
- 3 F. Sallas and R. Darcy, *Eur. J. Org. Chem.*, 2008, (6), 957–969.
- 4 M. Bauer, C. Fajolles, T. Charitat, H. Wacklin and J. Daillant, *Journal of Physical Chemistry B*, 2011, accepted.

- 5 M. Collot, M. Garcia-Moreno, C. Fajolles, M. Roux, L. Mauclair and M.J., *Tetrahedron Lett.*, 2007, **48**, 8566–8569.
- 6 R. Auzely-Velty, B. Perly, O. Tache, T. Zemb, P. Jehan, P. Guenot, J. P. Dalbiez and F. Djedaini-Pilard, *Carbohydr. Res.*, 1999, **318**, 82–90.
- 7 A. Klaus, C. Fajolles, M. Bauer, M. Collot, J.-M. Mallet and J. Daillant, *Langmuir*, 2011, **27**, 7580–7586.
- 8 M. Roux, R. Auzely-Velty, F. Djedaini-Pilard and B. Perly, *Biophys. J.*, 2002, **82**, 813–822.
- 9 K. Sabatini, J. Mattila and K.K., *Biophys. J.*, 2008, **95**, 2340–2355.
- 10 J. Davies and E. Rideal, *Interfacial phenomena*, Academic Press, New York, 2nd edition, 1963, 265.
- 11 J. Smaby, V. Kulkarni, M. Momsen and R. Brown, *Biophys. J.*, 1996, **70**, 868–877.
- 12 F. Goodrich, *Proceedings of the 2nd International Congress on Surface Activity* (Academic Press, London), 1957, 85–91.
- 13 D. Hoenig and D. Möbius, *J. Phys. Chem.*, 1991, **95**, 4590.
- 14 R. Lévy and M. Maaloum, *Nanotechnology*, 2002, **13**, 33–37.
- 15 FIGARO, Reflectometer at the ILL, <http://www.ill.eu/instruments-support/instruments-groups/instruments/figaro/>.
- 16 R. A. Campbell, H. Wacklin, I. Sutton, R. Cubitt and G. Fragneto, *Focus Point Eur. Phys. J.*, 2011, in press.
- 17 T. Charitat, E. Bellet-Amalric, G. Fragneto and F. Graner, *Eur. Phys. J. B*, 1999, **8**, 583–593.
- 18 T. Cubitt and G. Fragneto, *Appl. Phys. A: Mater. Sci. Process.*, 2002, **74**, s329–331.
- 19 B. Stidder, G. Fragneto and S. Roser, *Langmuir*, 2005, **21**, 9187–9193.
- 20 B. Koenig, S. Kureger, W. Orts, F. Majkrzak, N. Berk, J. Silverton and K. Gawritsch, *Langmuir*, 1996, **12**, 1343–1350.
- 21 O. Heavens, *Optical Properties of Thin Films*, Butterworth, 1955.
- 22 A. Nelson, *J. Appl. Crystallogr.*, 2006, **39**, 273–276.
- 23 P. Dynarowicz-Latka and K. Hac-Wydro, *Colloids Surf., B*, 2004, **37**, 21–25.
- 24 S. Ali, J. Smaby, M. Momsen, H. Bockmann and R. Brown, *Biophys. J.*, 1998, **74**, 338–348.
- 25 J. Zhao, D. Vollhardt, G. Brezesinski, S. Siegel, W. J., J. Li and R. Miller, *Colloids Surf., A*, 2000, **171**, 175–184.
- 26 D. Vaknin, K. Kjaer, J. Als-Nielsen and M. Lösche, *Biophys. J.*, 1991, **59**, 1325–1332.
- 27 C. Naumann, T. Brumm, A. Rennie, J. Penfold and M. Bayerl, *Langmuir*, 1995, **11**, 3948–3952.
- 28 J. Wu, T. Lin, C. Yang, U. Jeng, H. Lee and M.-R. R. Shih, *Colloids Surf., A*, 2006, **284–285**, 103–108.
- 29 L. Malaquin, T. Charitat and J. Daillant, *Eur. Phys. J. E*, 2010, **31**, 285–301.
- 30 Z. Leonenko, E. Finot, T. Dahms and D. Cramb, *Biophys. J.*, 2004, **86**, 3783–3793.
- 31 G. Fragneto, F. Graner, T. Charitat, P. Dubos and E. Bellet-Amalric, *Langmuir*, 2000, **16**, 4581–4588.
- 32 K. Kim, C. Kim and Y. Byun, *Langmuir*, 2001, **17**, 5066–5070.
- 33 P. Quinn and C. Wolf, *Biochim. Biophys. Acta, Biomembr.*, 2009, **1788**, 33–46.
- 34 T. Steiner and W. Saenger, *Carbohydr. Res.*, 1996, **282**, 53–63.
- 35 M. Caira, S. Bourne, W. Mhlongo and P. Dean, *Chem. Commun.*, 2004, (19), 2216–2217.
- 36 T. Loftsson and D. Duchène, *Int. J. Pharm.*, 2007, **329**, 1–11.
- 37 A. Harada, *Coord. Chem. Rev.*, 1996, **148**, 115–133.
- 38 G. Wenz, B. H. Han and A. Muller, *Chem. Rev.*, 2006, **106**, 782–817.
- 39 V. A. Baulin, A. Johnner and C. M. Marques, *Macromolecules*, 2005, **38**, 1434–1441.

Bibliography

- [1] T. M. Allen and P. R. Cullis. Drug delivery systems: Entering the mainstream. *Science*, 303(5665):1818–1822, March 2004.
- [2] Jesse V Jokerst, Tatsiana Lobovkina, Richard N Zare, and Sanjiv S Gambhir. Nanoparticle pegylation for imaging and therapy. *Nanomedicine*, 6(4):715–728, 2011.
- [3] Rainer Haag and Felix Kratz. Polymer therapeutics: Concepts and applications. *Angewandte Chemie International Edition*, 45(8):1198–1215, 2006.
- [4] Omathanu Pillai and Ramesh Panchagnula. Polymers in drug delivery. *Current Opinion in Chemical Biology*, 5(4):447–451, August 2001.
- [5] A. K. Patri, I. J. Majoros, and J. R. Baker. Dendritic polymer macromolecular carriers for drug delivery. *Current Opinion In Chemical Biology*, 6(4):466–471, August 2002.
- [6] Rainer H. Müller, Karsten Mäder, and Sven Gohla. Solid lipid nanoparticles (SLN) for controlled drug delivery - a review of the state of the art. *European Journal of Pharmaceutics and Biopharmaceutics*, 50(1):161–177, July 2000.
- [7] D. Lasic. *Stealth(®) Liposomes*. CRC Press London, 1995.
- [8] Eric Forssen and Michael Willis. Ligand-targeted liposomes. *Advanced Drug Delivery Reviews*, 29(3):249–271, February 1998.
- [9] M. L. Immordino, F. Dosio, and L. Cattel. Stealth liposomes: review of the basic science, rationale, and clinical applications, existing and potential. *International Journal of Nanomedicine*, 1(3):297–315, 2006.
- [10] R. D. Hofheinz, S. U. Gnad-Vogt, U. Beyer, and A. Hochhaus. Liposomal encapsulated anti-cancer drugs. *Anti-cancer Drugs*, 16(7):691–707, August 2005.
- [11] E. T. Castellana and P. S. Cremer. Solid supported lipid bilayers: From biophysical studies to sensor design. *Surface Science Reports*, 61(10):429–444, November 2006.
- [12] V. Kiessling, M. Domanska, D. Murray, C. Wen, and L. K. Tamm. Supported lipid bilayers: Development and applications in chemical biology. In *Wiley Encyclopedia of Chemical Biology*. John Wiley & Sons, Inc., 2008.

- [13] Alexandre Berquand, Pierre-Emmanuel Mazeran, Jacques Pantigny, Vanessa Proux-Delrouyre, Jean-Marc Laval, and Christian Bourdillon. Two-step formation of Streptavidin-Supported Lipid Bilayers by PEG-triggered vesicle fusion. fluorescence and atomic force microscopy characterization. *Langmuir*, 19(5):1700–1707, March 2003.
- [14] J. K. Vasir, M. K. Reddy, and V. D. Labhasetwar. Nanosystems in drug targeting: Opportunities and challenges. *Current Nanoscience*, 1(1):47–64, January 2005.
- [15] B. Alberts, A. Johnson, J. Lewis, M. Raff, K. Roberts, and Walter P. *Molecular Biology of the Cell*. Garland Science, 2007.
- [16] G. I. Bell. Models for specific adhesion of cells to cells. *Science*, 200(4342):618–627, 1978.
- [17] Nathan W. Moore and Tonya L. Kuhl. The role of flexible tethers in multiple ligand-receptor bond formation between curved surfaces. *Biophysical Journal*, 91(5):1675–1687, September 2006.
- [18] A. G. Moreira and C. M. Marques. The role of polymer spacers in specific adhesion. *Journal of Chemical Physics*, 120(13):6229–6237, April 2004.
- [19] Vladimir A. Baulin, Albert Johner, and Carlos M. Marques. Sliding grafted polymer layers. *Macromolecules*, 38(4):1434–1441, February 2005.
- [20] Akira Harada. Preparation and structures of supramolecules between cyclodextrins and polymers. *Coordination Chemistry Reviews*, 148:115–133, February 1996.
- [21] G. Wenz, B. H. Han, and A. Müller. Cyclodextrin rotaxanes and polyrotaxanes. *Chemical Reviews*, 106(3):782–817, March 2006.
- [22] S.J. Singer and G.L. Nicolson. The fluid mosaic model of the structure of cell membranes. *Science*, 175:720–731, 1972.
- [23] http://php.med.unsw.edu.au/cellbiology/index.php?title=Cell_Membranes_and_Compartment.
- [24] D. Nelson and M. Cox. *Principles of biochemistry*. Tenney S, 2005.
- [25] H. Ohvo-Rekilä and B. Ramstedt. Cholesterol interactions with phospholipids in membranes. *Progress in Lipid Research*, 41:66–97, 2002.
- [26] K. Simons and D. Toomre. Lipid rafts and signal transduction. *Nature Reviews Molecular Cell Biology*, 1(1):31–39, October 2000.
- [27] John F. Hancock. Lipid rafts: contentious only from simplistic standpoints. *Nat Rev Mol Cell Biol*, 7(6):456–462, June 2006.
- [28] J.N. Israelachvili. *Intermolecular and Surface Forces*. Academic Press, 1992.

- [29] E. Sackmann. Chapter 1 biological membranes architecture and function. In R. Lipowsky and E. Sackmann, editors, *Structure and Dynamics of Membranes*, volume Volume 1, pages 1–63. North-Holland, 1995.
- [30] Vladimir M. Kaganer, Helmuth Möhwald, and Pulak Dutta. Structure and phase transitions in langmuir monolayers. *Review of Modern Physics*, 71:779–819, 1999.
- [31] J. Zhao, D. Vollhardt, G. Brezesinski, S. Siegel, Wu J., J. Li, and R. Miller. Effect of protein penetration into phospholipid monolayers: morphology and structure. *Colloids and Surfaces A: Physicochemical and Engineering Aspects*, 171:175–184, 2000.
- [32] D. Vaknin, K. Kjaer, J. Als-Nielsen, and M. Lösche. Structural properties of phosphatidylcholine in a monolayer at the air/water interface. *Biophysical Journal*, 59:1325–1332, 1991.
- [33] F. Evans and H. Wennerström. *The colloidal domain*. Wiley-VCH, 1999.
- [34] Vasili Yaminsky, Tommy Nylander, and Barry Ninham. Thermodynamics of transfer of amphiphiles between the liquid-air interface and a solid surface wetting tension study of langmuir-blodgett films. *Langmuir*, 13(6):1746–1757, March 1997.
- [35] F. Jahnig. What is the surface tension of a lipid bilayer membrane? *Biophysical Journal*, 71(3):1348–1349, September 1996.
- [36] H. J. Butt, B. Cappella, and M. Kappl. Force measurements with the atomic force microscope: Technique, interpretation and applications. *Surface Science Reports*, 59(1-6):1–152, October 2005.
- [37] D. H. Murray, L. K. Tamm, and V. Kiessling. Supported double membranes. *Journal of Structural Biology*, 168(1):183–189, October 2009.
- [38] B. Stidder, G. Fragneto, and S. Roser. Effect of low amounts of cholesterol on the swelling behavior of floating bilayers. *Langmuir*, 21:9187–9193, 2005.
- [39] L. Malaquin, T. Charitat, and J. Daillant. Supported bilayers: Combined specular and diffuse x-ray scattering. *European Physical Journal E*, 31:285–301, 2010.
- [40] J. Schmitt, B. Danner, and Bayerl T.M. Polymer cushions in supported phospholipid bilayers reduce significantly the frictional drag between bilayer and solid surface. *Langmuir*, 17:244–246, 2001.
- [41] Claudia Steinem and Andreas Janshoff. Multicomponent membranes on solid substrates: Interfaces for protein binding. *Current Opinion in Colloid & Interface Science*, 15(6):479–488, December 2010.
- [42] T. Charitat, E. Bellet-Amalric, G. Fragneto, and F. Graner. Adsorbed and free lipid bilayers at the solid-liquid interface. *European Physical Journal B*, 8:583–593, 1999.
- [43] E. Sinner and W. Knoll. Functional tethered membranes. *Current Opinion Chemical Biology*, 5:705–711, 2001.

- [44] A.V. Hughes, S.J. Roser, M. Gerstenberg, A. Goldar, R. Stidder, B. Feidenhans, and J. Bradshaw. Phase behavior of dmpc free supported bilayers studied by neutron reflectivity. *Langmuir*, 18(21):8161–8171, 2002.
- [45] M. Eeman and M. Deleu. From biological membranes to biomimetic model membranes. *Biotechnology, Agronomy, Society and Environment*, 14:719–736, 2010.
- [46] R. Lipowsky. *Handbook of biological physics*, chapter Vol. 1. Elsevier, 1995.
- [47] E. Lifschitz. *Journal of Experimental and Theoretical Physics USSR*, 29:94, 1955.
- [48] Y. F. Dufrene, T. Boland, J. W. Schneider, W. R. Barger, and G. U. Lee. Characterization of the physical properties of model biomembranes at the nanometer scale with the atomic force microscope. *Faraday Discussions*, 111:79–94, 1998.
- [49] CA Helm, JN Israelachvili, and PM McGuiggan. Molecular mechanisms and forces involved in the adhesion and fusion of amphiphilic bilayers. *Science*, 246(4932):919–922, 1989.
- [50] W. Helfrich and R. Servuss. Undulations, steric interaction and cohesion of fluid membranes, 1984-01-01.
- [51] P. Bongrand. Ligand-receptor interactions. *Reports On Progress In Physics*, 62(6):921–968, June 1999.
- [52] D A Hammer and M Tirrell. Biological adhesion at interfaces. *Annu. Rev. Mater. Sci.*, 26(1):651–691, August 1996.
- [53] C. A. Helm, W. Knoll, and J. N. Israelachvili. Measurement of ligand receptor interactions. *Proceedings of the National Academy of Sciences of the United States of America*, 88(18):8169–8173, September 1991.
- [54] EL Florin, VT Moy, and HE Gaub. Adhesion forces between individual ligand-receptor pairs. *Science*, 264(5157):415–417, 1994.
- [55] R. Merkel, P. Nassoy, A. Leung, K. Ritchie, and E. Evans. Energy landscapes of receptor-ligand bonds explored with dynamic force spectroscopy. *Nature*, 397(6714):50–53, January 1999.
- [56] Nathan W. Moore, Dennis J. Mulder, and Tonya L. Kuhl. Adhesion from tethered ligand-receptor bonds with microsecond lifetimes. *Langmuir*, 24(4):1212–1218, February 2008.
- [57] J. Y. Wong, T. L. Kuhl, J. N. Israelachvili, N. Mullah, and S. Zalipsky. Direct measurement of a tethered ligand-receptor interaction potential. *Science*, 275(5301):820–822, February 1997.
- [58] Claus Jeppesen, Joyce Y. Wong, Tonya L. Kuhl, Jacob N. Israelachvili, Nasreen Mullah, Samuel Zalipsky, and Carlos M. Marques. Impact of polymer tether length on multiple ligand-receptor bond formation. *Science*, 293(5529):465–468, July 2001.

- [59] Jeremy I. Martin, Cheng-Zhong Zhang, and Zhen-Gang Wang. Polymer-tethered ligand-receptor interactions between surfaces. *Journal of Polymer Sciences B Polymer Physics*, 44(18):2621–2637, 2006.
- [60] S. Alexander. Adsorption of chain molecules with a polar head: A scaling description. *Journal De Physique*, 38(8):983–987, 1977.
- [61] P. G. de Gennes. Conformations of polymers attached to an interface. *Macromolecules*, 13(5):1069–1075, September 1980.
- [62] S. T. Milner, T. A. Witten, and M. E. Cates. A parabolic density profile for grafted polymers. *Europhysics Letters*, 5(5):413–418, March 1988.
- [63] A. M. Skvortsov, I. V. Pavlushkov, A. A. Gorbrunov, Y. B. Zhulina, O. V. Borisov, and V. A. Pryamitsyn. Structure of dense-grafted polymer monolayers. *Vysokomolekulyarnye Soedineniya Seriya A*, 30(8):1615–1622, August 1988.
- [64] Donald J. Cram. Preorganization-from solvents to spherands. *Angewandte Chemie International Edition*, 25(12):1039–1057, 1986.
- [65] Jean-Marie Lehn. Supramolecular chemistry - scope and perspectives molecules, supermolecules, and molecular devices (nobel lecture). *Angewandte Chemie International Edition*, 27(1):89–112, 1988.
- [66] Donald J. Cram. The design of molecular hosts, guests, and their complexes (nobel lecture). *Angewandte Chemie International Edition*, 27(8):1009–1020, 1988.
- [67] Cheol Moon, Young Min Kwon, Won Kyu Lee, Yoon Jeong Park, and Victor C. Yang. In vitro assessment of a novel polyrotaxane-based drug delivery system integrated with a cell-penetrating peptide. *Journal of Controlled Release*, 124(1-2):43–50, December 2007.
- [68] Hiroshi Ikeda, Takumi Sugiyama, and Akihiko Ueno. New chemosensor for larger guests based on modified cyclodextrin bearing seven hydrophobic chains each with a hydrophilic end group, 2007-04-01.
- [69] Guido H. Clever, Shohei Tashiro, and Mitsuhiko Shionoya. Light-triggered crystallization of a molecular host-guest complex. *Journal of the American Chemical Society*, 132(29):9973–9975, July 2010.
- [70] Wolfram Saenger. Cyclodextrin inclusion compounds in research and industry. *Angewandte Chemie International Edition*, 19(5):344–362, 1980.
- [71] Mikhail V. Rekharsky and Yoshihisa Inoue. Complexation thermodynamics of cyclodextrins. *Chemical Reviews*, 98(5):1875–1918, July 1998.
- [72] M. Villiers. Sur la fermentation de la fécule par l'action du ferment butyrique. *Comptes Rendus*, 112:536–538, 1891.
- [73] F. Schardinger. Bildung kristalliner Polysaccharide (Dextrine) aus Stärke-kleister durch Mikroben. *Centralblatt fuer Bakteriologie , Parasitenkunde und Infektionskrankheiten*, 29:188–197, 1911.

- [74] F. Cramer. *Einschlussverbindungen (Inclusion Compounds)*. Springer-Verlag: Berlin, 1954.
- [75] Jozsef Szejtli. Introduction and general overview of cyclodextrin chemistry. *Chemical Reviews*, 98(5):1743–1754, July 1998.
- [76] M. Del Valle. Cyclodextrins and their uses: A review. *Process Biochemistry*, 39:1033–1046, 2004.
- [77] Thorsteinn Loftsson and Dominique Duchène. Cyclodextrins and their pharmaceutical applications. *International Journal of Pharmaceutics*, 329(1-2):1–11, February 2007.
- [78] Gerhard Wenz. Cyclodextrins as building blocks for supramolecular structures and functional units. *Angew. Chem. Int. Ed. Engl.*, 33(8):803–822, 1994.
- [79] Wolfram Saenger, Joël Jacob, Katrin Gessler, Thomas Steiner, Daniel Hoffmann, Haruyo Sanbe, Kyoko Koizumi, Steven M. Smith, and Takeshi Takaha. Structures of the common cyclodextrins and their larger analogues beyond the doughnut. *Chemical Reviews*, 98(5):1787–1802, July 1998.
- [80] Toshio Nakagawa, Koji Ueno, Mariko Kashiwa, and Junko Watanabe. The stereoselective synthesis of cyclomaltopentaose. a novel cyclodextrin homologue with d.p. five. *Tetrahedron Letters*, 35(12):1921–1924, March 1994.
- [81] Axel Müller and Gerhard Wenz. Thickness recognition of bolaamphiphiles by α -cyclodextrin. *Chemistry - A European Journal*, 13(8):2218–2223, 2007.
- [82] Kenny B. Lipkowitz. Applications of computational chemistry to the study of cyclodextrins. *Chemical Reviews*, 98(5):1829–1874, July 1998.
- [83] H. Dodziuk. *Cyclodextrins and their complexes*. WILEY-VCA, 2006.
- [84] Gerhard Wenz. Recognition of monomers and polymers by cyclodextrins, 2009.
- [85] T. Loftsson and M. E. Brewster. Pharmaceutical applications of cyclodextrins .1. drug solubilization and stabilization. *Journal of Pharmaceutical Sciences*, 85(10):1017–1025, October 1996.
- [86] Kenneth A. Connors. The stability of cyclodextrin complexes in solution. *Chemical Reviews*, 97(5):1325–1358, August 1997.
- [87] Thorsteinn Loftsson, Már Másson, and Marcus E. Brewster. Self-association of cyclodextrins and cyclodextrin complexes. *Journal of Pharmaceutical Sciences*, 93(5):1091–1099, 2004.
- [88] L. Fielding. Determination of association constants (k-a) from solution nmr data. *Tetrahedron*, 56(34):6151–6170, August 2000.
- [89] Abdul Rauf Khan, Peter Forgo, Keith J. Stine, and Valerian T. D'Souza. Methods for selective modifications of cyclodextrins. *Chemical Reviews*, 98(5):1977–1996, July 1998.

- [90] Weihua Tang and Siu-Choon Ng. Facile synthesis of mono-6-amino-6-deoxy-[alpha]-, [beta]-, [gamma]-cyclodextrin hydrochlorides for molecular recognition, chiral separation and drug delivery. *Nat. Protocols*, 3(4):691–697, April 2008.
- [91] Ronald Palin, Simon J.A Grove, Alan B Prosser, and Ming-Qiang Zhang. Mono-6-(o-2,4,6-triisopropylbenzenesulfonyl)-[gamma]-cyclodextrin, a novel intermediate for the synthesis of mono-functionalised [gamma]-cyclodextrins. *Tetrahedron Letters*, 42(50):8897–8899, December 2001.
- [92] A. Gadelle and J. Defaye. Selective halogenation at primary positions of cyclomaltooligosaccharides and a synthesis of per-3,6-anhydro cyclomaltooligosaccharides. *Angewandte Chemie-international Edition In English*, 30(1):78–80, January 1991.
- [93] Maria T. Rojas, Rainer Koeniger, J. Fraser Stoddart, and Angel E. Kaifer. Supported monolayers containing preformed binding sites. synthesis and interfacial binding properties of a thiolated beta-cyclodextrin derivative. *Journal of the American Chemical Society*, 117(1):336–343, January 1995.
- [94] Wei Wang, Alan J. Pearce, Yongmin Zhang, and Pierre Sinaÿ. Diisobutylaluminium-promoted regioselective de-o-methylation of cyclodextrins: an expeditious entry to selectively modified cyclodextrins. *Tetrahedron: Asymmetry*, 12(3):517–523, March 2001.
- [95] Alan J. Pearce and Pierre Sinaÿ. Diisobutylaluminum-promoted regioselective de-o-benylation of perbenzylated cyclodextrins: A powerful new strategy for the preparation of selectively modified cyclodextrins. *Angewandte Chemie International Edition*, 39(20):3610–3612, 2000.
- [96] Thomas Lecourt, Jean-Maurice Mallet, and Pierre Sinaÿ. An efficient preparation of 6i,iv dihydroxy permethylated [beta]-cyclodextrin. *Carbohydrate Research*, 338(22):2417–2419, October 2003.
- [97] Ryuhei Nishiyabu and Koji Kano. Double self-inclusion by rotating glucopyranose units in per-o-methylated β -cyclodextrin moieties attached to a porphyrin in aqueous solution. *European Journal of Organic Chemistry*, 2004(24):4988–4985, 2004.
- [98] Thomas Steiner and Wolfram Saenger. Closure of the cavity in permethylated cyclodextrins through glucose inversion, flipping, and kinking. *Angewandte Chemie International Edition*, 37(24):3404–3407, 1998.
- [99] M. Caira, S. Bourne, W. Mhlongo, and P. Dean. New crystalline forms of permethylated β -cyclodextrin. *Chemical Communications*, 19:2216–2217, 2004.
- [100] M. Roux, S. Moutard, B. Perly, and F. Djedaini-Pilard. Lipid lateral segregation driven by diacyl cyclodextrin interactions at the membrane surface. *Biophysical Journal*, 93(5):1620–1629, September 2007.
- [101] F. Sallas and R. Darcy. Amphiphilic cyclodextrins - advances in synthesis and supramolecular chemistry. *European Journal of Organic Chemistry*, 2:957–969, 2008.

- [102] C. E. Granger, C. P. Felix, H. P. Parrot-Lopez, and B. R. Langlois. Fluorine containing beta-cyclodextrin: a new class of amphiphilic carriers. *Tetrahedron Letters*, 41(48):9257–9260, November 2000.
- [103] C. C. Ling, R. Darcy, and W. Risse. Cyclodextrin liquid-crystals - synthesis and self-organization of amphiphilic thio-beta-cyclodextrins. *Journal of the Chemical Society-chemical Communications*, 5(5):438–440, March 1993.
- [104] E. Memisoglu, A. Bochot, M. Sen, D. Duchene, and A. A. Hincal. Non-surfactant nanospheres of progesterone inclusion complexes with amphiphilic beta-cyclodextrins. *International Journal of Pharmaceutics*, 251(1-2):143–153, January 2003.
- [105] P. C. Tchoreloff, M. M. Boissonnade, A. W. Coleman, and A. Baszkin. Amphiphilic monolayers of insoluble cyclodextrins at the water/air interface. surface pressure and surface potential studies. *Langmuir*, 11(1):191–196, January 1995.
- [106] Sylviane Lesieur, Daniel Charon, Pierre Lesieur, Catherine Ringard-Lefebvre, Valérie Muguet, Dominique Duchène, and Denis Wouessidjewe. Phase behavior of fully hydrated dmpe-amphiphilic cyclodextrin systems. *Chemistry and Physics of Lipids*, 106(2):127–144, August 2000.
- [107] F. Sallas, K. Niikura, and S. I. Nishimura. A practical synthesis of amphiphilic cyclodextrins fully substituted with sugar residues on the primary face. *Chemical Communications*, 5(5):596–597, March 2004.
- [108] S. Moutard, B. Perly, P. Gode, G. Demailly, and F. Djedaini-Pilard. Novel glycolipids based on cyclodextrins. *Journal of Inclusion Phenomena and Macrocyclic Chemistry*, 44(1-4):317–322, December 2002.
- [109] Angelika Klaus, Christophe Fajolles, Martin Bauer, Mayeul Collot, Jean-Maurice Mallet, and Jean Daillant. Amphiphilic behavior and membrane solubility of a dicholesteryl-cyclodextrin. *Langmuir*, 27(12):7580–7586, June 2011.
- [110] J. Lin, C. Creminon, B. Perly, and F. Djedaini-Pilard. New amphiphilic derivatives of cyclodextrins for the purpose of insertion in biological membranes: The "cup and ball" molecules. *Journal of the Chemical Society-perkin Transactions 2*, 2(12):2639–2646, December 1998.
- [111] A. Angelova, C. Fajolles, C. Hocquelet, F. Djedaini-Pilard, S. Lesieur, V. Bonnet, B. Perly, G. Lebas, and L. Mauclair. Physico-chemical investigation of asymmetrical peptidolipidyl-cyclodextrins. *Journal of Colloid and Interface Science*, 322(1):304–314, June 2008.
- [112] Rachel Auzély-Velty, Bruno Perly, Olivier Taché, Thomas Zemb, Philippe Jehan, Pierre Guenot, Jean-Pierre Dalbiez, and Florence Djedaini-Pilard. Cholesteryl-cyclodextrins: synthesis and insertion into phospholipid membranes. *Carbohydrate Research*, 318(1-4):82–90, May 1999.

- [113] Michel Roux, Bruno Perly, and Florence Djedaini-Pilard. Self-assemblies of amphiphilic cyclodextrins. *European Biophysics Journal*, 36(8):861–867, 2007.
- [114] R. Auzély-Velty, F. Djedaini-Pilard, S. Désert, B. Perly, and Th. Zemb. Micellization of hydrophobically modified cyclodextrins. 1. micellar structure. *Langmuir*, 16(8):3727–3734, April 2000.
- [115] R. Auzely-Velty, C. Pean, F. Djeddaini-Pilard, T. Zemb, and B. Perly. Micellization of hydrophobically modified cyclodextrins: 2. inclusion of guest molecules. *Langmuir*, 17(2):504–510, January 2001.
- [116] M. Collot, M. Garcia-Moreno, C. Fajolles, M. Roux, L. Mauclaire, and Mallet J. Bis antennae amphiphilic cyclodextrins: The first examples. *Tetrahedron Letters* 48, 48:8566–8569, 2007.
- [117] M. Roux, R. Auzely-Velty, F. Djedaini-Pilard, and B. Perly. Cyclodextrin-induced lipid lateral separation in dmPC membranes: H-2 nuclear magnetic resonance study. *Biophysical Journal*, 82(2):813–822, February 2002.
- [118] Akira Harada. Cyclodextrin-based molecular machines. *Accounts of Chemical Research*, 34(6):456–464, June 2001.
- [119] Nobuhiko Yui, Ryo Katoono, and Atsushi Yamashita. Functional cyclodextrin polyrotaxanes for drug delivery, 2009.
- [120] Xiang Ma and He Tian. Bright functional rotaxanes. *Chemical Society Reviews*, 39(1):70–80, 2010.
- [121] T. Takata. Polyrotaxane and polyrotaxane network: Supramolecular architectures based on the concept of dynamic covalent bond chemistry. *Polymer Journal*, 38(1):1–20, 2006.
- [122] A. Yerin, E. S. Wilks, G. P. Moss, and A. Harada. Nomenclature for rotaxanes and pseudorotaxanes - (IUPAC recommendations 2008). *Pure and Applied Chemistry*, 80(9):2041–2068, September 2008.
- [123] Vincent Aucagne, David A. Leigh, Julia S. Lock, and Andrew R. Thomson. Rotaxanes of cyclic peptides. *Journal of the American Chemical Society*, 128(6):1784–1785, February 2006.
- [124] Pier Lucio Anelli, Peter R. Ashton, Neil Spencer, Alexandra M. Z. Slawin, J. Fraser Stoddart, and David J. Williams. Self-assembling [2]pseudorotaxanes. *Angewandte Chemie International Edition*, 30(8):1036–1039, 1991.
- [125] Sergey A. Nepogodiev and J. Fraser Stoddart. Cyclodextrin-based catenanes and rotaxanes. *Chemical Reviews*, 98(5):1959–1976, July 1998.
- [126] Jun Araki and Kohzo Ito. Recent advances in the preparation of cyclodextrin-based polyrotaxanes and their applications to soft materials. *Soft Matter*, 3(12):1456–1473, 2007.

- [127] Y. Liu, Y. L. Zhao, H. Y. Zhang, and H. B. Song. Polymeric rotaxane constructed from the inclusion complex of beta-cyclodextrin and 4,4'-dipyridine by coordination with nickel(II) ions. *Angewandte Chemie-international Edition*, 42(28):3260–3263, 2003.
- [128] M. B. Steinbrunn and G. Wenz. Synthesis of water-soluble inclusion compounds from polyamides and cyclodextrins by solid-state polycondensation. *Angewandte Chemie-international Edition In English*, 35(18):2139–2141, October 1996.
- [129] A. Harada and M. Kamachi. Complex-formation between poly(ethylene glycol) and alpha-cyclodextrin. *Macromolecules*, 23(10):2821–2823, May 1990.
- [130] J. Li, A. Harada, and M. Kamachi. Sol-gel transition during inclusion complex-formation between alpha-cyclodextrin and high-molecular-weight poly(ethylene glycol)s in aqueous-solution. *Polymer Journal*, 26(9):1019–1026, 1994.
- [131] Jie Wang, Li Li, Yunying Zhu, Peng Liu, and Xuhong Guo. Hydrogels assembled by inclusion complexation of poly(ethylene glycol) with alpha-cyclodextrin. *Asia-Pacific Jrnal of Chem. Eng*, 4(5):544–550, 2009.
- [132] A. Harada, J. Li, and M. Kamachi. Double-stranded inclusion complexes of cyclodextrin threaded on poly(ethylene glycol). *Nature*, 370(6485):126–128, July 1994.
- [133] G. Wenz, E. Vonderbey, and L. Schmidt. Synthesis of a lipophilic cyclodextrin-[2]-rotaxane. *Angewandte Chemie-international Edition In English*, 31(6):783–785, June 1992.
- [134] Jun Li, Xiping Ni, and Kam Leong. Block-selected molecular recognition and formation of polypseudorotaxanes between poly(propylene oxide)-poly(ethylene oxide)-poly(propylene oxide) triblock copolymers and α -cyclodextrin. *Angewandte Chemie International Edition*, 42(1):69–72, 2003.
- [135] Jun Li, Xiping Ni, Zhihan Zhou, and Kam W. Leong. Preparation and characterization of polypseudorotaxanes based on block-selected inclusion complexation between poly(propylene oxide)-poly(ethylene oxide)-poly(propylene oxide) triblock copolymers and α -cyclodextrin. *Journal of the American Chemical Society*, 125(7):1788–1795, February 2003.
- [136] A. Harada. Polyrotaxanes. *Acta Polym.*, 49(1):3–17, 1998.
- [137] P. Lo Nostro, L. Giustini, E. Fratini, B. W. Ninham, F. Ridi, and P. Baglioni. Threading, growth, and aggregation of pseudopolyrotaxanes. *Journal of Physical Chemistry B*, 112(4):1071–1081, January 2008.
- [138] Pierandrea Lo Nostro, Josias R. Lopes, and Camillo Cardelli. Formation of cyclodextrin-based polypseudorotaxane: Solvent effect and kinetic study. *Langmuir*, 17(15):4610–4615, July 2001.
- [139] Massimo Ceccato, Pierandrea Lo Nostro, and Piero Baglioni. α -cyclodextrin/polyethylene glycol polyrotaxane: A study of the threading process. *Langmuir*, 13(9):2436–2439, April 1997.

- [140] J. Horsky. Solubility and spectrophotometric investigation of alpha-cyclodextrin and poly(ethylene glycol) complexation. *European Polymer Journal*, 34(5-6):591–596, May 1998.
- [141] Guillaume Fleury, Cyril Brochon, Guy Schlatter, Guillaume Bonnet, Alain Lapp, and Georges Hadziioannou. Synthesis and characterization of high molecular weight polyrotaxanes: towards the control over a wide range of threaded [small alpha]-cyclodextrins. *Soft Matter*, 1(5):378–385, 2005.
- [142] Y. Okumura, K. Ito, and R. Hayakawa. Inclusion-dissociation transition in the complex formation between molecular nanotubes and linear polymer chains in solutions. *Physical Review Letters*, 80(22):5003–5006, June 1998.
- [143] Yasushi Okumura, Kohzo Ito, and Reinosuke Hayakawa. Theory on inclusion behavior between cyclodextrin molecules and linear polymer chains in solutions. *Polymer Advanced Technology*, 11(8-12):815–819, 2000.
- [144] Akira Harada, Jun Li, and Mikiharu Kamachi. The molecular necklace: a rotaxane containing many threaded [alpha]-cyclodextrins. *Nature*, 356(6367):325–327, March 1992.
- [145] T. Arai and T. Takata. One-pot synthesis of main chain-type polyrotaxane containing cyclodextrin wheels. *Chemistry Letters*, 36(3):418–419, March 2007.
- [146] T. Ooya, H. Mori, M. Terano, and N. Yui. Synthesis of a biodegradable polymeric supramolecular assembly for drug-delivery. *Macromolecular Rapid Communications*, 16(4):259–263, April 1995.
- [147] Tiejun Zhao and Haskell W. Beckham. Direct synthesis of cyclodextrin-rotaxanated poly(ethylene glycol)s and their self-diffusion behavior in dilute solution. *Macromolecules*, 36(26):9859–9865, December 2003.
- [148] Jun Araki, Changming Zhao, and Kohzo Ito. Efficient production of polyrotaxanes from α -cyclodextrin and poly(ethylene glycol). *Macromolecules*, 38(17):7524–7527, August 2005.
- [149] Miyuko Okada and Akira Harada. Preparation of β -cyclodextrin polyrotaxane: Photodimerization of pseudo-polyrotaxane with 2-anthryl and triphenylmethyl groups at the ends of poly(propylene glycol). *Organic Letters*, 6(3):361–364, February 2004.
- [150] Gerhard Wenz and Bruno Keller. Threading cyclodextrin rings on polymer chains. *Angewandte Chemie International Edition*, 31(2):197–199, 1992.
- [151] J. Terao, A. Tang, J. J. Michels, A. Krivokapic, and H. L. Anderson. Synthesis of poly(para-phenylenevinylene) rotaxanes by aqueous suzuki coupling. *Chemical Communications*, 3(1):56–57, January 2004.
- [152] Konstantin A. Udachin, Lee D. Wilson, and John A. Ripmeester. Solid polyrotaxanes of polyethylene glycol and cyclodextrins: The single crystal x-ray structure of PEG- β -cyclodextrin. *Journal of the American Chemical Society*, 122(49):12375–12376, December 2000.

- [153] Akira Harada, Jun Li, and Mikiharu Kamachi. Preparation and properties of inclusion complexes of polyethylene glycol with alpha-cyclodextrin. *Macromolecules*, 26(21):5698–5703, October 1993.
- [154] I. N. Topchieva, A. E. Tonelli, I. G. Panova, E. V. Matuchina, F. A. Kalashnikov, V. I. Gerasimov, C. C. Rusa, M. Rusa, and M. A. Hunt. Two-phase channel structures based on alpha-cyclodextrin-polyethylene glycol inclusion complexes. *Langmuir*, 20(21):9036–9043, October 2004.
- [155] A. A. Harada, J. Okada, M. M. nd Li, and M. Kamachi. Preparation and characterization of inclusion complexes of poly(propylene glycol) with cyclodextrins. *Macromolecules*, 28(24):8406–8411, November 1995.
- [156] Christophe Travelet, Guy Schlatter, Pascal Hébraud, Cyril Brochon, Alain Lapp, and Georges Hadziioannou. Formation and self-organization kinetics of α -cd/peo-based pseudo-polyrotaxanes in water. A specific behavior at 30 °C. *Langmuir*, 25(15):8723–8734, August 2009.
- [157] T. Ooya, H. Utsunomiya, M. Eguchi, and N. Yui. Rapid binding of concanavalin a and maltose-polyrotaxane conjugates due to mobile motion of alpha-cyclodextrins threaded onto a poly(ethylene glycol). *Bioconjugate Chemistry*, 16(1):62–69, January 2005.
- [158] T. E. Girardeau, T. J. Zhao, J. Leisen, H. W. Beckham, and D. G. Bucknall. Solid inclusion complexes of alpha-cyclodextrin and perdeuterated poly(oxyethylene). *Macromolecules*, 38(6):2261–2270, March 2005.
- [159] Michael J. Frampton and Harry L. Anderson. Insulated molecular wires. *Angewandte Chemie International Edition*, 46(7):1028–1064, 2007.
- [160] Tooru Ooya, Daisuke Inoue, Hak Soo Choi, Yuichiro Kobayashi, Scott Loethen, David H. Thompson, Young Ho Ko, Kimoon Kim, and Nobuhiko Yui. pH-responsive movement of cucurbit[7]uril in a diblock polypseudorotaxane containing dimethyl β -cyclodextrin and cucurbit[7]uril. *Organic Letters*, 8(15):3159–3162, July 2006.
- [161] Hoon Hyun and Nobuhiko Yui. Mono-, di-, or triazidated cyclodextrin-based polyrotaxanes for facile and efficient functionalization via click chemistry. *Macromolecular Rapid Communications*, 32(3):326–331, 2011.
- [162] A. Harada, Y. Takashima, and H. Yamaguchi. Cyclodextrin-based supramolecular polymers. *Chemical Society Reviews*, 38(4):875–882, 2009.
- [163] K. Sabatini, J. Mattila, and Kinnuen K. Interfacial behavior of cholesterol, ergosterol and lanosterol in mixtures with DPPC and DMPC. *Biophysical Journal*, 95:2340–2355, 2008.
- [164] J. Davies and E. Rideal. Interfacial phenomena. *Academic Press, New York*, (2nd edition):265, 1963.

- [165] J. Smaby, V. Kulkarni, M. Momsen, and R. Brown. The interfacial elastic packing interactions of galactosylceramides, sphingomyelins, and phosphatidylcholine. *Biophysical Journal*, 70:868–877, 1996.
- [166] F. Goodrich. Molecular interaction in mixed monolayers. *Proceedings of the 2nd International Congress on Surface Activity (Academic Press, London)*, pages 85–91, 1957.
- [167] <http://www.ksvnima.com/langmuir-and-langmuir-blodgett-troughs>.
- [168] S. Lecuyer, G. Fragneto, and T. Charitat. Effect of an electric field on a floating lipid bilayer: A neutron reflectivity study. *European Physical Journal E*, 21:153–159, 2006.
- [169] Martin Bauer, Thierry Charitat, Christophe Fajolles, Giovanna Fragneto, and Jean Daillant. Insertion properties of cholesteryl cyclodextrins in phospholipid membranes: a molecular study. *Soft Matter*, page DOI: 10.1039/CISM06346D, 2012.
- [170] D. Hoenig and D. Möbius. Direct visualization of monolayers at the air-water interface by Brewster Angle Microscopy. *Journal of Physical Chemistry*, 95:4590, 1991.
- [171] J. Meunier and S. Hénon. Microscope at the Brewster angle: Direct observation of first-order phase transitions in monolayers. *Review of Scientific Instruments*, 62:936–939, 1991.
- [172] M. Born. *Principles of Optics*. Pergamon Press Inc., 1959.
- [173] M. Harke, R. Teppner, and H. Motschmann. Description of a single modular optical setup for ellipsometry, surface plasmons, waveguide modes, and their corresponding imaging techniques including Brewster Angle Microscopy. *Review of Scientific Instruments*, 68:3130–3134, 1997.
- [174] G. Binnig, C. Quate, and C. Gerber. Atomic-force microscope. *Physical Review Letters*, 56:930–933, 1986.
- [175] R. Garcia and R. Perez. Dynamic Atomic Force Microscopy methods. *Surface Science Reports*, 47:197–301, 2002.
- [176] P. Samori. *Scanning Probe Microscopies Beyond Imaging*. WILEY-VCH, 2006.
- [177] F. L. Leite and P. S. P. Herrmann. Application of atomic force spectroscopy (AFS) to studies of adhesion phenomena: a review. *Journal of Adhesion Science and Technology*, 19(3-5):365–405, 2005.
- [178] B. Cappella and G. Dietler. Force-distance curves by atomic force microscopy. *Surface Science Reports*, 34(1-3):1–104, 1999.
- [179] Nanoscope v multimode - user manual, 2006.
- [180] J. E. Sader, I. Larson, P. Mulvaney, and L. R. White. Method for the calibration of atomic-force microscope cantilevers. *Review of Scientific Instruments*, 66(7):3789–3798, July 1995.

- [181] J. E. Sader, J. W. M. Chon, and P. Mulvaney. Calibration of rectangular atomic force microscope cantilevers. *Review of Scientific Instruments*, 70(10):3967–3969, October 1999.
- [182] R. Lévy and M. Maaloum. Measuring the spring constant of atomic force microscope cantilevers: thermal fluctuations and other methods. *Nanotechnology*, 13:33–37, 2002.
- [183] H. Hertz. Die berührung fester elastischer körper. *Reine Angewandte Mathematik*, 92:156–171, 1881.
- [184] K. Johnson, K. Kendall, and A. Roberts. Surface energy and the contact of elastic solid. *Proceedings of the Royal Society London*, 324:301–313, 1971.
- [185] B. B. Derjaguin, B. M. Muller, and Y. P. Toporov. Effect of contact deformation on the adhesion of particles. *Journal of Colloid Interface Science*, 53:314–326, 1975.
- [186] Shell Ip, James K. Li, and Gilbert C. Walker. Phase segregation of untethered zwitterionic model lipid bilayers observed on mercaptoundecanoic-acid-modified gold by afm imaging and force mapping. *Langmuir*, 26(13):11060–11070, July 2010.
- [187] X. Zhou and S. Chen. Theoretical foundation of X-ray and neutron reflectometry. *Physics Reports*, 257:223–348, 1995.
- [188] G. Fragneto-Cusani. Neutron reflectivity at the solid/liquid interface: Examples of applications in biophysics. *Journal of Physics: Condensed Matter*, 13:4973–4989, 2001.
- [189] J. Daillant and A. Gibaud. *X-Ray and Neutron Reflectivity: Principles and Applications*. Springer, 1999.
- [190] O. Heavens. *Optical Properties of Thin Films*. Butterworth, 1955.
- [191] A. Nelson. Co-refinement of multiple contrast neutron/x-ray reflectivity data using MOTOFIT. *Journal of Applied Crystallography*, 39:273–276, 2006.
- [192] Figaro. <http://www.ill.eu/instruments-support/instruments-groups/instruments/figaro/>.
- [193] R. Cubitt and G. Fragneto. D17: the new reflectometer at the ILL. *Applied Physics A*, 74:329.331, 2002.
- [194] F. Kasler. *Quantitative Analysis by NMR spectroscopy*. Academic Press London and New York, 1973.
- [195] M. Hesse, H. Meier, and B. Zeeh. *Spektroskopische Methoden in der organischen Chemie*. Thieme, 2005.
- [196] E. Kwan and S. Huang. Structural elucidation with NMR spectroscopy: Practical strategies for organic chemists. *European Journal of Organic Chemistry*, 1:2671–2688, 2008.

- [197] H. Desvaux, P. Berthault, N. Birlirakis, and M. Goldmann. ROESY hors-résonance: Une nouvelle méthode d'étude de la relaxation par RMN. *Comptes rendus de l'Académie des sciences Paris*, 317:19–25, 1993.
- [198] R. A. Dluhy and D. G. Cornell. In-situ measurement of the infrared-spectra of insoluble monolayers at the air-water-interface. *Journal of Physical Chemistry*, 89(15):3195–3197, 1985.
- [199] R. Mendelsohn, J. W. Brauner, and A. Gericke. External infrared reflection-absorption spectrometry monolayer films at the air-water-interface. *Annual Review of Physical Chemistry*, 46:305–334, 1995.
- [200] R. Mendelsohn and C. R. Flach. Infrared reflection-absorption spectroscopy of lipids, peptides, and proteins in aqueous monolayers. *Peptide-lipid Interactions*, 52:57–88, 2002.
- [201] R. Mendelsohn, G. R. Mao, and C. R. Flach. Infrared reflection-absorption spectroscopy: Principles and applications to lipid-protein interaction in langmuir films. *Biochimica Et Biophysica Acta-biomembranes*, 1798(4):788–800, April 2010.
- [202] Richard A. Dluhy, Susan M. Stephens, Suci Widayati, and Amy D. Williams. Vibrational spectroscopy of biophysical monolayers. applications of ir and raman spectroscopy to biomembrane model systems at interfaces. *Spectrochimica Acta Part A: Molecular and Biomolecular Spectroscopy*, 51(8):1413–1447, July 1995.
- [203] R. A. Dluhy. Infrared spectroscopy of biophysical monomolecular films at interfaces: Theory and applications (reprinted from physical chemistry of biological interfaces. *Applied Spectroscopy Reviews*, 35(4):315–351, 2000.
- [204] Daniel Blaudez, Thierry Buffeteau, Bernard Desbat, and Jean Marie Turllet. Infrared and raman spectroscopies of monolayers at the air-water interface. *Current Opinion in Colloid & Interface Science*, 4(4):265–272, August 1999.
- [205] C. R. Flach, A. Gericke, J. W. Brauner, and R. Mendelsohn. Quantitative irras determination of lipid acyl chain and helical peptide orientation in binary monolayers. *Biophysical Journal*, 72(2):WP340–WP340, February 1997.
- [206] C. R. Flach, J. W. Brauner, J. W. Taylor, R. C. Baldwin, and R. Mendelsohn. External reflection ftir of peptide monolayer films in-situ at the air/water interface - experimental-design, spectra-structure correlations, and effects of hydrogen-deuterium exchange. *Biophysical Journal*, 67(1):402–410, July 1994.
- [207] J. N. Israelachvili. Measurement of forces between surfaces immersed in electrolyte-solutions. *Faraday Discussions*, 65:20–24, 1978.
- [208] Jacob N. Israelachvili and Gayle E. Adams. Measurement of forces between two mica surfaces in aqueous electrolyte solutions in the range 0-100 nm. *Journal of the Chemical Society - Faraday Trans. 1*, 74:975–1001, 1978.

- [209] J. C. Froberg and T. Ederth. On the possibility of glue contaminations in the surface force apparatus. *Journal of Colloid and Interface Science*, 210(1):215–217, February 1999.
- [210] B. Derjaguin. Untersuchungen Äijber die reibung und adhÄdsion, iv, 1934-11-03.
- [211] J. N. Israelachvili. Thin film studies using multiple-beam interferometry. *Journal of Colloid and Interface Science*, 44(2):259–272, August 1973.
- [212] Samuel Tolansky. *Multiple-beam interferometry of surfaces and films*. Clarendon Press, 1948.
- [213] *Direct surface force measurement techniques*, volume 46. Springer, 2001.
- [214] T. L. Kuhl, D. E. Leckband, D. D. Lasic, and J. N. Israelachvili. Modulation of interaction forces between bilayers exposing short-chained ethylene-oxide headgroups. *Biophysical Journal*, 66(5):1479–1488, May 1994.
- [215] T. Steiner and W. Saenger. Crystal structure of anhydrous hexakis-(2,3,6-tri-O-methyl)-cyclomaltohexaose (permethyl- α -cyclodextrin) grown from hot water and from cold NaCl solutions. *Carbohydrate Research*, 282:53–63, 1996.
- [216] Stefan Immel and Frieder W. Lichtenthaler. Per-o-methylated α - and β -cd: Cyclodextrins with inverse hydrophobicity. *Starch/Stärke*, 48(6):225–232, 1996.
- [217] R. Vico, R. de Rossi, and B. Maggio. PM-IRRAS assessment of compression-mediated orientation of the nanocavity of monoacylated β -cyclodextrin in monolayers at the air-water interface. *Langmuir*, 11:8407–8413, 2010.
- [218] G. Coulon, J. Daillant, B. Collin, J. Benattar, and Y. Gallot. Time evolution of the free surface of ultrathin copolymer films. *Macromolecules*, 26:1582–1589, 1993.
- [219] H Rapaport, I. Kuzmenko, K. Lafont, S. Kjaer, P. Howes, J. Als-Nielsen, M. Lahav, and L. Leiserowitz. Cholesterol monohydrate nucleation in ultrathin films on water. *Biophysical Journal*, 81:2729–2736, 2001.
- [220] Bruno Demé and Lay-Theng Lee. Adsorption of a hydrophobically modified polysaccharide at the air-water interface: Kinetics and structure. *The Journal of Physical Chemistry B*, 101(41):8250–8258, October 1997.
- [221] C. Sultanem, S. Moutard, J. Benattar, F. Diedaini-Pilard, and B. Perly. Hydration of black foam films made of amphiphilic cyclodextrins. *Langmuir*, 20:3311–3318, 2004.
- [222] T. Shikata, R. Takahashi, and Y. Satokawa. Hydration and dynamic behavior of cyclodextrins in aqueous solution. *Journal of Physical Chemistry B*, 111:12239–12247, 2007.
- [223] M. Jana and S. Bandyopadhyay. Microscopic investigation of the hydration properities of cyclodextrin and its substituted forms. *Langmuir*, 25:13084–13091, 2009.

- [224] G. Romet-Lemonne, J. Daillant, P. Guenoun, J. Yang, and J.W. Mays. Thickness and density profiles of polyelectrolyte brushes: Dependence on grafting density and salt concentration. *Physical Review Letters*, 93:148301, 2004.
- [225] A. Kusmin, R. Lechner, M. Kammel, and W. Saenger. Native and methylated cyclodextrins with positive and negative solubility coefficients in water studied by SAXS and SANS. *Journal of Physical Chemistry B*, 112:12888–12898, 2008.
- [226] P. Dynarowicz-Latka and K. Hac-Wydro. Interactions between phosphatidylcholines and cholesterol in monolayers at the air/water interface. *Colloids and Surfaces B: Biointerfaces*, 37:21–25, 2004.
- [227] S. Ali, J. Smaby, M. Momsen, H. Bockmann, and R. Brown. Acyl chain-length asymmetry alters the interfacial elastic interactions of phosphatidylcholines. *Biophysical Journal*, 74:338–348, 1998.
- [228] Martin Bauer, Christophe Fajolles, Thierry Charitat, Hanna Wacklin, and Jean Daillant. Amphiphilic behavior of new cholesteryl cyclodextrins: A molecular study. *Journal of Physical Chemistry B*, page DOI: 10.1021/jp205917q, 2011.
- [229] B. Koenig, S. Kureger, W. Orts, F. Majkrzak, N. Berk, J. Silverton, and K. Gawritsch. Neutron reflectivity and atomic force microscopy studies of a lipid bilayer in water adsorbed to the surface of a silicon single crystal. *Langmuir*, 12:1343–1350, 1996.
- [230] C. Naumann, T. Brumm, A. Rennie, J. Penfold, and M. Bayerl. Hydration of DPPC monolayers at the air/water interface and its modulation by the nonionic surfactant $c_{12}e_4$: A neutron reflection study. *Langmuir*, 11:3948–3952, 1995.
- [231] J. Wu, T. Lin, C. Yang, U. Jeng, H. Lee, M.X-ray reflectivity Shih, and BAM studies on the LB film of mixed DPPC/DC-cholesterol monolayer. X-ray reflectivity and bam studies on the lb film of mixed dppc/dc-cholesterol monolayer. *Colloids and Surfaces A: Physicochemical and Engineering Aspects*, 284-285:103–108, 2006.
- [232] Z. Leonenko, E. Finot, T. Dahms, and D. Cramb. Investigation of temperature-induced phase transitions in dopc and dppc phospholipid bilayers using temperature-controlled scanning force microscopy. *Biophysical Journal*, 86:3783–3793, 2004.
- [233] G. Fragneto, F. Graner, T. Charitat, P. Dubos, and E. Bellet-Amalric. Interaction of the third helix of antennapedia homeodomain with a deposited phospholipid bilayer: A neutron reflectivity structural study. *Langmuir*, 16(10):4581–4588, May 2000.
- [234] P. Quinn and C. Wolf. The liquid-ordered phase in membranes. *Biochimica et Biophysica Acta - Biomembranes*, 1788:33–46, 2008.
- [235] F. L. Leite and O. Mattoso. The atomic force spectroscopy as a tool to investigate surface forces: Basic principles and applications. *Modern Research and Educational Topics in Microscopy*, 1:747–757, 2007.

- [236] M. Radmacher, M. Fritz, J. P. Cleveland, D. A. Walters, and P. K. Hansma. Imaging adhesion forces and elasticity of lysozyme adsorbed on mica with the atomic force microscope. *Langmuir*, 10(10):3809–3814, October 1994.
- [237] Sergi Garcia-Manyes and Fausto Sanz. Nanomechanics of lipid bilayers by force spectroscopy with afm: A perspective. *Biochimica et Biophysica Acta (BBA) - Biomembranes*, 1798(4):741–749, April 2010.
- [238] G. Blume and G. Cevc. Liposomes for the sustained drug release invivo. *Biochimica Et Biophysica Acta*, 1029(1):91–97, November 1990.
- [239] M. Winterhalter, P. M. Frederik, J. J. Vallner, and D. D. Lasic. Stealth(r) liposomes: From theory to product. *Advanced Drug Delivery Reviews*, 24(2-3):165–177, March 1997.
- [240] Akira Harada. Supramolecular assemblies through macromolecular recognition by cyclodextrins. *Supramolecular Science*, 3(1-3):19–23, March 1996.
- [241] Wolfgang H. Binder and Robert Sachsenhofer. Click chemistry in polymer and material science: An update. *Macromolecular Rapid Communications*, 29(12-13):952–981, 2008.
- [242] Takayuki Arai, Masanori Hayashi, Naoto Takagi, and Toshikazu Takata. One-pot synthesis of native and permethylated α -cyclodextrin-containing polyrotaxanes in water. *Macromolecules*, 42(6):1881–1887, 2009.
- [243] M. Tamura and A. Ueno. Energy transfer and guest responsive fluorescence spectra of polyrotaxane consisting of alpha-cyclodextrins bearing naphthyl moieties. *Bulletin of the Chemical Society of Japan*, 73(1):147–154, January 2000.
- [244] Carole Karakasyan, Marie-Claude Millot, and Claire Vidal-Madjar. Immobilization of a (dextran-adamantane-cooh) polymer onto [beta]-cyclodextrin-modified silica. *Journal of Chromatography B*, 808(1):63–67, August 2004.
- [245] D. Harries, D. C. Rau, and V. A. Parsegian. Solutes probe hydration in specific association of cyclodextrin and adamantane. *Journal of the American Chemical Society*, 127(7):2184–2190, February 2005.
- [246] Sophie Beugin, Katarina Edwards, Gï¿½ıran Karlsson, Michel Ollivon, and Sylviane Lesieur. New sterically stabilized vesicles based on nonionic surfactant, cholesterol, and poly(ethylene glycol)-cholesterol conjugates. *Biophysical Journal*, 74(6):3198–3210, June 1998.
- [247] S. Loethen, J. M. Kim, and D. H. Thompson. Biomedical applications of cyclodextrin based polyrotaxanes. *Polymer Reviews*, 47(3):383–418, 2007.
- [248] Kazuko Nakazono, Tomoyuki Takashima, Takayuki Arai, Yasuhito Koyama, and Toshikazu Takata. High-yield one-pot synthesis of permethylated α -cyclodextrin-based polyrotaxane in hydrocarbon solvent through an efficient heterogeneous reaction. *Macromolecules*, 43(2):691–696, January 2010.

- [249] Douglas A. Wicks and Zeno W. Wicks. Blocked isocyanates III: Part A. Mechanisms and chemistry. *Progress in Organic Coatings*, 36(3):148–172, July 1999.
- [250] D. A. Wicks and Z. W. Wicks. Blocked isocyanates III part B: Uses and applications of blocked isocyanates. *Progress In Organic Coatings*, 41(1-3):1–83, March 2001.
- [251] Julien Barrauet, Christine Gaillet, and Jacques Penelle. Easy one-pot synthesis of a reactive hydrogel from commercially available 2-isocyanatoethyl methacrylate and k2s2o5. *Macromol. Rapid Commun.*, 28(20):2007–2011, 2007.
- [252] Julien Barrauet, Romain Molle, Julien Babinot, and Jacques Penelle. Synthesis and characterization of a methacrylic polyelectrolyte capable of reacting with primary amines at room temperature in water. *Polymer*, 50(11):2335–2340, May 2009.
- [253] T. Ooya and N. Yui. Synthesis and characterization of biodegradable polyrotaxane as a novel supramolecular-structured drug carrier. *Journal of Biomaterials Science-polymer Edition*, 8(6):437–455, 1997.
- [254] M. Kunishima, C. Kawachi, J. Morita, K. Terao, F. Iwasaki, and S. Tani. 4-(4,6-dimethoxy-1,3,5-triazin-2-yl)-4-methyl-morpholinium chloride: An efficient condensing agent leading to the formation of amides and esters. *Tetrahedron*, 55(46):13159–13170, November 1999.
- [255] S. Hanessian, A. Benalil, M. Simard, and F. Belangergaripey. Crystal-structures and molecular-conformations of mono-6-azido-6-deoxya-alpha-cyclodextrin and mono-2-o-allyl-alpha-cyclodextrin - the formation of polymeric helical inclusion complexes. *Tetrahedron*, 51(37):10149–10158, September 1995.
- [256] Xin Chen, Tinglu Yang, Sho Kataoka, and Paul S. Cremer. Specific ion effects on interfacial water structure near macromolecules. *Journal of the American Chemical Society*, 129(40):12272–12279, October 2007.
- [257] H. C. Kolb, M. G. Finn, and K. B. Sharpless. Click chemistry: Diverse chemical function from a few good reactions. *Angewandte Chemie-international Edition*, 40(11):2004–2009, 2001.
- [258] C. W. Tornøe, C. Christensen, and M. Meldal. Peptidotriazoles on solid phase: [1,2,3]-triazoles by regiospecific copper(i)-catalyzed 1,3-dipolar cycloadditions of terminal alkynes to azides. *Journal of Organic Chemistry*, 67(9):3057–3064, May 2002.
- [259] Vu Hong, Stanislaw I. Presolski, Celia Ma, and M. G. Finn. Analysis and optimization of copper-catalyzed azide-alkyne cycloaddition for bioconjugation. *Angewandte Chemie International Edition*, 48(52):9879–9883, 2009.
- [260] Vsevolod V. Rostovtsev, Luke G. Green, Valery V. Fokin, and K. Barry Sharpless. A stepwise Huisgen cycloaddition process: Copper(I)-catalyzed regioselective “ligation” of azides and terminal alkynes. *Angewandte Chemie International Edition*, 41(14):2596–2599, 2002.

- [261] Fahmi Himo, Timothy Lovell, Robert Hilgraf, Vsevolod V. Rostovtsev, Louis Noodleman, K. Barry Sharpless, and Valery V. Fokin. Copper(I)-catalyzed synthesis of azoles. DFT study predicts unprecedented reactivity and intermediates. *Journal of the American Chemical Society*, 127(1):210–216, 2005.
- [262] Valentin O. Rodionov, Valery V. Fokin, and M. G. Finn. Mechanism of the ligand-free CuI-catalyzed azide-alkyne cycloaddition reaction. *Angewandte Chemie International Edition*, 44(15):2210–2215, 2005.
- [263] Jennifer L. Brennan, Nikos S. Hatzakis, T. Robert Tshikhudo, Valdemaras Razuamas, Shamkant Patkar, Jesper Vind, Allan Svendsen, Roeland J. M. Nolte, Alan E. Rowan, and Mathias Brust. Bionanoconjugation via click chemistry: the creation of functional hybrids of lipases and gold nanoparticles. *Bioconjugate Chemistry*, 17(6):1373–1375, November 2006.
- [264] Vu Hong, Nicole F. Steinmetz, Marianne Manchester, and M. G. Finn. Labeling live cells by copper-catalyzed alkyne-azide click chemistry. *Bioconjugate Chemistry*, 21(10):1912–1916, October 2010.
- [265] Jiayan Wu, Hongkun He, and Chao Gao. β -cyclodextrin-capped polyrotaxanes: One-pot facile synthesis via click chemistry and use as templates for platinum nanowires. *Macromolecules*, 43(5):2252–2260, March 2010.
- [266] S. Funasaka, K. Koji Kato, and T. Mukaiyama. Highly efficient method for the synthesis of carboxamides from carboxylic acids and amines using benzenesulfonic anhydride (BSA). *Chemistry Letters*, 36:1456–1457, 2007.
- [267] E. S. Kwak and F. A. Gomez. Determination of the binding of beta-cyclodextrin derivatives to adamantane carboxylic acids using capillary electrophoresis. *Chromatographia*, 43(11-12):659–662, December 1996.
- [268] Mohamed Guerrouache, Marie-Claude Millot, and Benjamin Carbonnier. Functionalization of macroporous organic polymer monolith based on succinimide ester reactivity for chiral capillary chromatography: A cyclodextrin click approach. *Macromol. Rapid Commun.*, 30(2):109–113, 2009.
- [269] Enrique Lallana, Eduardo Fernandez-Megia, and Ricardo Riguera. Surpassing the use of copper in the click functionalization of polymeric nanostructures: A strain-promoted approach. *Journal of the American Chemical Society*, 131(16):5748–5750, April 2009.
- [270] P. Shanmugam, M. Damodiran, K. Selvakumar, and P. T. Perumal. Synthesis of functionalized 1,2,3-triazole derivatives of 2-indolones from morita-baylis-hillman adducts of isatin via "click chemistry". *Journal of Heterocyclic Chemistry*, 46(5):919–924, September 2009.
- [271] N. W. Moore and T. L. Kuhl. Bimodal polymer mushrooms: Compressive forces and specificity toward receptor surfaces. *Langmuir*, 22(20):8485–8491, September 2006.

- [272] M. C. Fauré, P. Bassereau, L. T. Lee, A. Menelle, and C. Lheveder. Phase transitions in monolayers of psâŁšpeo copolymer at the airâŁšwater interface. *Macromolecules*, 32(25):8538–8550, December 1999.
- [273] M. M. Lozano and M. L. Longo. Complex formation and other phase transformations mapped in saturated phosphatidylcholine/dspe-peg2000 monolayers. *Soft Matter*, 5(9):1822–1834, 2009.
- [274] M. Winterhalter, H. Bürner, S. Marzinka, R. Benz, and J.J. Kasianowicz. Interaction of poly(ethylene-glycols) with air-water interfaces and lipid monolayers: investigations on surface pressure and surface potential. *Biophysical Journal*, 69(4):1372–1381, October 1995.
- [275] C. Barentin, P. Muller, and J. F. Joanny. Polymer brushes formed by end-capped poly(ethylene oxide) (peo) at the air-water interface rid d-2352-2010. *Macromolecules*, 31(7):2198–2211, April 1998.
- [276] T. Wiesenthal, T. R. Baekmark, and R. Merkel. Direct evidence for a lipid alkyl chain ordering transition in poly(ethylene oxide) lipopolymer monolayers at the air-water interface obtained from infrared reflection absorption spectroscopy. *Langmuir*, 15(20):6837–6844, September 1999.
- [277] C. R. Flach, F. G. Prendergast, and R. Mendelsohn. Infrared reflection-absorption of melittin interaction with phospholipid monolayers at the air/water interface. *Biophysical Journal*, 70(1):539–546, January 1996.
- [278] J. T. Reilly, J. M. Walsh, M. L. Greenfield, and M. D. Donohue. Analysis of FT-IR spectroscopic data - the voigt profile. *Spectrochimica Acta Part A-molecular and Biomolecular Spectroscopy*, 48(10):1459–1479, October 1992.
- [279] E. P. Enriquez and S. Granick. Chain flattening and infrared dichroism of adsorbed poly(ethylene oxide). *Colloids and Surfaces A-physicochemical and Engineering Aspects*, 113(1-2):11–17, August 1996.
- [280] M. Dissanayake and Roger Frech. Infrared spectroscopic study of the phases and phase transitions in poly(ethylene oxide) and poly(ethylene oxide)-lithium trifluoromethanesulfonate complexes. *Macromolecules*, 28(15):5312–5319, July 1995.
- [281] T. R. Baekmark, T. Wiesenthal, P. Kuhn, A. Albersdorfer, O. Nuyken, and R. Merkel. A systematic infrared reflection-absorption spectroscopy and film balance study of the phase behavior of lipopolymer monolayers at the air-water interface. *Langmuir*, 15(10):3616–3626, May 1999.
- [282] Havazelet Bianco-Peled, Yoav Dori, James Schneider, Li-Piin Sung, Sushil Satija, and Matthew Tirrell. Structural study of langmuir monolayers containing lipidated poly(ethylene glycol) and peptides. *Langmuir*, 17(22):6931–6937, October 2001.
- [283] J. Majewski, T. L. Kuhl, M. C. Gerstenberg, J. N. Israelachvili, and G. S. Smith. Structure of phospholipid monolayers containing poly(ethylene glycol) lipids at the

- air-water interface. *The Journal of Physical Chemistry B*, 101(16):3122–3129, April 1997.
- [284] Johan Marra and Jacob Israelachvili. Direct measurements of forces between phosphatidylcholine and phosphatidylethanolamine bilayers in aqueous electrolyte solutions. *Biochemistry*, 24(17):4608–4618, August 1985.
- [285] P. Kékicheff, H.K. Christenson, and B.W. Ninham. Adsorption of cetyltrimethylammonium bromide to mica surfaces below the critical micellar concentration. *Colloids and Surfaces*, 40:31–41, 1989.
- [286] T. Kuhl, Y. Q. Guo, J. L. Alderfer, A. D. Berman, D. Leckband, J. Israelachvili, and S. W. Hui. Direct measurement of polyethylene glycol induced depletion attraction between lipid bilayers. *Langmuir*, 12(12):3003–3014, June 1996.
- [287] S. T. Milner. Compressing polymer brushes - a quantitative comparison of theory and experiment. *Europhysics Letters*, 7(8):695–699, December 1988.
- [288] S. Balko, T. Kuhl, T. Patten, P. Costanzo, T. Kreer, A. Johner, and C. M. Marques. Pinning down the repulsive forces of polymer brushes. *preprint*, 2011. preprint.
- [289] L.H. Sperling. Front matter. In *Introduction to Physical Polymer Science*, pages i–xxx. John Wiley & Sons, Inc., 2005.
- [290] S. T. Milner, T. A. Witten, and M. E. Cates. Theory of the grafted polymer brush. *Macromolecules*, 21(8):2610–2619, August 1988.

Abstract

This work is aimed at the design and characterisation of a new family of tethered ligands, called sliding tethered ligands (STLs). They are based on topological complexes between polymers and amphiphilic cyclodextrins (CDs), which can be inserted into phospholipid membranes. At first we investigate the membrane insertion properties of amphiphilic cholesteryl CD derivatives, which are suitable membrane anchors for the STLs. With the help of neutron reflectivity it can be demonstrated that the CD residues show a remarkable conformational adaptability and that the CD cavities remain accessible upon insertion into lipid model membranes. We have developed a synthetic pathway to assemble the STLs from polyrotaxanes with a controlled low number of mono-modified azido- α -CDs, threaded on a polyethylene glycol (PEG) chain. Using newly developed in-situ capping methods the polyrotaxanes are endcapped with adamantane ligands, which can be recognized by a β -CD receptor. Furthermore a cholesteryl anchor is attached to the threaded CDs in order to enable the STLs to insert into membranes. We demonstrate that STLs readily insert into phospholipid (DPPC) model membranes using IR Absorption Reflection Spectroscopy and investigating the film morphology by Brewster Angle Microscopy and Atomic Force Microscopy. Applying neutron reflectivity it is shown, that for sufficiently high polymer densities the STLs form polymer brushes, which follow the scaling laws predicted by the mean field theory. Using the surface force apparatus it is evidenced that model membranes modified with STLs and cholesteryl β -CD receptors give rise to typical tethered ligand - receptor interaction profiles.

Résumé

Ce travail est destiné à la conception et à la caractérisation d'une nouvelle famille de ligands attachés, appelé "Sliding Tethered Ligands" (STLs). Ils sont à base de complexes topologiques entre des polymères et des cyclodextrines amphiphiles (CD), qui peuvent être insérées dans les membranes phospholipidiques. Au début, nous étudions les propriétés d'insertion membranaire des dérivés de CD amphiphiles modifiées avec du cholestérol, qui sont des ancrs membranaires appropriées pour les STLs. Avec l'aide de la réflectivité de neutrons on peut démontrer que les résidus de CD montrent une remarquable adaptabilité de conformation et que les cavités de CD restent accessibles lors de l'insertion dans des membranes modèles lipidiques. Nous avons développé une voie de synthèse pour assembler le STL à partir des polyrotaxanes avec un très bas nombre contrôlé des CDs mono-modifiées avec un groupe azido, enfilées sur une chaîne de polyéthylène glycol (PEG). En utilisant de nouvelles méthodes in situ les polyrotaxanes sont bouchonnés avec des ligands d'adamantane, qui peuvent être reconnus par des récepteurs de β -CD. Par ailleurs, une ancre membranaire de cholestérol est jointe aux CDs complexées afin de permettre au STLs à s'insérer dans les membranes. Nous démontrons que les STLs sont très bien ancrés dans des membranes modèles phospholipidiques (DPPC). Pour des densités de polymère suffisamment élevées les STLs forment des brosses de polymères qui suivent les lois d'échelle prédite par la théorie du champ moyen. En utilisant une machine de force, nous montrons que des membranes modèles modifiées avec des STLs et des récepteurs de cholestérol β -CD donnent lieu aux profils d'interaction typiques entre des ligands et des récepteurs.